AD-A120 813 PROCEEDINGS OF THE 1982 ARMY SCIENCE CONFERENCE HELD AT 1/6
THE UNITED STATES..(U) DEPUTY CHIEF OF STAFF FOR
RESEARCH DEVELOPMENT AND ACQUISITIO.. 18 JUN 82

UNCLASSIFIED F/G 5/2 NL

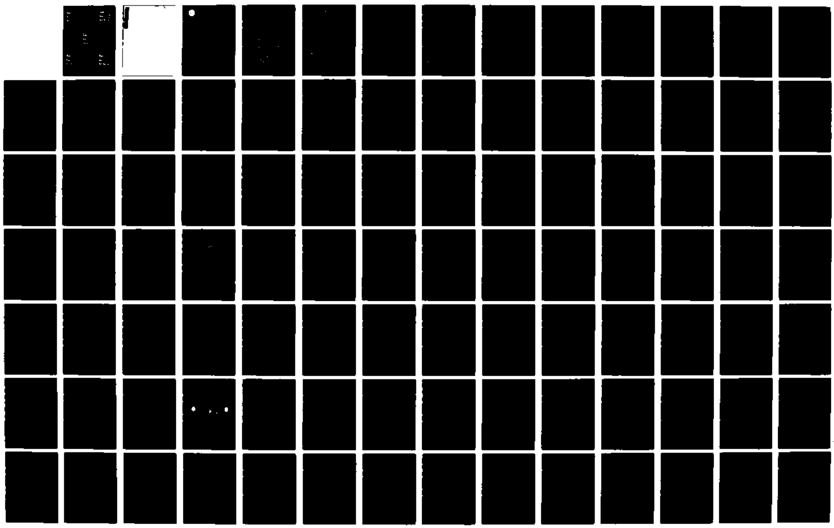

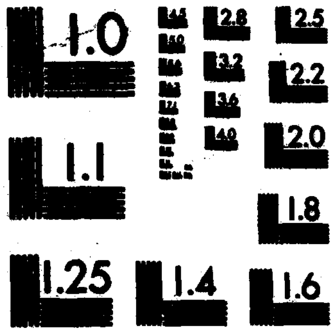

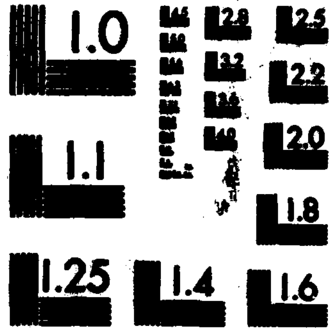

MICROCOPY RESOLUTION TEST CHART
NATIONAL BUREAU OF STANDARDS-1963-A

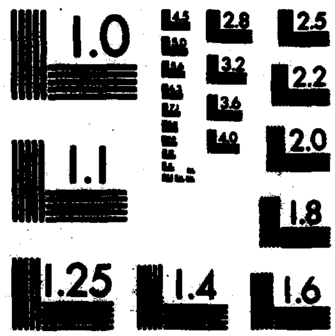

MICROCOPY RESOLUTION TEST CHART
NATIONAL BUREAU OF STANDARDS-1963-A

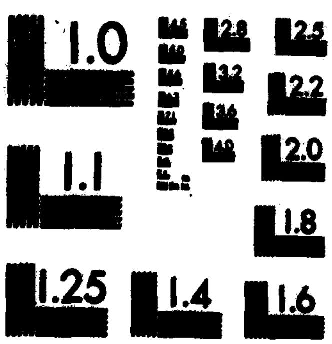

MICROCOPY RESOLUTION TEST CHART
NATIONAL BUREAU OF STANDARDS-1963-A

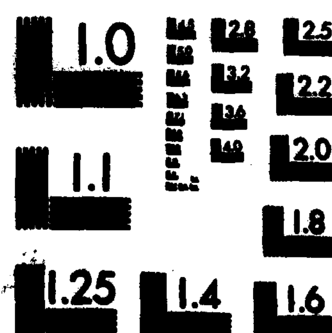

MICROCOPY RESOLUTION TEST CHART
NATIONAL BUREAU OF STANDARDS-1963-A

DEPARTMENT OF THE ARMY
OFFICE OF THE DEPUTY CHIEF OF STAFF
FOR RESEARCH, DEVELOPMENT, AND ACQUISITION
WASHINGTON, D.C. 20310

REPLY TO
ATTENTION OF

DAMA-ARZ-D

18 June 1982

SUBJECT: Proceedings of the 1982 Army Science Conference

SEE DISTRIBUTION

1. The thirteenth in a series of Army Science Conferences was held at the United States Military Academy, 15-18 June 1982. The conference presented a cross section of the many significant scientific and engineering programs carried out by the Department of the Army and provided an opportunity for Department of the Army civilian and military scientists and engineers to present the results of their research and development efforts before a distinguished and critical audience.

2. These Proceedings of the 1982 Army Science Conference are a compilation of all papers presented at the conference and the supplemental papers that were submitted. The Proceedings consist of four volumes, with Volumes I through III unclassified, and Volume IV classified.

3. Our purpose for soliciting these papers was:

a. To stimulate the involvement of scientific and engineering talent within the Department of the Army.

b. To demonstrate Army competence in research and development.

c. To provide a forum wherein Army personnel can demonstrate the full scope and depth of their current projects.

d. To promote the interchange of ideas among members of the Army scientific and engineering community.

4. The information contained in these volumes will be of benefit to those who attended the conference and to others interested in Army research and development. It is requested that these Proceedings be placed in technical libraries where they will be available for reference.

James H Merryman

JAMES H. MERRYMAN
Lieutenant General, GS
Deputy Chief of Staff for Research, Development, and Acquisition

i

DISTRIBUTION:

Office, Under Secretary of Defense for Rsch & Engineering, Wash, DC 20310
HQDA, ODCSRDA, ATTN: DAMA-ARZ-A, Washington, DC 20310
HQDA, ODCSRDA, ATTN: DAMA-ARZ-D, Washington, DC 20310
HQDA, Deputy Chief of Staff for Logistics, Washington, DC 20310
HQDA, Deputy Chief of Staff for Operations, Washington, DC 20310
HQDA, Deputy Chief of Staff for Personnel, Washington, DC 20310
HQDA, Asst Chief of Staff for Automation and Communication, Wash, DC 20310
HQDA, Assistant Chief of Staff for Intelligence, Washington, DC 20310
HQDA, Office of the Chief of Public Affairs, Washington, DC 20310
Office of the Surgeon General, ATTN: DASG-RDZ, Washington, DC 20310
Office, Chief of Engineers, ATTN: DAEN-RDZ-A, Washington, DC 20314
Office, Chief of Engineers, ATTN: DAEN-RDZ-B, Washington, DC 20314
Office, Chief of Engineers, ATTN: DAEN-RDM, Washington, DC 20314

COMMANDERS/DIRECTORS

- US Army Ballistic Missile Defense Systems Command, Huntsville, AL 35807
- US Army Computer Systems Command, Ft. Belvoir, VA 22060
- US Army Concepts Analysis Agency, Bethesda, MD
- US Army Operational Test and Evaluation Agency, Falls Church, VA 22041
- US Army Mat Dev & Readiness Cmd, ATTN: DRCDRA-ST, Alexandria, VA 22333
- US Army Mat Dev & Readiness Cmd, ATTN: DRCLD, Alexandria, VA 22333
  - US Army Armament R&D Cmd, Dover, NJ 07801
    - Ballistic Research Lab, Aberdeen Proving Ground, MD 21005
    - Chemical Systems Lab, Aberdeen Proving Ground, MD 21010
    - Large Caliber Weapons Systems Lab, Dover, NJ 07801
    - Fire Control & Small Caliber Weapons Systems Lab, Dover, NJ 07801
  - US Army Aviation R&D Cmd, St. Louis, MO 63166
    - USARTL, Ames Research Center, Moffett Field, CA 94035
    - USARTL, Aeromechanics Lab, Moffett Field, CA 94035
    - USARTL, Applied Technology Lab, Ft. Eustis, VA 23604
    - USARTL, Propulsion Lab, Cleveland, OH 44135
    - USARTL, Structures Lab, Hampton, VA 22665
    - US Army Avionics R&D Activity, Ft. Monmouth, NJ 07703
    - US Army Aviation Engineering Flight Activity, Edwards AFB, CA 93523
  - US Army Communications & Electronics Cmd, Ft. Monmouth, NJ 07703
    - Center for Communications Systems, Ft. Monmouth, NJ 07703
    - Center for Tactical Computer Systems, Ft. Monmouth, NJ 07703
    - Center for Systems Engineering & Integration, Ft. Monmouth, NJ 07703
  - US Army Electronics R&D Command, Adelphi, MD 20783
    - Atmospheric Sciences Lab, White Sands Missile Range, N 02
    - Combat Surveillance & Target Acquisition Lab, Ft. Monmo 07703
    - Electronics Technology & Devices Lab, Ft. Monmouth, NJ
    - Electronics Warfare Lab, Ft. Monmouth, NJ 07703
    - Ofc of Missile Electronic Warfare, White Sands Missile Range, NM 88002
    - Harry Diamond Laboratories, Adelphi, MD 20783
    - Night Vision & Electro-Optics Lab, Ft. Belvoir, VA 22060
    - Signals Warfare Lab, Vint Hill Farms Station, VA 22186
  - US Army Missile Command, Redstone Arsenal, AL 35898
    - US Army Missile Lab, Redstone Arsenal, AL 35898
  - US Army Mobility Equipment R&D Command, Ft. Belvoir, VA 22060

US Army Natick Laboratories, Natick, MA 01760
US Army Tank-Automotive Command, Warren, MI 48090
Tank-Automotive Systems Lab, Warren, MI 48090
Tank-Automotive Concepts Lab, Warren, MI 48090
US Army Test & Evaluation Command, Aberdeen Proving Ground, MD 21005
US Army Aberdeen Proving Ground, Aberdeen Proving Gnd, MD 21005
US Army Dugway Proving Ground, Dugway, UT 84022
US Army Electronic Proving Ground, Ft. Huachuca, AZ 85613
US Army Tropic Test Center, APO Miami 34004
US Army White Sands Missile Range, White Sands Missile Range, NM 88002
US Army Yuma Proving Ground, Yuma, AZ 85364
US Army Research Office, Research Triangle Park, NC 27709
US Army Materials & Mechanics Research Center, Watertown, MA 02172
US Army Human Engineering Lab, Aberdeen Proving Ground, MD 21005
US Army Mat Systems Analysis Activity, Aberdeen Proving Ground, MD 21005
US Army Foreign Science & Tech Center, Charlottesville, VA 22901
US Army Research, Development & Standardization Group (Europe)
US Army Satellite Communications Agency, ATTN: DRCPM-SC-11, Fort Monmouth, NJ 07703
US Army Training & Doctrine Cmd, ATTN: ATCD, Ft. Monroe, VA 23651
US Army Health Services Command, Ft. Sam Houston, TX 78234
Institute of Surgical Research, Ft. Sam Houston, TX 78234
US Army Medical R&D Command, Fort Detrick, Frederick, MD 21701
Aeromedical Research Lab, Ft. Rucker, AL 36362
Institute of Dental Research, WRAMC, Washington, DC 20012
Letterman Army Inst of Research, Presidio of San Francisco, CA 94129
Medical Bioengineering R&D Lab, Frederick, MD 21701
Medical Rsch Inst of Chemical Defense, Aberdeen Proving Gnd, MD 21010
Medical Rsch Inst of Environmental Medicine, Natick, MA 01760
Medical Rsch Inst of Infectious Diseases, Frederick, MD 21701
Walter Reed Army Inst of Research, Washington, DC 20012
Walter Reed Army Medical Center, Washington, DC
Armed Forces Radiobiology Rsch Inst, Bethesda, MD 20814
US Army Cold Regions Rsch & Eng Lab, Hanover, NH
US Army Construction Eng Rsch Lab, Champaign, IL
US Army Engineer Topographic Labs, Ft. Belvoir, VA 22060
US Army Engineer Waterways Experiment Station, Vicksburg, MS 39180
US Army Rsch Inst for the Behavioral & Social Sciences, Alex, VA 22333
ARI Field Unit, Ft. Benjamin Harrison, IN 46216
ARI Field Unit, Ft. Sill, OK 73503
ARI Field Unit, Presidio of Monterey, CA 93940

COMMANDANTS:
Academy of Health Sciences, ATTN: HSHA-CDM, Ft. Sam Houston, TX 78234
US Army Air Defense School, ATTN: ATSA-CDM-A, Ft. Bliss, TX 79916
US Army Armor Center, ATTN: ATZK-CD-SD, Ft. Knox, KY 40121
US Army Chemical School, ATTN: ATZN-CM-CS, Ft. McClellan, AL 36205
US Army Engineer School, ATTN: ATZA-CD, Ft. Belvoir, VA 22060
US Army Field Artillery School, Ft. Sill, OK 73503
US Army Infantry School, Ft. Benning, GA 31905
US Army Intelligence Center and School, Ft. Huachuca, AZ 85613

•US Army Logistics Center, Ft. Lee, VA 23801
US Army Ordnance Center and School, Aberdeen Proving Gnd, MD 21005
US Army Signal Center, Ft. Gordon, GA 30905
US Army Transportation School, ATTN: ATSP-CD-CS, Ft. Eustis, VA 23604

SUPERINTENDENT:
US Army Military Academy, ATTN: Technical Library, West Point, NY 10996

COPIES FURNISHED:
Defense Advanced Research Projects Agency, Arlington, VA 22209
Defense Technical Information Center, Alexandria, VA 22209
The Army Library, ATTN: ANRAL, Washington, DC
Chief, US Army Field Office, HQ AFSC/SDOA, Andrews AFB, MD 20331
Cdr, HQ Fort Huachuca, ATTN: Tech Reference Div, Ft. Huachuca, AZ 85613
Cdr, 1st COSCOM, HHC/SOTI, Ft. Bragg, NC 28303
Naval Air Systems Command (Code 310-A), Washington, DC 20361
Naval Research Library (Code 2627), Washington, DC 20361
Office of Naval Research (Code 102), Arlington, VA 22217
HQ US Marine Corps (Code RD-1), Washington, DC 20380
Air Force Systems Command, Andrews AFB, Washington, DC 20331
Lawrence Livermore Lab, Univ of California, Livermore, CA 94550
Los Alamos Scientific Lab, Los Alamos, NM 87544
Southwest Research Institute, San Antonio, TX 78228
United Nations Library, New York, NY 10017

PROCEEDINGS

OF THE

1982 ARMY SCIENCE CONFERENCE

UNITED STATES MILITARY ACADEMY

WEST POINT, NEW YORK

15-18 JUNE 1982

VOLUME III

Principal Authors P through Z

TABLE OF CONTENTS

PROCEEDINGS OF THE 1982 ARMY SCIENCE CONFERENCE

Author	Title	Vol	Page
Bingham, Gene J.	The Aerodynamic Influences of Rotor Blade Taper, Twist, Airfoils and Solidity on Hover and Forward Flight Performance	1	99
Binn, Leonard N.	See Lemon, Stanley M.	2	249
Black, Edward D.	See Porter, William L.	3	31
Bloom, Kenneth R.	See Zwick, H.	3	449
Borowick, John Bayha, William Stern, Richard A. Babbitt, Richard W.	Dielectric Waveguide Antenna	1	113
Bowden, Charles M.	MICOM Program in Light Control by Light	1	125
Brandt, W. E.	See Henchal, Erik A.	2	61
Brodman, Bruce W. Devine, Michael P.	Microbial Attack of Nitrocellulose	1	141
Brown, Douglas R.	An Empirical Model for Near Millimeter Wave Snow Extinction and Backscatter	1	147
Buser, R. G.	See Rohde, R. S.	4	177
Bushell, M. Manriquez, R. Merkel, G. Scharf, W. D.	Aurora Flash X-Ray Facility as a Source-Region EMP Simulator	1	159
Campana, Joseph E.	See Friedman, Joseph E.	1	415
Campbell, Donn V.	Control of Parasitic Currents on Radiating Systems	1	175
Campi, Morris	Design of Microstrip Linear Array Antennas by Computer	1	187
Carchedi, Steven	See Groff, John N.	4	97
Caslavsky, Jaroslav L. Viechnicki, Dennis J.	Resolution of Factors Responsible for Difficulty in Growing Single Crystals of YAG	1	201

Author	Title	Vol	Page
McKnight, W. B.	See Barr, Thomas A., Jr.	1	47
Meliza, Larry L.	See Miller, Jack H.	2	75
Melvin, W. S.	See Ayers, O. E.	1	17
Merkel, G.	See Bushell, M.	1	159
Meyers, William E.	See Setterstrom, Jean A.	3	215
Mikesell, Perry Knudson, Gregory B.	Plasmids of Legionella Species	2	385
Miller, Miles C.	Flight Instabilities of Spinning Projectiles Having Non-Rigid Payloads	2	393
Mirabelle, Rosemary	See Groff, John N.	4	97
Morgan, Robert L.	See Johnson, John L.	2	199
Murfree, J. A.	See Ayers, O. E.	1	17
Murphy, Newell R.	Armored Combat Vehicle Technology (ACVT) Program Mobility/Agility Findings	2	409
Nakano, Yoshisuke	See Lunardini, Virgil J.	2	263
Nietubicz, Charles J. Sturek, Walter B. Heavey, Karen R.	Computations of Projectile Magnus Effect at Transonic Velocities	2	425
Nolan, Raymond V.	Explosives Detection Systems Employing Behaviorally Modified Rats as Sensory Elements	2	441
Nomiyama, N. T.	See Rohde, R. S.	4	177
Norton, M. C.	See Rohde, R. S.	4	177
Obert, Launne P.	See Ratches, James A.	4	163
O'Connell, Robert L.	Soviet Land Arms Acquisition Model	4	125
O'Neill, Kevin	See Lunardini, Virgil J.	2	263
Oliphant, Joseph	See Lunardini, Virgil J.	2	263

AEROBIC POWER AND CORONARY RISK FACTORS IN 40 AND OVER AGED MILITARY PERSONNEL (U)

*JOHN F. PATTON, PH.D., JAMES A. VOGEL, PH.D.,
JULIUS BEDYNEK, COL, MC, DONALD ALEXANDER, MAJ, MC,
RONALD ALBRIGHT, CPT, MC

US ARMY RESEARCH INSTITUTE OF ENVIRONMENTAL MEDICINE
NATICK, MA 01760
OFFICE OF THE SURGEON GENERAL, WASHINGTON, DC 20310
DWIGHT D. EISENHOWER ARMY MEDICAL CENTER, FORT GORDON, GA 30905
MARTIN ARMY COMUMUNITY HOSPITAL, FORT BENNING, GA 31905

I. INTRODUCTION

The past few years have seen considerable attention given to the assessment of aerobic fitness and the quantification of aerobic training programs in young (less than 35 years of age) Army personnel (3,15). Physical training and fitness, however, have largely been ignored for the 40 and over age group. Until recently, such personnel for the most part did not have a specific fitness program and were not required to meet any minimum fitness standard. In October 1980, the Chief of Staff, US Army, initiated a new physical training program which emphasizes the development and maintenance of cardiorespiratory fitness through aerobic training for all age groups (17-60 years) on active duty. The goal of this program is for individuals aged 40 and over to achieve sufficient aerobic fitness during a 6-month training period to meet an age-adjusted standard for the two-mile run.

Since potential health risks of both physical training and testing are greater in personnel over the age of forty, the Army physical fitness program includes a mandatory medical and cardiac screen in order to try to predict and prevent untoward cardiovascular events. The screening procedure, which the Surgeon General has proposed to take place at the time of the biannual physical exam for personnel aged 40 and over, consists of a coronary risk factor assessment as developed by the Framingham Heart Study (9).

In order to validate multiple screening procedures to identify latent coronary artery disease in asymptomatic personnel prior to conditioning training, to assess aerobic fitness following 6-months of physical training, and to make projections as to materiel and personnel costs for an Army-wide screening program, a pilot study was conducted on 40 and over aged personnel at Ft. Benning, Georgia. This paper presents data that deals with two of the primary objectives of this study: the assessment of aerobic power and prevalence of coronary risk factors in a 40 and over aged population and, the effectiveness of the Army's new self-administered, unsupervised training program in promoting aerobic fitness.

II. METHODS

The experimental approach used in this study consisted of two testing sessions separated by a six-month training period. For the pre-training phase, 295 aged 40 and over male personnel (age range 40-53) who were available for the full six-months, volunteered to participate from approximately 600 individuals identified in this age group at Ft. Benning, GA. This sample consisted of 173 enlisted (grades E-4 to E-9) and 122 officer (grades 0-3 to 0-7) personnel who represented the typical cross-section of occupations common to any militrary installation.

During the pre-training period all subjects went through multiple, serial screening procedures to determine the prevalence of coronary risk factors and to preclude the presence of any cardiovascular disease prior to undergoing the 6-month training program. The screening included a resting 12-lead electrocardiogram (ECG), resting blood pressure, blood lipid profile to include cholesterol, triglyceride, and high density lipoprotein (HDL) determinations, fasting blood sugar, complete family medical history, smoking history ($\geq$ 10 cigarettes/day), history of medication and drug use, and a comprehensive physical examination performed by a physician to assess cardiovascular signs and symptoms. In addition, all subjects underwent a physician-supervised, multistage, symptom-limited exercise tolerance test using the US Air Force School of Aerospace Medicine (USAFSAM) treadmill protocol (23). This is a modified Balke procedure where the treadmill is set at a fixed speed of 90 m/min at 0% grade. With the speed kept constant, the grade is raised 5% every 3 min without interruption until the subject is unable to continue due to fatigue or exhaustion. To determine an individual's aerobic power, oxygen uptake was measured at each incremented stage in exercise intensity with the highest value achieved being taken as the maximal value. During the third min of each increase in intensity, the subject's expired air was collected through a mouthpiece attached to a low resistance breathing valve and into Douglas bags. An aliquot of expired air was analyzed with an Applied Electrochemistry S-3A oxygen analyzer and a Beckman LB-2 CO_2 analyzer. Expired air volumes were measured with a Collins chain-compensated gasometer. Body weight (kg) and height (cm) were determined and skinfold thickness (mm) measured at the subscapular, triceps, biceps, and suprailiac sites using Harpenden calipers. Age-adjusted regression equations were used to estimate percent body fat (5).

Individuals with abnormal treadmill results and those with normal results but who had abnormal cardiac findings or high risk factor analysis were excluded from the training program. Of the 295 subjects initially screened, 270 were cleared to take part in the Army's new *self-administered, individualized physical training* program (Army FM 21-20 Physical Readiness Training. Final Draft. Sect. IV page 3-1 thru 3-10, 1980). This program consists of a progressive walk/run mode of exercise where subjects enter the program, depending upon their initial level of physical activity, at one of three phases: preparatory, conditioning, or maintenance. Each of these phases consists of a progressive scale as to duration and frequency of exercise. Sedentary individuals enter the program in the preparatory phase while those who have been exercising enter either the conditioning or maintenance phase at an appropriate level.

Each subject was given a written description of the training program and provided guidance in choosing and implementing a regimen to fit his particular needs. A personal physical activity history was taken on each individual before and after the 6-months of training. For the purpose of data analysis, subjects in the pre-training phase were classified into one of the three following groups according to their level of physical activity: inactive, runs zero to 3 mi/wk; moderately active, runs greater than 3 but less than 10 mi/wk; and active, runs more than 10 mi/wk.

For a variety of reasons, e.g. retirements, medical profiles, temporary duty assignments, only 165 of the 270 subjects originally cleared were available for re-testing at the completion of the 6-months training. The efficacy of the training program was determined by repeating the measurement of maximal oxygen uptake using the same procedure as that used during the pre-training phase.

III. RESULTS

The results of this study are presented in two parts: first, a cross-sectional description of aerobic fitness, the prevalence of coronary risk factors and the relationship between fitness and risk factors in the 40 and over sample studied is presented, and secondly, a longitudinal evaluation is made of the effects of the six-month training program in enhancing aerobic fitness.

The mean data for age, anthropometric measures and the physiological responses to exercise for the enlisted and officer personnel and for the total sample studied during the pretraining period are presented in Table 1. No differences were seen in age or any of the anthropometric measures between the enlisted and officer groups. However, the enlisted group had a 9% lower $\dot{V}O_2$ max ($p < .05$) compared to the officers on both an absolute (l/min), and relative basis (ml/kg • min). The mean $\dot{V}O_2$ max of 38.1 ± 6.2 ml/kg • min represents a fairly typical aerobic fitness level for this age group. The range in $\dot{V}O_2$ max from 25.3 to 61.1 ml/kg • min suggests a large variation in fitness for this group. It is felt, therefore, that due to this range and the nature of the subject selection the sample is representative of 40 and over aged personnel throughout the Army.

TABLE 1. Age, anthropometric measures and maximal physiological responses to exercise prior to training (mean ± SD)

	Enlisted (n=168)	Officers (n=102)	Total (n=270)	Range
Age (yrs)	43.4 ± 2.7	44.5 ± 3.3	43.8 ± 3.0	40-53
Height (cm)	83.7 ± 12.7	83.9 ± 10.5	83.7 ± 11.4	56.6-115.7
Weight (kg)	177.7 ± 6.6	180.5 ± 6.7	178.9 ± 6.7	155-196
Body Fat (%)	26.2 ± 4.8	25.9 ± 4.4	26.0 ± 4.6	11.6-36.5
$\dot{V}O_2$ max (l/min)	3.04 ± 0.51	3.35 ± 0.48*	3.16 ± 0.52	1.71-4.58
$\dot{V}O_2$ max (ml/kg · min)	36.7 ± 5.5	40.3 ± 6.5*	38.1 ± 6.2	25.3-61.1
HRmax (BPM)	182 ± 9	181 ± 9	181.6 ± 9.2	157-203
$\dot{V}_E$ max (l/min BTPS)	119 ± 23	130 ± 23	123 ± 24	61-219

*$p < .05$ compared to enlisted

In Table 2 values of $\dot{V}O_2$ max are presented from various studies on healthy males between 40 and 55 years of age. Because of differences in physical activity history among the samples and in the techniques used to elicit $\dot{V}O_2$ max (treadmill vs. cycle ergometer), the results are not directly comparable. However, if one takes into account the lower values obtained using the cycle ergometer, it can be generally stated that a mean $\dot{V}O_2$ max is in the mid to upper 30's in ml/kg • min for this age group.

In Table 3 are presented the mean data and ranges for selected risk factors and the risk factor index calculated using the Framingham equations (9).

The prevalence of coronary risk factors for subjects divided into the two age groups 40-44 (n=196) and 45-53 (n=98) is presented in Table 4. Obesity (> 25% body fat), elevated serum cholesterol (> 200 mg/dl) and cigarette smoking (50% of subjects) appear to be the most predominant risk factors in both age groups. There was no difference between the two groups in the prevalence of obesity as nearly 64% of the individuals in both had body fat contents greater than 25%. Also, the percentage of low aerobically fit subjects ($\dot{V}O_2$ max < 35 ml/kg • min) was not different between the age groups and was 32.7% overall. Significant differences between the two groups were only seen in ECG abnormalities both at rest and after exercise and in the number of subjects with a risk factor index $\geq$ 5%. This latter difference is attributable almost entirely to the age difference of the groups and to the greater number of abnormal resting ECG in the older group since the other variables used to calculate the risk factor index (systolic blood pressure, fasting blood sugar, serum cholesterol, smoking history) were not different between groups.

Data comparing levels of cardiorespiratory fitness with coronary risk factor variables are shown in Table 5. The fitness levels correspond to the following ranges of $\dot{V}O_2$ max in ml/kg • min: very poor, < 30; poor, $\geq$ 30 < 35; fair, $\geq$ 35 < 40; good $\geq$ 40 > 45; excellent, > 45. Only statistically significant values related to the excellent level of fitness are included. Intergroup comparisons showed no significant differences between the good and excellent levels of fitness except for body weight, % body fat, and serum HDL levels. Further analyses demonstrated a significant difference between the very poor and poor categories for fasting blood sugar, body weight and % body fat. The good and fair levels of fitness differed significantly only with respect to the risk factor index and percent smokers. Differences between the poor and fair groups were shown in HDL levels, the cholesterol/HDL ratio and percent smokers. The fair to very poor groups differed significantly in body weight, % body fat, diastolic blood pressure, cholesterol/HDL ratio, fasting blood sugar, percent smokers and risk factor index.

TABLE 2. Comparison of $\dot{V}O_2$ max data from present study with other studies of 40-55 year-old males.

Investigator	Age (yr)	n	Testing Mode*	$\dot{V}O_2$ max (ml/kg • min)
Ribisl (18)	40.2	15	CE	40.1
Saltin et al. (19)	40.5	42	CE	37.5
Wilmore et al. (22)	40.5	16	CE	40.1
Naughton & Nagle (12)	41.0	18	CE	31.3
Hanson et al. (7)	48.9	7	CE	35.8
Pollock et al. (17)	48.9	15	TM	29.9
Froelicher et al. (6)	40 - 44	59	TM	34.0
	45 - 49	68	TM	33.5
	50 - 53	19	TM	34.0
Cumming et al. (2)	40 - 45	22	CE	31.9
	46 - 49	14	CE	30.4
	50 - 55	22	CE	30.0
Present Study	40 - 53	260	TM	38.1

*CE = Cycle Ergometer; TM = Treadmill

TABLE 3. Selected risk factors of subjects during the pretraining period (n=295)

Variable	Mean + SD	Range
Blood Pressure		
Systolic	124 ± 14	100-194
Diastolic	81 ± 9	55-120
Cholesterol (mg/dl)	215 + 38	95-354
HDL (mg/dl)	41.2 + 11.5	13.6-99.2
Chol/HDL	5.5 ± 1.6	1.0-9.9
Triglycerides (mg/dl)	159 ± 112	11-599
Fasting Blood Sugar (mg/dl)	98 ± 20	75-334
Risk Index (%)	3.4 ± 0.2	0.7-16.9

TABLE 4. Prevalence of coronary risk factors by age groups.

	Prevalence (Percent)		
Risk Factors	40-44	45-53	Total
% Body Fat			
> 25 ≤ 30	46.5	46.2	46.4
> 30	17.5	17.2	17.4
$\dot{V}O_2$ max (ml/kg • min)			
≥ 30 ≤ 35	23.5	25.6	24.2
< 30	7.1	11.1	8.5
Blood Pressure			
≥ 140/90 ≤ 160/95	18.0	17.4	17.8
> 160/95	7.2	4.1	6.1
Cholesterol (mg/dl)			
≥ 200 ≤ 250	46.7	37.8	44.0
> 250	14.9	23.5	17.8
Cholesterol/HDL			
≥ 6.0	33.3	32.7	33.1
Fasting Blood Sugar			
≥ 115 mg/dl	7.2	7.1	7.2
Triglycerides			
≥ 150 mg/dl	38.5	46.9	41.3
ECG Abnormalities			
At Rest	13.4	23.5+	16.8
At Exercise	6.6	17.0*	10.1
Cigarette Smoking	51.0	49.0	50.3
Positive Family History	27.6	23.5	26.2
Abnormal Cardiac Exam	38.6	50.5	42.8
Risk Factor Index			
≥ 5%	10.3	32.0**	26.7

+ $p < .05$; *$p < .01$; ** $p < .001$

TABLE 5. Physical fitness levels vs. anthropometric measures and coronary risk factors (Mean ± SD).

	Very Poor (n=22)	Poor (n=59)	Fair (n=86)	Good (n=58)	Excellent (n=32)
Age (yr)	44.5 ± 3.6	43.9 ± 2.7	44.1 ± 2.9	43.8 ± 3.4	42.8 ± 2.1
Hgt (cm)	180.6 ± 5.8	179.5 ± 6.3	178.0 ± 6.5	179.2 ± 7.5	178.4 ± 7.4
Wgt (kg)	95.5 ± 13.7**	85.6 ± 11.3**	83.4 ± 10.5**	82.0 ± 9.2*	76.0 ± 8.2
%BF	31.0 ± 4.4**	26.8 ± 4.2**	26.1 ± 4.2**	24.8 ± 4.4*	22.9 ± 3.9
SBP	129 ± 21*	124 ± 15	125 ± 13*	122 ± 12	119 ± 11
DBP	86 ± 12**	82 ± 8*	81 ± 8*	80 ± 9	77 ± 7
Chol (mg/dl)	222 ± 41*	224 ± 39*	217 ± 35*	205 ± 38	203 ± 37
HDL (mg/dl)	38.1 ± 10.9**	37.7 ± 7.6**	41.8 ± 10.4**	42.6 ± 13.4*	48.1 ± 14.3
CHOL/HDL	6.1 ± 1.8**	6.1 ± 1.5**	5.4 ± 1.5*	5.1 ± 1.6	4.6 ± 1.6
TRIG (mg/dl)	180 ± 109*	172 ± 115*	171 ± 138*	137 ± 76	122 ± 66
FBS (mg/dl)	110 ± 34**	98 ± 10	96 ± 11	94 ± 10	93 ± 8
Smokers (%)	77**	72**	48*	29	22
RF Index (%)	4.7 ± 3.5**	4.0 ± 2.5*	3.4 ± 2.1*	2.6 ± 1.8	2.5 ± 1.6

*p<.05; ** p<.01 when compared to excellent level of physical fitness. SBP -systolic blood pressure; DBP -diastolic blood pressure; CHOL - Cholesterol; TRIG - triglycerides; FBS - fasting blood sugar; RF - risk factor.

In order to quantify any change in aerobic power as a result of participating in the new self-administered, unsupervised training program, subjects were divided into three groups based on their initial level of physical activity as assessed by interview during the pre-training period. These three groups, with the number of subjects shown in parentheses, were as follows: inactive (140), runs zero to 3 mi/wk; moderately active (53), runs more than 3 but less than 10 mi/wk; and active (55), runs 10 or more mi/wk. Twelve individuals indicated that they participated in other activities, i.e., swimming, racquetball, tennis, etc., but they were not included in the activity estimation.

Table 6 presents the mean anthropometric and maximal physiologic data for subjects comprising the three activity groups prior to physical training. No differences were seen in body weight or % body fat among the three groups. $\dot{V}O_2$ max of the active group was 17% and 16% higher ($p < .01$) compared to the inactive group on an absolute (l/min) and relative (ml/kg • min) basis, respectively. The moderately active group also showed a significantly higher $\dot{V}O_2$ max ($p < .01$) compared to the inactive group. The interview procedure used to establish physical activity habits was effective, therefore, in separating individuals into three levels of aerobic fitness.

TABLE 6. Anthropometric and maximal physiological data for subjects grouped by physical activity history prior to training (Mean $\pm$ SD).

	Activity Group Inactive n = 140	Moderately Active n = 53	Active n = 55)
Age (yrs)	43.9 $\pm$ 3.1	43.5 $\pm$ 2.6	43.6 $\pm$ 3.1
Ht (cm)	178.0 $\pm$ 6.6	179.7 $\pm$ 6.9	179.6 $\pm$ 6.9
Wt (kg)	83.9 $\pm$ 12.8	83.2 $\pm$ 10.0	84.4 $\pm$ 11.0
% Body Fat	26.1 $\pm$ 4.7	25.9 $\pm$ 4.9	26.1 $\pm$ 4.1
$\dot{V}O_2$ max (l/min)	2.99 $\pm$ 0.46^{a,b}	3.31 $\pm$ 0.52	3.49 $\pm$ 0.49
$\dot{V}O_2$ max (ml/kg • min)	36.1 $\pm$ 5.3^{a,b}	39.8 $\pm$ 5.4	41.9 $\pm$ 6.7
HR max	182 $\pm$ 10^{b}	183 $\pm$ 9	178 $\pm$ 7
$\dot{V}_E$ max (l/min BTPS)	120 $\pm$ 23^{b}	125 $\pm$ 24	131 $\pm$ 24
Max TM Time (min)	14.6 $\pm$ 2.7^{a,b}	16.0 $\pm$ 2.7	16.8 $\pm$ 2.7

a = significantly different from moderately active group;
b = significantly different from active group. $p < .01$ ANOVA

Data on body composition and maximal responses to exercise determined before and after the 6-months prescribed training program are depicted for the three groups in Table 7. Of the 140 individuals who were initially classified as being inactive, only 78 (56%) were available for retesting. Thirty-four of these subjects indicated during a post-training interview that they had not participated to any significant degree in the program; forty-four subjects indicated that they participated to an extent that would be expected to produce a significant increase in $\dot{V}O_2$ max. There were no changes in body weight or % body fat in either of these subgroups upon retesting after 6 months. With respect to $\dot{V}O_2$ max, only a slight and insignificant increase (4.4%) was seen in those subjects who indicated they had participated in the program. For the moderately active and active groups, 76% (39 of 53) and 80% (44 of 55) of the subjects were retested, respectively. Neither of these groups showed any changes in aerobic power or body composition during the training period.

IV. DISCUSSION

This study represents perhaps the largest assessment of aerobic power using a direct measurement of $\dot{V}O_2$ max that has been performed in a 40 and over aged population. The results suggest that aerobic fitness of US Army personnel in this age group does not differ significantly from civilians of comparable age. This may not be surprising since members of the Army work in occupations similar to those found in the civilian sector of our society.

There have been few studies on other military populations to which the present results can be compared. In a select group of US Military Academy faculty and staff over 35 years of age, Kowal et al. (10) reported a $\dot{V}O_2$ max, using a treadmill protocol, of 41.4 and 50.6 ml/kg • min for low and high activity groups respectively. In USAF aircrewmen of similar age to those of the present study, Froelicher et al. (6) found an average $\dot{V}O_2$ max of 34.0 ml/kg • min using a treadmill protocol. Myles and Allen (11) in a survey of Canadian forces personnel aged 40-55 reported a mean value of 32.4 ml/kg • min using a submaximal predictive cycle ergometer test. If these data are corrected upward, however, by 15% for differences between cycle ergometer and treadmill as suggested by Shepard (20), then the results compare quite closely to the present data. While valid comparisons among studies are difficult due to differences in testing methods used to elicit $\dot{V}O_2$ max and in the physical activity history of the subjects it can generally be stated that a typical $\dot{V}O_2$ max for the 40 and over age group ranges from 35 to 40 ml/kg • min.

The data presented on the prevalence of coronary risk factors in 40 and over aged military personnel showed obesity, elevated blood cholesterol and cigarette smoking to be the most predominant factors. Obesity has been identified as one of the most prevalent health problems at all ages in the United States and has been shown to be a definite risk factor for development of coronary artery disease (8). The 63.8% prevalence of body fat content in excess of 25% (17.4% in excess of

TABLE 7. Anthropometric and maximal physiological data by activity group before and after 6-months training (mean ± SD).

		Activity Group			
		Inactive		Moderately Active	Active
		Nonparticipants	Participants		
		(N = 34)	(N = 44)	(N = 39)	(N = 44)
Weight (kg)	Pre-T*	84.0 ± 11.5	83.8 ± 11.8	84.6 ± 10.6	82.8 ± 11.1
	Post-T	83.4 ± 10.3	83.1 ± 10.9	84.5 ± 9.5	82.5 ± 10.2
% Body Fat	Pre-T	24.9 ± 5.6	26.2 ± 4.4	25.8 ± 4.9	25.7 ± 4.4
	Post-T	25.2 ± 5.0	26.7 ± 4.1	26.0 ± 4.3	26.0 ± 4.2
$\dot{V}O_2$ max(ml/kg•min)	Pre-T	35.9 ± 4.3	36.4 ± 5.5	40.3 ± 5.9	42.6 ± 6.7
	Post-T	36.3 ± 4.3	38.0 ± 5.4	39.8 ± 4.5	42.7 ± 6.3
HRmax (BPM)	Pre-T	179 ± 10	183 ± 11	183 ± 9	179 ± 7
	Post-T	178 ± 12	181 ± 9	180 ± 11	178 ± 9
$\dot{V}_E$ max (l/min BTPS)	Pre-T	125 ± 25	117 ± 22	128 ± 24	131 ± 26
	Post-T	127 ± 27	121 ± 24	130 ± 24	133 ± 28

*Pre-T = pre-training; Post-T = post training

30%) found herein would appear to be rather high. However, similarly high levels of body fat have been reported by others (1,10) for the 40 and over age group.

Plasma cholesterol has been shown to be an important risk factor with evidence suggesting a gradient of risk with increasing levels (8). In the present study, 61.8% of the total sample had serum cholesterol levels greater than 200 mg/dl with 17.8% being greater than 250 mg/dl. In a military population aged 35 and over, Denniston et al. (4) reported incidences of 45% for cholesterol levels greater than 200 mg/dl and 6% for those greater than 250 mg/dl.

Extensive data from several prospective studies have demonstrated a significant relationship between cigareette smoking and coronary artery disease (8). The high prevalence of smokers (50%) found in the present study is similar to that reported for other military populations (4) and represents the most predominant risk factor in this group. While some evidence suggests that cigarette smoking decreases with age (11), the prevalence of smokers did not change with age in the present study. While no conclusions can be drawn from such data, they do emphasize the cardiovascular risk of this factor in the military environment.

A direct inverse relationship between levels of cardiorespiratory fitness and variables related to an increased risk for coronary disease was seen. Since the data are cross-sectional in nature, a cause and effect relationship between physical activity and risk factor values cannot be inferred. However, a substantial difference between high and low levels of aerobic fitness is apparent. While the differences among the intermediate levels of fitness groups are less pronounced, these data strongly support the hypothesis that protection from coronary artery disease appears to be associated with a higher level of fitness (14). Assuming coronary risk factors are related directly to the frequency of coronary disease and that physical activity can affect these factors, then physical activity and thus the level of aerobic fitness may be important in reducing mortality from coronary artery disease. However, only longitudinal studies will show if decreasing the magnitude of these factors has any effect in reducing or delaying the onset of the disease.

A large body of data has accumulated over the past few years concerning the effects of physical training on cardiorespiratory fitness (16). These studies have shown that any improvement in $\dot{V}O_2$ max is directly related to the frequency, intensity, and duration of training. Depending on the quantity and quality of training, such improvement in $\dot{V}O_2$ max has been shown to range from 5% to 25%. Age in itself does not appear to be a deterrent to endurance fitness. Recent studies in subjects 20 to 63 yrs of age have shown that the relative change in $\dot{V}O_2$ max with training in middle-aged and older men is similar to that seen in younger age groups (17,19).

Based upon the available data, therefore, an increase of 10-15% in $\dot{V}O_2$ max could be expected for subjects who take part in aerobic training on a regular basis for 6 months (16). In the program evaluated in the present study, a large number of subjects (44%) who were initially designated as inactive did not participate in the program while those who were originally inactive but did participate showed only a 4.4% increase in $\dot{V}O_2$ max. This insignificant change suggests that these subjects did not train at an appropriate intensity, duration and frequency to stimulate the cardiorespiratory system.

While it is difficult to establish an acc rate "drop-out" rate since many subjects were unavailable for interview at the completion of the study, the percentage of nonparticipants in the inactive group is similar to data from other studies on non-compliance. Oldridge (13), in reviewing a series of studies on the compliance of apparently healthy male subjects, found an overall compliance of approximately 55% in training programs of 6 months or more in duration. While the Army recognizes the need for improved aerobic fitness in its 40 and over aged members, the results of this study suggest that the approach evaluated here to accomplish this end was not satisfactory. According to Wilmore (21), any successful exercise program must accomplish two major goals: (1) teach the participants why they should become physically active, and (2) motivate them to follow through with a training program.

Approximately 46% of the subjects who were initially tested indicated that they participated in their own personal training program. These subjects, who comprised the moderately active and active groups, had a $\dot{V}O_2$ max which can be considered good to excellent for their age (20). It is obvious, however, that much research is needed in the areas of education and motivation to find ways for those less physically fit to comply with self-administered training programs. In the military for the 40 and over aged soldier there is an absence of any occupationally-related requirement for physical fitness as well as a lack of a structured physical training program. These necessitate that participation in physical activity be left to individual initiative. The results of this study show, however, that merely providing subjects with a written program for the development of aerobic fitness, is unsatisfactory. This suggests that to improve participation in physical training in the Army will require an increased emphasis on supervision of the program and methods of positive reinforcement so individuals will maintain motivation and interest.

V. CONCLUSIONS

1. The level of aerobic power as measured by $\dot{V}O_2$ max in 40 and over aged Army personnel was not significantly different from that reported for civilian populations of comparable age.

2. The most prevalent coronary risk factors in the sample studied were obesity (63.8% with body fat content greater than 25%), serum cholesterol (61.8%

with levels greater than 200 mg/dl; 17.8% greater than 250 mg/dl), and smoking history (50.3% smokers).

3. An inverse relationship was found between levels of cardiorespiratory fitness and such coronary risk factors as blood pressure, serum cholesterol, obesity, fasting blood sugar and smoking history.

4. An unsupervised, self-administered, aerobic training program as described herein was ineffective in eliciting a significant improvement in aerobic power.

REFERENCES

1. Cooper, K.H., M.L. Pollock, R.P. Martin, S.R. White, A.C. Linnerud and A. Jackson. Physical fitness levels vs. selected coronary risk factors. A cross-sectional study. JAMA 236:166-169, 1976.

2. Cumming, G.R. and L.M. Borysyk. Criteria for maximum oxygen uptake in men over 40 in a population survey. Med. Sci. Sports 4:18-22, 1972.

3. Daniels, W.L., D.M. Kowal, J.A. Vogel, and R.M. Stauffer. Physiological effects of a military training program on male and female cadets. Aviat. Space Environ. Med. 50:562-566, 1979.

4. Denniston, J.C., R.E. Jackson, W.P. Morgan, M.U. Ramos, J.L. Szurek and J.A. Vogel. A survey of cardiopulmonary health and coronary risk factors in a select military population. Milit. Med. 141:440-444, 1977.

5. Durnin, J.V.G.A., and J. W. Wormsley. Body fat assessed from total body density and its estimation from skinfold thickness; measurements on 481 men and women aged from 16 to 72 years. Brit. J. Nutr. 32:77-92, 1974.

6. Froelicher, V.F., M. Allen and M.C. Lancaster. Maximal treadmill testing of normal USAF aircrewman. Aerospace Med. 45:310-315, 1974.

7. Hanson, J., B. Tabakian, A. Levy, and W. Nedde. Long-term physical training and cardiovascular dynamics in middle-aged men. Circulation 38:783-799, 1968.

8. Kannel, W.B., T.R. Dawber, A. Kagon, N. Revotskie and J. Stokes. Factors of risk in the development of coronary heart disease-six-year followup experience. The Framingham Study. Ann. Intern. Med. 55:33-50, 1961.

9. Kannel, W.B., D. McGee, and T. Gordon. A general cardiovascular risk profile: The Framingham Study. Amer. J. Cardiol. 38:46-51, 1976.

10. Kowal, D.M., J.A. Vogel, J. Paris, and J. Hodgdon. Exercise tolerance, coronary risk factors, and aerobic capacity of older military personnel. The Physician and Sports Medicine. 6:85-90, 1978.

11. Myles, W.S. and C.L. Allen. A survey of aerobic fitness levels in a Canadian military population. Aviat. Space Environ. Med. 50:813-815, 1979.

12. Naughton, J. and F. Nagle. Peak oxygen uptake during physical fitness program for middle-aged men. JAMA 191:103-105, 1965.

13. Oldridge, N.B. Compliance with exercise programs. In: Heart Disease and Rehabilitation. M.L. Pollock and D.H. Schmidt, Eds. Houghton Mifflin, Boston, MA. pp.619-629, 1979.

14. Paffenbarger, R.S. and W.E. Hale. Work activity and coronary heart mortality. New Eng. J. Med. 292:545-550, 1975.

15. Patton, J.F., W.L. Daniels and J.A. Vogel. Aerobic power and body fat of men and women during Army basic training. Aviat. Space Environ. Med. 51:492-496, 1980.

16. Pollock, M.A. The quantification of endurance training Programs. In: Exercise and Sports Sciences Reviews, J.H. Wilmore (Ed.). Academic Press, New York, NY, 1973.

17. Pollock, M.L., H.S. Miller, R. Janeway, A.C. Linnerud, B. Robertson, and R. Valentino. Effects of walking on body composition and cardiovascular function of middle-aged men. J. Applied Physiol. 30:126-130, 1971.

18. Ribisl, P. Effects of training upon the maximal oxygen uptake of middle-aged men. Intern. Z. Angew. Physiol. 27:154-160, 1969.

19. Saltin, B., L. Hartley, A. Kilbom, and A. Astrand. Physical training in sedentary middle-aged and older men. II. Scand. J. Clin. Lab. Invest. 24:323-334, 1969.

20. Shepard, R.J. World standards of cardiorespiratory performances. Arch. Environ. Health. 13:664-672, 1966.

21. Wilmore, J.H. Individual exercise prescription. Amer. J. Cardiology. 33:757-759, 1974.

22. Wilmore, J., J. Royce, R. Girandola, F. Katch, and V. Katch. Physiological alterations resulting from a 10 week program of jogging. Med. Sci. Sports 2:7-14, 1970.

23. Wolthuis, R.A., V. F. Froelicher, J. Rischer, I. Noguera, G. Davis, A.J. Stewart and J.H. Triebwasser. New practical treadmill protocols for clinical use. Amer. J. Cardiology 39:697-700, 1977.

EXPERT'S USE OF INFORMATION: IS IT BIASED?

RUTH H. PHELPS, PhD*
US Army Research Institute for the
Behavioral and Social Sciences
Alexandria, Virginia 22333

The quality of human information processing, judgment and decision making is rapidly becoming a critical concern for the Army due to both the development of increasingly complex weapon systems and availability of large volumes of information provided by automated sensor systems. In order to achieve operational effectiveness, the information processing capabilities of Army personnel must be comensurate with the technological sophistication of new weapon and information systems. Past research has shown, however, that even highly competent technical experts (engineers, physicians, scientists) are limited and often faulty information processors [1, 2, 3, 4, 5, 6, 7, 8]. Apparently these deficiencies are not the result of inadequate training in the specific fields of study, but are due to general limitations in human information processing skills and abilities, such as: inattention to various categories of information; inability to handle multiple sources of information, memory shortfalls; errors in drawing logical conclusions and inferences. Clearly, errors in human information processing can degrade the validity of even the expert's judgment, resulting in poor decisions that cost the Army money, soldier and materiel readiness, as well as operational effectiveness.

The purpose of this paper is to summarize two investigations of the ability of experts to logically utilize two different types of information used for Army decision making: (1) base rate (past frequency of occurrence) and (2) size of data sample (the number of cases on which the information is based). Past research has demonstrated that people in general [6] as well as some types of experts [2, 3, 5, 8] tend to ignore both base rate and sample size information when, in fact, this information is logically pertinent for making a decision or judgment. A few examples of military situations show how such biases would be costly. A strategic analyst predicts the likelihood of a Soviet invasion of Poland based only on the present configuration of troops and materiel, ignoring the past frequency (base rate) of this configuration when there was no invasion. A division commander, ignoring the relative unreliability of the small number of reports (size of data sample), directs an attack on Village A based on a single report indicating enemy location at Village A, while 7 out of 10 reports indicate enemy location at Village B. A systems engineer depends on the results of a single operational test, not realizing the potential unreliability of the results based on such a small sample of data.

Two specific questions about the use of base rate and sample size information by experts are addressed: (1) is the information used at all and (2) if so, how is it used (degree, consistency, pattern, etc.)? While previous research has focused on general analyses of a large number of individuals on a single problem, the methodology used in the present research emphasizes an in-depth study of the information processing for each individual on many problems. While this research used non-military problems, the results will reveal how experts, when required to solve a series of different problems (as in Army decision making), utilize base rate and sample size information. Experiment I investigated expert's use of base rate information, while Experiment II investigated their use of sample size information.[1]

EXPERIMENT I - USE OF BASE RATE INFORMATION

Method

Two groups participated in both Experiments I and II: the Expert Group was comprised of 15 PhD research psychologists having extensive training in statistics and scientific thinking employed by the US Army Research Institute and the Novice Group was comprised of 15 undergraduate students enrolled at the University of Maine. All participants were tested individually; all completed each experiment twice.

1. Details and more extensive interpretation of these two experiments, as well as other related experiments, can be found in "Use of Base Rate and Sample Size Information by Experts and Novices: Is it Biased?" by R. Phelps, J. Fetterman, C. Tolbert and S. Yachanin, obtainable from the author.

Participants were presented with the following story:

"At birth, a large percentage of babies require medical attention for any one of a variety of complications. These complications range in frequency and severity from mild and common problems to rare and serious birth defects. The detectability of these complications varies from those that are easily diagnosed, to those that are extremely difficult to diagnose. Tests can be conducted at birth to determine whether or not a baby has any of these conditions. The tests, however, vary in how well they predict the presence or absence of a given condition in any one baby.

Condition A occurs in approximately 100 of every 1000 births in the United States.

Test X has been developed to detect whether or not a child, at birth, has Condition A. The test is accurate 90% of the time, whether the baby has Condition A or not. That is, when a baby actually has Condition A the test is positive 90% of the time. When a baby does not have Condition A, the test is negative 90% of the time.

Given that the test has indicated that Condition A is present, what are the chances that a baby selected at random from all babies born in this country, in fact has Condition A?"

Two types of numerical information appear in the story: (1) the base-rate for Condition A (100/1000 in this example), and (2) the test accuracy or individuating information (90% in this example). Based on the information in the story, participants were to estimate the chances that a randomly selected baby, in fact, had Condition A.

For each problem the story remained the same but the numerical information varied. Each problem was constructed to conform to a cell in a 4 x 5 factorial design. There were four levels of base rate (.01, .10, .60, .90) and five levels of test accuracy (.01, .10, .50, .65, .90) resulting in 20 problems. There were 14 additional problems having levels different from those in the factorial; 10 of these appeared at the beginning and the remaining four were randomly mixed with the 20 experimental problems. None of these 14 problems were scored and, unknown to the participant, were included as practice and filler problems. Experimental problems appeared in the same random order for all participants. They made their probability estimates on an unmarked scale anchored at the ends by the phrases "absolutely impossible" and "absolutely certain".

Results

Both the relative use of the base rate and accuracy information and the information processing strategy used by each participant were assessed using three analytical measures: analysis of variance (ANOVA), W^2 (relative importance of each type of information) and an analysis of the shape of the plotted interaction of base rate and test accuracy information.

The ANOVA conducted for each participant showed that 26 of the total 30 participants used test accuracy information. However, contrary to previous findings, 26 of the 30 also used base rate information. Three single factor and 3 two factor information processing strategies were defined apriori and are summarized in Table 1. In Figure 1 example plots indicating the 3 different single factor strategies used to combine the base rate and test accuracy information are shown. In Figure 2, two strategies combining both types of information simultaneously (2 factor strategies) are shown; in the third plot (bottom panel) is shown the logically correct strategy. Beneath each plot is indicated the number of Expert and Novices using that strategy.

Four conclusions are drawn from the data contributing to Figures 1 and 2. First, most participants regardless of expertise used base rate information. Second, while all participants adopted very systematic strategies, there were at least 5 different types of strategies. Third, none adopted the logically correct strategy. Fourth, the Experts showed no differences from Novices in either the frequency in using base rate information or in their strategies.

TABLE 1

Definition of Strategies

Single Factor Strategies

1. Test Accuracy - only the test accuracy information is used, the base rate information is ignored as indicated by a main effect for accuracy but not base rate in the ANOVA. As shown in Figure 1, the plot appears as overlapping positively sloped lines.

2. Base Rate - only base rate information is used, as indicated by a significant effect for base rate but not test accuracy in the ANOVA. The plot in Figure 1 of this strategy appears as a set of flat parallel lines.

3. Interactive - only one factor is used at a time: base rates are used when test accuracy is low and accuracy is only used when base rate is low as indicated by significant main effects and interaction. The interaction plots as a converging set of lines.

Two Factor Strategies

1. Linear - both base rate and accuracy are used simultaneously but combined linearly as shown by significant main effects but no interaction The plot appears as parallel, positively sloping lines in Figure 2.

2. Multiplying - both base rate and accuracy are used simultaneously and are combined multiplicatively as shown by significant main effects and interaction. The interaction plots as a diverging fan of lines in Figure 2.

3. Logically Correct Strategy - solutions are calculated according to Bayes' theorem. The Bayesian solution plots as a barrel-shaped function as shown in the bottom panel, Figure 2.

SINGLE FACTOR STRATEGIES

ACCURACY STRATEGY

Experts: 2
Novices: 1

BASE RATE STRATEGY

Experts: 1
Novices: 2

INTERACTIVE STRATEGY

Experts: 5
Novices: 3

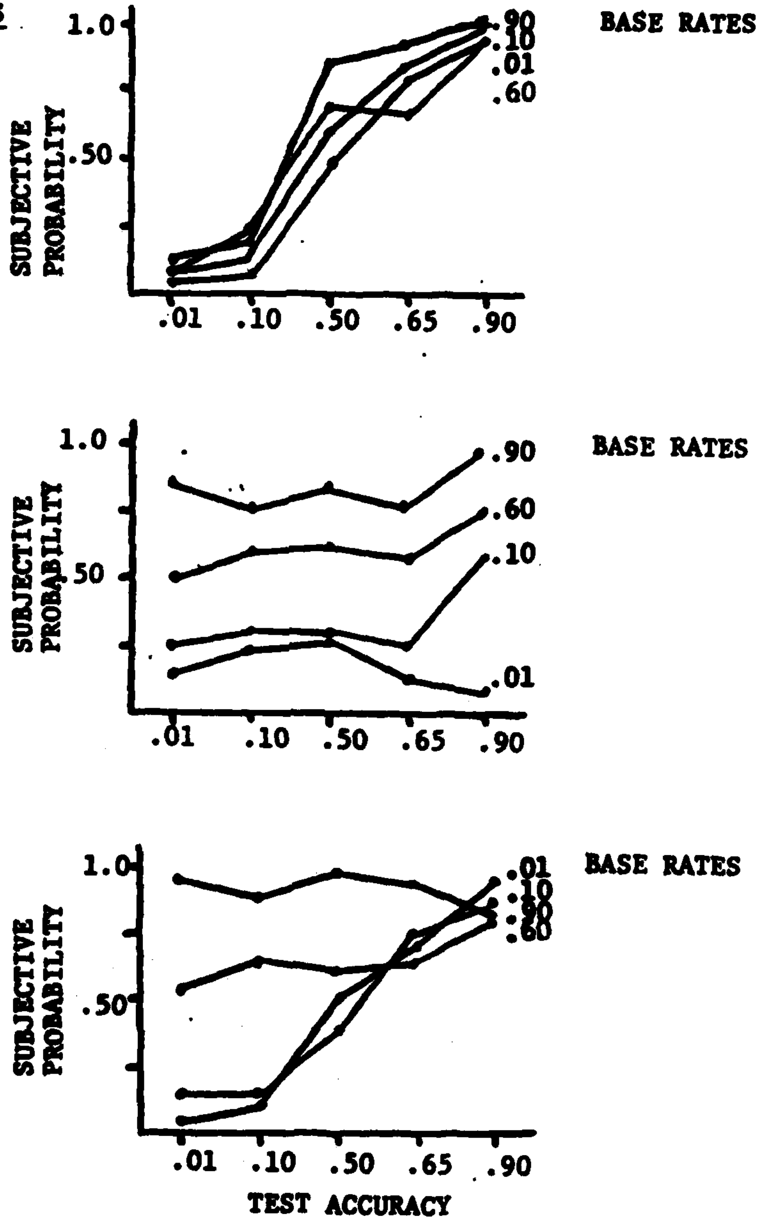

Figure 1. Plots of the Base Rate X Test Accuracy interaction for the three single factor strategies used by individual subjects. Each strategy is il-lustrated by data from a single subject. The number of Experts and Novices using each strategy is listed to the left of each plot.

TWO FACTOR STRATEGIES

LINEAR STRATEGY

Experts: 6
Novices: 7

MULTIPLYING STRATEGY

Experts: 1
Novices: 1

LOGICALLY CORRECT STRATEGY

Experts: 0
Novices: 0

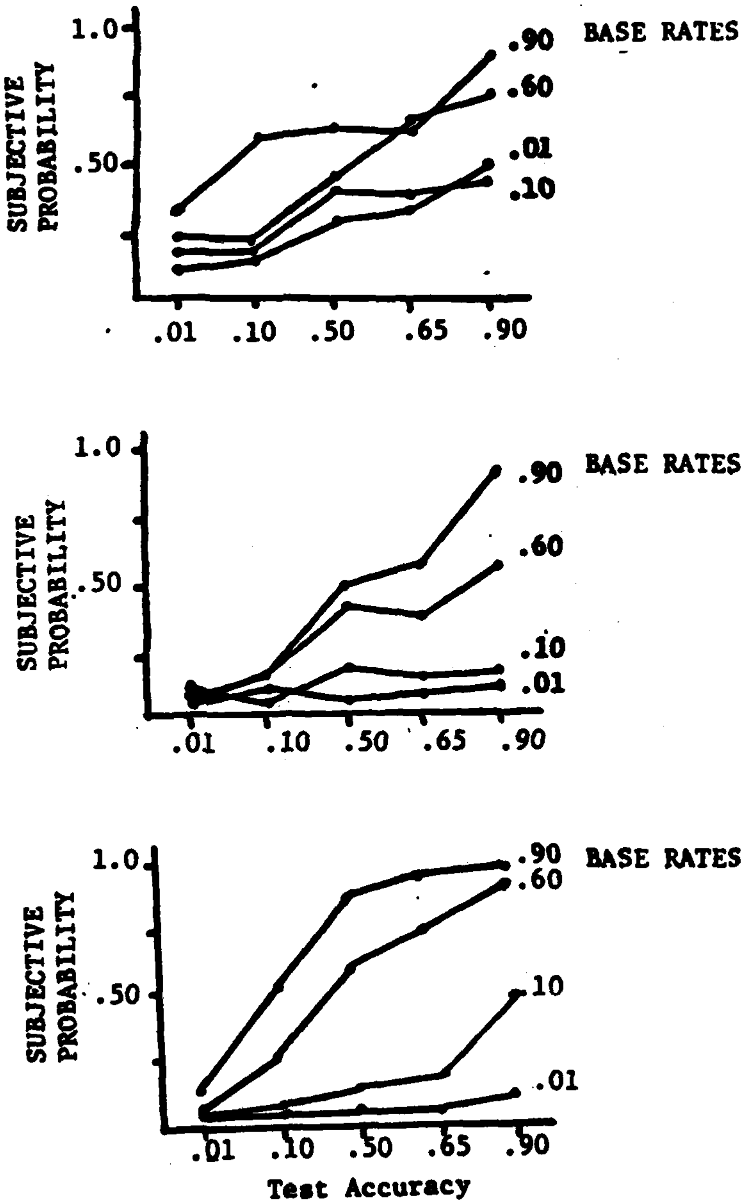

Figure 2. Plots of the Base Rate X Test Accuracy interaction for two factor strategies used by subjects (Top and Center). The bottom plot is the logically correct two factor solution derived from the application of Bayes' Theorem. The number of subjects using each strategy is shown to the left of each plot.

EXPERIMENT II-USE OF SAMPLE SIZE INFORMATION

Method

The same individuals participated in Experiment II as in Experiment I. They were presented with the following story:

> "A polling organization working for Candidate A was directed to estimate, in each of two states, the number of voters who will cast their ballots in favor of Candidate A in the fall election. In a sample of 10 voters from State X, 9 respondents said they would vote for Candidate A in the fall election. In a sample of 100 voters from State Y, 70 said they would vote for Candidate A in the upcoming election."

Two types of numerical information appear in the story: (1) the proportion of people preferring the candidate, and (2) the total number of people polled (sample size) for State X and State Y. The proportion information appeared in the story as the number preferring the candidate out of the total polled in that state (e.g., 90% in State X and 70% in State Y in the example cited above). Based on this information and the story, participants were to predict in which state the candidate had a better chance of winning and how confident they were in their prediction.

The story remained the same for all problems, while the two types of numerical information systematically varied. Each of the 81 test problems was constructed to conform to a cell in a 3x3x3x3 factorial design (4 factors, 3 levels each). The variations in factors and levels were: sample size for State X (levels: 10, 100, 500), sample size for State Y (levels: 10, 100, 500), proportion preferring the candidate in State X (levels: .01, .50, .90) and proportion preferring the candidate in State Y (levels: .01, .50, .90). There were 36 additional problems having levels different from those in the factorial; 20 of these appeared at the beginning and the remaining 16 were randomly mixed with the 81 test problems. None of these 36 problems were scored and unknown to the participants were included as practice and filler problems. Problems appeared in the same random order for all participants. They made their prediction and confidence estimates on an unmarked scale anchored at the endpoints with the phrases "Absolutely certain candidate will win in State X" and "Absolutely certain candidate will win in State Y"; the center point represented complete uncertainty.

Results

The relative utilization of sample size and proportion preferring the candidate as well as the information processing strategy used by each individual were both assessed using three analytical measures: analysis of variance (ANOVA), W^2 (relative importance of the types of information) and an analysis of the shape of the plotted interactions of sample size and proportion information.

In contrast to the results of Experiment I, in Experiment II there were large differences between the Expert and Novice groups in their use of sample size and proportion information. While all 30 participants used proportion information, 60% (9/15) of the Experts but none of the Novices used sample size information, based on the presence of significant effects in the ANOVA and the W^2 analysis. While proportion information was uniformly more important, the sample size information nevertheless reliably accounted for an average of 20% (range: 11%-to 36%) of the systematic variance for these 9 Experts. An examination of the W^2 values for each of the 30 participants shown in Table 2 reveals the large and regular discrepancy in the use of sample size information between the Expert and Novice groups.

All participants in the Novice and 40% of the Expert group used an information processing strategy characterized by a total and exclusive reliance on the subjective difference between the proportions preferring the candidate in State X and State Y. However, 60% of the Experts used a 2-step information processing strategy: first the subjective difference between the proportions for the two states is assessed, then this difference is moderated depending on the size of the samples drawn for State X and State Y. The strategy of this moderation is when either or both of the sample sizes for State X or Y is low, winning in both states is rated equally likely; however, when both sample sizes are 100 or more, judgments are based on the difference between proportions, just as in the proportion strategy. Thus it appears that more than half of the Experts but none of the Novices appreciate that proportions based on small samples are unreliable and are therefore unwilling to assign probabilities much greater than zero.

Table 2

Relative Importance of Sample Size and Proportion Information
(W^2 Values)

	EXPERT		NOVICE	
	Sample Size[a]	Proportion[b]	Sample Size	Proportion
01	.12	.59	0	.83
02	.08	.65	.03	.78
03	.36	.26	0	.69
04	.12	.53	0	1.0
05	.14	.24	.01	.60
06	0	.85	0	.84
07	.01	.81	0	.89
08	.18	.52	0	.83
09	.35	.27	0	.94
10	.02	.94	0	.67
11	.27	.32	.05	.61
12	.05	.31	0	.92
13	.11	.81	0	.97
14	.12	.42	0	.74
15	.04	.64	.08	.53
$\bar{X}$	.25	.53	.01	.79

a. based on the combined W^2 for sample size of State X and State Y

b. based on the W^2 for the Proportion State X and State Y interaction

DISCUSSION AND IMPLICATIONS

These two experiments have shown that when participants are allowed to solve several similar problems only varying in the specific numerical information: (1) both experts and novices use base rate information in contrast to previous reports; (2) there are large systematic differences in the information processing strategies; (3) none, regardless of expertise, used the logically correct information processing strategy for combining the base rate and test accuracy information;(4) only experts (60%) use sample size information, and; (5) even when sample size information is used, the strategy is extremely simplistic, not utilizing the complex implications of small unreliable samples.

Thus, these experiments show that information processing abilities of experts are better than expected for some types of problems and somewhat disappointing for others. However, the use of information is highly individualistic even within the same type of content area experts. Fortunately, the strategies used by both experts and relative novices are highly systematic and therefore amenable to scrutiny, evaluation, simulation and perhaps even modification. The problem is that complete reliance on even experts without some evaluation of the quality of the information processing could have detrimental repercussions.

On the brighter side, there are very constructive uses for the military application of these data and the methodology even though Army problems and personnel were not used in this research. At least three areas of Army concern are apparent: operational decision making, automated systems development, and training. These results as well as this methodology to study information processing could be used on those Army tasks, jobs and MOS's where information processing and integration are most critical. Then within each category of job/task, the requirements for improving the information processing abilities of personnel can be addressed through training, new systems and decision making aids.

By describing and assessing the information processing strategies and relative use of various categories of information, an evaluation of the strengths and weaknesses of Army personnel, systems, and doctrine can be made. And just as in other militarily significant skills (e.g., rifle marksmanship), the information processing skills can be targeted for additional training using the plotted strategies (as in Figures 1 and 2) as feedback to students (see [9] for a summary of the successful use of these techniques in training experts to use relevant and not irrelevant information). In addition new automated systems may either incorporate aids to help users to be logical information processors (see [3] for example of such an aid) or even bypass the user and allow the machine to process the types of information identified as exceptionally difficult for humans [1]. Furthermore automated systems developers should further find these results to be useful in simulating the human information processing component in testing prototype systems: the natural human errors made even by experts can be incorporated into alternative system evaluations. In conclusion, the description of how both experts and non-experts process information has potentially significant payoff for Army training, systems development and operations.

SUMMARY

Two experiments were conducted to compare the use of base rate and sample size information by experts and novices in making predictions about future events. Results showed that even though the majority of experts used both types of information, they used very simplistic information processing strategies. All participants regardless of expertise used highly systematic although individualistic strategies in making their predictions. These results and methodology can be used to assess and improve Army personnel information processing through training and automated systems development.

REFERENCES

1. Adelman, L., Donnell, M., Phelps, R. & Patterson, J. An interactive Bayesian decision aid: Toward improving the user-aid and user-organization interfaces. Manuscript submitted for publication, 1982.

2. Elstein, A., Shulman, L. & Sprafka, S. Medical Problem Solving. Cambridge, MA: Harvard University Press, 1979.

3. Kibler, A., Watson, S. , Kelly, C. & Phelps, R. A prototype decision aid for evaluating alternative courses of action for tactical engagement. (Technical Report Tr-78-A38). Alexandria, VA: US Army Research Institute for the Behavioral and Social Sciences, November 1978.

4. Leaper, D., Horrocks, J., Staniland, J. & deDombal, F. Computer assisted diagnosis of abdominal pain using "estimates" provided by clinicians. British Medical Journal, 1972, 2 350-354.

5. Lusted, L. Introduction to Medical Decision Making. Springfield, IL: Thomas, 1968.

6. Nisbett, R., Borgida, E., Crandall, R. & Reed, H. Popular induction: Information is not always informative, In J.S. Caroll & J. W. Payne (Eds.) Cognition and Social Behavior. Hillsdale, NJ: Lawrence Erlbaum, Assoc., 1976.

7. Nisbett, R. & Ross, L. Human Inference: Strategies and Shortcomings of Social Judgment. Englewood Cliffs, NJ: Prentice-Hall, Inc., 1980.

8. Tversky, A. & Kahneman, D. Judgment under uncertainty: Heuristics and biases. Science, 1974, 185, 1124-1131.

9. Shanteau, J. & Gaeth, G. Training expert decision makers to ignore irrelevant information: A comparison of lecture and interactive training procedures. (Report 81-1). Manhattan, KS: Kansas State University, 1981.

A RATIONALE FOR EVALUATION AND SELECTION OF ANTIOXIDANTS FOR PROTECTION OF RATION ITEMS OF DIFFERENT TYPES U

*DR. WILLIAM L. PORTER, DR. JOHN G. KAPSALIS, MS. ANN MARIE WETHERBY
MS. ANNE M. DROLET, DR. EDWARD D. BLACK
US ARMY NATICK RESEARCH & DEVELOPMENT LABORATORIES
NATICK, MA 01760

1. INTRODUCTION

Rancidity resulting from autoxidation of lipids (oxidation with atmospheric oxygen) in military ration items is a prime cause of rejection. Odor, color, flavor, and texture are degraded. For nearly fifty years scientists have searched for effective antioxidants and means of rating this effectiveness (1-4).

For the first forty years fats and oils were the lipids scrutinized. These are triglycerides of varying composition and are usually an artefact food, being expressed or extracted from plant or animal tissue. Frying oils, salad oils, lard and butter are examples. They have a low surface to volume ratio (LSV) and usually a low water content. Antioxidants were chosen for effectiveness in fats and oils and rated by accelerated shelf life tests using dry bulk fat or oil: the so-called Active Oxygen Method (AOM), Schaal Oven Test, and Oxygen Bomb Test. An antioxidant was considered uniformly good or bad, judged by these tests, with little regard for appropriateness in other lipids.

For the last twenty years, there has been growing attention to the protection of lipids dispersed in processed, whole tissue foods and in combination foods like baked goods, instant foods, and emulsions of the salad oil and whipped topping type. (5-13) This has been hastened by people's desire for quickly prepared convenience foods like TV or airline dinners, largely precooked and predisposed to autoxidation. The first oxidizing lipids in these foods are often polar lipids, like the phosphatides of membranes, or alternatively, highly emulsified triglycerides as in baked goods or whipped toppings. There is a characteristic high surface-to-volume ratio (HSV) and a preponderance of water as the continuous phase. The prevailing use of polyunsaturated triglycerides in these systems favors autoxidation. Chemically, the previous concentration on bulk systems, supposedly mixed and homogeneous, has given way to an interest in high surface systems, biphasic in nature with water or air as the continuous phase. Appropriate tests for antioxidants here are emulsions or dry high surface area systems. We have found that antioxidants can no longer be considered as uniformly effective, but vary in effectiveness, depending on the food situation.

Thus people's current desires for pre-processed convenience foods have changed the practices of antioxidant use and forced a hard look at new chemical principles supporting these practices. From an empirical, state-of-the-art method of choice, this laboratory has developed a broad scientific rationale for choice of appropriate antioxidants. This paper concerns that rationale, which, it should be noted, concerns only primary antioxidants, i.e., those that function by electron or hydrogen donation to interrupt free radical chains.

2. CHEMISTRY AND TYPES OF ANTIOXIDANTS

2.1 Chemistry of Autoxidation. Characteristic of the early years and the preoccupation with supposedly mobile, mixed and homogeneous lipid systems was the confident application of classical kinetic methods. Even oxidizing bulk oils are not now considered so homogeneous because of the importance of surface oxidation. Classical kinetics is even more suspect when applied to complicated whole food systems, where concentration is ill-defined because of anchoring of components and the preponderance of surfaces. However, certain model reactions must occur in any autoxidizing system and in its antioxidant termination. A few of the most important reactions and their relative rates are shown in Figures 1, 2, and 3 (12). The first, non-free radical step (Fig.1) is considered to be the addition of singlet oxygen (often generated by a photosensitizing catalyst like traces of chlorophyll or heme). This produces hydroperoxide, which may then be reductively split by trace metal as in Reaction 2 (5). Reaction 3 produces alkyl radical from activated methylene groups in unsaturated fatty acids. The well-known chain reactions of Figure 2 propagate the reaction. Radicals from ineffective antioxidants (not well stabilized by steric or resonance means) can cause chain transfer as in Reaction 3. Termination occurs by electron or hydrogen donation as in Figure 3, where AH is a well-stabilized antioxidant and BH is less so. A type of regenerative synergism is shown in Reaction 3, typical of the interaction between water-soluble reductones like ascorbic acid and more lipophilic primary antioxidants like the tocopherols or 3-t-butyl hydroxyanisole (BHA, Fig.4).

Stabilization of the antioxidant free radical resulting from the termination step is critical and may be accomplished both by steric hindrance and resonance as in the monohydric (and lipophilic) antioxidants like BHA or 3,5-di-t-butyl hydroxy toluene (BHT) (Fig. 4), or predominantly by mesomeric resonance in the free radical, as for t-butyl hydroquinone (TBHQ) or propyl gallate (PG) (Fig. 4). The main resonance forms are shown in Figure 5 for hydroquinone.

2.2 Types of primary antioxidants. Figure 4 illustrates the major four FDA-permitted synthetic antioxidants. BHA and BHT are monohydric phenols, TBHQ is dihydric, and PG is trihydric. Lipophilia, as measured by oil-water partition coefficient, generally decreases to the right in the figure

REACTION	REMARKS
-CH=CH-CH$_2$-CH=CH-CH$_2$- + SINGLET OXYGEN → -CH=CH-CH$_2$-CH(OOH)-CH=CH-	NON FREE RADICAL
ROOH + M^{n+} → RO· + OH^- + M^{n+1}	LARGE FOR Fe^{++}, Cu^{++}, Co^{++}
RO· + RH → ROH + R·	LARGE

Figure 1. Important reactions in initiation of surface autoxidation. Modified from Ref. 12

R· + O_2 → ROO·	VERY LARGE
ROO· + RH → ROOH + R·	INTERMEDIATE
A· + RH ⇌ AH + R·	CHAIN TRANSFER - RATE VERY SMALL FOR MOST HINDERED ANTIOXIDANTS

Figure 2. Important reactions in propagation. Modified from Ref. 12

ROO· + AH ⇌ ROOH + A·	LARGE - HINDERED OR POLYHYDRIC ANTIOXIDANT
ROO· + BH → ROOH + B·	LARGER - UNHINDERED MONOHYDRIC ANTIOXIDANT
AH + B· ⇌ A· + BH	PRIMARY SYNERGISM - RATE SMALL

Figure 3. Important reactions in termination by antioxidants Modified from Ref. 12

BHA BHT TBHQ PROPYL GALLATE

Figure 4. The major synthetic antioxidants in common food use. Ref. 24

although BHT is slightly more lipophilic than BHA. Both BHA and BHT are largely non-polar and are practically insoluble in water, while PG partitions about evenly between water and triglyceride (Table 1) (12). None of these have notable surface activity or amphiphilia, although TBHQ and PG have somewhat separated lipophilic and hydrophilic moieties.

Figure 6 illustrates the generic dihydric and trihydric phenols, whose substituted derivatives form the vast majority of antioxidant compounds found in nature. In particular, the ortho dihydric structure of catechol is found in the ubiquitous caffeic acid of coffee and oats, and the trihydric pyrogallol structure in gallic acid of tannins. The hydroquinone moiety occurs in flavonoids. All of these structures tend to be polar and hydrophilic, particularly as the salts of phenolic acids or the glycosides of flavonoids. Figure 7 shows some natural monohydric phenols which are antioxidants, like the abundant tocopherols. The three shown are volatile and highly flavored or pungent, but are very effective antioxidants in appropriate situations. Except for the tocopherols, lipophilic antioxidants are much less common than hydrophiles in nature, and often are volatile flavorants.

2.3 Solubility and surface activity. Substantial lipophilia can be conferred on any polar antioxidant moiety by the addition of a lipophilic side chain group, whether naturally occurring or synthetic. The long chain alkyl gallates are an example (Table 2) (25), lipophilia increasing exponentially with each added methylene or congener group. In addition, the molecules so formed possess amphiphilia, or surface energy, since they possess a pronounced polar moiety separated from a non-polar one. One measure of this tendency is the so-called "Hydrophilic-Lipophilic Balance" number, used in detergent formulation(14). In a surface active molecule, a large HLB number connotes greater water solubility and a tendency to form oil-in-water emulsions. Conversely, a low HLB number is associated with greater lipophilia. Although low HLB is associated with lipophilia in surface active compounds, the higher molecular weights preclude the volatility one might expect.

3. AUTOXIDATION AND ANTIOXIDANTS IN LOW SURFACE TO VOLUME RATIO (LSV) LIPID EXPOSURES

As was noted above, the autoxidation and antioxidant protection of bulk fats and oils was largely the target of the first forty years of effort. These are characterized by LSV exposure, by non-polar lipids, and a dry, non-polar environment. The compounds are triglycerides, which are often less polyunsaturated and oxidation prone than polar phosphatides. Above their melting point, which is the case in the typical antioxidant test for dry oils, they are mobile, mixed, and homogeneous on a macro scale. Such a test is the AOM (Active Oxygen Method), where air is bubbled through the oil at 100 C until peroxide value 70 is reached. For this situation we have found that, paradoxically, other things being equal, antioxidants of greater hydrophilia or ampiphiles of higher HLB are more effective than the lipophiles like BHA, BHT, and the tocopherols.

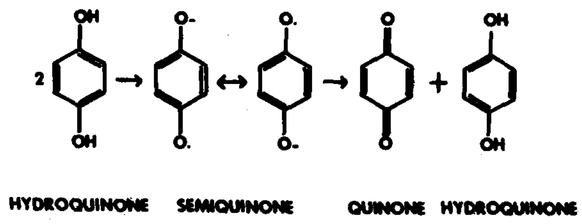

Figure 5. Semiquinone stabilization and dismutation
Ref. 24

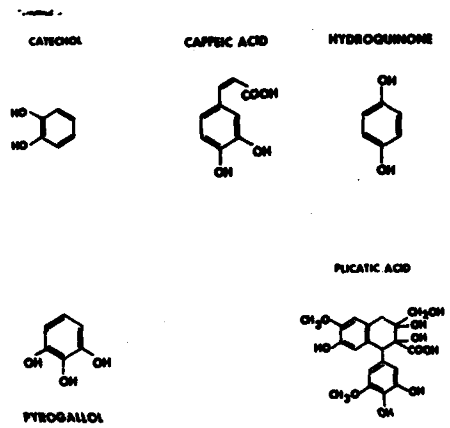

Figure 6. Dihydric and trihydric phenols.
Ref. 24

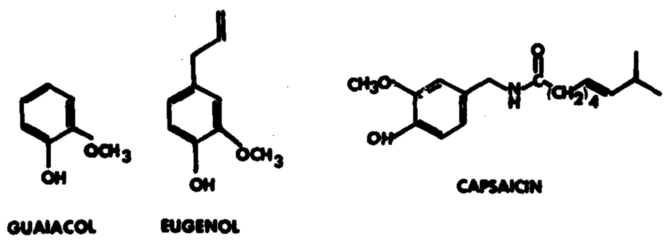

Figure 7. Volatile monohydric phenols.
Ref. 24

TABLE 1. Solubility of Antioxidants[a]

Solvent	BHT	BHA	TBHQ	PG
Water	Insol.	Insol.	<1	<1
Glycerol	Insol.	1	ca. 5	25
Propylene Glycol	Insol.	70	30	55
Methyl Linoleate	V. Sol.	V. Sol.	>10	1
Corn Oil	40	30	10	Insol.
Lard	50	40	5	1

[a]Ref. 12

TABLE 2. Butteroil/Water Partition Coefficient of Antioxidant at 40°C[a]

Antioxidant	Water	Milk Salt Solution
Ethyl Gallate	0.24	-
Propyl Gallate	1.33	0.84
Isopropyl Gallate	0.64	-
Butyl Gallate	5.8	3.9
Amyl Gallate	18.5	9.5
Hexyl Gallate	71.0	44.8
Nordihydroguaiaretic Acid	21.7	21.4
Butylated Hydroxyanisole	834	825

[a]Ref. 25

TABLE 3. Effect of Increasing Alkyl Chain Length on Antioxidant Activity of Substituted Hydroquinones[a]

Antioxidant (0.05 Wt % in Safflower Oil)	Oil Life (Time to PV 70)[b] AOM at 210°F Hours	Oil Life (Time to PV 70)[b] Storage at 110°F Days
None (Control)	9	21
Hydroquinone	39	191
Methylhydroquinone	69	330
Pentylhydroquinone	50	203
Octylhydroquinone	46	208
Dodecylhydroquinone	34	162

[a]Ref. 26

[b]Meq. peroxide/kg oil

Evidence for this "polar paradox" comes from tests of several homologous series of increasingly alkylated phenols. Innate potency of a given phenolic moiety results from a complicated balance of low reduction potential (hydrogen-donating tendency), high rate and low activation energy for the termination reaction (Fig. 2), and low chain transfer rate (steric hindrance and mesomeric resonance of the alkoxide free radical), among other factors. A homologous series with the same antioxidant moiety normalizes these effects and permits comparison of the effect of lipophilia or amphiphilia alone on effectiveness.

The lipophilic monohydric phenols like BHA, BHT, and 6-ethoxy-1,2-dihydro-2,2,4-trimethylquinoline (SANTOQUIN™) show very little to no activity in vegetable oils in AOM tests. The writer knows of no homologous series with these monohydric moieties. For the very active dihydric alkylated hydroquinone series, Table 3 (26) shows the relative effectiveness in AOM tests on safflower oil. Strictly speaking, hydroquinone itself is not a homologue, but in the remainder of the series, as lipophilia increases, activity declines with increasing chain length on a weight basis and remains virtually constant on a molar equivalent basis. It seems noteworthy also that hydroxyhydroquinone--again, not a strict member of this series, although exceedingly polar and water soluble--is the most effective of all hydroquinones tested in the AOM (89 hours).

Similar results for the ortho trihydric gallates are shown in Table 4 (26,27), where the low HLB dodecyl gallate has virtually no effect on induction period. Again, gallic acid is not a strict homologue of the rest of the series, but it is the most polar and water soluble and the most effective antioxidant in these dry oils. 1-galloyl glycerol, an even more highly polar compound, is even more effective in the AOM (15). Table 2 shows the oil/water partition ratios of these gallates and BHA.

Table 5 (28) shows similar partial homologous series for the ortho dihydric caffeic acid and for the mono-methoxylated analogue, ferulic acid. The same trend is evident, this time in oat oil. Several other series show similar trends. There are few exceptions to the rule that in dry vegetable oils and lard, the most polar member of a homologous series is the most effective antioxidant on a weight basis. Even on a molar equivalency basis, alkylation and lipophilia confer no advantage in this very non-polar exposure. In animal lard, the monohydrics BHA, BHT, and tocopherol show substantial activity in the AOM test, but the more polar dihydric and trihydric phenols remain superior (16).

4. HIGH SURFACE TO VOLUME LIPID EXPOSURES: EMULSIONS, MEMBRANES, DEHYDRATED FOODS

It was first noticed by Chipault (17) and by Uri(18,5) that antioxidants behave differently in emulsions than in dry oils. We at Natick Laboratories became interested in autoxidation in high surface situations in the early Sixties because of the large use of freeze-dried foods in stored military rations. Like several other workers(19-22) we have moved from carefully controlled simple model systems (linoleic acid in monolayer on

TABLE 4. Effect of Increasing Length of Alkyl Chain on Antioxidant Activity of Gallic Acid Esters

Antioxidant Treatment of Oil (% by Wt)	AOM Stability of Vegetable Oil (Hours to PV 70)					
	Cotton Seed[a]			Safflower[b]		
	Wt %	AOM	Control	Wt %	AOM	Control
Gallic Acid	-	-	-	0.05	27	9
Propyl Gallate	0.01	19	9	0.05	24	9
Hexyl Gallate	-	-	-	0.05	22	9
Octyl Gallate	0.01	11	8	-	-	-
Dodecyl Gallate	0.01	10	8	-	-	-

[a]Ref. 27

[b]Ref. 26

TABLE 5. Effect of Increasing Length of Alkyl Chain on Antioxidant Activity of Esters of Caffeic and Ferulic Acid[a]

Antioxidant (1 mg/100 mg oil)	Antioxidant Activity Oat Oil - Increase in Induction Period (Hrs/@100°C)
Control	(2)[b]
Caffeic Acid	90
Ethyl Caffeate	49
Dodecyl Caffeate	29
Hexacosyl Caffeate	29
Ferulic Acid	14
Hexacosyl Ferulate	2
Propyl Gallate	60

[a]Ref. 28

[b]Control shows actual induction period, not increase.

TABLE 6. Relative Effectiveness of Antioxidants in RBC Ghosts Perfusion Uptake Method - More Effective Compounds[a]

Compound	Mean Relative Effectiveness (REFF)	Mean Deviation[b]
Octadecyl Gallate	134	± 8
Topanol 354[c]	19	0.1
	60<REFF<90[e]	Indefinite
Phytyl Gallate	20<REFF<55[e]	Indefinite[d]
	53	5
BHA	15	1.1
	10	1.2
TBHQ	4.4	0.3
	5.0	0.2
α-Tocopherol	3.6	0.8
	4.7	1.2

[a]Ref. 24, 30

[b]Where N = 2, except as shown. Means and deviations are for two separate experiments per compound.

[c]3,5-di-t-butyl-4-hydroxy anisole.

[d]N = 4.

[e]Induction period ended during interruption in readings.

silica gel) through more advanced systems (freeze-dried red blood cell ghosts and lecithin liposomes) to more realistic situations (freeze-dried carrots). From this work, we have found that antioxidants differ greatly in effectiveness in high surface situations from their performance in dry oils. Indeed, paradoxically, in this more polar exposure, non-polar lipophiles like BHA, BHT, and Santoquin or low HLB amphiphiles are favored. Thus, the higher alkyl homologues in a series outperform the more polar lower members in protection of emulsions and membranes.

Antioxidant tests for this HSV exposure include oxygen uptake from freeze-dried or organic solvent-freed systems deposited on supports of high specific area like silica, carboxymethylcellulose, or microcrystalline cellulose. Emulsion tests may be monitored by spectrophotometry, polarography, or fluorescent detection of malonaldehyde. The systems are often characterized by a large excess of the continous phase, water, or the air space remaining after dehydration or organic solvent removal.

4.1 Linoleic Acid Monolayers on Silica. Our first work employed monolayers (Langmuir equivalent) of linoleic acid deposited under equilibrium conditions from petroleum ether solution, the excess of which was removed by decantation and a final dry nitrogen stream. Oxidation was conducted at 80°C in glass vessels closed with a rubber serum bottle stopper permitting headspace gas sampling. Oxygen content was determined on a gas partitioner. Under these conditions, pure linoleic acid autoxidizes in an apparent first order manner with no induction period, (29,32) unlike its behavior in low surface situations. Antioxidants pre-deposited on the activated silica from alcohol produce an induction period (time to an arbitrary oxygen uptake) and relative effectiveness (REFF) can be stated as

$$REFF = \frac{I_a}{I_c} - 1$$

where I_a = time to stated oxygen uptake with antioxidant

I_c = time without antioxidant

Figure 8 shows the apparent kinetics of oxygen uptake and the large relative effectiveness of BHA in contrast to the more polar caffeic acid and propyl gallate.

4.2 Red blood cell ghosts. We moved next to hemoglobin-free red blood cell ghosts, produced by the Dodge, Mitchell, Hanahan (23) method at pH7.4 in phosphate buffer. Ghosts are freeze-dried and for an antioxidant test are rehydrated by shaking for one hour at 20°C at 1 mg/ml in 20 mM phosphate buffer, pH 7.4, with or without antioxidants introduced from alcohol at 0.025 mg/ml final concentration in the buffer. The ghosts are centrifuged and washed in de-ionized water. Cobalt chloride is added at 0.3mg/ml and the suspension is freeze-dried. Oxygen uptake is studied by gas partition chromatography, and the results analyzed as in paragraph 4.1, above. Ghosts without cobalt are very refractory to autoxidation, but the reductive activation of peroxide by this metal promotes autoxidation strongly in these dry systems.

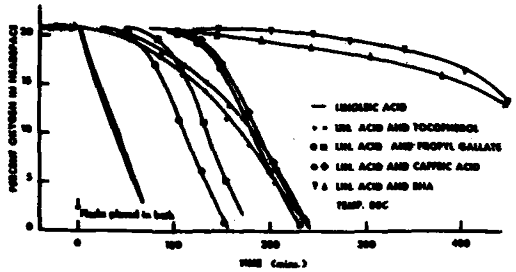

Figure 8. Effect of antioxidants on oxygen uptake of linoleic acid monolayers adsorbed on silica gel. Ref. 29.

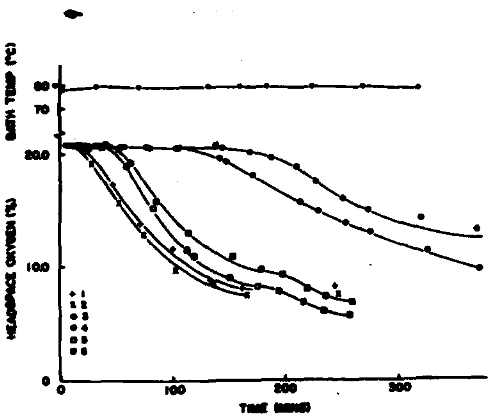

Figure 9. Effect of antioxidants on autoxidation of cobalt-activated freeze-dried red blood cell ghosts. (1,2) control; (3,4) BHA; (5,6) PG. Ref. 30.

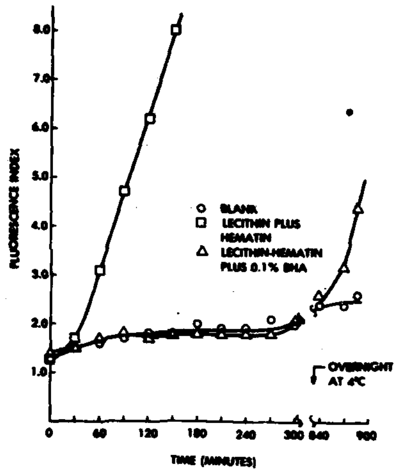

Figure 10. Antioxidant evaluation by oxidative polyamide fluorescence from soy lecithin liposomes. Ref. 31.

The superiority of BHA over propyl gallate in HSV systems is again demonstrated in Figure 9 for red blood cell ghosts. Low HLB amphiphiles are even more effective than the lipophiles BHA and Topanol 354 in this system, which is a realistic model of many whole food lipid and protein membranes. Table 6 shows this superiority and that of phytyl gallate, the phytol ester of gallic acid, synthesized by us specifically for membrane antioxidant effectiveness (24,30).

In both the silica monolayer and ghost systems, the quite volatile BHT is low in apparent effectiveness, but vapor phase uptake tests show that where it is retained in a closed system and not lost by sublimation, it is highly effective in both ghosts and freeze-dried carrots.

4.3 Lecithin liposomes. As a plant membrane model analogous to red blood cell ghosts, we have prepared sonicated soybean lecithin microdispersions and tested antioxidant activity in hematin-catalyzed samples at 65°C, monitoring autoxidation by solid sample measurement of the fluorescent compound formed between malonaldehyde (a breakdown product of peroxidized lipids) and polyamide powder.

We have used a sonicated aqueous dispersion (3 mg/ml) of either crude soybean lecithin (35% acetone solubles, largely triglyceride) or acetone-extracted soybean lecithin (3-5% acetone solubles). pH is 5.5 in 0.013M phosphate buffer. Sonication is done in a salt-ice cooled bath under a stream of dry nitrogen for a maximum of 20 minutes. Antioxidant in ethanol is added at 0.1% by weight of the dispersed lipid. The dispersions are then bubbled with glass-filtered air for thirty minutes. Hematin is added at zero time to give a final phosphatide-hematin ratio of 100/1. Twenty-five ml of the dispersion is placed in a covered Petri dish with a 2x3 cm strip of polyamide-coated plastic taped to the cover, powder side facing the solution. The dishes are placed in a 65°C draft oven and sampled at 30 minute intervals by removing the tape and reading the fluorescence in a solid sample attachment for a spectrofluorometer. Malonaldehyde arising from the oxidizing system forms an intense fluorescent amino-imino-propene compound with the amine end groups of the polyamide powder. Excitation wavelength is 360 nm and emission 425 nm. A 390 nm filter is used. A blank plate produces a characteristic diffraction pattern of bands in addition to the residual of the scattered excitation wavelength at 360 nm. The 360 scatter peak is used as an internal reference and fluorescence intensity is expressed as

$$\text{Fluorescence Index (F.I.)} = \frac{I_{430}}{I_{360}}$$

where I_{430} = intensity at 430 nm

I_{360} = intensity at 360 nm

F. I. values for both blank and sample are plotted on the same graph and their difference (ΔF.I.) is an integrative measure of malonaldehyde produced. Kinetics of fluorescence development are similar to those found with other indices (oxygen consumption, absorption at 233 nm, etc.) as are the effects of pro-and antioxidants. Analysis of relative effectiveness is similar to that in paragraph 4.1.

Figure 10 shows the time course of fluorescence development in an antioxidant-protected and a control sample. The control shows a short induction period attributable to the residual natural antioxidants in the soybean lecithin. In this case, BHA produces a very long period with virtually no fluorescence development.

Relative effectiveness of the most effective antioxidants in the lecithin microdispersion system is shown in Table 7 (31). Table 8 (31) displays the least effective compounds. Plainly, in this very polar system with a large preponderance of water (the dispersed lipid is only 0.3% of the continuous buffer phase) the lipophiles and the low HLB amphiphiles are much more effective than the more polar and hydrophilic phenolic acids, flavonoids and hydroquinone.

The lecithin dispersion has a net anionic charge, like most natural membranes. In addition, the phenolic acids are largely ionized at ph 5.5, and would be repelled by the micelles. However, this does not explain the low activity of hydroquinone, TBHQ, quercetin and methyl gallate, each of which is highly effective in dry oil tests.

5. THE POLAR PARADOX

The preceding results can be summed up in a rationale known as the "Polar Paradox". This states that, other things being equal, more polar and/or hydrophilic antioxidants and amphiphilic antioxidants of high HLB will be more effective in dry oils of low surface-to-volume ratio (LSV) and non-polar lipophilic antioxidants or amphiphiles of low HLB will be relatively more effective in dispersed phases of high surface-to-volume ratio (HSV), like emulsions, and the membranes of whole tissue foods, whether hydrated or dehydrated.

Obviously, this is a broad generalization, and it will be modified in the individual case by particulars of molecular structure, membrane or micelle affinity, susceptibility to loss or degradation during introduction, processing or storage (the low "carry-through" of the gallates in baking due to heat and alkalinity), and by mechanical barriers to introduction in real foods. However, the trend is unmistakable and to the writer at the present time, it is the most effective rationalization of the seemingly endless particulars of state-of-the-art antioxidant use.

Figure 11 (31) summarizes graphically the contrasting results of existing AOM tests and the lecithin microdispersion tests reported here for sixteen common synthetic and natural antioxidants.

In both LSV and HSV situations, it appears that autoxidation occurs largely at surfaces. Antioxidants of equal innate potency will differ in relative effectiveness to the degree that they reach and remain at that surface.

6. APPLICATIONS OF THE RATIONALE AT NATICK LABORATORIES

We have used the rationale in choice of appropriate antioxidants for two types of whole tissue foods; restructured meats and freeze-dried carrots.

6.1 Restructured meats. For reasons of economy and portion control, at Natick, less than prime meat parts are formed into thin flakes by a centrifugal flaking machine, mixed with salt and sodium tripolyphosphate to promote myosin exudation, then frozen, compressed into "logs", and sliced into restructured "steaks" for frozen packaged storage. The flaking, like grinding of ground beef, promotes autoxidation of membrane phospholipids through release of ferrous iron from the myoglobin, and the increase of air-exposed surface. Since this is an HSV situation, BHA or BHT are expected to be very effective in prevention of the so-called "warmed-over" flavor, and such was found to be the case.

6.2 Autoxidation of freeze-dried carrots. Because of the very great increase of gas-lipid interface occasioned by the freeze-drying process and the much longer storage periods which the spoilage-free freeze-dried foods can permit, autoxidation with attendant off odors (violet from β-ionone), texture changes, and decolorization occur rather rapidly if a completely anaerobic atmosphere is not maintained. Antioxidants can be introduced by a vapor-flush technique (24), and as expected in an HSV situation, lipophiles, in this case volatile ones like BHT or eugenol are very effective for the "once-open", vapor-tight package situation.

7. SUMMARY

Selection of appropriate antioxidants for lipid-containing ration items has hitherto been largely empirical. We have developed a broad, scientifically based rationale for this purpose and are currently putting it into practice. The rule states that, other things being equal, antioxidant applications are of two general types: (1) Dry, bulk oils and fats of the cooking and salad types, whether at storage or cooking temperature, having a low ratio of surface to volume. These are best protected by polar or hydrophilic antioxidants. (2) Emulsions and membranes, with a preponderant water or gas phase and a high surface-to-volume ratio. These are best protected by lipophilic, non-polar, or amphiphilic antioxidants with a low hydrophilic-lipophilic balance number (HLB).

Application of the above rationale to model systems and natural membranes (lecithin liposomes and red blood cells) allowed us to predict its applicability to restructured meat and freeze-dried carrots.

8. ACKNOWLEDGMENTS

The authors are indebted to Drs. Derek Ball, David Alabran, and J. Walter Giffee for valuable technical and editorial review. Thanks are also extended to Ms. Armande Arcand for careful preparation of the manuscript and final copy, and to Ms. Edna Albert for expert editorial review.

REFERENCES CITED

1. Olcott, H. S., J. Amer. Chem. Soc. (1934) 56, 2492.
2. Moore, R. N., Bickford, W. G., J. Amer. Oil Chem. Soc. (1952) 29, 1.
3. Everson, C. W., Miller, G. J., Quackenbush, F. W., J. Amer. Oil Chem. Soc. (1957) 34, 81.
4. Uri, N., "Antioxidants in Foods," Lea, C. H., Ed., p.722 Chem. and Ind., London, 1957.
5. Uri, N., "Autoxidation and Antioxidants," Vol. I, Sundberg, W. O., Ed., p. 133, Interscience Publishers, N.Y., 1961.
6. Chipault, J. R., "Autoxidation and Antioxidants," Vol. II Lundberg, W. O., Ed., p.477, Interscience Publishers, N.Y., 1962.
7. Schultz, H. W., Day, E. A., Sinnhuber, R. O., "Lipids and Their Oxidation," Schultz, H. W., Day, E. A., Sinnhuber, R. O., Eds., Symposium on Foods, Oregon State Univ., Avi Pub. Co., Inc., 1961.
8. Emanuel, N. M., Lyaskovskaya, Y. N., "The Inhibition of Fat Oxidation Processes," Pergamon Press, N.Y. 1965.
9. Scott, G., "Atmospheric Oxidation and Antioxidants," Elsevier Publishing Co., N.Y. 1965.
10. Stuckey, B., "Handbook of Food Additives," Furia, T., Ed., p. 209, Chem. Rubber Co., Cleveland, OH, 1968.
11. Labuza, T. P., "Kinetics of Lipid Oxidation in Foods," CRC Critical Reviews in Food Technology (1971) 2, 355.
12. Ragnarsson, J. O., "Accelerated Temperature Shelf Life Testing of Antioxidants in Dehydrated and Intermediate Moisture Systems," Ph.D Thesis, Univ. of Minn., 1976, Univ. Microfilms International, Ann Arbor, MI, 1977.
13. Ragnarsson, J. O., Labuza, T. P., Food Chem. (1977) 2, 291.
14. Adamson, A. W., "Physical Chemistry of Surfaces," 2d Ed., p. 520, Interscience Publishers, N.Y., 1967.
15. Takasagao, M., Horikawa, K., Masuyama, S., Yukagaku (1976) 25, 16.
16. Berner, D. L., Conte, J. A., Jacobson, G. A., J. Amer. Oil Chem. Soc. (1974) 51, 292.
17. Chipault, J. R., Mizuno, G. R., Lundberg, W. O., Food Technol. (1956) 10, 209.
18. Uri, N., "The Mechanism of the Oxidation of Linoleic Acid With Particular Reference to Metal Catalysis," IV Intern. Conf. on the Biochem. Problems of Lipids, Butterworths Sci. Publications, London, 1958.
19. Bishov, S. J., Henick, A. S., J. Food Sci. (1975) 40, 345.
20. Karel, M., Tannenbaum, S. R., Wallace, D. H., Maloney, H., J. Food Sci., (1966) 31, 892.
21. Labuza, T. P., Maloney, J. F., Karel, M., J. Food Sci. (1966) 31, 885.
22. Ragnarsson, J. O., Leick, D., Labuza, T. P., J. Food Sci. (1977) 42, 1536.
23. Dodge, J. T., Mitchell, C., Hanahan, D. J., Arch. Biochem. Biophys. (1963) 100, 119.

24. Porter, W. L., "Recent Trends in Food Applications of Antioxidants," Simic, M. G. and Karel, M., Eds., p. 295, Plenum Press, N.Y., 1980.
25. Cornell, D. G., Devilbiss, E. D., Pallansch, M. J., J. Dairy Sci. (1970) 53, 529.
26. Thompson, J. W., Sherwin, E. R., J. Amer. Oil Chem. Soc. (1966) 43, 683.
27. Sherwin, E. R., J. Amer. Oil Chem. Soc. (1976) 53, 430.
28. Daniels, D. G. H., Martin, H. F., J. Sci. Fd. and Agri. (1967) 18, 589.
29. Porter, W. L., Levasseur, L. A., Henick, A. S., J. Food Sci. (1977) 42, 1533.
30. Porter, W. L., Henick, A. S., Murphy, F., Colgan, R., Porfert, G., Lipids (1978) 13, 137.
31. Porter, W. L., Black, E. D., Drolet, A., Abstract No. 2, Division of Agricultural and Food Chemistry, 182d Ann. Meeting of Amer. Chem. Soc., N.Y., Aug. 1981.
32. Mead, J. F., Wu, G.-S., "Lipids," Paoletti, R., Porcellati, G., Jacini, G., Eds., p. 197, Raven Press, N.Y., 1976.

TABLE 7. Relative Effectiveness of Most Effective Antioxidants in Soy Lecithin Liposomes[a]

Compound	Mean[b]	Standard Deviation	Coef. of Variation
BHA	32	± 7.8	0.24
BHT	21	8.1	0.39
Ethoxyquin (San)	13	5.6	0.43
Propyl Gallate	11	3.8	0.35
Octyl Gallate	11	7.9	0.72
Dodecyl Gallate	10	6.0	0.60
Topanol	10	6.3	0.63
Ethyl Gallate	7	5.8	0.78

[a]Ref. 31

[b]Highest three values.

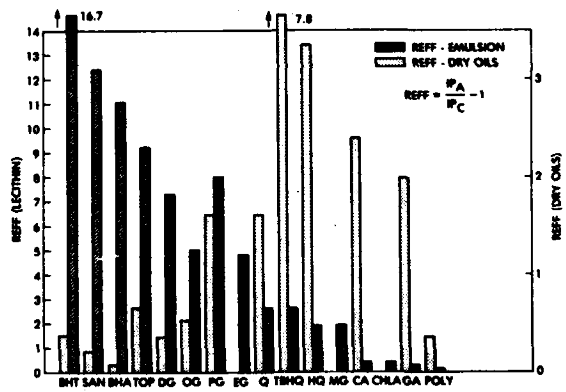

Figure 11. Relative effectiveness (REFF) of antioxidants in soy lecithin emulsions and dry vegetable oils. Ref. 31.

TABLE 8. Relative Effectiveness of Least Effective Antioxidants in Soy Lecithin Liposomes[a]

Compound	Mean[b]	Standard Deviation	Coef. of Variation
TBHQ.	4.9	± 4.4	0.90
Quercetin	4.1	1.7	0.41
Methyl Gallate	3.2	0.4	0.13
Hydroquinone	3.2	0.9	0.28
Gallic Acid	1.4	0.3	0.21
Caffeic Acid	1.4	0.2	0.14
Chlorogenic Acid	1.4	0.2	0.14
Poly AO™79	1.1	0.2	0.18

[a]Ref. 31

[b]Highest three values

HUMAN ENGINEERING LABORATORY AVIATION SUPPLY CLASS III/V MATERIEL (HELAVS III/V) FIELD TEST

ALAN M. POSTON
*PAUL F. GARRETT, JR., CPT
WILLIAM B. DeBELLIS
HARRY J. REED
JOHN M. GARINTHER
US ARMY HUMAN ENGINEERING LABORATORY
ABERDEEN PROVING GROUND, MD 21005

INTRODUCTION

In order to maintain aviation assets at a maximum capability, it is imperative that aircraft returning from missions be returned to their "mission ready" status as soon as possible. One aspect of this issue is the ability to rearm and refuel those returning aircraft. This issue is currently addressed by the concept of Forward Arming and Refueling Points (FARPs). FARPs, which will be established close to the forward line of troops or battle area, will preclude the need for aircraft to travel to rearward areas for this purpose, hence saving valuable mission time.

To this end, the US Army Human Engineering Laboratory (HEL) has embarked upon developing a data base related to the personnel and equipment issues in supplying and loading fuel and ordnance onto helicopters in forward areas. Efforts in this project were initiated in 1977 with background studies on FARP methodology and operation. Contact has been established and maintained with the Directorate for Combat Developments, US Army Aviation Center, Fort Rucker, Alabama, on the operation of aviation Class III/V materiel distribution. A coordination meeting was held to exchange information and ascertain priorities on developing data for aviation Class III/V materiel. As a result of this meeting, it was determined that loading of fuel and ordnance on gunships was the highest priority. Data on the refueling and rearming of the AH-64 is of particular importance since very little information is available in this area. Results of this field experiment will help establish a data base and provide inputs to field studies currently under consideration.

OBJECTIVES

The experimental objective was to obtain human performance data on helicopter refueling and rearming procedures. The data consisted of time measurements while refueling the helicopter and rearming the HELLFIRE missiles and 2.75-inch rockets. The experiment addressed the effects of crew size, day/night operations, and chemical/biological protective equipment on the refueling and rearming operations.

A second objective was to develop test methodologies which could be applied to the Aviation Performance Assessment in a Chemical Environment (APACHE) field study.

An additional objective was to evaluate the Division '86 Table of Organization and Equipment (TOE) staffing levels related to FARP operations. This data will assist the US Army Training and Doctrine Command in developing realistic TOEs for future attack helicopter units.

METHODOLOGY

Subjects

Participants in the experiment were male soldiers from the Materiel Testing Directorate, US Army Aberdeen Proving Ground. The military occupational specialties (MOSs) of those personnel differ from those found in the field performing FARP refueling and rearming operations. In order to alleviate this difference, each subject received extensive training in the specific duties to be performed during the evaluation.

Experimental Design

The experimental design was a completely random factorial (pqr) design with the dependent variable being task time. The three- and five-man crews were composed of randomly assigned individuals. The eight experimental conditions were as shown in Table 1. There were twelve trials for each of the eight experimental conditions. The order of presentation of each of the conditions was established through the use of a table of random numbers.

TABLE 1. Experimental Conditions.

3-Man Day CB	3-Man Day No CB	3-Man Night CB	3-Man Night No CB
5-Man Day CB	5-Man Day No CB	5-Man Night CB	5-Man Night No CB

PROCEDURES

Subject Training

Subjects were required to perform each specific task assigned until asymptotic efficiency was achieved as measured by the time to complete each task. The training required to reach the asympotic level is shown below in the order administered:

A. Day, No CB - Twenty-four runs
B. Day, Full CB Eight runs
C. Night, No CB - Ten runs
D. Night, Full CB - Eight runs

Training runs were conducted with three-man and five-man crews. The need for detail such as removal of 2.75-inch rocket shorting clips, proper handling of missiles, and safety checks was emphasized.

Initial Conditions/Assumptions

A. The following assumptions were made concerning ammunition:

1. HELLFIRE missiles are in closed but unlatched containers.
2. 2.75-inch rockets are in 19-unit containers or stacked on the ground.
3. Returning aircraft require full armament loads.
4. There are no malfunctioning missiles or rockets; i.e., rockets or missiles do not have to be off-loaded.

B. The following assumptions were made concerning refueling and grounding:

1. The Forward Area Refueling Equipment (FARE) systems are mounted on 5-ton trucks.
2. At least four full-fuel bladders containing JP-4 fuel are available.
3. Attack helicopters require 1500 lbs of fuel per mission at 6.56 lbs/gal.
4. All grounds are established; i.e., conductive.
5. Sufficient grounding rods and wire are within the unit.

C. The following assumptions were made concerning materiel and Class V loading:

1. Adequate Class III/V materiel and sufficient materiel handling equipment (MHE) are available.
2. Class III/V materiel will be positioned near the aircraft.
3. The five-man crew loading procedure would be to load all missiles first and then the rockets to preserve mission readiness.
4. The three-man crew loading procedure would be to load the left side armament first, the missiles next, and then the rockets to preclude interference with the fueler.
5. The HELLFIRE missiles are loaded in the sequence (upper inboard, lower inboard, lower outboard, upper outboard) per draft TM 9-1427-475-23.

D. The following assumptions were made concerning personnel:

1. The refueler is a 76W; the rearmers are 68Js and/or 68Ms.
2. Personnel perform only those tasks specified by their MOS.
3. Personnel from the three-man or five-man crews will not undertake supervisory or battle damage assessment tasks.

E. Additional assumptions:

1. The FARP is laid out before the arrival of five attack and three scout helicopters.
2. There is sufficient maneuver space within the FARP.
3. CB gear is sufficient for the threat.
4. No hardware flaws occur.
5. No maintenance is to be performed.
6. Night lighting (chemical wands) would be sufficient.

RESULTS AND DISCUSSION

Results

All data runs, both day and night, were recorded on cinema film at four frames per second. The specific task times were obtained by evaluation of those films after all trials were completed. In addition, overall trial times were obtained through the use of handheld digital timers.

By summing the mean percent change in time for each condition (dependent variable), the mean change in task time is obtained. The following general conclusions can be derived:

A. There was a 44-percent reduction in task time when a crew of five performed the rearming and refueling task as opposed to a crew of three.

B. There was an 11-percent increase in task time when the crew wore CB protective gear.

C. There was a 38-percent increase in task time when the rearming and refueling task was performed at night.

These effects were statistically significant at the 0.01 confidence level.

Table 2 shows the individual ordnance loading times. These times do not include any of the subsystem checks and related tasks and represent the time spent handling and loading munitions.

The greatest effect on the task times is the result of increasing the crew size to five people. However, across all conditions, the task times were affected more by having to perform tasks at night than by having the crew wear CB protective clothing. Significant interactions were evident, but they did not alter the conclusions drawn from the experiment.

DISCUSSION

Analysis of the data in Table 2 indicates that the mean time to load the left- and right-wing stores differs. The exact reason for this difference is not readily apparent but may be due to a number of reasons, including how the rockets were positioned, the type of missile shipping containers used to hold the missiles, and the presence of the 30mm loading equipment.

TABLE 2
Individual Ordnance Loading Times by Sides (Minutes)

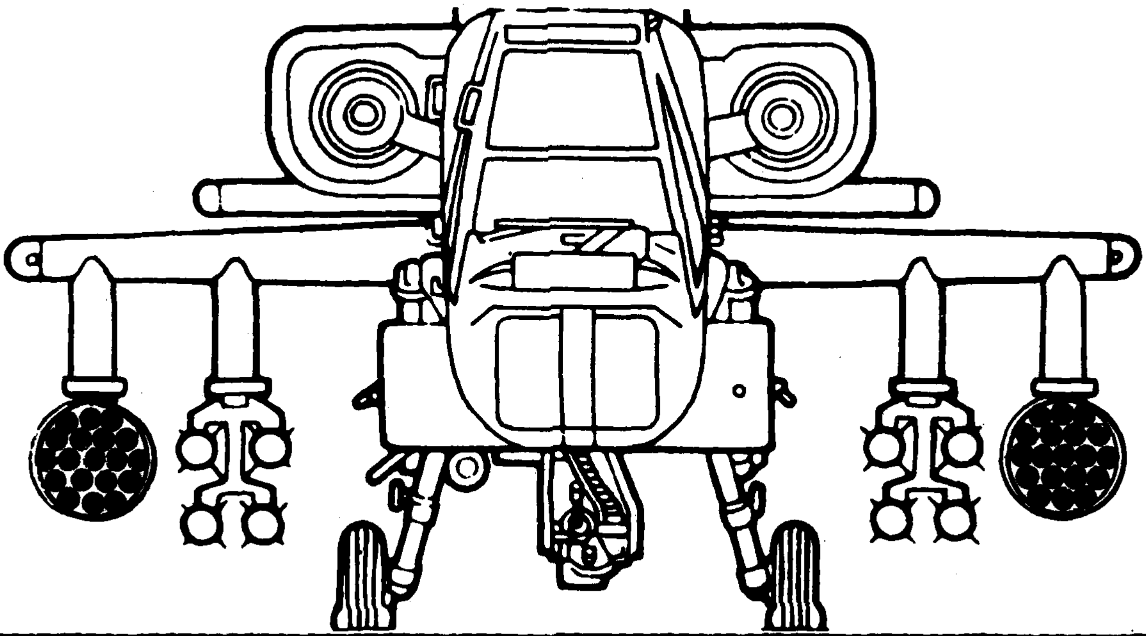

Right			Left	
Rockets	Missiles	Conditions	Missiles	Rockets
		Three-Man Crew		
2.38	2.11	Day without CB gear	2.11	2.30
2.76	2.40	Day with CB gear	2.65	2.76
3.24	2.91	Night without CB gear	3.49	3.12
3.42	3.25	Night with CB gear	3.32	3.34
		Five-Man Crew		
2.63	2.06	Day without CB gear	2.56	2.07
2.61	2.50	Day with CB gear	2.29	2.52
3.44	3.06	Night without CB gear	3.33	3.06
3.32	3.34	Night with CB gear	3.60	3.32

The ordnances to be loaded were positioned by placing the rockets on either side of the missiles, which were in the center. The nineteen rockets for left-side loading were housed in a circular container which was slightly elevated at its opening; while the rockets for right-side loading were stacked on a five-inch high pallet. The left-side rocket loading times, which were less than the right-side rocket loading times by approximately 6 percent, indicate that the use of the circular container and how it was positioned may have reduced the overall loading time.

The missiles for left-side loading were stowed in four of the newer metal containers which had been used for qualification tests and were slightly damaged. The missiles for right-side loading were stowed in three wooden shipping containers and one older fiberglass container. An analysis of the data indicates that the left-side loading times were approximately 8-percent greater than the right side. That difference may be attributed to the difference in container types.

Since one of the premises for the investigation was that the missiles would be readied for loading with "unlatched" containers, the above result would be more meaningful if a "latched" container condition could be obtained from the results. Therefore, a short investigation was accomplished to obtain the missile extraction times from latched containers. Again, the data from Table 2 was used but was now modified by subtracting extraction times from wooden and unlatched metal containers and adding the extraction times from latched containers.

These new times slightly affected the results, with the left-side missile loading times being an average of 7-percent higher than the right side. Therefore, a condition must have existed on the left side which caused this anomaly, as it was not expected. When the data films were reviewed, the only observed difference was that the metal containers' three-foot positioning arm was swung into the open space between the containers. While it cannot be stated with certainty, the missile positioning arm may have caused the difference in data since the 30mm loading equipment would have increased the right-side loading times.

Because the fuelers had, in most cases, completed their tasks before the three-man teams started to load the right-side missiles, a comparison of the right-side loading times gave some indication of the interference between the loading crew and the fueler. As a result, the fuelers' presence increased the crews' missile loading times by an average of 2 percent.

The correlary question to whether the fueler interfered with the ordnance loading was: "Did the ordnance loaders interfere with the fueler?" The fueler's activity time, either walking to and from the aircraft or preparing and securing fueling equipment, decreased an average of 3 percent when a five-man crew was employed. It was presupposed that the presence of two ordnance loaders on the right side would present an interference to the fueler with a resultant increase in task time. However, in consonance with the loader times, the fueler took an average of 15-percent longer when wearing CB gear and 25-percent longer when performing the task at night.

OBSERVATIONS

During the investigation, observations were made related to the rearming and refueling process. They are offered here with suggested improvements where appropriate.

Auxiliary Night Lighting

The initial experimental procedure called for the crews at night to use individual chemical illumination wands. These light sources provided illumination which was thought sufficient for the loading task without compromising the security of the area. However, after the first few night trials, the crews chose not to use them, as they presented a localized glow which interfered with their vision when brought adjacent to discrete areas requiring more illumination. In addition, the light wands could not be conveniently carried or positioned to provide sufficient lighting.

Missile Handholds

When the missile is exposed in its shipping container, it can not be extracted from the lid side or aft end of the container. As a result, the loader lifted the missile out either by grasping the aft attaching shoe or by grasping the two top fins. In similiar fashion, the second loader either lifted the missile out by cradling the optical seeker head or by grasping the forward attaching shoe. The HELLFIRE contractor indicated that the shoes should be able to take the strain, but preliminary loading procedures obtained from draft TM 9-1427-475-23 specify that the optical seeker head, attaching shoes, and fins are not suitable for lifting points.

If these points cannot be used for lifting, some type of handholds should be provided, not only for lifting but also for attaching the missiles to the launch rails.

Missile Attaching Procedure

The missiles have been designed to allow the missile to drop free of the launcher rails in a zero velocity launch situation. Specifically, the aft attaching shoe is narrower than the other two; and when the missile is fired, the aft shoe drops from a slot in the rails at the same time the middle shoe clears the forward end of the rails. Although this facilitates the launch procedure, it increases the complexity of loading the missile onto the launcher. The attachment procedure is more difficult than simply pushing the missile back onto the rails. The procedure prescribed by the contractor is for the loader holding the aft end of the missile to position the aft shoe in the slot in the rails while the loader holding the forward end of the missile rotates the missile axially to align the middle shoe with the rail opening, which aligns all attaching shoes and allows the missile to slip onto the rails. This has to be accomplished with the middle shoe approximately 1/4-inch forward of the launcher rail opening. The difficulty in this procedure is that during both day and night loadings, the aft loader cannot see the slot in the rail. Also, during the night, the forward loader cannot see to correctly align the middle attaching shoe.

Three suggestions are offered which might enhance attaching the missiles to the rails. Initially, provide a high contrast legend or decal on the side of the launch rails to indicate where the aft attaching shoe is to be placed. Secondly, mark the locking handles so they can be seen at night. Finally, chamfer the attaching shoes so that they slip onto the rails when precise alignment has not been obtained.

Training Missiles

During the investigation, each training missile was up- and down-loaded approximately 150 times. As crew training was progressing prior to actual test runs, it became evident that each attempt to attach the missile to the rails when slightly misaligned caused the aft edges of the attaching shoes to deform, preventing the missile from slipping onto the rails easily. Consequently, the attaching shoes had to be filed during testing to true up the shoes.

Providing a chamfer on the aft edges of the attaching shoes, as suggested earlier, should reduce, if not eliminate, this condition. It should be noted that this condition should not occur with the actual missiles which are normally only loaded once.

Rocket Handling

During the investigation, the loaders were allowed to develop their own rocket-carrying technique. There were two common procedures for rocket carrying. The first was for each loader to carry a single rocket and insert it into the launcher, taking turns until all 19 rockets were loaded. The second procedure was for one loader to pick up a single rocket and carry and transfer it to a second loader who then inserted it into the launcher. As these types of procedures were left up to the individual loader teams, no times were obtained as to which procedure was faster.

In addition, it should be noted that the longer rockets were used; and, as such, the rocket insertion tool was not used.

Space Between Wing Stores

It was observed that when the 19-tube rocket launcher was placed on the outboard rack, it restricted the movement of the loader around the missile launchers. This situation would appear to complicate the loading task. The loaders did not complain of the "tight" space, and no attempt was made to obtain missile-loading times without the rocket launchers in place or with two HELLFIRE launchers on the same side.

Stray Voltage Check

At the time of the investigation, precise procedures were not available for using the MARK IV modified tester for checking both missile and rocket system stray voltages. In addition, personnel involved with the operational testing of the AH-64 were using a voltmeter to check stray voltage on the rocket system, apparently because it was more sensitive.

Loading Time

An analysis is contained here to show that the loading time can be significantly reduced by positioning the ordnance as close as possible to the aircraft. As an example, the time to load missiles can be separated into three events: extraction time, transit time, and attaching time. The extraction time is the time to unlatch the container and lift the missile free; the transit time is the round-trip walking time between the container and the launcher; and the attaching time is the time to attach the missile to the launcher rails. The three-man team loaded eight missiles in 4.40 minutes with the containers placed outside of the rotor diameter approximately 38 feet from the launchers. Each missile can therefore be loaded in 0.55 minutes. When the extraction time of 0.12 minutes and transit time of 0.17 minutes are subtracted from the loaded time, the resulting attaching time is 0.26 minutes per missile.

If procedures would permit the helicopter to land with the containers 12 feet from the launchers, the transit time would be reduced to 0.05 minutes per missile and 8 missiles could possibly be loaded in 3.44 minutes. This is a 22-percent savings in time.

By a similar analysis, the time to load 38 rockets could be reduced to 2.76 minutes from 4.68 minutes, a 41-percent savings in time. As a result, the time to load ordnance would be reduced from 8.90 minutes to 6.20 minutes, which is a 30-percent savings in time because of the 68-percent reduction in walking distance.

Crew Comments

At various times during the data collection trials, the subjects were interviewed to get their thoughts and comments on the procedures established and equipment design issues. The following summarizes their comments:

A. Though they do not possess the MOSs identified for FARP personnel, they felt it would be easy to train an individual to perform the required tasks. It was estimated that this training would take less than one week.

B. There are times when the fueler is changing tanks that interference with the weapon loaders occurs.

C. The M-17 mask was difficult to work with. When looking downward, the mask and hence the eyeholes tend to rise up. Subjects reported they were sometimes looking cross-eyed.

D. It was difficult to open the gravity port fuel cap while wearing CB gloves.

E. When two different-sized people are teamed up to load the HELLFIRE missiles, the largest person should always be at the missile front. This will facilitate any need for moving between the pylons.

F. The subjects felt it would be very fatiguing to rearm and refuel more than one aircraft consecutively. This is especially true when wearing CB protective clothing.

G. The following are areas for improvement identified by the subjects:

1. A new design for attaching the HELLFIRE missiles to the launcher rail is desirable.

2. The method of locking the missile should be changed. Perhaps, an automatic system could be devised.

3. Consideration should be given to changing the loading sequence. That is, load the lower missiles first.

4. Provide a new CB mask which will allow greater vision.

5. Paint all missiles with the textured finish. This allows for better handling than the smooth finish.

6. Improved means of removing the HELLFIRE missiles from the new container are desirable.

CONCLUSIONS

A. From the analysis, it can be concluded that all three conditions evaluated did have an impact on rearming and refueling times. The crew-size change appears to have the most impact, followed by the day/night condition, and then the wearing of CB protective clothing.

1. Crew Size. The three-man crew consisted of two weapon loaders and one fueler. The five-man crew consisted of four weapon loaders and one fueler. The crew loaded 8 HELLFIREs and 38 2.75-inch rockets and simulated refueling.

a. Based on preliminary data, it is envisioned that loading the 30mm chain gun will take at least as long as loading the rockets. Hence, the three-man crew will not be able to meet the ten-minute turn-around time to load 8 HELLFIRE missiles and 320 rounds of 30mm ammunition and refuel as specified for the AH-64 in AMC-SS-AAH-H10000A.

b. A five-man crew may be able to meet this ten-minute turn-around time if 30mm reloading is conducted simultaneously with HELLFIRE missile reloading.

2. Day and Night Conditions Effects

a. There is an increase of 38 percent in the rearming and refueling time for a five-man crew at night over that during the day.

b. There is an increase of 36 percent in the rearming and refueling time for a three-man crew at night over that during the day.

3. Chemical and Biological Protective Clothing Effects

a. There is an increase of 7 percent in the rearming and refueling time for a five-man crew with CB gear over that without CB gear.

b. There is an increase of 16 percent in the rearming and refueling time for a three-man crew with CB gear over that without CB gear.

Note: The above data were taken under environmental conditions which were not severe enough to induce heat stress.

This data is summarized in Figure 1.

B. FARE Equipment

1. FARE equipment may not be capable of delivering 50 gal/min to two aircraft simultaneously using the current pumping system. Therefore, excluding 30mm considerations, refueling may be a longer process than rearming.

2. Two FAREs will be required for each FARP. The placement of a FARE on vehicles/trailers may enhance fuel availability to the aircraft.

C. HELLFIRE Missiles

1. The interface between the HELLFIRE missile and the launcher rails does not facilitate ease of loading. This is particularly true at night or when the crew is wearing CB protective clothing.

2. The design of the newer metal container makes it very difficult for the crew to extract the missiles. It is extremely difficult, if not impossible, for the missile to be extracted from the container without handling the fins, forward attaching shoe, or optical seeker head.

D. 2.75-inch Rockets. Given the fact that the new 19-rocket containers weighing about 575 pounds will come packed two to a pallet, consideration needs to be given as to how these containers will be moved around the FARP area.

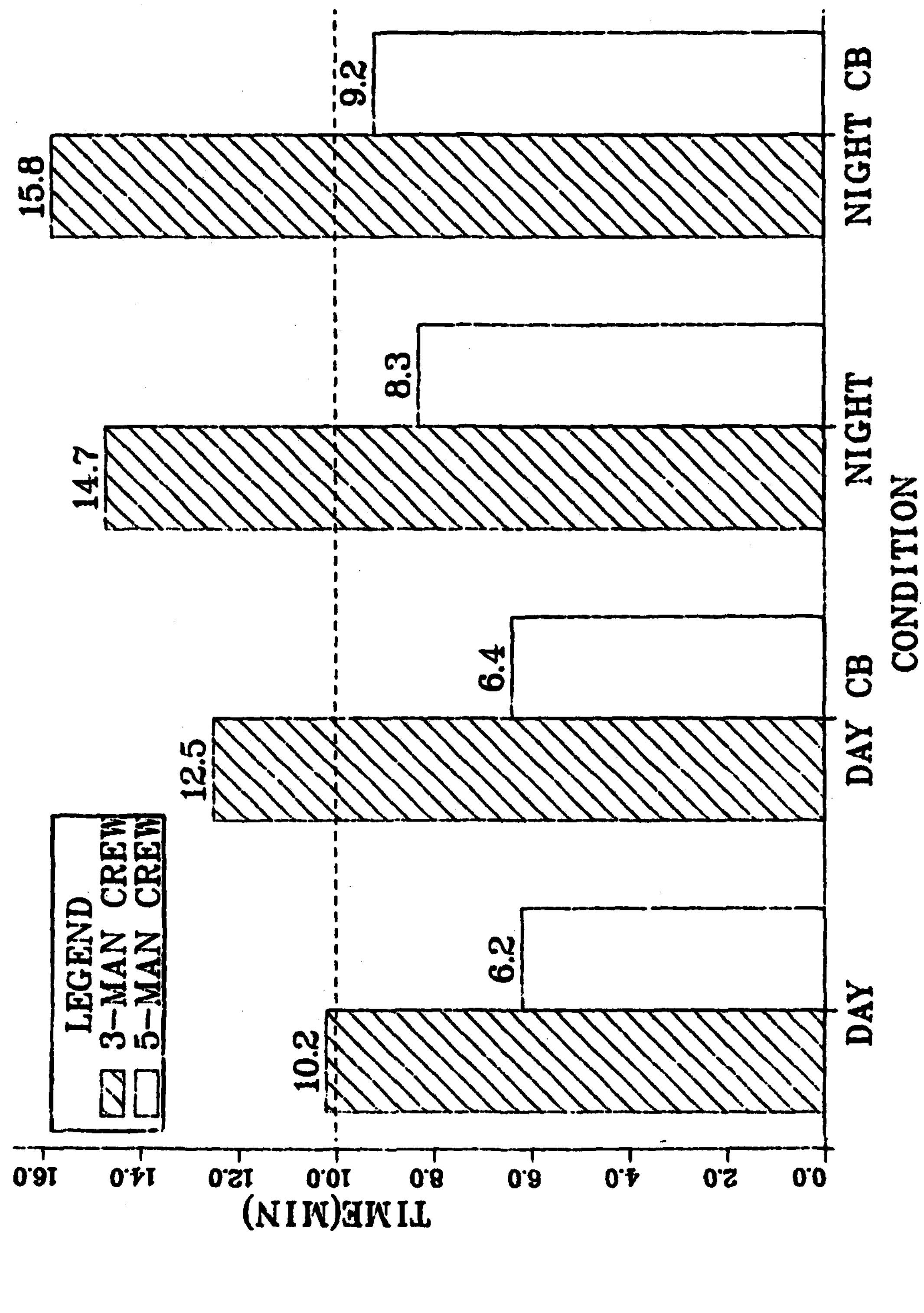

Figure 1. Mean Total Task Time.

RECOMMENDATIONS

Based on the FARP evaluation effort accomplished to date, it is recommended that the following issues and areas of future investigation be addressed in order to be able to fully assess the impact of operating in FARPs.

A. A similar investigation be repeated on an actual aircraft to determine the degradation due to a turning rotor blade, blowing dirt and grass, and the reduced ability to communicate due to the high noise environment.

B. A similar investigation be conducted under environmental temperature conditions expected on the battlefield to assess the crews' ability to perform under more realistic conditions.

C. Conduct an assessment of the time required to rearm the 30mm cannon in the forward area.

D. Assess the implications of performing simultaneous rearming and refueling. Similarly, assess the possibility of rearming missiles and rockets at the same time the 30mm cannon is being rearmed.

E. Evaluate the turn-around time for an entire attack team comprised of five attack and three scout helicopters.

F. Evaluate the impact on turn-around time of the following factors:

1. General maintenance performed on the aircraft.

2. Personnel performing duties outside of their MOS.

3. Additional crew size variations.

4. Aircrew personnel assist the rearming and refueling effort.

G. Develop a computer model of FARP operations. This would allow rapid assessment of the impact of varying certain parameters on rearm and refuel turn-around times.

BIOCHEMICAL INDICATORS OF INFECTION AND INFLAMMATION IN BURN INJURY (U)

*MICHAEL C. POWANDA, LTC, MSC, JOHN DUBOIS, MR., YSIDRO VILLARREAL, MR., MICHAEL M. LIEBERMAN, CPT, MSC†, BASIL A. PRUITT, JR., COL, MC
US ARMY INSTITUTE OF SURGICAL RESEARCH & CLINICAL INVESTIGATION SERVICE,
BROOKE ARMY MEDICAL CENTER†
FORT SAM HOUSTON, TEXAS 78234

The treatment of severe thermal trauma is very often complicated by infection which occurs readily in such patients (1,2). The loss of the skin barrier and the extensive metabolic and physiologic alterations in burn patients renders detection of infection more difficult and may allow colonization to be mistaken for infection. Three factors have been found in perchloric acid filtrates of whole blood taken from burned-infected rats, two of which appear to be useful indicators of the presence of infection and the third a measure of the presence of inflammation, irrespective of etiology (3,4). The following presents the data that the 398 nm absorbance factor and the λex 355, λem 420 fluorescent factor not only denote the presence of infection, but also reflect the severity of infection. Included is the evidence that these two factors require both plasma and cells for their generation as well as the attempts to ascertain which cell population is involved. The data from our initial studies to characterize the substances involved in the generation of these indicators are also presented.

METHODS AND MATERIALS

Rats used in these studies were obtained either from Holtzman or from Timco. The standard burn model of Walker and Mason (5) was used, and burn size varied as needed. Pseudomonas aeruginosa strain 12-4-4 was used to infect the burned rats. The biochemical indicators were quantitated as previously described (3) except that 0.2 ml of 30% H_2O_2 was added prior to the measurement of the 355/420 fluorescent factor. Seromucoid was measured using a modification of the method of Chandler and Neuhaus (6). Partial correlation and multivariate regression was accomplished using the BMDP biomedical computer programs.

RESULTS AND DISCUSSION

The preparation of samples of whole blood for the determination of these biochemical indicators starts with the addition of cold perchloric acid (PCA) to the whole blood; the final concentration of PCA is approximately 0.6 M. If plasma instead of whole blood were so treated, the resulting filtrate would contain the various carbohydrate-containing proteins which constitute the seromucoid fraction (7). Measurement of seromucoid concentration has been used to assess the severity of infection and/or injury (6,8,9,). Therefore, in some of the studies presented here, the concentration of seromucoid was also determined so as to provide an additional index of the severity of injury and/or infection. The biochemical indicators and seromucoid are all precipitated from their PCA filtrates by the addition of phosphotungstic acid (3,6) which suggests that the biochemical indicators may also be carbohydrate-containing proteins. There are a number of glycoproteins which are minor constituents of plasma; these proteins have not been extensively studied nor has their function been determined (9).

In order to assess the value of the newly discovered biochemical indicators of infection as compared to the seromucoid response to infection (7,8), the following study was carried out using fed and fasted rats. Twenty-four and 48 percent total body surface burns were produced, and one-half of each group of burned rats were inoculated with Pseudomonas. At 2 and 4 days, rats were killed and the blood analyzed for the biochemical indicators and the plasma for seromucoid. Figure 1 depicts the results of these analyses. On day 2, injury caused an increase in all indicators, while injury plus infection produced even greater changes. By day 4, the only significant increases in OD 398 and λex 355/λem 420 were the result of infection; there was little effect of injury. Seromucoid concentration as well as λex 280/λem 340 increased in response to injury alone, with somewhat greater changes due to injury plus infection. Fasting did not appreciably alter the extent of change in any of these indicators of infection and/or inflammation.

Table 1 summarizes the correlations between alterations in the indicators and burn size or the presence of infection. It is apparent that injury is a major factor in changes in concentration of these indicators on day 2, but on day 4, it is evident that the increases in OD 398 and fluorescence 355/420 are primarily in response to the presence of infection. This point is made clearer by Table 2, which shows the significance levels for the regression coefficients in Table 1. On day 4, OD 398 and fluorescence 355/420 do not respond significantly ($P < 0.01$) to burn size, but do respond to the presence of infection.

In order to assess whether the biochemical indicators of infection reflected the severity as well as the presence of infection, groups of rats were vaccinated or inoculated with immune serum and then challenged with strain 12-4-4 Pseudomonas. Table 3 shows the effect of vaccination with a strain-specific ribosomal vaccine (10) on the generation of biochemical indicators. The vaccine protects > 90% of the burned-infected

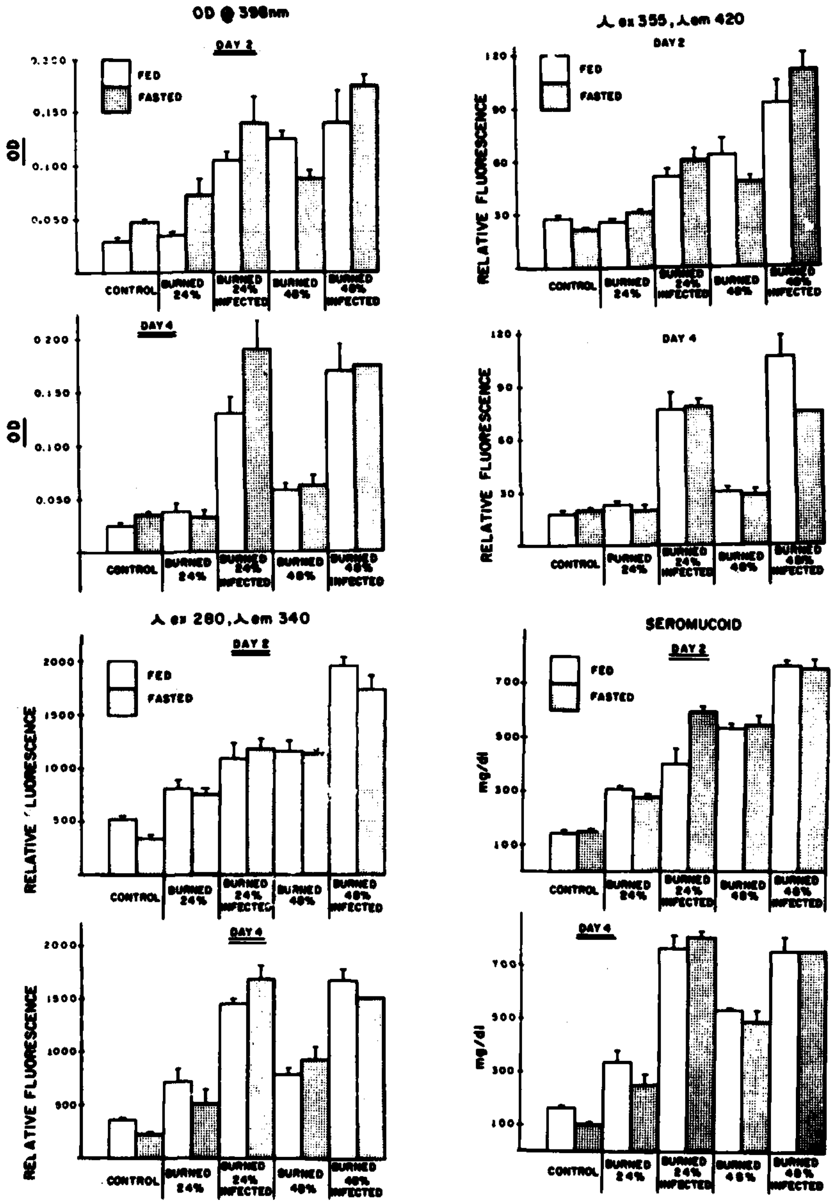

Figure 1. Alterations in putative biochemical indicators of infection and seromucoid following burn injury ± infection.

Table 1. Correlation of Dependent Variables with Burn Size or Presence of Infection

	Day 2		Day 4	
	Burn Size	Infection	Burn Size	Infection
Seromucoid	.849	.655	.588	.844
OD 398	.621	.648	.304	.805
280/340	.793	.681	.493	.793
355/420	.689	.665	.334	.867

Table 2. Significance Levels for Regression Coefficients

	Seromucoid	OD 398	280/340	355/420
Day 2: Burn size	.001	.001	.001	.001
Infection	.001	.001	.001	.001
Day 4: Burn size	.001	.070	.001	.014
Infection	.001	.001	.001	.001

Table 3. Effect of Vaccination with a Strain-Specific Ribosomal Vaccine on Generation of Biochemical Indicators

	Day 5				Day 7			
		Fluorescence		Sero-		Fluorescence		Sero-
	OD 398	280/ 340	355/ 420	mucoid mg/dl	OD 398	280/ 340	355/ 420	mucoid mg/dl
Control	.147 ±.006	602 ± 20	40 ± 2	518 ± 25	.166 ±.015	482 ± 31	53 ± 5	498 ± 24
Burned-infected	.616 ±.050	1367 ± 51	229 ±19	1227 ± 96	.493 ±.068	1358 ±106	298 ±30	1102 ±102
Burned-infected once vaccinated day -7	.499 ±.109	1325 ±105	195 ±41	916 ± 81	.191 ±.010	1433 ±147	146 ± 1	902 ± 46
Burned-infected twice vaccinated days -7, -2	.334 ±.031	1350 ± 76	135 ±11	867 ± 56	.164 ±.030	1408 ± 94	147 ±24	946 ± 78

n = 6; mean ± SEM

rats against death, while nonvaccinated burned-infected rats die between 7 and 10 days. Vaccination reduces the response of the 398 and 355/420 factors on day 5 and entirely abolishes the 398 response by day 7, while reducing the 355/420 response to 50% of the nonvaccinated rats. The 280/340 is unaffected by vaccination and seromucoid concentration only mildly suppressed. In contrast, treatment with a single injection of immune serum (11) which only lengthens the time to death but does not prevent it only slightly suppresses the production of all the indicators on day 4, but by day 7 there are no significant differences amongst the infected groups (Table 4).

Table 4. Effect of Treatment of Animals with Immune Serum on the Generation of Biochemical Indicators of Infection

	Day 4				Day 7			
		Fluorescence		Sero-		Fluorescence		Sero-
	OD 398	280/ 340	355/ 430	mucoid mg/dl	OD 398	280/ 340	355/ 420	mucoid mg/dl
Control	.110 ±.008	617 ± 17	38 ± 2	483 ± 5	.121 ±.013	317 ± 60	28 ± 1	496 ± 19
Burned-infected	.539 ±.013	1667 ± 76	169 ±12	1152 ± 84	.564 ±.063	1367 ±117	177 ±10	1107 ± 55
Burned-infected pre-immune serum	.561 ±.054	1558 ± 84	198 ± 5	1147 ± 25	.503 ±.045	1617 ±106	162 ±11	1047 ± 46
Burned-infected immune serum	.407 ±.043	1375 ± 76	133 ±14	899 ± 56	.453 ±.072	1633 ±136	150 ±12	1067 ± 46

n = 6; mean ± SEM; sera given i.p. on day 0

Our initial attempts at purifying the biochemical indicators as they existed in acid filtrates of whole blood were frustrated by the lability of these factors under these conditions and their tendency to disappear when the filtrates were neutralized. This led us to re-examine the question of the localization of these factors, i.e., whether in plasma or cell associated, and the requirements for the generation of each of these indicators.

Table 5 shows that the OD factor exists neither in the plasma nor the cell fractions but only when plasma and cells are mixed together. This is essentially true also for the 355/420 fluorescent factor. In contrast, the 280/340 fluorescent factor is found in plasma but not in cells, and in fact the addition of cells appears to interfere with its determination. Figure 2 displays the results of varying the concentration of plasma in the presence or absence of a constant amount of cells. The appearance of the OD 398 factor and the 355/420 fluorescent factor varies as a function of the amount of plasma present as long as cells are included. There is little 398 nm material detectable in the absence of cells, but there appears to be some 355/420 fluorescence even in the absence of cells. This may be due to factors released from the Pseudomonas in the infected animals. The 280/340 factor also varies as a function of plasma concentration, but the presence of cells serves to interfere with its detection.

Table 5. Localization of Biochemical Indicators

		Group		
Indicator	Sample	Control	Burned	Burned-Infected
Absorbance 398 nm	Whole blood	.096 ± .002	.123 ± .012	.617 ± .137
	Plasma	0	0	.012 ± .003
	Cells	.074 ± .019	.053 ± .010	.050 ± .012
	Plasma + cells	.060 ± .005	.047 ± .010	.324 ± .045
Fluorescence 280/340	Whole blood	395 ± 48	453 ± 21	1325 ± 65
	Plasma	1288 ± 75	1233 ± 29	3950 ± 129
	Cells	127 ± 25	103 ± 6	206 ± 118
	Plasma + cells	670 ± 53	613 ± 32	1588 ± 103
Fluorescence 355/420	Whole blood	21 ± 3	28 ± 2	143 ± 18
	Plasma	8 ± 1	10 ± 5	28 ± 5
	Cells	8 ± 1	8 ± 2	10 ± 2
	Plasma + cells	56 ± 6	56 ± 6	90 ± 6

n = 4; mean ± SD

Table 6 clearly demonstrates that it is the source of plasma, not of cells, which is critical in the generation of the biochemical indicators. Plasma from control or burned rats when mixed with cells from burned-infected rats does not promote generation of indicators. However, plasma from burned-infected rats when mixed with cells even from control rats produces the 398 and 355/420 factors. The possible advantage of this finding is that retrospective analyses of stored plasma samples from animals (and, one hopes, patients) suspected of having been infected can be carried out using normal cells, perhaps even from a different species.

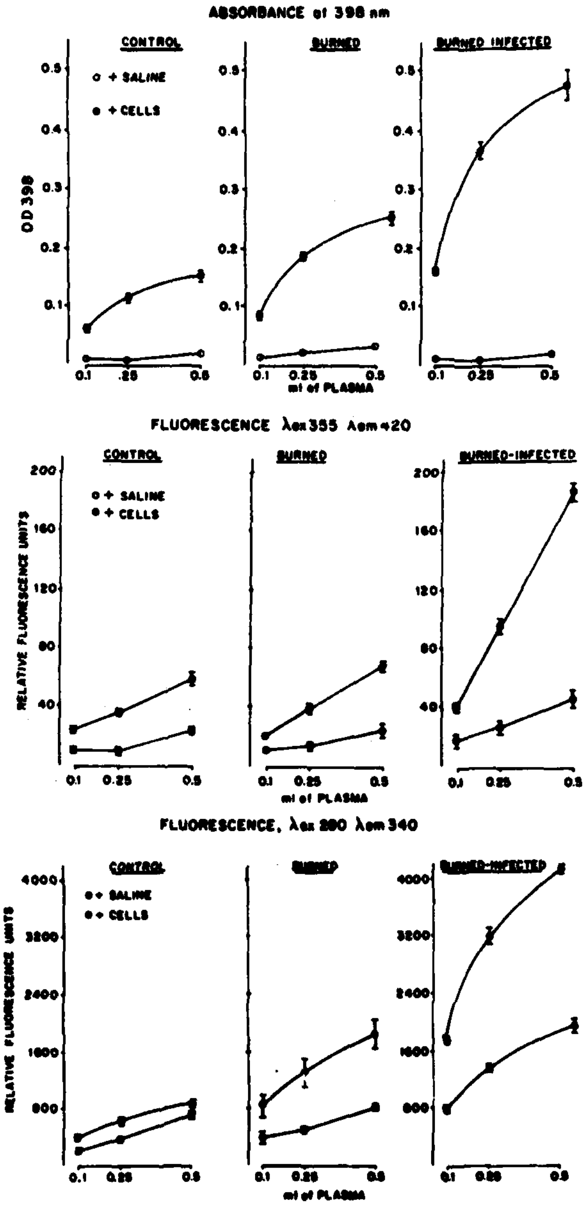

Figure 2. Titration curves for biochemical indicators of infection ± cells, cell concentration held constant.

Table 6. Generation of Biochemical Indicators Dependent on Source of Plasma, not of Cells

	OD 398	Fluorescence 280/340	Fluorescence 355/420
Plasma control + cells burned-infected	.047 ± .003	773 ± 40	28 ± 3
Plasma burned + cells burned-infected	.039 ± .006	720 ± 15	28 ± 3
Plasma burned-infected + cells burned-infected	.234 ± .027	2400 ± 177	111 ± 4
Plasma burned-infected + cells control	.255 ± .019	2338 ± 197	114 ± 11
Plasma burned-infected + cells burned	.239 ± .011	2375 ± 109	125 ± 11

n = 4; mean ± SEM

To ascertain what population of cells were requisite for the generation of the 398 and 355/420 factors, Ficoll-hypaque gradients were employed. It would appear that the erythrocyte fraction (which also contains granulocytes in this preparation) is the required fraction (Table 7). To assess whether the few granulocytes admixed with the erythrocytes could be responsible for the generation of the 398 and 355/420 factors, a Percoll gradient was utilized. Granulocytes plus plasma do not result in the production of the 398 and 355/420 factors whereas erythrocytes plus plasma do (Table 8).

The discovery that erythrocytes were one of the components responsible for the generation of the 398 and 355/420 indicators of infection led us to test whether hemoglobin or other heme-containing substances could participate in the generation of these indicators. Table 9 demonstrates that hemoglobin, methemoglobin, myoglobin and even hemin can all interact with plasma from burned-infected animals to generate the 398 nm indicator. Except for methemoglobin, all of these compounds can participate equally well in the production of the 355/420 fluorescent indicator. The inability of methemoglobin to generate appreciable quantities of 355/420 material does not seem to be due to the presence of iron in the ferric form since this is also true of hemin. None of the compounds, except for hemoglobin, generates much of the 398 nm or 355/420

Table 7. Ficoll Gradient Separation of Cells Responsible for Generation of Biochemical Indicators of Infection

	OD 398	Fluorescence 280/340	Fluorescence 355/420
Plasma + saline	.039 ± .006	3112 ± 123	46 ± 3
Plasma + cells	.199 ± .023	1838 ± 131	116 ± 4
Plasma + supernatant	.011 ± .003	1200 ± 20	37 ± 2
Plasma + lymphocyte/ monocyte band	.036 ± .010	52 ± 2	49 ± 4
Plasma + RBC pellet	.338 ± .014	35 ± 14	108 ± 3

n = 4; mean ± SEM

Table 8. Percoll Gradient Separation of Cells Responsible for Generation of Biochemical Indicators of Infection

Sample	OD 398 nm	Fluorescence 280/340	Fluorescence 355/420
Whole blood	559 ± .029	878 ± 21	118 ± 2
Plasma + packed cells	.463 ± .022	990 ± 35	89 ± 4
Plasma + erythrocytes	.399 ± .017	910 ± 31	81 ± 1
Plasma + monocytes/ lymphocytes	.018 ± .002	2667 ± 133	31 ± 1
Plasma + granulocytes	.020 ± .004	2100 ± 106	28 ± 1
Piasma + saline	.026 ± .003	3700 ± 68	26 ± 1

n = 6; mean ± SEM

Table 9. The Potential Role of Heme-containing Compounds in the Generation of Two of the Biochemical Indicators of Infection

Source of Ligand	+ Plasma		+ Saline	
	OD 398	355/420	OD 398	355/420
Cells	.745 ± .021	169 ± 1	.062 ± .004	7.3 ± 0.5
Hemoglobin	.580 ± .013	119 ± 4	.066 ± .010	36 ± 3
Methemoglobin	.495 ± .009	32 ± 1	.093 ± .003	6.3 ± 0.9
Myoglobin	.330 ± .011	145 ± 2	.043 ± .003	6.0 ± 0.4
Hemin	.819 ± .014	140 ± 2	.056 ± .005	1.8 ± 0.3

n = 4; mean ± SEM
Additions of ligands (other than cells) were 0.5 ml of a 2.3 mM solution

indicators when mixed with saline instead of plasma and even hemoglobin only produces some 355/420 fluorescence but little or no 398 absorbance. Though it appears that heme-containing compounds could substitute for erythrocytes in the assay of plasma for the 398 nm and the 355/420 indicators, it seemed advisable to continue to use erythrocytes until the plasma components had been purified and identified to eliminate the possibility of spurious results.

The findings that the source of plasma was the critical factor in the generation of the 398 and 355/420 indicators and that erythrocytes appear to be the cells which interact with the plasma substances in the presence of PCA to produce these indicators allowed us to pursue the following approach to the characterization and identification of the indicators. Rather than having to work with an unstable acid filtrate of whole blood, we could use plasma from burned-infected animals and employ classical techniques for the purification of proteins. The samples resulting from these procedures could then be assayed for the presence of the indicators by adding erythrocytes from normal animals followed by PCA. We first tried selective heat denaturation followed by ammonium sulfate fractionation. We found we could heat the plasma at 60° C for 30 minutes with no loss of activity (Table 10), but with about a 30% decrease in total protein content. The fact that the indicators were resistant to this treatment indicated that complement, which is inactivated under these conditions, is unlikely to be involved in the generation of the indicators. The heat treated plasma was then

Table 10. $(NH_4)_2SO_4$ Fractionation of Biochemical Indicators of Infection

Sample	OD 398 nm	Fluorescence 280/340	Fluorescence 355/420
Untreated plasma	.157	3700	80
	.167	3700	81
60°, 30' plasma	.157	3650	82
	.160	3700	84
0-20% $(NH_4)_2SO_4$	.024	320	9
	.027	350	11
	.025	300	8
20-40% $(NH_4)_2SO_4$	.110	2450	36
	.118	2500	38
	.119	2475	38
40-60% $(NH_4)_2SO_4$	.529	2700	355
	.512	2600	360
	.500	2650	350
60-80% $(NH_4)_2SO_4$	.223	4950	73
	.204	5000	71
	.199	5000	73
Remainder	.021	250	9
	.023	270	8
	.022	280	10

subjected to ammonium sulfate fractionation. The preponderance of 398 and 355/420 generating factors could be found in the 40-60% saturation range, with some tailing into the 60-80% fraction (Table 10). In contrast, fluorescence 280/340 was polydisperse, with the greatest amount being found in the 60-80% fraction but with considerable such fluorescence detectable in the 20-40% and 40-60% fractions. The polydisperse nature of the 280/340 fluorescence is consistent with such fluorescence resulting from the presence of tryptophan in the protein and the fact that most proteins contain tryptophan. Thus it would appear that changes in 280/340 that occur in response to injury as well as infection reflect changes in the concentration of more than a single protein.

Since the 40-60% ammonium sulfate fraction contained the preponderance of the 398 and 355/420 factors, an aliquot of this fraction was applied to a Sephacryl S-200 column in an attempt to further purify the factors responsible for the generation of these two indicators and refine our estimate of their molecular weight (Figure 3). Column chromatography revealed that the factors responsible for the generation of all three indicators appeared to have in common a component (or components) which eluted as a single peak. Using serum albumin, MW 66,300 daltons, to standardize the column, one could estimate that the majority of proteins involved in the generation of the indicators had an apparent MW of 70-75,000 daltons. There were, however, other fractions from the column which contained 280/340 fluorescence associated with molecules considerably larger than albumin; this too is consistent with the idea that increases in 280/340 fluorescence during inflammation reflect increases in a number of proteins. When erythrocytes were used to assay column fractions for the presence of the factor(s) involved in the generation of the 398 nm indicator, there was some activity found in the area of the chromatograph which contained substances of molecular weights considerably less than 12,000 daltons. Perhaps this represents degradation products of the primary component in the 70-75,000 dalton fraction. If hemoglobin were substituted for erythrocytes in the assay, then the 398 factor displayed considerable heterogenity with evidence for proteins of MW greater than 70-75,000 daltons being capable of generating the 398 factor.

At present we are continuing our efforts to purify, characterize and identify the plasma and cellular components which interact to generate the 398 and 355/420 indicators of infection. The available evidence indicates that these indicators are generated by the host in response to infection and not by the microorganism. One component of these indicators clearly is derived from erythrocytes, but the source of the plasma-borne component remains to be discovered. The plasma component could be synthesized de novo or merely in increased amounts by the liver as is the case for acute-phase proteins (12). Alternately the plasma component could be produced or released by cells of the reticuloendothelial system (13). Conceivably a substance already present in plasma could undergo transformation so as to be able to react with erythrocytes and generate a product which is soluble in 0.6 M perchloric acid. Another potential source for the plasma-borne component might be damaged cells. If damaged cells were a (rather than the) source of the plasma-borne component, this would explain why these indicators initially respond in some degree to injury but would not explain why these indicators rise dramatically in response to infection. Infection may elicit some tissue damage but certainly not to the extent that a 25% or 50% full-thickness burn would.

A preliminary survey of blood samples from burn patients indicates that some of these samples from very seriously ill patients appear to contain factors akin to those found in blood samples from burned-infected

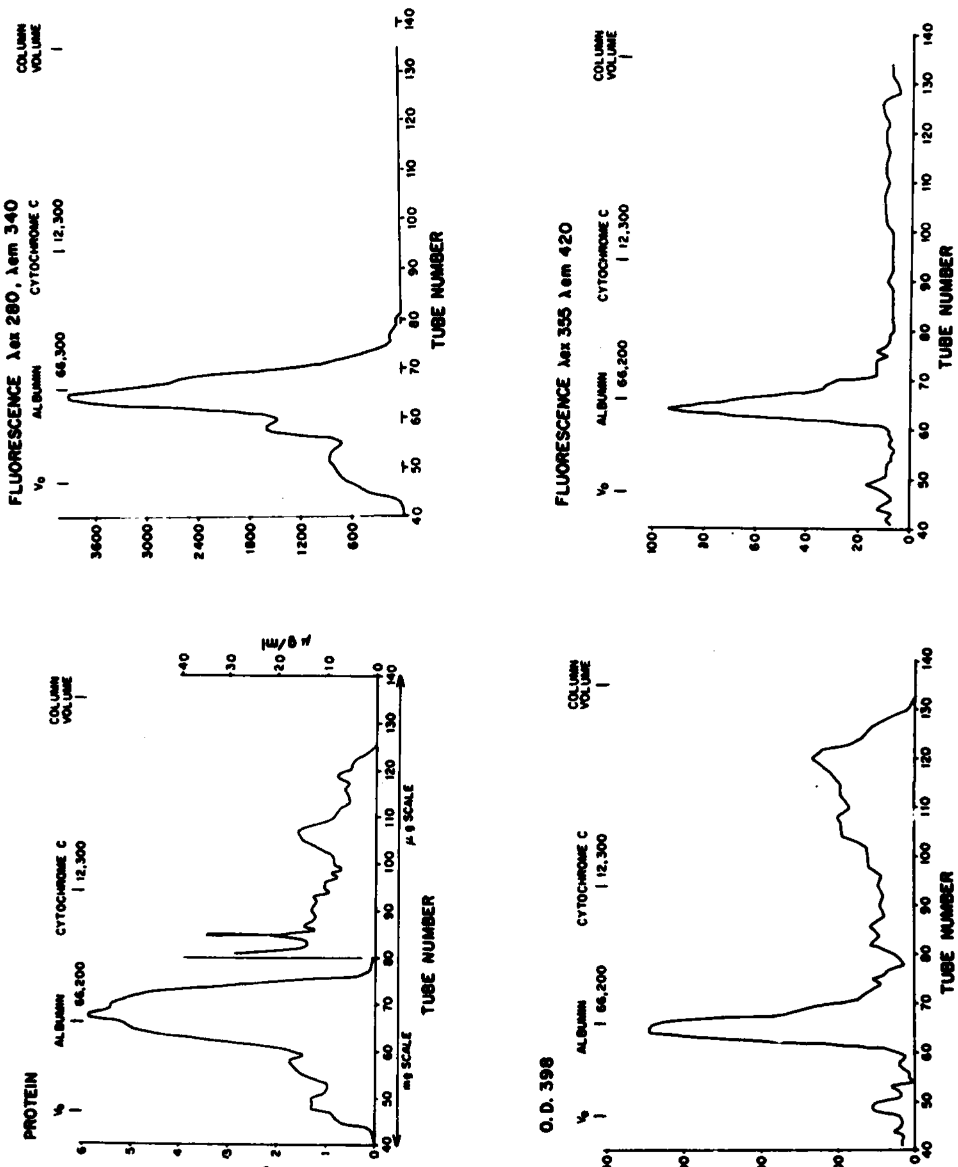

Figure 3. Separation of plasma-borne components of the biochemical indicators of infection on a Sephacryl S-200 column.

animals. A study is under way to assess whether these factors are truly indicative of infection in these patients or merely provide additional, but quantitative, evidence of the severity of the patient's condition.

REFERENCES

1. McManus WF, Goodwin CW, Mason AD Jr, Pruitt BA Jr: Burn wound infection. J Trauma 21:753-756, 1981.

2. McManus WF et al: Clinical operation, center for treatment of burned soldiers. US Army Institute of Surgical Research Annual Research Progress Report, FY 1980.

3. Powanda MC, Dubois J, Villarreal Y, Walker HL, Pruitt BA Jr: Detection of potential biochemical indicators of infection in the burned rat. J Lab Clin Med 97:672-679, 1981.

4. Powanda MC, Dubois J, Villarreal Y: Monitoring and modification of the metabolic and physiologic alterations associated with thermal injury in burned soldiers. US Army Institute of Surgical Research Annual Research Progress Report, FY 1981.

5. Walker HL, Mason AD Jr: A standard animal burn. J Trauma 8:1049-1051, 1968.

6. Chandler AM, Neuhaus OW: Synthesis of serum glycoproteins in response to injury. Am J Physiol 206:169-172, 1964.

7. Schultze HE, Heide K, Haupt H: Die mit Perchlorsaure nicht fallbaren Proteine des Humanserums. Clin Chim Acta 7:854-868, 1962.

8. Powanda MC, Cockerell GL, Moe JB, Abeles FB, Pekarek RS, Canonico, PG: Induced metabolic sequelae of tularemia in the rat: Correlation with tissue damage. Am J Physiol 229:479-483, 1975.

9. Berendt RF, Long GC, Abeles FB, Canonico PG, Elwell MR, Powanda MC: Pathogenesis of respiratory Klebsiella pneumoniae infections in the rat. Bacteriologic and histologic findings and metabolic alterations. Infect Immun 15:586-593, 1977.

10. Lieberman MM: Pseudomonas ribosomal vaccines: Preparation, properties, and immunogenicity. Infect Immun 21:76-86, 1978.

11. Lieberman MM, McKissock DC, Wright GL: Passive immunization against Pseudomonas with a ribosomal vaccine-induced immune serum and immunoglobulin fractions. Infect Immun 23:509-521, 1979.

12. Powanda MC, Moyer ED: Plasma protein alterations during infection: potential significance of these changes to host defense and repair systems. In Infection: The Physiologic and Metabolic Responses of the Host. M.C. Powanda and P.G. Canonico (eds.), Elsevier/North Holland Publishing Co., Amsterdam, 1981.

13. Powanda MC, Moyer ED: Selected aspects of protein metabolism in relation to reticuloendothelial system, lymphocyte and fibroblast function. In The Reticuloendothelial System: A Comprehensive Treatise. Vol. V - Physiology of the Reticuloendothelial System. S.M. Reichard and J.P. Filkins (eds.), Plenum Press, New York. In press, 1982.

AD-A120 813 PROCEEDINGS OF THE 1982 ARMY SCIENCE CONFERENCE HELD AT THE UNITED STATES..(U) DEPUTY CHIEF OF STAFF FOR RESEARCH DEVELOPMENT AND ACQUISITIO.. 18 JUN 82 2/6

UNCLASSIFIED F/G 5/2 NL

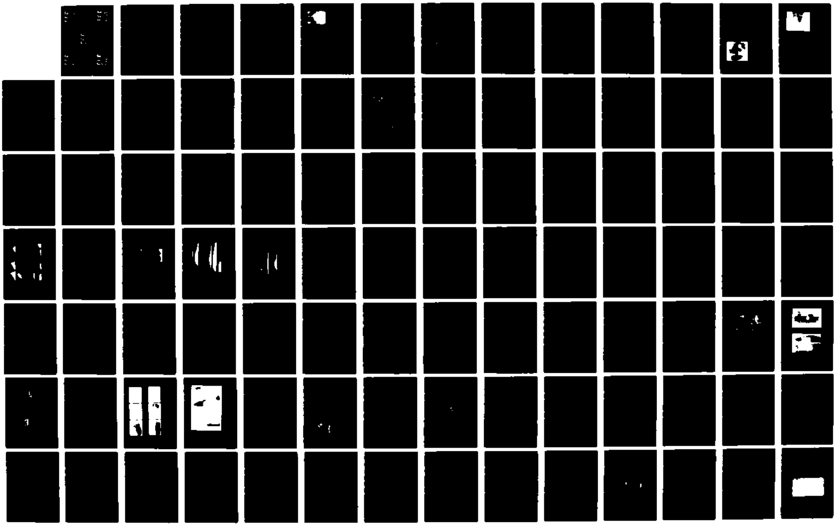

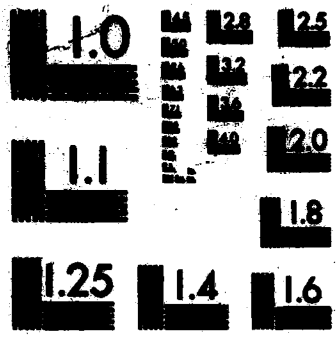

MICROCOPY RESOLUTION TEST CHART
NATIONAL BUREAU OF STANDARDS-1963-A

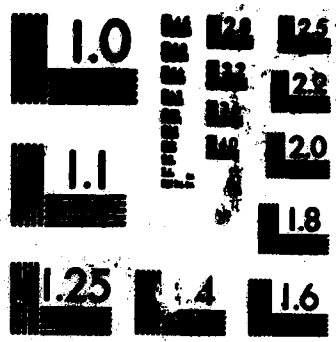

MICROCOPY RESOLUTION TEST CHART
NATIONAL BUREAU OF STANDARDS-1963-A

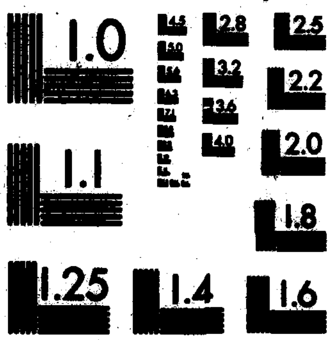

MICROCOPY RESOLUTION TEST CHART
NATIONAL BUREAU OF STANDARDS-1963-A

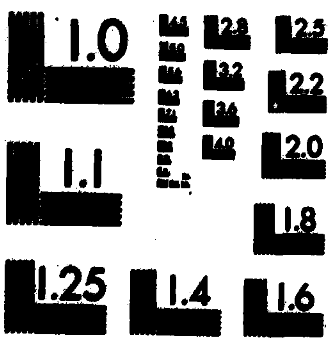

MICROCOPY RESOLUTION TEST CHART
NATIONAL BUREAU OF STANDARDS-1963-A

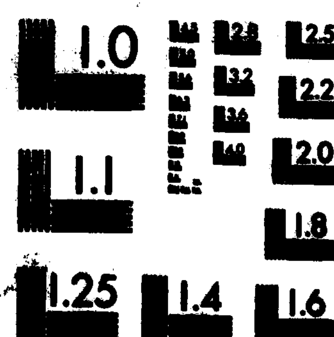

MICROCOPY RESOLUTION TEST CHART
NATIONAL BUREAU OF STANDARDS-1963-A

PSYCHOPHYSICS OF MODERN CAMOUFLAGE (U)

ALVIN O. RAMSLEY, MR.
*WALTER G. YEOMANS, MR.
U. S. ARMY NATICK RESEARCH AND DEVELOPMENT LABORATORIES
NATICK, MASSACHUSETTS 01760

INTRODUCTION

In October 1981 the Army began to issue the new Battle Dress Uniform. The most conspicuous feature of this garment is its Woodland Pattern that was designed to meet the Army's primary camouflage objectives for personnel in temperate regions, day and night, summer and winter.

Camouflage has the objective of reducing enemy perception of military installations, units, equipment, and personnel to enhance mission success, tactical advantage, and survival, itself, on the modern battlefield. To thwart the multiplicity and power of modern sensors, development of countermeasures can no longer rely on the intuitive methods of the past. Success in achieving the camouflage objectives for today's Army requires one to draw upon the resources of several scientific disciplines. Establishment of principles, criteria, and approaches emerges from basic understanding of relevant aspects of physics, ocular structure, psychology, and military science. Implementing the principles to produce real materials is primarily the task of chemistry and industrial technology.

This paper describes the application of psychophysical principles that led to the development of the Woodland Pattern. The scientific discipline that unifies the relevant physics, anatomy, and psychology of vision is called psychophysics. This is defined as "the branch of psychology that deals with relationships between physical stimuli and the resulting sensations and mental states"(1). For the purposes of this paper, the physical stimulus is electromagnetic radiation in the visible and near-infrared regions of the spectrum; the resulting sensations are the responses of a sensor and the person using it.

Of all the sensors a combat soldier encounters, the most versatile is the ubiquitous human eye; it is, as well, the ultimate sensor in using electro-optical devices. It is essential, therefore, that the design of camouflage measures be related to the visual process. In this study the camouflage objectives of the development were to minimize visual perception of soldiers by day and detection by image intensifier devices at night. Although the eye is far more complex, the processes that take place in a starlight scope can be dealt with by methods similar to those used for calculations related to color vision.

VISUAL ASPECTS

In-process reviews that led to the Required Operational Capability (ROC) document concluded that the shapes of individual elements of the camouflage pattern should be the same as those used in the tropical uniform that has been in the supply system for many years. Based on earlier field trials, the reviews also decided that the overall size of the pattern should be enlarged by 60 per cent compared to the older pattern(2). It was also believed that small changes in color from the earlier pattern would improve camouflage effectiveness for year-round use in temperate regions. The four colors of the new pattern are designated Light Green, Dark Green, Brown, and Black.

Selection of Colors

Application of psychophysical principles to questions of camouflage clothing began shortly after World War II. Extensive field trials demonstrated that Olive Drab field uniforms should be replaced by a greener color. The new target color, Olive Green (OG), was defined in Munsell terminology as 10Y3/3(3). Development of the standard OG color on fabrics of many kinds was guided by familiar colorimetric procedures(4). Selection of OG for monotone camouflage clothing and shelters has stood the test of time; it is still the US standard monotone field color for such items in both temperate and cold regions. Moreover, most nations have adopted very similar colors for these purposes. A more detailed historical review of the development of camouflage coloration is given in Reference 5.

During WW II the US Marines made some use of camouflage patterns for clothing in the Pacific, but it was not until the Vietnam era that the US Army did so for a tropical uniform. This uniform used a camouflage pattern that had been designed in 1948 by the Engineer R&D Laboratory (ERDL). Combat experience in Vietnam, however, proved that this design was too bright. Accordingly, the colors were toned down by Natick Laboratories in such a manner that the merged color more nearly approximated the OG color standard. The standard for this pattern is called NLABS-1; when that standard was depleted in 1979, a replacement was chosen, NLABS-2.

The merged color is that seen when a pattern is observed at a sufficient distance that the individual color elements can no longer be resolved by the eye. The method for calculating the merged color of a pattern is based on a summation of tristimulus values for each color, weighted by the fractional area in the pattern represented by each color, as described in Reference 5.

Because the Woodland pattern is intended to be used in temperate areas during both dormant and verdant seasons, colors were chosen so the merged color is somewhat duller than the OG target color, and closer in chroma to Forest Green, a monotone adopted by the Army for use on vehicles and other field items. In the design of surveillance countermeasures, the primary objective is reduction of contrast between the object to be protected and its surrounding background. For visual camouflage, where chromatic colors are used, quantitative measures of color difference as described in Reference 4 are generally employed to define contrast. Figure 1 shows the hue and the chroma in CIELAB color space for OG, Forest Green, the merged colors for ERDL, the two toned down versions (NLABS-1 and 2), and the Woodland pattern.

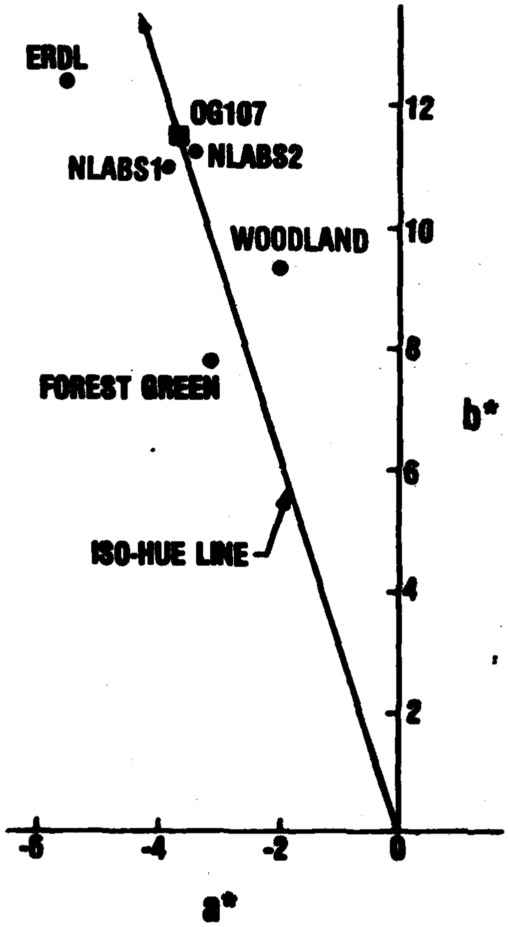

Figure 1. Chromaticity diagram for OG and Forest Green monotones and the merged colors for ERDL, NLABS-1, NLABS-2, and Woodland patterns.

Effective Range

A second factor in selecting the specific color for each of the pattern elements was based on the ability of the eye to resolve the individual areas. The assumption was made that, for the pattern to be effective it must be seen as a pattern; otherwise it would perform no differently than an equivalent monotone.

Fundamental to an understanding of how well the eye copes with this question is a knowledge of the structure of the retina. Figure 2 is a photograph of the central portion of a normal retina. The bright area near the edge of the image is the visually inert optic nerve [illegible]e darker region near the cent[illegible] [illegible]lled the *macula lutea*, a region [illegible]reatly increased concentration [illegible] cones and depletion of rods. In the center of the macular region is located a small, diffusely defined depression called the *fovea centralis*, an area about 0.5 mm in diameter. This rod-free region of the retina contains about 50,000 cones. This is the retinal region of maximum color difference

Figure 2. Normal macula.

discrimination and acuity. A more thorough description of this, the most important area of the retina, is given in Reference 6.

A typical element of the Woodland pattern may be 20 cm by 5 cm. When observed at 200 m, this element subtends an angle at the retina of only one milliradian (mr) by 0.25 mr and produces an image about 16μm by 4μm. Within this small image there will be only three to five cones of each of the three types; green-, red-, and blue sensitive. Considering the complexity of color vision, it is not surprising that the eye experiences difficulty in distinguishing color differences among neighboring elements viewed at considerable distance.

It has long been known qualitatively that small target colors give the eye greater difficulty in discriminating yellow-blue differences, approximately the b axis in Figure 1, than it does red-green or lightness differences. This phenomenon has been called "small angle tritanopia." Under such conditions of viewing, normal observers respond in a manner similar to one kind of color blindness, tritanopia. König reported studies of this as long ago as 1894 (7); among several more recent studies is that reported by MacAdam (8). In 1946 Blackwell reported an extensive study of contrast threshold for achromatic targets, thereby establishing a sound basis for dealing quantitatively with differences in lightness (9).

Judd and Yonemura (1969) reported a study of the small angle color discrimination problem in a manner that permits one to deal with all three axes in color space (10). Their method is based on u, v, W color space in which the axes are similar to, but not identical with, the a*, b*, L* axes otherwise used in this paper. Total color difference, ΔE, in this system is defined in Reference 4 as

$$\Delta E = (\Delta u^2 + \Delta v^2 + \Delta W^2)^{\frac{1}{2}} \qquad (1)$$

For small angles of view, they found that Equation 1 needed to be modified as follows

$$\Delta E' = \left[(k_2 \Delta u)^2 + (k_3 \Delta v)^2 + (k_1 \Delta W)^2\right]^{\frac{1}{2}} \qquad (2)$$

The significant contribution of the paper by Judd and Yonemura was the experimental determination of the dependence of the k-factors as functions of angular subtense. Figure 3 is adapted from their data by converting minutes of arc to the more convenient milliradians. By their modified equation, differences in the perceived colors of remote objects can be judged, regardless of their direction in color space. For example, for a

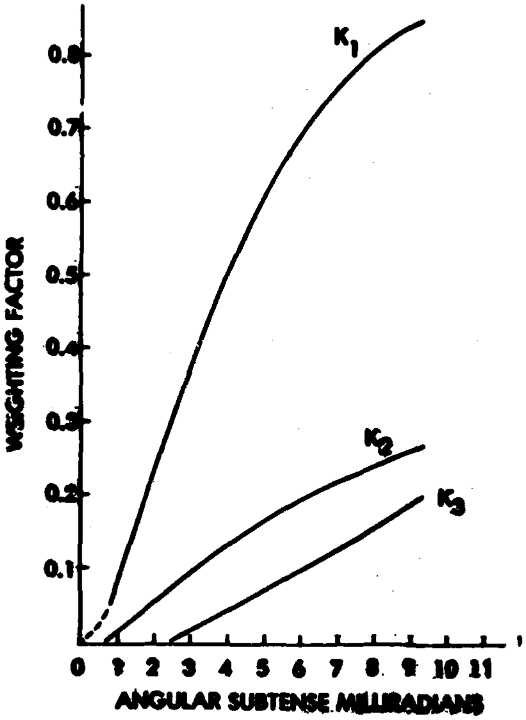

Figure 3. Dependence of K_1, K_2, and k_3 on angular subtense.

target that subtends 2 mr (a typical element of the Woodland pattern at 100 m) $k_3 = 0$; that is, the eye cannot distinguish any color differences along the yellow-blue axis of color space. Moreover, under these conditions k_1 and k_2 equal 0.22 and 0.05, respectively; only large lightness and red-green differences can be seen.

To estimate observation ranges at which the four-color pattern can actually be seen as four colors, we applied the method of Judd and Yonemura for the brown and dark green areas. These two colors were chosen because they are the most similar in lightness and comprise over 60 per cent of the total pattern. The range at which all four colors merge into a single monotone was estimated by comparing the brown and light green areas. The black area was not chosen for these comparisons because the individual black elements are small and represent only about 15 per cent of the pattern area. The next darkest area is the brown; the light green portion of the pattern is the lightest. Figures 4 and 5 summarize the calculations made for both the Woodland and the tropical pattern, NLABS-2. For these calculations, the controlling dimensions of the elements used were 20 cm and 12.5 cm, respectively. Because the ranges involved are rather short, atmospheric effects have been neglected.

Four subjects who were familiar with the camouflage development and also skilled in judging small color differences viewed both patterns on a clear day. They were asked to estimate (by pacing) the ranges at which each of the four-color patterns merged into a two-color pattern. They also were asked to estimate the range at which each pattern appeared as a monotone. The averages of these observations were that the four colors of the older NLABS-2 pattern blended into a two-color, light-dark design at about 100 m and into a monotone at about 175 m. For the Woodland pattern, these ranges were estimated at 140 and 260 m.

From Figures 4 and 5, it was concluded that the color differences that the observers could perceive under the field conditions at the limiting ranges in each case was about 0.8 u,v,W unit. Color differences of this magnitude, although readily perceptible under laboratory conditions, would, in most cases be considered good "commercial matches" by the textile industry. Both calculated data and the visual observations agree that the Woodland pattern "holds" at ranges 40 to 50 per cent longer than for the NLABS-2 pattern. On the basis of these results, it is predicted that the new Woodland pattern will provide the advantages of a disruptive design at significantly longer ranges in those terrains for which it is intended than the older NLABS-2 design which it replaces.

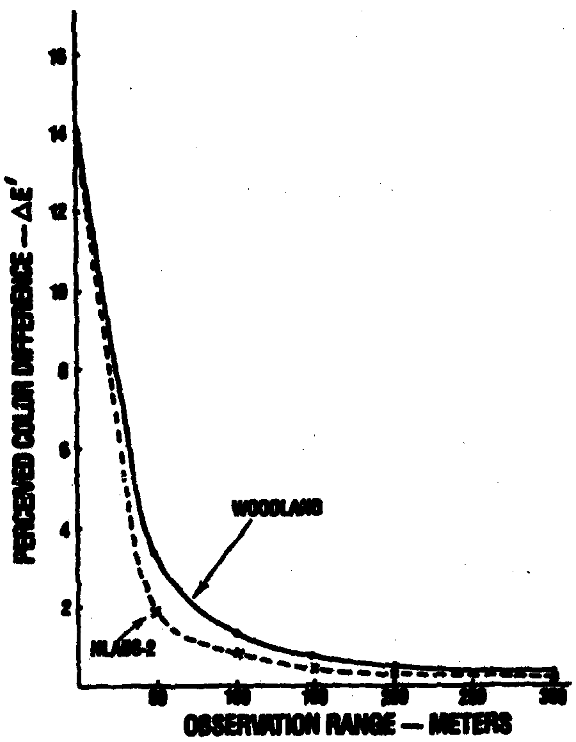

Figure 4. Perceived color differences between brown and dark green areas for the Woodland and NLABS-2 patterns.

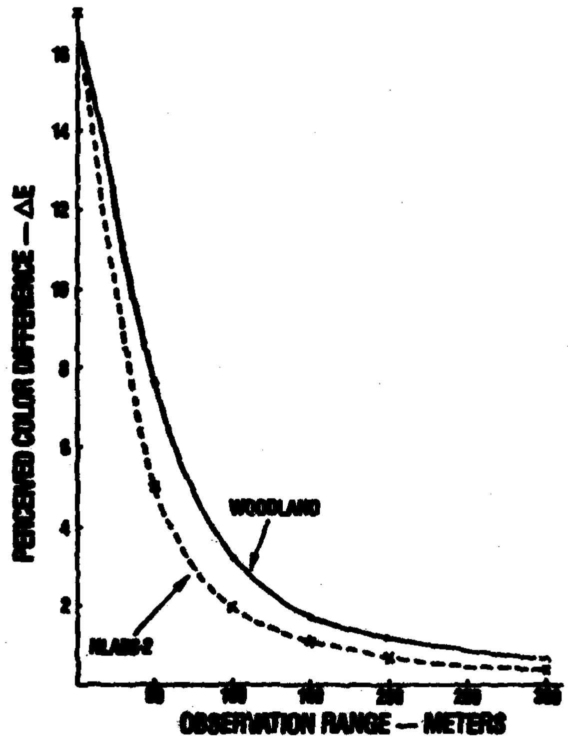

Figure 5. Perceived color differences between brown and light green areas for the Woodland and NLABS-2 patterns.

INFRARED ASPECTS

Psychophysical principles were also applied in reaching the second objective; to provide the soldier with camouflage protection at night as well as during the day. Although principles followed in designing the visual characteristics of the Woodland pattern are rather well quantified, this is not the case for infrared parameters. The reason for emphasis on infrared signatures of potential targets lies in the capability of certain devices to "see" in the dark by using infrared radiation. Three questions must be addressed. How can the relevant infrared entities be quantitatively related to what is seen? How can the infrared standard values best be defined? What are the infrared tolerances? The following develops a general methodology for handling these questions.

General Background

At night, two sensors are major threats to personnel: thermal imagers and image intensifiers. The former respond to infrared radiation emitted by objects and terrains through the 3 to 5 μm and 7 to 14 μm windows of the atmosphere. Unless special measures are taken, soldiers can readily be distinguished from cooler backgrounds with these devices. State of the art, however, is not yet able to furnish these measures in a practical way. On the other hand, no fundamental or practical barriers now prevent attainment of camouflage objectives to meet the threat of image intensifiers.

The underlying principles of image intensification form the basis for a variety of field devices ranging from drivers' night goggles to low light level television systems. The unit used in this study was an AN/PVS-2B Night Vision Sight, modified to provide automatic brightness control. This device is typical of items referred to as starlight scopes.

Because available radiation from the night sky is sufficient for their operation, starlight scopes require no auxiliary light sources, differentiating them from "active" devices. Radiation from the sky is reflected by an object in the same manner as visible light and imaged on photosensitive surfaces that emit electrons roughly in proportion to the intensity of the radiation incident on the tube. The electrons are accelerated through a micro-channel plate in a number of stages in a manner similar to that in a photomultiplier tube. Ultimately, an avalanche of electrons reaches a phosphor plate where a visible image is produced. By this process, the intensity of the original image has been amplified by a factor in excess of 10,000. The photo surfaces used in current image intensifier tubes are sensitive to both visible and near-infrared energy, covering a spectral range from less than 400 nm to about 900 nm. References 11 and 12 describe some of the salient features of both second and third generation starlight scopes, which are similar but not identical to the first generation deviee used in this study.

Quantitative Methods

Reduction of contrast is the major objective of camouflage. It is the variations in contrast that constitute an image, including those seen in a starlight scope. These images appear as a greenish monotone of varying levels of brightness, which allows use of the conventional definition of contrast, C. Although the term "contrast" developed within visual science, this study uses the principles to interpret images in a starlight scope.

$$C = (B - B_o)/B_o \tag{3}$$

B = brightness of an object and
B_o = brightness of the background

It is a purpose of this paper to describe general methods whereby the infrared factors that influence contrast seen in a starlight scope can be handled objectively. Three optical factors influence the variations in contrast one sees in these monotone images; spectral power distribution of the illumination, spectral sensitivity of the sensor, and spectral reflectance of the objects and terrains. Visual science relates similar factors for the eye in a quantitative manner to yield luminous reflectance, Y, a correlate of lightness, by the integration

$$Y = \int_{400}^{700} E_\lambda \quad \bar{y}_\lambda \quad R_\lambda \quad d\lambda \tag{4}$$

where E_λ = spectral power distribution of a specified illuminant, usually daylight
$\bar{y}_\lambda$ = photopic sensitivity function for the eye and
R_λ = spectral reflectance factors for objects.

Although Y may be correlated with brightness, the correlation is not linear. In visual colorimetry, a linear psychometric scale that is often used is defined in CIELAB terms as

$$L = 116\ (Y/Y_n)^{1/3} - 16 \tag{5}$$

where Y_n = integrated reflectance of a perfect white.

Available illumination in a battlefield varies widely at night and includes both natural and man made sources. To illustrate the methodology we have chosen two of the more common and extreme natural types; moonlight and the radiance of a clear moonless night sky. These approximate the extremes in spectral power distribution one may expect in a battlefield environment. Moonlight is similar to well-characterized sunlight mediated by the reflectance of the moon and effects of the earth's atmosphere. For the purpose of this paper we consider the spectral power distribution of moonlight to be equivalent to CIE illuminant D5500. A more complex situation exists for defining the distribution of the moonless night sky and that within shadows on a moonlit night. Published data show this varies widely due to unpredictable photochemical reactions of the upper atmosphere which generate much of the radiation (11-16). Although differing in detail, the data agree that the night sky radiates far more infrared energy than visible light. The curve shown in Figure 6 for a moonless clear sky is one synthesized from the referenced data. To a variable and small but often significant degree, the spectral quality of the ambient light is influenced by the reflections from the ground. Because vegetation strongly reflects near-infrared radiation, illumination from the sky may be further enriched in the infrared than the figure suggests, when surrounds consist of shrubs, trees, and other foliated material.

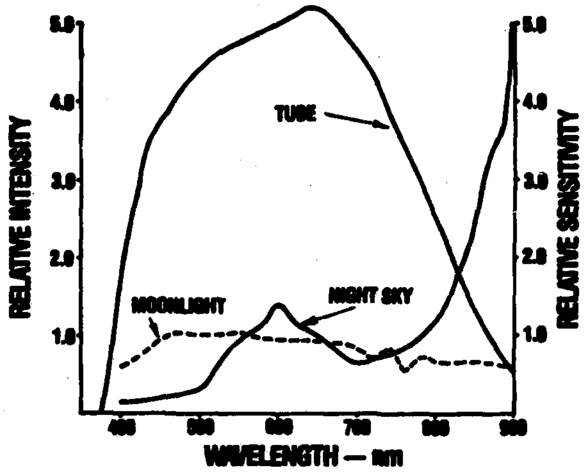

Figure 6. Selected spectral power distributions and the spectral sensitivity of a typical image intensifier.

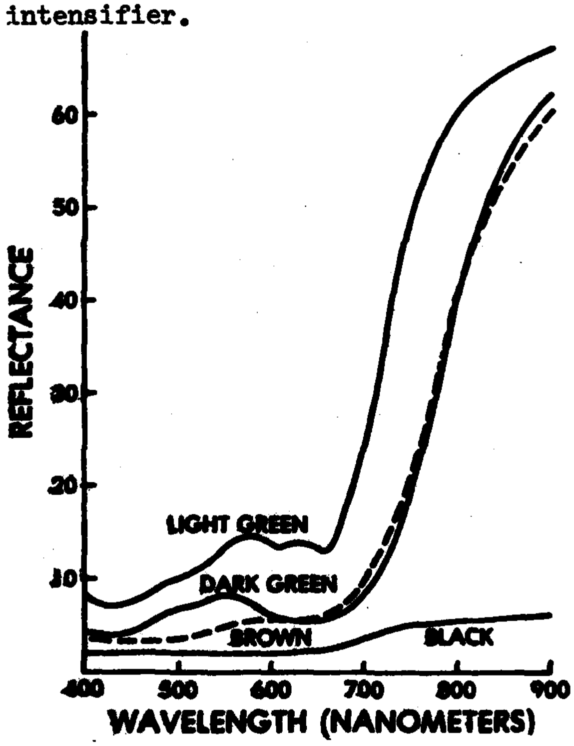

Figure 7. Spectral reflectance data for the Woodland pattern.

Among the many features of a starlight scope, its spectral sensitivity is of special interest to the researcher in camouflage. It is difficult to standardize on a particular set of values for this function for a number of reasons. Among these are variations in manufacture of a given tube type, variety of tube designs that actually are used, and influences of the optics of a given sensor design. Figure 6 shows a nominal sensitivity function for a typical second generation instrument (11, 12).

The third factor that determines contrasts in the image is the spectral reflectance of the objects represented in the image. An object that is characterized by a low reflectance curve is expected to appear darker in the image than one with a higher curve. This one factor over which a camouflage developer has some control is encumbered, however, by one constraint. Visual color requirements narrowly define the visible portion of the reflectance curves; only the infrared portion of the curve is a true variable for the researcher. Figure 7 shows reflectance curves of the four colors of the standard fabric for the Woodland pattern. Dyes were selected for printing the pattern to meet visual requirements and the infrared values derived from the method described in the next section.

Standard Values

The three factors of illumination, sensor, and object reflectance were related by integration in a manner analogous to that of Equation 4.

$$Ns = \int_{400}^{900} I_\lambda \quad S_\lambda \quad R_\lambda \quad d\lambda \qquad (6)$$

where, to avoid confusion with the terminology of color science, Y is replaced by Ns, connoting nighttime illumination and the starlight scope and

I_λ = spectral power distribution of moonlight or the night sky radiance,
S_λ = spectral sensitivity of the sensor.

Table I summarizes integrations using Equations 4 and 6 for visual (daytime) and starlight scope images, respectively. Integrations for Y

Table 1. Integrated Reflectance and Lightness for Several Specimens for Visual and Starlight Scope Observation

Specimen	Daylight Y(L)	Moonlight Ns(Ls)	Night Sky Ns(Ls)
Woodland Pattern			
Light Green	12.1(41.3)	18.3(49.9)	23.0(55.1)
Dark Green	6.9(31.5)	10.1(38.0)	13.3(43.2)
Brown	4.8(26.0)	9.2(36.3)	12.9(42.6)
Black	2.3(16.8)	2.8(19.0)	3.0(20.0)
Merged Pattern	6.5(30.6)	10.3(38.4)	14.1(44.4)
Munsell Grays			
N-3	6.1(29.6)	5.9(29.2)	5.8(29.0)
N-4	12.2(41.5)	11.8(41.0)	11.6(40.6)
N-5	20.4(52.3)	19.8(51.6)	19.4(51.2)
N-6	29.2(61.0)	28.3(60.2)	27.8(59.7)
N-7	43.1(71.6)	41.8(70.7)	41.0(70.1)
N-8	59.7(81.7)	57.9(80.6)	56.8(80.0)
Olive Green 507	7.9(33.8)	8.1(34.2)	9.1(36.3)
Olive Green 107	7.3(32.6)	6.7(31.1)	7.8(33.5)
Maple Leaf	8.1(34.3)	12.0(41.2)	16.4(47.5)
Hedge Leaf	11.2(39.9)	14.5(44.9)	19.3(51.1)
Aspen, summer (17)	5.8(28.9)	9.9(37.6)	13.8(44.0)
Soil, plowed (17)	6.0(29.3)	7.4(32.6)	9.0(36.0)
Meadow, summer (17)	9.5(36.9)	13.6(43.6)	18.9(50.6)

were based on the 1931 CIE Standard Observer and Source D6500; for Ns, the data that form the basis of Figure 6 were used for both moonlight and night sky illumination. Specimens that were evaluated include the four colors of the Woodland pattern, relevant monotone clothing fabrics, a series of

Munsell neutral gray samples, two leaves measured in the laboratory, and representative Krinov terrain data (17).

It is no more reasonable to expect that the contrasts observed visually in the image of a starlight scope are linearly related to the integrated reflectance values than they are for visual observation. In one attempt to explore possible linearity, values of Ns were converted to the lightness analog, Ls, using Equation 5. These data are also summarized in the table, in parentheses.

The following procedure was used to estimate optimum Ns or Ls values for the Woodland pattern to provide least contrast in a variety of temperate terrains at night. The Munsell gray scale identified in Table I was viewed through the starlight scope on both moonlit and moonless nights in a Massachusetts setting, a part of which is shown in Figure 8. Backgrounds consisted of miscellaneous brush up to eight feet in height and deciduous trees (primarily maple) up to 40 feet high. Observations were made both in early spring before leaves emerged and in the summer when foliage was in full bloom. N-3 was too dark under all conditions, except when placed directly in front of a dark shadow. The best matches to terrain elements such as tree trunks, twigs, and leaves were found for N-4 and N-5. N-6, N-7 and N-8 usually were conspicuously light.

Figure 8 is a photograph of three manikins taken at a distance of about 50 m on a moonless night in the setting described above. The Woodland patterned uniform is flanked by the durable press monotone OG-507 fatigues on the right and the NLABS-1 patterned uniform used in Vietnam on the left. Figure 8 clearly shows that, for the given scene on a moonless

Figure 8. Photograph taken through a starlight scope on a moonless night against a background of miscellaneous shrubs and tree. The three uniforms are, left to right, NLABS-1, the Woodland pattern, and the durable press OG-507. The dimness at the edges of the scene is an aberation of the photography.

Figure 9. Close up view of Woodland pattern showing three-level pattern seen through starlight scope.

night, the Woodland pattern is superior to the two uniforms it is replacing. Numerous observations were made in both deciduous and coniferous surrounds, in every season of the year, on moonless and moonlit nights, both clear and overcast. In every case the Woodland pattern showed less contrast with the backgrounds than the other two uniforms.

It was intended that the Woodland pattern should appear as a pattern when viewed with a starlight scope at night as it does visually in the day. Figure 8, the data of Table 1, and the personal observations confirm that the brown and dark green areas of the pattern are usually difficult to differentiate. What is seen, however, are three distinct levels of lightness that produce a three-level pattern, as shown in Figure 9. As in daylight, the black areas resemble shadows; the other areas resemble other commonly found terrain components. While the data of Table 1 are sparse, many night observations under a variety of conditions support the decisions that constitute the basis of specification requirements for procurement.

Allowable Tolerances

For the visual characteristics of the pattern, a series of textile samples have been selected to guide the inspectors in judging visual acceptability for each color. Because the uniform is worn in garrison as well as in the field, esthetic factors require the visual tolerances to be a bit tighter than they would be, if only combat conditions were considered. For the four colors of the Woodland pattern, the present tolerance ranges average about two CIELAB color difference units; somewhat less in hue, somewhat more in lightness. Both end-item purpose and the ability of the textile industry to produce large quantities of material were taken into account in establishing these tolerances.

It is essential that research also provide guidance to procurement on the range of variations in infrared reflectance that is acceptable. An effort to meet this need is being performed on two levels; one to provide immediate guidance to procurement, the other is a longer range effort to give a more fundamental basis for establishing the range. For the infrared aspects of the tolerances, only camouflage effectiveness and industry capability need to be considered.

To meet the immediate needs of procurement, the current specifications define acceptability in terms of a range of spectral reflectance factors at each wavelength in the infrared taken at 20 nm intervals. The weakness of this procedure lies in its failure to take account of the integrating operation of a starlight scope as expressed in Equation 6. A reflectance factor at one wavelength that is too low may be compensated by one or more higher values at other wavelengths. The method described below overcomes that weakness in the current method of inspection. Moreover, since the data derive from commercially produced visual tolerances, they illustrate the present industrial ability to control the infrared as well as visual characteristics.

Reflectance factors were measured from 400 to 900 nm for the visual tolerance samples for each of the three major colors and integrated by Equation 6. For the black area of the pattern, no lower limit is needed. Table 2 summarizes the ranges found for the three colors for Ns and Ls.

Table 2. Range of Ns and Ls for the Three Major Colors of the Woodland Pattern for two Night Illuminations.

	Moonlit Night		Moonless Night	
	Ns	Ls	Ns	Ls
Dark Green	8.0 to 10.1	(34.1 to 38.0)	11.0 to 13.3	(39.5 to 43.2)
Light Green	15.2 to 18.2	(45.8 to 49.7)	18.5 to 23.2	(50.1 to 55.3)
Brown	7.6 to 10.0	(33.0 to 37.9)	11.2 to 14.4	(40.0 to 44.9)

The ranges shown in Table 2 fall within the range of values shown in Table 1 for typical terrain elements. Taken with the black area, the data show that a three-level pattern will still be seen as long as reflectances remain within the ranges shown in Table 2. It was stated above that the dark green and brown areas were difficult to differentiate through a starlight scope. Table 2 shows acceptable variations in Ns for both areas are much larger than differences between the two areas in the standard. It may also be noted that, for reasons of color durability in use, the values for the standard lie near the upper limit of the tolerance ranges.

The above shows that the level of industrial control exercised in production of the Woodland pattern has been adequate to meet the infrared aspects of the objectives. These results, however, do not provide a total basis for establishing tolerance criteria for other applications, for example, a desert uniform. A general method must also consider the responses of the electro-optical device at various levels of illumination and its interaction with the eye of the observer. We have observed that the contrast threshold increases and resolution decreases as the light level falls. It remains to be determined quantitatively how instrument performance over a variety of conditions influence the criteria needed to produce satisfactory camouflage materials. This is part of the current research.

SUMMARY

Psychophysical principles were applied to several aspects in both the design and production of the recently adopted Woodland patterned Battle-Dress Uniform. These principles pertain to both visual and the near-infrared characteristics of the pattern.

- Well-known methods were applied to select each of the standard colors of the pattern and to define permitted variations in production.

- A little-known technique was modified to predict maximum visual range of effectiveness and to guide in final selection of colors.

- Basic principles of human vision were adapted to guide infrared aspects of the Woodland pattern. These relate to nighttime detectability by the starlight scope/eye interaction. The new methods were used to define both standard values and allowable variations.

These principles and the supporting dye formulation studies reported in Reference 5 have made possible the large scale production of acceptable fabrics. About 2,500,000 Battle Dress uniforms have now been procured. These provide troops with far better camouflage protection, both day and night, than they received in the past.

REFERENCES

1. College Dictionary, The Random House, New York, 1980.

2. Cottington, D.C., C. H. Ulrich and R. M. Wroblewski, MASSTER Camouflage Evaluation Program, Phase II; Verdant Camouflage Uniform Pattern Evaluation, MASSTER Test Report No. FM204B, Modern Army Selected Systems Test, Evaluation and Review, Ft. Hood, TX 76544, 21 Nov 75. AD-B008 620.

3. Munsell Book of Color, Macbeth Corporation, Newburgh, N.Y.

4. Judd, D. B. and G. Wyszecki, Color in Business, Science and Industry, John Wiley, New York, 1975.

5. Ramsley, A. O., Selection of Standard Colors for the Woodland Camouflage Pattern, NLABS/TR-81/030, NLABS, Natick, MA 01760, Sep 81. AD-B060 496L.

6. Wyszecki, G. and W. S. Stiles, Color Science, Wiley, New York, 1967.

7. Konig, A., Uber den menschlichen Sehpurpur und seine Bedeutung fur das Sehen, Sitzungsber. K. Preuss. Akad. Wiss. 30, 577-598 (1894).

8. MacAdam, D. L., Small field chromaticity discrimination, J. Opt. Soc. Amer., 49. 1143 (1959).

9. Blackwell, R. H., Contrast thresholds of the human eye, J. Opt. Soc. Amer., 36, 624 (1946).

10. Judd, D. B. and G. T. Yonemura, Target conspicuity and its dependence on color and angular subtense for gray and foliage surround, NBS Report No. 10130, National Bureau of Standards, Washington, Nov 69.

11. Csorba, I. P., Recent advances in image intensification: the generation 3 wafer tube, Applied Optics, 18, 2440 (1979).

12. Wiza, J. L., The microchannel plate, a shift to III and new terrain, Optical Spectra, 15, 58 (4 April 1981).

13. Ramsley, A. O., Camouflage of the Individual Soldier at Night, Tech. Rpt. 68-37-CM, NLABS, Natick, MA 01760, March 68 (AD 831 971).

14. Stark, A. M. and B. W. Manley, Feasibility Study of Emissive-Conductive Photocathode, CVD, Terminal Report, Feb 1964 (AD 441 168).

15. Hewlett-Packard Co., One-micron Photodetector, USAERDL, Ft. Belvoir, VA 22060, Oct 1966 (AD 809 471).

16. Vatsia, M. L., U. K. Stich and D. Dunlap, Night Sky Stearance from 450 to 2000 nanometers, Rept. No. ECOM-7022, US Army Electronics Command, Ft. Monmouth, NJ, Sep 72 (AD 750 609).

17. Krinov, E. L., Spectral Reflectance Properties of Natural Formations, Aero Methods Laboratory, Academy of Sciences, USSR, Translated by E. Belkov, National Research Council of Canada, Technical Translation 439, Ottawa, 1953 (AD 113 260).

Laser Flash Effects: A Non-Visual Phenomenon? (U)

*DAVID I. RANDOLPH, Ph.D, ELMAR T. SCHMEISSER, PhD., CPT MS
& EDWIN S. BEATRICE, M.D., COL MC
Letterman Army Institute of Research
San Francisco, CA 94129

Ruby and neodymium laser rangefinders, ground locator-designators and other devices which emit short (20 nsec) high energy flashes of laser radiation are currently being deployed to troop units in the field. Evidence of the effects of short laser pulses delivered in known quantities and spot sizes on the human retina has been limited to the treatment of proliferative diabetic retinopathy or other clinical states which involve abnormal ocular conditions(1). In these cases, the bulk of the laser energy is directed to the peripheral retina and, when necessary, to the capillary-free zone of the macula. No exposures are placed in the central fovea where visual acuity is best. The soldier using binoculars or other optical sighting devices in the combat environment would receive a laser flash directly in the fovea.

Research on flash effects with human subjects has been generally limited to white light, non-laser sources with large retinal spot sizes (2). The immediate effects upon the vision of individuals who receive foveal laser exposures (minimal spot size) is unknown. It is thus important to be able to predict accurately the biological and functional effects of these exposures, delineate the physical and physiological parameters and recommend a course of treatment for those thus exposed. Ultimately, these data should lead to techniques for preventing debilitating laser bioeffects.

Laser energy levels, wavelength, size of the affected area, pulse length, pulse repetition rate and other physical variables have been related to changes in the eye and skin since the mid 1960's (3,4)and have been primarily concerned with both gross and microscopic alterations in the tissue. Based upon these changes, inferences have been made about the functional effects, i.e. a lesion in the retina implied a loss of vision at that site.

In order to quantify the implied loss of vision, non-human primates have been trained to respond to acuity criteria for high and low stimulus contrast targets. Robbins et al (5) reported immediate (within 2 min) high target contrast visual acuity decrements in the rhesus monkey following foveal exposure to 100 msec pulses of helium-neon (633 nm), krypton (647 nm) and argon (514 and 488 nm) laser lines. The spot sizes varied between 150 and 300 µ. Recovery occurred after approx. 5 minutes. Similarly, Zwick et al (6) found decrements in both the high and low contrast visual acuity of trained rhesus monkeys within the first 2 to 3 min following exposure of the foveal area to a 532 nm Q-switched pulse. The laser had a repetitive pulse rate of 10 to 20 Hz, and produced minimal (50 µ) foveal lesions. They reported acuity recovered in 5 to 15 minutes following exposure. Merigan et al(7) showed that destruction of the fovea resulted in the loss of fine acuity at high luminance levels in the rhesus monkey. At lower target luminosity and for larger targets, no decrease in performance was noted. In a series of experiments designed to determine the effects of flashblinding stimuli upon the ability of both humans and rhesus monkeys to maintain compensatory tracking, Callin et al (8) reported that for the stimulus conditions (100 msec tungsten halogen flash and 20.7 µJ/flash), the average recovery time for each species was approx. 3 sec. A second study by this group using green or white (multiwavelength) laser pulses found no consistent effect upon tracking performance. The average flash recovery in those animals showing some disruption was approximately 2 sec. This was attributed solely to startle responses of the animals. Another interpretation of these data is that the fast recovery times exhibited by their trained animals was the result of the animal's ability to use parafoveal cues in tracking. This thus negated the central field flash effect. One method of determining foveal flash effects is to measure indirectly the integrity of the central retinal area by evaluating the cortical response to a pattern visual stimulus before and after a foveal laser exposure.

The pattern visual evoked potential (VEP) is an electrical response to a shifting stimulus composed of alternating light and dark bars recorded at the cortex. This potential primarily reflects activity in the fovea and the immediately surrounding macular area while suppressing perimacular involvement by insuring constant retinal illumination. Regan (9) has shown that the response of the electroencephalogram (EEG) to an alternating stimulus is one of entrainment of this signal at the alternating frequency. This phenomenon requires several seconds to appear following the onset of the stimulus. One hypothesis for this phenomenon is a neural recruitment of the retinal elements at the cortical level. The cortical elements then become synchronized to the signal.

Differences between human psychophysical data and corresponding electrophysiological results have been noted; recovery of the VEP is much faster than psychophysical recovery after response suppression by adaptation in a contrast threshold task (10). However, direct comparison of psychophysical and electrophysiological measures of contrast thresholds demonstrates a high correlation and indicates that the evoked potential can be an accurate reflection of perceptual experience (11 - 14).

The purpose of this study was twofold. First, determine if foveal flash effects could be identified and quantified by using an electrophysiological technique. Second, delineate those combinations of variables, such as spot size and energy level, which would yield immediate and short-term changes in the visual system.

METHODS

Subjects: Nine eyes of seven cynomolgus (*Macaca fascicularis*) monkeys were used in the present study. The animals were sedated by intramuscular injection of ketamine HCl (10 mg/kg) and premedicated with atropine (0.008 mg/kg). An intravenous catheter was established to administer and maintain the dose level of the paralytic agent pancuronium bromide. The animal was intubated and breathing was maintained by a small animal respirator. The breathing and the electrocardiogram were monitored on a single channel of the physiological amplifiers throughout the experimental session. The eye of interest was dilated with 2% cyclopentolate HCl and 10% phenylephrine HCl. The animal was placed on an animal holder whose plane of rotation was adjusted to be in the center of the cornea of the experimental eye. The head was fixed and a lid speculum installed. Corneal clarity was maintained by frequent washes of normal saline (approx. every 10 sec). The unused eye was kept closed throughout the procedure. At the conclusion of the experiment, the paralysis was reversed with neostigmine and atropine.

Apparatus: Figure 1A is a diagram of the system used in this study. A Holobeam Series 300 Q-switched Ruby laser operating at 694.3 nm with a pulse width of 20 nsec was coaxially aligned to the optics of a modified Zeiss fundus camera. Two spot sizes and two energy levels were chosen. The low dose level for minimal (50 µ: 0.2 degrees [°] visual angle) and large (500 µ: 2.0°) spot sizes were 18 and 178 µJ total interocular energy as measured at the cornea (TIE) respectively. At the higher dose level the TIE for the 50 and 500 µ retinal spot sizes were 39 and 422 µJ respectively. The fundus camera modification (Fig. 1B) consisted of a linear motion motor mounted on the side of the camera's optical system. The motor drove a high contrast square wave grating of either 1.6 or 2.8 cycles/degree visual angle in a square wave mode at 7 shifts/sec (3.5 Hz) in a focal plane conjunct with the retina. The normal field of view of the fundus camera is 30°. This was modified by the introduction of a field stop in the camera's final common path which reduced the projected grating to a stimulus diameter of 3.6° centered on the fovea. The VEP was recorded by a single subdermal needle electrode placed 1 cm superior to the inion and lateral to the midline referenced to linked ears. The

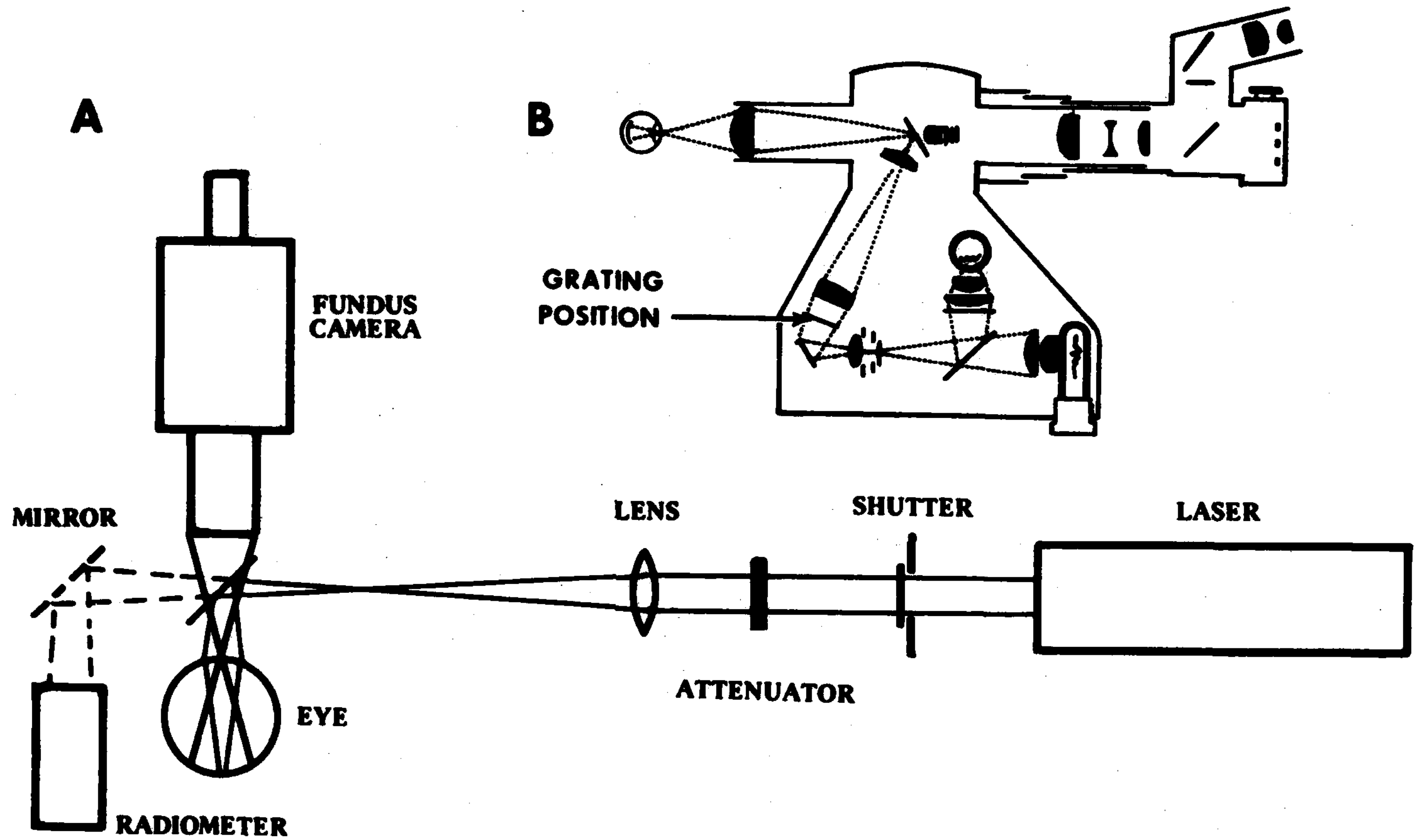

FIG. 1.A. Laser and stimulus system arrangement. B. Fundus camera diagram showing the position of the grating transparency.

signal was processed by a Grass 7P511 physiological amplifier. This signal was then recorded on FM magnetic tape while being analyzed on-line by a Nicolet MED-80 computer system and a PAR Vector Voltmeter. Off-line analysis was performed by playing back the taped signals into the MED-80 and/or Vector Voltmeter.

Procedure: The fovea was aligned with a reticle in the fundus camera field of view and the grating was focused onto the retina. Baseline VEPs were recorded in response to the oscillating grating. At this time, the aperture, if used, was introduced and further baseline data were obtained. During the stimulation, one or more single laser exposures was made to the fovea. Four measures of changes in the steady-state VEP were used, in addition to on-line observation of the averaged potential over short epochs. These measures were phase, magnitude, Pearson product moment correlation and the average standard deviation. Phase and magnitude traces were obtained by processing the VEP through the Vector Voltmeter synchronized with the 7 alteration/second grating stimulus. Changes in response phase reflect a change in the synchronization of the VEP and infer a loss of the ability of the visual system to follow the repetitive stimulus. The magnitude reflects the amplitude of the EEG component at the stimulation frequency. The Pearson correlation coefficient measure was obtained by comparing a pre-exposure averaged VEP (baseline) with sequential averaged VEPs (seven second epochs) recorded during the session. The correlation coefficient will theoretically approach 1.0 when the pre- and post-exposure VEP frequency elements show no difference in relative amplitude and phase. This measure is independent of absolute amplitude and ignores DC shifts. The average standard deviation measure is a mean variability estimate in relative units of the VEP processed in 11 sec bins (7 seconds averaging and 4 sec analysis time).

RESULTS

In the present study, under all of the stimulus and laser combinations: grating size (1.6 and 2.8 cycles/degree), field angular subtense (30° and 3.6°), high and low energy with large and small spot sizes, no immediate change in the VEP (i.e. within the first 5 sec) were observed. Neither were any long term effects noted for those conditions in which minimal spot, low or high energy flashes were combined with large stimulus field sizes (5 eyes). However, marked changes occurred in the VEP as the post-flash interval increased for those conditions in which the high energy, large spot size and/or small stimulating field was used (4 eyes).

Data are shown in Fig. 2 for four animals under four different sets of conditions. The first trace shows phase changes in the VEP of monkey B2. A 30° stimulus field produced a relatively stable phase locked response. The animal received a foveal exposure of 500 μ at 422 μJ, TIE.

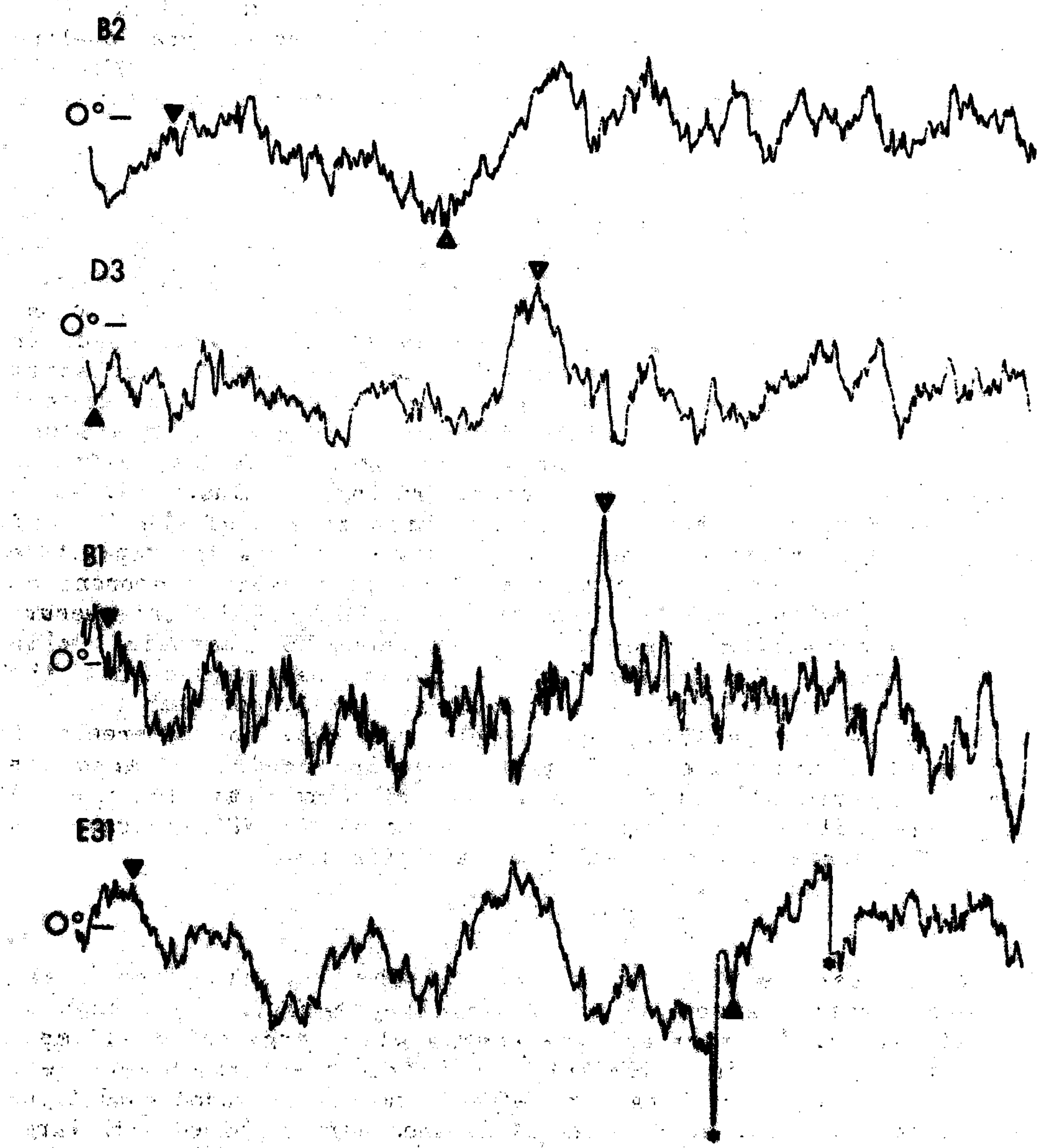

Fig. 2. Phase recordings from the vector voltmeter for 4 animals. Dark triangles indicate laser exposure; light triangles indicate response. Asterisks on trace E31 indicate manual shift into and out of the neighboring phase quadrant. Total time of traces is 204 sec. See text for description.

Little change in phase (digitized at 200 msec per point) was observed immediately after exposure. A later shift of 200° was noted which began approx. 45 sec after exposure and continued for 15 seconds. The second trace illustrates the response of monkey D3 to a Q-switched laser flash of low intensity (18 µJ) and minimal spot size (50 µ) with a test field of 3.6°. A large 90° phase shift occurred 90 seconds after the exposure. When the spot size of the laser exposure was increased to 500 µ (monkey B1) the 178 µJ T.I.E. flash produced a large sharp phase shift of approx. 180°, 106 seconds after the flash. The VEP quickly became resynchronized in this monkey and no further changes were observed. An increase in the laser energy to 422 µJ for the 500 µ spot size, 3.6° stimulus field condition produced a very large (approx. 250°) phase shift, 130 sec after the exposure (monkey E31). The asterisks in this trace mark the manual repositioning of the trace.

In addition to phase, three other measures of the changes in the VEP were recorded. These are shown in Fig. 3 for monkey D3. The first trace is a measure of the relative magnitude of the stimulus locked component of the VEP recorded simultaneously with the phase, phi (amplified from D3, Fig. 2). The point at which the magnitude approaches zero corresponds to the maximum of the phase shift. Line 3 shows the Pearson correlation coefficients for this epoch of data. A large decorrelation can be noted at the same time as the phase and magnitude shifts. The line marked sigma in Fig. 3 represents the variability of the VEP expressed as the mean of the standard deviations of the time-locked VEP 7 sec bin. The increased variability coincided with the shifts in magnitude, phase and correlation indices.

DISCUSSION

In the present study, little or no immediate flash effects were seen under any of the conditions used in this experiment. We have assumed that the VEP represents an ongoing, entrained response of the visual system to foveal events. Since we produced a visible change in the fovea with a Q-switched pulse, we would have expected to observe an immediate change in the VEP. This observation plus the fact that we observed a delayed change in the VEP leads to several possibilities. First, as Callin (8) has pointed out in his three studies of compensatory tracking performance, the flashes of laser light produced a momentary (2-3 sec) startle effect followed by a return to normal tracking behavior. In the curarized animal, this startle response would be absent. In Callin's (8) experiments, the animal's total tracking time was only 45 sec whereas in the present study, the effects did not appear until after 45 sec had passed. In addition, the data in the present study, as shown in Figs. 2 and 3, were recorded with time constants of sufficient length so as to mask a short 2-3 sec transient event.

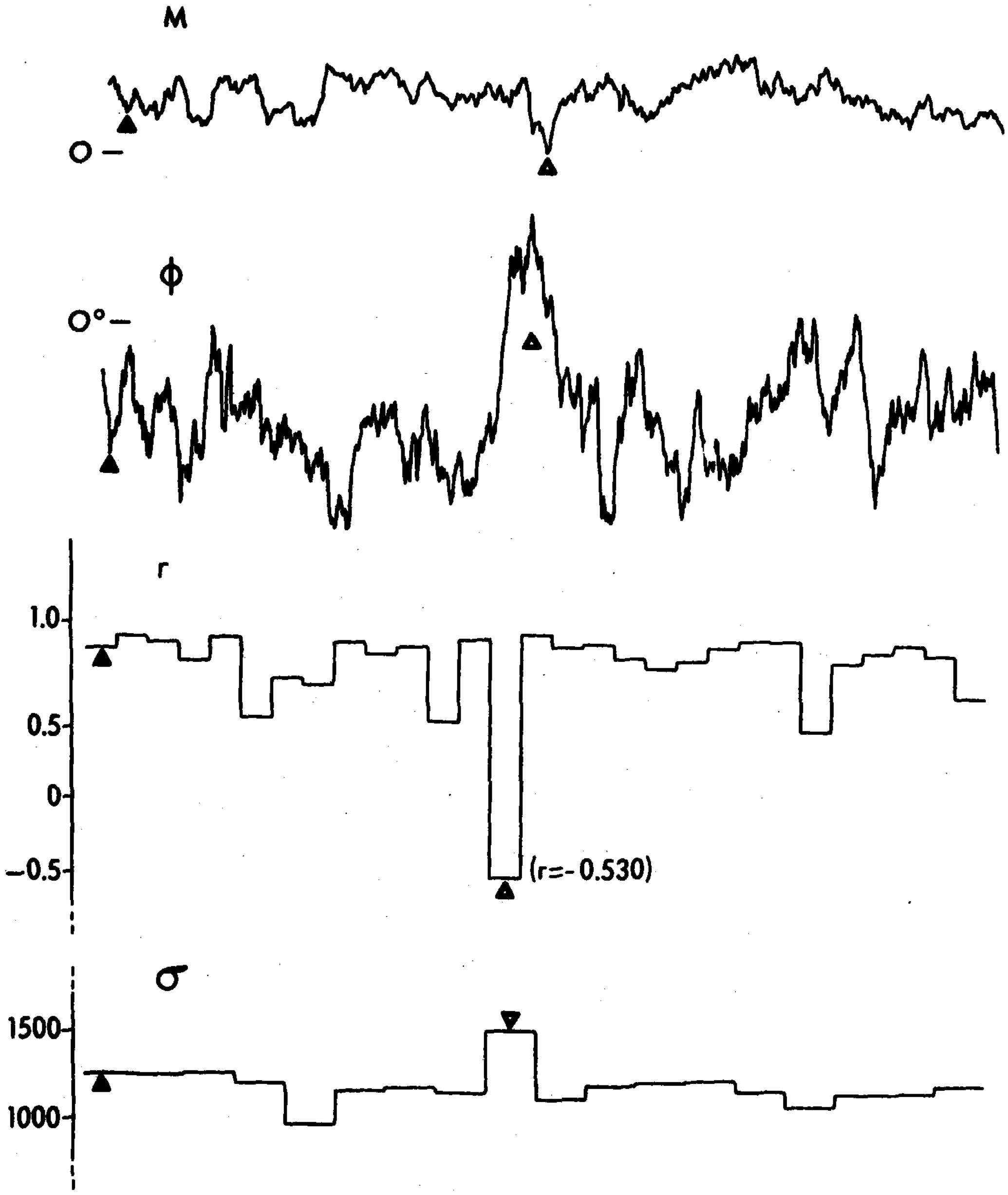

Fig.3. Analysis of animal D3 VEP. Magnitude (M), phase (phi), Pearson correlation coefficient (r) and average standard deviation (sigma) are shown. Dark triangles indicate laser exposure; light triangles indicate response. Total time of trace is 204 sec. See text for description.

Second, Zwick et al (6) showed data in which retinal lesions were produced by flashes resulting in visual acuity loss for considerable periods of time. Their immediate post exposure measures were the average of the first 2-3 min post flash acuity data and thus do not reflect the nearer term continuous monitoring of the retino-cortical response system. The perturbation reported in this paper may thus reflect the neurologic beginning of the phenomenon which was observed as an acuity decrement.

Third, the short Q-switched pulse may not have been sufficiently long to produce a measurable flash response. In the earlier studies (5,6,8), longer (100 msec) single pulses were placed in the fovea. In another study (7) the Q-switched 20 nsec pulses were delivered in a 120 msec train at a rate of 10 to 20 Hz. While a VEP response to the flash itself may have been present, it may not have been of sufficient duration or persistence to be detected.

A fourth consideration is the effect of the wavelength of the flash upon the response. The Q-switched ruby laser pulse produces a 694.3 nm pulse which is near the spectral perceptual limit of the primate visual system. Randolph (15) has shown that flash blindness production was far inferior for a red (620 nm) source than for blue, green or white light flashes of equivalent energy. The studies previously cited used visible wavelength flashes closer to the peak of visual sensitivity. Thus the wavelength of the flash source may have contributed significantly to the lack of any immediate response.

Fifth, while the higher energy laser flashes at both the 50 and 500 μ spot sizes produced visible alteration at the exposure site, the changes observed may have been limited to the non-visual cell layer, the retinal pigment epithelium, with little accompanying effect upon vision as measured by the VEP.

While all of the aforementioned factors may have contributed to the finding of no immediate VEP response differences, the nature of the delayed response is such as to suggest a dual mechanism. Initially, edema develops at the site of the laser injury and extends laterally. The delayed effects noted in this study may reflect the disentrainment or desynchronization of the cortical response due to the mechanical displacement of the retina by edema. The subsequent recovery of the response indices may reflect the re-entrainment of the cortical elements due to recruitment among surviving retinal elements and may be independent of possible changes in visual acuity i.e. a non-visual phenomenon.

CONCLUSIONS

The 20 nsec Q-switched ruby laser exposures centered on the fovea produced no immediate changes in the grating visual evoked potential for

50 and 500 µ spot sizes at two energy levels even when visible changes occurred at these sites.

The findings may have been the result of the ruby laser wavelength, which was near the visual sensitivity limit of the eye, or of the single Q-switched pulse which may have occurred too quickly to produce an immediate and/or sustained change in the cortical response.

The observed delayed effects and subsequent apparent recovery of the VEP may reflect the development of edema at the laser exposure site resulting in the desynchronization of the response for a period of time. This is followed by apparent recovery which was interpreted as recruitment of the spared retinal elements with subsequent neural re-entrainment at the cortical level.

REFERENCES

1. Diabetic Retinopathy Research Group (1981) Report No. 6: Design, methods and baseline results Invest. Ophthalmol. Vis. Sci. 21/1:1-109.

2. Davies J.M. & Randolph D.I. (1967) Proc. U.S. Army Natick Laboratories Flashblindness Symposium, Armed Forces-NRC Committee of Vision, Washington D.C.

3. Lund D.J., Stuck B.E. & Beatrice E.S. (1981) Biological research in support of project MILES. Institute Report No. 96, Letterman Army Institute of Research, Presidio of San Francisco, CA 94129.

4. Stuck B.E., Lund D.J. & Beatrice E.S. (1978) Repetitive pulse laser data and permissible exposure limits. Institute Report No. 58, Letterman Army Institute of Research, Presidio of San Francisco, CA 94129.

5. Robbins D.O., Zwick H. & Holst G.C. (1973) A method for producing foveal retinal exposures in an awake, task oriented rhesus monkey. Behav. Res. Meth. Instr. 5: 457-461.

6. Zwick H., Bloom K.R., Lund D.J. & Beatrice E.S. (1982) Laser ocular flash effects. In: Proc. Army Sci. Conf. DA-OCRD, West Point, NY, (this volume).

7. Merrigan W.H., Pasternak T. & Zehl D. (1981) Spatial and temporal vision of macaques after central retinal lesions. Invest. Ophthalmol. Vis. Sci. 21:17-26.

8. Callin G.D., Devine J.V. & Garcia P. (1981) Visual compensatory tracking performance after exposure to flashblinding pulses:I,II & III. Report SAM-TR-81-3, -7, -8, USAF School of Aerospace Medicine, Brooks Air

Force Base, TX 78235.

9. Regan D. (1977) Steady-state evoked potentials. J. Opt. Soc. Am. 67:1475-1489.

10. Mecacci L. & Spinelli D. (1976) The effects of spatial frequency adaptation of human evoked potentials. Vision Res. 16:477-479.

11. Bodis-Wollner I., Hendley C.D. & Kulikowski J.J. (1972) Electrophysiological and psychophysical responses to modulation of a grating pattern. Perception 1:341-349.

12. Franzen O. & Berkeley M. (1975) Apparent contrast as a function of modulation depth and spatial frequency: A comparison between perceptual and electrophysiological measures. Vision Res. 15:655-660.

13. Adachi-Usami E. (1979) Comparison of contrast thresholds of large bars and checks measures by VECPs and psychophisically as a function of defocusing. Albrecht v. Graefes Arch. klin. exp. Ophthalmol. 212:1-9.

14. Kojima M. & Zrenner E. (1980) Determinations of local thresholds in the visual field by recording the scotopic visually evoked potential in man. Ophthalmic Res. 12:1-8.

15. Randolph D.I. (1967) Electroretinographic and behavioral recovery time of cats to high intensity photic stimulation. In reference 2, pp 164-185.

In conducting the research described in this report, the investigation adhered to the "Guide for the Care and Use of Laboratory Animals," as promulgated by the Committee on Revision of the Guide for Laboratory Animal Facilities and Care, Insitute of Laboratory Animal Resources, National Research Council.

ACKNOWLEDGMENTS

The authors wish to thank SP6 Sharon L. Velez for her outstanding assitance in the preparation and monitoring of each animal, and to Ms Gail Escandarian for her assistance in the alignment and calibration of the laser.

VOICE INTERACTIVE SYSTEMS TECHNOLOGY AVIONICS (VISTA) PROGRAM (U)

LOCKWOOD W. REED
US ARMY AVIONICS RESEARCH AND DEVELOPMENT ACTIVITY
FORT MONMOUTH, N.J. 07703

INTRODUCTION

As the complexity of aircraft missions increases, there is a commensurate increase in the number of functions and operations to be performed by the pilot and crew of a given aircraft. Recently, military single-seat rotary aircraft have been proposed, compounding the problem of the man-machine interface.

This problem can be significantly reduced if the following three basic requirements can be satisfied: (1) the pilot can maintain hands on flight controls throughout the entire operation of the aircraft (2) the pilot's visual attention can be directed toward the flying of the aircraft (particularly important for Nap-of-the-Earth flight) (3) the pilot can still control all necessary aircraft subsystems under the conditions of (1) and (2).

Preliminary investigations by the Avionics Research and Development Activity (AVRADA) and many other governmental and industrial concerns have indicated that an integrated system of voice recognition and voice response can meet all the above requirements.

In order to investigate the potential advantages of Voice Technology, AVRADA has initiated a program entitled Voice Interactive Systems Technology Avionics (VISTA). The VISTA program is taking a phased approach to the introduction of voice recognition and response equipment into Army aircraft. Before detailing the phases of the VISTA program it would be appropriate to describe here the AVRADA facilities which will support the VISTA program. AVRADA maintains an extensive Computer aided Design and Audio Analysis Laboratory. The Audio Analysis Laboratory consists of two sound chambers (one Anechoic Fig 1, and one Sound Absorption Fig 2).

Each chamber is tied via audio signal and digital data lines into the test equipment rack (Fig 3) which contains signal measuring amplifiers, two audio spectrum analyzers, various filters and equalizers, and audio recording equipment. The equipment in the test rack is in turn connected to the main laboratory computer system (Fig 4) consisting of a 16-bit mini-computer, 17 terminals, line printer, parallel I/O to test equipment and 80 mbyte disk drive, and a high speed array processor. AVRADA's Audio Analysis laboratory contains one of the most extensive libraries of Army aircraft noise environment tape recordings. The recordings were taken in the field at various Army installations using AVRADA's portable audio analysis equipment which consists of a precision portable audio recorder, sound level meter with 1/3 octave and narrowband filter sets and strip chart recorder. Recordings were made in several OH-58, UH-1, AH-1, CH-47, OV-1D, CH-54, and a UH-60 aircraft in various modes of flight from hover to tactical maneuvers.

VISTA PROGRAM

The first phase of the VISTA program (Fig 5) consists of writing software for our in-house computer systems to aid in the testing and evaluation of voice recognizers (the software will be discussed in greater detail under test procedures), and the evaluation of selected off-the-shelf voice recognizers. The use of off-the-shelf recognizers has a twofold benefit. First, testing procedures applicable to all recognizers can be developed economically, and secondly, the performance of off-the-shelf recognizers can yield baseline cost/performance information to which more sophisticated recognizers can be compared. Recognizer testing during phase one will be performed exclusively in the Audio Analysis Laboratory. Testing in the aircraft will be limited to the generation of recognizer training/test tape recordings made in the aircraft to be used as a validation check on the accuracy of the chamber tests.

As the recognizer test/evaluation software and procedures are finalized, phase II of the VISTA program will begin (Fig 6). Phase II involves applying the testing software and procedures developed during Phase I to more sophisticated (and more costly) commercial and non-commercial voice recognizers. In addition, since high ambient noise is a prime concern for any attempted installation of voice recognition equipment in Army aircraft, testing will be performed by front-ending the above recognizers with off-the-shelf noise reduction devices in addition to the various noise canceling microphones already in use.

As the predictability of various voice recognizers is established, Phase III (Fig 7) of the VISTA program will begin with the installation of selected recognizers in AVRADA's Systems Testbed for Avionics Research (STAR) aircraft. The STAR aircraft (Fig 8) consists of a UH-60 helicopter modified to include a MIL-STD-1553 data bus, and various avionic subsystems (i.e., radio, navigation, night pilotage, etc.), all of which are connected to the common 1553 data bus. Sound recordings and measurements have been made in this aircraft and are being used in chamber environment simulations of the aircraft. Figure 9 shows the acoustic frequency spectrum taken in the aircraft at two locations, the cockpit and midship. The sound level has been measured at 103 db on the A weighted scale in the cockpit and 107 dBA amidships. Testing in the STAR aircraft will primarily be directed toward applications and operations for voice recognizers in the aircraft. To obtain meaningful results from the testing it will be necessary for the recognition equipment to be integrated into the aircraft data bus and to have access to all subsystems. To accomplish this and still have the flexibility of evaluating many different types of recognizers, a problem is created since most non-commercial and all commercially available recognizers do not have any MIL-STD-1553 data bus interface.

The approach taken to solve the problem is to install a general-purpose militarized computer (Fig 10) which will serve many functions. First, the computer will act as an intelligent interface providing the MIL-STD-1553 bus interface hardware and the data bus control software for the aircraft side of the integration. Second, since the large majority of commercial and non-commercial recognizers communicate via RS-232 or RS-422 hardware, the computer will provide several of these interfaces. Third, the operating system software of the computer will be designed so as to minimize the impact of changing from one recognizer to another. Fourth, the computer will contain all the software for a given control scenario. As an illustration, the use of a recognizer to control the onboard radios will be totally controlled by the computer. At any point in the scenario the computer will restrict the recognizer to a specific subset of its vocabulary to reduce the chance of false recognitions. When an utterance is made and the recognizer outputs its best guess, the computer will decide what to do with the response, what equipments are to be affected, and what 1553 data bus message will be sent. By dividing a control scenario into specific software modules keyed to generic recognizer responses, minimal impact on the computer software is achieved when changing voice recognizers. Only that software which extracts the generic information from a particular recognizer message need be changed.

To complement the contribution of the industrially available recognizers to the VISTA program, work will begin in house during Phase IV (Fig 11) to develop and test voice recognition and noise cancellation algorithms tailored to the Army aircraft environment. The high speed array processor mentioned previously will be used exclusively for voice recognition and noise cancellation algorithm testing, to permit real time response.

The emphasis of the VISTA program has been directed toward the voice recognition problem because technically it is the more risky half of an integrated voice interactive system. However, voice response does present unique problems of its own primarily in the area of human factors. Technically there are many implementations of voice response available, each offering certain advantages. For the most part, the selection of a given voice response unit is a tradeoff between intelligibility and digital storage capacity but even here the technology is converging in that new more memory efficient encoding algorithms are being developed and less expensive higher density memory chips are continually being introduced. The VISTA program is addressing voice response as an integrated complement to voice recognition. Presently a speech synthesizer is interfaced into AVRADA's computer facility for applications testing in the noise environment. The specific synthesizer used was selected for its ability to be programmed in-house. To this end a program was written (referred to as a Speech Editor) which enables various vocabularies to be stored on disk. These vocabularies can be accessed by several programs for intelligibility testing and applications testing in conjunction with the voice recognition equipment. Beginning in Phase III, various voice response units will be evaluated for intelligibility. Much of this intelligibility information should be available to the VISTA program through other Tri-Service efforts. The VISTA program will initially evaluate the available voice response intelligibility data for its application to the Army noise environment. Where data is still needed regarding the Army specific acoustical environment (i.e., radio and intercom systems as well as noise), the necessary testing will be performed under the VISTA program.

VISTA VOICE RECOGNIZER TESTING TECHNIQUES

At present the formulation of standards for recognizer testing is in its infancy and as yet no established recognizer testing standards or criteria exist. One of the chief difficulties in the formulation of standards for recognizer evaluation has been the determination of what criteria will yield meaningful information about the performance of voice recognizers in many diverse environments. This, unfortunately, creates the classic "chicken and the egg" problem for those who wish to apply this technology. The VISTA approach has been to devise a series of test and evaluation procedures applicable to the Army aircraft environment.

Figure 12 shows the typical test setup for recognizer testing. Recordings of aircraft noise are equalized and played into the sound absorption chamber. The output of a precision microphone, located in the chamber, is fed into a measuring amplifier and a spectrum analyzer to make adjustments in overall intensity and spectral content. The voice recognizer and a CRT terminal located in the chamber are connected to the Interactive Graphic Host Computer. Specialized software running on the host computer performs applications testing of the recognizers and recognizer comparative testing. Test results are then printed on the line printer.

The initial voice recognizer testing is limited to the two modes of recognizer operation--Unrestricted Vocabulary Search (UVS) and Restricted Vocabulary Search (RVS). UVS involves computer software which prompts the test subject (via CRT) with each word of a selected vocabulary. The computer permits the voice recognizer to search its entire vocabulary for a best match based on a predefined recognition threshold. If the utterance does not exceed the recognition threshold for any of the stored vocabulary words, a reject response is output from the recognizer to the computer. Likewise, if the voice recognizer perceives the utterance as noise, an appropriate response is output to the computer.

All responses generated by the recognizer are stored in a disk file. The RVS involves an Applications Simulation Program (ASP) running on the host computer. The ASP controls the voice recognizer as it would be in an actual aircraft application (i.e., radio control, navigation control, etc). At any point in the scenario the ASP restricts the voice recognizer to a specific subset of words in its vocabulary. Using radio control as an example, the ASP initializes to a command mode in which the user may request the status of a given radio. In command mode the recognizer is restricted to matching only those words which designate the various radios. At this point in the scenario it is neither necessary nor desirable to have the recognizer attempt to match an utterance to any other portion of the recognizer vocabulary. In actual field operation restriction of the vocabulary will decrease the occurrences of false matches by the recognizer and hence increase the reliability of the entire system. The RVS testing will give a measure of the relative reliability between restricted and unrestricted vocabularies as well as a closer measure of the performance which can be expected from a given recognizer in the field.

The following discussion describes a typical test session, delineating the test parameters and test results.

Radio control was selected as a candidate application because of the level of tasks to be performed and the fact that it is a non-flight control critical operation. Having selected radio control, the tasks to be performed were delineated and two basic functions were selected: the cycling of power and the selecting of frequency to a specific radio. The typical Army aircraft complement includes four radios: two VHF FM radios; one VHF AM radio and one UHF AM radio. Based on the above information, a vocabulary for the recognizer was devised (see Fig 13). It should be noted that the selected vocabulary contains two utterances which sound alike except for their endings ("Foxmike 1" and "Foxmike 2") and two utterances sound similar ("Victor" and "Enter"). These words were chosen to yield some information concerning the critical nature of sound alike words. Training patterns using the vocabulary of Figure 13 were made for several test subjects under four different conditions. The four conditions involve the use of two different microphones and training the recognizer with each microphone in the "Quiet" and in the "Candidate noise" environment. The noise environment selected for all training and testing is that of the UH-60 Black Hawk (the STAR testbed aircraft, see Fig 14). The training program resident on the host computer guides the test subject through the training process. After training is completed, the voice pattern stored in the recognizer is up-loaded into the host computer by a program called VOXDSK. VOXDSK handles all up-loading and down-loading of voice patterns.

Incorporated into VOXDSK is a mandatory request to the operator for header information concerning the test subject (Fig 15). The information includes the subject's name, the creation date and time of the voice pattern files, the condition of the test subject, the test conditions, the type of recognizer, the number of training passes and the number of words. VOXDSK reads the header file created by the operator and checks it for the required information. When VOXDSK is satisfied, it creates a composite file which includes the test subject header and the voice pattern (Fig 16). This self-documentation approach insures the traceability of voice pattern history and will minimize errors due to the incorrect use of voice pattern files. Having trained the recognizer, the testing procedures can now begin. This paper will be limited to a discussion of the procedures and preliminary results of the Unrestricted Vocabulary Search tests. The first step in the testing procedures is to create a test header file. This file is similar to the training header file except it refers to the specific test conditions which may be different from the training conditions. If a question mark is inserted into any information field (i.e., the "Date.Time" field) that data will be automatically requested from the operator at test time. Both the training and the test result files are uniquely numbered by a six-digit date field followed by a four-digit 24-hour time field separated by a period. When the test program runs, it creates a test results file. The operator is then prompted to enter the time of the test; the test program then looks up the voice pattern file used in the test and appends the training header to the test header in the test results file. For the UVS testing the subject is prompted, via the CRT, by the host computer with the vocabulary of Figure 13 stored in a prompt file. When the test subject responds to the prompt, the recognizer outputs its best match response (or no match response, if below the rejection threshold or noise) to the host computer. The host computer outputs all recognizer responses to the test results file for later comparison. When the data in the prompt file is exhausted, the testing program terminates. A comparison program automatically initiates at the termination of the test program and outputs all the header information contained in the test results file to the line printer; the program then begins comparing the response data in the test results file to the original prompt file. The results of the comparison are output to the line printer along with three columns of information (Fig 16). The information includes: an accuracy column with the number and percentage of totally correct responses; a reliability column which contains the number of totally correct responses plus the number of negative responses (a negative response is one in which either the recognition threshold is not exceeded or the recognizer perceives noise) and the percentage of same; and a latency column which is the difference information between reliability and accuracy. Because Reliability combines the total number of correct responses with the total number of negative responses it yields the percentage of the time (based on usage) the recognizer will not get the aircraft into trouble by going into the wrong mode of operation. The latency data yields the percentage of time a response would have to be repeated.

For the radio control vocabulary, an entire test run can be completed in an average of one minute and thirty-five seconds. For the same test conditions ten contiguous runs are performed by the computer in a total time of approximately 16 minutes. It is evident that, due to the rapidity of the testing procedures, many test condition variations can be tried in a relatively short period of time.

TEST RESULTS

The following discussion will be limited to the preliminary tests which were performed using the UVS technique. The results of those tests are summarized in Figures 17 and 18. The following conditions were adhered to for all testing: UH-60 noise at 103 dBA (Fig 17) and 107 dBA (Fig 18); microphone position just brushing the test subject's lips; the recognizer connected to the standard Army aircraft intercom system; the vocabulary of Figure 13 trained with five passes per word; approximately one second delay between word prompts; and a recognition threshold of 105 (NOTE: Each pattern is composed of 128 bits; a recognition threshold of 105 would require the recognizer to match 105 of 128 bits before outputting a match response).

The test results of Figures 17 and 18 represent the compilation of up to eighty tests per subject (10 iterations per test condition). They are ordered from the highest to the lowest accuracy for each test subject. It can be immediately observed that for each test subject, the highest recognizer accuracy was achieved for the vocabulary trained in the actual noise environment. This confirms the results of similar tests performed in different environments by other agencies. Another important feature of the test results is that in all cases, the Electret microphone achieves the most accurate results when the vocabulary is trained in the noise and the least accurate results when training in the noise is not employed. This apparent paradox can be explained by comparing the frequency response characteristics of each microphone (Fig 19). The Electret microphone has a broader frequency response; therefore, the contribution of noise to the pattern generated by the Electret microphone is more significant than the same pattern made in the noise with the M-87 microphone. Although the wider frequency response of the Electret microphone passes more noise, it also passes a greater portion of the low-frequency spectrum. This appears to account for the Electret microphone producing the most accurate recognition results for every test subject. The apparent ability to trace recognizer performance to microphone characteristics does provide a means of test result validation. As the number of test subjects increases, particular attention will be given to see if this trend continues.

Even now, a deviation from this trend is used to prompt a reexamination of a test subject's training pattern for accuracy.

RESEARCH AREAS

In the near-term testing of the VISTA program, we will be concentrating on the following areas: the front-ending of recognizers with off-the-shelf noise cancellation devices; the significance of Army aircraft vibration on human speech; the establishment of a restricted vocabulary for near-term application; the electrically vs acoustically mixing of noise and speech for training purposes; and the effect noise has on the character of human speech. The latter research area will be a joint effort by the Army (AVRADA, Ft Monmouth) and the Navy.

To date, many different techniques have been developed for the cancellation of noise. Many of these techniques have resulted in a significant loss in intelligibility; however, this loss of intelligibility, while significant to a human listener, may not affect voice recognition equipment. The VISTA program will therefore investigate the effects of applying existing noise cancellation techniques to voice recognizers.

The use of a reference voice will play a significant role in the investigation of vibration on human speech. The reference voice will be created using a recording of a selected subject played back through an artificial voice transducer. This reference voice will be used for training as well as testing the recognizer. Recordings will be made of test subjects and the reference voice in both the chamber aircraft noise environment and the actual aircraft noise environment. Because in actual flight the reference voice will not be subject to vibration, it is hoped that a comparison of the various test results will yield meaningful and repeatable information regarding the effects of vibration.

AVRADA will maintain a complete electrical hot bench of the STAR aircraft. This will provide an ideal environment for meaningful human factors work directed toward the implementation of voice recognition equipment in the Army aircraft environment. It is AVRADA's desire to enter into a cooperative arrangement with other governmental human factors agencies whereby those agencies would utilize AVRADA's STAR hot bench and STAR aircraft to perform human factors analyses in a relevant Army aircraft environment. Through this human factors work, a restricted vocabulary for near-term applications will be defined.

Because of the high ambient noise found in Army aircraft, it is undesirable to require training in the noise. Therefore, experiments will be conducted in electrically mixing the noise with the speech in the quiet for recognizer training. The resulting test data will be compared to the same test conditions using training patterns made by acoustically mixing the speech with the noise at the microphone. Because the speech in the former case will be generated in the quiet, as far as the test subject is concerned, any effect the noise has on the speech will not be reflected in the electrically mixed voice pattern. To investigate the effect of noise on speech, experiments will be conducted by subjecting the test subjects to noise via a high-quality headset. Care will be taken to insure that the test subject hears the same level and balance of sidetone (subject's own voice) and noise in the headset. The subject's voice, which is now essentially in the quiet (because the only noise is in the headset which has minimal leakage), will be recorded and analyzed for aberations traceable to the effect of the noise. The intent of the speech analysis is to determine if an apparatus can be devised to artificially shape speech produced in the quiet, giving it the characteristics of speech produced in the noise.

CONCLUSION

Although the preliminary test results are encouraging, it must be remembered that they were taken under ideal conditions. For all testing, the microphone was positioned just brushing the test subject's lips; however, a test was run with one test subject placing the microphone approximately four millimeters from the test subject's lips. The test results showed a 50% decrease in recognition accuracy for the same conditions as those with a microphone touching lips. Although the results are preliminary, it is apparent that the signal-to-noise ratio is a key factor in recognition accuracy. Another problem arises because of the automatic gain controls (AGC) found in most aircraft intercom systems. When there is no voicing for a period of time, the AGC increases the intercom sensitivity. If the first utterance spoken is intended for the recognizer it will likely be rejected because of the distortion caused by the AGC adjusting the gain during the utterance. This is demonstrated in the test results of all test subjects. No attempt was made to set the AGC before beginning the test; as a result, 90% of the first utterances were rejected which resulted in the lowering of the accuracy score by approximately 4%. The AGC has a release time of 10 seconds and the prompts are issued every second; therefore, after the first utterance the AGC has little effect. Some side tests were performed by making an utterance before signaling the computer to begin the test, and in each case the accuracy of the first test word increased to a point comparable to the other vocabulary words.

The VISTA program is the first in-depth attempt to apply voice recognition and response to the Army aircraft environment. Participation by other governmental agencies is being sought for cooperative efforts utilizing AVRADA facilities for the application of this technology to the Army aircraft environment.

Differentiation of Peripheral and Central Actions of Soman-Produced Respiratory Arrest

*DANIEL L. RICKETT, Ph.D., MAJ, NELSON L. ADAMS, MR.,
KENNETH J. GALL, MR., THOMAS C. RANDOLPH, SFC,
AND SIEGFRIED RYBCZYNSKI, MR.
Neurotoxicology and Experimental Therapeutics Branch
US Army Medical Research Institute of Chemical Defense
Aberdeen Proving Ground, MD 21010

The primary cause of death following exposure to lethal concentrations of organophosphorus chemical warfare agents is generally conceded to be cessation of respiration. Respiratory arrest may be mediated by actions at sites both within the peripheral nervous system and the central nervous system (CNS). These include airway obstruction by secretions, laryngospasm, or bronchoconstriction, and respiratory arrest through neuromuscular blockade of the muscles of respiration or arrest of normal activity within those areas of the CNS which control respiratory function. Although it is technically feasible to protect against the lethal effects of exposure to relatively low levels of nerve agents, this protection is offered at the unacceptable cost of prolonged incapacitation following treatment, regardless of the extent of exposure. Absolutely essential to development of a maximally effective and a minimally debilitating pretreatment and therapy regimen is identification and understanding of the sites and mechanisms of action of these agents, as well as the relative contributions of these actions, in the generation of lethal and incapictating effects.

Conventional thinking regarding the actions of nerve agents is that these compounds exert their effects through accumulation of acetylcholine (ACh) as a result of inhibition of acetylcholinesterase (1, 2). There is disagreement regarding the relative importance of central and peripheral actions of nerve agents in the production of respiratory arrest. Examination of the early literature yields support for the notions that respiratory arrest results from either airway obstruction (3-6), peripheral neuromuscular blockade (7-9), or central respiratory failure (10-12). This early confusion was clearly instrumental in leading DeCandole and his associates (13) to examine the lethal actions of a number of organophosphorus compounds including DFP, soman, sarin and tabun in a wide variety of animals. The conclusion of this study was that central respiratory failure seemed to be the predominant feature in cessation of respiration. This finding was supported, with few exceptions, in the subsequent literature concerning the lethal contribution of central and peripheral actions of nerve agents (cf, 14-17).

Pyridostigmine, a quaternary cholinesterase inhibitor not thought to readily penetrate the CNS, has more recently been found to offer enhanced protection against the lethal effects of nerve agents (18). This has rekindled the question of the relative importance of central versus peripheral sites of action. Additionally a number of reports are at variance with the "cholinesterase inhibition -- accumulation of acetylcholine" hypotheses for generation of respiratory arrest. As an example, Adams, Yamamura and O'Leary (19) reported that (a) brain acetylcholinesterase activity was unrelated to spontaneous recovery of central respiratory drive in nerve agent exposed, artifically ventilated guinea pigs, (b) additional nerve agent challenge failed to reinstate central arrest following spontaneous recovery, (c) significant depression of neuromuscular function and diaphragmatic block required agent doses which were far greater than the LD_{50}, and (d) the central protection offered by atropine sulfate was overcome by challenge levels which were well below those required to significantly impair neuromuscular function.

The cholinosensitivity of pontomedullary respiratory-related units is questionable. For example, Salmoiraghi and Steiner and others(cf, 20-22) have generally found these cells to be relatively unresponsive to iontophoretically applied ACh although cholinergic markers have been found to bind in areas where these cells are found (23). Bradley and his associates (24) found, as did Salmoiragi and Steiner, that these cells were responsive to directly applied physostigmine and that this responsiveness was not correlated with the cells' sensitivity to ACh. This lack of relationship between a cholinesterase inhibitor and ACh in altering cellular activity suggests that cholinesterase inhibitors might be having direct actions not related to inhibition of acetylcholinesterase.

Perhaps the most convincing demonstration of the central actions of nerve agents was provided by Stewart and Anderson (25). Using urethane anesthetized rabbits, they produced respiratory arrest by directly injecting sarin into the brainstem. The quantity injected was as little as one microgram, bilaterally. Respiratory arrest was not produced if either of the bilateral injections missed the target sites in either a rostral or dorsal direction, or if the injections were placed medial to the target area. Respiratory arrest occurred only following the second bilateral injection. Although these findings clearly suggest that the sarin-sensitive areas are bilaterally discrete, these areas do not correspond exactly with respiratory control areas identified by either electrical stimulation (26) or by microelectrode recordings (27).

Previous reports of the significance of central and peripheral nerve agent actions have tended to focus on limited aspects of the challenge. That is, while alterations in phrenic nerve activity and neuromuscular function have been reported for the same animals, there have been no reports in which most of the major contributing factors have been simultaneously examined. Furthermore, since the 1950's the majority of reports in this area have included the use of therapeutic drugs at some point during the course of nerve agent exposure or the development of signs and symptoms. Mechanisms of action were often inferred from what was known about the pharmacology of these drugs in unchallenged animals. Since the present study was the first of a projected series of studies, it was decided to use an animal preparation which was as intact as possible and whose sensitivity to nerve agents was similar to that of primates. It was also decided that the use of medications, other than those necessary to prevent pain, would complicate the interpretation of results. As a result of these considerations and because of the already existing technical database, we have used the Dial-urethane anesthetized, acute cat preparation.

Multiple unit activity of medullary respiratory-realted units found in the dorsal and ventral respiratory groups was recorded to assess CNS actions. Cells in these two areas were examined since they control patterned activity of spinal cord motor neurons which project to respiratory musculature (28). Furthermore, the integrity of synaptic connections in these areas could not be assumed to be unaffected by agent exposure. Whole nerve recordings of the intact phrenic nerve were made using sleeve electrodes. These electrodes were placed around the phrenic nerve at its emergence from C5-C6, on the side contralateral to unit recordings since the majority of medullary respiratory efferents have crossed projections and since the phrenic nerve is the major motor nerve for inspiratory drive. Electromyograms (EMG) and contractions were recorded from the diaphrgm leaflet receiving innervation via the monitored phrenic nerve. In this manner we simultaneously sampled CNS activity, its elicited motor nerve discharge and the resultant diaphragmatic EMG and contraction.

In order to assess respiratory states, air movement was indicated and recorded by means of a thermistor placed in a tracheal cannula. Cardiovascular status was examined by recording arterial blood pressure and gases, as well as electrocardiograms (ECG). Rectal temperature was monitored and regulated within the normal range using a heating pad. All parameters, with the exception of blood gases, were recorded on FM tape at a 5.0 kHz bandwidth. Data were analyzed off-line using locally generated programs for Nicolet MED-80 and Digital PDP-11/34 computers.

Following surgical preparation of the cat and placement of electrodes and transducers, time was allowed for stabilization of the preparation. Control recordings of all measures were then obtained in order to establish baseline conditions. This was followed by recordings during saline infusion, as a control for agent vehicle and volume, at a rate of one ml per minute via the femoral vein. Soman was prepared such that a volume of 15 mls contained one LD_{50} and was infused via the femoral vein at a rate of one ml per minute.

At the time that soman administration resulted in cessation of spontaneous respiration, the phrenic nerve was stimulated using suprathreshold current pulses, 0.5 sec train of one msec pulses at both 10 and 100 Hz, in order to test the functional integrity of the neuromuscular junction. The cat was then artifically respired and either administered Flaxedil in a dose sufficient to produce neuromuscular blockade or soman infusion was continued at one ml per minute but at a concentration of one LD_{50} per five mls.

Phrenic nerve stimulation was repeated once following Flaxedil administration. This was followed by direct diaphragmatic stimulation in order to test the integrity of muscular response. In those instances when soman infusion was continued, phrenic stimulation was repeated following delivery of each additional LD_{50}. Soman infusion was stopped when the diaphragm was completely refractory to indirect, that is phrenic nerve, stimulation. If the diaphragmatic neuromuscular junction was not completely blocked after 20 LD_{50}'s of soman had been delivered, Flaxedil and phrenic nerve stimulation were administered as above.

Figure 1 illustrates an example of what was routinely seen in the 10 cats used in this study and shows airflow, diaphragmatic contraction, intergrated diaphragmatic EMG, and integrated phrenic nerve discharge. The amplitude of these responses is reported as a percentage of control value. The activity of an inspiratory unit is shown as an average spike frequency histogram. Respiratory-related units were classified as either inspriatory, expiratory or phase spanning by correlating their discharge pattern with phrenic nerve discharge (29). Phrenic input of inspiratory units was verified using spike-contingent averaging of phrenic activity. The data in Figure 1 were derived, after the method of Smolders and Folgering (30), as an average of five respiratory cycles in which the inspiratory and expiratory portions were each divided into 100 equal time bins for averaging . It should be noted that airflow is actually a measure of air temperature at the tracheal cannula and thus does not accurately reflect flow.

Figure 1 illustrates that after 2 minutes, 2/15ths of an LD_{50}, very little has happened to any of these parameters. However, after seven minutes there is a clear phase shift in the discharge of the inspiratory unit. Note that the rate of discharge is dramatically enhanced during the expiratory portion of the cycle compared to the rate during the inspiratory portion. Since not all of the units recorded showed phase shift, the unit activity in Figure 1 is only an example of several effects on respiratory-realted unit activity. We have also observed loss of activity, both increased and decreased rates of discharge, conversion from phasic to tonic activity and recruitment of previously silent cells.

The other significant change after seven minutes of soman infusion is the development of "humping" in the diaphragmatic contraction. This is characteristic of organophosphate treated muscle although its significance is not fully understood. Note that during the apparent second contraction there is no apparent EMG activity. Both the phrenic nerve discharge and EMG are somewhat facilitated at this point, reflecting increased central

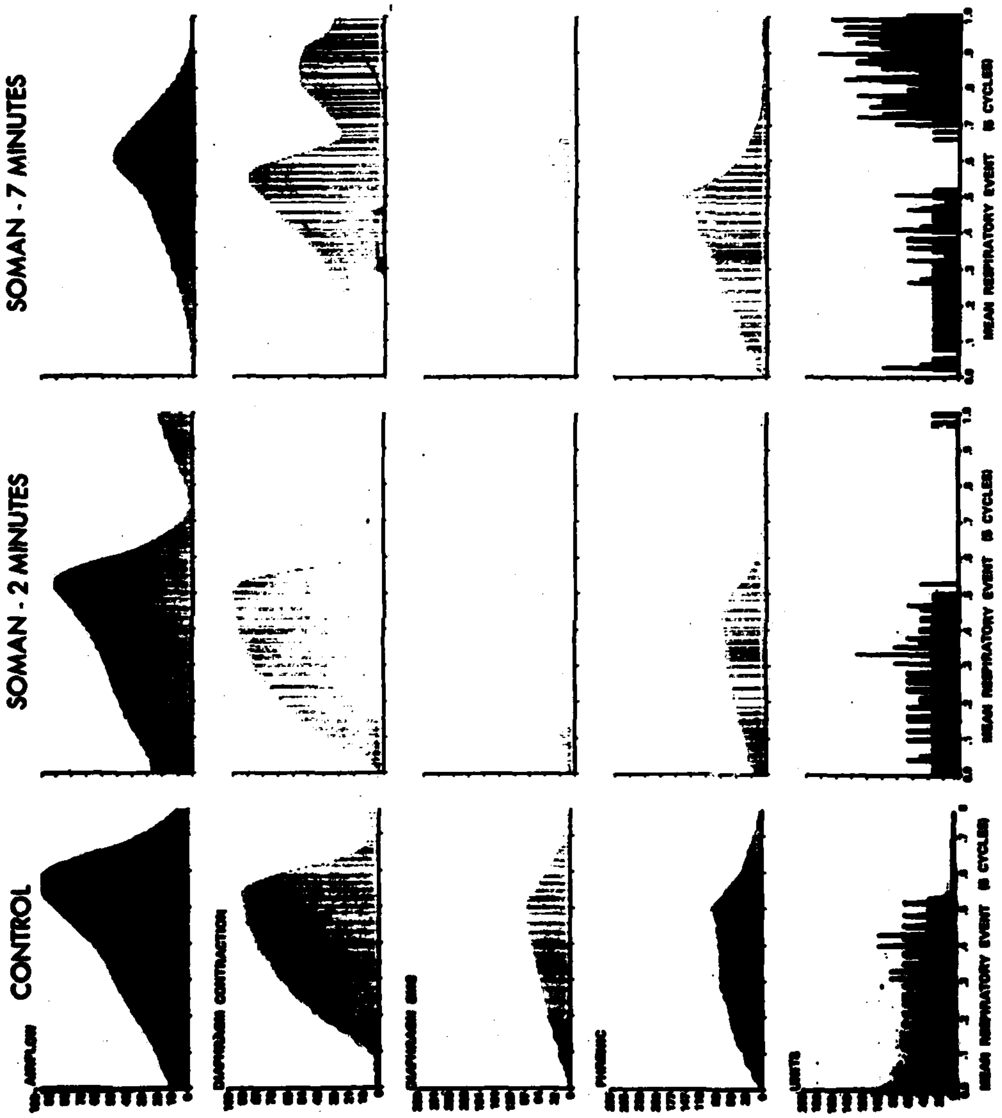

FIGURE 1. Response to Soman Infusion - 1 LD50 per 15 minutes

drive.

Figure 2 illustrates activity during continued soman infusion of the same cat whose data were reported in Figure 1. It can be seen that the "humping" has increased in amplitude such that the apparent second contraction appears as forceful as the primary contraction. Again both the EMG and phrenic activity are facilitated to a level approximately three times the control values. Perhaps most significantly, the unit from which we were recording has ceased firing.

After nine minutes, just prior to respiratory arrest in this animal, there is the appearance of random multiple unit noise being recorded from the unit electrode. These data were recorded by keeping the unit amplitude discriminator set at the same level throughout the period of recording. Examination of individual spike signatures revealed that the inspiratory-related unit, recorded in the earlier portions of the experiment, was no longer firing. In some instances we have seen units resume activity after a period of silence, although this discharge was generally more sporadic and less well regulated than normal. Integrated EMG and phrenic nerve activity continue to be facilitated above control levels. When respiration ceases medullary multiple unit activity appears to be random and there is an abrupt loss of phrenic nerve discharge. This results in an absence of EMG activity and no diaphragmatic contraction.

Figure 3 shows the results of suprathreshold stimulation of the phrenic nerve immediately following cessation of respiration. At both 10 and 100 Hz, this stimulation was sufficient to elicit a tetanic contraction. Figure 4 illustrates that after the administration of Flaxedil in this same cat, contractions were not elicited by phrenic stimulation. This verifies that our stimulation was indeed indirect. That is, diaphragmatic contraction was produced as a result of elicited activity in the phrenic nerve and not as a result of unrecognized current paths to the muscle. Furthermore, Figure 4 illustrates that direct stimulation of the diaphragm was effective for eleciting tetanic contractions.

In those instance where blood gases were analyzed, it was found that just prior to respiratory arrest, $PaCO_2$ was in the high normal range and PaO_2 was within the low normal range. Additionally, we have administered up to 20 LD_{50}s of soman without producing complete block of phrenic nerve elicited, diaphragmatic contractions, although the mean dose required to block was 14 LD_{50}s.

The observations from this study support the conclusion that soman-produced, acute respiratory arrest in unprotected animals is mediated within the CNS. Furthermore, lethal levels of soman exposure leave the neuromuscular junction functional. The major additional evidence provided by this study is that medullary respiratory-related units appear to be affected in a progressive manner. Initially, there appears to be an uncoupling of the regulation of unit activity, as exemplified by unit phase shift. This disruption of normal activity progresses in severity

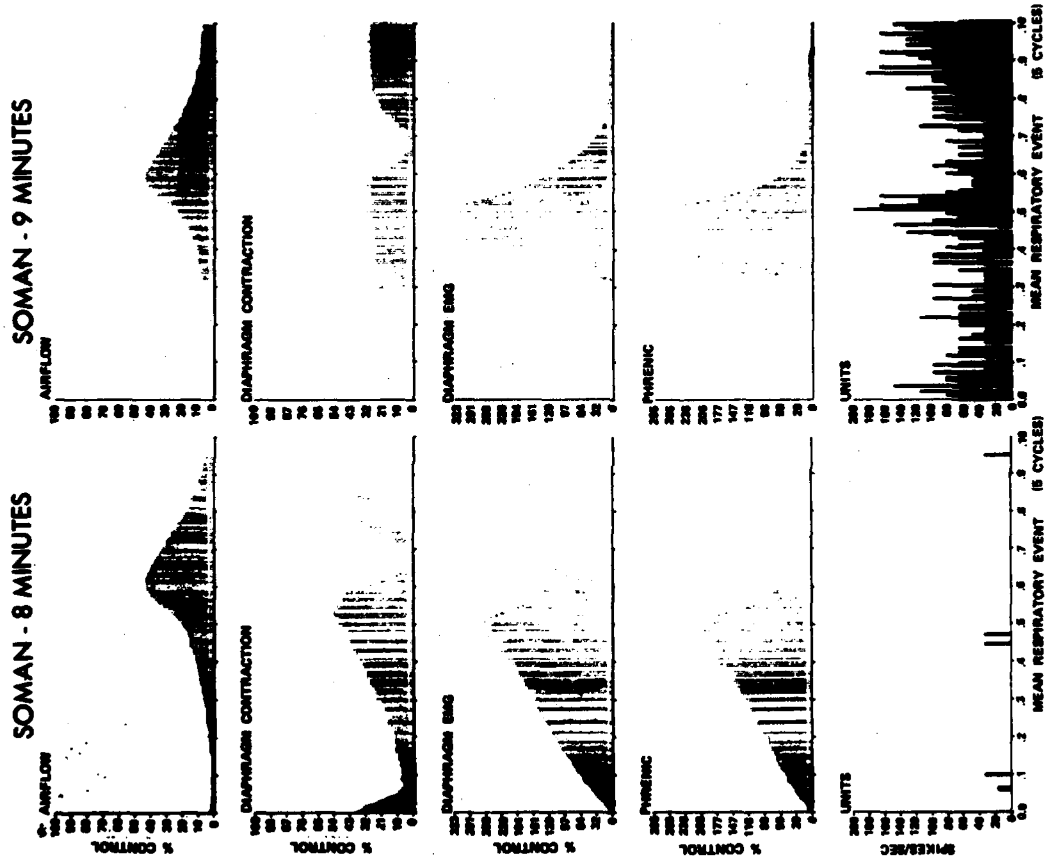

FIGURE 2. Continued response to Soman Infusion - 1 LD50 per 15 minutes

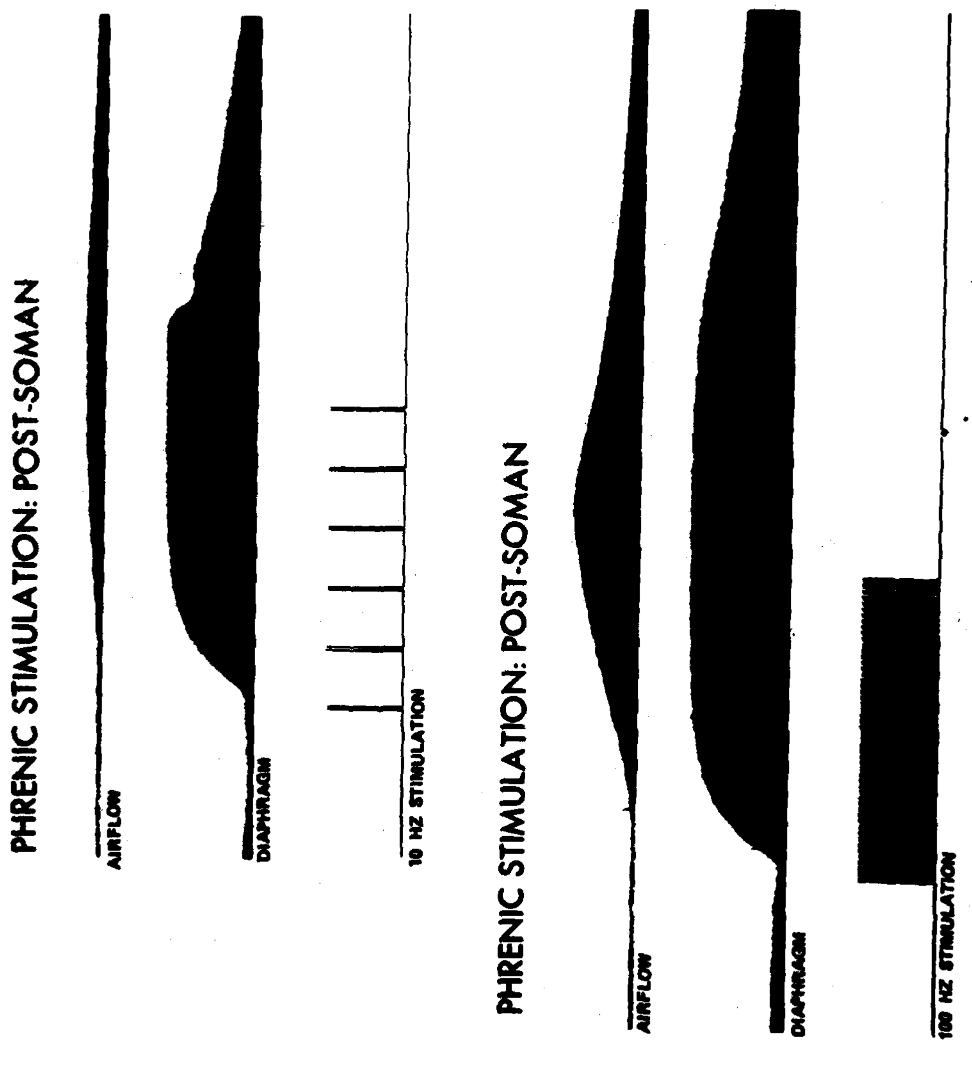

FIGURE 3. Diaphragm response following Soman-produced respiratory arrest

FIGURE 4. Diaphragm response following Soman-produced respiratory arrest and Flaxedil administration

until the system is incapable of sustained, organized respiratory effort. It was not until the cats were in severe respiratory distress that significant alterations were seen in the cardiovascular system.

The specific sites and mechanisms of soman's actions remain to be elucidated. The work by Stewart and Anderson (25), referred to earlier, certainly demonstrates that there are highly localized, nerve agent sensitive sites within the brain stem. Furthermore, Bay and his colleagues (31), working with the cat isolated brain stem preparation, reported unit phase shifts during the infusion of soman which were similar to those seen in the current study. Unfortunately these authors presented no data relating observed changes in respiratory-related unit activity with lethality. Thus, although not specifically controlled for in the present study, it is very unlikely that soman's respiratory depressant effects are mediated through actions on peripheral sensory systems.

As indicated in the introduction, the cholinosensitivity of medullary respiratory-related units is relatively vague due to the discrepancy between lack of responsiveness to iontophoresed ACh and apparent binding of QNB. If soman is exerting its actions on medullary areas regulating central respiratory drive, and if soman acts through cholinergic mechanisms, then this discrepancy will have to be resolved. A partial resolution to this issue is the proposal that within the CNS, with few exceptions, ACh acts primarily as a neuromodulator rather than as an event eleciting neurotransmitter (32). Additionally, Dev and Loeschcke (33, 34) have provided pharmacological evidence in support of a cholinosensitive mediation of both respiration and cardiovascular responses. Their findings were that chemosensitive zones residing on the ventral surface of the medulla are under a tonic cholinergic influence and that different structures possess nicotinic and muscarinic properties. The neuroanatomical relationships among these zones and more traditional pontomeduallary areas regulating respiration remains obscure.

The apparent sensitivity of respiratory-related units to direct application of cholinesterase inhibitors and the lack of correlation between this response and cellular cholinosensitivity suggests an alternative explanation of soman's action. That is, nerve agents may have direct actions on neural membranes and these actions may occur irrespective of specific neurotransmitter recognition sites. Kuba and Albuquerque (35) have shown that DFP blocks the nicotinic receptor-ionic channel complex of the frog neuromuscular junction. More recently, in collabortion with Albuquerque's group, we have shown that pyridostigmine is a channel active compound and that its reversal of DFP's effects on muscle is mediated largely through pyridostigmine's channel properties (36). Although demonstration of these properties at synaptic receptors of neural tissue remains to be accomplished, it is not unreasonable to believe that soman may have direct actions on neural membranes, and more specifically on ionic channels associated with both cholinergic and non-cholinergic receptors. Current and planned efforts in our laboratory are directed at identifying channel properties of nerve agents on neural tissue, identifying the direct actions of nerve agents on respiratory-related units and exploiting this information for the generation of effective, nondebilitating pretreatment and therapy to prevent nerve agent casualties.

REFERENCES

1. Harris, L.W., Stitcher, D.L. & Heyl, W.C. The effects of pretreatments with carbamates, atropine and mecamylamine on survival and on soman-induced alterations in rat and rabbit brain acetylcholine. Life Sci., 26: 1885-1891.
2. Koelle, G.B. Anticholinesterase agents. IN: The Pharmacological Basis of Therapeutics, L.S. Goodman and A. Gilman (Eds.), MacMillian Co., New York, 1970.
3. Heymans, C. & Jacob, J. Sur la pharmacologie du di-isopropyl-fluorophosphaonate (DFP) et le role des cholinesterases. Arch. Int. Pharmacodyn. Ther., 74: 233, 1947.
4. Verbeke, R. Nouvelles contributions a la pharmacologie du di-isopropylfluorophosphonate (DFP). Arch. Int. Pharmacodyn. Ther., 79:1-31, 1949.
5. Koelle, G.B. & Gilman, A. Anticholinesterase drugs. J. Pharmacol. Exp. Ther., 95: 166-216, 1949.
6. Holmstedt, B. Synthesis and pharmacology of dimethylamido-ethoxy-phosphoryl cyanide (Tabun) together with a description of some allied anticholinesterase compounds containing the N-P bond. Acta. Physiol. Scand., 25: 1-120, Supp. 90, 1951.
7. McNamara, B.P., Koelle, G.B. & Gilman, A. The treatment of di-isopropyl fluorophosphate (DFP) poisoning in rabbits. J. Pharmacol. Exp. Ther., 88: 27-33, 1946.
8. Lovatt-Evans, C. Neuromuscular block by anticholinesterases. J. Physiol. (London), 114: 6P, 1951.
9. Douglas, W.W. & Matthews, P.B.C. Acute tetraethylpyrophosphate poisoning in cats and its modification by atropine. J. Physiol. (London), 116: 202-218, 1952.
10. Modell, W. & Krop, S. Antidotes to poisoning by diisopropylfluorophosphate in cats. J. Pharmacol. Exp. Ther., 88: 34-38, 1946.
11. Modell, W., Krop, S., Hitchcock, P. & Riker, W.F. General systemic actions of diisopropylfluorophosphate (DFP) in cats. J. Pharmacol. Exp. Ther., 87: 400-413, 1946.
12. Freedman, A.M. & Himwich, H.E. DFP: site of injection and variation in response. Am. J. Physiol., 156: 125-128, 1949.

13. DeCandole, C.A., Douglas, W.W., Lovatt-Evans, C., Holmes, R., Spencer, K.E.V., Torrance, R.W. & Wilson, K.M. The failure of respiration in death by anticholinesterase poisoning. Brit. J. Pharmacol. Chemother., 8: 466-475, 1953.
14. Wright, P.G. An analysis of the central and peripheral components of respiratory failure produced by anticholinesterase poisoning in the rabbit. J. Physiol. (London), 126: 52-70, 1954.
15. Schaumann, W. & Job, C. Differential effects of a quaternary cholinesterase inhibitor, phospholine, and its tertiary analogue, compound 217-AO, on central control of respiration and neuromuscular transmission. The antagonism by 217-AO of the respiratory arrest caused by morphine. J. Pharmacol. Exp. Therap., 123: 114-120, 1958.
16. Stewart, W.C. The effects of sarin and atropine on the respiratory center and neuromuscular junctions of the rat. Can. J. Biochem. Physiol., 37: 651-660, 1959.
17. Meeter, E. & Wolthuis, O.L. The spontaneous recovery of respiration and neuromuscular transmission in the rat after anticholinesterase poisoning. Eur. J. Pharmacol., 2: 377-386, 1968.
18. Dirnhuber, P., French, M.C., Green, D.M., Leadbeater, L. & Stratton, J.A. The protection of primates against soman poisoning by pretreatment with pyridostigmine. J. Pharm. Pharmacol., 31: 295-299, 1979.
19. Adams, G.K., Yamamura, H.I. & O'Leary, J.F. Recovery of central respiratory function following anticholinesterase intoxication. Eur. J. Pharmacol., 38: 101-112, 1976.
20. Salmoiraghi, G.C. & Steiner, F.A. Acetylcholine sensitivity of cat's medullary neurons. J. Neurophysiol., 26: 581-597, 1963.
21. Denavit-Saubie, M. & Champagnat, J. The effect of some depressing amino acids on bulbar respiratory and non-respiratory neurons. Brain Res., 97: 356-361, 1975.
22. Kirsten, E.B., Satayavivad, J., St. John, W.M. & Wang, S.C. Alteration of medullary respiratory unit discharge by iontophoretic application of putative neurotransmitters. Br. J. Pharmacol., 63: 275-281, 1978.
23. Wamsley, J.K., Lewis, M.S., Young, W.S. & Kuhar, M.J. Autoradiographic localization of muscarinic cholinergic receptors in rat brainstem. J. Neurosci., 1: 176-191, 1981.
24. Bradley, P.B., Dhawan, B.N. & Wolstencroft, J.H. Pharmacological properties of cholinoceptive neurons in the medulla and pons of the cat. J. Physiol. (London), 183: 658-674, 1966.
25. Stweart, W.C. & Anderson, E.A. Effect of a cholinesterase inhibitor when injected into the medulla of the rabbit. J. Pharmacol. Exp. Ther., 162: 309-318, 1968.

26. Ngai, S.H. & Wang, S.C. Organization of the central respiratory mechanisms in the brain stem of the cat: Localization by stimulation and destruction. Am. J. Physiol., 190: 343-349, 1957.
27. Salmoiraghi, G.C. & Burns, B.D. Localization and patterns of discharge of respiratory neurons in brainstem of cat. J. Neurophysiol., 23: 2-13, 1960.
28. Cohen, M.I. Neurogenesis of respiratory rhythm in the mammal. Physiol. Rev., 59: 1105-1173, 1979.
29. Cohen, M.I. Respiratory periodicity in the paralyzed, vagotomized cat: hypocapnic polypnea. Am. J. Physiol., 206: 845-854, 1964.
30. Smolders, F.D.J. & Folgering, H.Th. Description of the firing pattern of respiratory neurons by frequency modulated interspike interval distributions. Eur. J. Physiol., 383: 1-8, 1979.
31. Bay, E., Adams, N.L., von Bredow, J.K.D. & Nelson, J.D. Respiratory phase shift of pattern in the medullary reticular formation after soman in the cat. Brain Res., 60: 526-532, 1973.
32. Krnjevic, K. Acetylcholine as modulator of amino-acid-mediated synaptic transmission. Prog. Clin. Biol. Res., 68: 127-141, 1981.
33. Dev, N.B. & Loeschcke, H.H. Topography of the respiratory and circulatory responses to acetylcholine and nicotine on the ventral surface of the medulla oblongata. Pflugers Arch., 379: 19-27, 1979.
34. Dev, N.B. & Loeschcke, H.H. A cholinergic mechanism involved in the respiratory chemosensitivity of the medulla oblongata in the cat. Pflugers Arch., 379: 29-36, 1979.
35. Kuba, K. & Albuquerque, E. Diisopropylfluorophosphate: suppression of ionic conductance of the cholinergic receptor. Science, 181: 853, 1973.
36. Pascuzzo, G.J., Rickett, D.L., Maleque, M.A. & Albuquerque, E.X. Actions of pyridostigmine (PYR) on the nicotinic receptor-ionic channel complex: antagonism of diisopropylfluorophosphate (DFP). Paper presented: 66th Annual Meeting, FASEB, New Orleans, 1982.

PROBABILISTIC SOLUTION FOR ONE-DIMENSIONAL PLANE WAVE PROPAGATION IN HOMOGENEOUS BILINEAR HYSTERETIC MATERIALS (U)

Behzad Rohani, Ph.D.
U. S. Army Engineer Waterways Experiment Station
Vicksburg, Mississippi 39180

INTRODUCTION

The ground shock calculation techniques currently used to predict the states of stress and ground motions induced in natural earth masses by explosive detonations are deterministic tools--that is, their input parameters (media stress-strain and strength properties, density, surface airblast loading, etc.) are specified as deterministic quantities or functions. In actuality, however, both the properties of earth materials and the characteristics of airblast pulses are random variables. Consequently, the randomness of these input variables indicates that the resulting states of stress and ground motion in natural earth masses are also random variables. Therefore the ground shock calculation problem should be treated probabilistically.

In general, airblast-induced ground motion from a surface burst can be analyzed as an axisymmetric two-dimensional (2D) problem. And, if the ratio of the propagation velocity of the airblast pulse traversing the ground surface is much greater than the propagation velocity of the stress wave in the medium (superseismic conditions), the near-surface ground motions outside the crater are predominantly vertical, in which case one-dimensional (1D) plane wave calculations are usually adequate for predicting free-field response. It is appropriate, therefore, as well as useful to commence an examination of probabilistic ground shock in terms of the 1D problem before examining the more cumbersome 2D problem.

A simple, yet powerful, deterministic model for predicting 1D wave propagation phenomena in earth media is the analytic solution for a bilinear hysteretic material loaded by a decaying surface airblast pulse developed by Salvadori, et al., in 1960 (Reference 1). Although the real stress-strain properties of soil are only approximated by this bilinear relationship, the solution accounts for the major observed features of stress wave propagation through earth materials--namely, the attenuation of stress and particle motion with depth. This paper is concerned with the conversion of this deterministic solution into a probabilistic solution using the method of partial derivatives (Reference 2). The method of partial derivatives greatly alleviates the burden of conducting brute force Monte Carlo analyses for probabilistic wave propagation problems. Furthermore, the partial derivative method has the advantage that it can be used to quantitatively rank the relative effects of input variabilities (uncertainties) on the dispersion of the output quantities, i.e., particle displacement, particle velocity, and stress.

DETERMINISTIC SOLUTION FOR ONE-DIMENSIONAL WAVE PROPAGATION IN BILINEAR HYSTERETIC MATERIALS

Description of bilinear model

The bilinear hysteretic model (Reference 1) was first used to approximate the stress-strain behavior of soils in states of uniaxial strain. The actual soil stress-strain curve during virgin loading is approximated as a straight line which is defined by modulus M_o . During unloading and subsequent reloading to a previous maximum stress level, the actual stress-strain relation is different from the loading relation and is approximated by another straight line, defined by modulus M_1 . When $M_o = M_1$, the model corresponds to a linear elastic material. The propagation velocity of a virgin loading stress wave is given by

$$C_o = \sqrt{M_o/\rho} \tag{1}$$

where ρ is the mass density of the material and the propagation velocity of an unloading or reloading stress wave is given by

$$C_1 = \sqrt{M_1/\rho} \tag{2}$$

The bilinear hysteretic material is therefore completely described by three material constants: M_o , M_1 , and ρ .

Boundary loading

The dynamic boundary load considered in Reference 1 allows the solution to be used for blast-type problems. It is a pulse characterized by an instantaneous rise to peak pressure (a shock front) followed by an exponential decay. Its expression is

$$P(t) = P_o \exp(-t/\tau) \tag{3}$$

where P_o is the peak applied pressure, t is time, and τ is the exponential time constant (time at which pressure has decayed to 0.3678 P_o).

The airblast pulse is therefore completely characterized by two parameters: P_o and τ.

Response of the medium to surface boundary loading

The 1D problem treated by this deterministic solution may be viewed as a semi-infinite body of bilinear hysteretic material uniformly loaded at its free surface by the pressure pulse $P(t)$ described above. Surface motion and stress are assumed to be zero before application of the load. According to Reference 1, the response of the medium in terms of time histories of stress σ and particle velocity $\dot{U}$ in the direction of propagating wave at a generic depth Z is given as

$$\sigma(Z,t) = P_o \exp\left[-\left(t - \frac{Z}{C_1}\right)\Big/\tau\right] + P_o \sum_{n=1}^{\infty} \alpha^n \left\{\exp\left[-\alpha^n\left(t - \frac{Z}{C_1}\right)\Big/\tau\right] - \exp\left[-\alpha^n\left(t + \frac{Z}{C_1}\right)\Big/\tau\right]\right\} \tag{4}$$

$$\dot{U}(Z,t) = P_o\left(\frac{1}{\rho C_o} - \frac{1}{\rho C_1}\right) + \frac{P_o}{\rho C_1}\exp\left[-\left(t - \frac{Z}{C_1}\right)\Big/\tau\right] - \frac{P_o}{\rho C_1}\sum_{n=1}^{\infty} \alpha^n \left\{2 - \exp\left[-\alpha^n\left(t - \frac{Z}{C_1}\right)\Big/\tau\right] - \exp\left[-\alpha^n\left(t + \frac{Z}{C_1}\right)\Big/\tau\right]\right\} \tag{5}$$

Integration of Equation 5 results in the following expression for particle displacement

$$\begin{aligned} U(Z,t) = {} & P_o\left(\frac{1}{\rho C_o} - \frac{1}{\rho C_1}\right)\left(t - \frac{Z}{C_o}\right) + \frac{P_o\tau}{\rho C_1}\left\{\exp\left[-\left(\frac{Z}{C_o} - \frac{Z}{C_1}\right)\Big/\tau\right] - \exp\left[-\left(t - \frac{Z}{C_1}\right)\Big/\tau\right]\right\} \\ & + \frac{P_o\tau}{\rho C_1}\sum_{n=1}^{\infty}\left\{2\alpha^n\left(\frac{Z}{C_o} - t\right)\Big/\tau + \exp\left[-\alpha^n\left(\frac{Z}{C_o} - \frac{Z}{C_1}\right)\Big/\tau\right] + \exp\left[-\alpha^n\left(\frac{Z}{C_o} + \frac{Z}{C_1}\right)\Big/\tau\right] \right. \\ & \left. - \exp\left[-\alpha^n\left(t - \frac{Z}{C_1}\right)\Big/\tau\right] - \exp\left[-\alpha^n\left(t + \frac{Z}{C_1}\right)\Big/\tau\right]\right\} \end{aligned} \tag{6}$$

The parameter α in Equations 4 through 6 is given by

$$\alpha = \frac{\sqrt{M_1/M_o} - 1}{\sqrt{M_1/M_o} + 1} \tag{7}$$

To account for the travel time of the wave to the depth of interest the initial value of t in Equations 4 through 6 must correspond to the arrival time t_a at that depth (i.e., these equations hold for $t \geq t_a$), which is given by

$$t_a = Z/C_o \tag{8}$$

Equations 4, 5, 6, and 8 (which relate the four dependent variables σ, $\dot{U}$, U, and t_a and the five independent variables M_o, M_1, ρ, P_o, and τ) provide the complete deterministic solution for 1D stress wave propagation in bilinear hysteretic materials. Note that since the stress and particle velocity maxima of this solution always occur at the wave front, t in Equations 4 and 5 can be replaced by t_a to obtain expressions for the peak stress σ_{max} and peak particle velocity $\dot{U}_{max}$ as a function of depth.

PROBABILISTIC ANALYSIS

The purpose of a probabilistic analysis is to develop a method by which the variability or uncertainties in the independent parameters in a particular problem can be evaluated or estimated in terms of their effects on the dispersion of the dependent (output) variables. A highly useful procedure for implementing such an analysis is to apply the method of partial derivatives, described in References 2 and 3, to a deterministic solution of the problem. The method gives approximations for the moments of the dependent variables in terms of functions of moments of the independent variables. That is if a random variable Y is functionally related to the random variables X_i

$$Y = Y(X_1, X_2, \ldots, X_n) \tag{9}$$

and if the X_i are uncorrelated, then according to the partial derivative method the approximations for the expected value of Y, $E[Y]$ and the variance of Y, $Var[Y]$, are

$$E[Y] \approx Y(\mu_1, \mu_2, \ldots, \mu_n) + \frac{1}{2} \sum_{i=1}^{n} \left. \frac{\partial^2 Y}{\partial X_i^2} \right|_{(\mu_1, \mu_2, \ldots, \mu_n)} Var[X_i] \tag{10}$$

$$\mathrm{Var}[Y] \approx \sum_{i=1}^{n} \left(\left. \frac{\partial Y}{\partial X_i} \right|_{(\mu_1,\mu_2,\ldots,\mu_n)} \right)^2 \mathrm{Var}[X_i] \tag{11}$$

where $(\mu_1,\mu_2,\ldots,\mu_n)$ denotes the respective mean of the random variables $(X_1,X_2,\ldots,X_n)$. The first term on the right-hand side of Equation 10 corresponds to the mean value of Y , i.e., the value of Y obtained using the mean values of all of the random variables. The second term represents the contributions to the expected value of Y due to uncertainties in the X_i . The second term is negligible if $\mathrm{Var}[X_i]$ and the nonlinearity in the function Y itself are not large. As pointed out in Reference 2, Equation 11 "may be interpreted as meaning that each of the n random variables X_i contributes to the dispersion of Y in a manner proportional to its own variance $\mathrm{Var}[X_i]$ and proportional to a factor $\left(\left. \frac{\partial Y}{\partial X_i} \right|_{(\mu_1,\mu_2,\ldots,\mu_n)} \right)^2$, which is related to the sensitivity of changes in Y to changes in X_i." This interpretation can be used to conduct sensitivity analyses to quantify and rank the relative effects of the input variabilities or uncertainties on the dispersion of the output quantities.

The partial derivatives in Equations 10 and 11 can be evaluated analytically if an explicit expression is available for the dependent variable Y . However, as pointed out by Mlakar (Reference 4), in many cases, even when an explicit relation for Y does exist, it is often more convenient to evaluate these partial derivatives numerically using finite-difference approximations. Following the method proposed by Mlakar (Reference 4), the partial derivatives may be expressed as

$$\frac{\partial Y}{\partial X_i} = \frac{Y(\mu_1,\ldots,\mu_i+kS_i,\ldots\mu_n) - Y(\mu_1,\ldots,\mu_i-kS_i,\ldots,\mu_n)}{2kS_i} \tag{12}$$

$$\frac{\partial^2 Y}{\partial X_i^2} = \frac{Y(\mu_1,\ldots,\mu_i-kS_i,\ldots,\mu_n)-2Y(\mu_1,\ldots,\mu_i,\ldots,\mu_n)+Y(\mu_1,\ldots,\mu_i+kS_i,\ldots\mu_n)}{(kS_i)^2} \tag{13}$$

$$i = 1,2,\ldots,n$$

The first partial derivative (Equation 12) is calculated from the functional values of Y at k standard deviation kS_i above and below the mean value of X_i (or μ_i) where k is a constant and S_i is the standard deviation of X_i . Similarly, the second partial derivative (Equation 13) is calculated from the mean value of Y and the functional values of

Y at kS_i above and below μ_i . The term kS_i therefore may be viewed as a finite-difference mesh spacing. The value of k is heuristically taken to be 1.0 in Reference 4. However, if either the standard deviation S_i or the nonlinearity in the function Y is large, smaller values of k should be tried until the results are no longer affected by further reductions in k . The probabilistic calculations reported in this paper (next section) were conducted using k = 0.5 . In order to determine the sensitivity of the results to variations in k several calculations were conducted for k varying from 1.0 to 0.1. These calculations indicated that an order of magnitude reduction in the value of k decreased the numerical results on the average by 6 percent and at most by 12 percent. Reducing the value of k from 0.5 to 0.1, however, changed the results of the calculations on the average by 1 percent and at most by 3 percent. For most practical problems it would therefore appear that a value of k within the range of 0.1 to 0.5 would be satisfactory.

For each of the dependent variables σ , $\dot{U}$, U , and t_a (Equations 4, 5, 6, and 8), Equations 12 and 13 can be used to calculate their first and second partial derivatives with respect to the five independent variables M_o , M_1 , ρ , P_o , and τ . These partial derivatives can then be used in Equations 10 and 11 to calculate the expected value and the variance of each of the dependent variables.

A computer program has been developed for the express purpose of numerically evaluating this complete system of equations. Within this program, computations are made at successive times at selected depths so that the time histories of the expected value and the variance of the dependent variables σ , $\dot{U}$, and U can be constructed. The program also computes and prints out the explicit contributions of each of the input (independent) random variables to the overall dispersion of the various output quantities (dependent variables).

NUMERICAL EXAMPLES

In this section we demonstrate the application of the above methodology for conducting probabilistic wave propagation analyses for bilinear hysteretic materials. Two numerical examples are presented. One is referred to as the "stiff soil" problem; the other is referred to as the "soft soil" problem. We consider the former problem first. The input quantities selected for the first problem consisting of the mean values μ_i and the coefficients of variation S_i/μ_i for the five independent variables M_o , M_1 , ρ , P_o , and τ are given in Table 1. The coefficients of variation specified for this problem are reasonable inasmuch as they have been encountered in actual practice. The bilinear material in this example problem is referred to as "stiff soil" because of the high value of the loading modulus M_o . The expected values $E[\sigma_{max}]$ and $E[\dot{U}_{max}]$ and

Table 1. Individual Contributions to Dispersion of Peak Stress Due to Uncertainties in Input Variables (Stiff Soil; $\alpha = 0.333$)

			$\left\lvert\frac{\partial\sigma_{max}}{\partial X_i}\right\rvert \frac{S_i}{E[\sigma_{max}]}$			
X_i	μ_i	S_i/μ_i	Z = 0.0 ft	Z = 10.0 ft	Z = 20.0 ft	Z = 40.0 ft
M_o	63.0 ksi	0.5	0.0	0.01905	0.03757	0.07286
M_1	252.0 ksi	0.5	0.0	0.00856	0.01690	0.03288
ρ	100.0 lb/ft^3	0.1	0.0	0.00209	0.00415	0.00812
P_o	0.1 ksi	0.1	0.1	0.10008	0.10010	0.09994
τ	0.05 sec	0.1	0.0	0.00420	0.00831	0.01627
			$E[\sigma_{max}]$ = 0.1 ksi	$E[\sigma_{max}]$ = 0.09570 ksi	$E[\sigma_{max}]$ = 0.09168 ksi	$E[\sigma_{max}]$ = 0.08441 ksi
			$V[\sigma_{max}]$ = 0.1	$V[\sigma_{max}]$ = 0.10246	$V[\sigma_{max}]$ = 0.10888	$V[\sigma_{max}]$ = 0.12980

Table 2. Individual Contributions to Dispersion of Peak Particle Velocity Due to Uncertainties in Input Variables (Stiff Soil; $\alpha = 0.333$)

			$\left\lvert\frac{\partial\dot{U}_{max}}{\partial X_i}\right\rvert \frac{S_i}{E[\dot{U}_{max}]}$			
X_i	μ_i	S_i/μ_i	Z = 0.0 ft	Z = 10.0 ft	Z = 20.0 ft	Z = 40.0 ft
M_o	63.0 ksi	0.5	0.23618	0.21932	0.20262	0.17008
M_1	252.0 ksi	0.5	0.0	0.00779	0.01546	0.03033
ρ	100.0 lb/ft^3	0.1	0.04544	0.04760	0.04970	0.05372
P_o	0.1 ksi	0.1	0.09074	0.09123	0.09164	0.09229
τ	0.05 sec	0.1	0.0	0.00384	0.00761	0.01502
			$E[\dot{U}_{max}]$ = 2.99 fps	$E[\dot{U}_{max}]$ = 2.85 fps	$E[\dot{U}_{max}]$ = 2.72 fps	$E[\dot{U}_{max}]$ = 2.48 fps
			$V[\dot{U}_{max}]$ = 0.25706	$V[\dot{U}_{max}]$ = 0.24266	$V[\dot{U}_{max}]$ = 0.22898	$V[\dot{U}_{max}]$ = 0.20447

the coefficients of variation $V[\sigma_{max}]$ and $V[\dot{U}_{max}]$ obtained for various depths from the probabilistic analysis of this problem are presented in Tables 1 and 2. These tables also list the individual contributions produced by the constituent random variables X_i to the dispersion of peak stress and peak particle velocity at different depths. These individual contributions are presented in the last four columns of Tables 1 and 2 in terms of the values of $\left|\frac{\partial\sigma_{max}}{\partial X_i}\right| \frac{S_i}{E[\sigma_{max}]}$ (Table 1) and $\left|\frac{\partial\dot{U}_{max}}{\partial X_i}\right| \frac{S_i}{E[\dot{U}_{max}]}$ (Table 2). Note that Equation 11 stipulates that these individual contributions would correspond to the coefficient of variation of peak stress (or peak particle velocity) if for each variable X_i the other four constituent variables were deterministic.

The input quantities for the second example problem are given in Table 3. The bilinear material used for this example problem is referred to as "soft soil" because of the low value of the loading modulus M_o. The probabilistic output quantities for this problem are presented in Tables 3 and 4.

The information presented in Tables 1 through 4 reveals several interesting trends regarding the dispersion of peak stress and peak particle velocity: (1) For the two soil materials considered in this paper, the coefficient of variation of peak stress $V[\sigma_{max}]$ increases with depth. On the other hand, the coefficient of variation of peak particle velocity $V[\dot{U}_{max}]$ decreases with depth. The rates of change of the coefficients of variation with depth, however, are more pronounced for the soft soil case. (2) As expected, at the ground surface only the variability in peak pressure P_o contributes to the dispersion of peak stress. With increasing depth, however, the variabilities in the other input variables also contribute to the dispersion of peak stress. Moreover, the contribution of the variability in P_o is (for all practical purposes) the same for all depths whereas the influence of the other input variables becomes more significant with increasing depth. These influences are stronger for the soft soil case. For both soils, the variabilities in peak pressure P_o and loading modulus M_o contribute most to the dispersion of peak stress. The combined variability in unloading modulus M_1, density ρ, and decay constant τ has a very small influence on the dispersion of peak stress. (3) The variability in loading modulus M_o contributes most to dispersion of peak particle velocity. Its influence, however, decreases with increasing depth. The variability in unloading modulus M_1 has a negligible effect on the dispersion of peak particle velocity but its influence increases with increasing depth. The combined variability in density ρ, peak pressure P_o, and decay constant τ has a small effect on the dispersion of peak particle velocity but its influence increases with increasing depth and is more pronounced for the soft soil case.

Table 3. Individual Contributions to Dispersion of Peak Stress Due to Uncertainties in Input Variables (Soft Soil; α = 0.714)

			$\left\lvert\frac{\partial\sigma_{max}}{\partial X_i}\right\rvert \frac{S_i}{E[\sigma_{max}]}$			
X_i	μ_i	S_i/μ_i	Z = 0.0 ft	Z = 10.0 ft	Z = 20.0 ft	Z = 40.0 ft
M_o	7.0 ksi	0.5	0.0	0.04475	0.08463	0.14888
M_1	252.0 ksi	0.5	0.0	0.00246	0.00451	0.00751
ρ	100.0 lb/ft^3	0.1	0.0	0.00819	0.01559	0.02777
P_o	0.1 ksi	0.1	0.1	0.10153	0.10263	0.10377
τ	0.05 sec	0.1	0.0	0.01640	0.03122	0.05555
			$E[\sigma_{max}]$ = 0.1 ksi	$E[\sigma_{max}]$ = 0.0834 ksi	$E[\sigma_{max}]$ = 0.0706 ksi	$E[\sigma_{max}]$ = 0.0525 ksi
			$V[\sigma_{max}]$ = 0.1	$V[\sigma_{max}]$ = 0.11249	$V[\sigma_{max}]$ = 0.13760	$V[\sigma_{max}]$ = 0.19195

Table 4. Individual Contributions to Dispersion of Peak Particle Velocity Due to Uncertainties in Input Variables (Soft Soil; α = 0.714)

			$\left\lvert\frac{\partial\dot{U}_{max}}{\partial X_i}\right\rvert \frac{S_i}{E[\dot{U}_{max}]}$			
X_i	μ_i	S_i/μ_i	Z = 0.0 ft	Z = 10.0 ft	Z = 20.0 ft	Z = 40.0 ft
M_o	7.0 ksi	0.5	0.23618	0.19938	0.16526	0.10806
M_1	252.0 ksi	0.5	0.0	0.00211	0.00391	0.00657
ρ	100.0 lb/ft^3	0.1	0.04544	0.05403	0.06186	0.07470
P_o	0.1 ksi	0.1	0.09074	0.09295	0.09479	0.09723
τ	0.05 sec	0.1	0.0	0.01497	0.02878	0.05195
			$E[\dot{U}_{max}]$ = 8.98 fps	$E[\dot{U}_{max}]$ = 7.43 fps	$E[\dot{U}_{max}]$ = 6.23 fps	$E[\dot{U}_{max}]$ = 4.57 fps
			$V[\dot{U}_{max}]$ = 0.25706	$V[\dot{U}_{max}]$ = 0.22703	$V[\dot{U}_{max}]$ = 0.20240	$V[\dot{U}_{max}]$ = 0.17162

It is worth pointing out that for the two example problems considered, the contributions of the second partial derivatives in Equation 10 to the expected values of the dependent variables σ , $\dot{U}$, U , and t_a are not very significant. In the case of stress, the contribution is negligible. For the other three dependent variables the contributions on the average are about 10 percent of the expected values and as high as 25 percent for the particle velocity at late times. The contributions are more pronounced for the soft soil problem.

To provide a feeling for the effects of input variability on the dispersion of particle displacement for the two problems considered, the results of the probabilistic calculations for surface displacement at $t = 0.15$ second are presented in Table 5. This tabulation shows that the variability in loading modulus M_o obviously contributes most to dispersion of particle displacement for both of the example problems. The combined effect of the variabilities in unloading modulus M_1 , density ρ , peak pressure P_o , and decay constant τ on the dispersion of particle displacement is small.

Table 5. Individual Contributions to Dispersion of Particle Displacement Due to Uncertainties in Input Variables ($Z = 0.0$ ft; $t = 0.15$ sec)

	Soft Soil, $\alpha = 0.714$			Stiff Soil, $\alpha = 0.333$		
X_i	μ_i	S_i/μ_i	$\left\lvert\frac{\partial U}{\partial X_i}\right\rvert \frac{S_i}{E[U]}$	μ_i	S_i/μ_i	$\left\lvert\frac{\partial U}{\partial X_i}\right\rvert \frac{S_i}{E[U]}$
M_o	7.0 ksi	0.5	0.29385	63.0 ksi	0.5	0.29738
M_1	252.0 ksi	0.5	0.05906	252.0 ksi	0.5	0.05999
ρ	100.0 lb/ft^3	0.1	0.04459	100.0 lb/ft^3	0.1	0.04595
P_o	0.1 ksi	0.1	0.08905	0.1 ksi	0.1	0.09175
τ	0.05 sec	0.1	0.02215	0.05 sec	0.1	0.04232
			E[U] = 10.92 in.			E[U] = 2.73 in.
			V[U] = 0.31661			V[U] = 0.32303

Typical time histories (wave forms) of the expected value and the coefficient of variation of stress, particle velocity, and particle displacement at $Z = 40.0$ feet are portrayed in Figures 1 through 3, respectively. The arrival times for these graphs correspond to $E[t_a] = 0.0257$

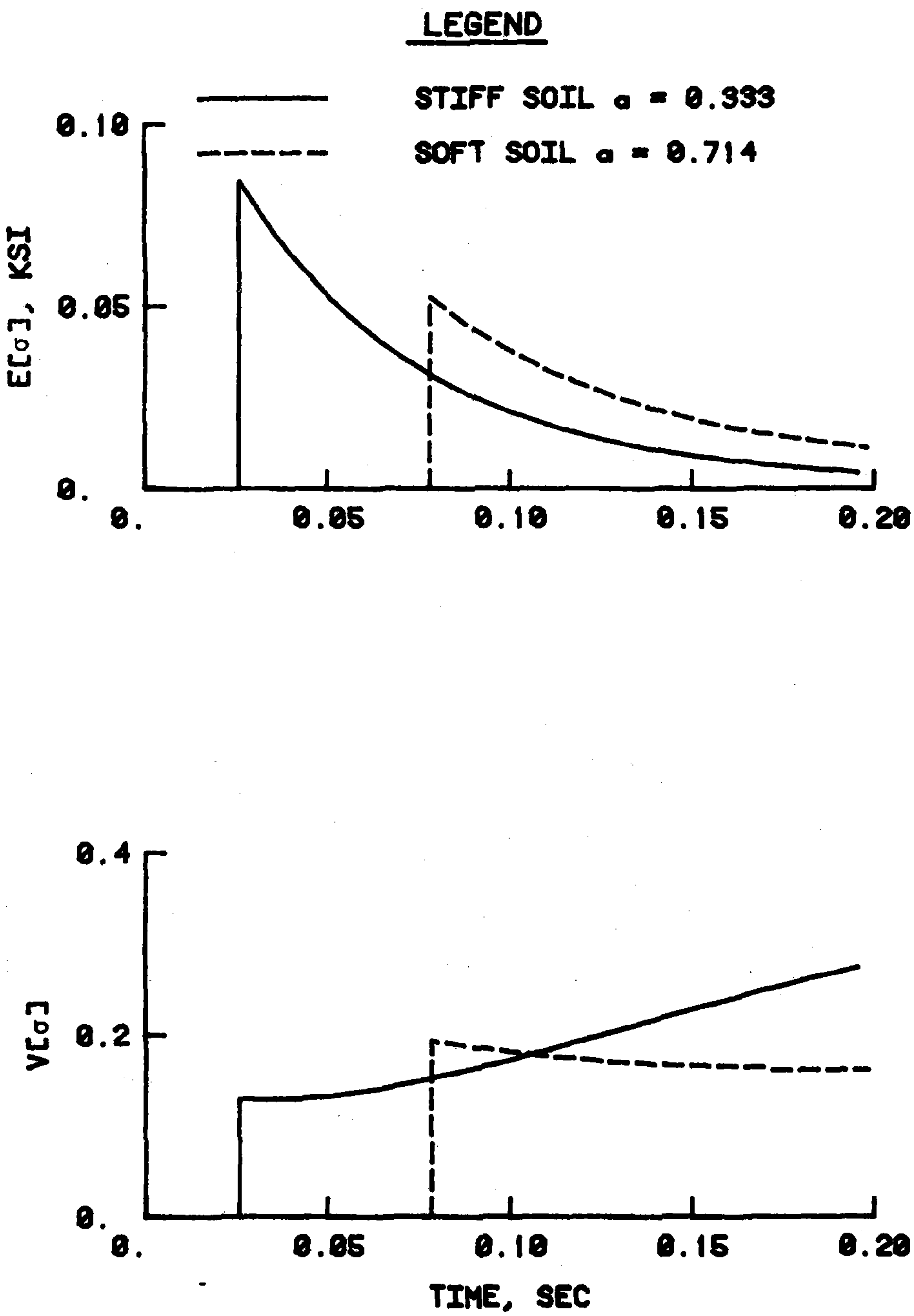

Figure 1. Time histories of E[σ] and V[σ] at Z = 40 feet.

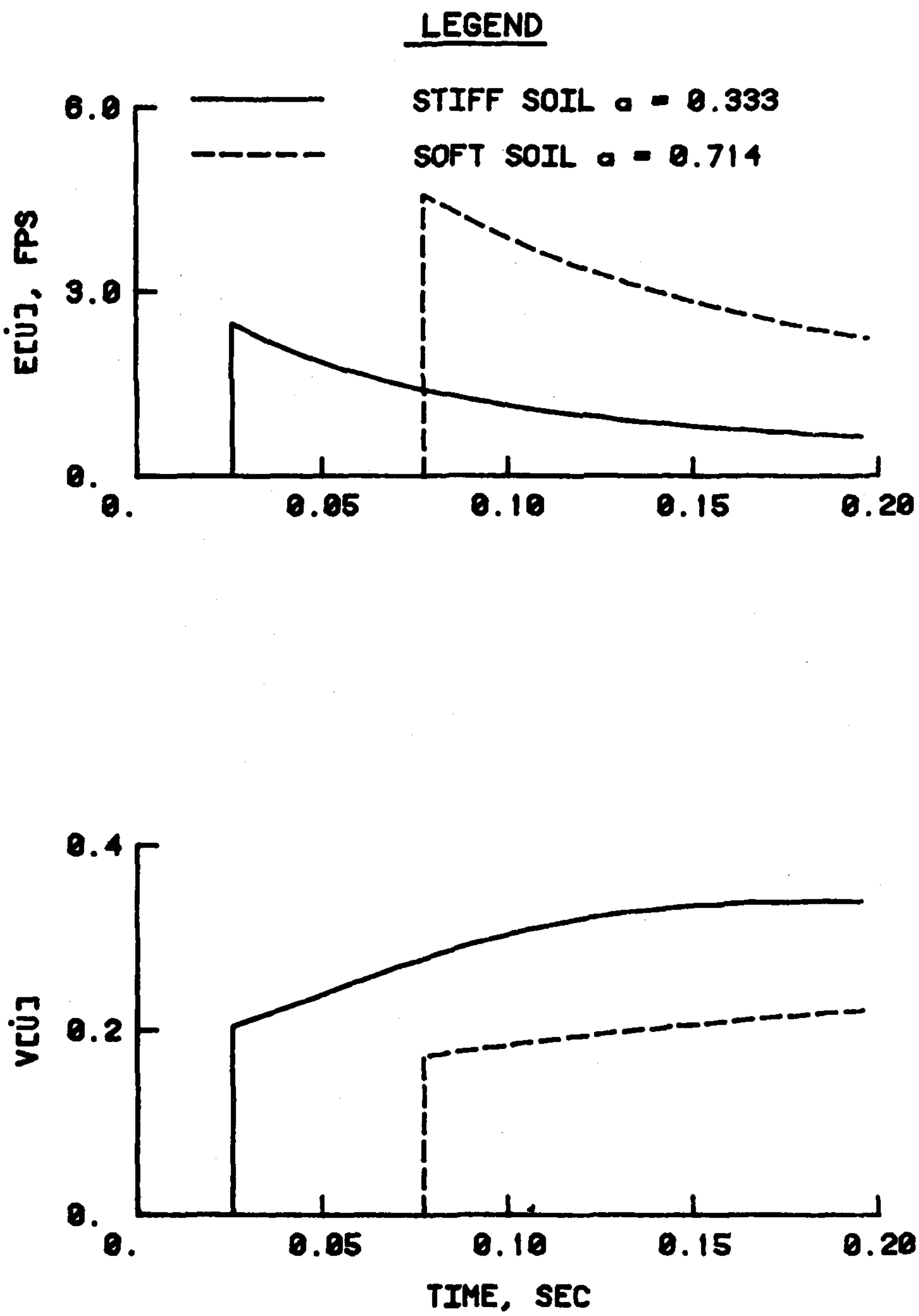

Figure 2. Time histories of E[U̇] and V[U̇] at Z = 40 feet.

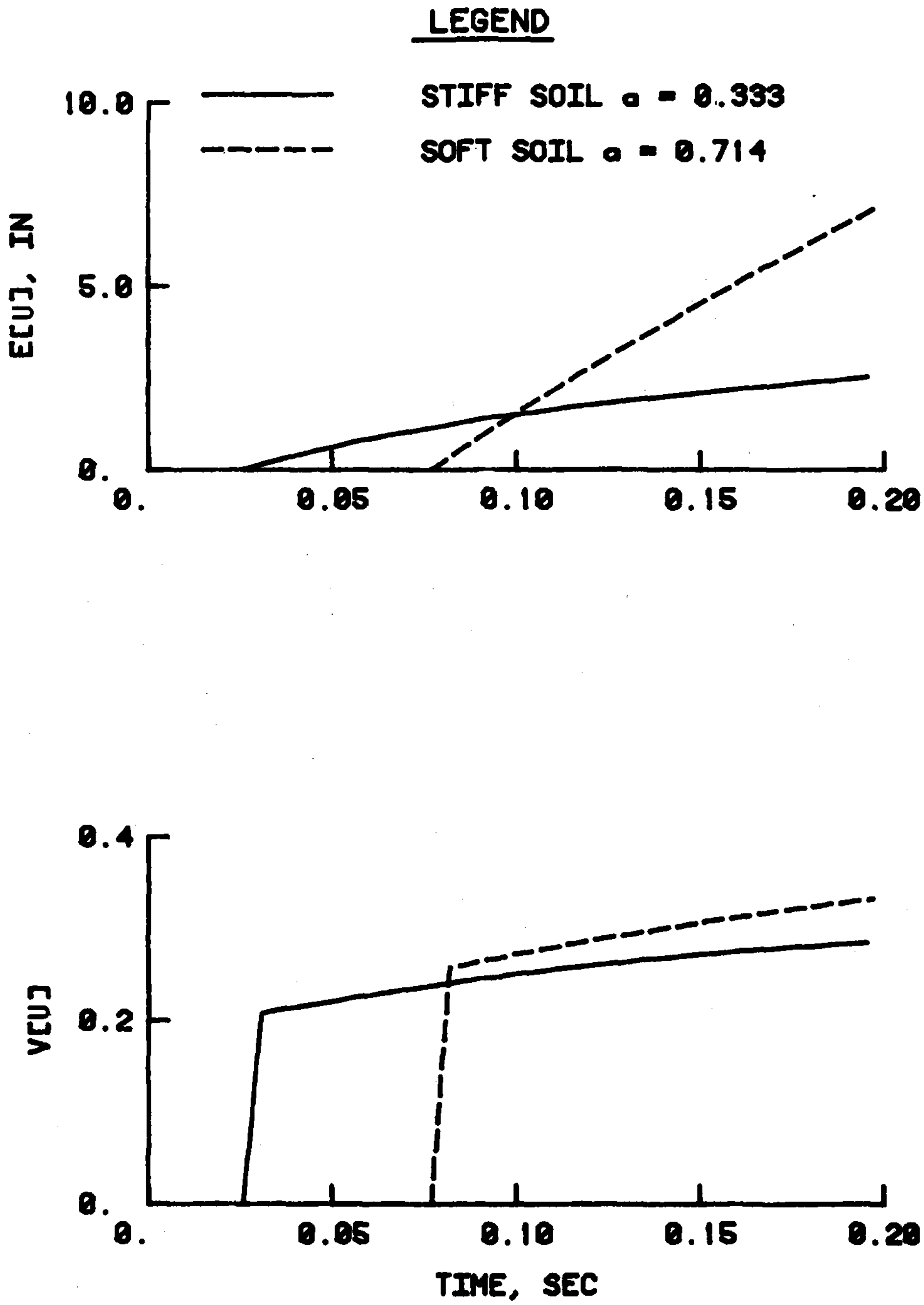

Figure 3. Time histories of E[U] and V[U] at Z = 40 feet.

second for the stiff soil and $E[t_a] = 0.0770$ second for the soft soil. The coefficient of variation of the arrival time is a function only of the variability in the independent variables M_0 and ρ and is equal to $V[t_a] = 0.2416$ for all depths and for both problems considered. The individual contributions to the dispersion of t_a due to uncertainties in M_0 and ρ are, respectively, 0.2373 and 0.0456. Therefore, the variability in M_0 contributes most to the dispersion of the arrival time. It is interesting to note from Figures 2 and 3 that the coefficients of variation of particle velocity and particle displacement, $V[\dot{U}]$ and $V[U]$, respectively, also increase with increasing time. In the case of stress (Figure 1), the coefficient of variation $V[\sigma]$ initially decreases with time and then increases at late times (thc soft soil history eventually turns upward at $t > 0.2$ second). The increase in $V[U]$ with time is important since the expected value of particle displacement $E[U]$ also increases with time.

Information of the type presented in Tables 1 through 5 and Figures 1 through 3 can be used to perform probabilistic analysis of airblast-induced ground shock and to construct reliability based safety factors for blast-resistant design purposes. Assuming that the probability distribution functions for each of the dependen' random variables are roughly bell-shaped, the normal distribution function can be used to conduct the desired probability analysis. For example, applying the rule-of-thumb that the probability that a variable lies within two standard deviation bounds of its mean is approximately 95 percent to the surface displacement predictions in Table 5, it can be stated $P[4.006 \text{ in.} \leq U \leq 17.834 \text{ in.}] = 0.95$ for the soft soil and $P[0.966 \text{ in.} \leq U \leq 4.493 \text{ in.}] = 0.95$ for the stiff soil. In the absence of the exact shape of the probability distribution function one could also use the Chebyshev inequality (Reference 2) for probability analysis.

CONCLUSIONS

The partial derivative method has been used to convert a deterministic analytic solution for stress wave propagation in homogeneous bilinear hysteretic materials subjected to an exponentially decaying surface airblast pulse into a numerical probabilistic solution. The probabilistic solution has been coded and used to conduct sensitivity analyses to rank the relative effects of input variabilities and uncertainties on the dispersion of output quantities (stress, particle velocity, and particle displacement). The analyses indicate that variability in the material loading modulus contributes most to the dispersion of particle velocity and particle displacement but its influence decreases with increasing depth. The variabilities in loading modulus and peak airblast pressure contribute most to the dispersion of peak stress; the influence of the former increasing with increasing depth and that of the latter remaining essentially constant with depth. The analyses also indicate that the coefficient of variation of particle velocity increases with time whereas the coefficient of variation of stress initially decreases with time and then increases at later times. At any given depth, of course, the expected values of stress and particle velocity decrease with time. The coefficient of variation of particle displacement increases with time, which is of particular interest since its expected value also increases with time.

ACKNOWLEDGEMENT

The work reported herein was conducted at the U. S. Army Engineer Waterways Experiment Station under the sponsorship of the Office, Chief of Engineers, Department of the Army, as part of Project 4A762719AT40, Task AO, Work Unit 024, "Ground Shock Prediction Techniques for Earth and Earth-Structure Systems."

REFERENCES

1. Salvadori, M. G., Skalak, R., and Weidlinger, P., "Waves and Shocks in Locking and Dissipative Media," Transactions, American Society of Civil Engineers, Vol 126, Part I, April 1960.

2. Benjamin, J. R. and Cornell, C. A., Probability, Statistics and Decision for Civil Engineers, McGraw-Hill, Inc., New York, 1970.

3. Haugen, E. B., Probabilistic Approaches to Design, John Wiley & Sons, Inc., 1968.

4. Mlakar, P. F., "Application of an Implicit Linear Statistical Analysis to the Estimation of the Resistance of a Reinforced Concrete Beam-Column," Miscellaneous Paper N-78-7, U. S. Army Engineer Waterways Experiment Station, CE, Vicksburg, Miss., 1978.

MEASURED EFFECTS OF TACTICAL SMOKE AND DUST ON PERFORMANCE OF A HIGH RESOLUTION INFRARED IMAGING SYSTEM

MR. JOHN A. ROTH
INSTRUMENTATION DIRECTORATE
WHITE SANDS MISSILE RANGE, NEW MEXICO 88002

I. INTRODUCTION

For centuries armies have relied on clouds of smoke and dust to screen their activities from the enemy. These obscurants have consisted both of those deliberately produced for that purpose, such as tactical smoke, and those produced by exploding shells, burning equipment, vehicular motion, and other normal battlefield events. Until recently the screening effects of such obscurants were only of importance in the visible portion of the spectrum. The introduction to the battlefield of electro-optical imaging systems, laser range finders and designators, and passive electromagnetic homing devices, most of which operate in the infrared portion of the spectrum between 1 and 12 microns, makes it of vital importance to determine the performance of these devices in the presence of obscurants.

The high interest in characterizing the performance of tactical E-O equipment in the presence of obscurants has led to a number of "Smoke" measurement programs being conducted in recent years, in which the obscuration effects of various materials, produced under controlled conditions, have been tested on various systems. One such test titled, "Battlefield Induced Contamination Test," (BICT), was conducted at White Sands Missile Range, NM during April and May, 1981 by the Atmospheric Sciences Laboratory (ASL) of the US Army Electronics Research and Development Command.

The Mobile Tracking Imaging Radiometer (MTIR), an instrumentation system being developed by the Instrumentation Directorate, WSMR, to support future High Energy Laser tests at the Range, participated in BICT at the request of ASL. The MTIR consists of a two-channel (3-5 and 8-12 micron) serial-scan, Forward-Looking Infrared imaging system (FLIR) mounted on a servopedestal attached to an instrumentation trailer.

II. HARDWARE DESCRIPTION

Two-Channel FLIR: The chief sensor of the MTIR is a serial-scan FLIR built by Honeywell Radiation Center (1). The FLIR is capable of producing imagery simultaneously in the 3-5 and the 8-12 micron bands. The scanner is located behind a 17-inch diameter, 84-inch focal length telescope which gives the system an instantaneous field-of-view of 60 microradians. Full field-of-view of the system is approximately one degree. The image from the telescope, after passing through the scanners is split by a dichroic beam splitter to the 3-5 and 8-12 detectors. The minimum resolvable temperature is approx. .2^{o}C at 8-12 micron and 3^{o}C at 3-5 micron (at 1 cycle/mr.). The detectors, which ride on a motorized table for focusing, are cooled by Joule-Thompson devices utilizing high pressure nitrogen gas. Each channel of the FLIR has two outputs. One output is adjustable in gain and level to produce the best image. The other output is fixed and is set for the best linear operation. Output of the FLIR is in standard video format and may be directly viewed on a standard TV monitor. A cutaway drawing of the FLIR is shown in Figure 1. Figure 2 is a photograph of the MTIR system.

TV Boresight System: A standard TV camera, equipped with a 6 to 1 zoom lens, is mounted above the FLIR system.

Recorders: Five Sony video cassette recorders are rack mounted in the trailer. All video outputs from the FLIR and the boresight TV camera may be simultaneously recorded. The recording system also includes an Ampex, studio-quality, reel-to-reel video recorder. A video matrix switch allows easy routing of the various video signals to selected monitors and recorders.

Blackbody Target: A heated, 18 by 18 inch, blackbody, mounted on a two-wheel trailer serves as the MTIR's calibration target. The target has a temperature uniformity of 1^{o}C and a temperature range of 40 to 500^{o}C. Figure 3 is a photograph of the target.

III. TEST DESCRIPTION

Field Layout: The BICT tests were conducted at the Dusty Infrared Test I (DIRT I) site, located in the far SE corner of WSMR, by ASL from 14 April through 13 May 1981. The test site consists of a 1.8km, north-south optical path with instrumentation pads at each end. A 200 by 300m cleared area, midway between the ends of the optical path, was utilized for the production of smoke and dust (2, 3). The MTIR was located at the south end of the optical path alongside of ASL's LIDAR van. The MTIR's blackbody target was located 600m to the north, at the beginning of the tests. Later it was moved to the northern end of the optical path

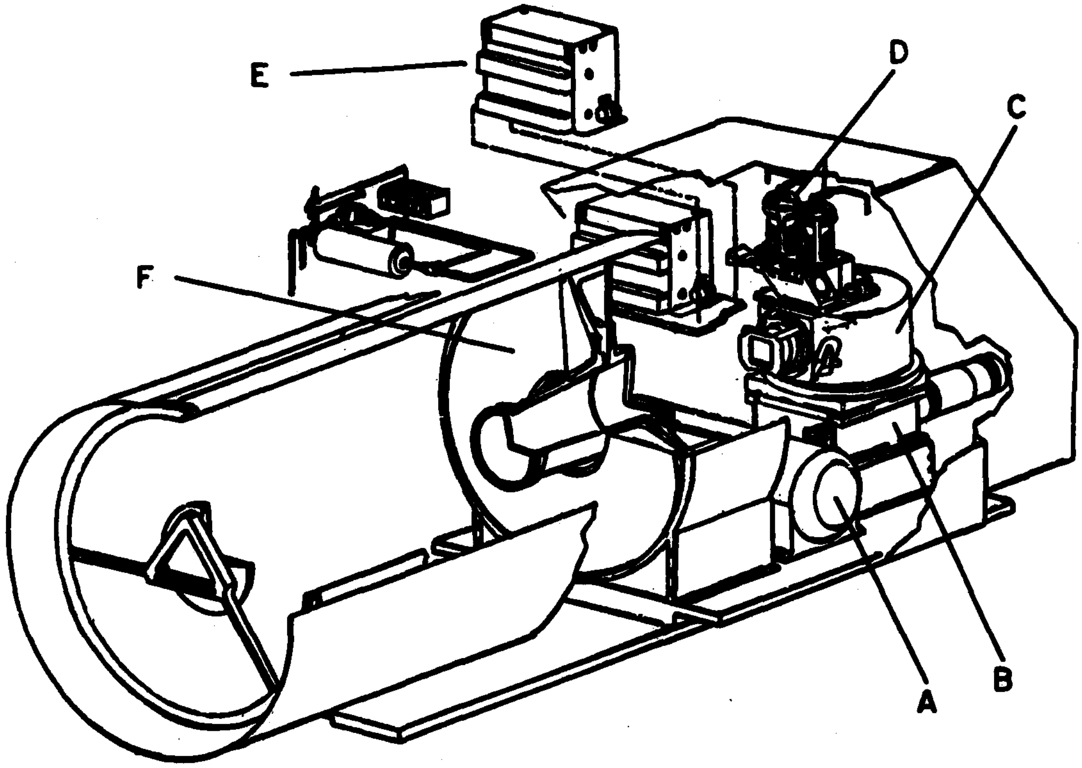

A. Nitrogen Bottle
B. Motor-Driven Focus Table
C. Scanner Housing
D. Detector Packages
E. Pre-Amplifiers
F. 17-in. Primary Mirror

Figure 1: Cutaway Drawing of Two-Channel FLIR.

when it was feared that it would be damaged by shrapnel. The backstop, utilized by the LIDAR to reflect 1.06 micron energy from its YAG laser back to its receiver, was also located at the northern end of the test path. Figure 4 is a sketch (not to scale) of the field configuration.

Smoke and Dust Generation: Five series of smoke tests were conducted during the BICT tests. These were: The production of hexochloroethane (HC) smoke from ignited M1 and M2 canisters, the detonation of canisters containing XM825, a developmental long-duration smoke producing device containing felt wedges saturated with white phosphorus, static firing of pole-mounted projectiles containing bulk white phophorus (WP), the impact of 155mm white phosphorus shells fired into the test area by two M198 howitzers (LF), and Fire Products, the production of smoke from burning

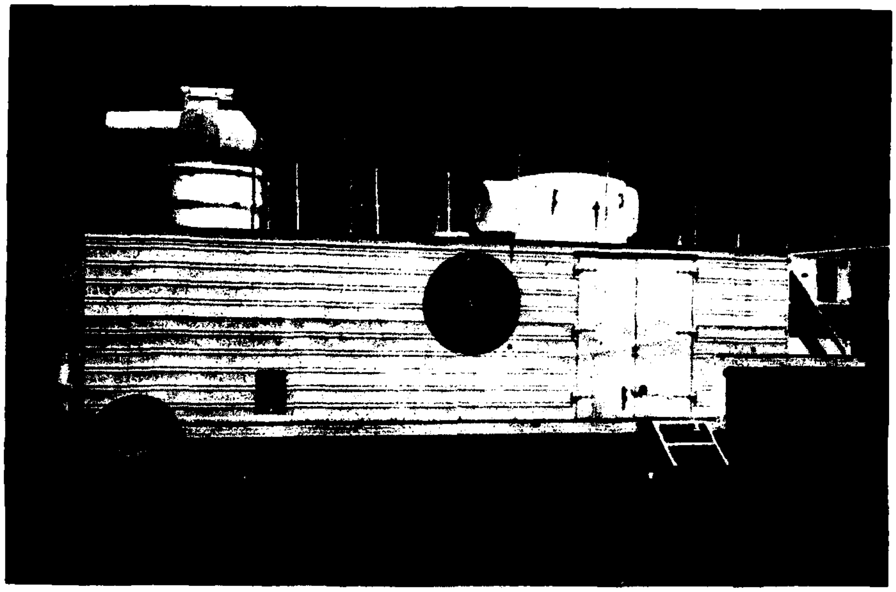

Figure 2: Mobile Tracking Imaging Radiometer (MTIR)

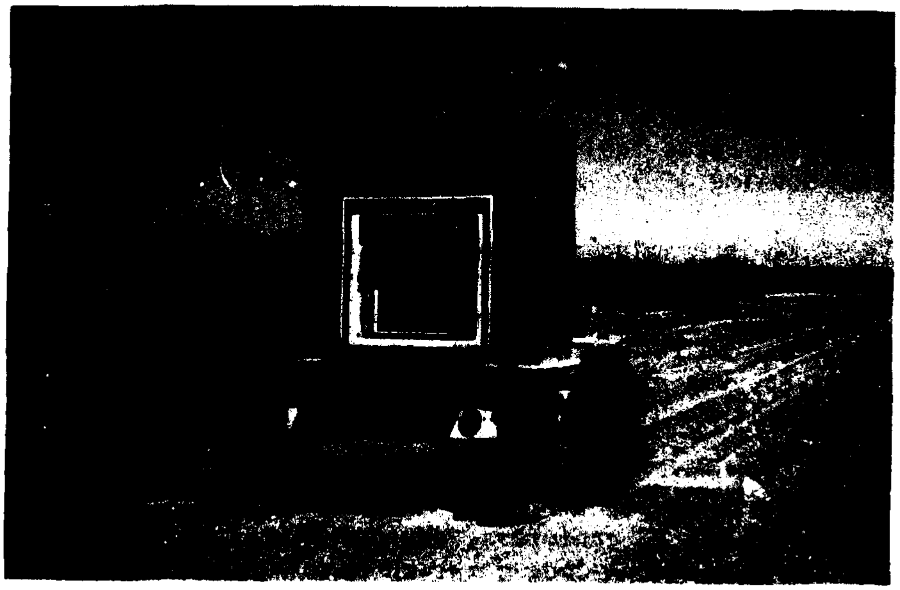

Figure 3: Trailer Mounted Blackbody Target

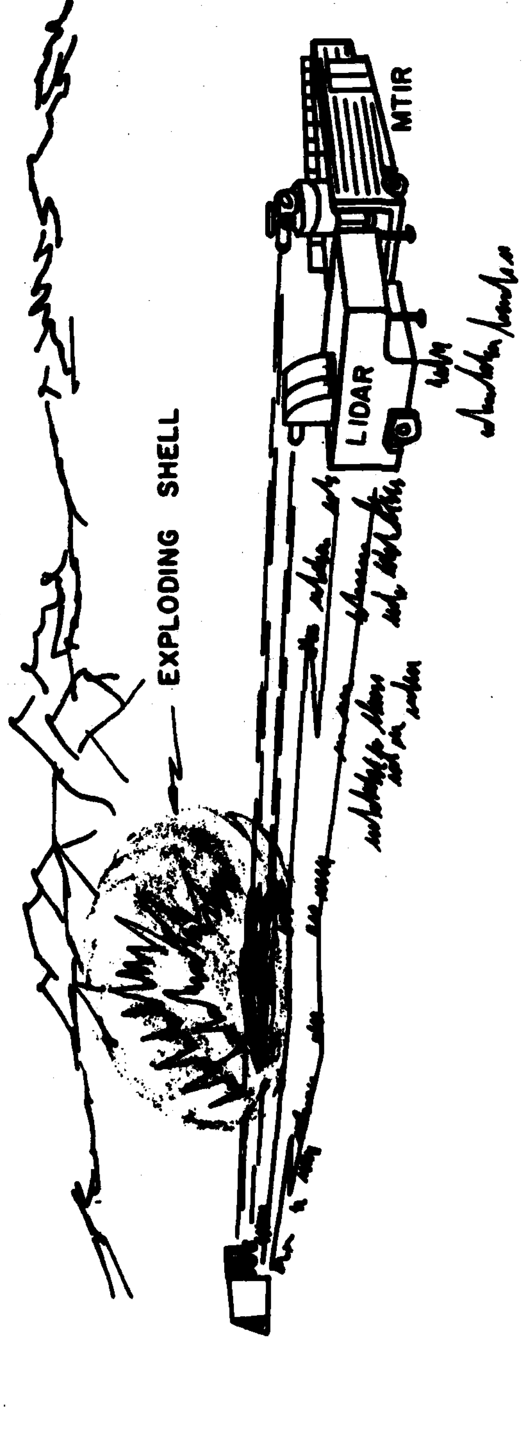

FIGURE 4. FIELD TEST CONFIGURATION FOR IR TRANSMISSION AND CONTRAST MEASUREMENTS

tires and diesel fuel.

Dust clouds were produced in the test area by running tactical vehicles in racetrack patterns at distances from 13 to 27 meters to one side of the line-of-sight. M-47 tanks, armored personnel carriers, and shop trucks were utilized.

Data Collection: Data was collected by the MTIR during all of the test series with the exception of the Fire Products test when it removed to support a High Energy Laser test off-range. Data collection consisted of aiming the FLIR at the blackbody target, which was heated to approximately 70°C to simulate a vehicle warmed by engine heat, and simultaneously recording the FLIR output channels and the standard video image before and during the smoke, or dust, cloud development. Timing was inserted on the linear outputs of the FLIR and video camera for later data correlation.

Data Handling: For analysis purposes the imagery recorded on the cassette recorders was transferred to the Ampex recorder, which has an excellent single frame capability. The image intensity of the heated blackbody and the cool, low emissivity housing of the blackbody were read, at one second intervals, utilizing a Colorado Video Model 321 video analyzer. The ratio of the two readings, the image contrast, was plotted, along with the LIDAR transmissivity data obtained from ASL, as a function of time (4). Since the dust clouds produced during the tests stayed close to ground level and did not sufficiently intercept the LIDAR's backstop reflector, the contrast of a white building to its dark background was read from the standard video camera output for comparing this part of the test.

IV. RESULTS

The TV monitor photographs of Figures 5 and 6 illustrate the type of imagery recorded during the tests. The photos on the far left of Figure 5 were taken from the MTIR's video camera and show the scene looking north along the optical path during test HC-7, both before and after development of the smoke cloud. The cross hairs cover the blackbody target position. The large white rectangle in the background is the LIDAR backstop. The photos in the middle and to the left are from the FLIR's 8-12 and 3-5 channels respectively and show the excellent HC smoke penetration at these wavelengths. These photos were taken after passing the FLIR signals through the video analyzer. The white rectangle near the middle of the vertical line is the heated blackbody target. The photos of Figure 6 were taken at the start of test WP-10. The white area in the far right of the video camera image (upper photo) is an exploding bulk white phosphorus shell. The lower photo is an 8-12 micron image recorded .02 seconds later and shows a low jet of hot smoke, almost invisible in the video image, about to obscure the target. The detonation is not visible

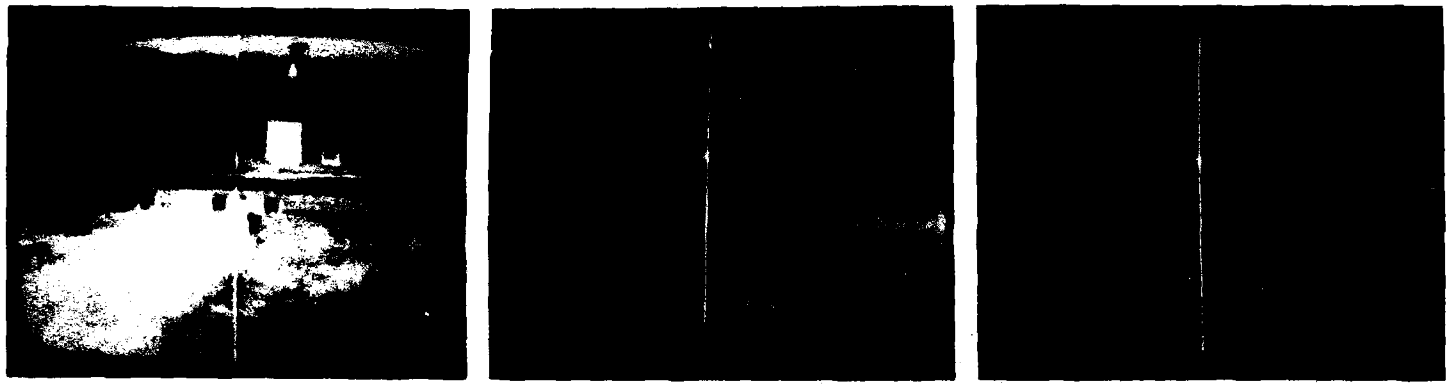

Video 8-12 Micron 3-5 Micron

Optical Path Clear

Video 8-12 Micron 3-5 Micron

Optical Path Obsured By Thick Smoke

Figure 5: Standard Video and FLIR Images Recorded During Test HC 7, Before and After Smoke Cloud Formation.

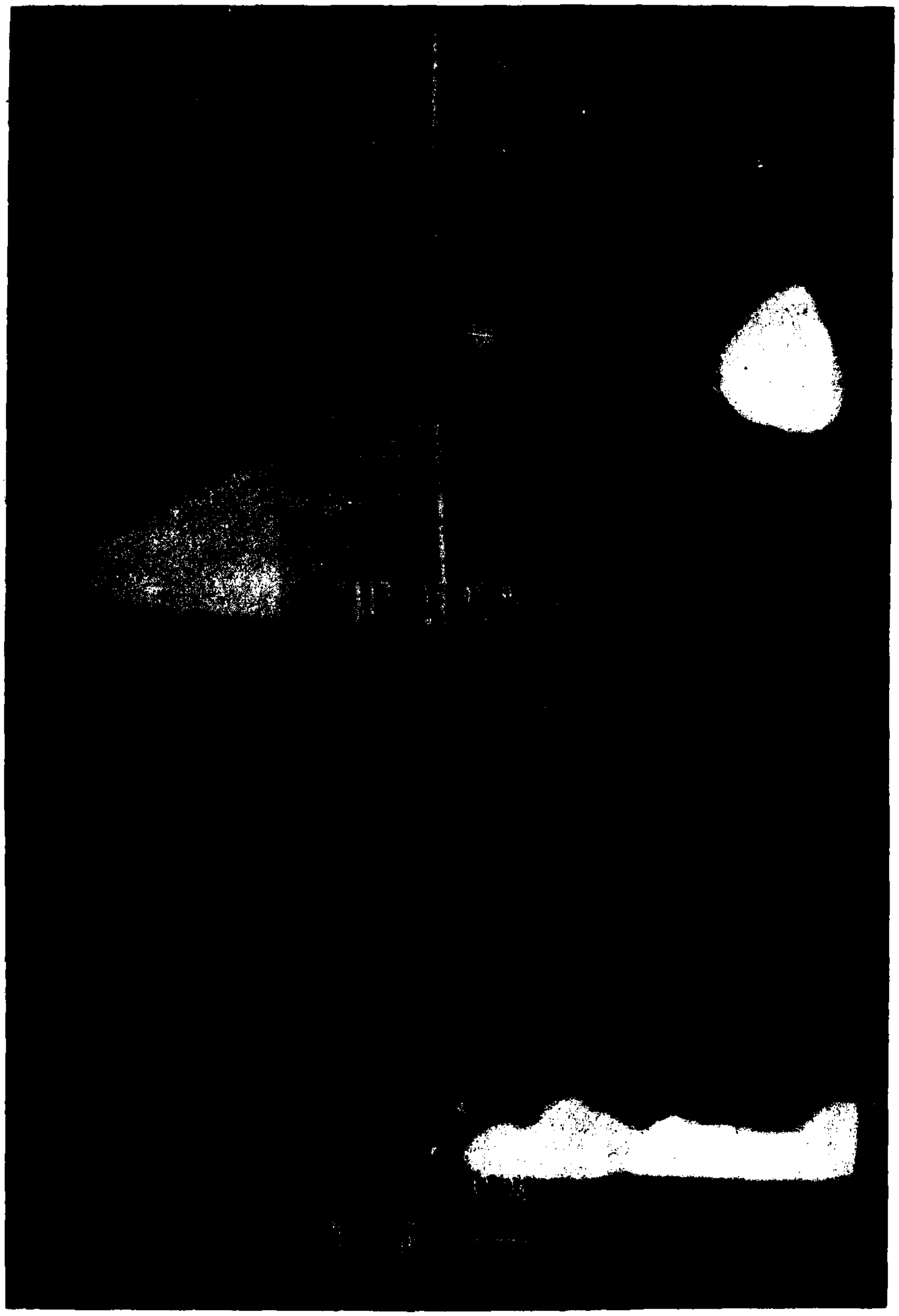

Figure 6: Explosion of a White Phosphorus Shell During Test WP-10.

in the 8-12 micron image due to the FLIR's smaller field-of-view.

Figure 7 is a plot of FLIR image contrast and 1.06 micron transmission versus time for test HC 11. The sharp drop in the transmission curve indicates the arrival of the smoke cloud in the optical path. Figure 8 represents data recorded during tests XM-10. While contrast reduction is apparent in the FLIR images early in the test at no time was the target completely obscured in either IR band. It is interesting to note that the 3-5 micron image, while of lower contrast due to the lower sensitivity of the FLIR in this band, seems less effected by the XM smoke than does the 8-12 micron imagery. Figures 9 and 10 show data recorded during tests WP-10 and LF-4. Both of these tests involved the explosion of bulk white phosphorus shells. Total obscuration of the target, in both FLIR bands, was experienced during test WP-10 for an extended period of time. The nearness of the WP detonations to the optical path resulting in hot smoke in the line-of-sight is partly responsible for the total loss of contrast. During test LF-4, smoke from two WP rounds drifted across the optical path. Image contrast was lost only briefly at 8-12 micron and for longer periods at 3-5 micron.

Figure 11 compares the contrast of visible and 8-12 micron imagery through dust raised by two armored personnel carriers running in a racetrack pattern west of the optical path. Soil dampness inhibited the formation of dust clouds thick enough to completely obliterate the visible contrast during most of the test. The 8-12 micron contrast curve closely follows that from the visible imagery and indicates some dust penetration potential.

V. CONCLUSIONS

Results of the tests show that HC smoke screens do not effectively screen against infrared imaging systems operating in the 8-12 and 3-5 micron bands. Contrast is reduced, but not obliterated in either band, by XM smoke. Smoke produced by the explosion of bulk white phosphorus shells is effective in blocking FLIR imagery if the detonation takes place near enough to the line-of-sight so that the smoke is hot. Dust Clouds are effective obscurants in the 8-12 micron band.

REFERENCES

1. I.R. Abel, "Radiometric Accuracy in a Forward Looking Infrared System", Optical Engineering, Vol 16, No. 3, May-June 1977.

2. B.W. Kennedy, R. Peña, D. Hoock, and R. Sutherland, "Test Plan for Battlefield Induced Contamination Tests", US Army Electronics Research and Development Command, Atmospheric Sciences Laboratory, White Sands Missile

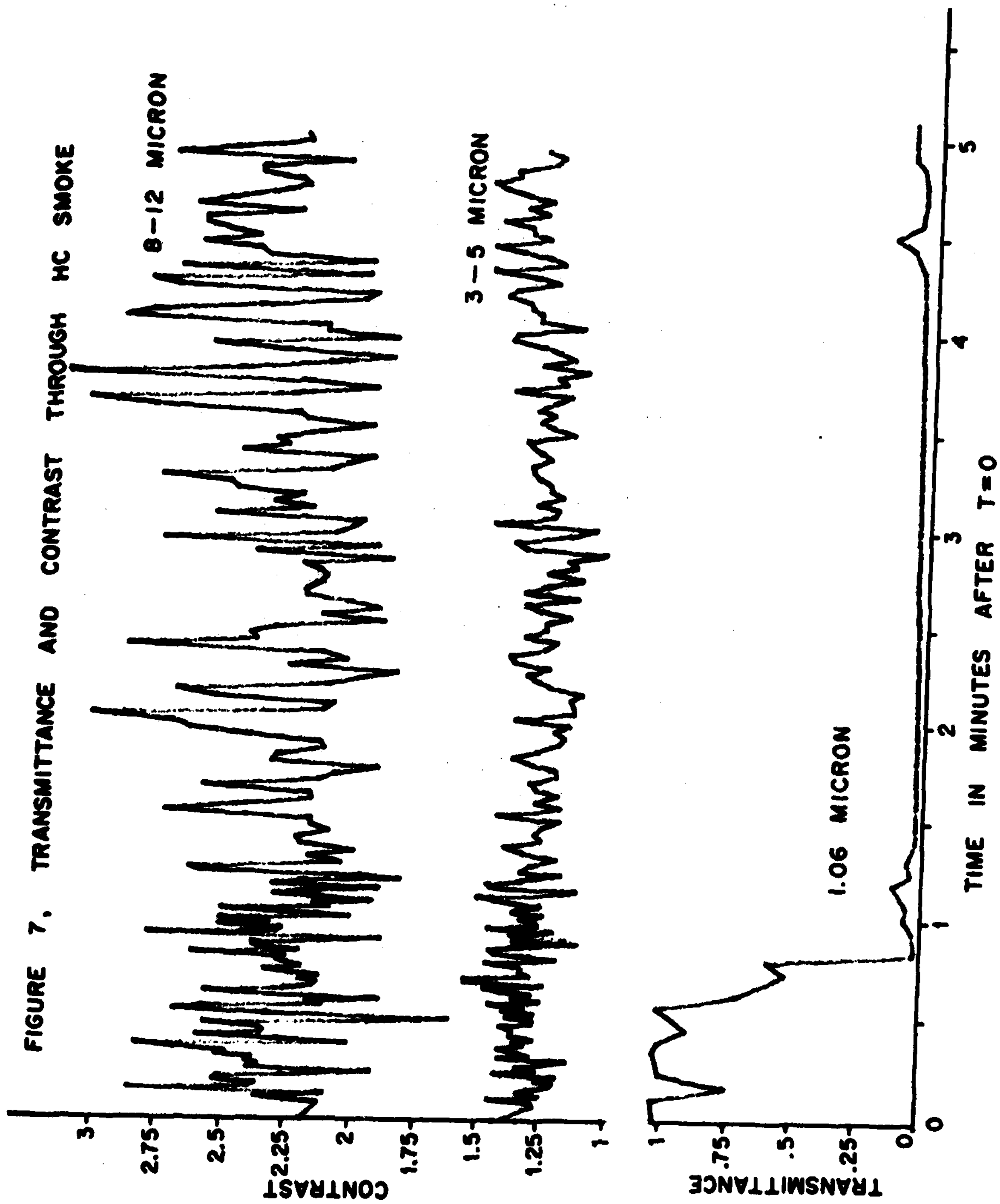

FIGURE 7. TRANSMITTANCE AND CONTRAST THROUGH HC SMOKE

FIGURE 8. TRANSMITTANCE AND CONTRAST THROUGH XM SMOKE

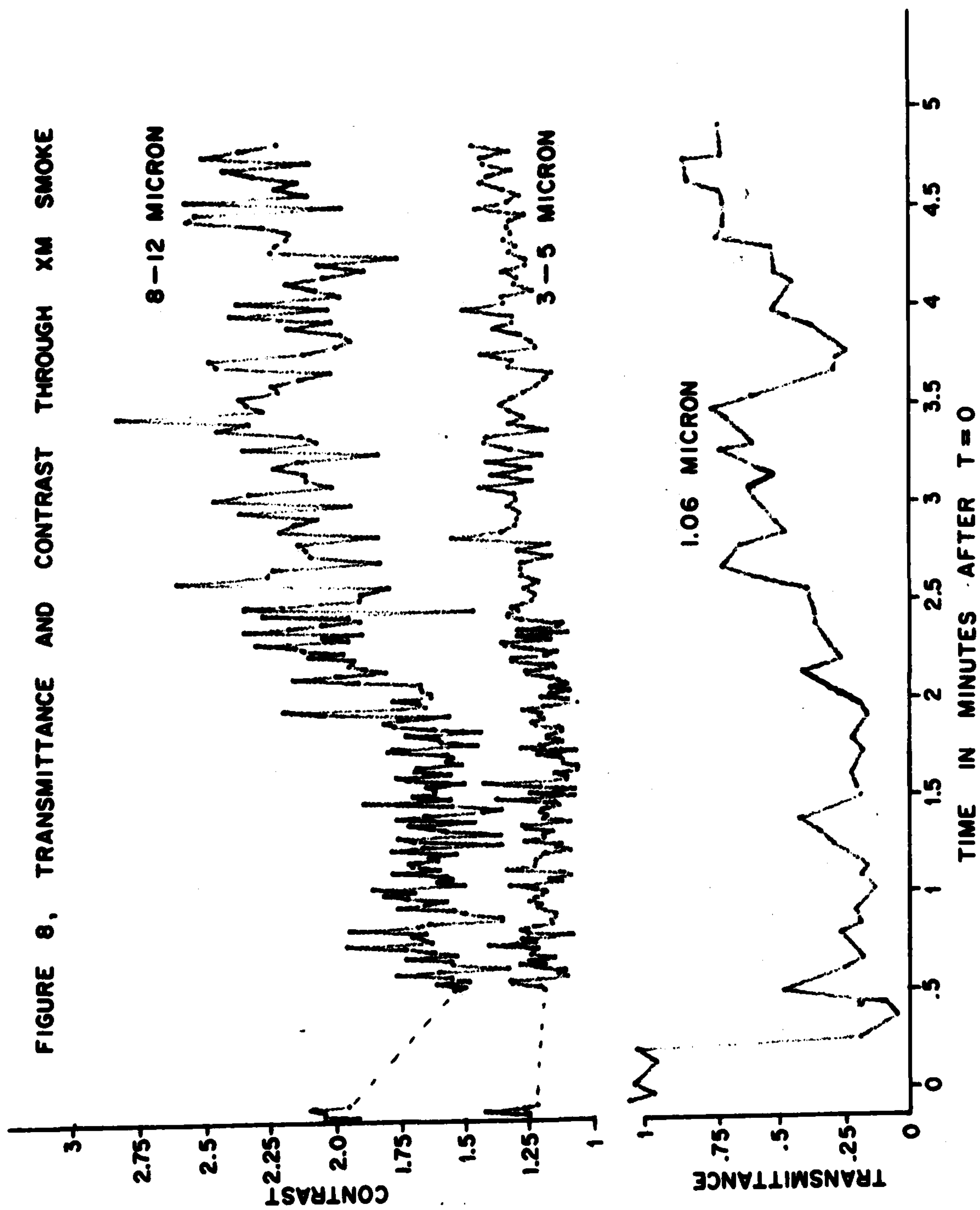

FIGURE 9. TRANSMITTANCE AND CONTRAST THROUGH WP SMOKE

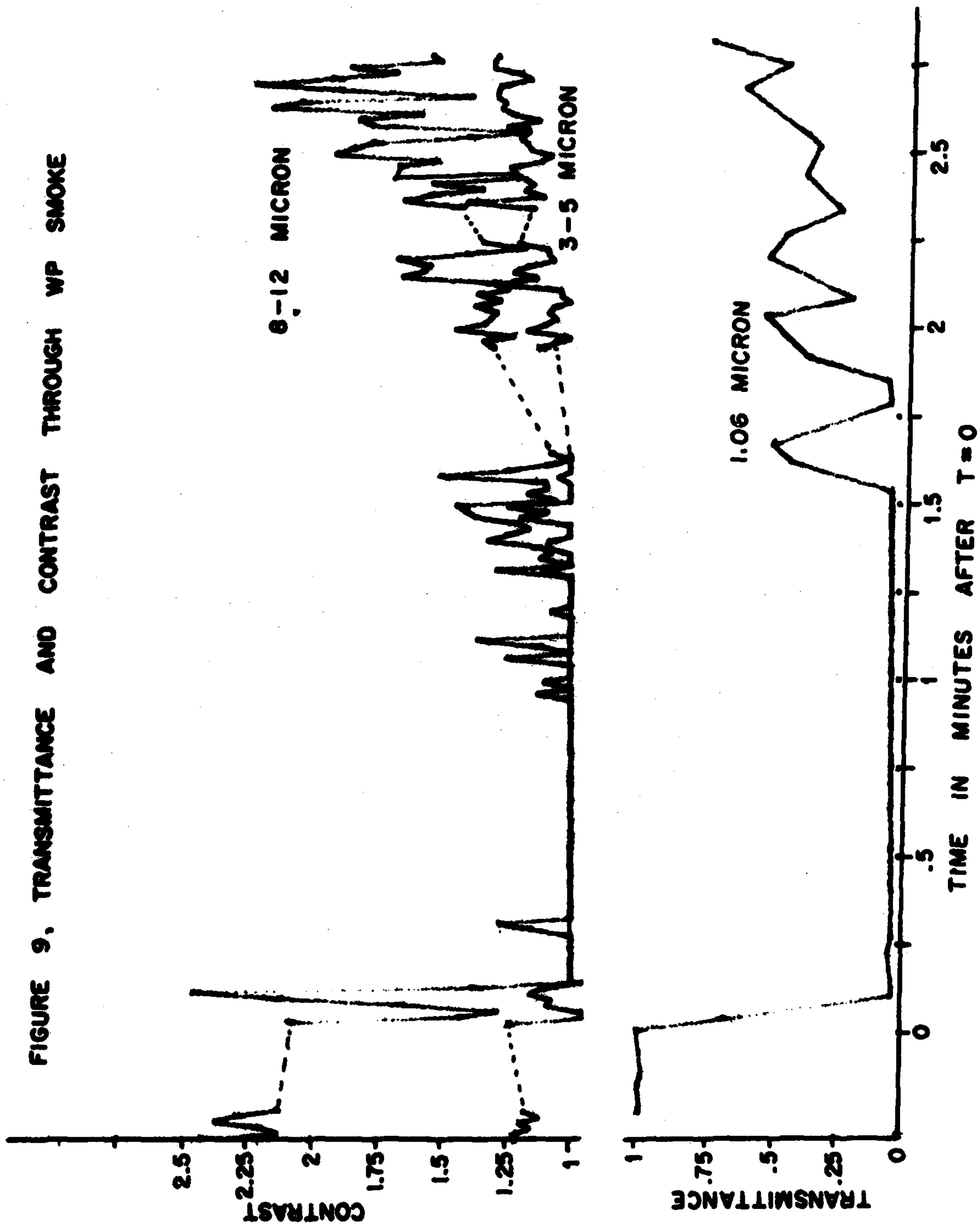

FIGURE 10. TRANSMITTANCE AND CONTRAST THROUGH LF SMOKE

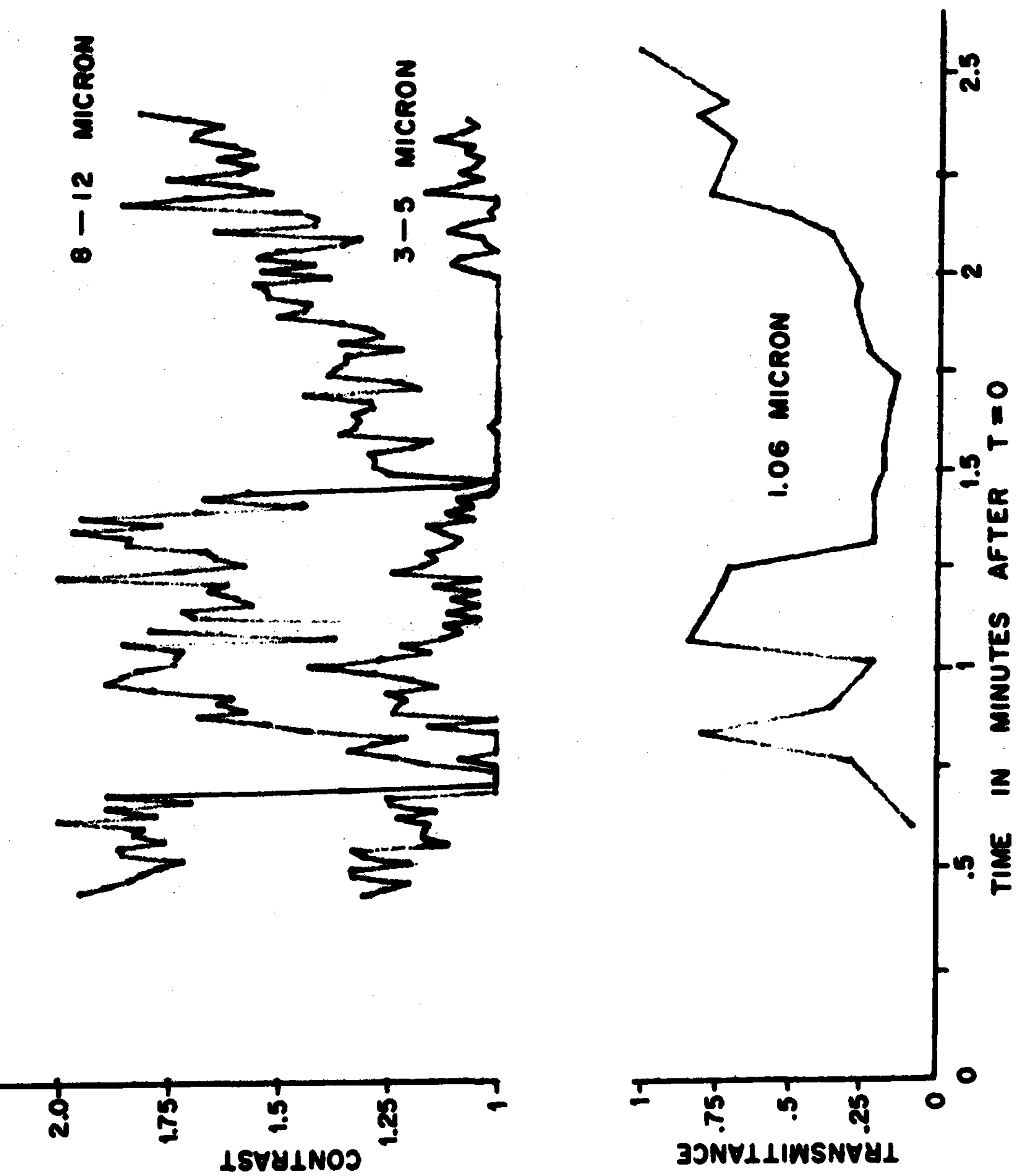

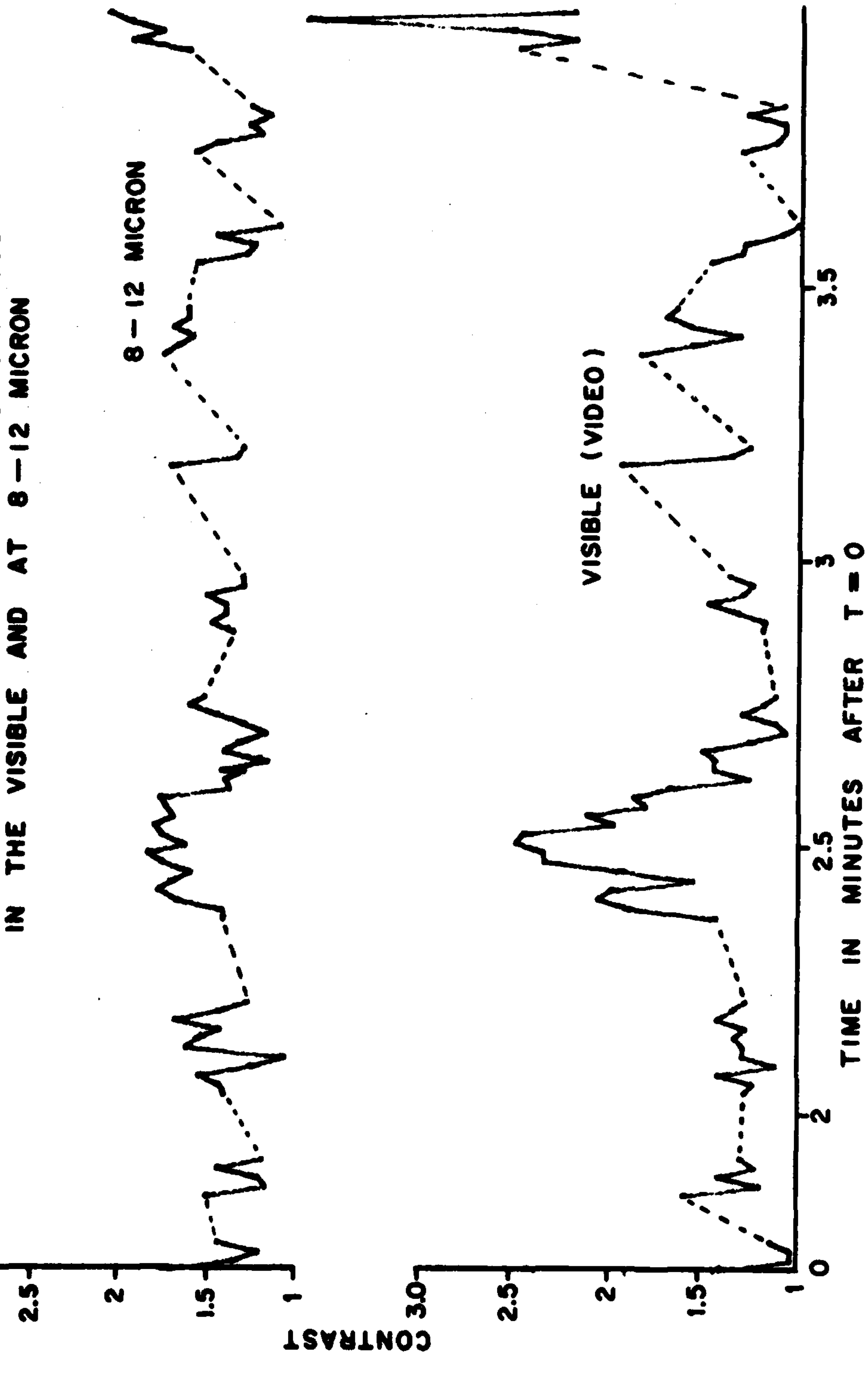

FIGURE 11. CONTRAST THROUGH VEHICULAR CAUSED DUST IN THE VISIBLE AND AT 8—12 MICRON

Range, NM 88002, February 1981.

3. B.W. Kennedy, "Battlefield Induced Contamination Test, Project Summary", US Army Research and Development Command, Atmospheric Sciences Laboratory, White Sands Missile Range, NM 88002, August 1981. (Internal Report).

4. R. Rubio, E. Measure, and D. Knauss, "LIDAR Smoke Transmissivity Data", US Army Electronics Research and Development Command, Atmospheric Sciences Laboratory, White Sands Missile Range, NM 88002. (Undated Draft Report).

PROPERTIES OF $SOCl_2$ ELECTROLYTE SOLUTIONS (U)

MARK SALOMON, Ph D
US ARMY ELECTRONICS TECHNOLOGY AND DEVICES LABORATORY, ERADCOM
FORT MONMOUTH, NEW JERSEY 07703

INTRODUCTION

A number of types of lithium secondary and primary nonaqueous batteries are under development in the Power Sources Division at Fort Monmouth. Military applications for portable power sources range from communications to laser designators and night vision devices. For the latter two applications, the lithium-thionyl chloride battery has been identified as a highly promising system. The battery was initially shown (1) to be capable of providing very high energy densities at various rates of discharge as shown in Figure 1. In this figure the discharge characteristics are

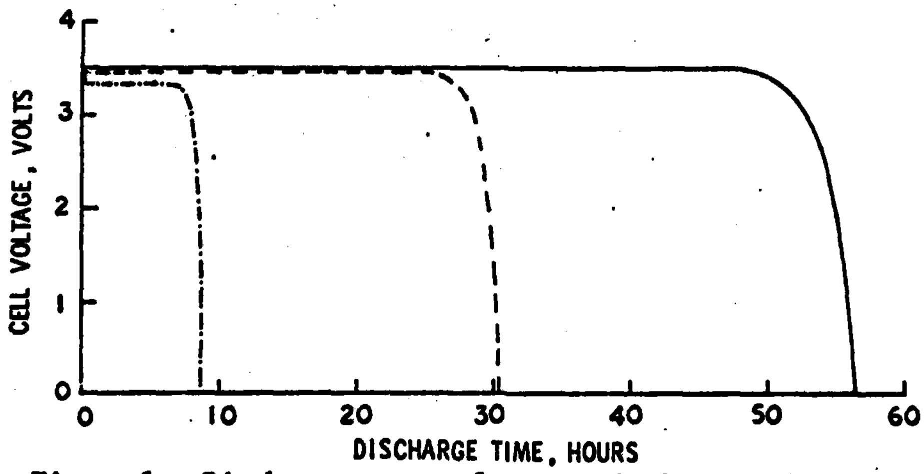

Figure 1. Discharge curves for a typical Li-$SOCl_2$ cell.

given for a Li-$SOCl_2$ cell containing 1.5 mol dm^{-3} $LiAlCl_4$ electrolyte, and at current densities of 1, 2, and 5 mA cm^{-2}. Operating voltages under current drain are around 3.4 V, and the discharge curve is remarkedly flat over the operational life of the cell. The end of the practical cell life can easily be identified by the rapid decrease in cell potential, and is due, in part, to precipitation of the cell product LiCl into the porous carbon cathode therefore physically blocking the cathode reactant ($SOCl_2$) from the porous cathode. Subsequent researches on the Li-$SOCl_2$ cell have identified additional technical problems such as voltage delays, safety, and low temperature performance. These technical problems are interdependent in the sense that improvement in one area will also result in incremental improvements in other areas. For example, researches on improving low temperature performance involve the selection of new conductive electrolytes which will not precipitate out as the temperature decreases. By improving the conductivity, simultaneous improvements are expected in safety because of less heat generation due to lower cell resistance, and increased cell capacity if the new electrolyte decreases the rate of formation of LiCl at the cathode. This latter effect can be achieved by employing electrolytes in which the cation will not precipitate as the chloride in solutions with a high chloride ion concentration.

Since there are virtually no detailed studies on the general physical chemistry of electrolyte solutions in $SOCl_2$, the initial phase of the program to develop new electrolytes was to determine those factors which govern both conductivities and solubilities.

EXPERIMENTAL

Materials: Thionyl chloride was purified as described in (2). Purified $LiAlCl_4$ was supplied by W. K. Behl of this laboratory and purified as described in (1). "Pure" grade $AlCl_3$ was sublimed before use. Tetraalkylammonium salts (R_4NX where X = Cl, ClO_4) were recrystallized from an appropriate solvent and vacuum dried. Tetraphenyl arsonate and tetraphenyl borate salts were prepared by metathesis starting with either Ph_4AsCl or $NaBPh_4$, and followed by recrystallization and vacuum drying. "Pure" grade LiCl, NaCl, and KCl were dried at 115°C prior to use. All solvents used in the crystallizations were either AR grade (methanol, ethylacetate, ether, petroleum ether, chloroform), twice fractionated (water, ethanol), or highly purified commercial products (acetone, acetonitrile). All salts and $SOCl_2$ were stored in an argon filled dry box (O_2 and H_2O content less than 1 ppm).

Dielectric Constant Measurements: The static dielectric constants at 15°, 25°, and 35°C were measured by the comparison method (3). The cell, which utilized Type 304 stainless steel, consisted of concentric steel electrodes threaded onto a Teflon base which also formed part of a water jacket. The cell capacities were measured at 1 MHz by a substitution method with a General Radio 1606-B bridge and 722-D and 1422-ME precision capacitors. The cell constants were determined from measurements with air, benzene, and tetrahydrofuran. The cell was filled with $SOCl_2$ in the dry box, sealed with a Teflon stopper, and removed to the laboratory for capacitance measurements at 15°, 25°, and 35° ± 0.1°C.

Conductance Measurements: Dip type conductivity cells with smooth Pt electrodes were modified to permit sealing with a 10/20 ST Pyrex stopper and to permit immersion in a water bath thermostated at 25 ± 0.03°C. An Altrex model RC-18A conductivity bridge was used for the measurements: the stated accuracy of this bridge is ± 0.05%. All solutions were prepared by volume in the dry box at 22-27°C, and concentration corrections to 25°C were made using the temperature coefficient of the density for the pure solvent (4). The overall precision in the molar conductivities (Λ) is estimated to be around 1-2%.

Saturated solutions of LiCl, NaCl, and KCl were prepared by adding $SOCl_2$ to an excess of salt in the dry box. The solutions were stored at room temperature for 72 h with periodic shaking. When the dry box reached a temperature of around 30°C for several hours, the saturated solutions were transferred to the conductivity cells with a small amount of solid. The cells were then sealed and removed from the dry box to the laboratory for measurements at 25°C. Two measurements were made for each salt, and the mean electrolytic conductivities (after correcting for the electrolytic conductivity of the solvent) were used to compute the solubilities as described below.

RESULTS AND DATA ANALYSES

The static dielectric constants at 15°, 25°, and 35°C are, respectively, 9.65, 9.23, and 8.77D. These results were fitted by least squares to the following smoothing equation

$$\epsilon/D = -3.88 + 3903/(T/K) \quad [1]$$

The molar conductivities, Λ, for the highly soluble salts were calculated from the experimental electrolyte conductivities after correcting for the electrolytic conductivity of the pure solvent: at 25°C $\kappa(SOCl_2)$ 5×10^{-9} S cm^{-1} (5). The results of these measurements are summarized in Figures 2-4 in which the molar conductivities are plotted against the square root of the concentration (all concentration units are mol dm^{-3}). In all cases the conductivity curves are non-linear and fall well below the limiting law curve. This type of behavior is well known and is identified with the existence of ion pairs. The conductivity data were, therefore, treated in terms of an ion pairing model in which the equilibrium between ion pairs, MX, and the ions M^+ and X^- is defined as

$$MX \rightleftharpoons M^+ + X^- \qquad K_D \quad [2]$$

The conductivity data for the salts over the concentration range of 0.01 to 5×10^{-5} mol dm^{-3} were analyzed by empirical forms of the Fuoss-Hsia (6) equation

$$\Lambda = \Lambda^{\infty} - S(\alpha c)^{1/2} + E\alpha c\ln(\alpha c) + J_1\alpha c + J_2(\alpha c)^{3/2} - \alpha c y_{\pm}^2/K_D^{\infty} y_n \quad [3]$$

or the Fuoss-Onsager (6) equation

$$\Lambda = \Lambda^{\infty} - S(\alpha c)^{1/2} + E c \ln(\alpha c) + J\alpha c - \alpha c y_{\pm}^{2}/K_{D}^{\infty} y_{n} \qquad [4]$$

In eqs [3] and [4], α is the degree of dissociation, c the total concentration in mol dm^{-3}, $y_{\pm}$ the mean molar activity coefficient, and y_n the activity coefficient of the neutral ion pair. The J's are empirical constants evaluated as described below. In all of the present calculations, y_n was estimated as $\exp(0.3A\alpha c)$ where A is the Debye-Huckel constant (12.64 $mol^{-1/2}$ $dm^{3/2}$ at 25°C). y_n values for all concentrations employed in the present calculations are essentially unity. The mean molal activity coefficients were estimated from the Davies (7) equation:

$$\log y_{\pm} = -A(\alpha c)^{1/2}/[1 + (\alpha c)^{1/2}] + 0.3A\alpha c \qquad [5]$$

K_D^{∞} and Λ^{∞} values for each salt were determined by a pit-mapping method in which the standard deviations in the observed molar conductivities, σ_{Λ}, were minimized. σ_{Λ} is defined as

$$\sigma_{\Lambda} = \left\{\sum(\Lambda_{obs} - \Lambda_{calc})^{2}/(N - 3)\right\}^{1/2} \qquad [6]$$

For a given Λ^{∞} and K_D^{∞}, α and $y_{\pm}$ were evaluated for each concentration by an interation method using eqs [5] and

$$K_D^{\infty} = \alpha^{2} c y_{\pm}^{2}/(1 - \alpha) y_{n} \qquad [7]$$

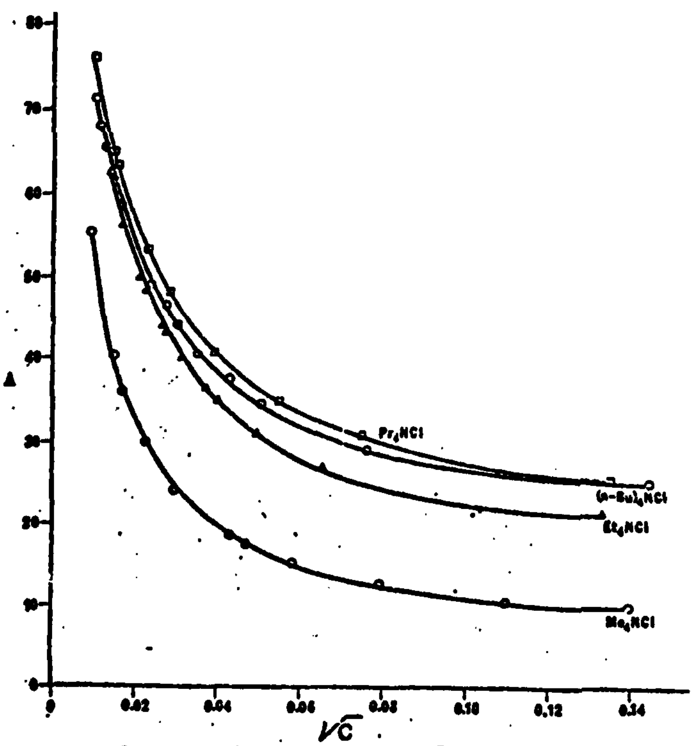

Figure 2. Conductivities of tetraalkylammonium chlorides.

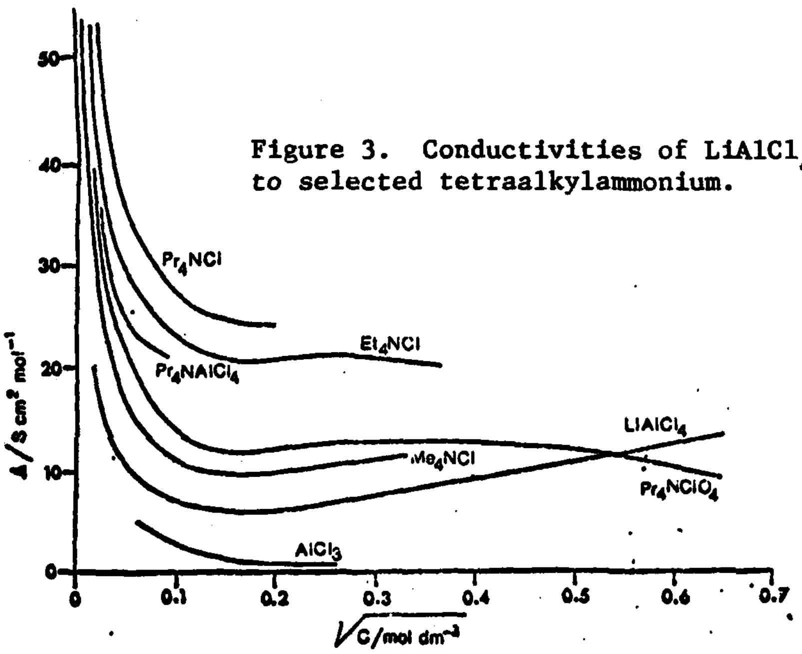

Figure 3. Conductivities of $LiAlCl_4$ and $AlCl_3$ compared to selected tetraalkylammonium.

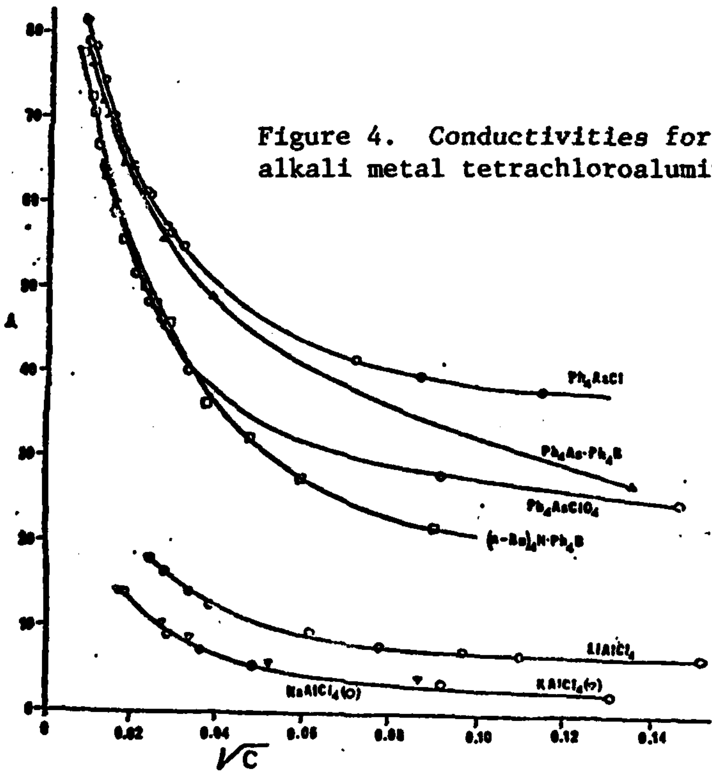

Figure 4. *Conductivities for tetraphenyl salts and alkali metal tetrachloroaluminates.*

The J values were evaluated by the least squares method and the calculations repeated until the minimum in the pit was found. The refined values for Λ^{∞} and K_D^{∞}, and the J's and σ_Λ are in Table 1.

Table 1. **Results of Analyses Based on Equations (3) - (4) at 25°C**

salt	$\Lambda^{\infty}(\sigma)^a$	$10^4 K_D^{\infty}(\sigma)^a$	$\sigma\Lambda$	$10^{-5}J_1$	$-10^{-5}J_2$	R^d
Me_4Cl	128.6 (1.3)	0.220 (0.004)	0.43	1.824	17.95	0.457
Et_4NCl	117.3 (0.6)	0.750 (0.006)	0.22	2.074	33.23	0.991
$n\text{-}Bu_4NCl$	103.6 (0.9)	1.25 (0.02)	0.41	1.507	15.63	0.968
Ph_4AsCl	102.0 (0.6)	2.20 (0.04	0.38	1.634	18.97	0.982
$n\text{-}Bu_4NBPh_4$	94.4 (0.3)	2.43 (0.04)	0.23	0.850	-0.374	0.089
$n\text{-}Bu_4NBPh_4$ [b]	94.4 (0.3)	2.43 (0.04)	0.23	0.858	------	0.999
Ph_4AsBPh_4	94.4 (0.5)	3.9 (0.1)	0.36	1.151	8.886	0.960
Ph_4AsPic [c]	92.6 (0.1)	4.5 (0.04)	0.13	1.138	8.599	0.999
LiCl	85.1					
NaCl	88.6					
KCl	91.4					

a. Results based on eq. [3] except as noted; Λ^{∞} units are S cm^2 mol^{-1} and K_D^{∞} units are mol dm^{-3}.

b. Results based on eq. [4].

c. Pic = picrate.

d. Correlation coefficient for least squares fit to eqs [3] or [4].

The solubilities for the slightly soluble salts LiCl, NaCl, and KCl were calculated from the Onsager equation corrected for ion pairing:

$$\Lambda = \Lambda^{\infty} - S(\alpha c)^{1/2} - \alpha y_{\pm}^2 c/K_D^{\infty} \qquad [8]$$

Eq. [8] was solved by an interative method along with eq. [5] noting that $\Lambda = 1000\kappa/c_{satd}$, and varying K_D^{∞} within reasonable limits. Table 2 shows the effect of choice of K_D^{∞} on the calculated solubilities, c_{satd}. Within experimental error for the measured κ's of the saturated solutions, it is found that c_{satd} is essentially constant for K_D^{∞} values > 1 X 10^{-5} mol dm^{-3}. For all the solutes studied in the present work, values of K_D^{∞} were always found to be greater than 2 X 10^{-5} mol dm^{-3}, and is reasonable to take a lower limit of K_D^{∞} = 1 X 10^{-5} dm^{-3} for LiCl, NaCl, and KCl. On this basis it is estimated that

$$c_{satd}(LiCl) = 2.2 \times 10^{-6}\ mol\ dm^{-3}$$

$$c_{satd}(NaCl) = 4.6 \times 10^{-7}\ mol\ dm^{-3}$$

$$c_{satd}(KCl) = 2.7 \times 10^{-7}\ mol\ dm^{-3}$$

Whereas c_{satd} values are dependent upon the choice of K_D^{∞}, values of the thermodynamic solubility product constant, K_{s0}^{∞}, are independent of K_D. Since K_{s0}^{∞} is simply defined as $(\alpha c y_{\pm})^2$, it turns out (as it should) that K_{s0}^{∞} is independent upon the choice of K_D^{∞}. The results for 25°C are:

$$K_{s0}^{\infty}(LiCl) = 3.3 \times 10^{-12}\ mol^2\ dm^{-6}$$

$$K_{s0}^{\infty}(NaCl) = 2.0 \times 10^{-13}\ mol^2\ dm^{-6}$$

$$K_{s0}^{\infty}(KCl) = 7.1 \times 10^{-14}\ mol^2\ dm^{-6}$$

Table 2. Calculated Solubilities for NaCl as a Function of K_D^{∞}

K_D^{∞}	1×10^{-3}	1×10^{-4}	1×10^{-5}	5×10^{-6}	1×10^{-6}
$10^7 c_{satd}$	4.57	4.59	4.77	4.97	6.57
α	1.000	0.996	0.958	0.919	0.695
$y_{\pm}$	0.981	0.981	0.981	0.981	0.981

DISCUSSION

The analysis of the conductivity data for $AlCl_3$ solutions in terms of the simple dissolution reaction

$$AlCl_3 + SOCl_2 = SOCl^+ + AlCl_4^- \overset{K_D^{\infty}}{=} (SOCl^+)(AlCl_4^-)$$

was not successful, i.e., σ_A values were generally large and insensitive to values of K_D^{∞}. This inability to fit the data to this simple dissolution mechanism is attributed to both the experimental error and to the probability that dissolution is more complex and involves such species as Al_2Cl_6, $Al_2Cl_7^-$, etc.

This complex chemistry of $AlCl_3$ systems in $SOCl_2$ is being studied in greater detail.

The results of the calculations for Λ^{∞} and K_D^{∞} given in Table 1 show that all salts are highly associated in $SOCl_2$, and that an anomaly exists in K_D^{∞} for $(C_3H_7)_4NCl$. Based soley on ion size (electrotatics), it is expected that K_D for $(C_3H_7)_4NCl$ will be smaller than for $(C_3H_7)_4NClO$ and $(C_3H_7)_4NAlCl_4$. The reverse behavior is attributed to a strong interaction between Cl^- and the solvent, i.e., to the formation of a charge transfer (CT)-complex denoted as $SOCl_2 \cdot Cl^-$. CT-complexes between $SOCl_2$ and halide ions have been identified by Wasif and co-workers (8), and the nature of these complexes have also been described by the author (9). When sulfur is bonded to highly electronegative atoms such as oxygen or chlorine, there results a large lowering of the energy levels of the d orbitals on the sulfur which enables the sulfur to act as a π-accepter. In terms of Pearson's concepts (10), $SOCl_2$ behaves as a "hard" Lewis acid and coordinates with a Lewis base such as Cl^- via (3d-3p)π bondings. Additional stabilazation occurs via back-bonding to the 3d orbitals of Cl^- as shown in previous MO calculations on the interaction between Cl^- and the sulfite ester $(CH_2O)_2SO$ (9). Combined with the above results it is concluded that future studies on improved electrolytes for Li-$SOCl_2$ batteries should include salts possessing large cations and hard Lewis basic anions.

The molar conductivities of individual ions at infinitesimal ionic strength, λ^{∞}, are of great interest since their comparative values relate only to ion-solvent interactions. The direct evaluation of λ^{∞} values requires transference number data which, together with numerous other data, are not available for $SOCl_2$ solutions. λ^{∞} values were, therefore, evaluated empirically using the assumption that $\lambda^{\infty}(Ph_4As^+) = \lambda^{\infty}(BPh_4^-)$ which turns out to be identical to the assumption (11-13) that $\lambda^{\infty}(n\text{-}Bu_4N^+) = \lambda^{\infty}(BPh_4^-)$. The results are given in Table 3. There is no question that the Stokes equation, and hence the constancy of the Walden product $\lambda^{\infty}\eta^{\circ}$, fails when comparing various solvent systems due to the varying nature of the ion-solvent interactions. This is demonstrated in Table 4 where values for Cl^- and ClO_4^- are compared for selected solvents. The order of solvents listed in this table was chosen so as to reflect the changing nature of Cl^- solvation compared to that of ClO_4^-. The fact that $\lambda^{\infty}(Cl^-) > \lambda^{\infty}(ClO_4^-)$ in water, formamide and propylene carbonate can simply be attributed to the greater "hydrodynamic" radius of ClO_4^-. For those cases where $\lambda^{\infty}(Cl^-)$ is equal to or less than $\lambda^{\infty}(ClO_4^-)$, it is clear that the solvation of Cl^- is changing relative to that of ClO_4^-. The factors giving rise to this phenomena are varied. For example, in $SOCl_2$ there is evidence, as discussed above, that the solvent can form weak charge transfer complexes with Cl^- but not with ClO_4^- (9-11). In most aprotic solvents in which anions are poorly solvated (11), ion-solvent interactions are generally strongly governed by mutual polarizabilities (12-14). In methanol, the interaction with Cl^- is more extensive than with ClO_4^- due to an entropic effect: i.e., a greater "net ordering" as described previously (14,15).

Table 3. Molar Conductivities and Stokes Radii for Individual Ions in $SOCl_2$

ion	λ^∞/S cm^2 mol^{-1}	r_s/Å [b]	ion	λ^∞/S cm^2 mol^{-1}	r_s/Å [b]
Ph_4As^+ [a]	47.2	2.78	Li^+	29.7	4.41
BPh_4^- [a]	47.2	2.78	Na^+	33.0	3.98
$n\text{-}Bu_4N^+$	47.2	2.78	K^+	35.8	3.66
$n\text{-}Pr_4N^+$	51.0	2.57	Cl^-	55.6	2.36
Et_4N^+	61.7	2.12	ClO^-	55.2	2.37
Me_4N^+	73.0	1.80	Pic^-	47.4	2.77
			$AlCl_4^-$	46.0	2.85

a. From assumption that $\lambda^\infty(Ph_4As^+) = \lambda^\infty(BPh_4^-)$.

b. Calculated from eq. [9].

Table 4. Values for Cl^- and ClO_4^- at 25°C in Selected Solvents

solvent	$\lambda^\infty(Cl^-)$	$\lambda^\infty(ClO_4^-)$
H_2O	76.4	67.4
formamide	17.1	16.5
propylene carbonate	21.0	19.6
dimethyl sulfoxide	24.0	24.1
$SOCl_2$	55.6	55.2
sulfolane (30°C)	9.3	6.7
acetylacetone	38.0	49.8
methanol	52.4	70.8
acetonitrile	98.7	103.7
acetone	105.2	115.3

With very few exceptions, the molar conductivities of the alkali metals increase as the crystal radii increase according to $Li^+ > Na^+ > K^+ > Rb^+ > Cs^+$. It also turns out that for most aprotic solvents, the Walden product $\Lambda^\circ\eta^\circ$ is fairly constant for the alkali metals in a given solvent, but varies markedly from solvent to solvent. To account for this behavior, one cannot employ crystal radii in the Stokes equation, but rather "hydrated" or "Stokes" radii, r_s, defined in the usual manner by the equation

$$\Lambda^\circ\eta^\circ = 0.820z^2/r_s \qquad [9]$$

The Stokes radii listed in Table 3 was calculated from eq [9].

REFERENCES

1. W. K. Behl, J. A. Christopulos, M. Ramirez, S. Gilman, J. Electrochem. Soc., 120, 1619 (1973).
2. L. Friedman and W. P. Wetter, J. Chem. Soc. (A), 36 (1967).
3. L. Hartshorn and P. A. Oliver, Proc. Roy. Soc. (London), Ser. A, 123, 664 (1929).
4. M. Salomon, J. Electrochem. Soc. 128, 233 (1981).
5. According to Dr. H. V. Venkatasetty (private communication), $\kappa(SOCl_2)$ is around 3-5 x 10^{-9} S cm^{-1} at 25°C.
6. See R. Fernandez-Prini, "Physical Chemistry of Organic Solvent Systems," Chap. 5.1, A. K. Covington and T. Dickinson, editors, Plenum Press, London, (1973).
7. C. W. Davies, "Ion Association," Butterworths, London, (1962).
8. A. Salama, S. B. Salama, M. Sobier, and S. Wasif, J. Chem. Soc. (A), 1112 (1971).
9. M. Salomon, J. Phys. Chem. 79, 429 (1975); 79, 2000 (1975).
10. R. G. Pearson, J. Am. Chem. Soc. 85, 3533 (1963).
11. C. M. Criss and M. Salomon, J. Chem. Educat. 53, 763 (1976).
12. A. J. Parker, Chem. Revs. 69, 1 (1969).
13. B. G. Cox, G. R. Hedwig, A. J. Parker and D. W. Watts, Aust. J. Chem., 27, 477 (1974).
14. C. M. Criss and M. Salomon, "Physical Chemistry of Organic Solvent Systems," Chap. 2.4, eds. A. K. Covington and T. Dickinson, Plenum Press, London, 1973.
15. C. M. Criss, J. Phys. Chem. 78, 1000 (1974).

*SCHUSCHEREBA, BEATRICE

AUTORADIOGRAPHY OF PRIMATE RETINA AFTER Q-SWITCHED RUBY LASER RADIATION (U)

*STEVEN T. SCHUSCHEREBA, BS
EDWIN S. BEATRICE, M.D.,COL MC
LETTERMAN ARMY INSTITUTE OF RESEARCH
PRESIDIO OF SAN FRANCISCO, CALIFORNIA 94129

INTRODUCTION

Biological implications in the use of laser devices by the Army has been the subject of study in the last two decades. For laser systems operating in the visible and near-infrared spectral region, the retina is the most vulnerable part of the body, and retinal effects have been extensively characterized ophthalmoscopically, histologically, and functionally (1-7). These effects vary from severe damage, accompanied by massive retinal hemorrhaging and extrusion into the vitreous (6), to small retinal burns characterized by focal retinal opacities (5) to changes in visual function (7) with or without morphologic changes.

A principal concern of laser bioeffects investigations has been mechanism and recovery processes of retinal tissue after damage by laser radiation near the visible damage threshold. Adams et al. (2), in their study of threshold exposure limits, found that extremely low output energies from a Q-switched ruby laser (70 μJ at the cornea) produced extensive changes in the rhesus monkey retina when examined by electron microscopy. These changes included formation of bizarre fingerprint-like whorls in the outer segments at the base of the outer segment in the photoreceptor cells. This is in sharp contrast to the highly ordered arrangement in normal photoreceptors. The low levels of coherent radiation were thought to effect the formation of the outer segment membranes. Similar findings are observed in aged human retinas (8).

Young (9) studied outer segment formation by autoradiography, a technique that used radioactive amino acids as precursors for proteins, and discovered that an enormous amount of metabolic effort is devoted to a process that supports visual function. Rods, which subserve scotopic vision (vision in dim light), and cones, which subserve photopic vision (vision in bright light), expend most of their energy on the repeated replacement of their photon-capturing devices, the outer segments. Proteins were synthesized in the inner segment and migrated into the outer segment where they were assembled into membranous discs that comprised the outer segment stack. Opsin, the rod visual pigment protein, comprised most of the protein in rod outer segments. Smaller quantities of proteins are produced in the nucleus and very little in other parts of the cell. The question of whether or not near threshold laser light exposure can alter photoreceptor metabolism has long been pondered. Marshall (1) first reported, for suprathreshold Q-switched ruby laser exposures of the retina, that protein synthesis (in vitro) was inhibited in photoreceptor inner segments and nuclei; however, no work has been reported on the effects of laser light on outer segment synthesis rates. It seems that knowledge of how lasers alter normal biologic function and cellular dynamics is an important area of study that should parallel other studies of ophthalmoscopic, histologic, and functional changes. The study of photoreceptor metabolism after Q-switched ruby laser radiation might give additional information regarding damage mechanisms involving metabolic activities. An understanding of the metabolism of damaged retinal tissue might suggest methods of treatment for such injury. In addition, such an understanding may also pave the way for preventive measures against injury. To gain insight into how lasers affect photoreceptor metabolism a study was undertaken to examine laser-induced retinal changes in outer segment renewal rates by autoradiography.

The work objectives of this study were: 1) to evaluate the recovery of Rhesus monkey retinal rods (similar in retinal structure to the human) after exposure (20 nsec pulse duration, 1000 μm beam spot-size) to a range of Q-switched ruby laser radiation (suprathreshold to subthreshold for retinal damage as evidenced by ophthalmoscopy), 2) to correlate morphologic damage by both light and electron microscopy with biochemical abnormalities observed by autoradiography, 3) to assess the degree of sensitivity provided by autoradiography and 4) to postulate possible damage and recovery processes.

MATERIALS AND METHODS

The Q-switched ruby laser system was employed (4). This system had been previously used to determine ED_{50} levels for 1000 μm diameter exposures (10) and transmission electron microscopy studies (2). The output beam diameter was 1.7 mm with beam divergence of one milliradian. A 20 diopter convex lens placed at twice the focal length of the lens (10 cm) produced a 2.2 mm beam on the cornea with a 67 mr divergence resulting in 1000 μm retinal irradiance diameter for a single 20 nsec pulse. An ultrafast detector and oscilloscope were used to measure each exposure. A helium-neon (He-Ne) laser of low output energy was aligned colinearly to aim the ruby beam on the retina at predetermined loci.

A Rhesus monkey was anesthetized with halothane. The pupils were dilated and corneal transparency was maintained by irrigation with normal saline. The retina was viewed and photographed through a Zeiss fundus camera immediately before and after laser exposure. An artifactual optical target marker in the fundus camera coaligned with the He-Ne laser was used to denote the exact lased area on fundus photographs.

Single 20 nsec laser exposures were made in the left fovea (756 µJ) and concentrically around the macula at 1000, 400, 200, and 100 µJ (Figure 1). Two and a half days lapsed and a similar exposure scheme was repeated with the exposure sites located in a circle 3 mm internal to the first. Within one hour of the last exposure, the animal was injected with 70 mCi of ^{3}H-L leucine-4,5 (specific activity, 30,000-60,000 mCi/mmol) in 2 ml of 2% ethanol via the catheterized right saphenous vein. Two and a half days after the ^{3}H-leucine injection, eyes were enucleated.

One square millimeter blocks (of lesions and controls) were dissected and fixed in Karnovsky's fixative (11). All tissue processing and autoradiography were performed by a previously described technique (9).

The total length of the rod outer segments and the distance from the outer-inner segment junction to the center of the transverse band of radioactivity on the outer segments in autoradiographs were measured by an ocular micrometer at X1000 (Figure 2). Rod outer segment renewal rates (ROSRRs) were determined by dividing the total outer segment length by the distance of the band of label from the outer-inner segment junction multiplied by the number of days after injection. Slides with lesions of maximum diameter for each exposure site and adjacent controls were selected. Measurements were taken at 50 µm intervals across given radii of the lesions from the established center. Measurements were in microns on five rods at each interval for each lesion and control.

Outer nuclear layer grain counts (ONLGCs) were tabulated and compared only within the same section (i.e. grain counts of the lesion center were compared with grain counts at the lesion edge). Counts were made on two different sections from two different slides for each lesion. The difference between the two areas was computed as a percent difference.

The the retinal pigment epithelium (RPE) thickness was measured using a linear reticle at X1000. A minimum of five measurements, approximately 10 µm apart, were taken from the lesion center and periphery on three sections.

RESULTS

Little histopathologic difference existed between the 2.5 and 5-day lesions, with the exception that the 5-day lesions were smaller in size. In general, a decreasing severity in pathology occurred with decreasing exposure energy and with increasing distance from the lesion center. The most remarkable morphologic findings were that cones were more easily and

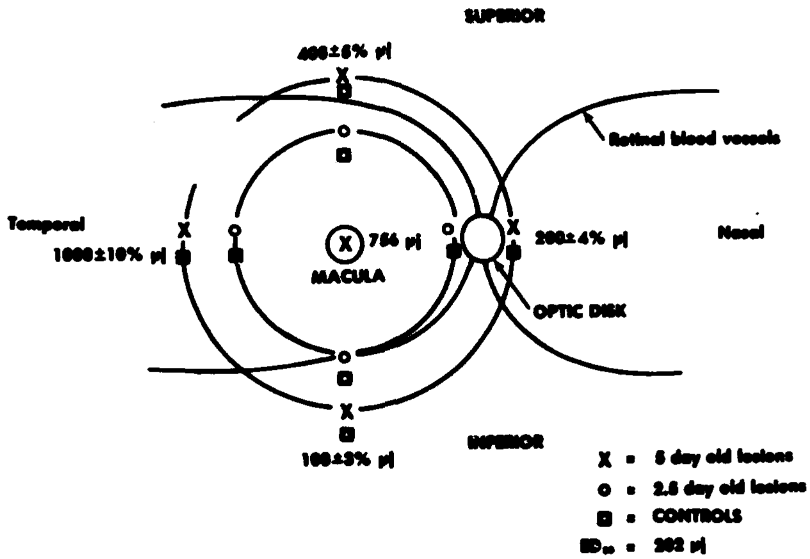

Figure 1. Fundus schematic of right-eye and laser exposure locations

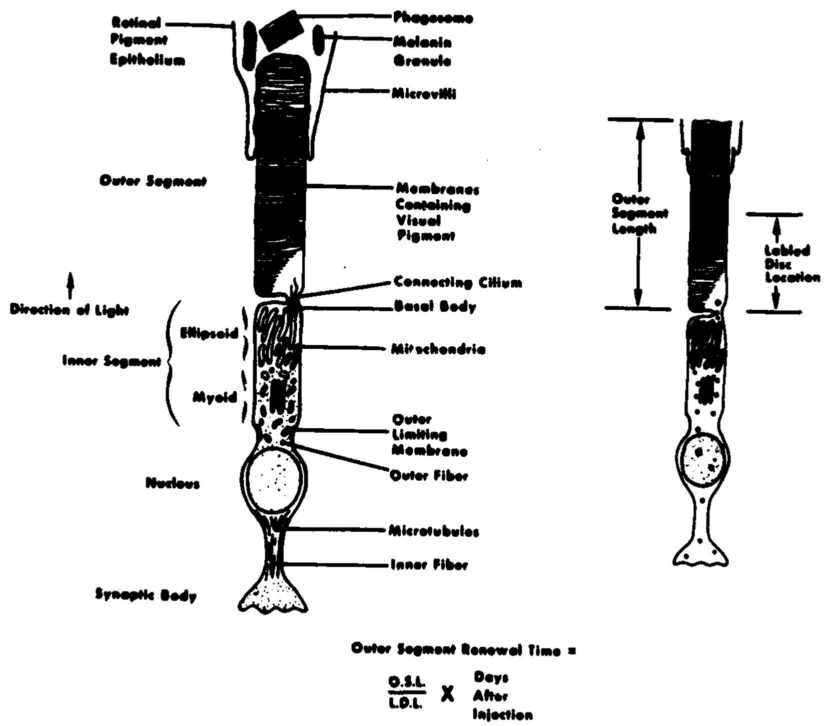

Figure 2. Diagram illustrating the components of a vertebrate visual cell. Formula for estimating rod outer segment renewal is at the bottom of the figure.

Table I

Pathologic findings in a rhesus monkey retina (9 lesions, 5 sites*) after irradiation with a Q-switch ruby laser (694.3 nm) Plus sign (+) indicates presence of characteristic; blank space indicates absence of characteristic

MORPHOLOGIC CHARACTERISTICS†	EXPOSURE ENERGY (μJ)								
	1000		756	400‡		200		100	
days after exposure	2.5	5	5	2.5	5	2.5	5	2.5	5
Hemorrhage (subretinal and preretinal)	+	+							
Loss of photoreceptors	+	+	+						
Vacuolization and depigmentation in choroid	+	+	+						
Melanin granule fracture	+	+							
Cellular proliferation of RPE	+	+	+			+	+		
Pyknotic photoreceptor nuclei	+	+	+						
Cone inner segment disruption	+	+	+			+			
Dissolution of outer segments	+	+	+						
Inclusion material in the outer receptor fibers			+						
Inner retina vacuoles	+	+	+						
Outer segments in the inner segments			+						
Melanin granule clumping	+	+	+	+	+	+	+	+	+
Pyknotic RPE nuclei	+	+	+	+	+	+	+		
Lamellar disarray of outer segments	+	+	+	+	+	+	+	+	+
Pyknotic outer segment debris						+	+		
Vacuolated inner segments	+	+	+	+	+	+	+	+	
Macrophages in subretinal space	+	+	+			+	+	+	
Hypopigmentation of RPE	+	+	+	+	+	+	+	+	+
Retraction of outer segments from the RPE	+	+	+	+	+	+	+		
Decreased length and thinning of outer segments	+	+	+	+	+	+	+	+	+
Reduced RPE thickness	+	+	+	+	+	+	+	+	+
Disorganized RPE microvilli	+	+	+	+	+	+	+	+	+

* Only one lesion was placed in the macula and analyzed 5 days later.

† Efforts have been made to list the characteristics by a decreasing order of severity, i.e. damage to retina, and arbitrarily divided the characteristics into groups of five.

‡ The distortion of the beam energy profile produced a distorted energy deposition and an under-represented response in the retina.

more severely disrupted than rods and that cones in the macula showed outer segments in their inner segments. The remainder of the pathologic findings are summarized in Table I.

Mean RPE thickness values for all the 2.5 and 5-day lesions showed that the RPE thickness was reduced as the function of the exposure energy in the center of the lesion (Figure 3). An increase in RPE thickness occurred at the periphery of all the lesions. The range of RPE change in the macula was comparable to the values obtained for the 200 µJ extramacular lesions which suggests an attenuation effect to the RPE.

In contrast to the histologic findings, large autoradiographic variations occurred between the 2.5 and 5-day lesions. In the 1000 µJ 2.5 day lesion center (Figure 4), a decrease in label intensity was noted in the rod outer segment band as well as in the outer nuclear layer. The inner retina and RPE cells in the center of the 1000 µJ 5-day lesion showed a greater label uptake than peripheral or unexposed regions. With increasing distance from the edge of the 1000 µJ lesion to the center, cone inner segments contained less label (Figure 4).

Many undulating peaks occurred in the band of label in the 400 µJ lesions. These peaks suggested a distortion in the geometry of the laser beam energy distribution. In the 200 µJ lesions the label intensity in the rod outer segment band was decreased in the center of the lesion. In the 100 µJ lesions, the band of label was fragmented laterally.

All of the 2.5-day lesions showed less inhibition in ROSRRs with decreasing exposure energy (Figure 5). All the 5-day lesions showed more nearly normal ROSRRs (Figure 6). In either the 2.5 or 5-day 1000 µJ lesions, almost no rod outer segment renewal was taking place. Only the 5-day 1000 µJ lesion showed some rods with label in the outer segments. In the 5-day 200 and 100 µJ lesions, ROSRRs were increased 10-15% above the normal rate.

Calculated times for complete outer segment renewal are based on measurements taken on photoreceptors (Table IIA) and are given in Table IIB. Since outer segment lengths were slightly variable, depending upon the region of the retina where the outer segments were measured, estimated normal and abnormal renewal times varied accordingly. Rod outer segment renewal time projections are based on the development of events in the 2.5 and 5-day lesions and are expected to vary and develop further. After high energy laser exposure (1000 µJ), rods will take about three times as long to synthesize and renew their normal complement of outer segment discs. Laser exposures at 200 and 100 µJ (subvisible lesions) cause rods to synthesize and renew their normal complement of outer segment discs more rapidly (Table IIB).

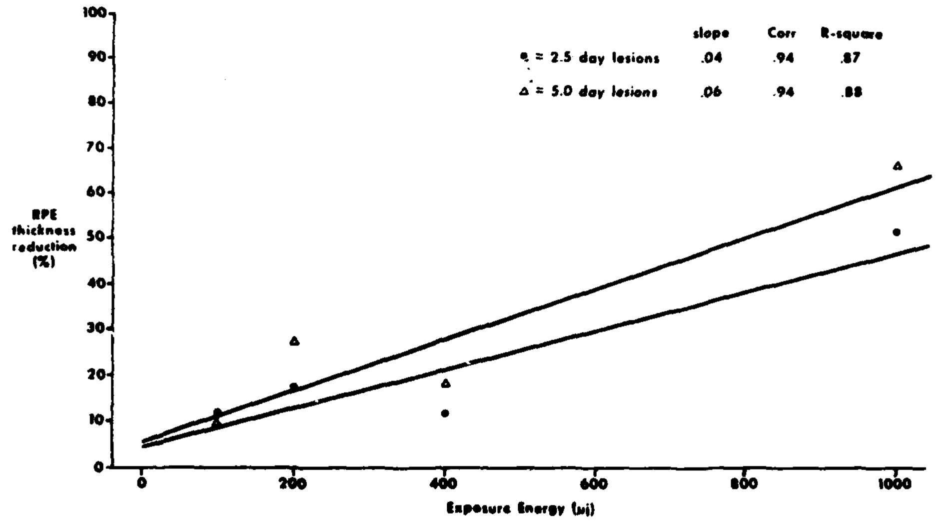

Figure 3. The effect of Q-switched ruby laser radiation on retinal pigment epithelium thickness in lesion centers.

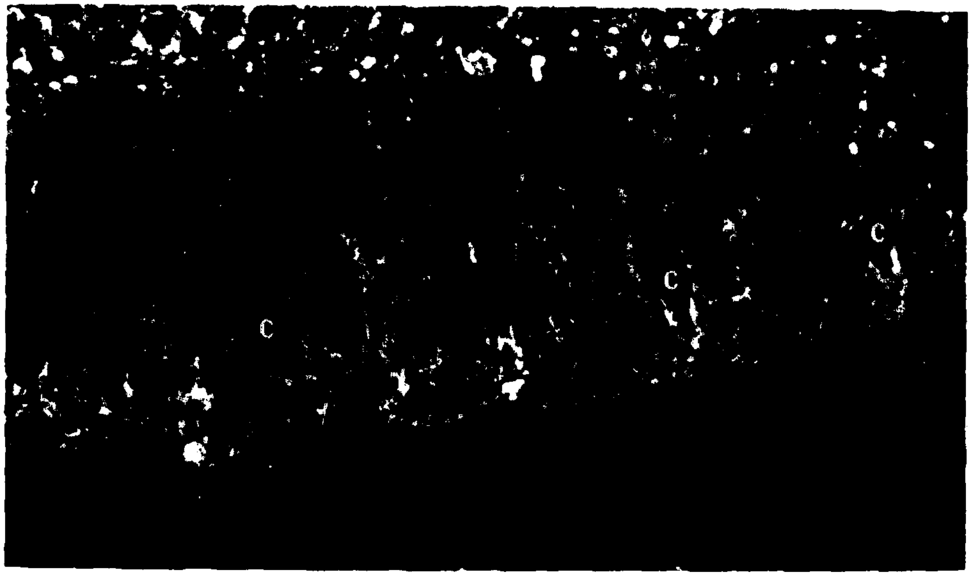

Figure 4. 1000 µJ, 2.5-day lesion. Lesion center is to the right. The following retinal layers are indicated in the photograph: outer plexiform layer (op), outer nuclear layer (on), photoreceptor inner segments (is) and outer segments (os). Cones (c) show increasing severity of inner segment degeneration and decreasing amount of label uptake left to right. Arrows indicate band of rod cuter segment label which disappears on the right. The amount of label in the outer nuclear layer on the right is less than on the left. Hemorrhage (H). Bar = 50 µm.

AD-A120 813 PROCEEDINGS OF THE 1982 ARMY SCIENCE CONFERENCE HELD AT THE UNITED STATES..(U) DEPUTY CHIEF OF STAFF FOR RESEARCH DEVELOPMENT AND ACQUISITIO.. 18 JUN 82 3/

UNCLASSIFIED F/G 5/2 NL

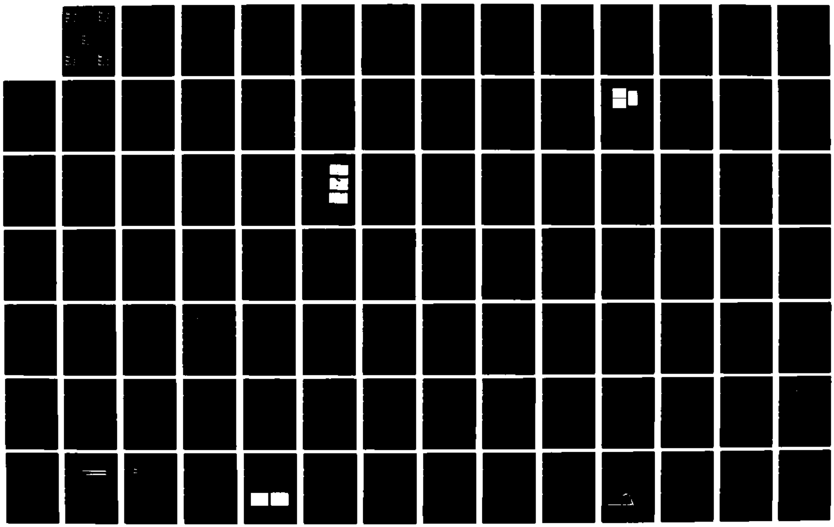

MICROCOPY RESOLUTION TEST CHART
NATIONAL BUREAU OF STANDARDS-1963-A

MICROCOPY RESOLUTION TEST CHART
NATIONAL BUREAU OF STANDARDS-1963-A

MICROCOPY RESOLUTION TEST CHART
NATIONAL BUREAU OF STANDARDS-1963-A

MICROCOPY RESOLUTION TEST CHART
NATIONAL BUREAU OF STANDARDS-1963-A

MICROCOPY RESOLUTION TEST CHART
NATIONAL BUREAU OF STANDARDS-1963-A

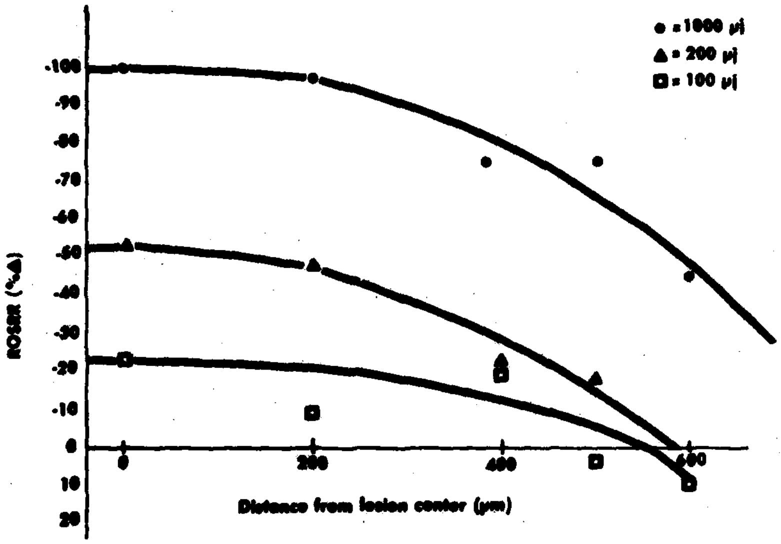

Figure 5. Two and a half day lesions show a decreased inhibitory effect with decreased exposure energy.

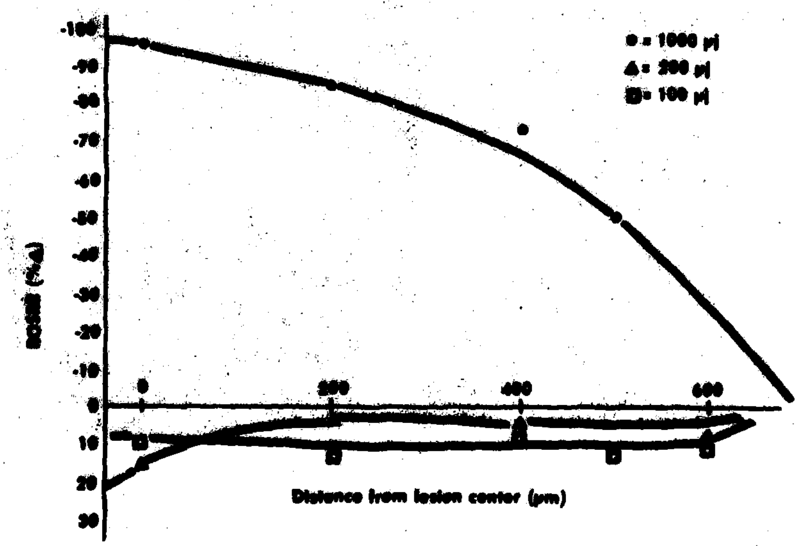

Figure 6. Five-day lesions show a recovery effect at the 200 and 100 µJ levels.

Table IIA

Location of labeled discs and length of rod outer segments

Exposure Energy (µJ)	Fundus Site	Lesion* (days after exposure)	Labeled disc† location (µm)	Outer segment‡ length (µm)
1000	Temporal	A 2.5	2.0	26.0
		B 5.0	2.3	30.0
400	Superior	A 2.5	2.3	30.0
		B 5.0	8.6	34.1
200	Nasal	A 2.5	5.6	30.0
		B 5.0	8.6	30.6
100	Inferior	A 2.5	7.1	35.0
		B 5.0	9.2	32.6

* 1 animal, 1 eye
† Distance from the base of the outer segment to the location of the center of the heavily labeled band (see Figure 2) in the center of the lesion (values represent the average of the center and 200 µm from the center data points).

‡ See Figure 2

Table IIB

Renewal time after injection of ^{3}H-leucine in Fundus

Fundus Site	Lesion* (days after exposure)	Rod outer segment renewal time (days)	
		Estimated time with exposure†	Estimated time without exposure‡
		lesion @ 1000 µJ	
Temporal	A 2.5	32.5	8.0
	B 5.0	32.6	9.3
		lesion @ 400 µJ	
Superior	A 2.5	11.4	9.3
	B 5.0	9.9	10.5
		lesion @ 200 µJ	
Nasal	A 2.5	13.4	9.3
	B 5.0	8.9	9.4
		lesion @ 100 µJ	
Inferior	A 2.5	12.3	10.8
	B 5.0	8.7	10.1

* 1 animal, 1 eye.
† Formula: (Outer segment length divided by distance from outer segment to center of labeled band) x (days after injection) = renewal rate. Measurements can be obtained from Table IIA.

‡ Distance from outer segment to labeled band, based on findings in control = 8.1 µm. Same formula† is applied with 8.1 µm as divisor.

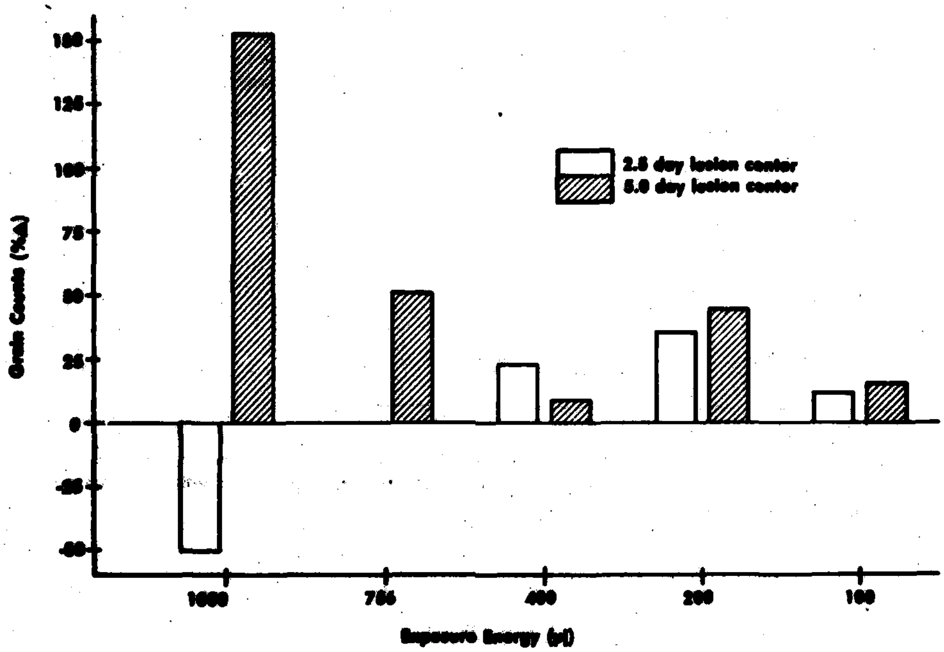

Figure 7. Grain counts over outer nuclear layer nuclei in lesion center as compared with the lesion periphery (600 μm from center).

ONLGCs from the centers of lesions were compared with values from the lesion periphery (600 μm from the lesion center) (Figure 7). ONLG^s for the 2.5-day 1000 μJ lesion centers showed a marked reduction (-50%), while all the other lesions showed an increase. At 5 days, the ONLGCs showed an exposure-energy dependent trend, although not linear (counts decreased with decreasing exposure energy, i.e. 1000 > 200 > 100 μJ); however, these counts were elevated above normal more so than the 2.5-day counts. The greatest percent increase in the ONLGCs occurred in the 5-day 1000 μJ lesion (+153%); the macula showed the next highest increase (+51%).

A comparison of the percent ; ·:e in ROSRRs with the percent increase in ONLGCs indicates that a... the 5-day lesions had a back log of leucine in the outer nuclear layer (ONL).

DISCUSSION

Because disc formation is steady, it is possible to predict, from a single radiolabel injection, the length of time necessary for the labeled discs to be displaced along the entire length of a rod outer segment, and thus the time required for complete outer segment renewal. Two autoradiographic variables, ROSRRs and ONLGCs, gave remarkable insight to the extent of alteration as a function of laser exposure energy and as a function of the amount of recovery with time.

Tso et al. (12) have shown that lasers preferentially alter cone morphology. In our study, we confirm that cones are damaged more severely than adjacent rods. In addition, by comparing the relative amounts of inner segment label between adjacent rods and cones, cones showed less label uptake. Unfortunately, cone outer segment synthesis processes could not be evaluated, as membrane precursor proteins yield only a diffuse scattering of newly synthesized molecules throughout the existing membranes and photoreceptor (13). Nevertheless, our study appears to be the first to correlate both morphologic and metabolic sensitivity for cones over rods. As part of a recovery response some macular cones showed newly formed outer segment membranes in their inner segments. These have previously not been described for laser exposed retinas.

In the 5-day 200 μJ (ED_{50}) and 100 μJ lesions the upper limit of 10-15% above normal in ROSRRs indicated a maximum recovery response. Upper limits to membrane rod outer segment addition have been reported in other autoradiographic studies (14) to result from exposure to elevated ambient temperatures and from exposure to constant light. Several things are suggested by an upper limit increase in rod outer segment synthesis: 1) that a critical inner segment factor regulates outer segment synthesis and that this factor is rate-limiting; 2) that the upper limit reflects an increased aging process; and 3) that the upper limit in membrane synthesis may not be sufficient to meet the repair demands of the photoreceptors and as a result photoreceptor cytoplasmic efficiency would be decreased. This may manifest itself as the continued production of altered outer segment membranes many months after laser light exposure (2). Longer term studies need to clarify if this increased synthesis rate persists, increases, or returns to normal.

Increases in outer nuclear layer label are greater with increasing time after laser insult and with increasing exposure energy. Such data have not been previously reported and indicate that protein synthesis sites in the inner segment have been altered and that protein precursors accumulate in the inner portion of the photoreceptor. The more extensive the inactivation of membrane synthesis centers, as with increasing exposure energy in the inner segment, the greater is the amount of label shunting to the inner photoreceptor regions. Alternatively, the increased outer nuclear layer label after exposure may reflect increased synthesis due to repair processes. The large decrease below normal in outer nuclear layer label concentration 2.5 days after 1000 µJ exposure may represent a reduced efficiency in membrane transport function in addition to decreased protein synthesis. This is most likely related to the thermal effect of laser radiation.

Our results suggest that inhibition involves two primary photoreceptor processes: 1) the active transport of amino acids, or perhaps passive diffusion across membranes, and 2) inactivation of intracellular protein synthesis centers (i.e., ribosomes or critical enzymes). Floyd et al. (15) have reported that Q-switched ruby laser pulses ablated particles from the surfaces of membranes. Marshall (1) in an in vitro autoradiography study reported that inhibition of protein synthesis after Q-switched ruby laser exposure was thermally dependent and most likely occurred at the ribosomal level. It would seem reasonable then that inhibition of protein synthesis in membrane renewal may also involve the ablation of ribosomes from the rough endoplasmic reticulum and thus uncouples protein synthesis. Furthermore, if Q-switched ruby laser pulses ablate surface particles from membranes then alterations in the composition of membrane proteins, and therefore transport functions, could account for the reduced amount of label seen at 2.5 days after exposure in both the photoreceptor nuclei and outer segments. Alternatively, the concentration or activity of an enzyme(s) may be the sensitive endpoint.

The extent of inhibition and recovery as revealed by the shifting pattern of black grains, which represent membrane precursor molecules in retinal laser lesions, show that rod outer segment renewal rates are more sensitive to the 694.3 nm laser radiation than label uptake by nuclei. The large quantities of label accumulation in the outer nuclear layer may serve as a reservoir for the critical rate-limiting reaction in the inner segment. The maximum upper limit to synthesis in rod outer segments may continue for an unknown period of time in an attempt to deplete this reservoir which may be directly related to the repair demand. Whether this is the case will require further studies.

In general, inhibition of membrane renewal processes in this study is consistent with the thermal and mechanical damage theory of retinal tissue in laser lesions (1,16).

In summary, the morphologic findings are consistent with both the thermal and mechanical disruption of retinal tissue in laser lesions. Cones are both morphologically and metabolically more sensitive than rods to 694.3 nm radiation. In a recovery response, cones synthesize outer segments in their inner segments. An attenuation effect to the RPE and an increased absorption effect are suggested in the macula. Rod outer segment renewal rates are initially more sensitive to Q-switched ruby laser radiation at 694.3 nm than label uptake by the outer nuclear layer. Near-threshold lesions show a recovery response in ROSRRs by indicating a small maximum upper limit increase, while a large backlog of protein precursors accumulate in the outer nuclear layer. Inhibition in protein synthesis may occur at the ribosomal level, while recovery involves some critical rate-limiting step. Low-level (subvisible ophthalmoscopically) retinal laser lesions show an increased aging process and altered metabolism, which suggest an increased sensitivity of analysis with autoradiography and reevaluation of the ophthalmoscopically determined ED_{50}. The Army may discover that these findings may have implictions for retinal conditions detected in users of laser devices.

*SCHUSCHEREBA, BEATRICE

REFERENCES

1. MARSHALL, J. Thermal and mechanical mechanisms in laser light damage to the retina. Invest. Ophthalmol. 9:97-115, 1970.

2. ADAMS, D.O., BEATRICE, E. S., BEDELL, R. B., Retina: Ultrastructural alterations produced by extremely low levels of coherent radiation. Science 177:58-60, 1972.

3. HAM, W. T. Jr., MILLER, H. A., RUFFOLO, J. J. Jr., CLARKE, A. M. Sensitivity of the retina to radiation damage as a function of wavelength. Photochem. Photobiol. 29:735-743, 1979.

4. FRISCH, G.D., BEATRICE, E. S., HOLSEN, R.C. Comparative study of argon and ruby retinal damage thresholds. Invest. Ophthalmol. 10:911-919, 1971.

5. LAPPIN, P.W., COOGAN, P.S. Histologic evaluation of ophthalmoscopically subvisible retinal laser exposures. Invest. Ophthalmol. 9:537-542, 1970.

6. GIBBONS, W. D., ALLEN, R.G. Retinal damage from suprathreshold Q-switch laser exposure. Health Physics 35:461-469, 1978.

7. ZWICK, H., BEDELL, R.B., BLOOM, K. Spectral and visual deficits associated with laser irradiation. Mod. Prob. Ophthalmol. 13:299-306, 1974.

8. MARSHALL, J., GRINDLE, J., ANSELL, P.L., BORWEIN, B. Convolution in human rods: an ageing process. Br. J. Ophthalmol. 63: 181-187, 1979.

9. YOUNG, R.W. The renewal of rod and cone outer segments in the rhesus monkey. J. Cell Biol. 49:303-318, 1971.

10. BEATRICE, E.S., Retinal Damage by a Q-switched ruby laser for large spot diameters, Report M70-22-1, Philadelphia, PA, Frankford Arsenal, 1970.

11. KARNOVSKY, M.J. A formaldehyde-gluteraldehyde fixative of high osmolality for use in electron microscopy. J. Cell Biol. 27: 137A, 1965.

12. TSO, M.O., M., WALLOW, I. H. L., POWELL, J.O., ZIMMERMAN, L.E., Recovery of rod and cone cells after photic injury. Trans. Am. Acad. Ophthalmol Otolaryngol, 76:1247-1262, 1972.

*SCHUSCHEREBA, BEATRICE

13. ANDERSON D.H., FISHER, S.K. The photoreceptors of diurnal squirrels: outer segment structure, disc shedding, and protein renewal. J. Ultrastruct. Res. 55: 119-141, 1976.

14. HOLLYFIELD, J. Membrane addition to photoreceptor outer segments: progressive reduction in stimulatory effect of light with increased temperature. Invest. Ophthalmol. Vis. Sci. 18:977-981, 1979.

15. FLOYD, R.A., KEYHANI, E. , CHANCE, B. Membrane structure and function II. Alterations in photoinduced absorption changes after treatment of isolated chloroplasts with large pulses of the ruby laser. Arch. Biochem. Biophys. 146: 627-634, 1974.

16. GOLDMAN, A.I., HAM, W.T., MUELLER, Jr. H.A., Mechanisms of retinal damage resulting from exposure of rhesus monkeys to ultrashort laser pulses. Exp. Eye Res., 21:457-469, 1975.

METHODS FOR EVALUATING GUN-POINTING ANGLE ERRORS AND MISS DISTANCE PARAMETERS FOR AN AIR DEFENSE GUN SYSTEM (U)

*PAUL M. SCHWARTZ, PhD
US ARMY ABERDEEN PROVING GROUND
ABERDEEN PROVING GROUND, MD. 21005

PART I. Coordinate frames, system and instrumentation data; gun angles.

COORDINATIZATION. The basic reference frame used to coordinatize target position and resolve gun-pointing direction into azimuth and elevation components every .1 second is an (east, north, gravity vertical up) system centered in the vehicle at the point C on the turret axis at the ground height of the gun trunnion, $F(C/\mathcal{X},\mathcal{Y},\mathcal{Z})$. Government trackers at known range coordinates acquire target position in their own frames. For a stationary pass, each vehicle sits on a prescribed pad, its turret axis approximately over a point on the pad with known range coordinates. These sets of coordinates, together with the trunnion height, permit the conversion from tracker frame coordinates to reference coordinates, which are further subject to a low-pass digital filter [1, Sec 5.1]. For a moving vehicle pass, in addition vehicle position is provided by a government tracker (also filtered), and $F(C/\mathcal{X},\mathcal{Y},\mathcal{Z})$ becomes a moving frame.

All velocity-related parameters are computed solely from target coordinates available every .1 second in the reference frame. Target velocity components $(\dot{x},\dot{y},\dot{z})$ are associated to each target position vector (x,y,z) by differentiation of a moving fitted polynomial arc. The so-called level plane is spanned by $C, \mathcal{X}, \mathcal{Y}$; target azimuth α_T in the level plane has vertex C, initial ray direction $\mathcal{Y}$, with a positive clockwise (viewed from above) sense of rotation to its terminal side; target elevation ε_T has vertex C , and initial ray in the level plane. So $\tan\alpha_T = x/y$, $\tan\varepsilon_T = z/\sqrt{x^2+y^2}$, and time differentiation yields the angular rates $\dot{\alpha}_T$, $\dot{\varepsilon}_T$ in terms of x,y,z.

The computation of the components of the range rate and range-angular velocity resolution of target velocity runs as follows. Set $\mathbf{r}=(x,y,z)$ and $\mathbf{v}=(\dot{x},\dot{y},\dot{z})$; for a non-zero vector $\mathbf{a}$ let $\|\mathbf{a}\|$ denote its length and $\mathbf{a}^0$ the unit vector in the direction of $\mathbf{a}$. Resolving $\mathbf{v}$ into two components, one along the range vector $\mathbf{r}$ and the other perpendicular to $\mathbf{r}$ in the plane spanned by $\mathbf{r}$ & $\mathbf{v}$, get $\mathbf{v}=\frac{1}{\|\mathbf{r}\|^2}\left[(\mathbf{r}\cdot\mathbf{v})\mathbf{r}+\mathbf{r}\times(\mathbf{v}\times\mathbf{r})\right]$ (*) . On the other hand, from a standard elementary mechanics set-up, get $\mathbf{v}=\dot{r}\,\mathbf{r}^0+r\dot{\theta}\hat{\theta}$, where $r=\|\mathbf{r}\|$, $\hat{\theta}$ is that vector in the plane spanned by $\mathbf{v}$, $\mathbf{r}$ leading $\mathbf{r}$ by 90°, and $\dot{\theta}$ is the angular velocity of the range vector. Indeed, (*) shows that the coefficient of $\mathbf{r}^0=\mathbf{r}\cdot\mathbf{v}/\|\mathbf{r}\|$, precisely the time derivative $\dot{r}$ of the range. From the definition of $\hat{\theta}$, it follows that $\hat{\theta}=\mathrm{sgm}(\dot{x}y-x\dot{y})\left[\mathbf{r}\times(\mathbf{v}\times\mathbf{r})\right]^0$; as $\|\mathbf{r}\times(\mathbf{v}\times\mathbf{r})\|=\|\mathbf{r}\|\cdot\|\mathbf{v}\times\mathbf{r}\|$, $\dot{\theta}=\mathrm{sgm}(\dot{x}y-x\dot{y})\frac{\|\mathbf{v}\times\mathbf{r}\|}{r^2}$.

GUN AZIMUTH & ELEVATION ANGLES. To obtain gun-pointing direction errors and miss distance results, it is necessary to resolve real-time gun-pointing direction into azimuth and elevation angles wrt the reference frame. Usually this is just a matter of out-of-level compensation. A representative situation for an air defense tank is discussed here.

The turret frame $F(C/\mathfrak{x}_T,\mathfrak{y}_T,\mathfrak{z}_T)$ is defined as follows: $\mathfrak{y}_T$ is the turret axis direction given by the gun vector direction at 0 turret elevation, $\mathfrak{x}_T$ points in the direction of the trunnion to the right of $\mathfrak{y}_T$ (looking down), $\mathfrak{z}_T=\mathfrak{x}_T\times\mathfrak{y}_T$ (turret vertical up). The attitude of the turret frame wrt the reference frame is determined only to the extent of specifying turret pitch and roll relative to the gravity vertical axis $\mathfrak{z}$.

Gun azimuth and elevation in the reference frame is computed using the following data:

Pitch angle θ, with typical sign conventions + or - according as the turret front moves up or down;
Roll angle ϕ, with typical sign conventions + or - according as the right side moves up or down;
Gun resolver elevation ε_t off the turret plane;
Target angles wrt turret frame---
α_t = target azimuth wrt turret frame (lead traverse), with typical sign conventions + or - according as the target lies to the right or left of the gun elevation plane;
e_T = target elevation off turret plane;
Target position in the reference frame.

The desired azimuth α_G and elevation ε_G are computed in the following 3 steps.

Step 1. Quadrant elevation ε_G (signed) from $\varepsilon_t, \theta, \phi$
Attitude data: gyro pitch θ, roll ϕ

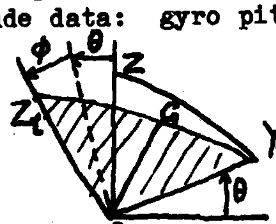

$\vec{CZ_t}$ represents turret vertical
$\vec{CZ}$ represents gravity vertical (on reference unit sphere)
$\vec{CY_t}$ represents nominal turret centerline (gun pointing direction at 0 turret el)

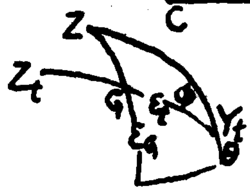

Gun elevates in plane CZ_tY_t

ϕ = dihedral angle between planes Z_tCY_t & ZCY_t

$$\therefore \sin\varepsilon_G = \cos\varepsilon_t \sin\theta + \sin\varepsilon_t \cos\theta \cos\phi$$

Step 2. Lead azimuth magnitude λ from $\varepsilon_G, \varepsilon_t, e_T, \varepsilon_T, \alpha_t$

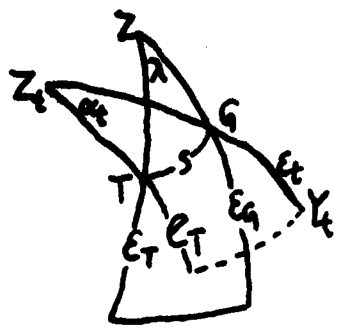

$\vec{CT}$ represents target direction
S = target-gun angle in slant plane
From $\triangle TZ_tG$

$$\cos S = \sin\varepsilon_t \sin e_T + \cos\varepsilon_t \cos e_T \cos\alpha_t$$

From $\triangle TZG$

$$\cos S = \sin\varepsilon_T \sin\varepsilon_G + \cos\varepsilon_T \cos\varepsilon_G \cos\lambda$$

$\therefore \lambda$ (unsigned) is determined

Step 3. α_G. It remains only to determine on which side of the vertical plane ZCG containing the gun direction the target lies. Let the true vertical point Z have turret angles α', ϵ'. Note that α' and ϕ have opposite signs.

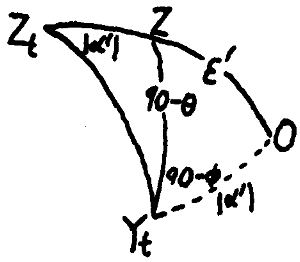

From $\Delta Y_t Z O$

$$\sin\epsilon' = \cos\theta\cos\phi,$$
$$\cos\epsilon'\cos\alpha' = \sin\theta;$$
$$\sin|\alpha'| = \tan\epsilon'\tan\phi, \text{ so}$$
$$\cos\epsilon'\sin\alpha' = -\cos\theta\sin\phi.$$
$$\therefore \overrightarrow{CZ} = -\cos\phi\sin\theta\, x_T + \sin\theta\, y_T + \cos\theta\cos\phi\, z_T$$

$\overrightarrow{CG} \times \overrightarrow{CZ}$ is a normal to the vertical plane containing the gun direction pointing to the right of the plane (viewed from above). So the target lies to the right or the left of this plane according as

$$\overrightarrow{CT}\cdot(\overrightarrow{CG}\times\overrightarrow{CZ}) \geq 0 \text{ or } < 0.$$

Since the turret coordinates of all vectors of the triple product are known, the scalar can in fact be computed.

$\therefore \quad \alpha_G = \alpha_T \mp \lambda \mod 2\pi$ according as the target lies to the left or right of the vertical gun plane.

The attitude data may be available from both on-board system and government-supplied gyros. Target angular position in the turret frame is available from the system's optic sight or track radar, subject to tracking errors. A government-supplied tracker, PAMS, operating in the NIR region, is available for turret tracking with considerably reduced tracking errors.

PART II. Ballistics; ideal gun-pointing direction, system gun-pointing direction errors.

BALLISTICS. The equations of motion of a projectile considered as a particle acted on by an axial drag force, horizontal wind, gravity, rotation of the earth, and subject to a drift owing to aerodynamic forces not deriving from axial drag or crosswind deflection are developed in [2]. That development is not repeated here, but a summary of the trajectory equations, the acquisition and use of metro, and the numerical integration method is set down.

The ballistic frame $F(O/\mathfrak{Z}_B, \mathfrak{X}_B, \mathcal{Y}_B)$ with generic coordinates (Z, X, Y) is defined thus: O represents the vertical projection of the attachment of the gun to its elevating axis to zero MSL, $\mathfrak{X}_B$ = downrange direction, i.e., vertical projection of the current gpd, $\mathcal{Y}_B$ = gravity vertical up direction, $\mathfrak{Z}_B$ = crossrange direction, to the right of the current gpd.

Let t=current projectile time of flight,
(Z, X, Y)=ballistic coordinates of projectile at time t,
w_X, w_Z=downrange, crossrange wind components at projectile position (Z, X, Y) (data actually obtained as a function of altitude above MSL),
ρ=air density at (Z, X, Y) (data source as for wind),
$K_D(M)$=drag coefficient expressed as function of current Mach number M,
C=ballistic coefficient,
$E = \frac{\rho K_D}{C} \times$projectile speed relative to air (retardation),
g=nominal gravitational acceleration,
K=drift constant,
$\lambda_1, \lambda_2, \lambda_3$ =coriolis terms,
V_0=muzzle velocity,
ε =gpd elevation angle off the level plane,
s =MSL altitude of gun attachment,
ℓ =barrel length.

In the ballistic frame, the equations of motion of the projectile read

$$\ddot{X} = -E(\dot{X} - w_X) + \lambda_1 \dot{Y}$$
$$\ddot{Y} = -E\dot{Y} - g - \lambda_1 \dot{X}$$
$$\ddot{Z} = -E(\dot{Z} - w_Z - 2Kt\cos\varepsilon) + 2K\cos\varepsilon + \lambda_2 \dot{X} + \lambda_3 \dot{Y},$$

with initial conditions

$$X(0) = \ell\cos\varepsilon, \; Y(0) = s + \ell\sin\varepsilon, \; Z(0) = 0$$
$$\dot{X}(0) = V_0\cos\varepsilon, \; \dot{Y}(0) = V_0\sin\varepsilon, \; \dot{Z}(0) = 0.$$

For the situation here, the reference origin=the gun attachment; if the gpd has azimuth α wrt the reference frame, the change of coordinates relating ballistic and reference coordinates is given by

$$\begin{pmatrix} Z \\ X \\ Y \end{pmatrix} = \begin{pmatrix} c\alpha & -s\alpha & 0 \\ s\alpha & c\alpha & 0 \\ 0 & 0 & 1 \end{pmatrix} \begin{pmatrix} x \\ y \\ z+s \end{pmatrix}.$$

Acquisition and use of metro data. All data is obtained and used as function of altitude; details concerning units, conversion of temperature, pressure, and humidity to density are omitted.

Surface metro. Here wind speed, windward, temperature, pressure, and humidity are acquired at the surface near the time of testing. Wind data is converted to ballistic coordinates in the current frame; ground air temperature T_s and ground air density ρ_s are used to convert the temperature and density values that the ICAO standard [2] assigns to various altitudes to ICAO adjusted values by additive scaling with T_s and multiplicative with ρ_s, respectively.

Metro aloft. For firing passes, winds aloft radiosonde metro is used when available. Here wind speed, windward, temperature, density are obtained at prescribed altitudes $Y_1 < \cdots < Y_m$ near the time of testing. Wind components in the current ballistic frame, temperature, and pressure for a required altitude are obtained by linear interpolation on altitude.

Numerical integration of the trajectory equations. A numerical solution of the trajectory equations is based on the following rationale. Let $\Delta t =$ a prescribed small time increment; currently $\Delta t = .1\,sec$. Consider the elapsed times of projectile flight $t_i = i\Delta t, i = 0, 1, 2, \ldots$. Ballistic coordinates and their derivatives are computed only at the discrete times t_i; so known values of $Z, \dot{Z}, X, \dot{X}, Y, \dot{Y}$ at t_i and the metro data associated to altitude $Y(t_i)$ determine $E(t_i)$ and so $\ddot{X}, \ddot{Y}, \ddot{Z}$ at t_i. The assumption that acceleration remains constant throughout the interval $[t_i, t_i + \Delta t = t_{i+1})$ permits the immediate integration of $\ddot{X}, \ddot{Y}, \ddot{Z}$ there, yielding values of $\dot{Z}, Z, \dot{X}, X, \dot{Y}, Y$ at t_{i+1}. The initial conditions start the procedure, and from what has just been said, the procedure can be continued until stopped by some prescribed termination condition. Projectile position and velocity at non-discrete times are obtained by linear interpolation on time. Note that at termination projectile time of flight, velocity components are automatically available.

Ballistic coefficients, drag coefficients, drift constants, and nominal muzzle velocities for the rounds used during testing are supplied by the ballistics section. Actual muzzle velocities during firing may be obtained from a government-supplied muzzle velocity radar.

IDEAL GUN-POINTING DIRECTION.
An ideal intercept algorithm providing gpd azimuth and elevation wrt the reference frame required to intercept any target on the flight path not too near the end is now explicated. Based on the capability of generating the gpd required to intercept a stationary point target by a point round with miss distance $<$ prescribed small tolerance, the premier idea in intercepting a moving target by a projectile-firing weapon can readily be implemented: find the future position on the flight path where the target time of flight from its present position matches the projectile time of flight resulting from the gpd required to intercept that future position. Currently, this algorithm produces dynamic gpd resulting in $|$(target time of flight) - (projectile time-of-flight)$|$ $< 10^{-10}$ sec and miss at intercept $<$ .4 inch.

Stationary intercept algorithm. Given a stationary target with reference coordinates $\mathcal{P}^* = (x^*, y^*, z^*)$, it is required to generate gun aim angles in the reference frame producing a trajectory terminated at point $\mathfrak{P} = (x, y, z)$ according to the stop condition ground range of $\mathfrak{P} \approx$ ground range of $\mathcal{P}^*$, satisfying the near intercept condition (I) $\min(|x^*-x|, |y^*-y|, |z^*-z|)$ < prescribed tolerance ϵ. Currently, $\epsilon = .01m$. Aim azimuth, elevation angles $(\alpha_i, \varepsilon_i)$, $i = 0, 1, 2, \ldots$ are generated successively as follows. The initial angles are just $\alpha_0 = \alpha^*$=azimuth of $\mathcal{P}^*$, ε_0=elevation of $\mathcal{P}^*$+superelevation (provided by the statistics section, based on a LS curve fit to trajectory angle of fall, as determined by the ballistics of the round under standard conditions, vs slant range). For the iteration, suppose that $(\alpha_i, \varepsilon_i)$ produces a terminal projectile position with reference coordinates $\mathfrak{P}_i = (x_i, y_i, z_i)$. If the coordinates satisfy (I) stop and deliver $(\alpha_i, \varepsilon_i)$ as the required angles. Otherwise, either (1) $\min(|x^*-x_i|, |y^*-y_i|) \geq \epsilon$ or (2) $|z^*-z_i| \geq \epsilon$ and the improving aim angles $(\alpha_{i+1}, \varepsilon_{i+1})$ are obtained as follows. If (1) does not hold take $\alpha_{i+1} = \alpha_i$; if (1) does hold, the azimuth $\tilde{\alpha}$ of $\mathfrak{P}_i$ differs enough from the azimuth α^* to make an azimuth correction to α_i by simply adding the miss azimuth $\alpha^* - \tilde{\alpha}$ to the old az - formally α_{i+1} is given by $\alpha_{i+1} \equiv \alpha_i + \alpha^* - \tilde{\alpha} \bmod 2\pi, 0 \leq \alpha_{i+1} < 2\pi$. If (2) does not hold, take $\varepsilon_{i+1} = \varepsilon_i$; if (2) holds, likewise make an elevation correction to ε_i, by adding on the miss elevation $\varepsilon^* - \tilde{\varepsilon}$, to obtain ε_{i+1}, where $\tilde{\varepsilon}$ is the elevation of $\mathfrak{P}_i$ (& ε^* the el of $\mathcal{P}^*$).

Dynamic intercept algorithm. Target position is available every Δt second (currently $\Delta t = .1$). Given a present target position (in reference coordinates) $\mathcal{C}_j$ corresponding to a present discrete clock time, it is required to intercept the future target flight path by firing at the present instant. Target position $\mathcal{C}_{j+\nu}$, $\nu = 1, 2, 3, \ldots$, is available $\nu\Delta t$ sec ahead of the present instant; the future target flight path - parametrized by target time of flight from the present position - is taken to be the polygonal train joining $\mathcal{C}_j, \mathcal{C}_{j+1}, \mathcal{C}_{j+2}, \ldots$, with constant velocity in the interior of the segment $\langle \mathcal{C}_{j+\nu}, \mathcal{C}_{j+\nu+1} \rangle$. So $\mathcal{C}_{\nu,\lambda} = \mathcal{C}_{j+\nu} + \lambda(\mathcal{C}_{j+\nu+1} - \mathcal{C}_{j+\nu})$, $0 \le \lambda \le 1$ on $\langle \mathcal{C}_{j+\nu}, \mathcal{C}_{j+\nu+1} \rangle$ has target time of flight $\nu\Delta t + \lambda\Delta t$. Let $\tau_{\nu,\lambda}$ = projectile time of flight to an intercept of $\mathcal{C}_{\nu,\lambda}$ for a trajectory initiated at the present instant (available from the static algorithm). Ideally we would require the determination of $\mathcal{C}_{\nu,\lambda}$ so that $\tau_{\nu,\lambda} = (\nu+\lambda)\Delta t$; but this is certainly not realistic numerically, so we relax the intercept condition to (D) $|\tau_{\nu,\lambda} - (\nu+\lambda)\Delta t| <$ small prescribed tolerance δ — currently $\delta = 10^{-10}$ sec.

The rationale for the algorithm is based on the following considerations. Suppose that 2 successive positions $\mathcal{C}_{\bar\nu,\lambda_1}$ and $\mathcal{C}_{\bar\nu,\lambda_2}$, $0 \le \lambda_1 < \lambda_2 \le 1$ on the same segment have been obtained admitting an undershoot (projectile arrives at location after target) $\tau_{\bar\nu,\lambda_1} < (\bar\nu+\lambda_1)\Delta t$ at $\mathcal{C}_{\bar\nu,\lambda_1}$, and an overshoot (projectile arrives at location before target) $\tau_{\bar\nu,\lambda_2} > (\bar\nu+\lambda_2)\Delta t$ at $\mathcal{C}_{\bar\nu,\lambda_2}$. If either time of flight difference satisfies (D), stop and deliver the aim angles $(\alpha_j, \varepsilon_j)$ of the trajectory as the so-called ideal angles producing the desired intercept. Otherwise, it is a reasonable presumption to expect an intercept somewhere between $\mathcal{C}_{\bar\nu,\lambda_1}$ and $\mathcal{C}_{\bar\nu,\lambda_2}$. We know that the target time of flight to positions

$\mathcal{C}_{\bar\nu,\lambda_1} + \mu(\mathcal{C}_{\bar\nu,\lambda_2} - \mathcal{C}_{\bar\nu,\lambda_1})$, $0 \le \mu \le 1$, on the segment $\langle \mathcal{C}_{\bar\nu,\lambda_1}, \mathcal{C}_{\bar\nu,\lambda_2} \rangle$ is $\bar\nu\Delta t + [\mu(\lambda_2 - \lambda_1) + \lambda_1]\Delta t = (\bar\nu\Delta t + \lambda_1\Delta t) + \mu[(\bar\nu\Delta t + \lambda_2\Delta t) - (\bar\nu\Delta t + \lambda_1\Delta t)]$, where the barycentric combination of the end-point times of flight is the same as that giving the intermediate point's coordinates as a combination of the end-point coordinates. Proceeding under the temporary assumption that the projectile time of flight to an intermediate point is likewise the same barycentric combination of end-point projectile times of flight, get a unique solution $\bar\mu$, $0 < \bar\mu < 1$, of the equation $\tau_{\bar\nu,\lambda_1} + \mu(\tau_{\bar\nu,\lambda_2} - \tau_{\bar\nu,\lambda_1}) = \bar\nu\Delta t + [\mu(\lambda_2 - \lambda_1) + \lambda_1]\Delta t$ determining where target time of flight = projectile time of flight under the tentative assumption. Note that the alternating under/overshoot conditions ensures $0 < \bar\mu < 1$; the corresponding point on $\langle \mathcal{C}_{\bar\nu,\lambda_1}, \mathcal{C}_{\bar\nu,\lambda_2} \rangle$ is $\mathcal{C}_{\bar\nu,\lambda_3}$, where $\lambda_3 = \bar\mu(\lambda_2 - \lambda_1) + \lambda_1$. Now drop the temporary assumption and regard $\mathcal{C}_{\bar\nu,\lambda_3}$ as a candidate intercept point. Compute $\tau_{\bar\nu,\lambda_3}$ and test the time of flight difference $(\bar\nu+\lambda_3)\Delta t - \tau_{\bar\nu,\lambda_3}$ against condition (D).

If (D) is satisfied, stop and deliver the aim angles $(\alpha_j, \varepsilon_j)$ of the trajectory yielding $\tau_{\bar{\nu},\lambda_3}$ as the ideal intercept angles. If (D) is not satisfied, we have an under-or overshoot at $\mathscr{C}_{\bar{\nu},\lambda_3}$; taking that one of $\mathscr{C}_{\bar{\nu},\lambda_1}, \mathscr{C}_{\bar{\nu},\lambda_2}$ with the opposite under/overshoot condition, we have reproduced the initial state of affairs (with a smaller distance between the points). Thus the rationale and the formal procedure for iterating.

It remains only to start the algorithm by finding two successive discrete clock time target positions $\mathscr{C}_{j+\bar{\nu}}, \mathscr{C}_{j+\bar{\nu}+1}$ exhibiting the alternating under/overshoot condition. This is done by computing all $\tau_{\nu,0}, \nu = 0,1,2,\ldots$ (projectile times of flight to the present and future discrete target positions), and determining $\bar{\nu} \geq 1$ by the conditions $\tau_{\nu,0} > \nu\Delta t$ for $\nu = 0,\ldots,\bar{\nu}-1$; $\tau_{\bar{\nu},0} \leq \bar{\nu}\Delta t$ Clearly $\tau_{\nu,0} > \nu\Delta t, \nu = 0$; if $\tau_{\nu,0} > \nu\Delta t$ for all $\nu \geq 0,1,2,\ldots$ no interception is possible, so this state of affairs is used as the criterion for terminating ideal intercept angle calculation.

Gun-pointing angle errors. Ideal intercept angles (α, ε) and actual gun angles $(\alpha_G, \varepsilon_G)$ wrt the reference frame as derived in Part I are compared to yield signed errors as follows. The signed elevation error is just $\varepsilon_G - \varepsilon$; so positive if the gun actually points above the ideal elevation, negative if the gun points below. Azimuth error is signed so that positive means the actual is leading the ideal, negative means a lag, provided that the target flight path admits a determination of crossing.

PART III. Miss Distance and Related Parameters.

At discrete clock times separated by Δt sec (currently $\Delta t = .1$) target position in the reference frame is available to a maximum of n points (currently $n \leq 1000$: target flight time considered $\leq$ 100 sec); so we have n target coordinates $\mathscr{C}_1, \ldots, \mathscr{C}_n$ at clock times $C_1, \ldots, C_n$, where $C_i = C_{i-1} + \Delta t$. Consider a projectile trajectory, with system gun angles $(\alpha_G, \varepsilon_G)$ wrt the reference frame, initiated at the clock time C_j. Suppose that we have continuous, rectifiable arcs $\mathscr{C}^j, \mathscr{P}^j$, parametrized by elapsed time of flight $t, 0 \leq t \leq (n-j)\Delta t$, reckoned from the present instant C_j, representing target, projectile flight paths, respectively. At elapsed time t, the target-to-projectile miss vector is just $m(t) = \mathscr{P}^j(t) - \mathscr{C}^j(t)$. So theoretically, there is a smallest τ_m at which the miss distance $\|m(t)\|$ assumes its minimum value: $\|m(\tau_m)\| = \min_{0 \leq t \leq (n-j)\Delta t} \|m(t)\| =$ the minimum miss distance. Further assuming differentiability of both arcs we can obtain target and projectile velocity at minimum miss time τ_m. If τ_m is an interior point (as expected), we also have $\frac{d}{dt}\|m\|^2 = m \cdot \dot{m} = 0$: this leads directly to the introduction of the so-called normal plane and a single shot hit probability set-up in the normal plane.

MINIMUM MISS VECTOR. The construction of $\mathscr{C}^j, \mathscr{P}^j$, and the numerical procedures used to obtain τ_m, $m(\tau_m)$, velocities follow. Introduce the distinguished elapsed times $t_\nu = \nu\Delta t, \nu = 0, \dots, n-j$. As before, $\mathscr{C}^j$ is taken as the polygonal train joining $\mathscr{C}_j, \dots, \mathscr{C}_n$ with intervalwise parametrization $\mathscr{C}^j(t_\nu + \lambda\Delta t) = \mathscr{C}_{j+\nu} + \lambda(\mathscr{C}_{j+\nu+1} - \mathscr{C}_{j+\nu}), 0 \le \lambda \le 1$, in $[t_\nu, t_{\nu+1}], \nu = 0, \dots, n-j$. Velocity at time t_ν is just the velocity $\dot{\mathscr{C}}_{j+\nu}$ already numerically obtained, as described in Part I; for interior points $\mathscr{C}_{j+\nu} + \lambda(\mathscr{C}_{j+\nu+1} - \mathscr{C}_{j+\nu})$ velocity is obtained by linear interpolation on the relative position barycenter λ, if needed. From the numerical trajectory computations, projectile position $\mathscr{P}_\nu$ and velocity $\dot{\mathscr{P}}_\nu$ are available in reference coordinates at the discrete times t_ν. Just as for the target flight path, the projectile trajectory $\mathscr{P}^j$ is taken as the polygonal train joining $\mathscr{P}_j, \dots, \mathscr{P}_n$, parametrized as for the target flight path, with velocity obtained at interior points of a segment $\langle \mathscr{P}_{j+\nu}, \mathscr{P}_{j+\nu+1} \rangle$ as for target velocity.

$\|m(t_k + \lambda\Delta t)\|^2 = \|\mathscr{P}_k - \mathscr{C}_k + \lambda[(\mathscr{P}_{k+1} - \mathscr{C}_{k+1}) - (\mathscr{P}_k - \mathscr{C}_k)]\|^2$ is just a quadratic function of $\lambda, 0 \le \lambda \le 1$, so the minimum value m_k and the point $t_k + \lambda_k\Delta t$ of attainment where m assumes its minimum value over the interval $[t_k, t_{k+1}]$ are readily computed. The discrete minimization problem: find the smallest index l such that $m_l = \min_{k=0,1,\dots,n-j-1} m_k$, is trivially solvable (by computer). So we have minimum miss time τ_m, the minimum miss vector $m(\tau_m)$ (in reference coordinates), and other required values $\mathscr{C}^j(\tau_m), \mathscr{P}^j(\tau_m), \|\mathscr{C}^j(\tau_m)\|$.

NORMAL PLANE. HIT PROBABILITY.

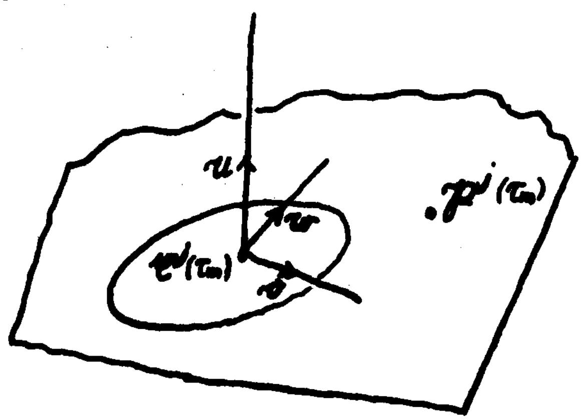

Let $\mathcal{U} = \mathcal{m}(\tau_m)^0$ As we have seen at the beginning, in theory $\mathcal{m}(\tau_m)\cdot\mathcal{U}=0$. The numerical procedures used do not strictly guarantee this; however, for minimum miss distances $\|\mathcal{m}(\tau_m)\| \leq 30m$, it has been observed that usually $|\mathcal{m}(\tau_m)\cdot\mathcal{U}|$ computes out $<.01m$, invariably $|\mathcal{m}(\tau_m)\cdot\mathcal{U}|<.1m$; for minimum miss distances $>30m$, the magnitude is unpredictable. We will proceed assuming $\mathcal{m}(\tau_m)\cdot\mathcal{U}=0$. This simply says that at minimum miss the projectile lies in the plane passing through the target perpendicular to the relative velocity vector $\dot{\mathcal{m}}(\tau_m) = \dot{p}^j(\tau_m) - \dot{\mathcal{C}}^j(\tau_m)$, the so-called normal plane. A two-dimensional coordinate frame $F(\mathcal{C}^j(\tau_m)/\mathcal{V},\mathcal{W})$ in the normal plane is introduced as follows. With $\mathcal{U} = u_1\mathcal{X}+u_2\mathcal{Y}+u_3\mathcal{Z}$, set $\mathcal{V}=(u_1^2+u_2^2)^{-\frac{1}{2}}(-u_2\mathcal{X}+u_1\mathcal{Y})$ in the free normal plane and parallel to the ground, $\mathcal{W}=(\mathcal{U}\times\mathcal{V})^0$; generic coordinates, (v,w,) wrt this frame are called normal coordinates, with v being regarded as a horizontal or azimuth miss distance component, w as a vertical or elevation component. The normal coordinates of the projectile at minimum miss are $(v_0, w_0) = (\mathcal{m}(\tau_m)\cdot\mathcal{V}, \mathcal{m}(\tau_m)\cdot\mathcal{W})$.

To arrive at a set-up leading to a simple single shot hit probability, we assume that random projectile location in the normal plane has random normal coordinates (V,W) following a bivariate normal distribution where (1) the center of the distribution is taken as (V_0, W_0) , the computed normal coordinates of the projectile at minimum miss; (2) the standard deviations σ_V, σ_W are normal axes distance dispersions obtained from an average of normal axes mil dispersions derived by the statistics section from PINS & miss distance radar scorings - the target range $\|\mathcal{C}^j(\tau_m)\|$ at minimum miss is required for the customary mils-to-meters conversion.

A target region in the normal plane is obtained as follows. First the target is mathematically represented as the region enclosed by an ellipsoid in 3 space defined as follows:

center= $\mathcal{C}^j(\tau_m)$;

longitudinal axes in the direction $\mathcal{V}$ of target velocity at miss, with semi-axis length a: $\mathcal{V} = \dot{\mathcal{C}}^j(\tau_m)^0 = r_1\mathcal{X}+r_2\mathcal{Y}+r_3\mathcal{Z}$;

traverse axis parallel to the ground, direction $\mathcal{Y} = \dfrac{-r_2\mathcal{X}+r_1\mathcal{Y}}{\sqrt{r_1^2+r_2^2}}$, with semi-axis length b;

vertical axis directed by $\mathcal{S}=(\mathcal{V}\times\mathcal{Y})^0$, with semi-axis length c.

The definition of $\mathcal{V}$ adequately accounts for target yaw and pitch, but in the absence of any data the definition of $\mathcal{Y}$ amounts to assuming zero roll. The ellipsoid is projected in the direction $\mathcal{U}$ onto the normal plane in accordance with the notion of presented area, resulting in a target region given by the interior of an ellipse $\alpha V^2+\beta VW+\gamma W^2=1$. The straightforward but tedious calculations required to produce the coefficients α,β,γ from the definition of the target ellipsoid are omitted.

Quite abstractly, the desired single shot hit probability is just $Prob\{\alpha V^2 + \beta V \cdot W + \gamma W^2 \leq 1\}$. If the covariance turns out negligible, the cross-product term of the quadratic form in normal, independent random variables can be removed by a rotation of axes, and the equivalent probability is evaluated by the well known Grubbs approximation [3]. Otherwise the double integral representing the probability is readily computed numerically.

References

[1] Programs for Digital Signal Processing, IEEE Press 1979.

[2] "Method for Calculating Exterior Ballistic Trajectories..", Development and Proof Services Report No. DPS-416, L. Heppner, 1962.

[3] "Approximate Circular and Noncircular Offset Probabilities of Hitting", Operations Research, 12, pp 51-62, F. E. Grubbs, 1964.

Effects of Vegetation and Battlefield Obscurants on Point-to-Point Transmission in the Lower Millimeter Wave Region (30-60GHz)

FELIX K. SCHWERING, DR., *ROBERT A. JOHNSON, 1LT(P),
NIKOLAUS ROKKOS AND GERALD M. WHITMAN, DR.
US ARMY COMMUNICATIONS-ELECTRONICS COMMAND
FORT MONMOUTH, NJ 07703
EDMOND J. VIOLETTE AND RICHARD H. ESPELAND
US DEPARTMENT OF COMMERCE
NATIONAL TELECOMMUNICATION AND INFORMATION ADMINISTRATION
INSTITUTE FOR TELECOMMUNICATION SCIENCES
BOULDER, CO 80303

1. Introduction

The Center for Communication Systems of the US Army Communications-Electronics Command is developing mm-wave radio systems for tactical and strategic communication/data transmission. These systems are designed to operate in the frequency bands of 35-39GHz and 54-58GHz. It is well known that atmospheric effects, battlefield obscurants, and vegetation affect transmission in the lower mm-wave region much less than they affect transmission in the optical range (laser beams). But in order to define performance standards and equipment specifications for mm-wave radios, a data base on propagation effects for this frequency region needs to be established.

The effects of atmospheric absorption, rain, and fog have been studied previously [1], [2]; snow effects on mm-wave propagation are presently investigated in the SNOW 1 and 1A experiments. This paper reports on recent studies on mm-wave transmission through vegetation and through battlefield obscurants such as smoke, dust and artillery shell detonation clouds.

The vegetation experiments [3] were conducted at three frequencies simultaneously, i.e., at 9.6, 28.8 and 57.6 GHz, using special test instrumentation available at ITS, Boulder, CO. They involved measurements over propagation paths through coniferous and deciduous groves, where in the latter case, the tests were repeated under summer and winter conditions; further test runs investigated the effects of dry, wet and windy weather conditions on foliage penetration.

The effects of battlefield obscurants on mm-wave propagation conditions were studied with available mm-wave radios operating in the 38 and 60 GHz bands [4]. Experiments at Grafenwoehr, FRG, were concerned with propagation through smoke and dust, while test runs at Ft. Polk, LA, investigated airborne dust and debris effects produced by artillery shell detonations (DIRT III).

The experiments were complemented by theoretical studies to establish parameter dependencies and assist in the interpretation of measured data. The results of the investigation shows that mm-wave links are capable of providing reliable communication/data transmission in the battlefield environment.

2. Vegetation Experiments

The instrumentation for the measurement program is shown in Figure 1. Both transmitting and receiving terminals are mounted in four-wheel-drive vans for mobility in rough terrain. The RF components are supported on erectable track-mounted carriages to permit ready adjustment of height above ground. In addition, the transmitter mounting permits two meters of horizontal travel to allow variability along this coordinate.

The directional antennas are scaned in elevation and azimuth by a remote-controlled positioner at the receiver terminal to provide data on the intensity of off-angle scatter from foliage and ground reflection effects.

Three frequencies, 9.6, 28.8, and 57.6 GHz, are used simultaneously to obtain frequency dependent data to aid in developing transmission loss models for specific types of vegetation. Both vertical and horizontal antenna polarization are mechanically selectable at each terminal which permits measurements for each case, including cross polarization. Beamwidths of the transmitting antennas are 10^{o} at all frequencies. Receiving antenna beamwidths are 4.8^{o} at the 9.6 GHz frequency and 1.2^{o} at 28.8 and 57.6 GHz. A 70 dB dynamic range and a minimum sensitivity of -100 dBm is available at all frequencies.

The data recorded from these measurements consists of received signal amplitudes from both azimuthal and elevation scans at transmitter and receiver heights from 1 to 9 meters above ground. The transmitter antennas were normally fixed at a zero angle (on-path) pointing and the receiving antennas were scanned at $\pm 20^{o}$ in the azimuthal plane and $\pm 15^{o}$ in the elevation plane. In most test, the transmit and receive antennas were positioned at the same height above ground.

The significant results and observations from this study are listed in the following summary statements with specific illustrations shown in

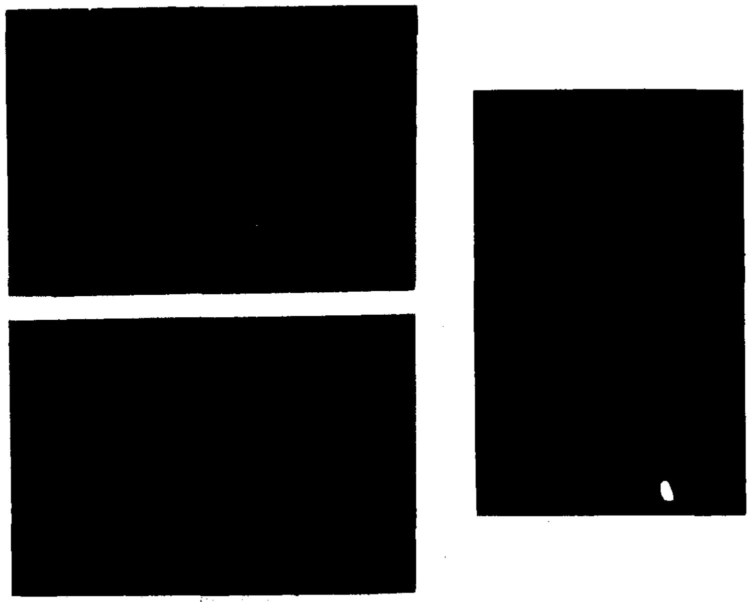

Fig. 1. Transmitting and receiving equipment used for the vegetation measurements.

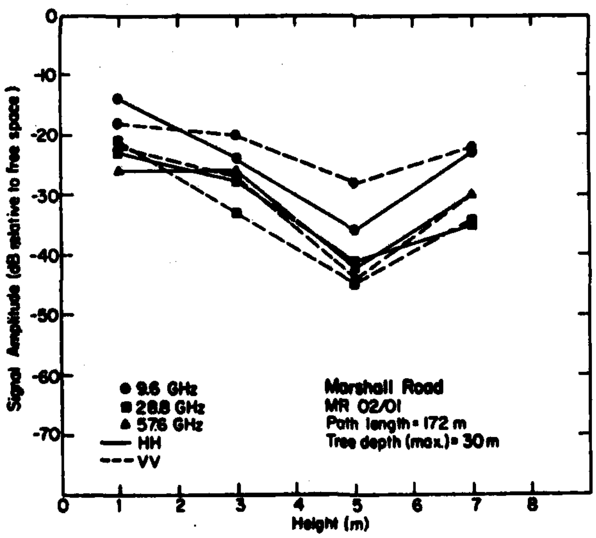

Fig. 2. Signal amplitude as a function of height for a cottonwood grove (HH polarization and VV polarization).

Figures 2 through 5:

a. The measured signal loss (dB/m) through trees in foliage exceeds predicted loss obtained from extrapolation of data from numerous sources at frequencies between 100 and 9000 MHz. These extrapolated values indicate only 1/3 to 1/10th the dB/m loss measured in the frequency range of 10 to 60 GHz. The term dB/m means dB loss per meter of measured foliage depth on a path, independent of the total path length. These studies have indicated a need to establish a method for determining depth of foliage. This aspect must be examined when comparing results.

b. Diffraction theory has a $\sqrt{f}$ dependence which sometimes is used to predict vegetation loss (dB/m) at higher frequencies. Although our results show that vegetation losses clearly increased (on the average) at these frequencies, the rate was less than $\sqrt{f}$ over the 10 to 60 GHz frequency range. Normalized losses due to vegetation (dB/m) show a trend to decrease as the foliage path is lengthened which appears consistent with measurements at lower frequencies and with theoretical predictions.

c. The measured vegetation loss, in nearly all cases, as observed in Figure 2 was less at the 1 and 2 meter heights than at heights greater than 2 meters. This is the result of no leaves or sparse leaves at the 1 and 2 meter height and the general absence of underbrush on the sites used for these tests. Also, for trees and bushes, vegetation loss difference as a function of antenna polarization was very slight, whereas for tall grass, horizontal polarization clearly provides less loss. When comparisons of vegetation loss were made of deciduous groves, with and without foliage, the groves in summer foliage produced about 3 times as much loss in dB/m as the same groves in their defoliated state. Figure 3 shows an example of these observations.

d. An important factor is the dependence of received signal on spatial variance. Signal amplitude variations as large as 42 dB, see Figure 4, and typically 30 dB were observed for small displacements (≈ 25 cm) of the transmitter antennas in either the horizontal or vertical plane. There is considerable evidence that these deep fades are results of two relatively strong multipath signals adding destructively. Exposed (free of leaf cover) trunks and branches appear to be the source of the multipath.

e. Observations during windy periods (15 to 20 km/h) on a path with 10 or more meters of foliage depth produced signal variations (scintillations) of up to 15 dB with periods of less than 5 seconds. In addition, 8 dB fades of longer periods (1 to 5 minutes) were noted in gusting winds. The time series records in Figure 5, illustrate typical scintillations.

f. An increase in vegetation loss was noted during a rain on a single observation when water covered, or droplets formed, on leaves and branches

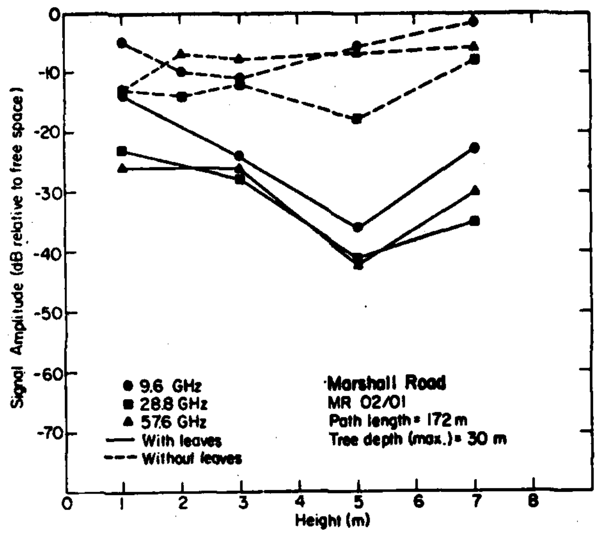

Fig. 3. Signal amplitude as a function of height for a cottonwood tree grove, with and without foliage (HH polarization).

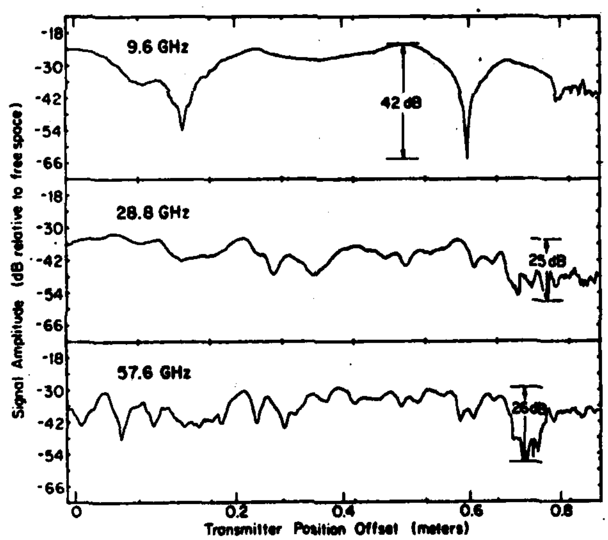

Fig. 4. Signal amplitude relative to transmitter antenna horizontal displacement. (MR01/01, path length = 152 m, height = 1 m, tree depth = 40 m, polarization = VV.)

of a willow tree. The signal loss increase was 3 to 5 dB at 9.6 GHz and 15 to 20 dB at 28.8 GHz; however, these maximum losses occured several minutes after the shower started, indicating perhaps a delay in wetting of leaves and branches contributing to propagation in sheltered regions. Moisture condensation prevented a measurement at 57.6 GHz. A wet snow fell during a conifer path observation and much of it stayed on the branches; however, no detectable signal change was noted.

g. Depolarization of signals propagated through exposed tree trunks showed less change than through leafy foliage where depolarized signal level increased by as much as 20 dB.

h. For a path with high loss due to foliage, a stronger received signal was observed when a common off-path volume (clear of tall trees) was illuminated. In the observed case a common scatterer, perhaps a bush or terrain feature in a clearing produced a side scatter signal level higher than the direct-path signal.

Additional data and a detailed discussion on these experiments can be found in a recent report [3].

3. Vegetation Theory

This theory treats vegetation (forests) as a random medium and uses a transport equation approach to analyze mm-wave propagation in this medium. The approach allows multiple scattering effects to be taken fully into account, while interference effects are neglected, a simplification which is justified by the experimental results; see Figure 4.

Transport theory splits the total field intensity into two components, the coherent (median) component and the incoherent (zero mean) component. While the coherent component possesses the same polarization properties as the incident field, the incoherent component is described by using a formulation in terms of the four Stokes' parameters. The theory thus leads to a system of four coupled integro-differential equations for the specific intensities of the incoherent component. However, by making reasonable assumptions concerning the statistical scattering characteristics of the forest medium, it is shown that for the first Stokes' parameter a single, uncoupled equation is obtained which is identical to the conventional scalar transport equation. The first Stokes' parameter is the quantity of primary interest since it is by definition the total intensity of radiation, i.e., it represents the sum of the intensities associated with two orthogonal polarizations.

The scalar transport equation has been solved for the case of a plane wave impinging upon the planar interface between an air half space and a forest half space characterized as a statistically homogeneous random

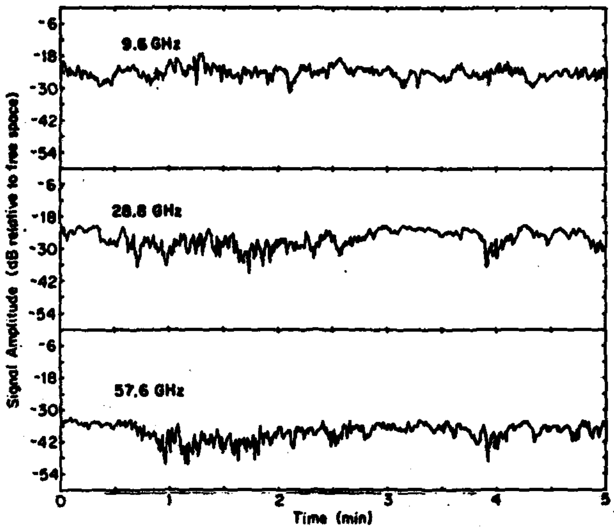

Fig. 5. Time series records of received signal amplitude during windy conditions.

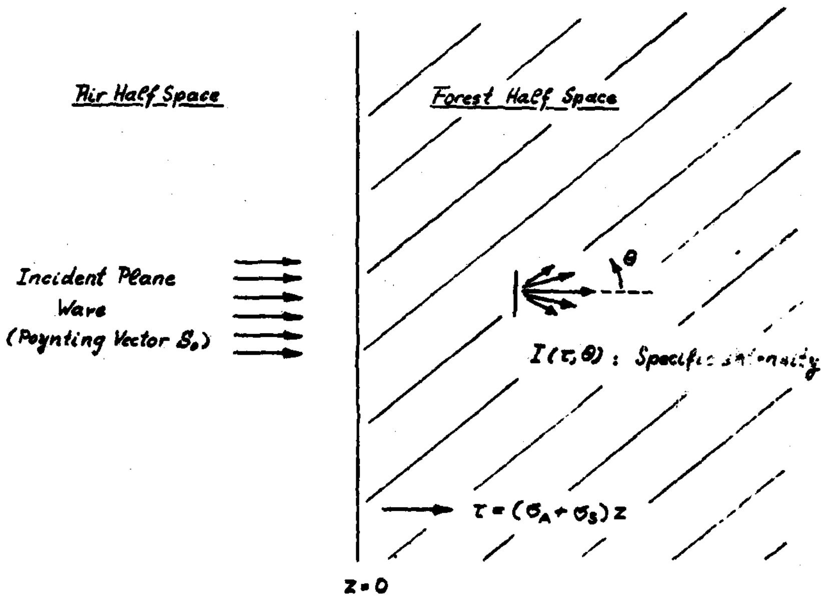

Fig. 6. Theoretical model: Plane wave normally incident upon planar interface separating air half space from statistically homogeneous random medium.

σ_A, σ_S : absorption and scatter cross section per unit volume.

$\tau = (\sigma_A + \sigma_S) z$: normalized distance into medium.

medium with an isotropic scatter function; see Figure 6. In the analysis of this model two approaches were taken:

a. A first order multiple scattering approximation (for small penetration depths) in conjunction with an asymptotic solution (for large penetration depths). This approach yields explicit expressions for the range dependence of both the coherent and incoherent field components, and for the directional spectrum of the incoherent component. Results are shown in Figures 7 and 8.

b. A rigorous method which represents the specific intensity by a series expansion in terms of Tschebyscheff polynomials. Computer evaluation of this theory has confirmed the trends indicated by the approximate theory and improved numerical accuracy.

The theory shows that at large penetration depths the forward scattered wave trains yield the major contribution to the received field intensity (Figure 7) and that the range dependency of this intensity is complex and not determined by a constant attenuation rate (Figure 8). A comparatively high attenuation rate at small penetration depth gradually reduces to a lower attenuation rate at larger distances.

A similar trend has also been observed at VHF and lower frequencies; but the underlying mechanism is completely different. While at VHF, the decreasing attenuation rate is due to the so-called up-over-down mechanism i.e., to the excitation of a low-attenuation lateral wave guided by the forest-to-air interface (Tamir theory), the effect at mm-waves is caused by the interaction of the coherent and incoherent field intensities: The coherent component dominates at small penetration depth but is attenuated due to both absorption and scatter, and therefore decreases rapidly. The incoherent component on the other hand scatters into itself and therefore decreases due to absorption only (though over an extended path). Hence this component, having a lower attenuation rate, will dominate at larger distances. At small distances of course the incoherent component is of low magnitude since it is generated by the scattering of the coherent component.

A rigorous theory using a scatter function with a strong forward component (and an omni-directional background) is presently being evaluated. Since in a forest environment all scatter objects are large compared to a mm-wavelength, strong forward scattering may be a more realistic assumption than the use of an isotropic scatter function.

4. Smoke and Dust Experiments

Field experiments on mm-wave propagation through smoke and dust were performed at Grafenwohr, West-Germany, during May-June 1979. Tactical

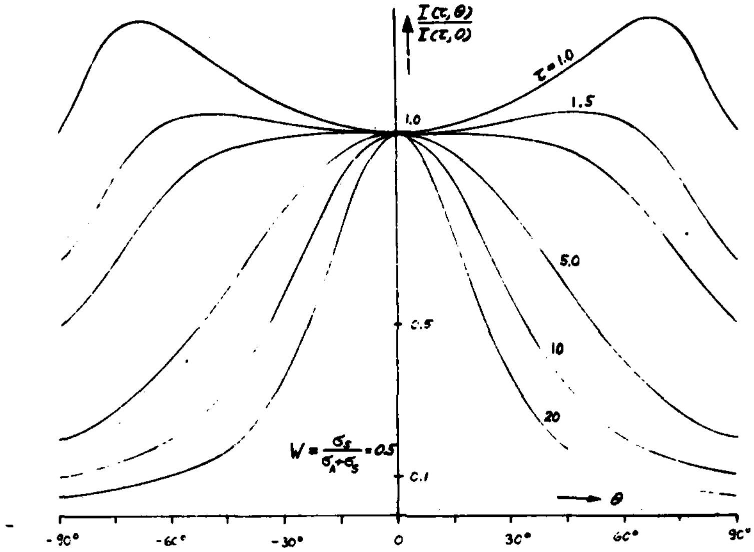

Fig. 7. Specific intensity I of incoherent component as function of θ for various τ and W = 0.5. Isotropic scattering assumed.

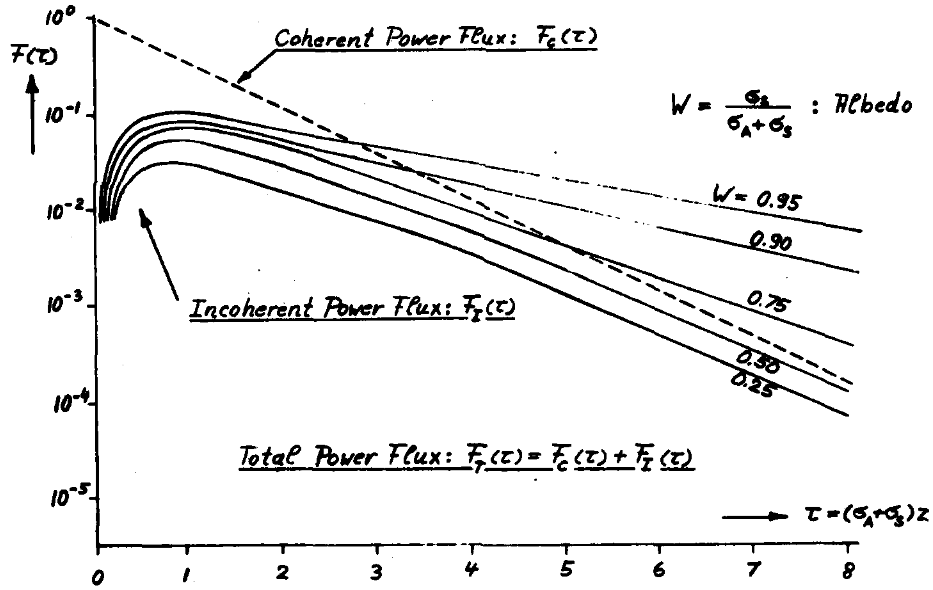

Fig. 8. Power flux in forward direction as function of τ . Isotropic scattering assumed.

$F_c(\tau)$: Magnitude of Poynting vector of coherent component;

$F_I(\tau)$: Forward flux of incoherent component.

radios developed by CENCOMS for the 38 GHz band were used in these tests. Characteristics of these radios are listed in Table 1; the data on 60 GHz radios is included in the table for use in Section 5.

Table 1
Millimeter Wave Radio Characteristics

Characteristics		38 GHz Radio	60 GHz Radio
Frequency		38.5 GHz	59.7 GHz
Transmit Power		50 mW	40 mW
Receiver Sensitivity			
Bandwidth (voice/video)		4/10 MHz	4/10 MHz
Beamwidth		5.5°	3.0°
Range	clear:	30/14 km	1.7/1.2 km
(voice/video)	15 mm/h rain:	5/3.5 km	1.3/0.95 km

The tests were conducted over a 2.75 km transmission path. In a first sequence of experiments an intense dust cloud was produced by an Armored Personnel Carrier driven parallel or perpendicular to the transmission path. A second test investigated propagation through a smoke (labeled HC) derived from tetrachlorine and zinc powder. A third experiment was performed over a shorter path of 500 m length and tested a smoke provided by German technicians; its chemical composition was not revealed.

Measured data show that HC smoke or a cloud of dust having an extension of several hunderd meters will cause an attenuation of less than 0.3 dB. The smoke used in the third test was slightly less transparent; but attenuation remained below 1 dB. The experiments thus confirm the effectiveness of mm-wave beams in penetrating through dust and smoke.

5. Dirt III Experiments

The Dirt III experiments were conducted at Ft Polk, Louisiana, during April 1980. CENCOMS participated in these experiments to investigate the effect of dust and debris clouds, produced by artillery shell detonations, on the performance of mm-wave communication links. Two such links, operating at 38 GHz and 60 GHz, respectively, were studied using the radios of Table 1. The radios were tripod-mounted i.e., at a height of $\sim$1.5 m above ground. The transmission path had a length of approximately 850 m. At this distance the (clear air) fade margin was 25 dB for the 38 GHz radios and 9 dB for the 60 GHz link.

The testing consisted in measuring received power (or AGC) as a function of time after detonation of artillery shells that were placed either directly below the line-of-sight (LOS) or at a lateral distance of 10 m or 20 m off the LOS. The munitions were either buried or placed on the ground. The distances of the detonation site from the two terminals of each link were approximately 600 m and 250 m. Both Russian and American artillery rounds were used. The sizes of the rounds were 122 mm and 152 mm for the Russian and 105 mm and 155 mm for the American munitions. Figure 10 shows a timesequence of the dirt and debris cloud of a typical surface detonation.

As an example of measured data, Figure 9 shows a stripchart recording of the AGC output of the 38 GHz and 60 GHz radios in response to a 122 mm, buried, on-axis detonation. Note that the time coordinate increases from right to left. On the recording, attenuation levels of 1, 3, 6 and 10 dB are indicated. In Table 2, the amount of time during which the attenuation was greater than these levels is listed for the 38 GHz radios and for the (worst) case of on-axis detonations. It is apparent that signal strength recovers to nearly normal levels within a few seconds. Similar tables were compiled for off-axis explosions and for the 60 GHz link.

Table 2

Effect of on-axis detonation cloud on signal transmission at 38 GHz:

Maximum attenuation A_{max}, and time t_n for which attenuation exceeded n dB

Shell size (mm)	Placement (B: buried, S: surface)	A_{max} (dB)	t_{10}	t_6	t_3	t_1
			(seconds)			
122	S	10.5	0.12	0.25	1.00	1.50
105	S	5.8	—	—	0.78	3.4
152	S	20.0	0.25	0.94	1.56	4.38
155	B	22.1	0.16	0.94	1.56	8.13
122	B	21.5	0.31	0.63	0.78	4.06

Also shown in Table 2 is the maximum attenuation A_{max} occuring immediately after the detonation. For the 38 GHz radios this attenuation remained within the fade margin of 25 dB so that communication could be maintained at all times. For the 60 GHz radios, on the other hand, A_{max} exceeded the fade margin of 9 dB in several instances (of on-axis detonations) and communication was temperarily interrupted. Outage times howeveer remained below 1 second. For off-axis explosions at distances of 10 m and 20 m from the LOS, the maximum attenuation did not exceed 6 dB and 3 dB respectively, and no outages occured at either frequency. It can thus be stated the the effect of artillery shell detonation clouds on mm-wave communication is minimal. As a general rule, such effects will decrease further with increasing link length.

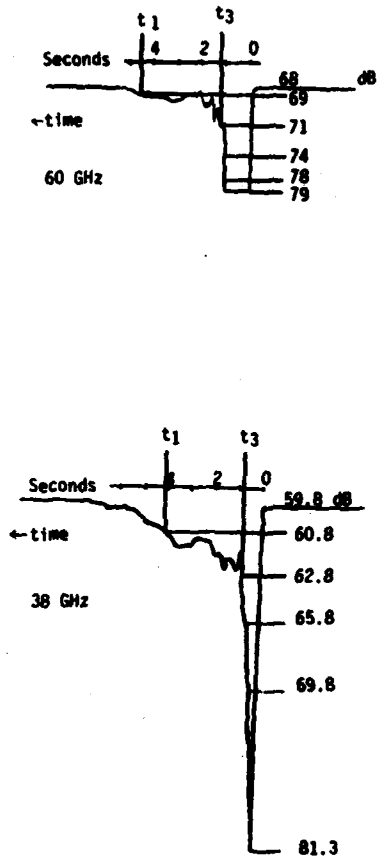

Fig. 9. Stripchart recording of 122 mm, buried, on-axis event: Attenuation vs. time

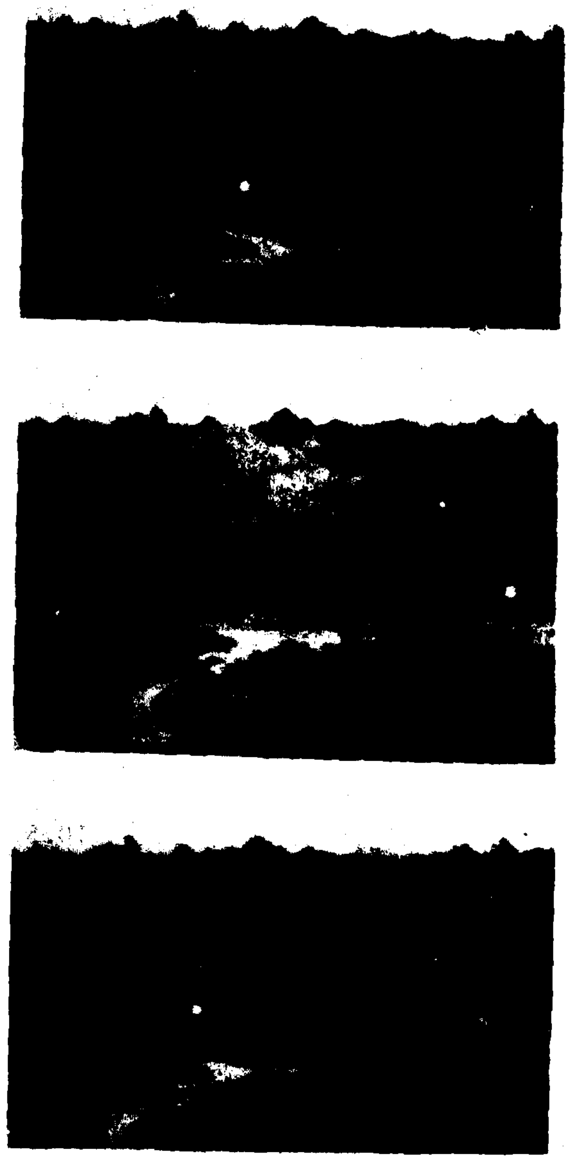

Fig. 10. Typical time sequence of detonation cloud

As a consistent trend it was observed that, in the case of on-axis detonations, buried shells produced stronger attenuation than munitions exploded on the surface, while for off-axis detonations the situation was reversed. This is easily explained by the fact that buried detonation tend to expell particulate matter in the vertical direction thus producing a more collimated explosion cloud than surface explosions which generate laterally more extended clouds. Collimation of the explosion cloud also explains an effect observed for on-axis detonations, that a second, smaller attenuation maximum occurs approximately 4 seconds after a buried explosion. This attenuation peak is attributed to the heavier pieces of dirt and debris thrown almost vertically into the air and passing the vicinity of the LOS a second time while falling back to the ground. In general the experiments show that strong mm-wave attenuation, as it occurs immediately after the detonation, is caused by the larger and heavier particulate matter which however remains airborne for a short time span only. Lighter particles, which remain suspended in the air for a longer period of time, have negligible effect on mm-wave transmission as evidenced by the smoke and dust experiments reported in Section 4.

A detailed discussion of the Dirt III mm-wave experiments can be found in a recent report [4], which also presents an analytical approach allowing generalization of experimental results to other geometrical situations. The analysis is based on a description of the size of the explosion cloud and its distance from the LOS in terms of the Fresnel zones of the radio link in the plane (normal to the LOS) where the detonation cloud has its center.

6. Conclusions

Experimental investigations supported by theoretical studies confirm that mm-wave links are capable of providing highly reliable communication in the battlefield environment. Specifically

a. Millimeter wave transmission through a line of trees or placement of radios at moderate depths into woods (for camouflage purposes) will be possible, although at the price of a reduced transmission distance. The range reduction well depend on vegetation depth and density.

b. Millimeter wave attenuation by smoke and dust is minimal and not likely to noticeably affect link availability.

c. Artillery shell detonations may temporarily interrupt signal transmission but only under unfavorable circumstances, i.e., if the explosion occurs below ground and the detonation cloud intercepts the line-of-sight. Even under these conditions, outage times will be less than 1 second.

These results apply to voice, video as well as data transmission.

References:

1 J. R. Clark, W. Sollfrey, S. Katz, Performance of Tactical Millimeter Wave Radio Links, Rand Corp Techn. Report N-1461-Army, June 1980.

2 R. K. Crane, Prediction of Attenuation by Rain, IEEE Trans. on Communications, Vol. COM-28, pp. 1717-1733, September 1980.

3 E. J. Violette, R. H. Espeland, A. R. Mitz, F. A. Goodknight, SHF-EHF Propagation through Vegetation on Colorado East Slope, R&D Techn. Report CECOM-81-CS020-F, June 1981.

4 R. A. Johnson, N. Rokkos, Some Measurements on the Effects of Battlefield Obscurants on Millimeter Wave Radio Communication, R&D Techn. Report CECOM-TR-81-1, August 1981.

CONTROLLED RELEASE OF ANTIBIOTICS FROM BIODEGRADABLE MICROCAPSULES FOR WOUND INFECTION CONTROL

JEAN A. SETTERSTROM, Ph.D.,* U. S. ARMY INSTITUTE OF DENTAL RESEARCH,
WALTER REED ARMY MEDICAL CENTER, WASHINGTON, D. C. 20012
THOMAS R. TICE, Ph.D., DANNY H. LEWIS, Ph.D., and WILLIAM E. MEYERS, Ph.D.,
SOUTHERN RESEARCH INSTITUTE, BIRMINGHAM, ALABAMA 35255

INTRODUCTION

Improved methods to prevent and treat infection in contaminated wounds following traumatic injury are of military significance. Combat wounds are characterized by a high incidence of infection due to the inevitable presence of devitalized tissue and foreign body contaminants. Infection in these wounds is most effectively suppressed the first four hours after injury when an increased blood supply transports phagocytic cells and bactericidal factors to the injured area.(1) After four hours, vascular permeability decreases sharply and a fibrous coagulum forms at the base of the granulating wound which blocks antibiotics in the serum from penetrating the area.(2) To control infection, systemic antibiotics must be administered early when circulation is optimal. If treatment is delayed, a milieu for bacterial growth is established and complications associated with established infections occur.(3) Once infections are established, it becomes difficult to administer systemic antibiotics for an extended time, at levels that are safe, yet effective at the wound site. An ideal mode of antibiotic delivery to a contaminated wound would have the following characteristics: (1) local application in a single dose would be possible; (2) it would provide an initial burst of antibiotic for immediate tissue perfusion; and (3) it would provide a sustained and effective tissue level at the wound site. An antibiotic delivery system that fulfills these criteria is currently being developed and evaluated.

Unless topically active, drugs are distributed through the body in plasma, and the amount of drug that hits its target, is only a small part of the total drug in the body. This ineffective use of the drug is compounded in the trauma patient by hypovolemic shock, which produces a low perfusion rate of blood to tissues.(4) The ability to administer controlled quantities of a drug to a local area for a sustained time, via a biocompatible, biodegradable vehicle, provides an opportunity to evaluate a potentially advantageous method of antibiotic delivery to contaminated or infected tissue. Historically, the first success with topical antibiotics occurred at Pearl Harbor in 1941 when promptly debrided wounds, which were sprinkled with sulfanilamide, yielded low infection rates. Following inappropriate use, however, concretions of sulfa formed in the tissue causing infection rates to rise.(5) Such failures in the use of topical antibiotics are now believed to have occurred because improper drugs were used, or the method of administration failed to release drugs in an effective concentration. In recent years, topical antibiotics have been shown to be lifesaving in the prophylaxis and treatment of burn infections because the antibiotic can be applied repeatedly to the infected area, assuring a constant source of drug. The role of topical antibiotics in deep tissue wounds, however, has had less dramatic success. In contrast to burn therapy, an infected, deep tissue wound cannot be repeatedly treated with topical antibiotics unless the infected area is surgically re-exposed. The effect of single doses of antibiotics, in the form of powders, sprays, or lavages, are short-term because they are rapidly removed from the site and excreted. Nevertheless, studies have shown repeatedly that when risk of infection is high, topical antibiotics applied in this way do have an effect in reducing infection rates.(6-9) Until the recent development of sustained release systems, the opportunity to locally release drugs in tissues for sustained periods was not possible. Consequently, the theoretical advantages of such a system could not be evaluated.

The ability to control the release of an antibiotic at the wound site assures direct contact between effective antibiotic levels and the infecting microorganisms for a sustained period of time. Many drugs have a therapeutic range, above which they are toxic and below which they are ineffective. Oscillating drug levels that are commonly observed following systemic administration may cause alternating periods of ineffectiveness and toxicity. A sustained-release preparation can maintain the drug in the desired therapeutic range by means of a single dose. The presence of nonviable tissue, decreased blood flow subsequent to shock, and nonspecific drug binding to body proteins while en route to targeted sites, all decrease the amount of a drug that will reach a wound when the antibiotic is administered systemically. The local delivery of sustained, therapeutic amounts of antibiotic theoretically minimizes these problems. Furthermore, it would be unnecessary to administer multiple doses of potentially toxic antibiotics. Drugs with short half-lives might be used more efficiently and undesirable side effects would be minimized.

It is the goal of this study to develop microcapsules that slowly release effective therapeutic doses of antibiotics in a wound over a 14-day period, by which time the microcapsules will have been biodegraded. It is the purpose of this paper to report the *in vivo* results obtained using recently formulated prototype microcapsules.

All initial efforts in the development of the controlled antibiotic release system have used ampicillin with lactide/glycolide copolymer as the drug vehicle. This copolymer is ideally suited for *in vivo* drug release since it elicits a minimal inflammatory response, is biologically compatible, and degrades under physiologic conditions.(10) The degradation products are nontoxic and readily metabolized. All microcapsules currently formulated exist as free-flowing microspheres (<250 microns in diameter) consisting of ampicillin anhydrate coated with a poly (DL-lactide-co-glycolide) excipient having a lactide:glycolide ratio of 68:32. Microcapsules of this size can be administered directly to a wound by a shaker-type dispenser or aerosol spray. The rate of biodegradation is controllable because it is related to the molar ratios of the constituent polymers and to the surface area of the microcapsules.

MATERIALS AND METHODS

Microencapsulation Process

Both solvent evaporation and phase separation methods were used in formulating the microcapsules.(11) The microencapsulation process will be described in detail in a subsequent publication, therefore, only a brief description of the process follows. In the solvent evaporation process, ampicillin anhydrate (Bristol Laboratories) was suspended in a polymer solution prepared by dissolving poly (DL-lactide-co-glycolide) in an acetone and methylene chloride solvent. This mixture was then added to a stirred aqueous solution of poly (vinyl alcohol) to form a stable oil-in-water emulsion. The oil microdroplets which formed contain drug, polymer, and polymer solvent. Removal of the polymer solvent by evaporation resulted in solid microcapsules. The poly (DL-lactide-co-glycolide) was synthesized from DL-lactide and glycolic acid. In the phase separation method the antibiotic was suspended in a dilute polymer solution. A non-solvent for both polymer and drug was added to precipitate the polymer onto suspended drug particles in order to produce the microcapsules.

Analytical Procedures Used to Characterize the Microcapsules

Before *in vivo* testing of the microcapsules, the antibiotic content (core load) and *in vitro* release kinetics were evaluated. The core loads were determined by dissolving milligram quantities of microcapsules in methylene chloride and extracting the antibiotic with four volumes of water. The drug dissolved in the water was assayed by direct spectrophotometry, ninhydrin-based colorimetry, or microbiologic techniques. The study of the *in vitro* release rate of the antibiotic was performed by placing known amounts of microcapsules in flasks containing deionized water and agitating at 37°C. Aliquots periodically removed from the receiving fluid were assayed for drug content. A reagent prepared as a ninhydrin-hydrinatin solution was used in a colorimetric assay to evaluate the antibiotic content of the receiving fluid. Reactions of this reagent with antibiotic solutions of various concentrations developed a color proportional in intensity to the antibiotic content.

Using both microencapsulation processes, ^{14}C-labeled ampicillin anhydrate microcapsules were synthesized.(12) These radiolabeled microcapsules provided an accurate method for determining ampicillin core loadings and *in vitro* release profiles.

In Vivo Evaluation of Microcapsules

Ampicillin microcapsules formulated by both the solvent evaporation and phase separation processes were evaluated *in vivo* to determine the effect of the locally released drug on artificially induced wound infections. Experiments were performed on male Walter Reed strain albino rats, weighing 250-300 grams, that were anesthetized with sodium pentobarbital. The right hind leg was razor-shaved, scrubbed with Betadine, and swabbed with 70% isopropyl alcohol. A wound 2.5 to 3.0 cm in length and 5.0 mm deep was made in the thigh muscle, after which, 0.2 g of sterile dirt was added. The muscles were traumatized by pinching uniformly with tissue forceps, and inoculated with known quantities of *Staphylococcus aureus* ATCC 6538P and *Streptococcus pyogenes* ATCC 19615. The artificially contaminated wounds were treated by layering sterile, preweighed amounts of microencapsulated antibiotic directly on the wound and suturing the skin closed. Groups of animals with treated wounds (ampicillin-loaded microcapsules), untreated wounds, wounds packed with unloaded microcapsules, and wounds packed with unencapsulated antibiotic were evaluated at daily intervals.

After the effectiveness of microcapsules A681-31-1 was established, a dose-response experiment was performed wherein doses of microcapsules ranging from 0.5 to 0.05 g were applied to wounds. Sixty-eight rats were divided into five groups (A through E); four groups of 15 rats and one group of 8 rats. All rats were infected on the same day with the same quantitated bacterial suspension to assure uniform inoculum in all wounds. Wounds in the group of 8 rats (Group A) were treated with 0.5 g of ampicillin microcapsules. Rats in Groups B, C, and D were treated with 0.25, 0.10, and 0.05 g, respectively. Rats in Group E remained untreated. Bacterial counts were performed on homogenized, preweighed tissue that was removed aseptically from the wound sites. Tissue from varying distances around the wound site and serum removed by cardiac puncture were assayed for antibiotic content. This was performed by placing disks saturated with known quantities of serum or tissue homogenates on the surface of Muller-Hinton agar previously seeded with standardized amounts of *Sarcina lutea* ATCC 9341. Following incubation at 37°C, inhibition zones were measured. Freshly diluted stock solutions containing known quantities of ampicillin anhydrate served as standards. Diameters of the inhibition zones were converted to antibiotic concentrations using standard curves generated by plotting the logarithm of the drug concentration against the zone diameters.

RESULTS AND DISCUSSION

The ampicillin microcapsules evaluated *in vivo* are listed in Table 1. The doses applied to each wound and the ampicillin core loadings (wt%) for each batch of microcapsules evaluated are shown in Table 2. With time, all microcapsules tested effectively reduced bacterial counts in contaminated wounds. However, microcapsules produced by the phase separation process were optimally effective in eliminating infection. An infection was considered eliminated when the wound site was bacteria free at 14 days. When 0.5 g of microcapsules (A382-140-1) were applied to wounds infected with *Staphylococcus aureus* and *Streptococcus pyogenes*, 60% of the wounds were sterile by 14 days. The remaining wounds were infected with *Staphylococcus aureus* only, since *Streptococcus pyogenes* was eliminated from all wounds by 48 hours. Wounds treated with an amount of powdered ampicillin equivalent to the core load amount, but not encapsulated within the DL-PLGA microcapsules, remained infected. Although 40% of the wounds remained contaminated at 14 days, the bacterial counts for these wounds were significantly lower than those observed for wounds treated with topical ampicillin powder or unloaded microcapsules (Table 3).

Results of the dose-response experiment performed to determine the smallest effective dose for microcapsules A681-31-1 are shown in Table 4. The bacterial counts listed in this table are for *Staphylococcus aureus* only, since all doses of microcapsules (A681-31-1) also eliminated *Streptococcus pyogenes* by 48 hours. At 7 days the wounds treated with encapsulated ampicillin remained infected with *Staphylococcus aureus*. By 14 days all wounds treated with encapsulated ampicillin were sterile; whereas, all untreated wounds remained infected. Doses of encapsulated ampicillin as small as 0.05 g per wound successfully eliminated *Staphlococcus aureus*. Based on the ampicillin core load, this quanity of microcapsule (0.05 g) contained approximately 9.05 mg (9050 μg) of ampicillin. If released uniformly over 14 days approximately 646 μg of ampicillin would be released into the wound. Kinetic studies of ampicillin released from C^{14} labeled ampicillin anhydrate microcapsules formulated by the phase separation process showed that only 60% of the total reservoir of ampicillin was released by 14 days. Considering this, approximately 387 μg of ampicillin was available for release per day. The amounts of ampicillin detected in muscle tissue removed from wounds treated with 0.05 g of microcapsule were 54, 60, and 21 μg/g of tissue at 2, 7, and 14 days respectively. This amount is theoretically more than adequate to effectively control the growth of *Staphylococcus aureus* since the minimal inhibitory concentration sufficient to kill 95% of all strains *in vitro* is 0.5 μg/ml. An *in vitro* ampicillin level as low as 0.05 μg/ml, or 10 times less, will inhibit 97% of all strains of *Streptococcus pyogenes*.

Microcapsules produced by the solvent evaporation process had low ampicillin core loadings (3.0-4.5 wt%). Kinetic studies showing the *in vitro* release of ampicillin from these microcapsules indicated that only 40% of the ampicillin was released by 14 days.(13) Nevertheless, these microcapsules eliminated infections and decreased bacterial counts when applied to infected wounds. However, even though large doses were applied (1.0-0.7 g microcapsule/wound) ampicillin was not detected in serum. Rats treated with high core loaded microcapsules produced by phase separation (A681-31-1) at a dose of 0.25 g/wound, had serum ampicillin levels present the first 4 days after treatment (Figure 2). Those treated with 0.5 g per wound had serum ampicillin levels 7 days post-treatment. No serum ampicillin was detected in rats treated with 0.10 g of microcapsule per wound or less.

The microcapsules currently evaluated have been formulated with 68:32 poly(DL-lactide-co-glycolide). The bioresorption time for unsterilized microparticles of that polymer is approximately 3-4 months *in vivo*. These microcapsules deliver drug at an efficacious rate over a target period of 2 weeks; however, they also release drug at a very slow rate for over 30 days following this initial 2 week period. Once infections in wounds are eliminated, the antibiotic and microcapsules are no longer wanted in the tissue. Therefore, new microcapsules consisting of 50:50 poly(DL-lactide-co-glycolide are being formulated. It is expected that these microcapsules will begin to biodegrade immediately following administration, and be completely degraded by 30 days. The more rapid biodegradation should reduce or eliminate the slow release of ampicillin that is occurring past 14 days.

In conducting the research described in this report, the investigators adhered to the "Guide for the Care and Use of Laboratory Animals" as promulgated by the Committee on the Guide for Laboratory Animal Facilities and Care, of the Institute of Laboratory Animal Resources, National Academy of Sciences, National Research Council.

Commercial materials and equipment are identified in this report to specify the investigative procedures. Such identification does not imply recommendation or endorsement or that the materials and equipment are necessarily the best available for the purpose. Furthermore, the opinions expressed herein are those of the author and are not to be construed as those of the U. S. Army Medical Department.

ACKNOWLEDGMENTS

The authors are grateful to Maria A. Derevjanik and Jerry S. G. Harrington for their excellent technical assistance.

TABLE 1. *IN VIVO* AMPICILLIN MICROCAPSULES EVALUATED

CAPSULE NUMBER	MICROENCAPSULATION PROCESS	MICROCAPSULE SIZE, μ
9306-142-1	Solvent Evaporation	<250
A026-62-1	Solvent Evaporation	63-250
A382-140-1	Phase Separation	45-106
A681-31-1	Phase Separation	45-106

TABLE 2. AMPICILLIN CONTENT AND DOSE OF MICROCAPSULES APPLIED TO WOUNDS

IN VIVO EXPERIMENT	CAPSULE NUMBER	MICROCAPSULE DOSE/WOUND (AMPICILLIN EQUIVALENT)	ANTIBIOTIC CORE LOAD (WT%)
(EFFICACY)	9306-142-1	1.0 g (30.9 mg)	3
(EFFICACY)	A026-62-1	0.7 g (32.9 mg)	4.5
(EFFICACY)	A382-140-1	0.5 g (113 mg)	18.5
(DOSE-RESPONSE)	A681-31-1	0.50 g (110 mg) 0.25 g (45.25 mg) 0.10 g (18.10 mg) 0.05 g (9.05 mg)	18.1

TABLE 3. *STAPHYLOCOCCUS AUREUS* PRESENT IN WOUNDS FOLLOWING TREATMENT WITH MICROCAPSULES A382-140-1, UNLOADED MICROCAPSULES, OR UNENCAPSULATED AMPICILLIN

DAYS POST TREATMENT	MICROCAPSULES	UNLOADED MICROCAPSULES	UNENCAPSULATED AMPICILLIN
	(AVERAGE NUMBER* OF ORGANISMS PER GRAM OF TISSUE†)		
2	$6.3 \pm 2.6 \times 10^6$	$1.3 \pm 1.5 \times 10^7$	$4.2 \pm 2.4 \times 10^6$
6	$4.7 \pm 2.2 \times 10^5$	$1.0 \pm 5.5 \times 10^6$	$5.3 \pm 7.0 \times 10^6$
8	$7.3 \pm 3.3 \times 10^4$	$4.5 \pm 9.7 \times 10^8$	$5.4 \pm 7.5 \times 10^6$
14	$9.4 \pm 0.6 \times 10^3$ §	$4.7 \pm 9.8 \times 10^5$ ×	$1.8 \pm 3.2 \times 10^6$

* Mean $\pm$ Standard Deviation, n=5

† 6.0×10^9 *Staphylococcus aureus* inoculated/wound

§ 3 of 5 wounds sterile

× Lowered due to competitive inhibition by superinfecting gram negative rods

When a regression curve was drawn using the data shown (log concentration of bacteria vs time) the linear component approached significance. This component represented the steady decrease in bacteria/gram of tissue observed in rats treated with microcapsules A382-140-1. When one outlier was removed from each group, significance ($p<0.05$) was observed.

TABLE 4. AVERAGE NUMBER OF *STAPHYLOCOCCUS AUREUS*/GRAM OF TISSUE PRESENT IN WOUNDS TREATED WITH DECREASING AMOUNTS OF MICROENCAPSULATED AMPICILLIN (A681-31-1)

GROUP	MICROCAPSULE DOSE (g)/WOUND	TOTAL AMPICILLIN AVAILABLE (mg)	Bacteria Per Gram of Tissue (mean ± S.D.,* n=5) 48 HOURS	7 DAYS	14 DAYS
A	0.5	90.50	$3.7 \pm 1.4 \times 10^{6}$	$7.7 \pm 10.0 \times 10^{3}$	0
B	0.25	45.25	$5.9 \pm 10.0 \times 10^{3}$	$8.2 \pm 14.0 \times 10^{3}$	0
C	0.10	18.10	$2.1 \pm 3.0 \times 10^{6}$	$1.8 \pm 3.4 \times 10^{4}$	0
D	0.05	9.05	$6.8 \pm 4.7 \times 10^{5}$	$4.4 \pm 3.8 \times 10^{4}$	0
E	0.00	0.00	$1.8 \pm 1.8 \times 10^{6}$	$3.5 \pm 4.3 \times 10^{6}$	$6.4 \pm 9.6 \times 10^{5}$

*Standard Deviation

1.5×10^{10} *S. aureus* inoculated/wound

Figure 1. Ampicillin Concentrations Detected in Homogenized Muscle Tissue (Deep) at 2, 7, and 14 Days Following Wound Site Treatment with Microencapsulated Ampicillin (A 681-31-1)

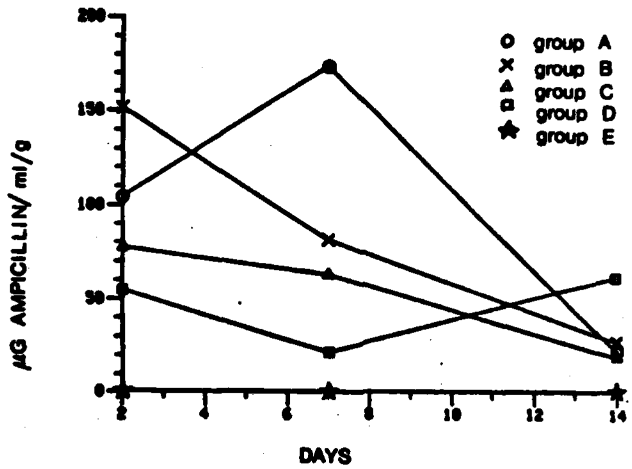

Figure 2. Ampicillin Concentrations Detected in Serum at 2, 4, 7, and 14 Days Following the Application of Microencapsulated Ampicillin (Batch A 681-31-1) to Infected Wounds

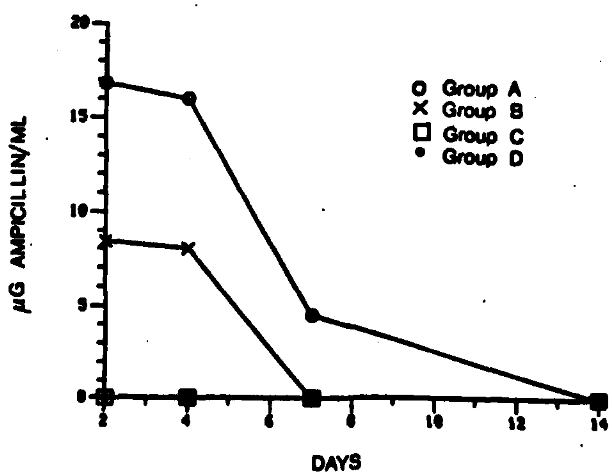

REFERENCES

1. Burke, J. F.: "Infection" IN: *Fundamentals of Wound Management.* T. K. Hunt and J. E. Dunphy (Ed.), Appleton-Century-Crofts, New York, N.Y., 1979.

2. Burke, J. F.: *Surgery* 50:161, 1961.

3. Rodeheaver, C., M. T. Edgerton, M. B. Elliott, L. D. Kurtz, and R. F. Edlich. *Am J Surg* 127:564, 1974.

4. Gelin, L. E. and J. R. Border. *J Trauma* 10:1078, 1970.

5. Heisterkamp, C., J. Vernick, R. L. Simmons, and T. Motsumoto: *Mil Med* 134:13, 1969.

6. Ryan, E. A.: *Brit J Surg* 54:324, 1967.

7. Glotzer, D. J.: *Arch Surg* 100:589, 1970.

8. Waterman, N.G., R. S. Howell, and M. Babich: *Arch Surg* 97:365, 1968.

9. DiGiglia, J.W., G. L. Leonard, and J. L. Ochsner. *Surgery* 67:836, 1970.

10. Cutright, D. E., B. Perez, J. Beasley III, W. E. Larson, and W. R. Posey: *Oral Surg* 37:142, 1974.

11. Tice, T. R., W. E. Meyers, D. H. Lewis, D. R. Cowser, and J. A. Setterstrom: 8th International Symposium on Controlled Release of Bioactive Materials, Abstracts, 1981.

12. Valcavi, V.: *J Labeled Comp* 8:687, 1972.

13. Lewis, D.H., W. E. Meyers, T. R. Tice, and T. O. Dappert: Annual Progress Report, 1981. (Unpublished)

ELECTRICAL PROPERTIES OF HEATED DIELECTRICS (U)

*EDWARD J. SHARP, DR.
LYNN E. GARN, DR.
NIGHT VISION AND ELECTRO-OPTICS LABORATORY
FORT BELVOIR, VIRGINIA 22060

INTRODUCTION

For the past decade there has been a great deal of work devoted to understanding the pyroelectric and piezoelectric mechanisms in several of the high polymers, most notably in the material poly(vinylidene fluoride), PVF_2. At the present time PVF_2 has the highest piezo-pyroelectric response among polymeric materials. Since the early work on the pyroelectric properties of PVF_2 by Nakamura and Wada (1) and Bergman et al (2), considerable effort has been expended in attempts to improve the pyroelectric response of this polymer for numerous practical applications including reflectivity measurements (3), a photocopy process (4), infrared radiation detection (5),(6), thermal imaging with a pyroelectric vidicon (7),(8), intrusion and fire detection (9), and non-linear optical devices (2). In spite of this intense activity the nature of the mechanism (or mechanisms) of pyroelectricity in PVF_2 is not fully understood (10),(11). To a large extent much of the confusion surrounding the understanding of the electrical behavior of this important material is due to ambiguous results associated with the interpretation of different measurement techniques used to explore its properties.

Several techniques have been used in the past to accurately determine the pyroelectric properties of dielectric materials (4),(12),(13),(14). Some of these techniques have been reviewed recently regarding their usefulness in the characterization of pyroelectric materials intended for use as infrared radiation detectors or as targets in a pyroelectric vidicon (PEV) (8). As radiation detectors, pyroelectric materials must exhibit a current response that is completely reversible and reproducible when subjected to small temperature changes.

There are numerous materials which exhibit a large non-pyroelectric current response (non-reversible) when they are heated (15). There are also many materials which are capable of exhibiting both non-pyroelectric and pyroelectric responses simultaneously when they are heated. Since only the reversible pyroelectric current contributes to infrared response, it is obvious that any technique used to evaluate such materials for use as infrared radiation detectors must provide the capability for distinguishing the current contributions associated with pyroelectric behavior and those associated with non-pyroelectric behavior and to permit the determination of their individual magnitudes.

Typically PVF_2 film is only weakly pyroelectric in the as received condition. When PVF_2 is subjected to an applied electric field (poling), significant pyroelectric response can be generated in the film and this response may be further enhanced or degraded by additional or simultaneous thermal and mechanical treatments (stretching). A recent review article on PVF_2 by Das-Gupta (16) discusses these poling techniques and their subsequent effects on the structure, pyroelectric behavior, and the possible models to explain this behavior.

It has been reported (8),(17) that the first thermal cycle of a poled PVF_2 sample will yield a predominantly non-pyroelectric current (thermally stimulated current or conductivity, TSC) (15) as a function of temperature and that the second and subsequent thermal cycles yield a reversible pyroelectric current (4). The shape of the first thermal cycle current curve depends upon the poling procedure (18). Here we describe a new method which allows the analysis and evaluation of electric currents such as pyroelectric currents and thermally stimulated currents arising from heated dielectric materials. This method can be applied to materials that exhibit only pyroelectric currents, materials that exhibit only non-pyroelectric currents, or materials that exhibit a combination of the two types of currents. Pyroelectric current is directly proportional to the derivative of temperature with respect to time. Non-pyroelectric current, in general, is either constant or within small temperature intervals nearly proportional to the temperature. These assumptions have been verified (19),(20) mathematically in certain temperature and frequency ranges and experimentally for a number of different dielectric materials, several of which will be discussed here. Poly(vinylidene fluoride) has been selected as one of the materials since it is an important material from an applications point of view. It also lends itself well to demonstrating the strength and validity of the following treatment and measurements.

THEORY

For the present we assume that non-pyroelectric currents can be represented by

$$i_\ell = i_o + RT \,, \tag{1}$$

where i_o is a constant, non-pyroelectric, temperature independent current. The term RT is also non-pyroelectric, but it increases linearily with temperature T; R, being a temperature coefficient. It has been shown previously (20) that within small temperature intervals TSC can be approximated by this form. Equation [1] is used because it is general and applies to any non-pyroelectric current that may be present.

The pyroelectric current can be written as (12),(14)

$$i_\pi = pA\frac{dT}{dt} \quad , \qquad [2]$$

where p is the pyroelectric coefficient A, the sample area and dT/dt the time derivative of the temperature.

In a material where both currents are present the total current can be written as

$$i_T = i_o + RT + pA\frac{dT}{dt} \; . \qquad [3]$$

In typical measurements of TSC and pyroelectric current, the sample temperature is $T_o + bt$, where T_o denotes the initial absolute temperature of the sample and bt is the temperature change introduced when the sample is heated at a constant rate b for a time t (14),(21),(22). If, in addition to this normal method of heating, a small sinusoidal temperature component of amplitude T_1 and angular frequency ω is imposed on the sample, the temperature becomes

$$T = T_o + bt + T_1 \sin(\omega t) \; . \qquad [4]$$

The total current from the sample under these heating conditions can now be written as a sum of an ac-current and a dc-current as

$$i_T = [i_o + R(T_o + bt) + pAb] + [RT_1 \sin(\omega t) + pAT_1 \omega \cos(\omega t)]. \; [5]$$

For sufficiently large frequencies the term Rbt is nearly constant during the period of a heat wave and is therefore included in the dc-current term. It is important to note that the term $RT_1 \sin(\omega t)$, which is in phase with the sinusoidal component of temperature, comes from the non-pyroelectric part of Eq. [3]. On the other hand, the term $PAT_1 \omega \cos(\omega t)$ comes from the pyroelectric component of Eq. [3] and the resulting current precedes the sinusoidal temperature wave by 90°. Thus ac-components of non-pyroelectric currents are in phase with the temperature, whereas ac-components of pyroelectric currents precede the temperature by 90°. The ac portion of the current given by Eq. [5] can be written as

$$i_{ac} = i_1 \sin(\omega t + \theta) \; , \qquad [6]$$

where

$$i_1 = (i_n{}^2 + i_p{}^2)^{1/2} , \qquad [7]$$

$$i_n = RT_1 , \qquad [8]$$

$$i_p = pAT_1\omega , \qquad [9]$$

$$\theta = \tan^{-1}(i_p/i_n) = \tan^{-1}(pA\omega/R) . \qquad [10]$$

The amplitudes of the non-pyroelectric and pyroelectric currents are given by i_n and i_p respectively. The amplitude of the ac-current i_1 therefore depends upon the amplitude of both the pyroelectric current and the non-pyroelectric current. An examination of the amplitude of the ac-component i_1 is not sufficient to determine if the current is pyroelectric or non-pyroelectric. The phase difference θ between the temperature and current waves must be determined to establish which type of current is present. For example, in a purely pyroelectric material i_n will be zero and $\theta = 90^o$, and for a material with no pyroelectric response i_p will be zero and $\theta = 0^o$. When a material exhibits both types of currents the extrema of the ac-current precede the extrema of the temperature by a phase angle somewhere between 0^o and 90^o. Thus if we measure the phase of the ac-current with respect to the temperature wave, we can determine if the current is pyroelectric or non-pyroelectric and we can use Eq. [7] and [10] to compute the fraction of current associated with each effect. These components are:

$$i_p = i_1 \sin(\theta) , \qquad [11]$$

$$i_n = i_1 \cos(\theta) . \qquad [12]$$

It has been shown that the TSC arising from numerous relaxation processes has the following time and temperature dependence (15),(21),(22).

$$i_b = C \exp\left[\frac{-E}{kT} - B \int_0^t \exp\left(\frac{-E}{kT}\right) dt\right] . \qquad [13]$$

where the constants C and B depend on the origin of the TSC. This relation assumes a single relaxation time of the form $\tau = \tau_o \exp[E/kT]$ where τ_o is a constant, E is an activation energy, and k is Boltzmann's

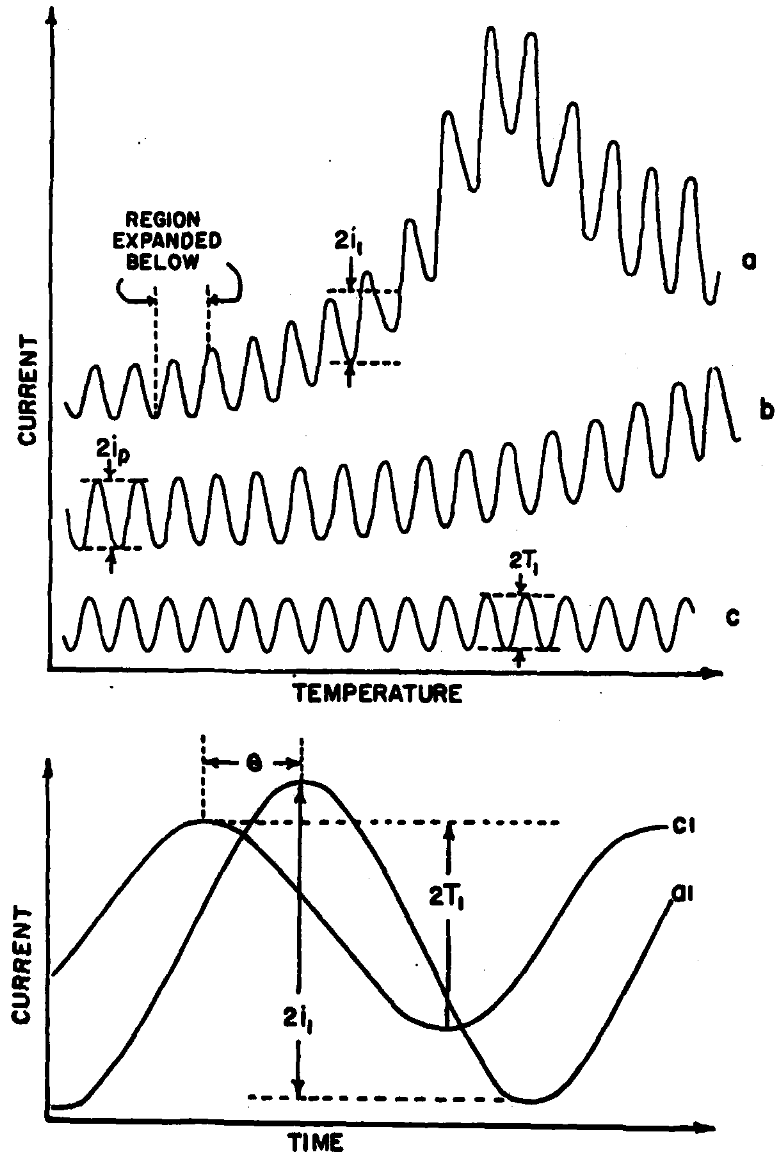

Figure 1. Sketch of actual data for a pyroelectric material such as PVF_2. A small section of the current versus temperature data is expanded in the lower set of curves to illustrate the observed phase shift, θ. Curve (a) represents the current arising from a first thermal cycle, curve (b) is the current arising from subsequent theral cycles, and curve (c) is the ac-temperature wave.

constant. This assumption is consistent with our observations of TSC curves of PVF_2 samples rested equal lengths of time (18). There is some temperature T_m at which maximum TSC occurs for a sample heated at a constant rate b, ($T = T_o+bt$) determined by maximizing Eq. [13] with respect to t. The value of T_m depends strongly upon the rest time after poling and in general the TSC decreases sharply for $T > T_m$ (18).

It has been previously shown (20) that within small temperature intervals the TSC given by Eq. [13] is a linear function of temperature for a constant heating rate of the form $T = T_o+bt$. For temperatures of the form given by Eq. [4] i_b is non-pyroelectric and can be represented by Eq. [1]. Where the period of the sinusoidal temperature wave and the heating rate can be chosen such that i_o and R change very little during several periods of the heat wave (20). The value of R is then expressed as:

$$R = \frac{i_b E}{k(T_o + bt)^2} \quad . \qquad [14]$$

It is useful to examine the influence of the temperature dependence of R on the magnitude and phase of the ac-current. We can rewrite the expression for the amplitude of the ac-component i_1 in terms of the pyroelectric and non-pyroelectric current amplitudes given by Eqs. [8] and [9].

$$i_1 = \left[\left(\frac{i_b E T_1}{k(T_o + bt)^2}\right)^2 + (pA\omega T_1)^2\right]^{1/2} , \qquad [15]$$

where R has been written in the form given by Eq. [14]. Since i_b has the characteristic TSC dependence on temperature, the non-pyroelectric amplitude and therefore the ac-component i_1 will increase as i_b increases to its maximum at T_m. As the temperature is increased beyond T_m, i_b decreases to zero and the first term in Eq. [15] vanishes and i_1 is then equal to the amplitude of the pyroelectric current. The change in i_b with temperature does not influence i_p but it does influence the phase angle. Since θ decreases as R increases, θ will reach a minimum when i_b is a maximum at the temperature T_m. The amplitude and phase of the ac-current, i_1, and θ, can be measured directly and compared with computed values.

To better understand this procedure, Fig. 1 is presented. It represents an actual display of data taken on a sample that exhibits both TSC and pyroelectric response such as a PVF_2 sample might have. This figure is used to identify the various parameters associated with the theory and to demonstrate how to extract the information necessary to apply the theory from a typical sample of recorded data.

When a sample is thermally cycled for the first time curves (a) and (c) are recorded concurrently. Curve (a) is the total current, pyroelectric and non-pyroelectric, released from the sample as it is heated under the conditions given by Eq. [4]. Curve (c) is a recording of only the sinusoidal portion of the applied temperature, $T_1 \sin(\omega t)$, which oscillates about (T_o+bt). For each subsequent thermal cycle the current, curve (b), and a new curve (c) are recorded so that phase measurements can be made. It is important to note that curve (a) as shown in Fig. 1 is representative of those obtained on PVF_2. In materials which exhibit only pyroelectric response curves (a) and (b) will be identical. At selected temperatures (T_o+bt, see Eq. [4]) throughout the thermal cycle, usually every 10°C, new curves (c1) and (a1) are recorded to graphically magnify the phase difference betweeen them.

The analysis of data is simplified by noting that A and k are constants, ω and T_1 are fixed by the temperature wave period, and the quantity (T_o+bt) is just the measurement temperature at some time t during the thermal cycle. The values of the three quantities remaining in the expression for the ac-current amplitude, i_b, E, and p along with the phase difference can be extracted from the data as follows: the pyroelectric coefficient, p, can be estimated using second run current dc-values (18). This, together with the values of A, T_1, and ω, provides a computed value for the amplitude of the ac-pyroelectric current component $pAT_1\omega$. If the dc-component of the curve (a) is measured and the dc-component of curve (b) is subtracted off (18), the resulting current i_b can be subjected to the usual (21), (22) TSC analysis and a determination of the activation energy can be made. The amplitude of the non-pyroelectric ac-current can be computed from Eq. [8]. The values i_n and i_p can now be used to compute i_1 and θ which may then be compared with the measured values.

EXPERIMENTAL RESULTS

We have examined two ferroelectric materials in the temperature range 0°C to 80°C: triglycine sulfate (TGS), $(NH_2CH_2COOH)_3 \cdot H_2SO_4$, and lithium tantalate, $LiTaO_3$. Samples of each material were prepared from 50 m thick wafers having circular nichrome electrodes deposited on both sides so that they formed capacitors with an area of 0.6cm^2. Fine wire leads were silver-epoxied to non-overlapping tabs extending from the circular electrodes and the samples were poled at room temperature with dc-electric fields of 10^3 - 10^4 V/cm for both materials.

TGS exhibits Curie behavior in this temperature range at ~ 49°C but $LiTaO_3$ does not since it is a high-temperature ferroelectric with a Curie temperature $T_c \approx 618$°C (23),(24). Figure 2 shows the measured ac- and dc-components of pyroelectric current for lithium tantalate as a function of temperature from 0°C to 80°C for 5, 10, 20, 50, 100, and

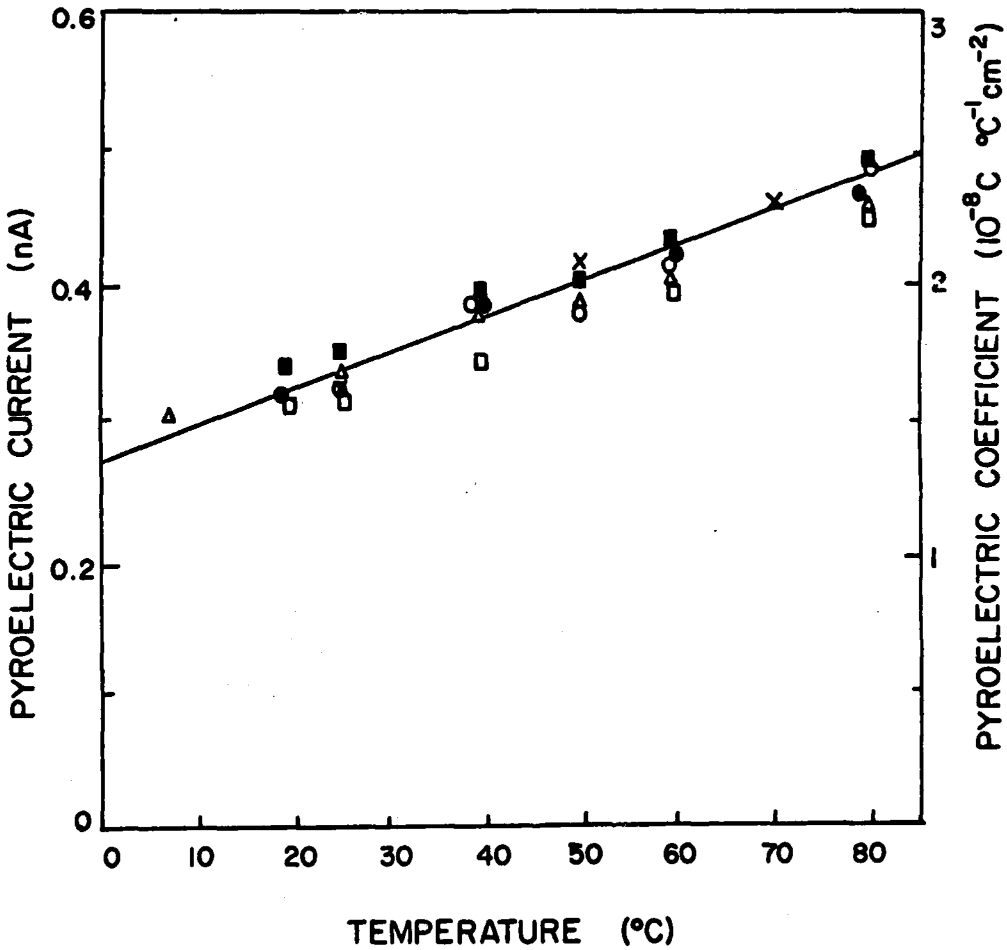

Figure 2. Pyroelectric current as a function of temperature for $LiTaO_3$. The values of the pyroelectric coefficients associated with these currents are also shown. Here the straight line is the measured dc-value of the pyroelectric current and the ac-values are for different temperature wave periods as: (5 sec-X), (10 sec-■), (20 sec-□), (50 sec-△), (100 sec-●), and (200 sec-○).

200 sec temperature wave periods. The value of the pyroelectric coefficient for $LiTaO_3$ at 25^oC is in agreement with the values reported by other workers (14),(24),(25), $1.76x10^{-8} C/cm^2$ to $1.9x10^{-8}$ C/cm^2 ^oC.

The pyroelectric coefficients for TGS obtained from the measured ac and dc-components of the current are compared in Fig. 3. The value of the pyroelectric coefficient, $p = 3x10^{-8}$ C/cm^2 ^oC obtained at 23^oC agrees well with the values reported by others, (25),(26), $2.8x10^{-8}$ C/cm^2 ^oC and $2\text{-}3.5x10^{-8}$ C/cm^2 ^oC. The markedly different pyroelectric response curves for TGS and $LiTaO_3$ shown in Figs. 2 and 3 stem from the fact that TGS exhibits Curie behavior in the measurement temperature range. Even though the measured pyroelectric response of TGS varies nearly two orders of magnitude and $LiTaO_3$ varies only slightly, there is good agreement between the ac and dc-current components for both materials.

The phase difference for these two materials is determined graphically as described earlier and these values are shown in Fig. 4 from 0^oC to 80^oC. The $\pi/2$ phase shifts at all temperatures indicate that i_1 has no non-pyroelectric ac-component and thereby confirms that the materials are purely pyroelectric.

Hundreds of PVF_2 samples were prepared from 6 m thick biaxially oriented film and electroded to form capacitors in the same manner as the ferroelectric materials. These samples were then poled at relatively high fields, $1.3x10^6$ V/cm, at room temperature. This procedure assured that the samples were well poled as described by Day et al (27).

The currents from these samples were recorded as a function of temperature from 0^oC to 80^oC at a 2^o/min heating rate in the presence of a small low-frequency sinusoidal temperature wave. Each specimen was measured several times and data similar to that depicted in Fig. 1 was obtained for each sample. Pyroelectric coefficients obtained at room temperature of $1x10^{-9}$ C/cm^2 C^o are in good agreement with those of a number of other workers for similarily poled samples (27),(28). Following the analysis procedure outlined earlier, the phase shifts for the first thermal cycles of identically poled and rested samples are shown in Fig. 5 for temperature wave periods of 5, 20, 50, and 100 seconds.

Note that in these curves the position of the maximum phase shift from $\pi/2$ corresponds to the maximum value of i_b (TSC current) as can be seen from Eqs. [10] and [14]. The position of T_m for well-poled samples prepared at room temperature depends on the rest time, t_r, through the phenomenological relationship $T_m = 309 + 6.5 \log(t_r)$ which has been extracted from the data of Ref. (18). For samples rested three days, $t_r = 72$ hours, T_m corresponds to $\sim 47^oC$ as indicated in the phase-shift data of Fig. 5. The absolute value of the phase angle is dependent upon the temperature-wave-period as seen from Eq. [10] and is also in evidence in Fig. 5.

Second and subsequent thermal cycles yield $\pi/2$ phase shifts for these same samples indicating reversible and reproducible pyroelectric behavior. Figure 6 shows a plot of the computed and measured phase

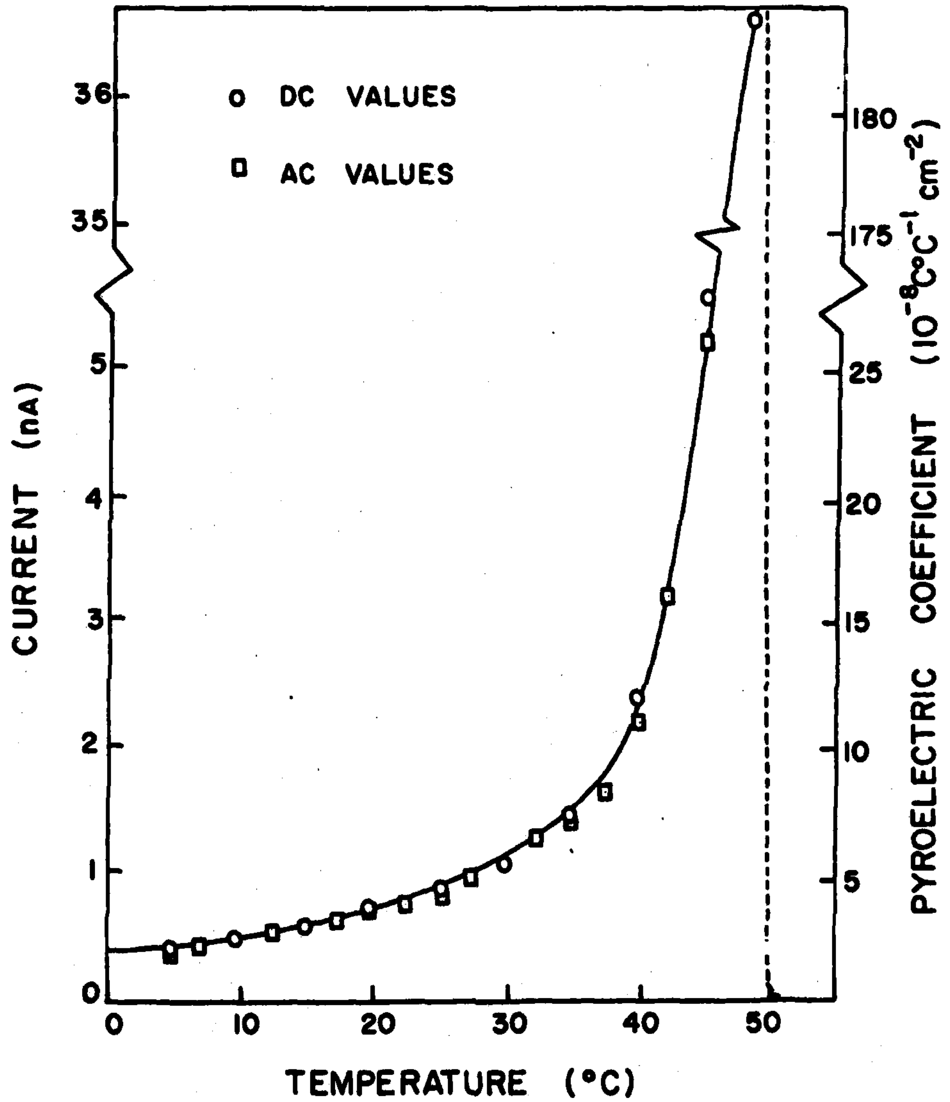

Figure 3. Measured ac and dc-pyroelectric current and corresponding pyroelectric coefficients for triglycine sulfate for a 20-second temperature wave period.

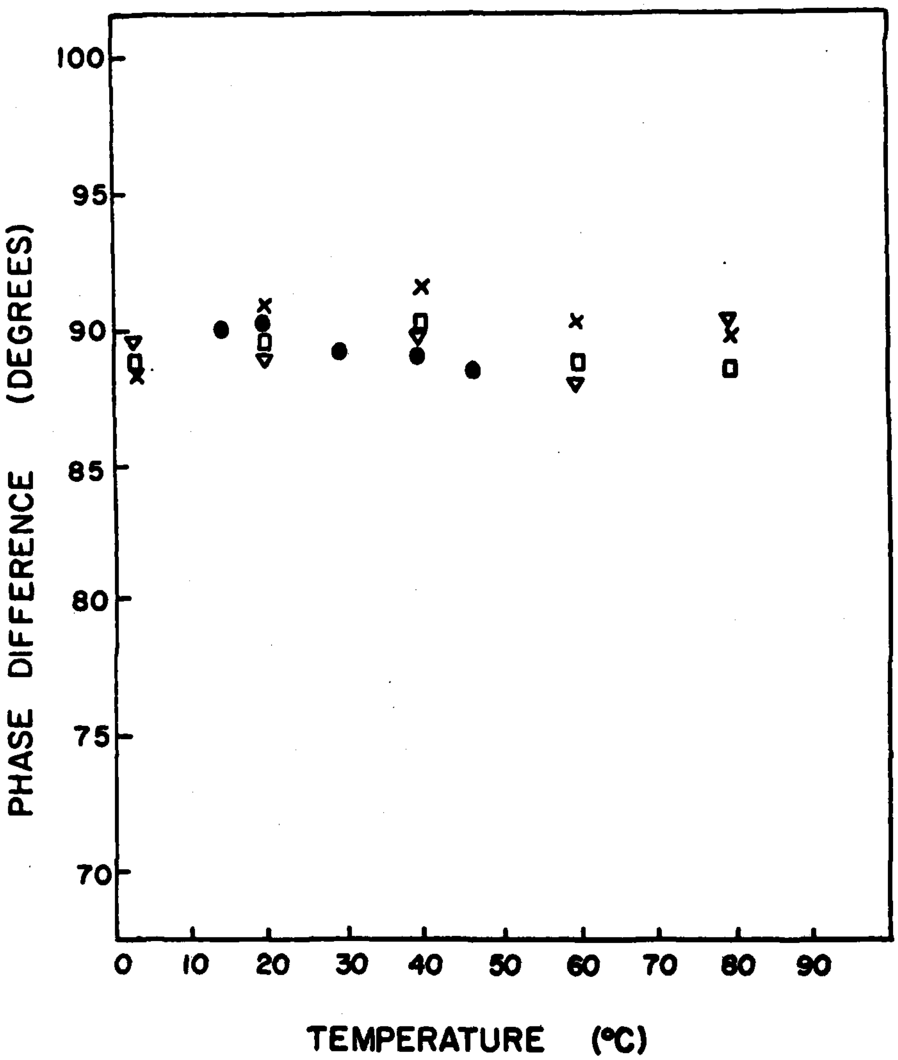

Figure 4. Phase difference between measured current and applied ac-temperature wave as a function of temperature for TGS (20 sec-●) and $LiTaO_3$ (5 sec-X), (50 sec-□), and (200 sec-Δ).

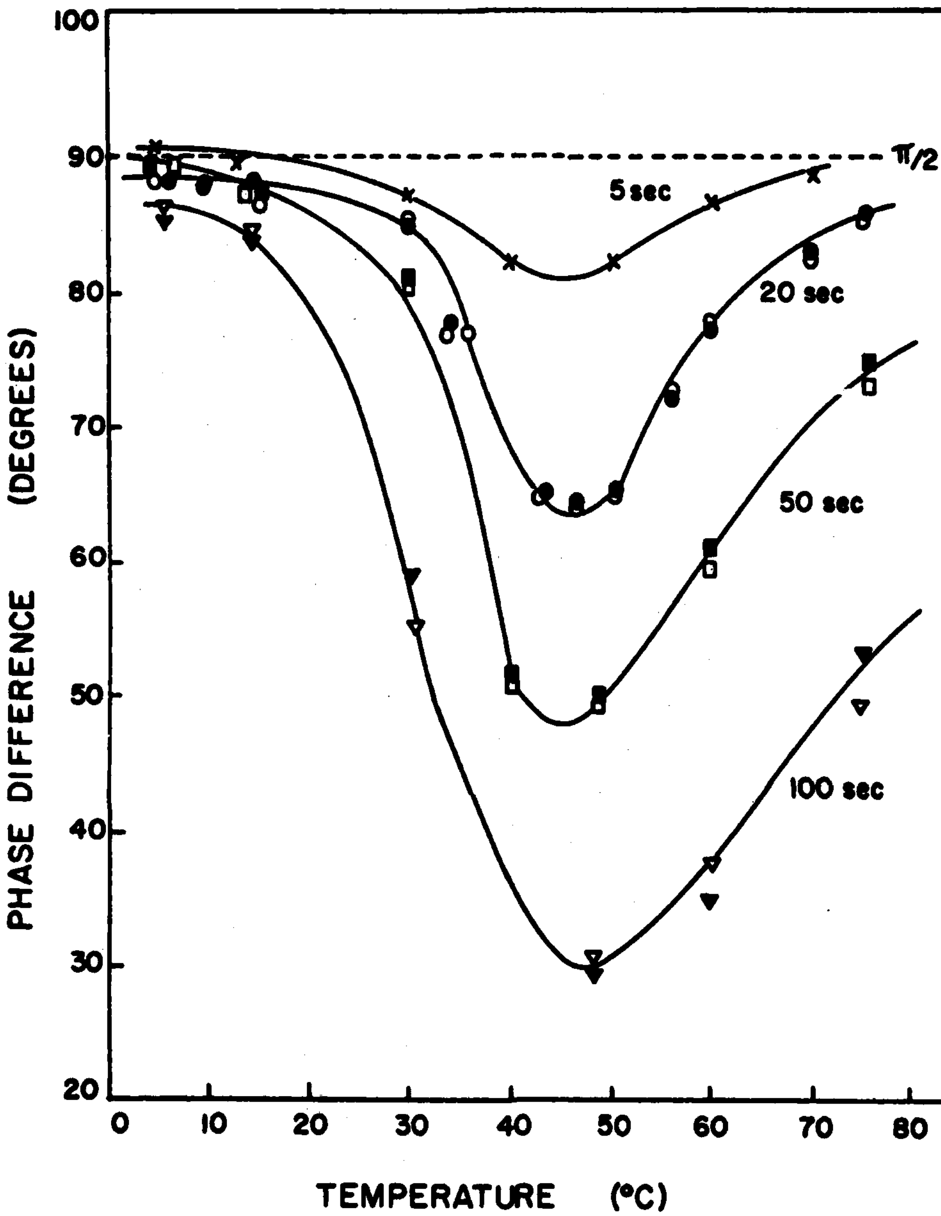

Figure 5. First thermal cycle phase difference between measured current and ac-temperature waves as a function of temperature for identically poled PVF_2 samples. Here solid points are computed from Eq. [10] and the open points are determined graphically from the data.

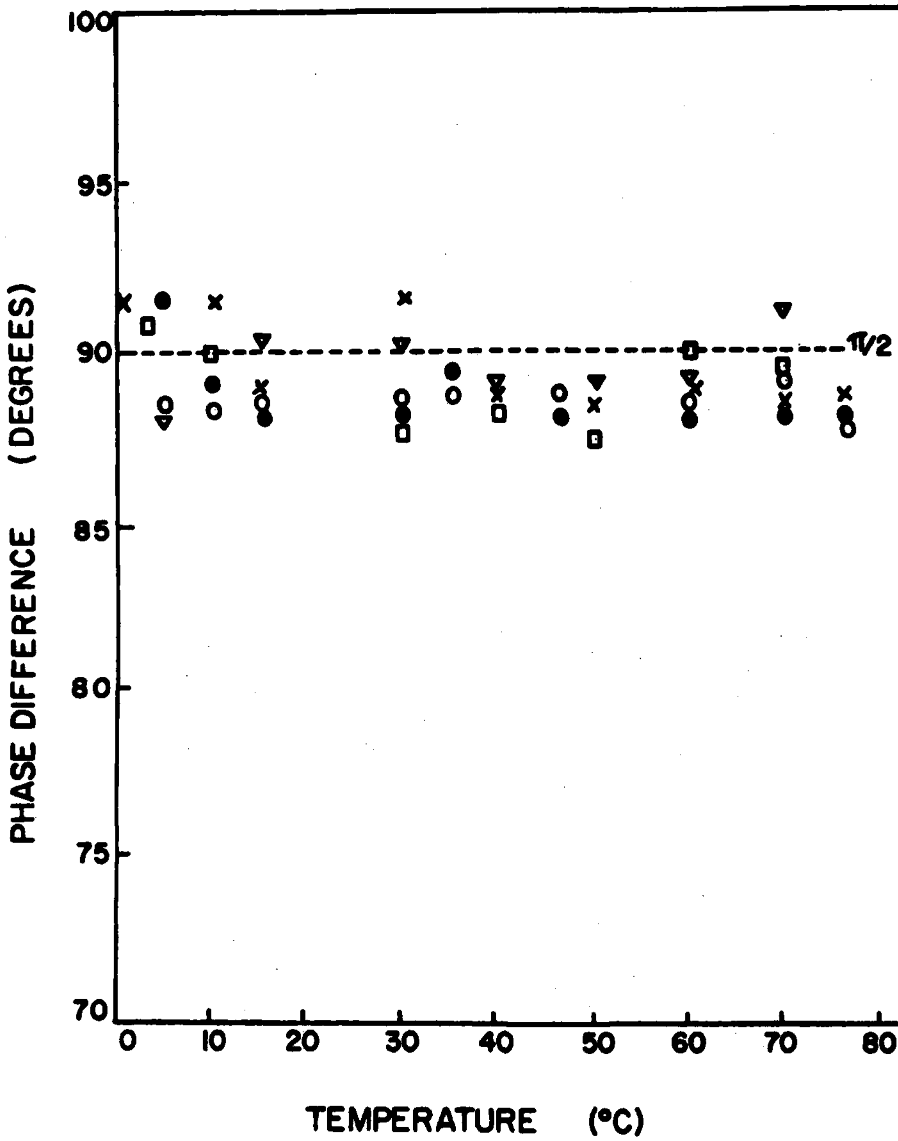

Figure 6. Computed (solid points) and measured (open points) phase differences of the second and third thermal cycles for identically poled PVF_2 samples. Here (20 sec-X), third run; (20 sec-0), (5 sec-Δ), and (50 sec-□), all second run; and (20 sec-●), computed second run.

shifts of the second and third thermal cycles for temperature wave periods of 5, 20, and 50 seconds.

CONCLUSIONS

A method has been described which allows one to analyze complicated currents emanating from warmed dielectrics. This technique is easily applied for temperature waves of certain amplitude and frequency limits and permits an accurate assessment of dielectric materials being examined for specific applications, such as infrared detectors or vidicon targets, where it is necessary to know the current magnitude and relaxation properties as a function of temperature and temperature changes.

The low-frequency temperature wave method is a direct dynamic measurement of the pyroelectric coefficient. This method eliminates the need for measurements of specific heats, dielectric constants, and radiation absorption coefficients as well as identifying the effects due to irreversible currents which occur when samples are heated at a constant rate.

REFERENCES

1. Nakamura, K. and Wada, Y., J. Polym. Sci. A29:161 (1971).
2. Bergman, J. G. Jr., McFee, J. H., and Crane, G. R., Appl. Phys. Letter , 18:203 (1971); McFee, J.H., Bergman, J. G. Jr., and Crane, G.R., Ferroelectrics, 3: 305 (1972).
3. Blevin, R. W. and Geist, J., Appl. Opt., 13:2212 (1974).
4. Bergman, J. G. Jr., Crane, G. R., Ballman, A. A., and O'Bryan, H. M. Jr., Appl. Phys. Letters, 21:497 (1972).
5. Glass, A. M., McFee, J. H., Bergman, J. G. Jr., J. Appl. Phys., 42:5219 (1971).
6. Peterson, R. L., Day, G. W., Gruzensky, P. M., and Phelan, R. J. Jr., J. Appl. Phys., 45:3296 (1974).
7. Stephens, A. W., Levine, A. W., Fech, J. Jr., Zrebiec, T. J., Cafiero, A. V., and Garofalo, A. M., Thin Solid Films, 20:361 (1974).
8. Garn, L. E., and Sharp, E. J., IEEE Trans. Parts, Hybrids, Packag., PHP-10:208 (1974).
9. Stern, J. and Edleman, S., Tech. News Bull. NBS, 56:52 (1972).
10. Wada, Y., and Hayakawa, R., Japan J. Appl. Phys., 15:2041 (1976).
11. Das-Gupta, D. K., and Duffy, J. S., J. Appl. Phys., 50:561 (1979).
12. Chynoweth, A. G., J. Appl. Phys., 27:78 (1956).
13. Glass, A. M., J. Appl. Phys., 40:4699 (1969).
14. Byer, R. L., and Roundy, C. B., IEEE Trans. Sonics Ultrason., SU-19:333 (1972).

15. Creswell, R. A., Perlman, M. M., and Kabayama, M. A., in Dielectric Properties of Polymers, edited by Karasz, F. E., (Plenum, New York, 1972), p. 295ff.
16. Das-Gupta, D. K., Ferroelectrics, 33:75 (1981).
17. Burkhard, H., and Pfister, G., J. Appl. Phys., 45:3360 (1974).
18. Sharp, E. J., and Garn, L. E., Appl. Phys. Letters, 29:480 (1976).
19. Garn, L. E., Dissertation, American Univ., (1977).
20. Garn, L. E., and Sharp, E. J., (submitted to J. Appl. Phys.).
21. Creswell, R. A., and Perlman, M. M., J. Appl. Phys., 41:2365 (1970).
22. Perlman, M. M., J. Appl. Phys., 42:2645 (1971).
23. Glass, A. M., Phys. Rev., 172:564 (1968).
24. Lines, M. E., and Glass, A. M., Phys. Rev. Letters, 39:1362 (1977).
25. Glass, A. M., Appl. Phys. Letters, 13:147 (1968).
26. Taylor, R. G. F., and Boot, H. A. H., Contemp. Phys., 14:55 (1973).
27. Day, G. W., Hamilton, C. A., Peterson, R. L., Phelan, R. J. Jr., and Mullen, L. O., Appl. Phys. Letters, 24:456 (1974).
28. Das-Gupta, D. K., and Doughty, K., J. Appl. Phys., 49:4601 (1978); IEEE, Trans. Industry Appl., IA-14:448 (1978); J. Appl. Phys., 51:1733 (1979).

A NEW INTERACTIVE, COMPUTER-CONTROLLED METHOD FOR INVESTIGATING THERMAL REACTIONS FOR THE 'THERMODETOXIFICATION' AND RESOURCE RECOVERY OF SURPLUS CHEMICALS (U)

WENDEL J. SHUELY, MR.
CHEMICAL SYSTEMS LABORATORY, USAARRADCOM
ABERDEEN PROVING GROUND, MD 21010

1. INTRODUCTION.

We are faced with increasingly difficult scientific and technological problems and some of these problems require new approaches to scientific experimentation in order to furnish possible solutions. A number of difficult scientific problems are posed by the technological problems concerning disposal of hazardous wastes.

The background of the disposal problem can be separated into several broad areas of concern and these have been well documented: (a) the extent and scope of the surplus chemical and hazardous waste problem (1); (b) the propagation of definitions, categories, and various regulatory lists of compounds (2); (c) the emphasis on resource recovery and the tracking of the safe disposal of wastes (3); and (d) the importance of thermal methods in the spectrum of disposal techniques (4).

A new method of low temperature thermal disposal has been suggested (5). The concept of low temperature thermodetoxification is directly based on a series of publications by a group of investigators at Mississippi State University (led by M. Kennedy). In the process of studying chemical and thermal destruction of 20 to 30 pesticides for EPA, they realized that the various high temperature incineration and combustion techniques were not necessary to detoxify most pesticides. Examples of advantages cited for low temperature methods are that energy, equipment cost, and the complexity of the reaction products could be reduced. They successfully demonstrated that low temperature thermal conversion of surplus compounds could produce simple products and the term "thermodetoxification" first appeared in one of these publications.

Their major problem was that adequate methods were not available to obtain the basic thermal reaction data needed to characterize these thermodetoxification reactions. They used five methods of thermal treatment and six methods of instrumental analysis, (5) however, the thermal reaction data obtained were not very useful. For example, the initial decomposition temperature by different methods differed by an average of 60 degrees C over a range of 120 degrees C, or about 50%. No reaction rate data, temperature vs rate data, or other activation parameters were obtained. In addition, the methods often could not distinguish between physical processes and reactions. Therefore, there are problems with the available methodology and there is a need for new, adequate techniques. This basic research investigation for the US Army Toxic and Hazardous Materials Agency (USATHAMA) was directed at attempting to develop improved techniques.

The scope of this review must be limited to a summary of theory, results, and conclusions. Complete descriptions of materials, procedures, instrumentation, and kinetic computations will be published in the future.

2. THEORY.

2.1 Temperature scanned thermogravimetric analysis

The EPA investigations at the U. of Mississippi employed some thermal analytical techniques to good advantage. These linear programmed temperature (e.g., dynamic) analyses offer significant, well documented advantages (6), however, the methods have the limitations discussed in section 2.2.

A basic research investigation was proposed to improve the kinetic data available from dynamic thermal analysis. The focus was directed specifically to thermogravimetric analysis (TGA) in which sample weight-loss is measured as the temperature is scanned. The approach used was to create a system in which the computer directly interacted with the thermal chemical process. The concept is based on the design of an interactive computer control system so that experimentation could be performed in a novel manner.

2.2 Interactive control instrumentation.

Conventionally, chemical kinetic data have been obtained in the traditional scientific manner. Independent variables are carefully measured or maintained at a constant value and their effects are determined by measurements of the dependent variable. For example, in the dynamic TGA experiment, temperature is the independent variable;

temperature is scanned in a deliberate manner and the dependent variables of weight-loss or rate of weight-loss measured. The concept proposed here is to specify a predetermined value for a dependent variable one wishes to determine (rate) and automatically control the independent variable (temperature) to maintain the predetermined value. By monitoring all the variables, the functional relationships among them can be determined in the usual manner.

Increased capabilities in analog electronics, digital electronics, and computer science have increased the potential for experimentation that involve such manipulation or complex control of the independent variables to improve some aspect of the measurement process. An important class of such instrumentation is that in which a computer serves as an interactive component which provides computations, logical decisions, and calculated experimental adjustments. Computer interaction widens the range of experimentation in which the independent variables can be manipulated to adjust the dependent variable to attain certain values and improve the sensitivity, precision, analysis time, and other experimental factors. Therefore, experimentation was approached in this new, non-traditional manner and the dependent and independent variables were interchanged. This was accomplished through an instrument interface and minicomputer software which were designed to reverse these variables. The reaction rate was specified and temperature was varied by real-time, interactive computer adjustment. In this manner, experimental parameters were maintained at optimum values for the measurement of the reaction rate.

This application of computer control to reaction kinetics of organic melts was inspired by analogous investigations into manual and automatic step heating of inorganics in the analysis of weight-loss transformations from the solid-state. These are most often approximated as zero order processes and proceed at a constant rate when held under isothermal conditions. Manual (7) electrofluidic (8), and electro-optical (9) apparatus have been employed in these studies.

2.3 Advantages of computer-control of thermal reactions to a constant rate (8).

There are two fundamental objectives in studies of the thermal decomposition kinetics. First, the major qualitative objective is the assignment of a coherent set of temperature, time, and weight data to a single chemical process, e.g., discrimination between reactions. A second goal is to obtain accurate quantitative values of temperature, time, and weight so that values of activation energy, frequency factor, rate constants, and reaction order can be calculated.

Each of these objectives can be evaluated in terms of (a) the deviation of thermodynamic processes during decomposition from equilibrium and (b) the chemical reaction heat effects that both obscure successive reactions and systematically distort temperature and mass data.

2.3.1 Deviation from equilibrium during decomposition.

2.3.1.1 Effect on reaction discrimination.

Fundamental physical processes in TGA are influx of heat and efflux of mass (gaseous decomposition products). The ideal thermodynamic conditions for the determination of reaction kinetics is for the process to proceed at all times under equilibrium or, at least, quasi-equilibrium conditions. This requires uniform heat flux into the sample. A conventional linear temperature ramp causes an ever-changing reaction rate. This can be seen by inspecting the thermogram (figure 1A) and its first derivative (figure 1B). In the first stage of weight-loss, the rate increases rapidly to the maximum and then decreases rapidly. The spectrum of rates measured over the decomposition temperature range is quite wide. The second stage shows another typical variation in the weight-loss and derivative curves. Figure 1C shows weight-loss at a constant rate and the derivative curve (figure 1D) shows a steady, constant rate of weight-loss.

Figure 1.

IDEALIZED THERMOGRAMS AND THEIR FIRST DERIVATIVES

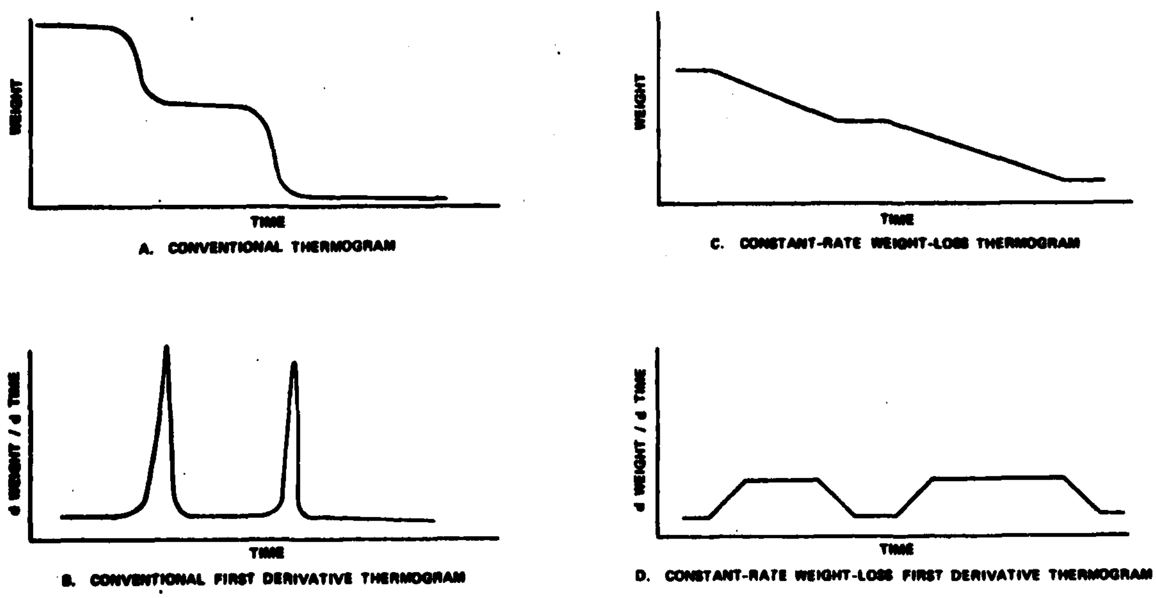

A computer-controlled TGA method would provide slow, constant-rate (figure 1C, D) weight-loss kinetics in order to attain quasi-equilibrium thermodynamic conditions during kinetic measurements. A reaction occurring at near equilibrium conditions would minimize temperature gradients and improve temperature homogeneity within the sample. With all loci in the sample nearer to the same temperature, the reaction and physical processes will proceed in a more uniform manner and more nearly in concert on a molecular level. Measurements of macroscopic weight-loss will then lead to improved discrimination between two consecutive reactions. The isolation of the reaction steps will increase, separate stages can be identified, and a defined set of weight, time, and temperature data can be assigned to a segment of the thermogram.

Inspection of the first derivative of the thermogram in figure 1B also shows that not only is the maintenance of temperature homogeneity a problem when the rate varies widely during a decomposition process, but mass efflux or gas evolution will occur under nonequilibrium conditions. The difference in rate can be large between the maximum rate at the peak and the initial or final rates. There would be different rates of gas diffusion through the fluid to the sample surface, different pan buoyancy effects, and different gas concentrations over the sample at various times and temperatures (extent of reaction). These gas efflux effects would contribute to loss of resolution between two reactions.

2.3.1.2 Effect on data accuracy.

The errors in accuracy that can be decreased by maintaining reaction conditions closer to equilibrium with computerized TGA instrumentation might be described as systematic lag errors. The errors are caused by the time difference between the kinetic event and the detection by temperature and weight transducers (thermal conductivity and mass transfer delays, respectively). The thermocouple temperature is usually "ahead" of the sample temperature. The escape of gas from the balance pan usually lags the formation of the gas molecule in a decomposition reaction.

A small, constant offset or lag is not a serious error. However, at the maximum rate, (the peak top in figure 1B) the lag between gaseous product formation and exit from the sample pan could be quite different from the lag at the lower initial or final rates. This difference will affect the kinetic parameters calculated from the rate data obtained at different reaction extents.

One might assume that a linear temperature program would lead to a very steady thermal flux into the sample from the furnace.

However, this flux is being applied to an ever-decreasing mass. Early in the decomposition reaction, the recorded temperature will be more "ahead" of the actual sample temperature due to the larger thermal mass of the sample. The smaller, decomposed sample mass will be closer to the thermocouple temperature at the end of the reaction. This uneven offset is, again, a source of anomalous differences in rates calculated from different sections of the thermolysis curve. A constant-rate temperature profile for a first order decomposition would have a slower initial temperature rise and a faster rise at the end to drive the reaction to completion. One can see that the lag at the end of the reaction will again be low since the small sample mass will be better able to keep up with an accelerating temperature profile. In addition, the initial temperature profile will be relatively slow and the larger mass at the beginning of the thermolysis will not lag the oven temperature as much as a faster linear ramp.

2.3.2 Reaction heat effects during decomposition.

In the investigation of a decomposition reaction, the reaction heat can be either exothermic or endothermic, large or small. Even if DTA or DSC analyses are available to characterize the direction and magnitude of the reaction heat, the error due to sample self-heating or self-cooling will still be present and distort the kinetic data. If the temperature difference due to sample heat of reaction is greater than the temperature difference between two successive reactions, then the discrimination between the two reactions will not be detected by formation of a weight-loss plateau between their decomposition curves. The existence of two separate reactions will be missed and a single, "apparent" activation energy will be erroneously assigned to the two reactions.

A computer-assisted method that controlled the reaction rate would signal for less heater wattage when an exothermic reaction heat raised the sample temperature above the measured temperature. Conversely, if an endothermic reaction caused self-cooling, the reaction rate would decrease and the computer alogrithm for constant weight-loss would signal for more heat from the furnace.

2.3.3 Advantages of a computer-controlled rate in the calculation of kinetic parameters.

The above description of processes during a weight-loss reaction is based on a microscopic or molecular viewpoint. An operational discussion of the inaccuracies inherent in kinetic calculations from conventional programmed TGA data is contained in a monograph on polymer decomposition. The quotations shown below demonstrate that the reaction rates are too rapid (too steep) near the middle portion of the weight-loss curve for accurate calculations.

(a) "Derived data for the Teflon degradation were obtained only up to about 50 percent conversion, since beyond this conversion the slopes of the primary thermograms became too steep to be utilized satisfactorily." (10)

(b) "However, in using this method, (Freeman-Carroll calculation method) it is necessary to measure steep slopes accurately." (10)

(c) "A major disadvantage of this method (Ozawa type calculation) is the necessity to determine slope accurately from the primary thermogram." (10)

It can be seen from the above that the reaction rate is too rapid at certain sections of the conventional TGA thermogram and this influences the accuracy of the kinetic calculations. The computer-controlled technique furnishes a moderate slope that allows more accurate calculations.

3. RESULTS AND DISCUSSION.

3.1. Testing the computer-controlled method with reference compounds and comparison with conventional TGA data.

A rare opportunity for a direct comparison between conventional TGA and the computer-controlled system exists. Gyore and Ecet (11) determined the activation energy of malonic acid using a conventional TGA method. Fortunately, malonic acid is one of the compounds qualifying as a reference material because of its well characterized activation energy. Therefore, there is a good isothermal reference value with which to compare the conventional programmed temperature and computer-controlled method. Gyore and Ecet made 13 runs at program rates of 0.8 to 8.4 degrees per minute, in air or argon and at a variety of sample weights. They reported that all conditions gave similar results. Their conditions were roughly duplicated herein by using 10 mg samples, an air atmosphere, and an equivalent extent-of-reaction calculation interval.

A comparison of a computer-controlled and conventional thermogram of malonic acid decomposition (Gyore and Ecet (11)) is presented in figures 2 and 3 respectively.

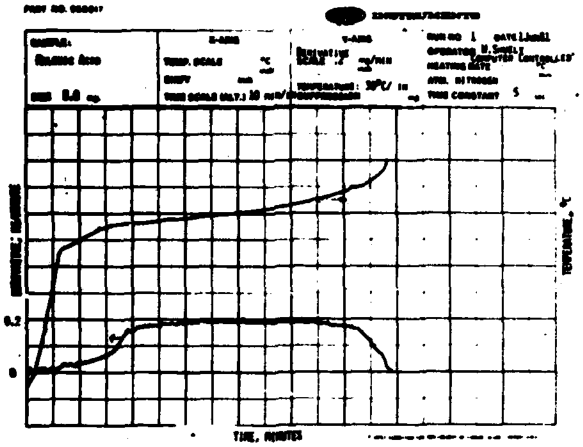

Figure 2. Computer-Controlled Malonic Acid Thermogram

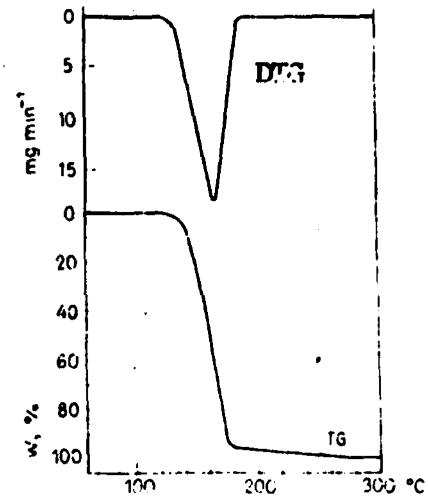

Figure 3. Conventional Malonic Acid Thermogram

Arrhenius plots from the data obtained with the computer-controlled and conventional method are presented in figures 4 and 5 .

A comparison of activation energies is shown in table 1.

Table 1

DEVIATION OF ACTIVATION ENERGIES DETERMINED BY PROGRAMMED TEMPERATURE TGA FROM ISOTHERMAL REFERENCE VALUES

METHOD	ACTIVATION ENERGY	95% CONFIDENCE INTERVAL	DEVIATION FROM REFERENCE VALUE (38.6 ± 0.15)	PERCENT DEVIATION OVER ACTIVATION ENERGY RANGE (25 to 45 Kcal/mole)	STATISTICALLY DIFFERENT FROM REFERENCE VALUE (alpha = 0.05)
	Kcal/mole		Kcal/mole		
CONVENTIONAL TGA	40	NOT REPORTED	+3.4	+17%	YES
COMPUTERIZED TGA	38.8	± 0.7	+0.2	+ 1%	NO

Gyore and Ecet used three different computational methods to analyze their data and all gave essentially 40 Kcal/mole. This is 3.4 Kcal/mole higher than the reference value of 36.6 $\pm$ 0.15 Kcal/mole (12). For perspective, the 17% deviation over an activation energy range of 20 Kcal/mole is reported. This gives a more realistic measure of the accuracy since the activation energy of this type of compound usually only ranges from 25 to 45 Kcal/mole. A t-test found the reference value significantly different from the value of 40 Kcal/mole. For the computer-controlled reaction rate system, a mean value of 36.8 was obtained. The 95% confidence interval was $\pm$ 0.7 Kcal/mole, which is very good for a temperature-scanned thermal method. The deviation from the reference value was 0.2 Kcal/mole which is about 1% when taken over a 20 Kcal/mole range. There was no significant difference between the reference value and computer-controlled TGA value by a t-test at an alpha value of 0.05.

Simulation calculations were programmed to compute the theoretical temperature profile for a reaction controlled to a constant rate of weight-loss. Input parameters were activation energy, activation entropy, order and rate of weight-loss. Figure 6 shows the accelerating profile produced by the simulation calculations for malonic acid kinetic data. It can be seen that the temperature profile matches that measured with malonic acid in figure 2.

3.2 Examples of computer-controlled rate data and activation parameters of hazardous waste compounds.

An example of one of the applications of computer-controlled rate system to a candidate hazardous waste compound is presented in figure 7. The conversion is controlled to a weight-loss rate of 0.2 mg/min. Note the derivative signal rises to 0.2 mg/min and is then parallel to the time axis. The weight signal is a straight, diagonal line; this can be compared to the idealized data in figure 1.

An example of a computer printout of activation parameters is given in table 2 for Dicamba.

Table 2 . Example of Computer Print-out of Kinetic Activation Parameters for Dicamba

		ACTIVATION			
TEMPERATURE	RATE	ENERGY	ENTROPY	ENTHALPY	FREE ENERGY
131.13	0.186E-03	38.49	18.15	37.69	30.35
154.09	0.467E-02	38.49	18.04	37.64	29.94

FIGURE 4 . ARRHENIUS PLOT OF TEMPERATURE VS RATE CONSTANT

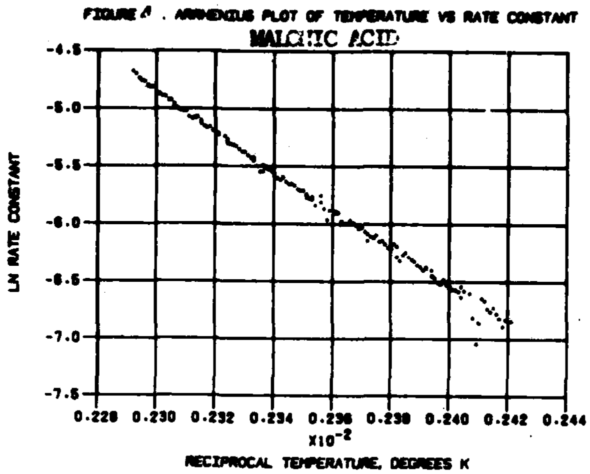

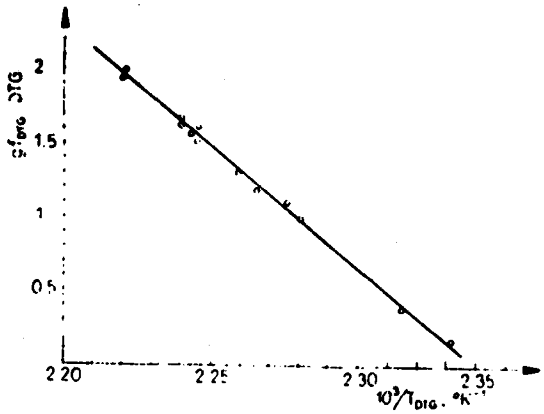

Figure 5. Malonic Acid Arrhenius Plot from Conventional TGA Data

Figure 6 . Computer Calculated Simulation of Computer-Controlled Constant Rate of Weight-loss for Malonic Acid

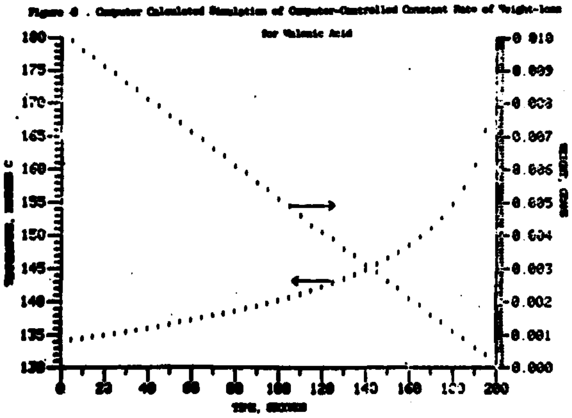

Figure 7 . Computer-Controlled Constant Rate of Weight-Loss Experiment with Dinoseb

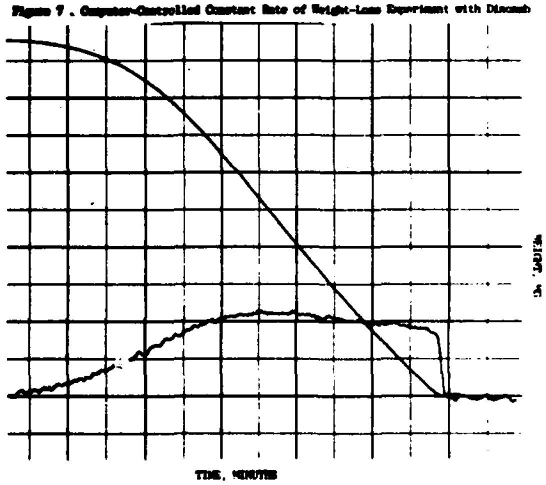

3.3 Potential application of the computer-controlled rate method.

It was of interest to obtain an estimate of: (a) the ability of the computerized method to detect and isolate candidate thermal disposal reactions that were simple and "clean" and (b) the fraction of compounds that might be amenable to low temperature thermal disposal or resource recovery.

Since reaction mechanisms are open to continous refinement, a final value for the first estimate above is not likely. However, table 3 contains the best current estimates for this group of compounds. About 38 of 50 or 76% have been completely to considerably isolated from consecutive and concurrent processes (table 3, Number 1,2,3). The others appear to be characterized by complex processes or extreme reaction heats. Therefore, it appears that up to 76% of the compounds might be candidates for low temperature thermal disposal or resource recovery.

Table 3. Operational Classification of 50 Pesticides for Thermal Disposal Kinetic Studies Based on Preliminary Analysis with a Computerized Thermal Instrument System.

Reaction Classification	Number of Compounds
1. Isolated single reactions with measurable kinetics	14
2. Isolated consecutive reactions with measurable kinetics	13
3. Partially isolated consecutive reactions with measurable kinetics over most of the thermal conversion	11
4. Reactions requiring further computerized TGA experimentation and data analysis and possible assistance from other techniques	7
5. Reactions with extremely high heats of reaction, presenting a difficult TGA kinetic measurement problem.	5

Table 4 contains a comparison of initial decomposition temperature estimates from previously published studies sponsored by the EPA with these computerized TGA data, sponsored by USATHAMA. The average difference was 101°C. The computerized TGA method would be expected to detect the initial decomposition at a lower temperature because the method: (a) is more sensitive (b) is a temperature scanned method (c) has been tested and calibrated with thermal reference compounds.

Table 4. Comparison of Previous (EPA) Thermal Disposal Decomposition Data with Computerized Thermogravimetric Data (USATHAMA)

	Procedural Decomposition Temperatures, °C			
	Initial		Final	
Pesticide	EPA(5)	USATHAMA	EPA	USATHAMA
Zineb	200	130	nd	160
Dicamba	210	115	nd	225
Picloram	225	165	nd	220
Carbaryl	250	145	nd	210
Atrazine	250	140	nd	205
2,4-D	300	135	nd	240
Bromocil	250	150	nd	265

Average Difference: 101 $\pm$ 34 (sd)°C

nd = not determined

Table 5 presents two examples showing reduced toxicity of the product relative to the pesticide reactant. These were the two compounds (of the seven in table 4) with toxicity data for both pesticide and product under similar conditions. Other toxicity data for various routes of administration or species appear to show reduced toxicity, however, interpretation of this data requires a specialist and is beyond the scope of this investigation.

Table Example of Investigated Compounds Showing Reduced Toxicity of the Product Relative to the Reactant (Oral-rat Data (12))

Reactant	LD50 mg/kg	Product	LD50 mg/kg	LD50 Ratio
Dinoseb	25	2-sec-butylphenol	2700	108
Carbaryl	250	1-naphthol	2590	10

4. CONCLUSIONS:

A basic research investigation is in progress to develop a computer-controlled thermogravimetric method for investigating thermal reactions. The new method is needed for the study of the low temperature conversion of surplus hazardous compounds to less toxic compounds. The following conclusions have been obtained.

1. A computer-controlled system has been created to improve the measurement of weight-loss kinetics by thermogravimetric instrumentation. The control algorithm has been successful in producing a constant rate of weight-loss. The complex, nonlinear temperature profiles executed by the computer furnish reaction rates that are optimal for accurate measurement and avoid conditions in which the rate is either too rapid or too slow for accurate measurement.

2. The computer-controlled thermogravimetric system can measure and compute kinetic activation parameters of reference compounds that are not significantly different from those determined with an independent, isothermal method. The precision of the data obtained with the new method is not as good as that of the more difficult and time consuming isothermal, manometric methods; the precision is better than that of the conventional dynamic TGA methods.

3. The computer-controlled rate method maintains the advantages of a temperature scanning technique while also providing the improved conditions for kinetic measurements. In addition, an increase in temperature scanning efficiency has been achieved. The computer scans the temperature more rapidly when there is no weight-loss detected, therefore, measurements are obtained during about 75% of the analysis time. During conventional linear-temperature-programmed experiments

reaction data is collected less than 25% of the analysis time.

4. The control algorithm allows real-time, interactive temperature compensation for sample self-heating or self-cooling due to heat-of-reaction effects. The system response is satisfactory for moderate reaction heats. Extreme reaction heats can be reproducibly detected but cannot be automatically compensated at this time.

5. The system can be applied to survey and measure thermal reactions of surplus hazardous wastes such as pesticides. Data is being obtained on the thermal conversion of pesticides into compounds that are less toxic. These compounds present the opportunity for resource recovery or afford a reduced disposal problem. The results obtained are also the basic data needed for other thermal disposal techniques such as pyrolysis, incineration, and combustion.

6. Experiments with 50 pesticides demonstrated that the computer-controlled system can detect and isolate reactions for kinetic measurements in about 75% of these compounds. Consequently, it appears that a significant number of hazardous, surplus pesticides may be converted to other compounds by low temperature methods. Such methods may possess net advantages over chemical, incineration, pyrolytic, or other destruction methods.

7. The computer-controlled non-linear temperature scan detects initial and final procedural decomposition at significantly lower temperatures than previously published, conventional studies. The ability of the new method to reproduce data obtained from isothermal studies of reference compounds suggests that these lower values are more accurate.

8. It has been hypothesized that some rather complex, toxic molecular structures might be converted to simplier, less toxic products by application of the minimum thermal energy. This concept appears promising from the limited toxicological comparisons available at this time.

LITERATURE CITED

1. Maugh, Thomas. Toxic Waste Disposal; A Gro-'ng Problem. Science. 204(25) 19-823 (1979).

2. Cheremisinoff, Paul N. and Holcomb, William F. Management of Hazardous and Toxic Wastes. Pollution Engineering. April 1976.

3. Barnhart, Benjamin J. The Disposal of Hazardous Waste. Environmental Science and Technology. V12. No. 10. (1978).

4. Miller, Thomas A. CPT, MSC. USAMEERU Report No. 73-01. Problem Definition Study: Evaluation of Health and Hygiene Effects of the Disposal of Pesticides and Pesticide Containers. August 1972. UNCLASSFIED Report.

5. Stojanovic, B. J., Hutto, Fay, Kennedy, M.V. and Shuman, F. L. Jr. Mild Thermal Degradation of Pesticides. J. Environ. Quality, Vol 1, No. 4, 397-401 (1972).

6. Wendlandt, Wesley Wm. Thermal Methods of Analysis. John Wiley & Sons. New York. 1974.

7. Zuda, A., The Technique of Step Heating Applied to Thermal Analysis. Thermochimica Acta, Vol. 8, 217-224, (1974).

8. Rouquerol, J., Critical Examination of Several Problems Typically Found in the Kinetic Study of Thermal Decomposition Under Vacuum. Journal of Thermal Analysis, Vol. 5, 203-216, (1973).

9. Paulik, F. and Paulik, J. Thermogravimetric Investigations, Under Quasi-Isothermal and Quasi-Isobaric Conditions, by Means of the Derivatograph. Hungarian Scientific Instruments, Vol. 28, 1-5, (1973).

10. Reich, L. and Stivala, S. Elements of Polymer Degradation. McGraw-Hill Book Co. 1971.

11. Gyore, J. and Ecet, M. Kinetic Equations for the Thermal Decomposition of Crystalline Malonic Acid. J. Thermal Anal. Vol. 2, 397-409 (1970).

12. Clark, Louis Watts. Kinetics of Decarboxylation of Malonic Acid and Other Acids. J. Phys. Chem. 68(10) 3048-3052 (1964).

13. Lewis, Richard J. and Tatken, Rodger L. Editors. Registry of Toxic Effects of Chemical Substances. NIOSH. 1979.

Near Millimeter Wave Radiation from a Gyromonotron

Joseph D. Silverstein, Ph.D.
U.S. Army Electronics Research and Development Command
Harry Diamond Laboratories
Adelphi, MD 20783

Introduction

The emergence of the gyrotron [1], or cyclotron resonance maser (CRM), as a highly efficient and powerful source of millimeter waves has made it attractive for applications in communications, radar, and rf heating of fusion plasmas. In this tube the output frequency is determined by the cyclotron frequency imparted to a beam of electrons by an applied magnetic field. When these electrons traverse an rf cavity of appropriate size they are caused to form azimuthal bunches in such a way that they impart a large fraction of their energy to the electromagnetic field in the cavity. However, there is no intrinsic requirement to limit the size of the rf structure to the radiation wavelength as with conventional tubes, thus allowing for very large power densities.

Recently the Department of Defense (DOD) has increased emphasis on operating certain radar and EW systems in the near millimeter wave (NMMW) spectral region between 0.3 and 3.3 mm. Basically, the reason for this is that the NMMW region offers an attractive compromise between the high resolution capabilities of midinfrared systems and the low propagation loss characteristics of microwave operation. Until the present time the only reported operations of NMMW gyrotrons have been in the Soviet Union. The impressive results obtained there with these tubes include output power of 1500 W cw at 0.9 mm, 2400 W cw at 1.9 mm, and 1.1 MW pulsed at 3 mm, all with efficiencies around 10% or greater [2]. An important aspect of the DOD NMMW effort is a collaboration between Harry Diamond Laboratories and the Naval Research Laboratory in the building of a gyromonotron, or gyrotron oscillator, designed to operate at a wavelength, λ, of 1.25 mm (240 GHz) with output power in the 1 to 10- kW range and with an efficiency of about 10%. The present paper describes the design of this tube and the results obtained in early tests.

Design

1. Magnetic Field

The magnetic field required for a cyclotron frequency of 240 GHz with a 30- kV beam voltage is approximately 90 kG. Magnetic fields of that magnitude can readily be generated in laboratory environments both by room temperature and superconducting magnets, with the latter being particularly convenient for gyrotron experiments. However, for most applications involving fielded systems it may be desirable to reduce the required magnetic field to the greatest extent possible. It is, in fact, possible to reduce this field by a factor of 1/n, where n is an integer, by designing the gyrotron to operate at the nth harmonic of the cyclotron frequency. A number of gyrotrons operated at the second harmonic have exhibited very encouraging output power and efficiency [3]. It was therefore decided to design the present tube for optimum operation at the second harmonic, with an eye towards testing gyrotrons at even higher harmonics in the future should the present tube prove successful. A superconducting magnet capable of generating up to 60 kG was chosen for the experiment.

2. Cavity Design

The electrons traverse the gyrotron cavity in the form of a hollow beam whose thickness is about twice the Larmor radius and whose radius is the guiding center radius of the electrons. When the transverse component of electron momentum is larger than the axial one the electrons can efficiently transfer kinetic energy to the TE modes of the cavity. This energy transfer is most efficient for TE modes near cutoff [1]. In order to avoid any possible heat dissipation and voltage breakdown problems at an output power of 10 kW the minimum cavity radius must be about 0.3 cm. These criteria, together with the operating frequency of about 240 GHz, then lead to the requirement of operating this gyrotron at a rather high order TE mode.

3. Threshold Power

The beam-wave coupling and oscillation-start conditions were calculated using the linear theory of Chu [4], which has recently been extended to include non-azimuthally symmetric TE modes [5]. Figs. (1a) and (1b) show the results of these calculations for the experimental parameters being employed. These are

(a) beam voltage, $V = 30$ kV,
(b) ratio of transverse to axial electron momentum in the cavity, $\alpha = 1.5$,

(c) ratio of cavity length to cavity radius, L/b = 8,
(d) ratio of electron beam guiding center radius to cavity radius, r_e/b = 0.38, and
(e) cavity radius, b = 0.328 cm.

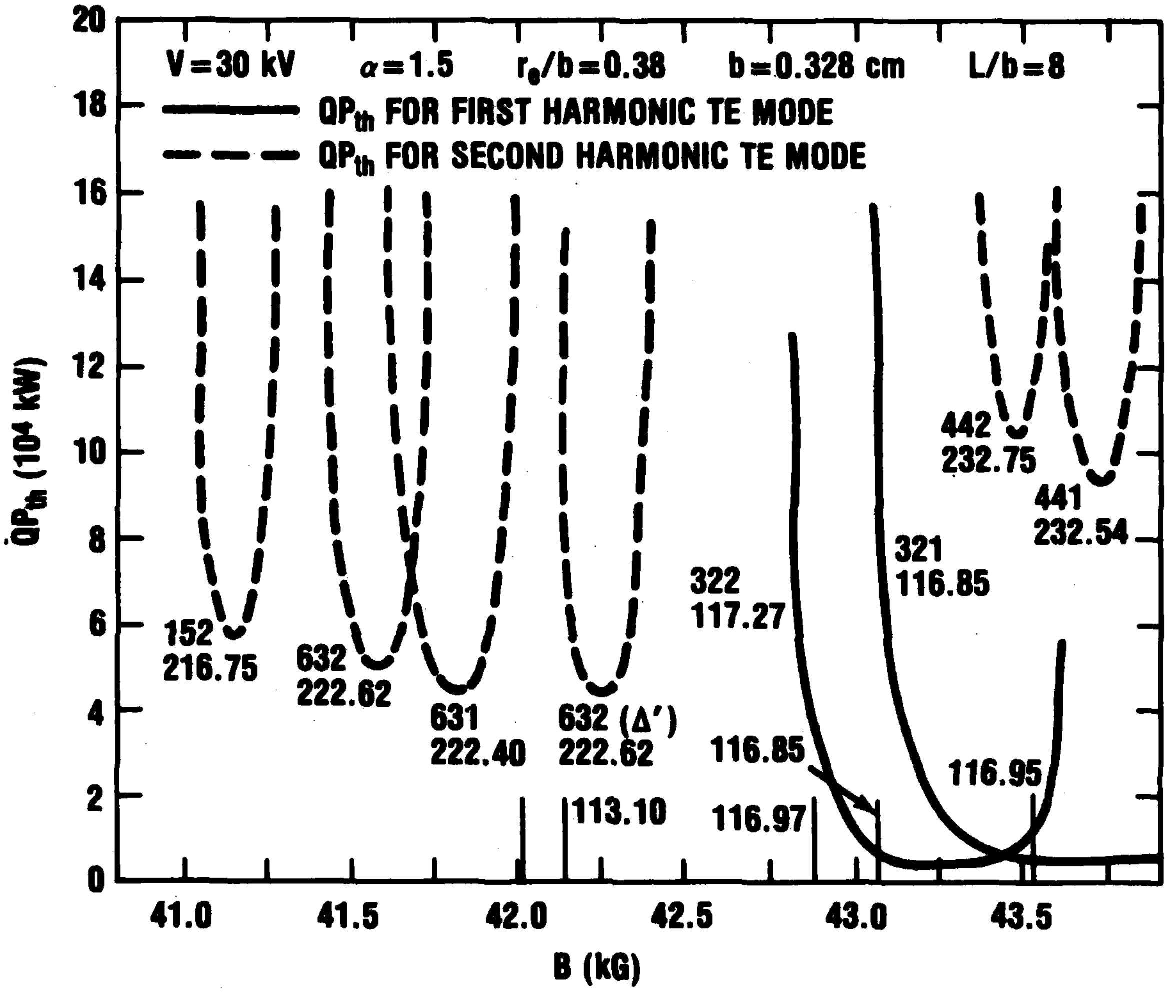

Fig. 1a Predictions of linear gyrotron cavity theory for loaded Q times threshold power vs. applied magnetic field. The vertical lines are values of magnetic field at which N-band signals were observed. The theoretical curves are labelled by the TE cavity mode, the frequency in GHz, and in some cases, Δ', which is a phase shift parameter discussed in reference [4]. The numbers labelling the vertical lines are measured frequencies in GHz.

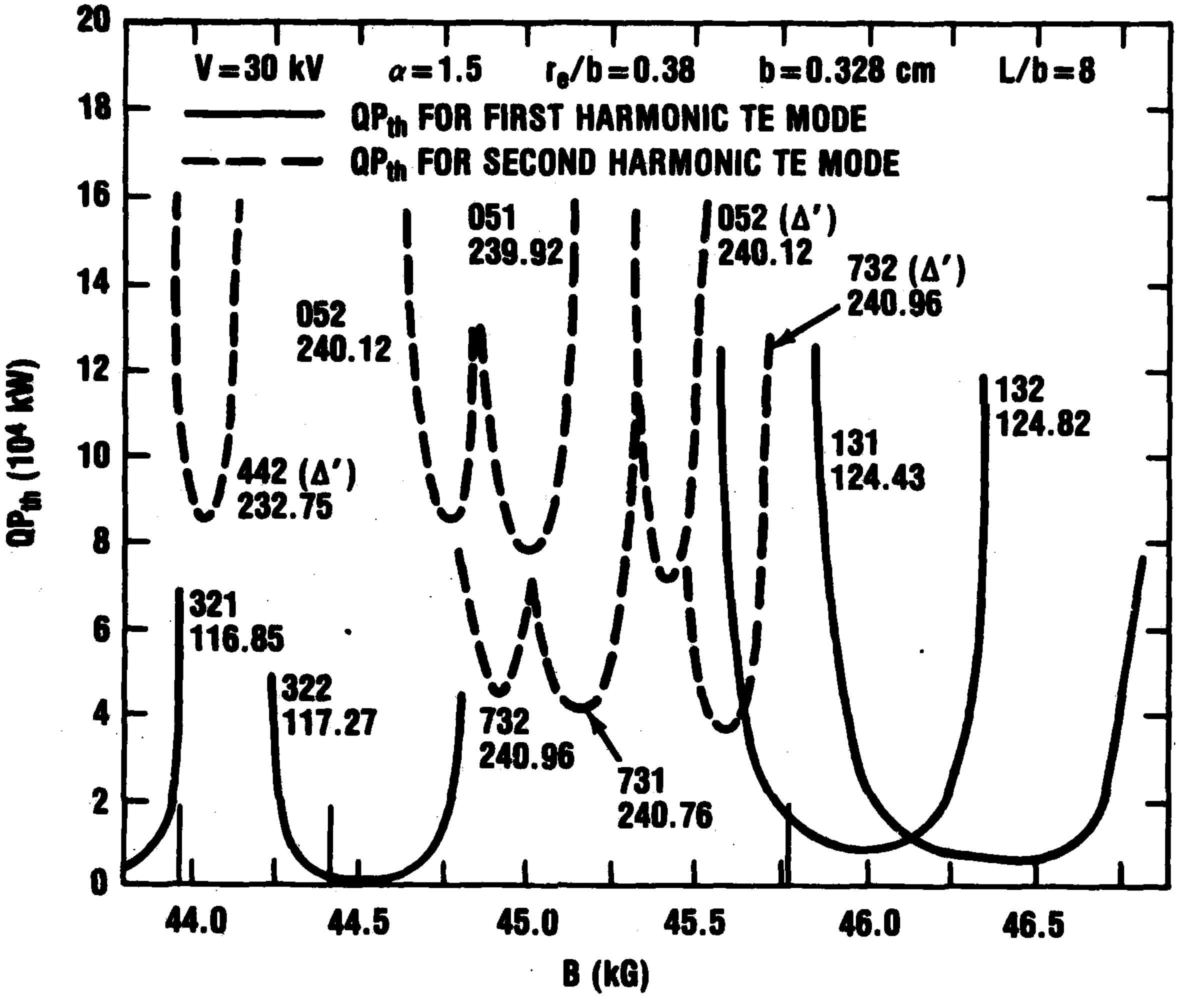

Fig. 1b Predictions of linear gyrotron cavity theory for loaded Q times threshold power vs. applied magnetic field. The vertical lines are values of magnetic field at which N-band signals were observed. The theoretical curves are labelled by the TE cavity mode, the frequency in GHz, and in some cases, Δ', which is a phase shift parameter discussed in reference [4]. The numbers labelling the vertical lines are measured frequencies in GHz.

The curves in these figures are plots of cavity loaded Q times threshold power vs. applied magnetic field, the latter ranging from 40.8 to 43.9 kG in Fig. (1a) and from 43.9 kG to 47.1 kG in Fig. (1b). It is obvious from these figures that a multitude of both first and second harmonic modes oscillating around 120 GHz and 240 GHz, respectively, should be obtainable from this tube.

In order to obtain the threshold current from the data of Fig. (1) it is necessary to know the loaded Q of the cavity for the various modes at their respective oscillating frequencies. These have not been measured. However, they have been estimated using standard expressions for ohmic Q and the theory of Vlasov et al [6] for the coupling Q. The results of these estimates for the modes occurring at applied magnetic fields near 45 kG are shown in Table 1.

4. Power and Efficiency

The optimum power and efficiency expected from the gyrotron when it is oscillating in a particular mode are obtained from computer simulations of the electron orbits in the assumed electromagnetic field. These calculations have not as yet been done for the minimum threshold, second harmonic modes at 45 kG, namely the TE_{731} and TE_{732} modes. However, simulations have been performed for second harmonic gyrotron oscillations in the TE_{051} mode [7]. All geometric and electrical parameters used in those calculations are essentially the same as those of the present experiment except for the guiding center radius of the electron beam. Fortunately, certain scaling laws have been derived [8] from a large number of gyrotron oribit simulations which enable one to relate the predicted efficiency and power for oscillations in various TE modes at fixed values of n, α, V, and L/λ. Applying these scaling laws to the TE_{051} mode data, one obtains the following estimates: 11% efficiency, with an output power of 3 kW at a beam current of 0.8 A for the TE_{731} mode, and 11% efficiency, with an output power of 9 kW at a beam current of 2 A, for the TE_{732} mode.

5. Tube Construction

Fig. (2) shows the overall layout of the tube and a plot of the axial magnetic field inside the dewar of the superconducting magnet. At the extreme left of Fig. (2) is the magnetron injection electron gun, which operates at a cathode voltage of -30 kV and a control anode voltage of about -18 kV. Fig. (3) shows an assembly drawing of the gun. Fig. (4) shows a detailed drawing of the input guide which the electron beam traverses on its way to the cavity. It contains mode filters consisting of rings made of Ceralloy, a beryllia material [8], separated by smaller i.d. beam scraping rings made of oxygen-free, high conductivity (OFHC) copper. The i.d. of the rings were decreased going toward the cavity to accommodate the converging beam. Fig. (4) also shows the pumping path in

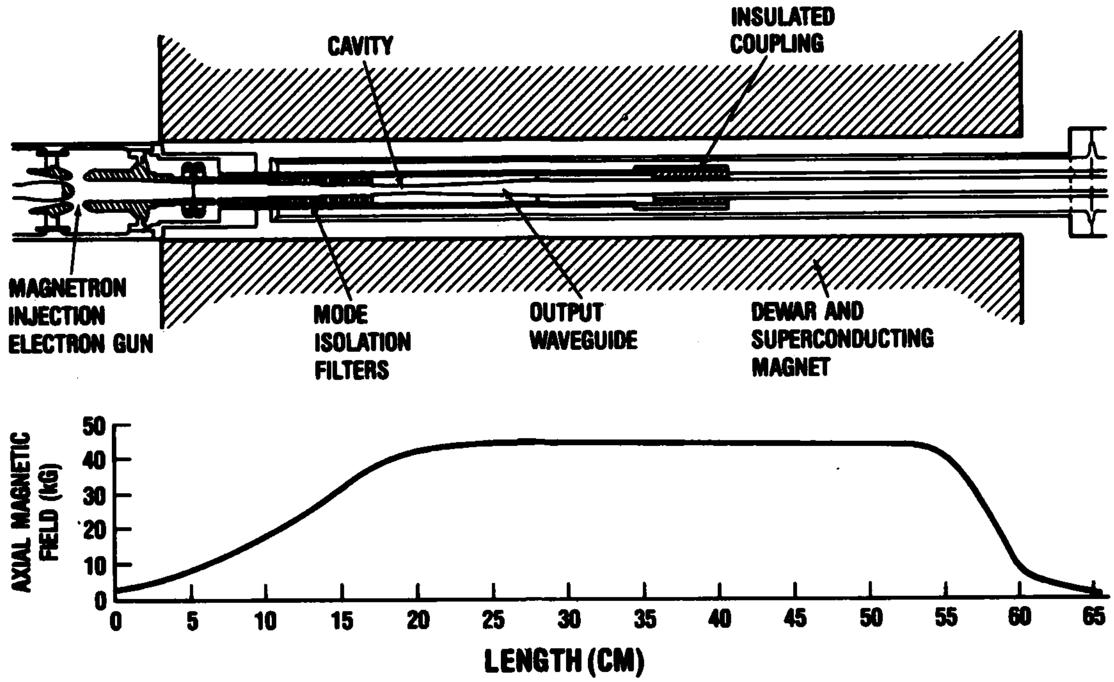

Fig. 2 Layout of tube and axial variation of applied magnetic field.

this tube which, although it resulted in a high pumping impedance, nevertheless allowed sufficiently low pressures, of the order of 10^{-8} torr, to be attained.

The geometry in the region of the cavity is shown in Fig. (5). The OFHC copper rings immediately preceding the cavity have an i.d. of 0.508 cm compared to a cavity diameter of 0.655 cm. Thus, all the modes whose thresholds are shown in Figs. (1a) and (1b) are in cutoff in this ring region. The detailed cavity and tapered waveguide geometry shown in Fig. (5) was used to calculate the cavity loaded Q results given in Table 1.

Fig. (2) shows that most of the output waveguide is insulated by a dielectric coupling ring so that the waveguide can act as a Faraday cup, enabling one to measure the electron beam current traversing the cavity. Electrons reaching the output waveguide are collected on its walls due to the diverging field of the superconducting magnet and to the transverse field of a permanent magnet immediately preceding the exit window. The window is made of fused quartz and has a thickness of $3\lambda/2$ for resonant transmission.

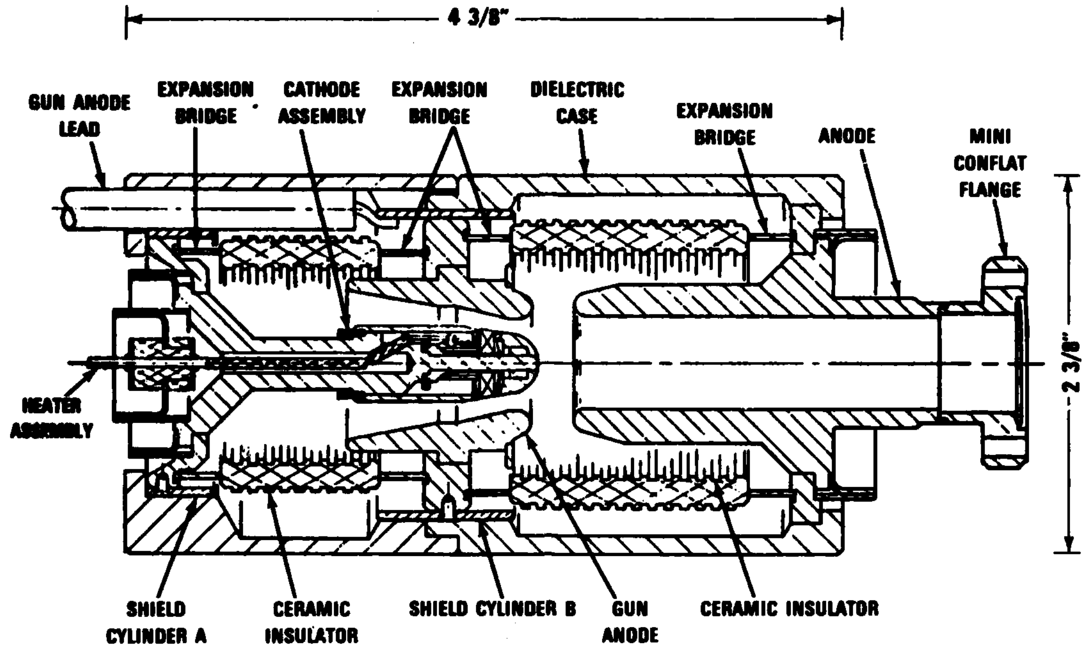

Fig. 3 Assembly drawing of magnetron injection electron gun.

Test Results

In initial tests with this gyrotron the cavity geometry was the same as that shown in Fig. (5), except that the i.d. of the OFHC copper and Ceralloy rings immediately preceding the cavity was 0.254 cm and 0.381 cm, respectively. Radiation was coupled out of the gyrotron by a 5-cm long conical horn having a 5-degree taper. The latter should provide good directivity as well as a good match between the wave impedance of the TE modes propagating in the 0.953-cm (3/8-in.) i.d. gyrotron output waveguide and the 377-ohm impedance of free space.

Fig. (6) shows the average power recorded in the initial tests with a Scientech 362 power meter as the applied magnetic field was varied between 43.5 and 46.5 kG. Power measurements with this detector have been found to be quite reliable in the NMMW region [10]. The vertical scale in this figure was converted to peak power values by the known duty cycle, which was typically 2×10^{-5} (2-μs pulse, 10 Hz). Fig (7) shows the peak power recorded by a crystal detector in a Y-band (170 to 260-GHz) mount for the same range of applied magnetic field. It can be seen that only the

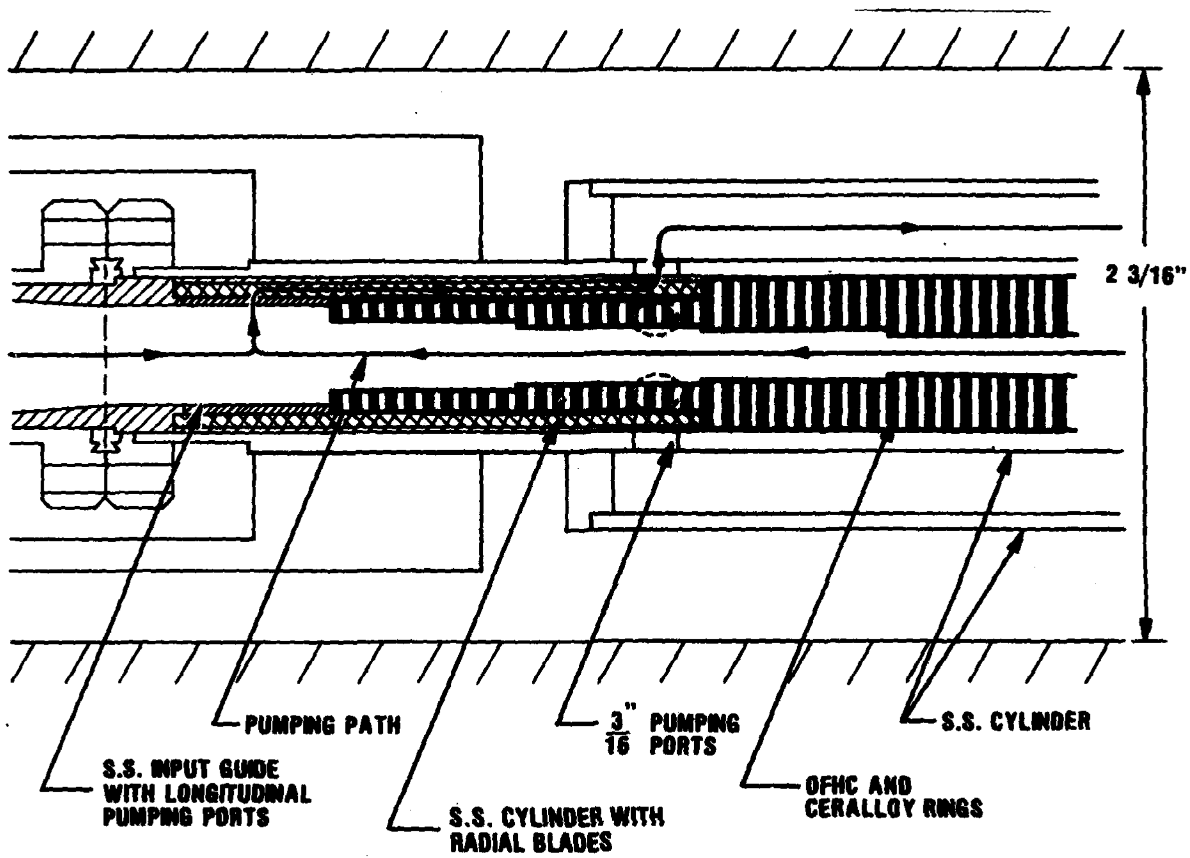

Fig. 4 Detail of input waveguide showing mode suppressor and scraper rings and pumping path.

radiation at around 45 kG was observed, implying that this was second harmonic radiation, whereas the radiation at around 44.0 and 46.0 kG seen in Fig. (6) are first harmonic and are cut off to the detector. The difference in the relative intensities of the two components of the radiation at 45 kG in Figs. (6) and (7) is not understood. The identification of the radiation at 45 and 46 kG was confirmed in other measurements made with a variety of interferometers and wavemeters. In particular, the radiation at 45 kG was analyzed by means of an optical, semiconfocal Fabry-Perot interferometer similar to one that has proven to be quite successful for various types of NMMW spectroscopy [11]. The average wavelength measured was 1.26 mm (238 GHz) and the linewidth estimated from the width of the Fabry-Perot peaks was about 1.7 MHz.

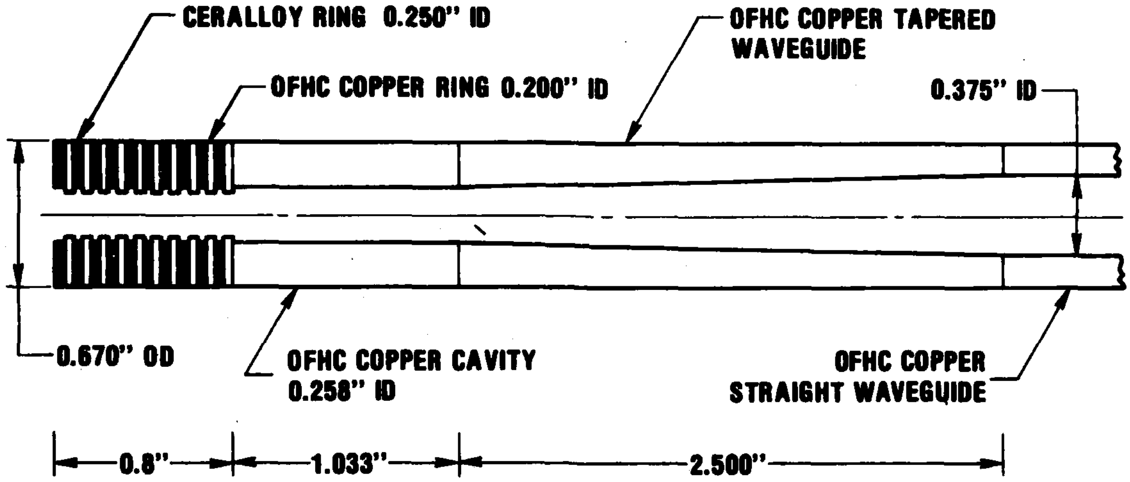

Fig. 5 Geometry of cavity showing the tapered output waveguide and mode supressor and scraper rings immediately preceeding the cavity.

The i.d. of the OFHC copper rings immediately preceding the cavity in the tests described above had to be enlarged when it was found that the electron beam had significantly damaged these rings. In fact, the average diameter of the beam entering the cavity was measured with thin tantalum witness plates and found to be about 0.267 cm with a thickness of about 0.025 cm. The i.d. of these rings was therefore enlarged to 0.508 cm, the size shown in Fig. (5). Besides avoiding any further beam damage to the ring, this change also increased the ratio of collector current to cathode current to nearly one, whereas it was no greater than about 0.4 previously. This geometry change also resulted in a much better tube vacuum and generally more stable tube operation than was experienced previously.

In tests employing the new cavity geometry a high gain Ka-band (26.5 to 40 GHz) horn was placed at the exit of the gyrotron output horn. The output of the Ka-band horn was then transmitted over a Ka-band waveguide section about 6 m long to the control console. By means of a waveguide switch the radiation could then be detected either in a Y-band (170 to 260 GHz) mounted or N-band (90 to 140 GHz) mounted crystal detector through appropriate tapered waveguide sections. Although copious signals were obtained with the N-band detector, none were obtained with the Y-band detector as the applied magnetic field was varied between 39 and 46 kG. The test for Y-band signals was repeated with the Y-band detector placed

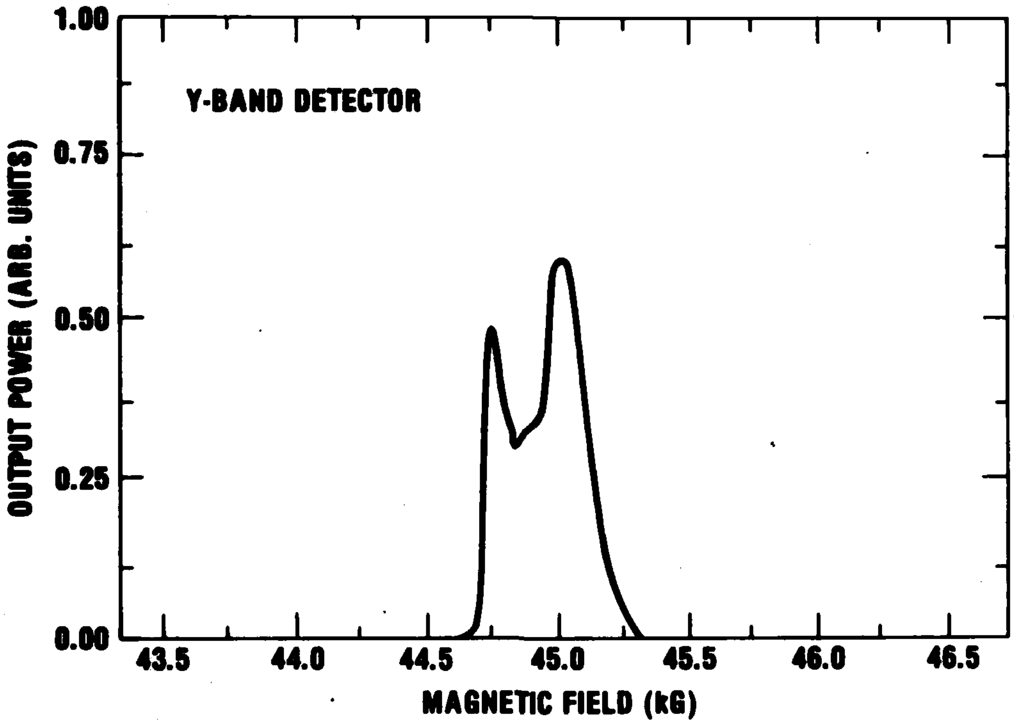

Fig. 6 Output power measured with Scientech 362 calorimeter vs applied magnetic field with cavity geometry employing 0.254 cm id copper scraping rings immediately preceeding the cavity.

at the exit of the gyrotron output horn in order to bypass the 6 m long Ka-band waveguide, which might have attenuated the signal down to a level at which it was indistinguishable from the noise. However, once again no signals were obtained throughout the same range of applied magnetic field.

The dashed lines in Figs. (1a) and (1b) indicate the values of applied magnetic field at which N-band detector signals were recorded, and the number labelling some of them is the frequency measured with a Fabry-Perot wavemeter. Fig. (8) shows a set of typical pulses obtained during the experiment with the new cavity geometry. On the left the top and bottom traces are a control anode voltage, and collector current, pulse, respectively, and on the right is a detector pulse. The short duration of the detector pulse compared to the other two is not understood at present.

A number of power measurements with the new cavity geometry were made, again using the Scientech 362 calorimeter. At a collector power of 22.5 kW, the peak power measured at 42.9 kG and 45.9 kG was 700 W and 500 W, respectively.

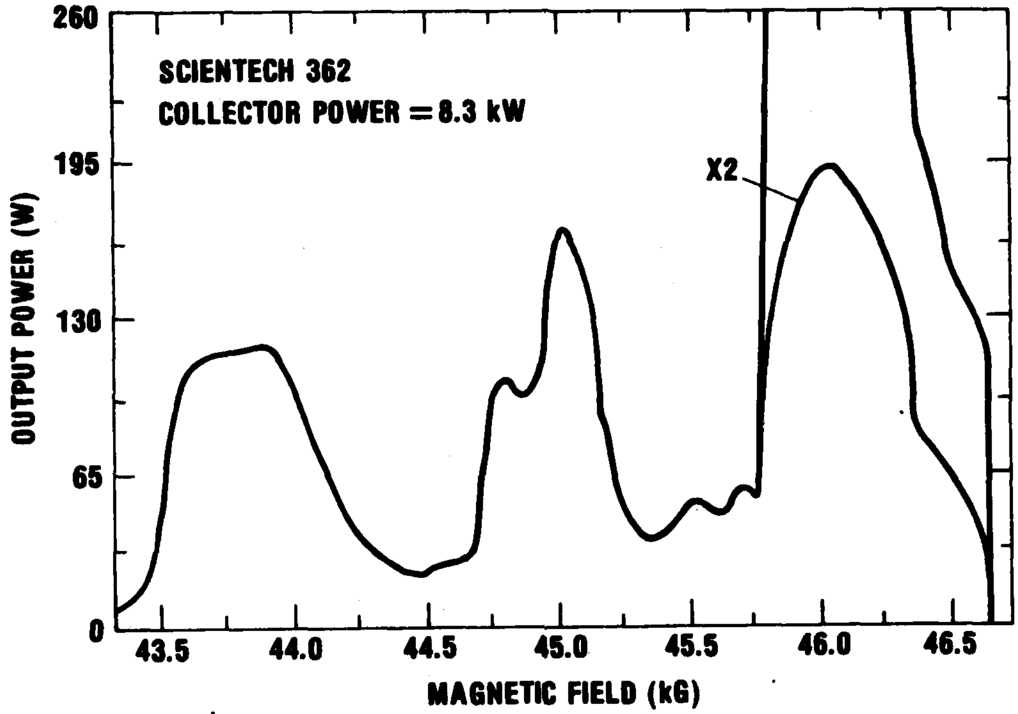

Fig. 7 Output power measured with Y-band (170 to 260 GHz) detector vs applied magnetic field with cavity geometry employing 0.254 cm id copper scraping rings immediately preceeding the cavity.

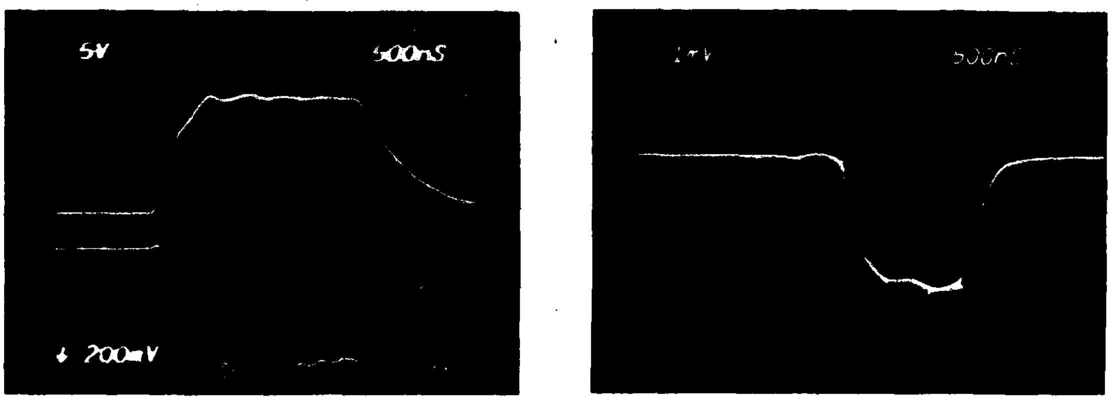

Fig. 8 Left: top trace--control-anode-to-cathode voltage (5.45 kV/div) bottom trace--collector current (5 A/div). Right--detector signal (uncalibrated).

Discussion

The second harmonic output power and efficiency of the gyrotron with 0.254-cm i.d. copper rings preceding the cavity was quite low, as is evidenced in Fig. (6). In addition, although Fig. (1a) indicates that at 45.0 kG oscillations should occur at 241 GHz at the second harmonic in the TE_{732} mode, the frequency of the radiation measured at this field value was 238 GHz. Frequency measurements of the radiation at 44 and 46 kG were not sufficiently accurate to make a corresponding comparison for those data. It is possible that these discrepancies can be due to the fact that much of the radiation produced in these early tests was excited by electrons whose guiding center radii were much smaller than the 0.12 cm corresponding to the average beam radius. Such an occurrence might be the result of a slight misalignment of the tube from the magnetic field axis. In view of the fact that the average beam diameter was larger than the i.d. of the rings preceding the cavity, such a misalignment might have been necessary in order that 40% of the electrons can penetrate the ring opening and reach the collector, as was observed.

Fig. (1a) shows that two N-band signals were observed near 42.1 kG, one of whose frequencies was measured to be 113.1 GHz. These data are puzzling, since no first harmonic mode with a low enough threshold is predicted at that magnetic field value. The other N-band signals indicated in Figs. (1a) and (1b), however, seem to be consistent with the threshold power predictions. A direct comparison, however, must await a measurement of threshold power for these oscillations.

Conclusion

Reasonably powerful and efficient first harmonic oscillations have been obtained from this gyrotron at values of beam current, applied magnetic fields, and frequencies mostly consistent with the linear gyrotron theory. This implies that the predictions for cavity Q times threshold power from the theory are, at least approximately, correct for the first harmonic. On the other hand the second harmonic oscillations predicted by this theory were not observed for the cavity geometry of Fig. (5). One must conclude that either the theory is not equally as reliable for second harmonic interactions, or that the Q values for the modes in the present cavity are much lower than those estimated in Table 1. Measurements of threshold power and of cavity Q will hopefully help clarify the issue and eventually lead to efficient second harmonic radiation from this gyrotron.

Acknowledgment

The author is indebted to M. E. Read and K. R. Chu of the U. S. Naval Research Laboratory for their advice and constant encouragement in this work, and to Robert M. Curnutt of the Harry Diamond Laboratories for his tireless assistance in the performance of these experiments.

Table 1. Estimated Loaded Q and Threshold Current, I_{th}, for TE Modes near B=45 kG

TE Mode	Harmonic	Frequency (GHz)	B(kG)	Q	I_{th}(A)
3 2 2	1	117.27	44.7	3400	0.05
7 3 2	2	240.96	45.0	3400	0.44
7 3 1	2	240.76	45.3	9600	0.14
1 3 2	1	124.82	46.2	300	1.11

References

[1] V. A. Flyagin, A. V. Gaponov, M. I. Petelin, and V. K. Ulpatov, IEEE Trans. Microwave Theory Tech., vol. MTT-25, pp 514-521, June 1977.

[2] A. A. Andronov, V. A. Flyagin, A. V. Gaponov, A. L. Gol'denberg, M. I. Petelin, V. Usov, and V. K. Ulpatov, Infrared Phys., Vol. 18, No. 5/6, pp. 385-393, Dec. 1978.

[3] N. I. Zaytsev, T. B. Pankratova, M. I. Petelin, and V. A. Flyagin, Radio Eng. Electron. Phys., Vol. 19, No. 5, pp. 103-107, May 1974; H. Z. Guo, C. Z. Chen, S. C. Zhang, and D. S. Wu, Int. J. Electron. vol. 54, No. 4, pp.485-492, Oct. 1981.

[4] K. R. Chu, Phys. Fluids, vol. 21, pp. 2354-2364, Dec. 1978.

[5] K. R. Chu, private communication.

[6] S. N. Vlasov, G. M. Zhislin, I. M. Orlova, M. I. Petelin, and G. G. Rogacheva, Radiophys. Quantum Electron., Vol. 121, No. 8, pp. 972-978, Aug. 1969.

[7] J. D. Silverstein, M. E. Read, and A. T. Drobot, IEEE Trans. Microwave Theory Tech., Vol. MTT-28, No. 9, pp. 962-966, Sept. 1980.

[8] M. E. Read, K. R. Chu and K. J. Kim, NRL Memorandum Report 4349, Nov. 1980.

[9] Obtained from Ceradyne, Inc., Santa Ana, CA 92705.

[10] F. B. Foote, D. T. Hodges, and H. B. Dyson, Int. J. IR and MM Waves, vol. 2, No. 4, pp. 773-782 July, 1981.

[11] E.P. Valkenburg and V. E. Derr, Proc. IEEE, vol. 54, No. 4, pp. 493-498, April, 1966.

TERRAIN VISUALIZATION BY SOLDIERS (U)

ZITA M. SIMUTIS, DR., AND HELENA F. BARSAM, MS.
US ARMY RESEARCH INSTITUTE FOR THE
BEHAVIORAL AND SOCIAL SCIENCES
ALEXANDRIA, VIRGINIA 22333

Reading a military map is an important, but often difficult, soldiering task. Map reading requires not only reading and mathematical skills, but also complex problem-solving and perceptual skills. Soldiers must be able to read map symbols and special map vocabulary, calculate and estimate distance and direction, be aware of geographic orientation, and understand the meaning and interpretation of contour lines. Contour lines are mechanisms by which military maps represent land formations and relief. Soldiers must be able to quickly use the two-dimensional contour lines to visualize the three-dimensional terrain over which they must navigate. Soldiers must also be able to translate the spatial information in the environment to a two-dimensional contour line pattern so that they can isolate a current location.

The ability to visualize the three-dimensional terrain from its two-dimensional contour line representation is the most complex cognitive skill required of the map reader. This skill, called terrain visualization, is also the most difficult map reading skill to train. Map users report difficulty visualizing the terrain from contour lines (1) and trainers generally agree that there are large individual differences in this ability.

All enlisted soldiers receive limited map reading instruction during Basic Training. Some soldiers receive additional training, also limited in time, during Advanced Individual Training. For many soldiers, however, map reading skills must be developed on the job. Where formal map reading training exists, much of the classroom time must be spent teaching mathematical techniques and the special symbols required for map reading. Little time is left for developing and practicing terrain visualization skills.

Current techniques for training terrain visualization vary, and include having soldiers read sections of map reading manuals, presenting slides of contour maps and associated terrains, or providing field experience in which the trainer walks with a group of students and indicates land formations and associated contour line patterns on a map. Trainers and commanders in the field have stated that along with apparent individual differences in spatial abilities, extended experience with a variety of terrains and contour line representations is a major factor in the development of terrain visualization skills (2). Thus, techniques which can broaden and increase terrain visualization experience in a short time period could lead to improved map reading training and performance.

One technique with high potential for improving terrain visualization skills is the use of computer graphics. Recent developments in computer technology can provide a means to simulate field experience and enable soldiers to practice terrain visualization with a large variety of terrains. Computers can generate contour line maps and present their three-dimensional representations quickly and realistically on a graphics display. For example, computer-based terrain visualization techniques used in this research allow a soldier to view a simplified contour map in the upper half of a computer display, place and rotate a cursor at any location on the map, and subsequently view simulated three-dimensional terrain corresponding to the cursor's position and direction. In effect, the soldier sees a graphic representation of what he or she would see if actually standing at that map location looking in that particular direction. Figure 1 shows an example of one simplified map, cursor position and direction, and associated terrain visualization. Techniques such as these are exciting and offer many potential applications within the Army.

As with any other technology, however, simply putting costly computer graphics systems into the classroom to assist in training will not necessarily lead to improved terrain visualization performance. Instructional developers and trainers must know how to effectively use the technology as a training tool.

The purpose of this research was to explore the application of computer graphics to terrain visualization problems using two training techniques. Individual differences in spatial abilities were also considered because researchers have shown that although spatial ability is generally not related to overall intelligence level, it plays a critical role in the performance of spatially related tasks (3).

Enlisted soldiers with limited terrain visualization training were first tested on their spatial ability and divided into three spatial ability groups, either high, medium or low. All soldiers were given about one hour of computer-assisted instruction in map fundamentals required for terrain visualization. Half the soldiers in each spatial group then either actively (that is, made their own decisions about cursor position and direction) or passively (that is, the computer randomly made the decisions) practiced with

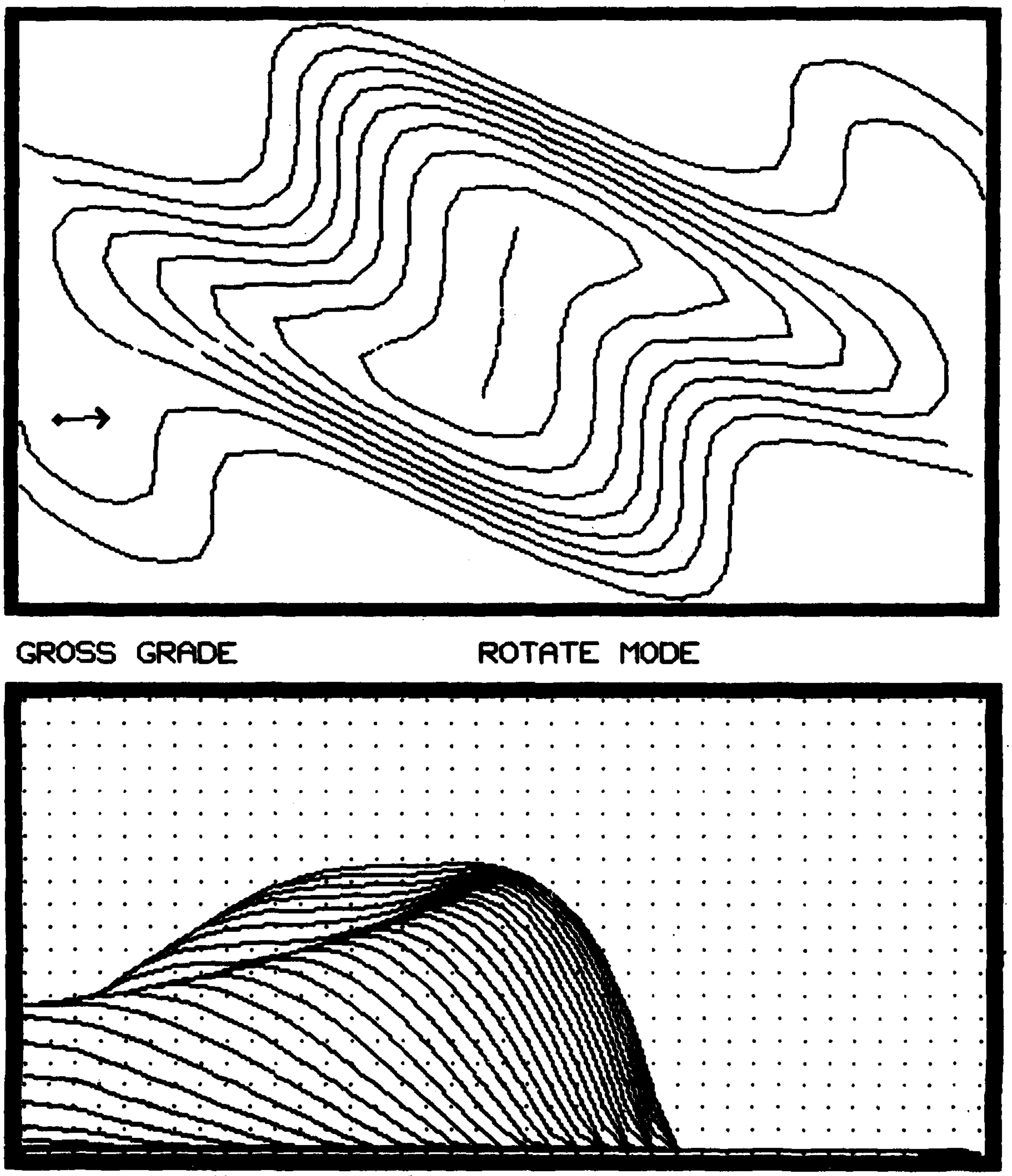

Figure 1. Example of computer display of contour map and associated terrain visualization.

computer-based terrain visualization techniques. Finally, all soldiers were tested on an ARI developed paper-and-pencil terrain visualization test.

METHOD

Subjects and Design

Sixty enlisted soldiers (6 females, 54 males) stationed at Ft Belvoir, VA participated in the research. All soldiers had limited training and/or experience in map reading and terrain visualization. Their ages ranged from 17 to 33 with mean age at 21.9 years. Soldiers were tested on spatial subtests from the Kit of Factor-Referenced Cognitive Tests (4) prior to the experiment. Soldiers were divided into three spatial ability groups (high, medium, or low) based on their spatial scores. Soldiers in each spatial group were then randomly assigned to one of two terrain visualization training conditions, either active or passive. Thus, the design was a 2-by-3 factorial design consisting of six groups with 10 soldiers per group.

Computer-Based Training Materials

With US Army Research Institute for the Behavioral and Social Sciences (ARI) assistance, the University of Illinois ROTC unit developed a series of computer-based lessons for training ROTC students in map reading.[1] The lessons were developed using the University of Illinois PLATO Computer-Based Education System. More information about this system can be found in Reference 5. The authors modified two of these lessons for use in this research. Elevation, Relief and Terrain Features covers topics required for terrain visualization, such as, elevation, relief, contour lines, slope, and terrain features. Interpretation of Contour Lines provides practice in terrain visualization as described earlier. In addition to providing three dimensional views as shown in Figure 1, ground profiles can be generated in the bottom half of the screen by moving the cursor across the map in the upper half of the screen. Rather than drawing the three-dimensional views from digitized map data bases as many other systems do, this lesson approximates the views by calculating bivariate normal probability density functions.

Training Conditions

Two versions, active and passive, of the Interpretation of Contour Lines lessons were developed for terrain visualization practice. The

---

[1]Major John Organek provided the ideas and direction. David Lesny and Gary Turner implemented the ideas. ARI provided computer time, terminals, and technical advisory service.

general approach was to have soldiers view one of four simplified contour maps and subsequently see the ground profile or land formation associated with a specific place on the map. All soldiers saw the same contour maps and were permitted to view the terrain of two of these maps in ground profile for ten minutes per map. The remaining two maps provided three-dimensional terrain visualization practice for twenty minutes per map.

Active Practice. Under the active practice condition, soldiers were freely allowed to explore each contour map, selecting the ground profiles and three dimensional visualizations they wished to see. Soldiers made all decisions about cursor position and direction. Soldiers could view as many displays per map as they wished until the time limit expired.

Passive Practice. Under the passive practice condition, the soldiers' role was to watch displays randomly chosen from positions at the edge of the map frame boundaries directed toward the map center. In all other respects the training conditions were identical: maps were identical, time of viewing each map was identical, and soldiers could view as many displays per map as they wished until the time limit expired.

Terrain Visualization Test Materials

Three subtests from ARI's Relief Assessment Test (6) were used to test soldiers' post-training terrain visualization performance. This paper-and-pencil test was originally developed to assist cartographers in assessing the effects of map design changes. The three selected subtests, each with twelve test items, were:

(1) Landform Identification. The user identifies landforms beneath the tips of arrows overprinted on map segments. The landforms to be identified (hill, valley, spur, depression, and saddle) are illustrated in pencil sketches.

(2) Ridge Valley Identification. The user determines whether lines overprinted on map segments run along: (a) a uniform up slope, (b) a uniform down slope, (c) a convex up slope, or (d) a concave down slope.

(3) Terrain Visualization. The user selects the scene one would see if standing at an arrowtip overprinted on a map segment, looking in the direction shown by the arrow.

Procedure

Spatial Pretest. Soldiers were pretested on the subtests of the spatial test (4) in groups of about seven soldiers prior to training. Administration of the test required one hour. After soldiers completed the tests, arrangements were made for them to return to complete the experiment.

The sample mean and standard deviation of all 60 soldiers' scores on the spatial test were calculated and spatial ability groups were determined from these measures. The high spatial ability group had scores greater than one-half standard deviation above the mean (52-116). Medium ability soldiers had scores greater than one-half standard deviation below the mean but no more than one-half standard deviation above the mean (24-51). Low spatial ability group members had scores less than one-half standard deviation below the mean (0-23). Half the soldiers in each spatial group were randomly assigned to one of the two training conditions, either active or passive.

Training. In groups of about seven, soldiers received a general orientation to the experiment, and completed a biographic information survey about their previous map reading experiences or training, subjective opinion of their perceived ability to read maps and explore unfamiliar areas, as well as information about age, rank, and time in service. Soldiers were all assigned a code number so that the information supplied by the soldiers as well as all experimental scores would be anonymous.

Soldiers were then seated at PLATO terminals in the Education Center, Ft Belvoir, VA, and signed onto the computer system. All lessons and instructions were delivered on-line via a computerized routing sequence. Soldiers were presented with material in a sequenced order with options for reviewing the instructions only. After a lesson was completed, the soldiers were routed directly to the next appropriate lesson.

All soldiers worked on the self-paced Elevation, Relief, and Terrain Features lesson for about one hour. Soldiers then practiced terrain visualization with the version of Interpretation of Contour Lines appropriate to their assigned group, either active or passive, for exactly one hour.

Terrain Visualization Test. After completing all training, all soldiers answered the 36 items from the subtest of the ARI Relief Assessment Test. The test was self-paced and all soldiers completed the test. Testing time ranged from 30 to 150 minutes. Scores on the test, corrected for guessing, served as the measure of soldiers' terrain visualization performance level after training.

RESULTS

Soldiers' adjusted scores on the subtests of Relief Assessment Test are shown in Table 1 as a function of spatial ability and training condition. The data were analyzed using a two-way between-subjects analysis of variance.

AD-A120 813 PROCEEDINGS OF THE 1982 ARMY SCIENCE CONFERENCE HELD AT THE UNITED STATES..(U) DEPUTY CHIEF OF STAFF FOR RESEARCH DEVELOPMENT AND ACQUISITIO.. 18 JUN 82 4/6

UNCLASSIFIED F/G 5/2 NL

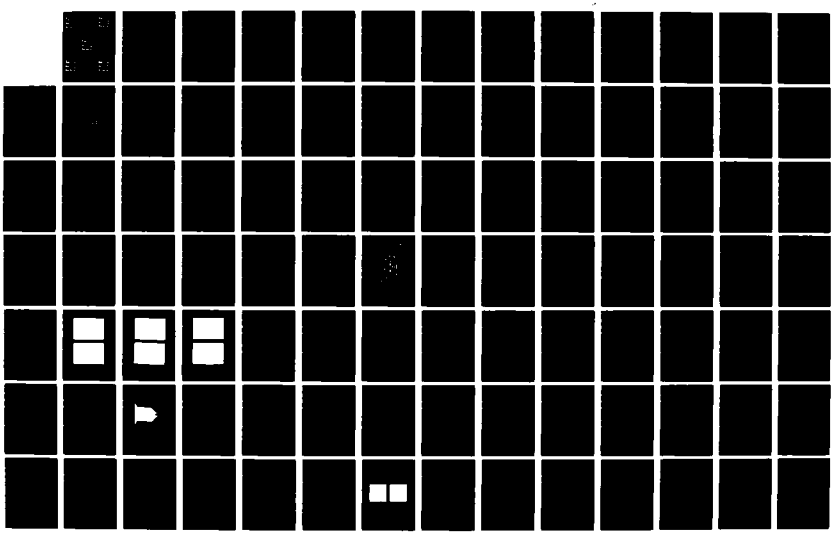

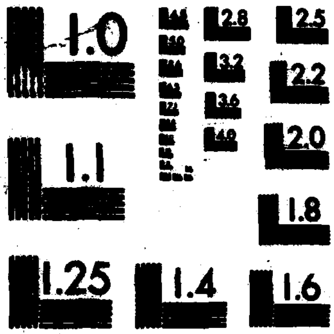

MICROCOPY RESOLUTION TEST CHART
NATIONAL BUREAU OF STANDARDS-1963-A

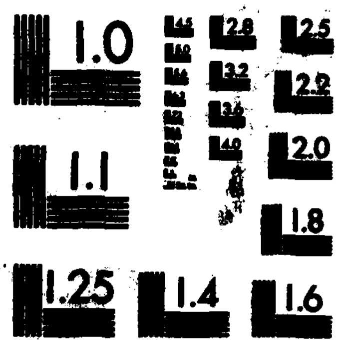

MICROCOPY RESOLUTION TEST CHART
NATIONAL BUREAU OF STANDARDS-1963-A

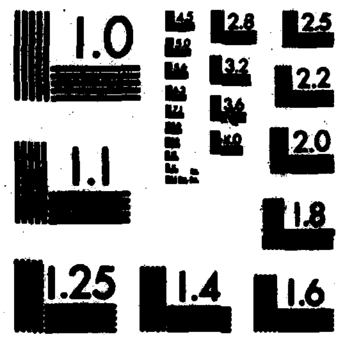

MICROCOPY RESOLUTION TEST CHART
NATIONAL BUREAU OF STANDARDS-1963-A

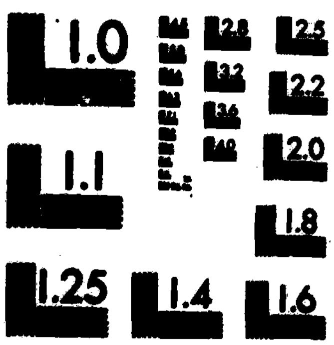

MICROCOPY RESOLUTION TEST CHART
NATIONAL BUREAU OF STANDARDS-1963-A

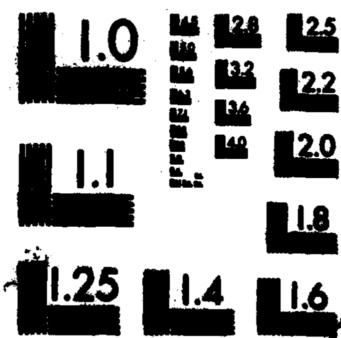

MICROCOPY RESOLUTION TEST CHART
NATIONAL BUREAU OF STANDARDS-1963-A

Because the overall analysis of variance showed a significant interaction between spatial ability and training condition, F (2,54) = 4.42, $p < .02$, tests of simple effects and orthogonal comparisons were performed.

Table 1. Soldiers adjusted scores on the ARI Relief Assessment Subtest as a function of training condition and spatial ability level.[a]

Spatial Ability	Training Condition: Active	Training Condition: Passive
High	17.895	9.508
Medium	5.031	5.648
Low	1.728	1.610

Note. Maximum Score = 36

[a] n = 10 for each cell.

High spatial ability soldiers had higher adjusted scores than medium or low spatial ability soldiers under the active, F (1,54) = 49.63, $p < .001$, and the passive, F (1,54) = 8.14, $p < .001$, terrain visualization training conditions. Although adjusted scores were higher for medium spatial ability soldiers than for low spatial ability soldiers, the differences were not significant under the active, F (1,54) = 1.93 and the passive, F (1,54) = 2.88, training conditions.

High spatial ability soldiers who actively practiced terrain visualization during training had higher adjusted scores than soldiers who passively practiced, F (1,54) = 12.43, $p < .001$. Indeed, for these soldiers active practice resulted in performance almost twice as high as passive practice. Type of practice during terrain visualization training clearly had no effect for medium F (1,54) = .07, or low spatial ability soldiers, F (1,54) = .001.

DISCUSSION

In this research we found effects of spatial abilities and computer-based graphic training techniques on terrain visualization performance. High spatial ability soldiers were better able to perform terrain visualization tasks after two hours of computer-based training and practice than were lower spatial ability soldiers. When high spatial ability soldiers were allowed to actively select the three-dimensional views and ground profiles to be generated by the computer, their performance on terrain visualization tasks nearly doubled. Active practice, however, did not improve the performance of the medium and low spatial ability soldiers. The terrain visualization performance of these soldiers was identical under both training conditions.

One reasonable explanation for these results is as follows: the active practice training group differed from the passive group in that the active group was able to choose the views that they wanted to see rather than simply being presented with random views. This active choice process allowed an individual to impose structure in the learning situation in the absence of any pre-existing structure, but only if the individual had sufficient spatial abilities to select information-rich views. It may be that what was critical to learning in the active terrain visualization practice was not simply being able to choose, but rather the structure itself that resulted from the choosing. For soldiers in the active practice group having high spatial abilities allowed choices that resulted in a reasonably structured learning situation. Because they lacked the same level of visual skills, however, our lower spatial ability soldiers could not make good choices of views to see, so that their choices were essentially random. Furthermore, our high spatial soldiers in the passive condition found it difficult to impose any structure on the learning situation because they only saw random views.

This reasoning suggests an instructional technique that could improve the efficency of computer graphic terrain visualization practice for all spatial ability level soldiers: improve the level of structure inherent to the practice itself. For example, the computer could initially guide soldiers in selecting views, showing them how small changes in cursor position or direction change the terrain display. Using more sophisticated techniques, the computer could individualize the amount and type of structure for soldiers of different spatial ability levels.

It may be, however, that entirely different techniques, as yet unknown, are required to train lower spatial ability soldiers in terrain visualization skills. Lower spatial ability soldiers also may need more time than higher spatial ability soldiers to actively practice terrain visualization skills. Finally, it is possible that lower spatial ability soldiers may never perform as well as high spatial ability soldiers at terrain visualization, no matter how sophisticated the training technique or the technology used to deliver the training.

This research also serves as an example of the need to consider characteristics of trainees and the training methods to be used when investing in a new technology to be used for training. On the surface, using a computer display which allows a soldier to move around on a contour map and see changes in terrain as one travels appears to be a better training technique than showing soldiers points on a contour map with slides (or computer simulations) of associated terrains. Our research has shown that it is, but only for soldiers with high spatial abilities. This does not mean that computer graphics technology is not a viable technology for training terrain visualization to soldiers of lower spatial ability. It means that before optimal use of the technology can be made, we need a better understanding of individual differences in spatial and terrain visualization processes, and development of instructional techniques appropriate to meet these individual differences.

REFERENCES

1. Skop, J. Investigation of user requirements pertinent to relief portrayal. Army Map Service, Corps of Engineers. Final Report, 1958.

2. Army's FORMIDABLE Conference, Ft Benning, GA, February 1978.

3. McGee, M.G. Human spatial abilities: Psychometric studies and environmental, genetic, hormonal, and neurological influences. Psychological Bulletin, 1979, 86, 889-918.

4. Ekstrom, R.B., French, J.W., Harman, H.H., & Dermen, D. Manual for Kit of factor-referenced cognitive tests. Princeton, N.J.: Educational Testing Service, 1976.

5. Smith, S.G., & Sherwood, B.A. Educational uses of the PLATO computer system. Science, 1976, 192, 344-352.

6. Potash, L.M., Farrell, J.P., Jeffery, T. A technique for assessing map relief legibility. The Cartographic Journal, 1978, 15, 28-35.

Calculation on Optical Effect of Matter from First Principles Using Group Theoretical Techniques (U)

Orazio I. Sindoni, Dr.
Chemical Systems Laboratory
Aberdeen Proving Ground, MD 21010

1. INTRODUCTION.

Scattering of light by molecules is commonly dealt with through Rayleigh-Debye theory.[1,2] Such approach is known to be applicable to molecules whose effective index of refraction is close to unity and to imply a number of approximations which may have rather severe effects.[3,6] In this paper we face the problem by adapting the method devised by Johnson,[7] and successfully used to calculate the electronic states of large molecules,[8] to the scattering of electromagnetic waves. Accordingly, we model a molecule as a cluster of spherical scatterers, possibly of different radii and refractive indexes. A plane electromagnetic wave, incident to the cluster, undergoes multiple scatterings which we account for by expanding the scattered wave in a multicentered series of vector harmonics. The expansion coefficients turn out to be the solutions of the system of linear equations obtained by expanding both the incident field and that within the spheres in a series of vector harmonics, and imposing the boundary conditions across the surface. Due to the presence of the incident plane wave, the above system is nonhomogeneous.

The method outlined above does not require any approximation, except for the truncations of the expansions in vector harmonics, in order to get a system of finite order. For large clusters and for convergency reasons, however, one might have to solve rather large systems. Anyway, if the cluster possesses symmetry properties, as is the case for actual molecules, one can use group theoretical techniques to get the system in factorized form. By expanding both the incident and the scattered field in symmetry-adapted combinations of vector harmonics, indeed, the system factorizes in much the same way as quantum mechanical secular equations,[9] except that the inhomogeneous terms are not independent of the row index of the multidimensional irreducible representations. As a consequence, we have to solve all the systems arising out of the factorization procedure. It will become apparent, however, that this peculiarity of the present problem does not cancel the undoubted advantages of the group theoretical techniques.

2. MULTIPOLAR EXPANSION OF THE FIELD.

The cluster whose scattering properties we want to study is composed of N non-magnetic spheres whose centers lie at $\underset{\sim}{R}_\alpha$ and whose radii and (possibly complex) refractve indices are b_α and n_α, respectively. We refer the cluster to a fixed set of axes and choose the direction of incidence of the incoming plane wave through direction cosines of its wavevector. A straightforward calculation along the lines sketched by Jackson[10] allows us to write the field of a circularly polarized plane wave of wavevector $\underset{\sim}{k}$ as

$$\underset{\sim}{E}_\eta^{(i)} = \sum_{LM} W_{\eta LM}(\hat{k})[j_L(kr)\underset{\sim}{X}_{LM}(\hat{r}) + \eta\frac{1}{k}\nabla\times j_L(kr)\underset{\sim}{X}_{LM}(\hat{r})] \tag{2-1a}$$

$$i\underset{\sim}{B}_\eta^{(i)} = \eta\underset{\sim}{E}_\eta^{(i)} \tag{2-1b}$$

with $\eta = \pm 1$ according to the polarization and

$$W_{\eta LM}(\hat{k}) = 4\pi i^L(\underset{\sim}{e}_1 + i\eta\underset{\sim}{e}_2)\cdot\underset{\sim}{X}^*_{LM}(\hat{k}) \tag{2-2}$$

where $\underset{\sim}{e}_1$ and $\underset{\sim}{e}_2$ are unit vectors orthogonal to $\underset{\sim}{k}$ and to each other. In the above equations the vector spherical harmonics, $\underset{\sim}{X}_{LM}$, are defined according to Jackson.[10]

The field scattered by the cluster is expanded in a multicentered series of multipoles including only outgoing spherical waves at infinity:

$$\underset{\sim}{E}_\eta^{(s)} = \sum_\alpha\sum_{LM}[A^\alpha_{\eta LM}h_L(kr_\alpha)\underset{\sim}{X}_{LM}(\hat{r}_\alpha) + B^\alpha_{\eta LM}\frac{1}{k}\nabla\times h_L(kr_\alpha)\underset{\sim}{X}_{LM}(\hat{r}_\alpha)] \tag{2-3a}$$

$$i\underset{\sim}{B}_\eta^{(s)} = \sum_\alpha\sum_{LM}[B^\alpha_{\eta LM}h_L(kr_\alpha)\underset{\sim}{X}_{LM}(\hat{r}_\alpha) + A^\alpha_{\eta LM}\frac{1}{k}\nabla\times h_L(kr_\alpha)\underset{\sim}{X}_{LM}(\hat{r}_\alpha)] \tag{2-3b}$$

with $\underset{\sim}{r}_\alpha = \underset{\sim}{r} - \underset{\sim}{R}_\alpha$. The superscript(1) on the spherical Hankel functions of the first kind will be omitted throughout for simplicity. As regards the field within the spheres we remark that the present theory is not restricted to homogeneous spheres, provided the n_α's are spherically symmetric. Therefore, within the α - th sphere we can write[11]

$$\underset{\sim}{E}_\eta^{(t)\alpha} = \sum_{LM}[C^\alpha_{\eta LM}R^\alpha_L(r_\alpha)\underset{\sim}{X}_{LM}(\hat{r}_\alpha) + \frac{1}{n_\alpha^2}D^\alpha_{\eta LM}\frac{1}{k}\nabla\times S^\alpha_L(r_\alpha)\underset{\sim}{X}_{LM}(\hat{r}_\alpha)] \tag{2-4a}$$

$$i\underset{\sim}{B}_\eta^{(t)\alpha} = \sum_{LM}[D^\alpha_{\eta LM}S^\alpha_L(r_\alpha)\underset{\sim}{X}_{LM}(\hat{r}_\alpha) + C^\alpha_{\eta LM}\frac{1}{k}\nabla\times R^\alpha_L(r_\alpha)\underset{\sim}{X}_{LM}(\hat{r}_\alpha)] \tag{2-4b}$$

where R_L^α and S_L^α are the solutions, regular at $r_\alpha = 0$, of the equations

$$\left[\frac{d^2}{dr_\alpha^2} - \frac{L(L+1)}{r_\alpha^2} + k^2 n_\alpha^2\right](r_\alpha R_L^\alpha) = 0 \qquad (2\text{-}5a)$$

and

$$\left[\frac{d^2}{dr_\alpha^2} - \frac{2}{r_\alpha n_\alpha}\frac{dn_\alpha}{dr_\alpha}\frac{d}{dr_\alpha} - \frac{L(L+1)}{r_\alpha^2} + k^2 n_\alpha^2\right](r_\alpha S_L^\alpha) = 0 \qquad (2\text{-}5b)$$

respectively. Of course, for uniform n_α's, $R_L^\alpha(r_\alpha) \equiv S_L^\alpha(r_\alpha) \equiv j_L(K_\alpha r_\alpha)$ with $K_\alpha = kn_\alpha$.

3. SYMMETRY ADAPTED MULTIPOLAR EXPANSION OF THE FIELD

The expansion coefficients in equations (2-3) and (2-4) are solutions of the system of linear nonhomogeneous equations obtained by imposing on $\underset{\sim}{E}$ and $\underset{\sim}{B}$ the customary boundary conditions at the surface of each one of the spheres. However, by first exploiting the symmetry properties of the cluster and thus putting equations (2-1) and (2-3) in symmetry-adapted form, we shall get the above system in factorized form.

First of all we partition the cluster into sets of spheres which are transformed into each other by the symmetry operations. This does not imply renumbering of the spheres but only association of each site index, α, to the appropriate set index, σ. Then we construct symmetrized combinations out of the vector harmonics centered at the sites of each set. To this end we remark that if $f_L(kr)$ is a spherical Bessel or Hankel function then

$$f_L(kr)\underset{\sim}{X}_{LM}(\hat{r}) = -f_L(k\hat{r})\underset{\sim}{T}_{LL}^{M}(\hat{r}) \qquad (3\text{-}1a)$$

$$\nabla\times f_L(kr)\underset{\sim}{X}_{LM}(\hat{r}) = -ik\left[\sqrt{\frac{L+1}{2L+1}}f_{L+1}\underset{\sim}{T}_{LL+1}^{M} - \sqrt{\frac{L+1}{2L+1}}f_{L-1}\,\underset{\sim}{T}_{LL-1}^{M}\right] \qquad 3\text{-}1b)$$

the $\underset{\sim}{T}$'s being irreducible spherical tensors.[12] Therefore, both the magnetic and the electric 2^L-pole fields transform according to the representation $D^{(L)}$ of the full rotation group.[12,13,27] Accordingly, let S be a symmetry operation such that

$$S\underset{\sim}{R}_\alpha = \underset{\sim}{R}_\beta$$

with α and β in the same set, of course, and let O_s be the associated operator, then[14] if S is a proper rotation

$$O_s f_L(kr_\alpha)\underset{\sim}{X}_{LM}(\hat{r}_\alpha) = f_L(kr_\beta)\sum_{M'} D_{M'M}^{(L)}(S)\underset{\sim}{X}_{LM'}(\hat{r}_\beta) \qquad (3\text{-}2a)$$

$$O_s\nabla\times f_L(kr_\alpha)\underset{\sim}{X}_{LM}(\hat{r}_\alpha) = \sum_{M'}\nabla\times f_L(kr_\beta)D_{M'M}^{(L)}(S)\underset{\sim}{X}_{LM'}(\hat{r}_\beta). \qquad (3\text{-}2b)$$

However, if S is an improper rotation one must take into account that the parity of $f_L \underset{\sim}{X}_{LM}$ is $(-)^L$ while that of $\nabla \times f_L \underset{\sim}{X}_{LM}$ is $(-)^{L+1}$. Therefore for improper rotations, the right-hand side of equation of (3-2a) must be multiplied by $(-)^L$ and the right-hand side of equation (3-2b) by $(-)^{L+1}$ and the argument in $D^{(L)}_{M'M}$ must be understood as the proper rotational part of S. As a consequence, if the symmetry group of the cluster also includes harmonics belonging to the rows of the ν-th irreducible representation, one has to apply the projection operators[15,16]

$$P^{\nu}_{pq} = \frac{g_\nu}{g}\sum_S D^{(\nu)*}_{pq}(S)O_S \tag{3-3}$$

both to the magnetic and the electric 2^L poles. Thus we can write

$$\underset{\sim}{H}^{\nu p\sigma}_{NL} = \sum_{\alpha\in\sigma}\sum_{M\in N} a^{\nu p\alpha}_{NLM} h_L(kr_\alpha)\underset{\sim}{X}_{LM}(\hat{\underset{\sim}{r}}_\alpha) \tag{3-4a}$$

$$\underset{\sim}{K}^{\nu p\sigma}_{N'L} = \sum_{\alpha\in\sigma}\sum_{\bar{M}\in N'} b^{\nu p\alpha}_{N'L\bar{M}} \frac{1}{k}\, \nabla\times h_L(kr_\alpha)\underset{\sim}{X}_{LM}(\hat{\underset{\sim}{r}}_\alpha) \tag{3-4b}$$

for the combinations of magnetic and electric 2^L poles, respectively, centered at the sites of the σ-th set. The superscripts ν, p indicate that the combination belongs to the p-th row of the ν-th irreducible representation and the index N recalls, when appropriate, that one can get more than one set of basis functions for a given L. The scattered field can thus be written in symmetrized form as

$$\underset{\sim}{E}^{S}_{\eta} = \sum_{\nu p}\sum_{\sigma L}\left[\sum_N A^{\nu p\sigma}_{\eta NL}\,\underset{\sim}{H}^{\nu p\sigma}_{NL} + \sum_{N'} B^{\nu p\sigma}_{\eta N'L}\,\underset{\sim}{K}^{\nu p\sigma}_{N'L}\right] \tag{3-5a}$$

the corresponding expression for $i\underset{\sim}{B}^{(s)}_{\eta}$ being obtained through the Maxwell equation $i\underset{\sim}{B} = \frac{1}{k}\nabla\times\underset{\sim}{E}$; the index η denotes the polarization as in the preceding section.
Comparison of equation (3-5) with equation (2-3) shows that

$$\sum_{\nu p}\sum_N A^{\nu p\sigma}_{\eta NL} a^{\nu p\alpha}_{NLM} = A^{\alpha}_{\eta LM}\ ,\ \sum_{\nu p}\sum_N B^{\nu p\sigma}_{\eta NL} b^{\nu p\alpha}_{NLM} = B^{\alpha}_{\eta LM} \tag{3-6}$$

Furthermore, since we work with unitary irreducible representations, as shown by the structure of the operators, equation (3-3), the coefficients $a^{\nu p\alpha}_{NLM}$ have the property

$$\sum_{\alpha\in\sigma}\sum_M (a^{\nu p\alpha}_{NLM})^* a^{\nu p\alpha}_{N'LM} = \delta_{NN'}\ ,\sum_{\alpha\in\sigma}\sum_M (b^{\nu p\alpha}_{NLM})^* b^{\nu p\alpha}_{N'LM} = \delta_{NN'} \tag{3-7}$$

Now we have to decompose the incident field into parts belonging to the rows of irreducible representations of the symmetry group of the cluster. This is easily done for the projection operators, equation (3-3), have the completeness property[15,16]

$$\sum_{\nu}\sum_{p} \mathcal{P}^{\nu}_{pp} = 1 \tag{3-8}$$

Thus we can write

$$\begin{aligned} \underset{\sim}{E}^{(i)}_{n} &= \sum_{LM} W_{\eta LM}(\hat{\underset{\sim}{k}}) \sum_{\nu p}\left[\mathcal{P}^{\nu}_{pp}\, j_L(kr)\underset{\sim}{X}_{LM}(\hat{\underset{\sim}{r}}) + \eta \frac{1}{k}\mathcal{P}^{\nu}_{pp}\nabla\times j_L(kr)\underset{\sim}{X}_{LM}(\hat{\underset{\sim}{r}})\right] \\ &= \sum_{\nu p}\sum_{LM} W_{\eta LM}(\hat{\underset{\sim}{k}})\left[\underset{\sim}{J}^{\nu p}_{LM} + \eta \underset{\sim}{L}^{\nu p}_{LM}\right], \end{aligned} \tag{3-9}$$

and an analgous equation for $i\underset{\sim}{B}^{(i)}_{n}$, where

$$\begin{aligned} \underset{\sim}{J}^{\nu p}_{LM} &= \frac{g_\nu}{g}\sum_{S} D^{(\nu)*}_{pp}(S)\sum_{M'} D^{(L)}_{M'M}(S) j_L(kr)\underset{\sim}{X}_{LM'}(\hat{\underset{\sim}{r}}) \\ &= \sum_{M'} c^{\nu p}_{LMM'}\, j_L(kr)\underset{\sim}{X}_{LM'}(\hat{\underset{\sim}{r}}) \end{aligned}$$

and

$$\underset{\sim}{L}^{\nu p}_{LM} = \sum_{M'} A^{\nu p}_{LMM'} \frac{1}{k}\nabla\times j_L(kr)\underset{\sim}{X}_{LM'}(\hat{\underset{\sim}{r}}).$$

This completes the symmetrization procedure because equation (2-4) need not be symmetrized for reasons that will become clear in the next section.

4. EQUATIONS FOR THE COEFFICIENTS

We are now able to write the equations for the coefficients $A^{\nu p\sigma}_{\eta NL}$ and $B^{\nu p\sigma}_{\eta NL}$ of the scattered wave, equation (3-5), by imposing to $\underset{\sim}{E}$ and $\underset{\sim}{B}$ the appropriate boundary conditions at the surface of each one of the spheres. To this end we rewrite equations (3-5) and (3-9) in terms of vector harmonics centered at a single site, say $\underset{\sim}{R}_{\alpha}$, through the use of the appropriate addition theorems.[17,18] Indeed, near the surface of the α-th sphere belonging to the σ-th set we have

$$\begin{aligned} \underset{\sim}{E}^{(s)}_{n} = \sum_{\nu p\sigma}\sum_{L}\Bigg\{ & \sum_{N} A^{\nu p\sigma}_{\eta NL}\sum_{M\in N} a^{\nu p\alpha}_{NLM} h_L(kr_\alpha)\underset{\sim}{X}_{LM}(\hat{\underset{\sim}{r}}_\alpha) + \sum_{N'} B^{\nu p\sigma}_{\eta N'L}\sum_{\bar{M}\in N'} b^{\nu p\alpha}_{N'L\bar{M}}\frac{1}{k}\nabla\times h_L(kr_\alpha)\underset{\sim}{X}_{L\bar{M}}(\hat{\underset{\sim}{r}}_\alpha) \\ & + \sum_{N}\sum_{\tau} A^{\nu p\tau}_{\eta NL}\sum_{\beta\in\tau}\sum_{M\in N} a^{\nu p\beta}_{NLM}\sum_{L'M'}\left[H^{\alpha\beta}_{L'M'LM}\, j_{L'}(kr_\alpha)\underset{\sim}{X}_{L'M'}(\hat{\underset{\sim}{r}}_\alpha) + K^{\alpha\beta}_{L'M'LM}\frac{1}{k}\nabla\times j_{L'}(kr_\alpha)\underset{\sim}{X}_{L'M'}(\hat{\underset{\sim}{r}}_\alpha)\right] \\ & + \sum_{\tau}\sum_{N'} B^{\nu p\tau}_{\eta N'L}\sum_{\beta\in\tau}\sum_{\bar{M}\in N'} b^{\nu p\beta}_{N'L\bar{M}}\left[K^{\alpha\beta}_{L'M'L\bar{M}}\, j_{L'}(kr_\alpha)\underset{\sim}{X}_{L'M'}(\hat{\underset{\sim}{r}}_\alpha) + H^{\alpha\beta}_{L'M'L\bar{M}}\frac{1}{k}\nabla\times j_{L'}(kr_\alpha)\underset{\sim}{X}_{L'M'}(\hat{\underset{\sim}{r}}_\alpha)\right]\Bigg\} \end{aligned} \tag{4-1}$$

$$\begin{aligned} \underset{\sim}{E}^{(i)}_{n} = \sum_{LM} W_{\eta LM}(\hat{\underset{\sim}{k}})\sum_{\nu p}\sum_{M'}\Bigg\{ & c^{\nu p}_{LMM'}\sum_{L''M''}\left[J^{\alpha}_{L''M''LM'}\, j_{L''}(kr_\alpha)\underset{\sim}{X}_{L''M''}(\hat{\underset{\sim}{r}}_\alpha) + L^{\alpha}_{L''M''LM'}\frac{1}{k}\nabla\times j_{L''}(kr_\alpha)\underset{\sim}{X}_{L''M''}(\hat{\underset{\sim}{r}}_\alpha)\right] \\ & + \eta d^{\nu p}_{LMM'}\sum_{L''M''}\left[L^{c}_{L''M''LM'}\, j_{L''}(kr_\alpha)\underset{\sim}{X}_{L''M''}(\hat{\underset{\sim}{r}}_\alpha) + J^{\alpha}_{L''M''LM'}\frac{1}{k}\nabla\times j_{L''}(kr_\alpha)\underset{\sim}{X}_{L''M''}(\hat{\underset{\sim}{r}}_\alpha)\right]\Bigg\} \end{aligned} \tag{4-2}$$

and analogous expressions for $i\underset{\sim}{B}_\eta^{(s)}$ and $i\underset{\sim}{B}_\eta^{(i)}$. In equation (4-1) we define

$$H^{\alpha\beta}_{L'M'LM} = (1-\delta_{\alpha\beta})\sum_\mu C(1,L',L';-\mu,M'+\mu)4\pi\sum_\lambda i^{L'-L-\lambda} I_\lambda(L',M'+\mu;L,M+\mu)$$

$$\times\, h_\lambda(kR_{\alpha\beta})Y^*_{\lambda M'-M}(\hat{\underset{\sim}{R}}_{\alpha\beta})C(1,L,L;-\mu,M+\mu) \qquad (4\text{-}3a)$$

$$K^{\alpha\beta}_{L'M'LM} = -i\sqrt{\frac{2L'+1}{L'}}\,(1-\delta_{\alpha\beta})\sum_\mu C(1,L',L'+1;-\mu,M'+\mu)4\pi\sum_\lambda i^{L'-L-\lambda+1}$$

$$\times\, I_\lambda(L'+1,M'+\mu;L,M+\mu)h_\lambda(kR_{\alpha\beta})Y^*_{\lambda M'-M}(\hat{\underset{\sim}{R}}_{\alpha\beta})C(1,L,L;-\mu,M+\mu) \qquad (4\text{-}3b)$$

with $\underset{\sim}{R}_{\alpha\beta} = \underset{\sim}{R}_\beta - \underset{\sim}{R}_\alpha$, while in equation (4-2) $J^\alpha_{L'M'LM}$ and $L^\alpha_{L'M'LM}$ are identical to $H^{\alpha\beta}_{L'M'LM}$ and $K^{\alpha\beta}_{L'M'LM}$ respectively but for the substitution of j_λ to h_λ and $\underset{\sim}{R}_\beta=0$. The quantities

$$I_\lambda(L'M';LM) = \int Y^*_{L'M'}\,Y_{LM}Y_{\lambda M'-M}d\Omega$$

are the well-known Gaunt integrals.[19]
Now, taking the dot product of equations (4-1), (4-2) and (2-4) in turn with $\underset{\sim}{r}_\alpha\, Y^*_{\ell m}(\underset{\sim}{r}_\alpha)$ and $\underset{\sim}{r}_\alpha \times \underset{\sim}{X}^*_{\ell m}(\underset{\sim}{r}_\alpha)$ we get the radial and the tangential components of the field at the surface of the α-th sphere. Imposition of the boundary conditions and integration over the angles yields, for each ℓ,m six equations among which the coefficients of the internal field, $C^\alpha_{\eta\ell m}$ and $D^\alpha_{\eta\ell m}$, are easily eliminated. This circumstance, on one hand clarifies the inessentiality of the symmetrization of the internal field, and on the other hand yields, for each ν, p, r_α a system involving only the A's and B's as unknowns:

$$\sum_\tau\sum_{\beta\epsilon\tau}\sum_L\left\{\sum_N\sum_{M\epsilon N}\left(\delta_{L\ell}\delta_{Mm}\delta_{\sigma\beta}\left[R^\beta_L\right]^{-1} + H^{\alpha\beta}_{\ell m LM}\right)a^{\nu p\beta}_{NLM}A^{\nu p\beta}_{NL} + \sum_{N'}\sum_{\bar{M}\epsilon N'}K^{\alpha\beta}_{\ell m L\bar{M}}\, b^{\nu p\beta}_{N'L\bar{M}}B^{\nu p\tau}_{\eta N'L}\right\}$$

$$= -\sum_{LM}\sum_{M'}W_{\eta LM}(\hat{\underset{\sim}{k}})\left[\eta c^{\nu p}_{LMM'}L^\alpha_{\ell m LM'} + d^{\mu p}_{LMM'}J^\alpha_{\ell m LM'}\right] \qquad (4\text{-}4a)$$

$$\sum_\tau\sum_{\beta\epsilon\tau}\sum_L\left\{\sum_{N'}\sum_{\bar{M}\epsilon N'}\left(\delta_{L\ell}\delta_{Mm}\delta_{\sigma\beta}\left[S^\beta_L\right]^{-1} + H^{\alpha\beta}_{\ell m L\bar{M}}\right)b^{\nu p\beta}_{N'L\bar{M}}B^{\nu p\beta}_{\eta N'L} + \sum_N\sum_{M\epsilon N}K^{\alpha\beta}_{\ell m LM}\,a^{\nu p\beta}_{NLM}A^{\nu p\tau}_{\eta NL}\right\}$$

$$= -\sum_{LM}\sum_{M'}W_{\eta LM}(\hat{\underset{\sim}{k}})\left[c^{\nu p}_{LMM'}L^\alpha_{\ell m LM'} + \eta d^{\mu p}_{LMM'}J^\alpha_{\ell m LM'}\right] \qquad (4\text{-}4b)$$

where we define

$$R_\ell^\alpha = \left[\frac{j_\ell(kr_\alpha)\frac{d}{dr_\alpha}(r_\alpha R_\ell^\alpha) - R_\ell^\alpha\frac{d}{dr_\alpha}(r_\alpha j_\ell(kr_\alpha))}{h_\ell(kr_\alpha)\frac{d}{dr_\alpha}(r_\alpha R_\ell^\alpha) - R_\ell^\alpha\frac{d}{dr_\alpha}(r_\alpha j_\ell(kr_\alpha))}\right]_{r_\alpha=b_\alpha} \qquad (4\text{-}5a)$$

$$S_\ell^\alpha = \left[\frac{j_\ell(kr_\alpha)\frac{d}{dr_\alpha}(r_\alpha S_\ell^\alpha) - n_\alpha^2 S_\ell^\alpha\frac{d}{dr_\alpha}(r_\alpha j_\ell(kr_\alpha))}{h_\ell(kr_\alpha)\frac{d}{dr_\alpha}(r_\alpha S_\ell^\alpha) - n_\alpha^2 S_\ell^\alpha\frac{d}{dr_\alpha}(r_\alpha h_\ell(kr_\alpha))}\right]_{r_\alpha=b_\alpha} \qquad (4\text{-}5b)$$

Since the spheres within a set are identical to each other, R_ℓ^α and S_ℓ^α do not actually depend on α but only on the set index, σ. Therefore, from now on these quantities will be indicated by R_ℓ^σ and S_ℓ^σ, respectively. Equation (4-4) can be put in a more symmetrical form through the use of equation (3-6). Indeed, multiplication of equation (4-4a) by $(a_{n\ell m}^{\nu p\alpha})^*$, and of equation (4-4b) by $(b_{n\ell m}^{\nu p\alpha})^*$, and summation over the α's belonging to the σ-th set and over m yield for each ν, p, τ the equations

$$\sum_s \delta_{rs}\left[R_s\right]^{-1} + H_{rs}^{\nu}(m)\, A_{ns}^{\nu p} + \sum_{s'} K_{rs'}^{\nu}(m,e)\, B_{ns'}^{\nu p} = -P_{nr}^{\nu p} \qquad (4\text{-}7a)$$

$$\sum_{s'}\left(\delta_{r's'}\left[S_{s'}\right]^{-1} + H_{r's'}^{\nu}(e)\right) B_{ns'}^{\nu p} + \sum_s K_{r's}^{\nu}(e,m)\, A_{ns}^{\nu p} = -Q_{nr'}^{\nu p} \qquad (4\text{-}7b)$$

In equation (4-7) we put, for the sake of simplicity,

$$r \equiv (\sigma,\ell,n),\ s \equiv (\tau,L,N),\ r' \equiv (\sigma,\ell,n'),\ s' \equiv (\tau,L,N')$$

and define

$$H_{rs}^{\nu}(m) = \sum_{\alpha m}\sum_{\beta M}(a_{n\ell m}^{\nu p\alpha})^* H_{\ell mLM}^{\alpha\beta}\, a_{NLM}^{\nu p\beta} \qquad (4\text{-}8)$$

$$K_{rs}^{\nu}(m,e) = \sum_{\alpha m}\sum_{\beta M}(a_{n\ell m}^{\nu p\alpha})^* K_{\ell mLM}^{\alpha\beta}\, b_{NLM}^{\nu p\beta} \qquad (4\text{-}9)$$

with an obvious meaning of the parameters e, m. The quantities $H_{rs}^{\nu}(e)$ and $K_{rs}^{\nu}(m,e)$ are identical to $H_{rs}^{\nu}(m)$ and $K_{rs}^{\nu}(e,m)$ respectively, except for the mutual exchange of the a's with the b's.
Moreover

$$P_{nr}^{\nu p} \sum_{LN}\sum_{\alpha m}\sum_{M'} W_{nLN}(\hat{k})\left[nc_{LMM'}^{\nu p}\, L_{\ell mLM'}^{\alpha} + d_{LMM'}^{\nu p}\, J_{\ell mLM'}^{\alpha}\right]\left(a_{n\ell m}^{\nu p\alpha}\right)^*$$

$$Q_{nr'}^{\nu p} = \sum_{LN}\sum_{\alpha m}\sum_{M'} W_{nLN}(\hat{k})\left[c_{LMM'}^{\nu p}\, L_{\ell mLM'}^{\alpha} + nd_{LMM'}^{\nu p}\, J_{\ell mLM'}^{\alpha}\right]\left(b_{n'\ell m}^{\nu p\alpha}\right)^*$$

We remark that in equations (4-7) and (4-8) the superscript p on

$\tilde{H}$ and $\tilde{K}$ is missing. As will be shown later, these quantities are actually independent of the row index so that p has been dropped.

5. THE CROSS SECTIONS

Once the coefficients $\mathcal{A}_n^{\nu p\sigma}$ and $\mathcal{B}_n^{\nu p\sigma}$ are known, all the scattering properties of the cluster can easily be calculated. For this purpose, symmetry is not essential and we can revert to the unsymmetrized expansion of the scattered field through equation (3-6). It is convenient to express the scattered field in terms of vector harmonics centered at a single point through the addition theorem already used in the preceding section.[18] If $\underset{\sim}{R}_o$ is the vector position of the chosen point and $\underset{\sim}{r}_o = \underset{\sim}{r} - \underset{\sim}{R}_o$

$$\underset{\sim}{E}_n^{(s)} = \sum_\alpha\sum_{LM} \Bigg\{ A^\alpha_{nLM} \sum_{L'M'} \left[\mathcal{J}^{0\alpha}_{L'M'LM}\, h_{L'}(kr_0)\underset{\sim}{X}_{L'M'}(\hat{\underset{\sim}{r}}_0) + \mathcal{L}^{0\alpha}_{L'M'LM}\, \frac{1}{k}\nabla\times h_{L'}(kr_0)\underset{\sim}{X}_{L'M'}(\hat{\underset{\sim}{r}}_0) \right]$$

$$+ B^\alpha_{nLM} \sum_{L'M'} \left[\mathcal{L}^{0\alpha}_{L'M'LM}\, h_{L'}(kr_0)\underset{\sim}{X}_{L'M'}(\hat{\underset{\sim}{r}}_0) + \mathcal{J}^{0\alpha}_{L'M'LM}\, \frac{1}{k}\nabla\times h_{L'}(kr_0)\underset{\sim}{X}_{L'M'}(\hat{\underset{\sim}{r}}_0) \right] \Bigg\}$$

$$= \sum_{L'M'} \left\{ \tilde{A}_{nL'M'}\, h_{L'}(kr_0)\underset{\sim}{X}_{L'M'}(\hat{\underset{\sim}{r}}_0) + \tilde{B}_{nL'M'}\, \frac{1}{k}\nabla\times h_{L'}(kr_0)\underset{\sim}{X}_{L'M'}(\hat{\underset{\sim}{r}}_0) \right\} \tag{5-1}$$

and an analogous expression for $i\underset{\sim}{B}_n^{(s)}$ with

$$\tilde{A}_{nL'M'} = \sum_\alpha\sum_{LM} \left[A^\alpha_{nLM}\mathcal{J}^{0\alpha}_{L'M'LM} + B^\alpha_{nLM}\mathcal{L}^{0\alpha}_{L'M'LM} \right] \tag{5-2a}$$

$$\tilde{B}_{nL'M'} = \sum_\alpha\sum_{LM} \left[A^\alpha_{nLM}\mathcal{L}^{0\alpha}_{L'M'LM} + B^\alpha_{nLM}\mathcal{J}^{0\alpha}_{L'M'LM} \right] \tag{5-2b}$$

$\mathcal{J}^{o\alpha}_{L'MLM}$ and $\mathcal{L}^{o\alpha}_{L'M'LM'}$ are given by equation (4-3) but for the substitution of j_λ to h_λ. Equation (5-1) is valid provided that $r_o > R_{o\alpha} \equiv |\underset{\sim}{R}_\alpha - \underset{\sim}{R}_o|$, i.e., in the region outside a sphere centered at $\underset{\sim}{R}_o$ and including the whole cluster. Therefore choosing $\underset{\sim}{R}_o = 0$ and thus letting the center of the expansion (5-1) coincide with the center of symmetry of the cluster, the radius of the above sphere is minimized. Anyway the coefficients $\tilde{A}$ and $\tilde{B}$, unlike those of the field scattered by a single sphere, depend on the direction of the incident wavevector, $\underset{\sim}{k}$. As a consequence all the quantities of interest depend both on $\underset{\sim}{k}$ and on the scattered wavevector, $\underset{\sim}{k}_s = k\underset{\sim}{r}$, except, of course, the scattering, absorbtion and total cross-sections which depend only on $\underset{\sim}{k}$. A straightforward calculation shows, in fact, that

$$\sigma_n^{(s)} = \frac{2\pi^2}{k^2} \sum_{L'M'} \left\{ |\tilde{A}_{nL'M'}|^2 + |\tilde{B}_{nL'M'}|^2 \right\} \tag{5-3a}$$

$$\sigma_\eta^{(abs)} = \frac{2\pi^2}{k^2} \sum_{L'M'} \left\{ 2|W_{\eta L'M'}|^2 - |\tilde{A}_{\eta L'M'} + W_{\eta L'M'}|^2 - |\tilde{B}_{\eta L'M'} + W_{\eta L'M'}|^2 \right\} \quad (5\text{-}3b)$$

$$\sigma_\eta^{(tot)} = \frac{4\pi^2}{k^2} \sum_{L'M'} \mathrm{Re} \left\{ W^*_{\eta L'M'} (\tilde{A}_{\eta L'M'} + \tilde{B}_{\eta L'M'}) \right\} \quad (5\text{-}3c)$$

Finally, we notice that the cross sections depend on the polarization of the incident wave, η, as explicitly indicated in equation (5-3).

6. DISCUSSION

In the preceding sections we used group theory to put the system for the coefficients of the scattered wave in factorized form. Let us now rewrite equation (4-7) matrixwise as

$$\begin{vmatrix} \underset{\sim}{R}^{-1} + \underset{\sim}{H}^{\nu}(m) & \underset{\sim}{K}^{\nu}(m,e) \\ \underset{\sim}{K}^{\nu}(e,m) & \underset{\sim}{S}^{-1} + \underset{\sim}{H}^{\nu}(e) \end{vmatrix} \begin{vmatrix} A^{\nu p} \\ B^{\nu p} \end{vmatrix} = \begin{vmatrix} P^{\nu p} \\ Q^{\nu p} \end{vmatrix} \quad (6\text{-}1)$$

in self explanatory notation. Clearly the dependence on p of the right-hand side of equation (6-1) forces us to solve all the systems arising from the factorization procedure. Nevertheless, the matrix on the left-hand side of equation (6-1) does not depend on p, just as in the case of a secular problem. The p-independence of R and S, indeed, follows from their very definition, equation (4-5). These quantities occur even in the theory of electromagnetic scattering from a single sphere[20] and are the electromagnetic analog of the elements of the transition-matrix in quantum scattering theory.[21] $\underset{\sim}{H}^{\nu}$ and $\underset{\sim}{K}^{\nu}$, in turn are the symmetrized counterparts of and , equation (4-3), which are the matrix elements in the site and angular momentum representation of G, the dyadic Green's function for free space propagation of spherical vector waves. The p-independence of $\underset{\sim}{H}$ and $\underset{\sim}{K}$ is then a direct consequence of the invariance of $\underset{\sim}{G}$ under the symmetry operations. Therefore, the matrix on the left of equation (6-1), which can be interpreted as the inverse of the transition matrix for the whole cluster,[22] turns out to be independent of p. This circumstance greatly reduces the computational work in the case of multidimensional irreducible representations. Anyway the computational work needed to solve our scattering problem depends on the number of spheres in the cluster and on the number of L-values included in the expansion of the scattered field, equation (2-3) or (3-5). For a cluster of N spheres and including multipoles up to the order L_M, the dimension of the unsymmetrized system is $d = 2N(L_M + 1)^2 - 2N$, while if group theory is used, the order of the factorized systems depends on the group of the cluster. As an example let us consider a cluster of 5 spheres with point group T_d (the SO_4^{--}, CH_4 molecules have just this structure). Table 1 shows the order of the symmetrized systems and that of the unsymmetrized one for values of L up to 4. Anyway, from the work of Mie[23] and of Debye[24] we know that, for a sphere of radius, b, $L_M = 1$ is quite sufficient for a good description of the scattered field, provided that $Kb \ll 1$. Now, since our cluster is meant to modellize a molecule, the radius of the spheres can hardly exceed 3 Å so that in the visible and infrared range $Kb_\alpha < 10^{-3}$ for any α. Therefore, even allowing for the effect of multiple-scatterings, $L_M = 3$ should be quite sufficient to achieve fairly converged values of the scattered field.

Table 1

L_M	1	2	3	4
A_1	1	2	6	10
A_2	1	2	6	10
E	2	8	12	20
F_1	4	10	19	30
F_2	4	10	19	30
U	30	80	150	240

Dimension of the symmetrized and unsymmetrized systems for L_M up to 4 for a cluster of 5 spheres with a point group Td. The entry U means unsymmetrized while the other entries indicate the irreducible representations in the notation of Hamermesh.[15]

7. COMPUTER CODES

The method described has been implemented through computer algorithms whose practical application we briefly describe. The first code has a main program named SYMULT and subroutines PRMUTE, PRJECT, FUNCTION DL, PRJPW, ORTHOG. The second main program, named MUSCA, has subroutines RESYCO, REPAPW, GHMT, GJMT, GHGK, GIGL, SHMME, SKMME, SPQ, MULAM, CROSSE, CMES, ZOTS, WLM, RSINV, AUXIL, FUNCTION DCLEB, RBF, RNF, CBF, POLAR, SPHAR, DCMLIN, COMPLEX FUNCTION DCDOT.

SYMULT only reads the input data and calls the subroutines, which actually perform the mathematical computations, and finally prints the output, which consists of the following quantities:

1. Names of the operations for the group, , with the corresponding parameters: ω, angle of rotation, λ, μ, ν direction cosines; and the permutations induced on the sites of a given set by the operations of . For the operations of group and associated operator ecc we refer to eqs. (3-2a) (3-2b) and following explanations.

2. Coefficients of the independent combinations of magnetic and electric multipoles centered at the sites of the given set, such quantities are computed from eqs. (3-4a), (3-4b).

3. The projections of the magnetic and electric multipoles included in the expansion of the incident plane wave, as are shown in eqs (3-9).

These quantities are written on a file and are the input data for MUSCA, whose output consists of the following quantities:

1. The total cross section, computed from eq (3-5c)
2. The scattering cross section, from eq (3-5a)
3. The absorption cross section, from eq (3-5b)
4. The coefficients of the scattered wave for each representation, the $A_{nNL}^{\nu p\sigma}$ and $B_{nNL}^{\nu p\sigma}$ of eq (3-6), which are the unknown quantities in our solution and thus, with their knowledge we are able to fully describe the properties of the cluster, as stated in section 5.

Following are some data obtained from these programs (outputs of SYMULT and MUSCA) for the case of the point group Td (SO_4^{--}) and comparison is made with experimental data.

ACKNOWLEDGEMENT

The author wishes to acknowledge the participation in this study of the following people: Prof. Ferdinando Borghese, Prof. Paolo Denti and Dr. Giuditta Toscano of the University of Messina, Institute of the Structure of the Matter, Messina, Italy.

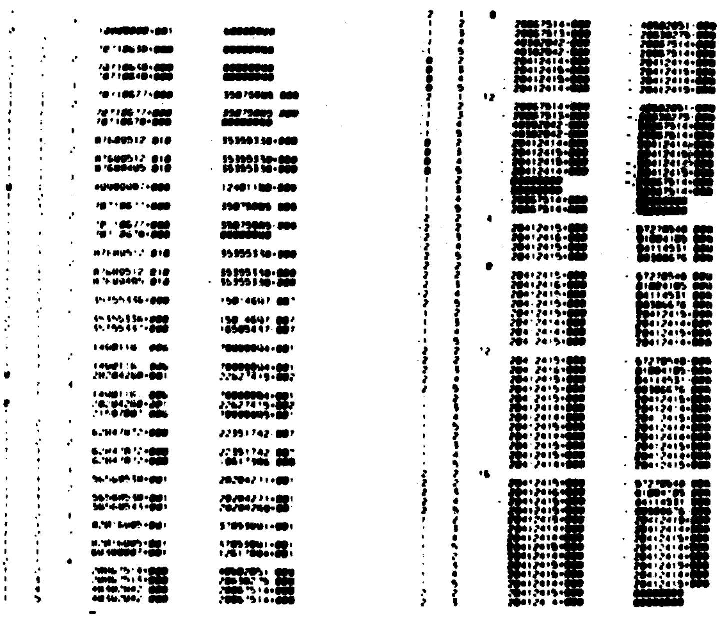

sample output from Musca

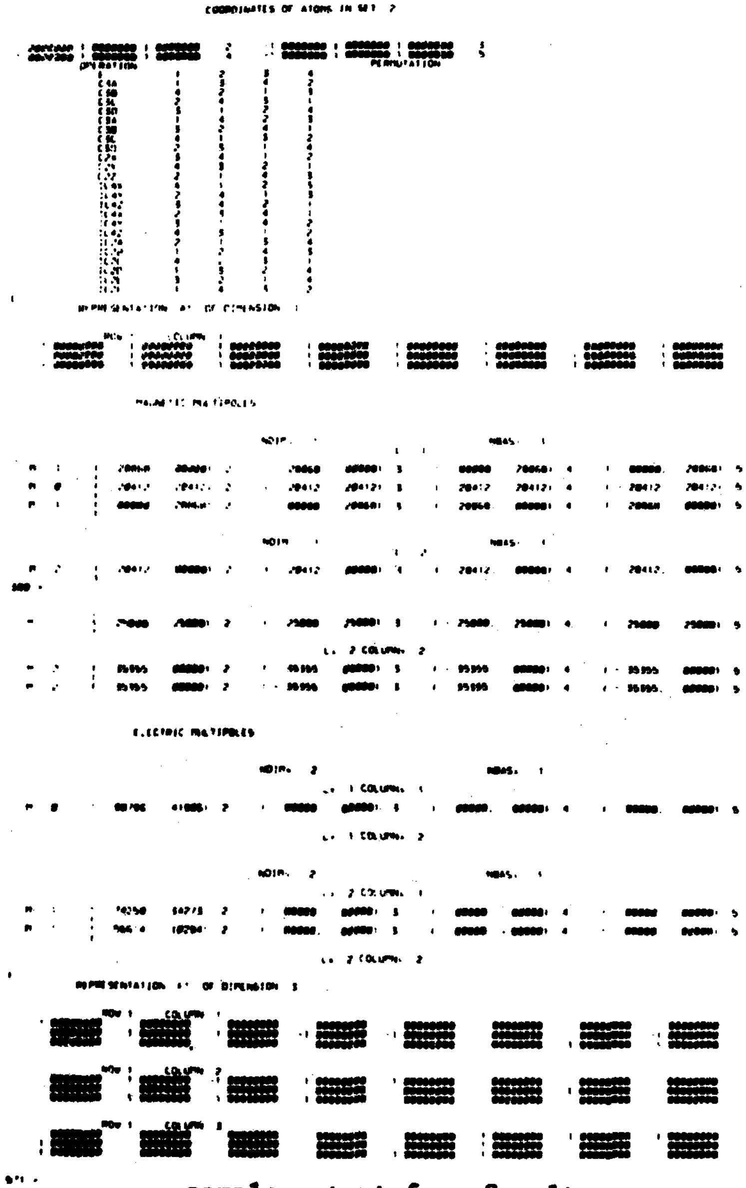

sample output from Symult

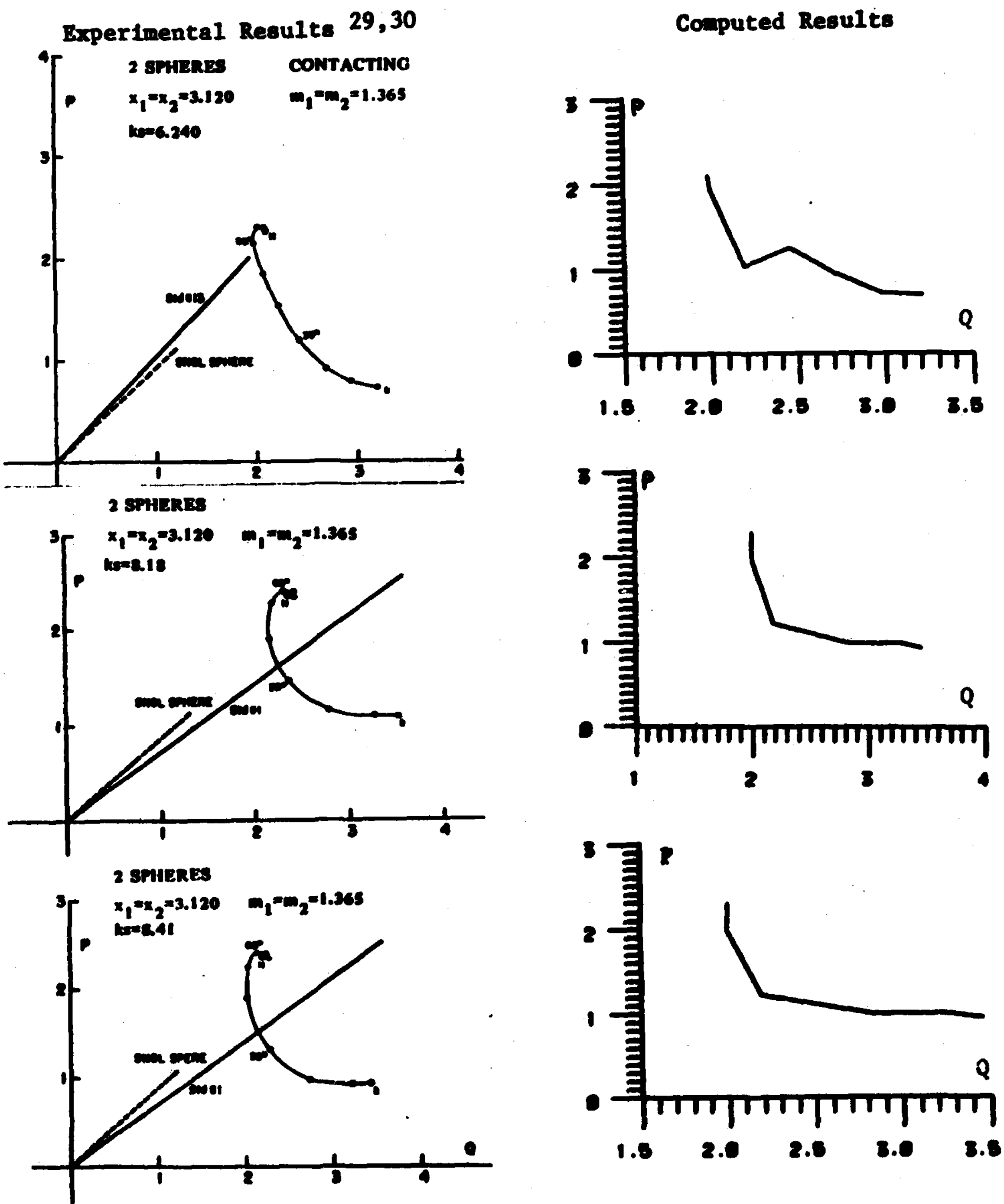

Comparison of experimental and computed results for $P=Im[\sigma(\theta)]$ and $Q=Re[\sigma(\theta)]$ with $\theta=0$

LITERATURE CITED

1. Lord Rayleigh. Phil. Mag. 12, 81 (1881); Proc. Roy. Soc. A84, 25 (1910); ibid. A90, 219 (1914); ibid. A94, 365 (1918).
2. Debye, P. Ann. Phys. 46, 809 (1915).
3. Kerker, M., Faone, W. A., and Matijevic, E. J. Opt. Soc. Am 53, 758 (1963).
4. Faone, W. A. Kerker, M. A., and Matijevic, E. "Electromagnetic Scattering", edited by M. Kerker, Pergamon Press, Oxford. 1963.
5. Heller, W. "Electromagnetic Scattering" edited by M. Kerker, Pergamon Press, Oxford, 1963.
6. Barber, P. W. and Wang, Dao-Sing. Appl. Optics 17, 787 (1978).
7. Johnson, K. H. J. Chem. Phys. 45, 3085 (1966); Int. J. Quantum Chemistry S1, 361 (1967).
8. Liberman, D. A. and Batra, I. P. J. Chem. Phys. 59, 3723 (1973); Herman F., Williams, A. R. and Johnson, K. H. J. Chem. Phys. 61, 3508 (1974).
9. Heine, V. Group Theory. Pergamon Press, Oxford. 1964.
10. Jackson, J. D. Classical Electrodynamics. John Wiley & Sons, New York. 1975.
11. Wyatt, J. P. Phys. Rev 127, 1837 (1962); ibid. 134, AB1 (1964).
12. Rose, E. M. Multiple Fields. John Wiley & Sons, New York. 1955.
13. Edmonds, A. R. Angular Momentum in Quantum Mechanics. Princeton University Press, Princeton, NJ 1957.
14. Diamond, J. B. Chem Phys. Letters 20, 63 (1973).
15. Hamermesh, M. Group Theory. Addison-Wesley Publishing Co., Reading, MA. 1962.
16. Cornwell, J. F. Group Theory. North Holland Publishing Co., Amsterdam. 1969.
17. Cruzan, O. R. Q. Appl. Math. 20, 33 (1962).
18. Borghese, F., Denti, P., Toscano, G., and Sindoni, O. I. J. Math.Phys. 21 (12), 2754, (1980).
19. Gaunt, J. A. Proc, Cambridge Phil. Soc. 24, 328 (1928); Condon, E. V. and Shortley, G. H. The Theory of Atomic Spectra, p 75. Cambridge University Press, Cambridge England. 1951.
20. Stratton, J. A. Electromagnetic Theory. McGraw-Hill Book Co., New York. 1941.
21. Wu, T. Y. and Ohmura, T. Quantum Theory of Scattering, pp 15, 317. Prentice-Hall Inc., Englewood Cliffs, NJ. 1962.
22. Waterman, P. C. Phys. Rev. D3, 825 (1971).
23. Mie, G. Ann. Phys. 25, 377 (1908).
24. Debye, P. Ann. Phys. 30, 57 (1909).
25. Norman, R. J. Math Phys 7, 1841 (1966).
26. Hansen, W. W. Phys Rev, 47, 139 (1935).
27. Rose, E. M. Elemental Theory of Angular Momentum. John Wiley & Sons, New York. 1957.
28. Slater, J. C. Quantum Theory of Atomic Structure. Appendix 20. McGraw-Hill Book Co., New York. 1960.
29. D. W. Schuerman, R. T. Wang, B. A. Gustafson, and R. W. Schaefer, App. Opt. 20, 23, 4039 (1 December 81).
30. D. W. Schuerman, R. T. Wang, ARCSL-CR-81003, November 81.

SYNTHESIS AND EVALUATION OF PHOSPHAZENE FIRE RESISTANT FLUIDS

*R. E. SINGLER, T. N. KOULOURIS, A. J. DEOME,
H. LEE, D. A. DUNN AND P. J. KANE
U.S. ARMY MATERIALS AND MECHANICS RESEARCH CENTER
WATERTOWN, MASSACHUSETTS 02172
M. J. BIEBERICH
DAVID TAYLOR NAVAL SHIP RESEARCH AND DEVELOPMENT CENTER
ANNAPOLIS, MD 21402

INTRODUCTION

The Army and Navy have a critical need for improved fire resistant (FR) materials in combat applications. This need includes synthetic hydraulic fluids and lubriciants as replacements for conventional products used in tanks, helicopters and Naval surface ships. Cyclic phosphazene fluids synthesized at AMMRC, may satisfy these stringent requirements. Evaluation of these fluids is being conducted at the David Taylor Naval Ship R&D Center as part of a program to find replacements for fluids such as triarylphosphates covered under specifications MIL-H-19457C.

Cyclic phosphazenes are ring compounds of alternating phosphorus and nitrogen atoms which have two substitutents attached to phosphorus. Representative structures (I and II) are shown below. In these structures R can be halogen, pseudohalogen, or various organo substituents.

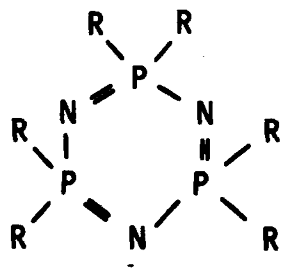

I

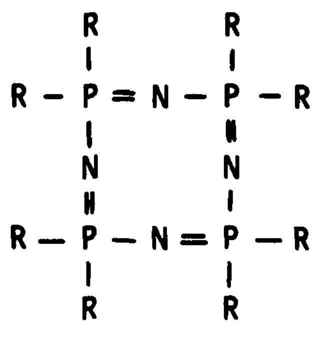

II

At first glance, the phosphazenes would appear attractive in applications where fire resistance and thermal stability are important factors. Due to the presence of phosphorus, nitrogen, and quite often halogen, the phosphazenes are inherently fire resistant. With the proper selection of aryloxy or fluoroalkoxy substitutents, thermally and hydrolytically stable compounds have been prepared (1).

With the support of the US Navy, Bureau of Ships, Kober and coworkers (2) previously synthesized a series cyclic phosphazenes from the reaction of phosphonitrilic chloride trimer and tetramer (I and II, R=Cl) with mixtures of sodium perfluoroalkoxides and aryloxides. Although some of the fluids showed promise for the intended applications, the work was discontinued because the phosphazenes did not show a substantial improvement over the current fire resistant fluids. Furthermore, some of the fluids were prone to crystallize upon long standing or had poor hydrolytic stability and materials compatibility.

A change in requirements plus a continuing need for improved fire resistant fluids (3, 4) has prompted us to reinvestigate the potential of the cyclic phosphazenes. This paper describes our work to prepare fire resistant phosphazene fluids with low pour points, good hydrolytic stability and systems compatibility.

EXPERIMENTAL

<u>Synthesis and Chemical Characterization</u>. The general procedure was similar to the one employed by Kober, Lederle and Ottman (2).

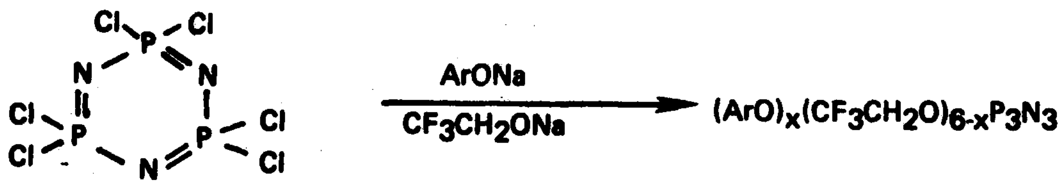

III IV

However, several important changes were made. For the initial study, phosphonitrilic chloride trimer (III) and trifluoroethanol were used throughout and only the phenol was changed. The phenols (ArOH) used were m-chlorophenol and m-trifluoromethylphenol. In contrast to the earlier work (2) which employed an azeotropic removal of water formed during the reaction of potassium hydroxide and the phenol, sodium salts of trifluoroethanol and the phenols were formed using sodium hydride in anhydrous dioxane or tetrahydrofuran (THF). Three modes of addition of reactants were investigated:

Mode 1. Addition of trimer to a mixture of ArONa and CF_3CH_2ONa.

Mode 2. Addition of a mixture of ArONa and CF_3CH_2OHa to the trimer.

Mode 3. Sequential addition of ArONa to the trimer, followed by CF_3CH_2ONa.

Finally, the ratio of ArONa and CF_3CH_2ONa was varied in order to minimize crystallization and optimize viscosity and pour points.

Table 1 shows the results for the reaction of trimer and sodium salts of trifluoroethanol and m-chlorophenol. When the trimer was added to the sodium salts (Mode 1), very little of the mixed substituted products, $(ArO)(CF_3CH_2O)P_3N_3$, was obtained. Reversing the mode of addition changed the product composition dramatically. Mode 2 resulted in an increase in % oil recovery from 18 to 62. Further increases were achieved by using the sequential addition Mode 3.

The aryloxy content, X, was determined through nuclear magnetic resonance (NMR). Analysis by gas chromatography - mass spectroscopy (GC-MS) revealed that the samples were mixtures of components X=0, 1, 2, 3 with molecular ions at 729, 757, 785 and 813, respectively. Detection of X=4, 5 and 6 was not obtained by GC-MS due to the low volatility of the cyclic phosphazenes. Further analysis using high pressure liquid chromatography (HPLC) revealed additional components, possibly X=4 and 5.

The reaction products were redistilled in order to remove the X=0, 4, 5, and 6 components, so as to minimize crystallization and lower the pour point. The final sample, labeled 1422-32, was supplied to the David Taylor Naval Ship R&D Center for evaluation. Proton NMR showed X=1.95, in good agreement with elemental analysis (Figure 1). The GC-MS analysis showed the principle components to be X=1, 2, 3. Analysis by HPLC (Figure 2) revealed at least seven components, which is consistent with the various isomers that could result from this complex reaction process.

Synthesis of a second candidate fluid was done using the second and third reaction modes (Table II). The proportion of m-trifluoromethylphenol was decreased in an attempt to lower the pour point of the product. Some hexakis(trifluoroethoxy)cyclotriphosphazene (IV, X=0) was formed which could be removed by vacuum distillation. The product yields and distributions were similar to those obtained for the first sample (Table 1).

TABLE I

SYNTHESIS OF ( $-O)_X(CF_3CH_2O)_{6-X}P_3N_3$

Reaction Mode	Isolated Fraction No.[b]	Relative Yield %	Physical State[c]	Aryloxy Content X	Absolute % Yield of Oil Distillates
1 (3/3)[a]	1	36	Solid	< 0.5	18
	2	25	Oil	0.71	
	3	2	Oil	2.2	
	Residue	36	Semisolid	5.1	
2 (3/3)[a]	1	13	Solid	0.57	62
	2	43	Oil	1.6	
	3	36	Oil	2.7	
	Residue	9	Oil	4.2	
3 (3/3)[a]	1	8	Oil	1.5	68
	2	53	Oil	2.6	
	3	25	Oil	3.2	
	Residue	14	Oil[d]	4.1	
3 (2/4)[a]	1	17	Oil[e]	0.77	81
	2	68	Oil	1.9	
	3	5	Oil	2.7	
	4	9	Oil	3.0	
	Residue	-	-	-	

[a] Mole ratio m-chloro phenol/trifluoroethanol.

[b] Vacuum distillation over a range 100-250°C between 0.2 and ~0.1 mm Hg.

[c] At room temperature. Oil samples were generally water clear. Upon refrigeration, some fractions became cloudy or crystallized (below).

[d] Residue was eventually distilled at higher vacuum (~0.05 mm) to give an oil.

[e] Solidified at -10°C.

Table II

SYNTHESIS OF (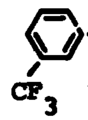 $-O)_X(CF_3CH_2O)_{6-X}P_3N_3$

Reaction Mode	Isolated Fraction No.[b]	Relative Yield %	Physical State[c]	Aryloxy Content X	Absolute % Yield of Oil Distillates
2	1	3	Oil[e]	0.67	83
(3/3)[a]	2	50	Oil	2.32	
	3	15	Oil	3.38	
	4	33	Oil	4.48	
	Residue	-	-	-	
2	1	10	Oil[e]	0.57	74
(2.5/3.5)	2	24	Oil	1.62	
	3	48	Oil	3.88	
	4	-	-	-	
	Residue	19	Oil[d]	4.07	
3	1	10	Oil	1.45	78
(2.5/3.5)	2	31	Oil	2.15	
	3	38	Oil	2.86	
	4	14	Oil	3.19	
	Residue	8	Oil[d]	4.53	
3	1	6	Oil[e]	0.45	80
(2.3/3.7)	2	51	Oil	1.9	
	3	43	Oil	2.9	
	Residue	-	-	-	

[a] Mole ratio m-trifluoromethyl phenol/trifluoroethanol.

[b] Vacuum distillation over a range 100-250°C between 0.2 and ~0.1mm Hg.

[c] At room temperature. Oil samples were generally water clear. Upon refrigeration, some fractions became cloudy or crystallized (below).

[d] Residue was eventually distilled at higher vacuum (~0.05) to give an oil.

[e] Solidified at -10°C.

The reaction products were combined and redistilled to obtain two samples, 1422-36 and S208-47-3 for evaluation at DTNSRDC. Proton NMR for 1422-36 showed X=2.18, which was in good agreement with the elemental analysis (Figure 3). The GC-MS revealed five components, X=1, 2, 3 (Figure 4). In this case, separation into two components each for X=2 and 3 was obtained. The HPLC showed at least six and possibly seven components (Figure 5). Partial fraction by HPLC and reexamination by GC-MS made it possible to assign molecular weights to some of the components in Figure 5.

The sample S208-47-3 was a higher boiling fraction than 1422-16. For S208-47-3, NMR showed X=3.30. This corresponds to X=2 (minor), 3 (major), 4 (minor) in structure (IV).

The fluid evaluation for the samples supplied to DTNSRDC is given in Table III. Sample number 1422-32 corresponds to structure (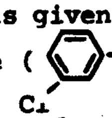 $-O)_{1.95}$ $(CF_3CH_2O)_{4.05}P_3N_3$ and numbers 1422-36 and S208-47-3 correspond to structure (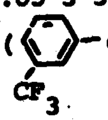 $-O)_X(CF_3CH_2O)_{6-X}P_3N_3$, X=2.18 and 3.30, respectively.

The samples have excellent fire resistance as measured by high pressure autogeneous ignition tests (AIT). Samples 1422-32 and 1422-36 have acceptable pour points and hydrolytic stability. While these fluids are not acceptable in every respect, synthetic modifications can improve viscosity characteristics and most likely elastomer compatibility (Viton).

CONCLUSION

Phosphazene fluids have potential for military applications requiring improved fire resistance in hydraulic systems, engines and transmission components. Further synthesis is planned which includes modification of the aryloxide/fluoroalkoxide ratio and investigation of other phenols. Large scale synthesis and hydraulic pump loop tests are being planned using the most promising candidates from this laboratory synthesis-dharacterization and fluid evaluation programs.

REFERENCES

1. H. R. Allcock, "Phosphorus-Nitrogen Compounds" Academic Press, New York, 1972.

2. N. Lederle, E. Kober, and G. Ottman, J. Chem. Eng. Data, 11, 1966, p. 221; contract NObs-90092, (AD608144) 1964.

3. R. Singler, "Potential of Phosphazenes as Hydraulic Fluids", NASA "Conference on Hydraulic Fluids", Ames Research Center, California, NASA TMX-73142, 1976, p. 179.

4. "Fire-Resistant Hydraulic Fluids in Enclosed Marine Environments", National Research Council, NMAB-345, 1979.

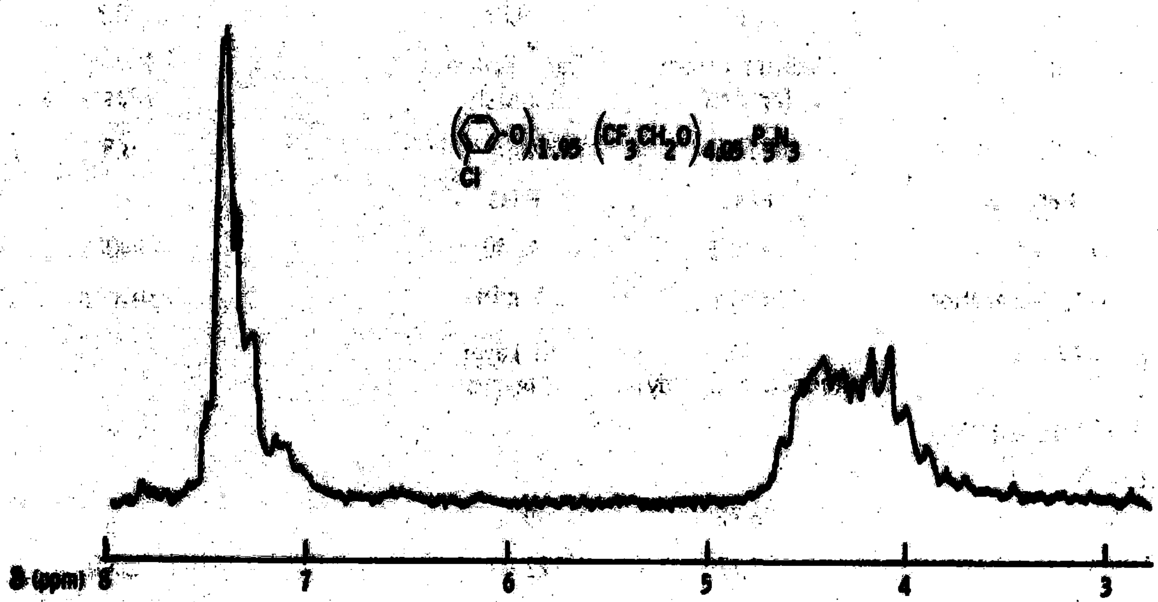

FIGURE 1. Proton 90 MHz NMR of 1422-32. Elemental Analysis, (Theory) Found: C, (30.55) 30.25; H (2.06) 2.34; Cl (9.02) 8.47; F (29.00) 29.06.

TABLE III

PHOSPHAZENE FLUID EVALUATION CRITICAL PROPERTIES

PROPERTY	FLUID 1422-32	FLUID 1422-36	FLUID S208-47-3	MIL-H-19457C REQUIREMENT
Viscosity,[a] Centistokes				
40°C	23.53	22.79	53.97	43-50
100°C	3.4	3.5	4.7	4.8 min
Pour Point,[b] °C	-37	-30	-16	-18
High Pressure AIT,[c] °F	558	630	640	450
Acid Number[d] (max) mg KOH/g	0.057	0.018		0.1 max
Hydrolytic Stability[e]				
Δ TAN mg KOH/g	-0.022	-0.01		+0.2
H_2O Layer, mg KOH	0.85	0.11		5.0
Cu wt Loss mg/cm^2	0.14	0.02		0.3
Appearance Cu	Medium Brown Tarnish	Dark Brown Tarnish		Brown (Pass)
Insolubles, wt %	0.008	None		0.5
Emulsion Characteristics[f]	Pass	Pass		
Layers (ml)	39/40/1	40/40		40/40/≤3
Time to Separation	5 min	5 min		30 min
Appearance	Oil Layer Remained Cloudy	Oil Layer Cleared		
Elastomer Compatibility, % Volume Swell				
Buna N	26.26	0.82		g
Viton I	7.77	22.60		±5.0
Viton II	21.55	16.15		±5.0
EPR	2.06	0.07		±5.0

(a) ASTM D-445; (b) ASTM D-97; (c) High Pressure Autogeneous Ignition, 1500 psi, 100% Oxygen; (d) ASTM D-974; (e) MIL-H-19457C, par. 4.5.2; (f) ASTM D-1401; (g) Current Fluid > 100%

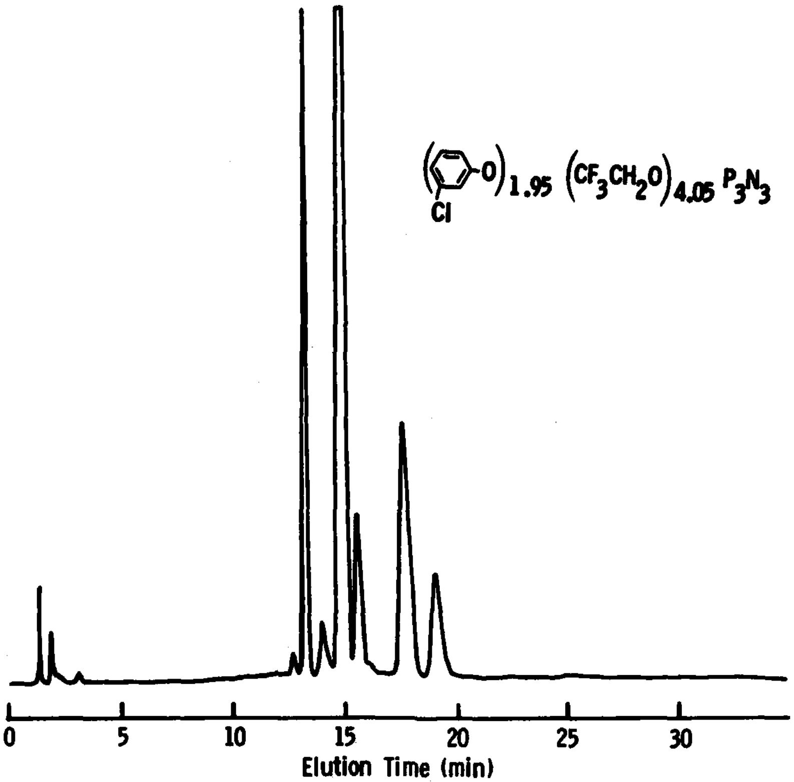

FIGURE 2. Reverse Phase HPLC of 1422-32. Column: micro Bondapak C_{18}. Solvent Gradient CH_3CN-H_2O. Detector: UV 210 nm.

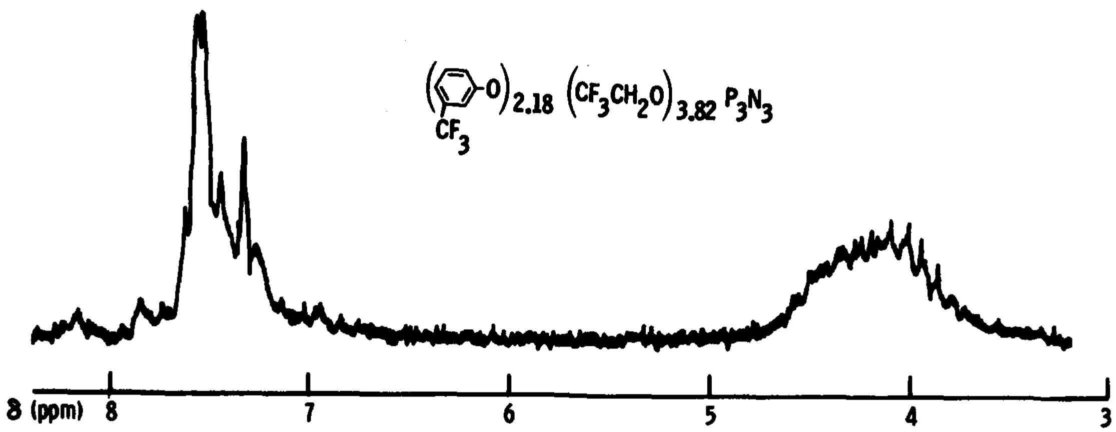

FIGURE 3. Proton 90 MHz NMR of 1422-36. Elemental Analysis (Theory) Found: C (31.82) 31.70;H (1.91) 1.92;Cl (0) 0.06;F (39.56) 39.10.

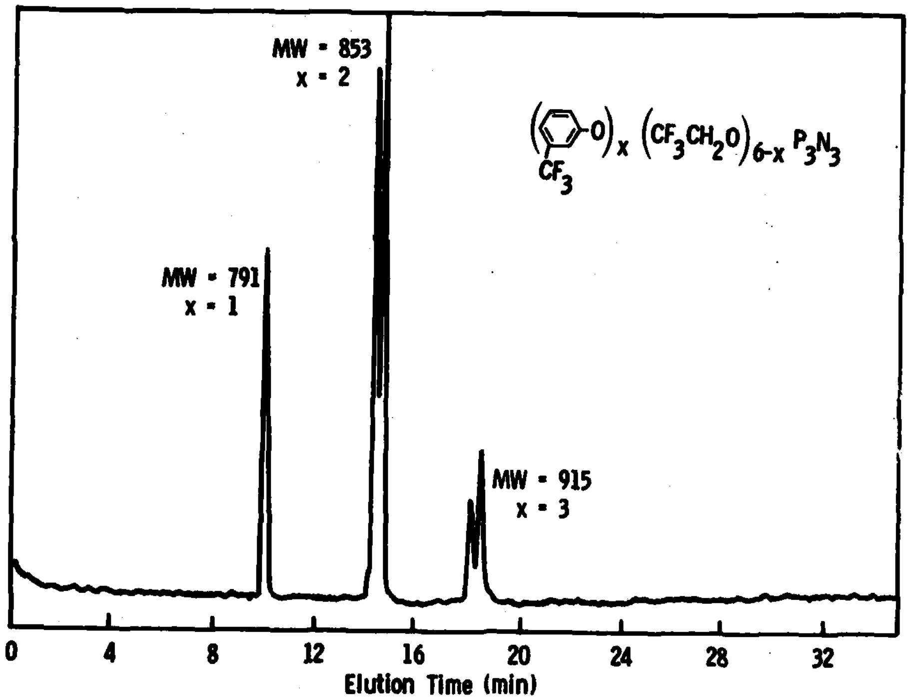

FIGURE 4. GC-MS of 1422-36. Column: OV-225
Temperature: 8°C/min 100-260°C, continuous.

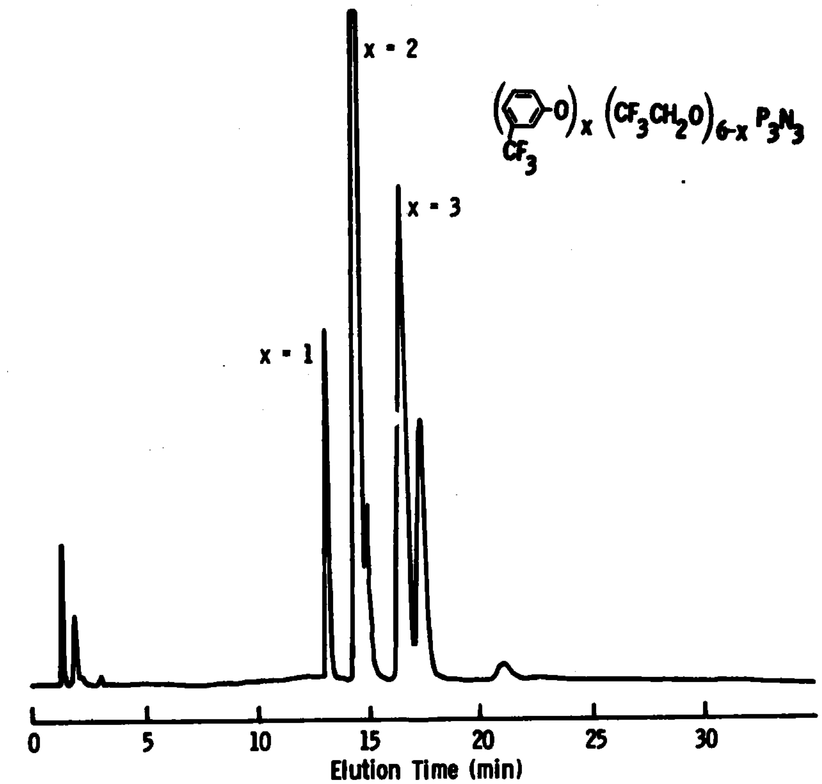

FIGURE 5. Reverse Phase HPLC of 1422-36. Column: micro Bondapak C_{18} Solvent Gradient: CH_3CN-H_2O. Detector: UV 210 nm.

A METHOD OF POLYMER DESIGN AND SYNTHESIS FOR SELECTIVE INFRARED ENERGY ABSORPTION (U)

Alvin Smith
U.S. Army Construction Engineering Research Laboratory
Champaign, Illinois 61820

INTRODUCTION

Infrared-absortion spectroscopy is extensively used in polymer chemistry in the study of reaction processes, structure, morphology, qualitative and quantitative composition, molecular configuration, and other features. The rapid growth of the technique since the mid-1940's attests to its usefulness.

In the method, electromagnetic radiation in the infrared region (greater than $\lambda = 0.7\ \mu m$) interacts with mass in vibrational and rotational modes. The interactions with molecules or groups of atoms within molecules causes transitions between the vibrational and/or rotational states with a resulting characteristic absorption of energy or spectral "signature." The spectrum produced relates the intensity of energy absorption at particular wavelengths by specific groups of atoms and provides an insight into the structure and configuration by providing both the types of groups and their concentrations. Infrared-absorption spectroscopy may be used alone as an analytical method; however, it is often combined with Raman and mass spectroscopy or with nuclear magnetic resonance to obtain more detailed information.

The present study presents a procedural method of designing and synthesizing polymers intended to selectively absorb energy in particular bands of the infrared spectrum. Thus, filters may be prepared that can be used to mask or alter the signatures of infrared-emitting objects and, in effect, camouflage these objects against observation by attenuating or altering the infrared energy that is allowed to be transmitted to a detector.

In addition to the molecular design of the polymer, a change in the physical form by foaming is studied to determine this effect on the overall efficiency of the attenuating properties of the filter. An advantage of foaming the polymer is the ability to make essentially self-supporting filter enclosures for infrared emitters. The most obvious uses of selectively absorbing infrared filters are in military camouflaging applications and as photographic filters analogous to the visible light filters commonly used.

THEORETICAL

Infrared radiation energy causes only the vibrational and rotational energy state transitions described earlier; it is incapable of causing electron energy level changes. The transitions effected cause the molecules to react as a vibrating system of springs and masses that can be reasonably approximated as a simple harmonic system which can be analyzed by quantum mechanics techniques such as the Schrodinger wave equation with the condition

$$\nu = \frac{E_2 - E_1}{hc}$$

in which ν is the wave number,* E_1 and E_2 are discrete energy values of the two transition states, h is Planck's constant, and c is the velocity of light. Only vibrations resulting in changes in dipole moments cause infrared absorptions of a fundamental nature; overtone and combination vibrations may occur, but their intensities are generally much lower. The intensity of absorption is proportional to the square of the magnitude of the changing dipole moment in the vibration or rotation.

---

*The wave number is conventionally defined as $10^4/\lambda$ where λ is between 1 and 500μm; it allows better numerical description than does the wavelength λ.

The number of possible vibrations in a polymer system containing N atoms is 3N wave numbers. Of these, six values represent whole molecule vibration or rotation transitions so the total number of possible absorptions becomes 3N-6 in most cases. Not all vibrations are detectable in the infrared spectrum due to a lack of proper response by the molecule or group to the infrared energy or to precedent Raman (electrical polarizability) activity or molecular symmetry. It is possible to calculate all of the individual values for all of the vibration frequencies from atomic masses and geometric positions (chemical bond lengths and bond angles) and the force constants of the bonds if some of the values are independently provided from other sources such as mass spectroscopy and nuclear magnetic resonance.

The translations of vibrational or rotational energy via mass displacement occur as bond stretching (symmetric and asymmetric), deformation (symmetric bending), wagging, twisting, and rocking as defined and illustrated by Bikales [1]. In relatively simple polymer molecules such as polyethylene, the motions are well defined. More complex molecules, especially network or crosslinked polymers with a large number of different types of groups, present much more formidable problems of exact analytical description. Nearest neighbor interactions, hydrogen bonding, van der Waals forces, residual strain, and steric hindrances all may cause shifting of the absorption band in the spectrum, broadening of the band, or combination with other nearby bands with a concomitant alteration of the absorption intensity.

The amount of infrared energy that is absorbed (converse of transmitted) as an infrared beam is passed through a material depends linearly upon the incident radiation intensity and non-linearly upon the number of absorbing molecules or groups in the path. The functional relationship is given by the Beer-Lambert law [2] in which logarithms are required to give the correct quantitative value of absorption. Since the effect of the logarithm is less pronounced when weak absorption occurs, the difference in peak absorption can be used to describe the number of absorbing molecules or groups. The reverse is not true, however, since strong absorption results in very large changes in the logarithmic value of transmission, and care must be exercised in interpreting the results quantitatively in terms of the number of functional absorbing groups in the light path.

Given that each polymer group has characteristic absorption properties, it is then theoretically possible to select groups by type and quantity and to synthesize polymers such that absorption will occur at specific bands in the spectrum. As a result, infrared radiation incident on one side of a layer of such a material can be absorbed as it passes through the material with the shape and/or overall transmitted spectrum intensity significantly tailored to suit a desired result.

Relatively little work has been reported on the intentional design of polymers to absorb infrared energy over a substantial portion of the near and intermediate portions of the spectrum. Exceptions include long- and short-pass and interference filters designed principally for use in the study of the infrared spectrum itself [3].

EXPERIMENTAL

The experimental procedure used was selected to satisfy three objectives. First, a polymer system was selected to afford as much flexibility in design as practical. Second, the designed polymer was synthesized. Third, the infrared-absorption spectrum of the polymer was studied with the polymer as a film and as varying thicknesses of foam to determine whether the polymer absorbed as designed and to compare the performance of the film and the foam.

Polymer groups were cataloged with respect to their infrared absorption bands. The selected groups and references are given in Table 1. The groups, their vibrational modes and principal absorption bands are listed in Table 2. These tables do not cover the entire range of possibilities, but rather reflect a selection sufficiently broad to cover a reasonable portion of the infrared spectrum from wave number 4000 cm^{-1} to about wave number 700 cm^{-1}. More than 100,000 infrared spectra are available for comparison reference of polymer group absorption in the ASTM and Sadtler collections [2].

An examination of the composition of numerous polymers showed that the polyurethane family offered a great number of opportunities for inclusion of many of the desired groups. (As a contrast, polyethylene contains only CH_2 groups with no possibility of other groups other than CH_3 at the chain ends.) Furthermore, the polyurethanes are generally readily synthesized as both films and foams by using commercially available isocyanates and a wide variety of reactants that contain ether C-O, ester -C(=O)-O, phosphate PO_4^{-3}, amine NH, amide-C(=O)-NH_2, sulfur S-H, halogen C-X, silicon Si-H, Si-C, Si-O, and other groups. The general absorption assignments of the various groups are given in Table 2. As can be seen, these groups cover the entire spectrum from about 3600 cm^{-1} to 700 cm^{-1} wave numbers.

The polyurethane was formulated using a polymethylenepolyphenylisocyanate and polyether polyol. The chemistry and reactions are described in [4]. Thin films of the formulated polyurethane were cast on a Teflon slab. Low-density foams were made of the same formulation but by necessity, the foams also contained silicone surfactant and monofluorotrichloromethane as a cell control and foaming agent, respectively. The foam was sliced into thin sheets of various thicknesses prior to testing.

Transmission spectra of the specimens were made on a Perkin-Elmer Infrared Spectrometer, Model 283B. The transmission method was selected over other techniques such as attenuated total reflectance or as particles dispersed and consolidated in potassium bromide pellets as described by Bikales [1]. The transmission mode represents the anticipated use as a filter and was thus considered the most appropriate test procedure. Comparable absorption spectra were obtained for the film and foam specimens; thus, the method appeared satisfactory.

EXPERIMENTAL RESULTS

A composite spectrograph of the film and foam specimens is shown as Figure 1. Curve 1 at the top of the graph is the transmission spectrum of a thin film (0.0178 mm) of the polyurethane polymer. Absorption peaks (which appear as valleys in the curve) are strong at numerous wave numbers, especially at about 1075 cm^{-1}, 1220 cm^{-1}, 1525 cm^{-1}, 1710 cm^{-1}, 2900 cm^{-1}, and 3300 cm^{-1}. The presumed absorbing groups are identified in the upper margin. Curves 2 through 5 are increasingly greater thicknesses of foam (0.0218 mm through 0.0533 mm) of the same polymer and, as can be seen, they retain the same general absorption features as the film, but the absorption peaks become less pronounced as the thickness increases and more total absorption occurs. A sufficiently thick specimen would totally block transmission and the whole spectrum would be absent, just as no specimen in the beam would allow complete transmission.

The somewhat erratic trace of the curves is probably due to reflective scattering of the beam; small deviations in the curve are not satisfactory for assignment of absorption groups or indicative of the dipole activity required for infrared absorption. These small deviations should be considered as artifacts of the test or ignored completely for the purposes of this paper.

A single experiment was conducted under field conditions to verify findings in the laboratory. The experiment compared the observability of two operating 60-kW diesel drives generator sets; one set was enclosed by sheets of polyurethane foam approximately 50 mm thick, and the other set was bare. The enclosed set was shielded along the sides and over the top only so as to not interfere with either cooling air flow from end to end or exhaust gas emission.

The test was conducted for a 26-hour period to include a complete solar day. Temperature measurements were made at various points on the skin of the unenclosed set and at corresponding geometric points on the enclosed set and its shield. Background temperatures of soil, vegetation, and air were also measured.

Analysis of the thermographs thus assembled showed a sharp contrast between the thermal profile of the bare set and the background, whereas the thermal profile of the surface of the foam enclosure was practically identical with the background. Thus, the enclosure effectively filtered or masked the thermal output from the generator and would prevent observation from directions other than directly at the unenclosed ends.

DISCUSSION

The multiple absorption peaks shown in Figure 1 are the result of the variety of different groups present in the polyurethane polymer. In addition to the prominent peaks described, many smaller peaks are evident. The overall absorption spectrum is essentially the form that was desired and could effectively filter an emission spectrum of an infrared source.

The foam specimens absorbed more than the equivalent solid film, as shown in Table 3. The increased absorption is attributed to substantial scattering caused by the large number of angles described by cell walls in the foam. Incidence of the beam with the cell walls increases reflection to the sides and backward.

The results of this study support the hypothesis that selectively absorbent polymers can be designed and made. Foamed polymer appears to be superior to a film of the same material of the same thickness when used as a filter for infrared radiation. It is believed that effective masking filters for emitters could be made to a particular specification to absorb much of the infrared spectrum within the range described in this paper.

While it was not a part of this study, it is known that colorants, dyes, pigments, and fillers can also be incorporated into a polymer (film or foam) to further alter the absorption properties.

Field utility of foamed polymers was deemed feasible based on the results of the single experiment described. Obviously, more study will be required to design an optimum system for general application.

SUMMARY

A method of designing a polymer to be selectively absorbing in the infrared electromagnetic spectrum was studied. The design was intended to give as much absorption as possible in the region of 4000 cm^{-1} to 700 cm^{-1} wave numbers. A polyurethane polymer was synthesized which showed absorption in this range with numerous fairly prominent absorption peaks. Foam made of this polymer showed the same absorption characteristics but appeared to be more efficient as a total filter for the whole range, particularly at a thickness of about 1.9 mm or greater.

A field experiment showed promise for effectively camouflaging thermal sources such as operating generator sets by enclosing them with polyurethane foam sheets.

ACKNOWLEDGEMENTS

The author is grateful for the support of the Army's In-Laboratory Independent Research Program for the financial support of this work, to Prof. R. P. Wool of the University of Illinois at Urbana-Champaign for his helpful guidance and suggestions, and to Mr. Rich Lampo and LT O. S. Marshall, co-workers who greatly assisted in the study.

REFERENCES

1. Bikales, N. M., Characterization of Polymers, Interscience, New York (1971), pp 127-129, 133.

2. Rabek, J. F., Experimental Methods in Polymer Chemistry, Interscience, New York (1980), pp 212, 224.

3. Wolfe, W. L. and G. J. Zissis (ed.), The Infrared Handbook, Office of Naval Research, Department of the Navy, Washington (1978), pp 7-103 - 7-110.

4. Saunders, J. H. and K. C. Frisch, Polyurethanes, Chemistry and Technology - Part 1 Chemistry, John Wiley and Sons, New York (1962).

5. Bellamy, L. J., The Infrared Spectra of Complex Molecules, 3rd Edition, Chapman and Hall, London (1975).

6. Colthup, N. B., L. H. Daly, and S. E. Wiberley, Introduction to Infrared and Raman Spectroscopy, Academic Press, New York (1964).

7. Dolphin, D. and A. Wick, Tabulation of Infrared Spectral Data, Wiley-Interscience, New York (1977).

8. Hummel, D. O., Applied Infrared Spectroscopy, Chap. 2.2 in D. O. Hummel, Ed., Polymer Spectroscopy, Monographs in Modern Chemistry, Vol. 6, Verlag Chemie, Germany (1974).

9. Hummel, D. O., Infrared Spectra of Polymers, Polymer Reviews, Vol. 14, Wiley-Interscience, New York (1966).

10. Bellamy, L. J., Advances in Infrared Group Frequencies, Methuen & Co., London (1968).

11. Szyanski, H. A., IR: Theory and Practice of Infrared Spectroscopy, Plenum Press, New York (1964).

12. Krimm, S., "Infrared Spectra of High Polymers," *Fortschr. Hochpoly.-Forsch*, 2, 51 (1960).

13. Zbinden, R. Infrared Spectroscopy of High Polymers, Academic Press, New York (1964).

14. Hummel, D. O. and F. Scholl, Infrared Analysis of Polymers, Resins, and Additives: An Atlas, Vol. 1, Part 2, Wiley-Interscience, New York (1969).

15. Whetsel, K. B., "Near Infrared Spectrophotometry," *Appl. Spectros. Rev.* 2, 1 (1969).

16. Tadokoro, H. and M. Kobayashi, "Vibrational Analysis of Highly Ordered Polymers," Chap. 2.2 in D. O. Hummel, Ed., Polymer Spectroscopy, Monographs in Modern Chemistry, Vol. 6, Verlag Chemie, Germany (1974).

17. Szymanski, H. A. and R. E. Erickson, Infrared Band Handbook, 2nd Edition, IFI/Plenum, New York (1970).

18. Fox, J. J. and A. E. Martin, *Proc. Roy. Soc.* A175, 208, 234 (1940).

19. McKean, D. C., *Chem. Comm.*, 1373 (1971).

20. Francis, S. A., *J. Chem. Phys.* 19, 942 (1951).

21. Wilmshurst, J. K., *J. Chem. Phys.*, 26, 426 (1957).

22. Wright, W. B., *J. Org. Chem.* 24, 1362 (1959).

23. McMurry, H. L. and Thorton, V., *Anal. Chem.* 24, 2318 (1952).

24. Jones, R. N., *Spectrochim, Acta*, 9, 235 (1957).

25. Sheppard, N., in Advances in Spectroscopy, Vol. 1, Interscience, New York, p. 288 (1959).

26. Potts, W. J. and R. A. Nyquist, *Spectrochim. Acta*, 15, 679 (1959).

27. Davison, W. H. T. and Bates, J., *J. Chem. Soc.*, 2607 (1953).

28. Pinchas, S., *Anal. Chem.* 27, 2 (1955).

29. Katritzky, A. R., *Quart. Rev*, 13, 353 (1959).

30. Mason, P., *J. Chem. Soc.* 22 (1961).

31. Stewart, J. E., *J. Chem. Phys.*, 30, 1259 (1959).

32. Flett, M. S. C., *Spetrochim. Acta*, 19, 509 (1963).

33. Murthy, A. S. N. and C. N. R. Rao, "Spectroscopic Studies of the Hydrogen Bond," *Appl. Spectros. Rev.* 2, 69 (1969).

34. Stuart, A. V. and G. B. B. M. Sutherland, *J. Chem. Phys.*, 24, 559 (1956).

35. Matsubara, I., Y. Itch, and M. Shinomiya, *J. Polymer Sci.*, B4, 47 (1966).

36. Simpson, D. M. and G. B. B. M. Sutherland, *Proc. Roy. Soc.*, A199, 169 (1949).

37. Varsanyi, G., Vibrational Spectra of Benzene Derivatives, Academic Press, New York (1969).

38. Kniseley, R. N., V. A. Fassel, and E. E. Conrad, *Spectrochim. Acta*, 15, 651 (1959).

39. Wright, N. and M. J. Hunter, *J. Am. Chem. Soc.*, 69, 803 (1947).

40. Smith, A. L., *Spectrochim. Acta*, 16, 87 (1960).

41. Altona, and Hageman, Rec., *Trav. Chim. Pays Bas*, 88, 33 (1969).

42. Rentley, F. F., N. T. McDevitt, and A. L. Rozek, *Spectrochim. Acta*, 20,105 (1964).

43. Carrington, R. A. G., *Spectrochim. Acta* , 16, 1279 (1960).

44. Sheppard, D., *Trans. Faraday Soc.*, 46, 429 (1950).

45. Daasch, L. W. and D. C. Smith, *Anal. Chem.* 23, 853 (1951).

Table 1

List of Groups of Interest and Applicable References

Group	References
-CH	5,6,7,15,26,28,29
CH_2	5,6,7,15,18,20,22,23,24,25,26,27
Ch_3	5,6,7,11,15,18,19,20,21
C-X (X = halogen)	5,41,42
C-C	5,36
C-C (aromatic)	5,6,7,37
C=C	5,6
C≡C	5
C-N	5,6,8,35
C≡N	5
NH	5,6,7,8,10,15,33
NH_2	5,6,7,15,31,32
C-O	5,6,8,34
C=O	5,6,7,8,10
OH	6,7,10,15,34
P-H	6,45
PO_4^{-3}	6
P=O	5,45
Si-H	6,38
Si-O	6,39,40
Si-C	6,40
Si-X	6,40
SO_4^{-2}	6
C-S	6,44
ONO_2, NO_3^{-1}	5,6,43

Table 2

Tabulation of Groups With Principal Vibrational Modes and Absorption Bands

Group	Association	Stretching, cm^{-1}	Deformation, cm^{-1}	Wagging, cm^{-1}
C-H	Aliphatic	2880-2900 (w)	1315-1350 (w)	
	aromatic	3030 (w m)	700-900 (s) out-of-plane 100-1300 (m) in-plane	
	alkynes	3267-3340 (s)	610-680 (s)	
	alkenes	3000-3030 (m)	trans 965 990 (s) out-of-plane cis 650 730 (m) trans 1285-1300 (m) in-plane cis 1395-1430 (m) in-plane	
	Halogen carbon	3000	1200-1215 intensifies	
	carbonyl esters, Amides	2900-2930	1400	
CH_2		2916-2936 (s) asym 2843-2063 (m) sym	1450-1475 (m)	
CH_3	Aliphatic	2952-2972 (s) asym 2862-2882(m) sym	1450-1475 (m) asym 1370-1380 (m) sym	
	Aromatics	2920-2930 (m) asym 2860-2870 (m) sym		
C-F		1000-1400 (vs)		
C-Cl		650-730 (m to s)		
C-Br		510-700		
C-I		485-600		
C-C		1140-1250 (s)		
$\ddot{C}$-C		1440-1625 (w m)	ring stretching	
C=C		1638-1692 (w m)		
C≡C		2100-2260 (m w) depending on substitution		
C-N	Amines, aliphatic	1032-1090 (m) asym		
	aromatic	1250-1360 (s) asym		
	Guide primary	1310-1430 (w)		
	secondary	1270 (s) as Amide III	1515-1570 (s)	
C≡N	Alkyl	2240-2260 (s)		
	Aryl	2220-2240 (s)		

Table 2 (Cont'd)

N-H	Secondary amines	3310-3360 (w)	1550-1650 (w)	700-750 (m)
	Secondary amines	3140-3480 (m)	1200-1305 (m) Amine III	700-740 (m)
	Urethanes	3250-3340 (m)	1200-1305 (m)	700-740 (m)
NH^2	Amines	3330-3400 (w)	1575-1660 (m)	750-850 (s)
	Amides	3350 (m)	1620-1650 (s)	600-750 (s)
C-O	Ethers, alkyl	1060-1150 (vs)		
	aromatic	1230-1270 (vs)		
	alkyl/aryl	1010 1050 (s)		
	vinyl	1200-1225 (s)		
	Esters	1160-1210 (s)		
	Acetate	1230-1260 (s) asym		
		1035-1060 (s) asym		
	Caromates, alkyl/alkyl	1240-1280		
	alkyl/aryl	1211-1248		
	aryl/aryl	1205-1221		
C=O	Amides, ureas, urethanes, carbon acids, carbonates, etc.	1600-1700 (s)		600-700
OH	Alcohols	3300 (s)	1260-1350 (s)	1260-1350 (s)
	Carboxy acids	3000 (s)	875-960 (m)	
	Phenols	3200-3250	1211-1320 (s)	
			1180-1260 (s)	
P-H		2275-2320 (m)	1080-1090 (m)	910-940 (m)
PO_4^{-3}		1000-1100 (s)		
P=O		1110-1250		
Si-H		2100-2250 (m)	800-950 (m)	800-845 (m)
Si-O	Siloxanes (open-chain)	1024-1055 (s)		
		1076-1095 (s)		
	Alkoxy	1100 (m)		
	Silanols	830-910 (s)		
Si-C	Methyl Siloxanes	660-850 (m)		
	Si-phenyl	1100-1125 (s)		
Si-X	(X = Halogen)	820-945 (s)		
SO_4^{-2}		1080-1125 (s) asym		
C-S	Aliphatic	570-705 (m w)		
	Aromatic	1090		

Table 2 (Cont'd)

ONO_2	Nitro	1270-1285 (s) Sym	745-760 (m) 690-710 (m)
NO_3^{-1}	Nitrate	1350-1380 (s) 815-835 (m)	

Table 3

Equivalent Solid Film/Foam Thickness and Relative Absorption at 3000 cm^{-1}

Foam Thickness, mm	Film Thickness Equivalent, mm	% Absorption
0.61	0.0178*	16.5*
0.76	0.0218	40
1.04	0.0305	79
1.50	0.0432	90
1.91	0.0533*	96*

*It is readily apparent that a three-fold increase in equivalent thickness causes almost a six-fold increase in absorption at this wave number. Essentially, the same ratio occurs all along the spectrum of 4000 cm^{-1} to 700 cm^{-1}.

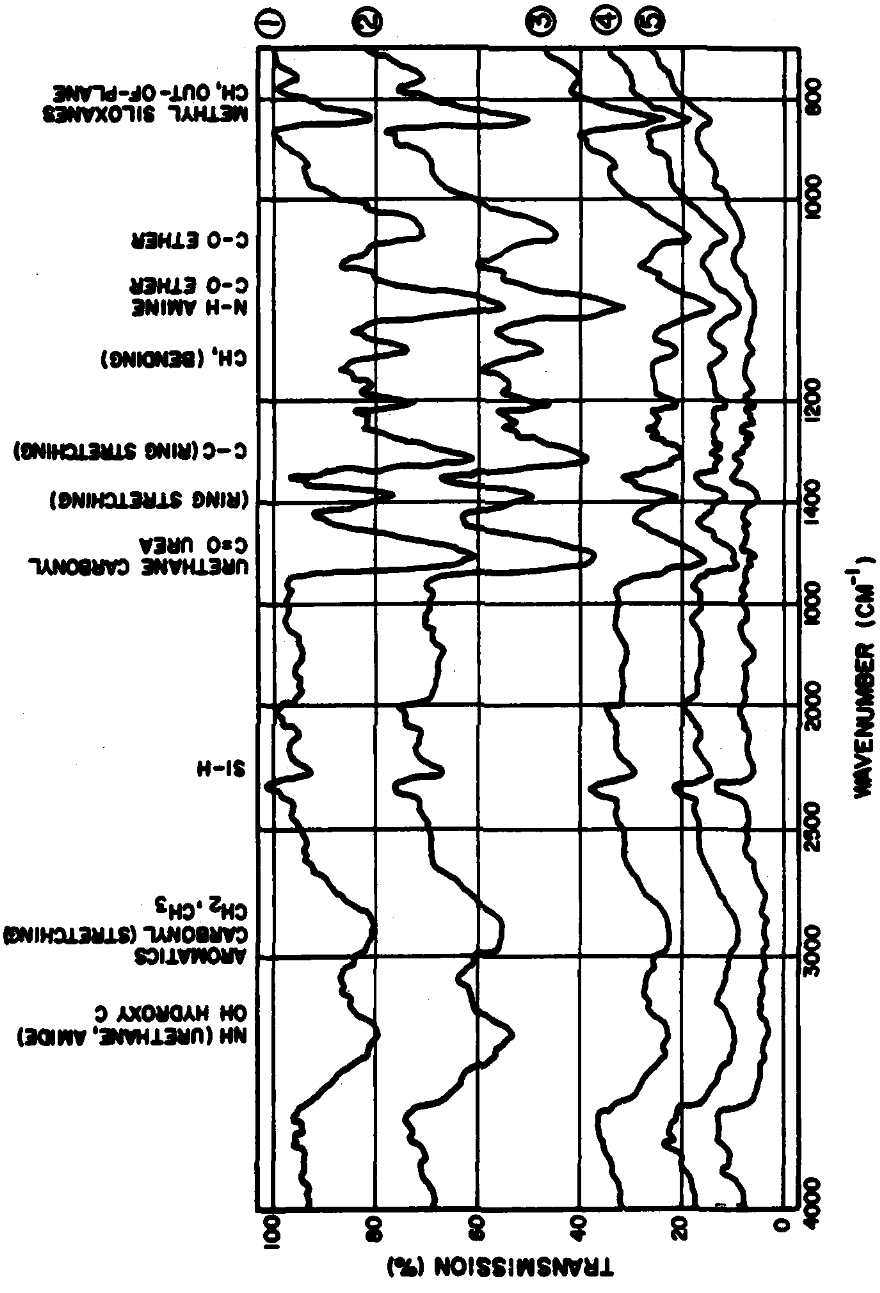

Figure 1. Comparison of Polyurethane Film and Foam Absorption Spectra

CAEADS -- COMPUTER-AIDED ENGINEERING AND ARCHITECTURAL DESIGN SYSTEM (U)

JANET H. SPOONAMORE*
U.S. ARMY CONSTRUCTION ENGINEERING RESEARCH LABORATORY
CHAMPAIGN, IL 61820

The U.S. Army Corps of Engineers Construction Engineering Research Laboratory is developing the Computer-Aided Engineering and Architectural Design System (CAEADS) to support the design of military facilities. CAEADS' support will start with initial requirements for a facility, and continue through concept and final design and the production of construction drawings, specifications and cost estimates. The CAEADS system will be integrated based on a central source of design information used by all the disciplines in the design process: users, project planners, architects, engineers, specification writers, and cost estimators and drafters.

In October of 1981, the integration of the concept design tools of the CAEADS system was completed and a test initiated involving 200 projects in the Military Construction Army (MCA) FY84 program. This integrated system, called Concept CAEADS, is used to support preliminary design, from project requirements through to the 25 percent design level. Concept CAEADS provides tools for project information retrieval, facility layout, functional evaluation, energy evaluation, cost estimating and production of drawings. During the period 1 October 81 to 1 February 82, one architectural engineering firm tested and used Concept CAEADS to design to 25 percent these 200 MCA projects. The findings of the test suggest that substantial design cost reductions will be realized. The purpose of this paper is to report on the Concept CAEADS test objectives and findings and describe the development of a further integration of design tools -- Predesign and Final Design CAEADS.

Background

The Corps of Engineers is the largest construction industry in the world. Each year, the Corps' MCA program includes several hundred projects consisting of some 50 facility types in various stages of planning, design or construction. For several years, total MCA construction has grown both in volume and technical complexity. Keeping construction costs low given increasing demands for energy and concerns for safety, accessibility, and efficiency in an environment of rising construction labor and material costs is a great challenge. This challenge means the Corps must design the best possible facilities, reuse these "best" designs, and manage construction programs to optimize on repetition. Further quality can be gained and time saved by using automated tools to support design layout, analysis and drawing production on repetitive, "similar" projects. The CAEADS system is being developed to meet this objective; i.e., to reduce design costs and increase the quality of design.

Computer-Aided Design Technology

Computer-aided design (CAD) tools for engineering and construction have been adapted mainly from manufacturing and business applications; software for accounting, specification production and drafting are presently available. These individual tools now are being linked using a geometric description of the design, i.e., a central source of data. Computer graphics and geometry are used like balsa-wood models, but can do much more -- functional analysis, quantity take-offs, statistical analysis, and heating and cooling analysis, etc. For example, using the geometric operations, interferences between the layout of structural elements and heating, ventilating, and air conditioning (HVAC) ducts can be detected. According to Engineering News-Record (December 1981), CAD may bring the most profound changes in standard procedures the design profession has ever seen (1).

CAEADS focuses on assembling hardware and software tools affordable by and compatible with the architect/engineer (A/E) organizations that will be using the system on Corps projects (2).

The benefits an integrated system such as CAEADS will offer the Corps are far-reaching. The MCA design process can be shortened and strengthened using CAEADS. CAEADS can increase productivity, and help the Corps exploit the opportunity of repetition of similar designs. (Repetition is especially amenable to automation.) CAEADS allows more analyses to be performed to detect design errors such as interferences in construction, poor layout, etc. CAEADS also gives the Corps an efficient way to make continual evaluations to trade off expected construction costs and operating energy costs. CAEADS will produce benefits and savings in the design, construction and operation and maintenance of facilities.

Concept CAEADS Description

CAEADS has only recently become available as an integrated system. Over the past several years, CERL and other Corps organizations have developed specific, stand-alone application tools under the CAEADS umbrella. The systems include the Design Information System (DIS), developed by the Office of the Chief of Engineers; the Automated Budget Estimating System (ABES) and the Computer-Aided Cost Estimating System (CACES), developed by the U.S. Army Engineer Division, Middle East (Rear); and the CERL-developed DD 1391 Processor, the Systematic Evaluation of Architectural Criteria (SEARCH), the Computer-Aided Facility Layout System (SKETCH), the Building Loads Analysis and Thermodynamics (BLAST) System, and the Computer-Aided Specification Preparation System (EDITSPEC).

Concept CAEADS integrates automated tools for use at the early stages of design, primarily the functional layout and analysis phases. Figure 1, "CAEADS Concept Design," depicts these tools. The system helps designers organize project information, lay out design alternatives, analyze for compliance to functional requirements, evaluate energy consumption and costs, estimate direct project costs and produce scaled drawings. Concept CAEADS provides a 3-dimensional data base from which final design can be initiated.

In the concept design phase, the designer will generate one or more conceptual design solutions. Each alternative is evaluated and reviewed to assure it complies with the facility users' needs and other design criteria.

The Concept CAEADS design process includes the following steps:

1. The DIS module is used to review the MCA project design information in a given fiscal year and identify projects that can use "as-designed" standards. Project information is maintained at a summary level in the DD 1391 Processor data bases.

2. The SKETCH module is used to develop custom layouts or to modify standards. The system provides layout tools for rooms, walls, doors, windows, ceilings, floors, furniture and equipment, thermal zones and associated construction materials.

3. The SEARCH evaluation modules are used to check alternatives to assure they comply with a project's functional requirements. These include area, walking distance, acoustic separation, visual control and handicap accessibility codes.

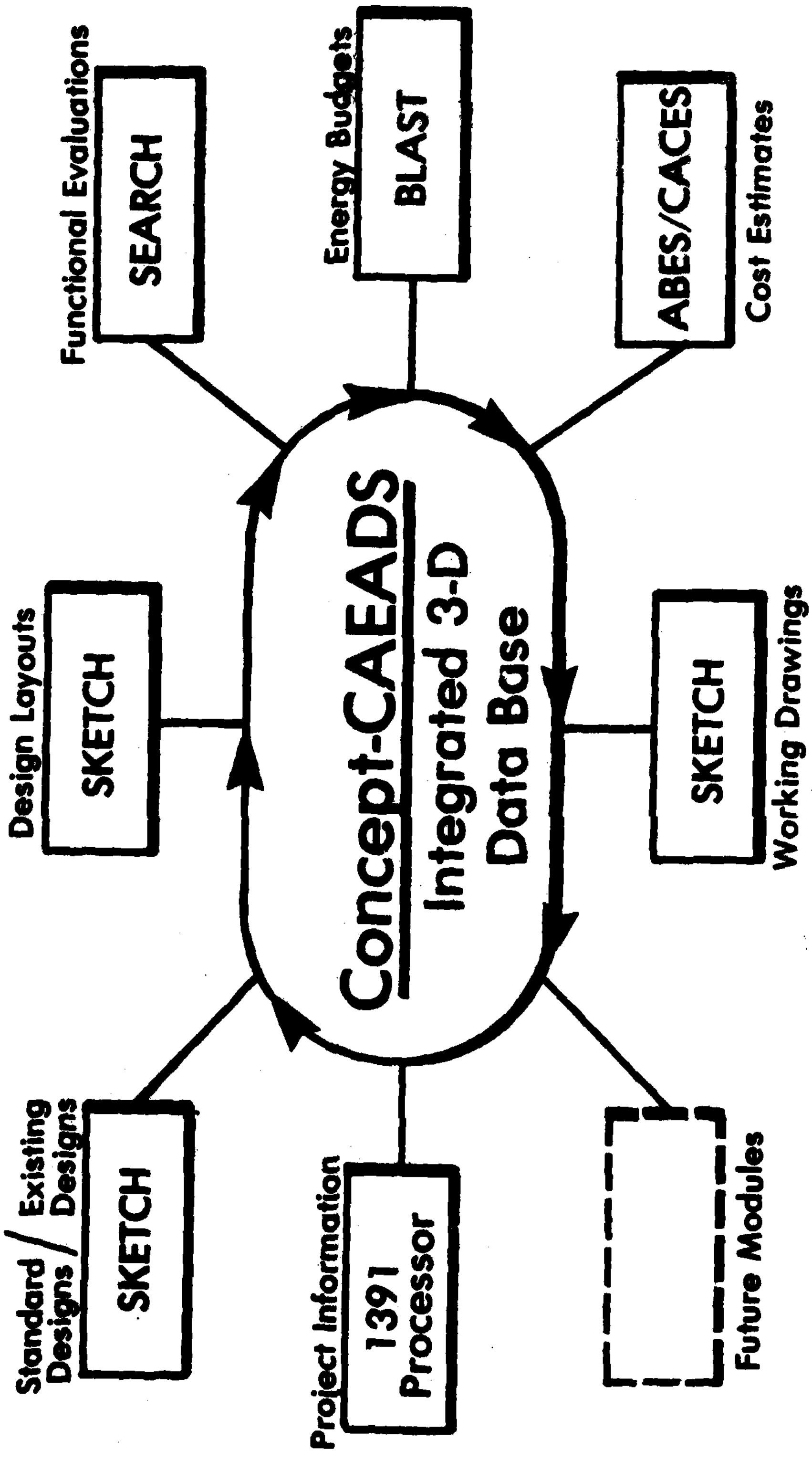

Figure 1. CAEADS Concept Design

4. The BLAST module analyzes alternatives for energy consumption and costs (3). BLAST predicts consumption based on simulated geographic weather and building operations.

5. The ABES/CACES modules prepare preliminary cost estimates for each alternative. A data base library of construction and unit costs is maintained in the system.

Designers access Concept CAEADS using low-cost graphics workstation terminals. Layouts are entered using the terminal thumbwell movements; displays are shown on the terminal screen. Hardcopy plots of final layouts can be produced. The functional evaluation, energy usage and cost estimate reports also are produced by the system at this workstation.

Concept CAEADS currently operates on timesharing services at the University of Michigan, Michigan State University, and the Mid-East Rear Division.

Concept CAEADS Test Objectives

The test of the Concept CAEADS system had three objectives:

1. Determine the usability of a system like CAEADS.

2. Determine the costs and benefits of applying CAEADS to a design workload.

3. Determine the design workload distribution which would ensure the highest payoff using CAEADS.

Usability

A system like CAEADS may or may not be accepted and properly used by practitioners, although it closely supports normal design practice. Human factor issues are very important. The use of automation in architectural/engineering practice historically has been very low compared to other professions. But with the initiation of computer-aided drafting in the A/E community, it seems likely that a CAD system will be accepted and used. Only the essential differences between automated drafting and automated design tools need to be explored. Table 1, "Summary of Concept CAEADS Versus Automated Drafting," shows the differences between drafting tools and design tools. The Concept CAEADS test helped determine whether these design tools could be incorporated into practice, in much the same way as drafting tools have been.

Table 1

Summary of Concept CAEADS Versus Automated Drafting

Automated Drafting (Typical turn-key system)

- o Drawing tools
  - Definition of levels/pages
  - Definition of repeating group of elements
  - Layout of elements
    - o Annotation
    - o Points
    - o Lines
    - o Polygons
    - o Polyhedron
    - o Group of elements
  - Modification of above (changes or deletions)
  - Line-weighting, cross-hatching, fill, font selection, paragraphing, formatting.
  - Dimensioning notation (semi-automatic)
  - Accuracy controls (snapping to grids, points)
- o Plotting tools
  - Selection of scale, region to be plotted.
- o Association of elements to nongraphic data

Concept CAEADS

- o Design tools
  - Definition of project criteria
    - o Room areas/proximities/visual control
    - o Handicap criteria
    - o Location
  - Layout of alternative plan elements
    - o Floors, ceilings, roofs, doors, windows, equipment/furniture or groups of these
    - o Selection of materials for above
    - o Automatic generation of room polygons
    - o Definition of room names and HVAC zones (plants, air handling)
    - o Stretching/shrinking capability
    - o Accuracy controls (snapping to grids, points, angles)
- o Analysis tools
  - Calculation of layout against project criteria
  - Calculation of quantities and direct costs
  - Calculation of heating/cooling BTUs
- o Plotting tools
  - Automatic generation of scaled drawings
- o Translation of elements into graphic data for further lineweighting, dimensioning, annotation, fill and font selection.

The test showed that Concept CAEADS could be applied directly to design practice. Training on the system (i.e., learning the system functions and applying them to the design efforts) went well throughout the course of the test. Only simple problems occurred during the test, including computer "downtime," causing work stoppage; minor system errors; and user difficulties in not understanding how the system operated. During the first several weeks of the test, the A/E staff quickly adapted to the new functions offered by Concept CAEADS.

Midway through the test, the A/E staff was asked to fill out a questionnaire about the system's utility and ease of use. The questionnaire also asked the A/Es to compare Concept CAEADS to manual and automated drafting approaches, and to suggest improvements. The users who actually operated the system included three architects and one mechanical engineer. These persons used the SKETCH system to do floor plan layouts and to specify HVAC zones and building materials. They also ran off the SEARCH drawings, BLAST energy profiles and ABES/CACES cost estimates.

The questionnaire results indicated the staff felt the system was useful for adapting past project or definitive layouts to meet established criteria. They also felt the system's strong evaluation features were useful. Their negative reactions focused on several of the user protocol procedures, which they felt slowed their performance. Based on their recommendations, many of these procedures already have been enhanced and are now much easier to perform.

Costs/Benefits

The use of Concept CAEADS on 200 MCA project designs produced considerable savings over current practice. It should be noted that savings were realized not only from use of the system, but also from the consolidated design workload on which the system was used. The costs for the 200 projects included design personnel costs, computer timesharing services costs, equipment rental costs and software maintenance/training personnel costs. These costs are shown in Table 2, "Concept CAEADS Test Costs." Costs using current methods of design practice were derived from typical project design costs incurred in the past. An average cost for 25 percent project design (on similar design workloads) was approximately $16,000 using current manual methods. The number of completed projects in the test workload was 113 out of the original 205 started. Ninety-two projects were cancelled during the progress of the work. On the average, these 92 projects were completed to about 10 percent. The costs to perform the design using current practice are shown in Table 3, "Current Practice Costs."

Table 2

Concept CAEADS Test Costs

Costs	
Design personnel	$200,000
Automated data processing timesharing	100,000
Equipment rental	16,000
Software maintenance/training	40,000
	$356,000

Table 3

Current Practice Costs

Projects	Cost/Project	Total
113	$16,000	$1,808,000
92	6,400	588,800
	TOTAL	$2,396,800

Table 3 shows that more than $2 million in cost savings were realized using Concept CAEADS.

Design Workload Distribution

As mentioned earlier, the users of the Concept CAEADS system felt the system was amenable to adapting designs based on definitive or past project layouts, and that design workload distribution was an important ingredient in realizing high-payoffs from automation. Table 4, "Project Distribution," shows the range and scope of facilities designed. This workload included new construction of building projects.

Table 4

Project Distribution

Category Code		Number of Projects	Approximate Square Feet
141	Field operations	5	9,000
		2	13,000
		2	18,500
		1	4,000
171	Headquarters	1	4,000
		6	12,000
		2	17,000
		1	25,000
		1	28,000
		1	35,000
211	Hangars	6	Ranges (25,000 - 63,000) Average (41,500)
214	Vehicle maintenance	9	4,000
		2	14,000
		2	19,000
		1	26,000
		1	29,000
		2	33,000
		1	49,000
		2	225,000
219	Maintenance -- FE	1	12,000
		1	12,000
		1	28,000
		1	34,000
610	Administration	2	3,500
		1	35,000
		1	85,000
722	Dining	3	8,000
		3	12,000
		1	16,000
		1	48,000

Table 4 (Cont'd)

Category Code		Number of Projects	Approximate Square Feet
723	Company administration	4	5,000
		1	14,000
		1	19,000
		2	24,000
		1	29,000
		1	34,000
		2	43,000
		1	71,000
		1	78,000
724	Officers housing	1	52,000
730	Fire stations	2	5,000
		2	6,000
740	Morale support	19	Ranges (3,000-62,000)
	o Child care		Average (30,000)
	o Eduction/library		
	o Physical fitness centers		
	o Recreation centers		

As expected, there was considerable variation in layout time required to modify drawings versus original custom design layout. The online usage data collected during the test revealed an average of 12 hours per layout (minimum 0, maximum 24 hours) with a standard deviation of 15. Having access to a central library of design layouts and tools to modify these floor plans for specific project requirements and location gave designers the opportunity to "reuse" designs. This approach resulted in the lowest possible design costs at no sacrifice to quality.

Further Developments

This extensive test answered several questions. CAEADS easily can be incorporated into design practice -- it is usable. It is cost effective and the repetitive workload of the MCA program is especially amenable to high-cost avoidance.

Two main questions arose during the test which must be answered. First, project design information is sometimes lacking at the start of the design process. How can this project requirement information best be collected and organized for design initiation? Much of this data is generated by the Army installation user, and ultimately is documented in the Project Development Brochure (PDB). Proposed construction projects must be approved and contained in the Installation Master Plans (including the approved site). A new module of CAEADS -- Predesign CAEADS -- will be developed to integrate the tools to support the development of project requirements (functional and technical requirements), the analysis of supporting utility requirements compared to capacity and environmental and economic impact analysis. Predesign CAEADS will be used primarily by Corps district offices supporting installations preparing MCA project information.

A second question posed during the test regards the transition of the concept design into final design (usually performed under A/E services). Given project designs completed to concept level, a means must be provided to transfer these designs to the many A/E firms which ultimately will provide working drawings, specifications and detailed design analysis. The system which will provide this transition is called Final Design CAEADS. This system will integrate several of the stand-alone systems previously mentioned (BLAST, CACES, EDITSPEC) and a sophisticated 3-dimensional modeling data base for representing the design. The 3-dimensional data base provides a central source of data from which specifications can be prepared, quantities calculated for detailed cost estimates and analysis performed (structural, electrical and mechanical). The system ARCH:MODEL, developed by the University of Michigan Architectural Research Laboratory, will provide the data base handling and geometric modeling tools needed for fully representing and retrieving the elements of design, i.e., doors, windows, ceiling, roof, foundations, structure, mechanical and mechanical/electrical conduit (4). ARCH:MODEL's geometric operations on 3-dimensional polyhedra allow for checking interferences in building system layout. Presently, an interface has been developed to transfer concept-level floor plans into a 3-dimensional model of the facility design. Figures 2 through 8 depict the development of a design using ARCH:MODEL.

Conclusions

The recent test of Concept CAEADS has provided a unique opportunity to evaluate the impacts of CAD on a wide range of project design workloads. The findings of the test show the usability of CAD in design practice and the benefits of CAD applied on a consolidated concept design workload. Development of the Predesign and Final Design modules of CAEADS will be performed over the next 5 years.

References

(1) Engineering-News Record, December 3, 1981, "Computer-Aided Everything," pp 34-61.

(2) "Computer-Aided Engineering and Architectural Design System (CAEADS), Volume I: Summary," U.S. Army Construction Engineering Research Laboratory, Champaign, IL, CERL-TR-P-97, Jan 1979.

(3) "The Building Loads Analysis System Thermodynamics (BLAST) Program, Version 2.0: Users Manual, Volume I," U.S. Army Construction Engineering Research Laboratory, Champaign, IL, CERL-TR-E-153, June 1979.

(4) "ARCH:MODEL, Version 1-2, Geometric Modeling Relational Database System," Architectural Research Laboratory, College of Agriculture and Urban Planning, University of Michigan, Ann Arbor, Michigan, July 1981.

Figure 2. Transfer of layout to 3-dimensional model (includes ceramic floor tiles for passive solar design).

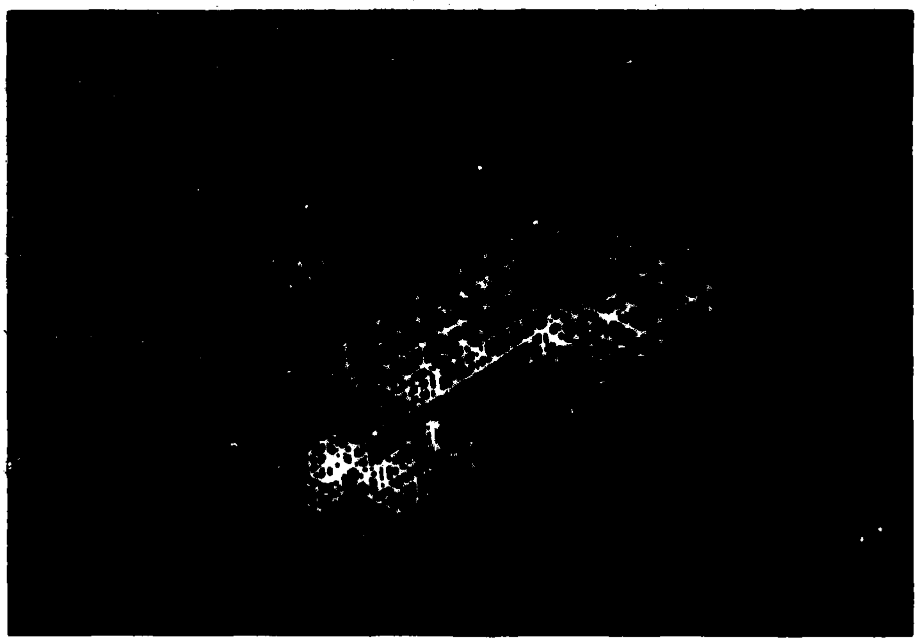

Figure 3. Extrusion of walls into 3-dimensional polyhedron.

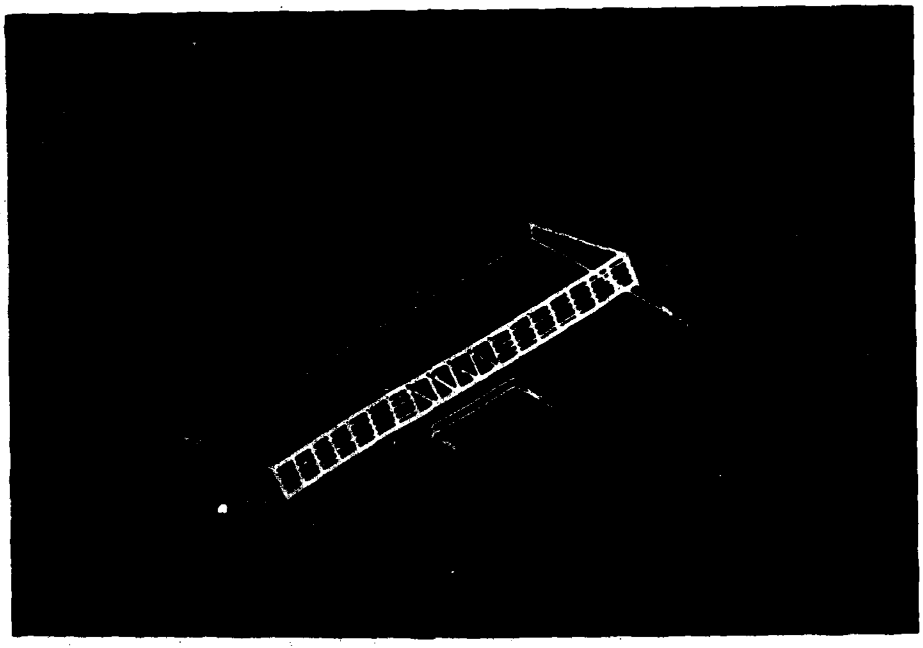

Figure 4. Roof section laid out in SKETCH and extruded. Louver windows and solar collection panels are built in 2-dimensions and placed on roof.

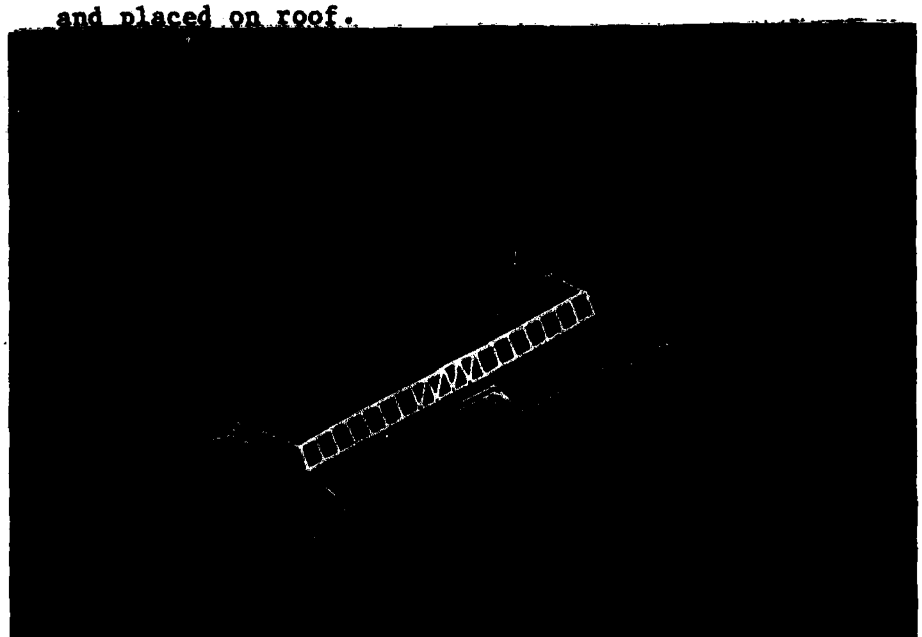

Figure 5. Roof is placed on building and berms are placed on north, west and east sides.

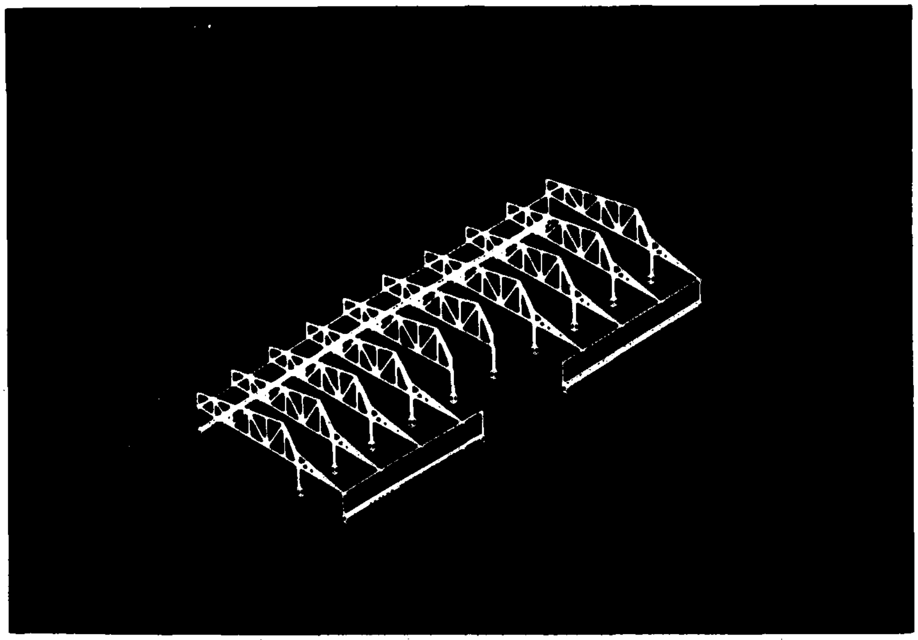

Figure 6. Footings, foundations, columns, and girders are sketched and extruded. Presently, sizing and layout are calculated outside CAEADS. Eventually, an automated interface will be provided.

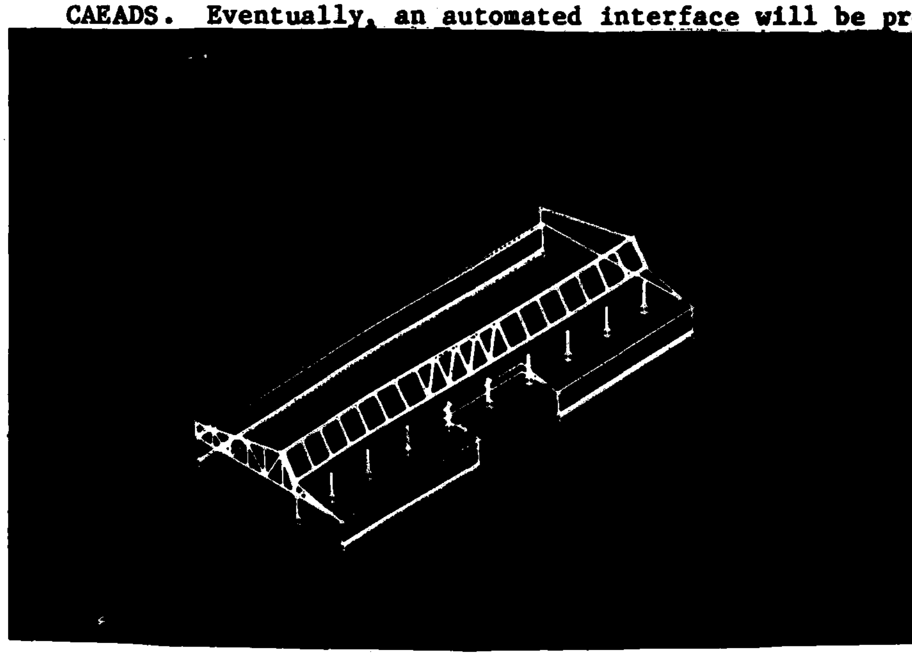

Figure 7. Conflicts in placement of components can be detected, e.g., the girder and roof.

VISCO-ELASTIC BEHAVIOR OF INCENDIARY COMPOSITIONS UNDER BALLISTIC LOADING

WALTER H. SQUIRE
LAMONT W. GARNETT
FIRE CONTROL & SMALL CALIBER WEAPON SYSTEMS LABORATORY
U.S. ARMY ARRADCOM, DOVER, NJ 07801

BACKGROUND

The defeat of both personnel and materiel type targets on the modern battlefield is accomplished in the most cost effective means through the terminal effects of blast, fire, and fragmentation. These terminal effects are quite easily realized through the functioning of a high explosive projectile. While the terminal effects of gun-launched, high explosive projectiles is a well-accepted fact, munition designers must incorporate independent safing, arming, and functioning mechanisms into the munition. In general, gun-launched, high explosive projectiles are required to be safe from accidental or premature initiation during transportation and handling and while being fed into the weapon. However, once the projectile has been launched and directed toward the target, an arming mechanism is required to render -- on a reliable and predictable basis -- the projectile in a state for functioning given its interaction with the target. Lastly, when the high explosive does engage the target, a functioning mechanism must be provided to initiate the explosive charge in a high order detonation. Traditionally, these performance requirements for independent safing, arming, and functioning are accomplished through a conventional mechanical or electrical fuze. Specific safety requirements for the generic cannon caliber ammunition class of fuzes are provided in reference (1).

Unfortunately, recent tactical trends (i.e. proximity of friendly personnel in the immediate area from which a high explosive projectile has been launched) and a wide diversity of targets on the modern battlefield have driven fuze designers to great lengths in providing for a spectrum of safing, arming, and functioning envelopes in a particular fuze design. A typical cannon caliber projectile fuze (i.e. a fuze which is used on 20 through and including 40mm ammunition) is shown in Figure 1. As is readily seen, safety and performance requirements have dictated a rather complex and sophisticated mechanism. When one considers the relative density of which cannon caliber ammunition is produced on a yearly basis and the cost of a conventional mechanical or electrical fuzing -- resulting from complexity and sophistication -- the motivation is obvious for simpler and less expensive fuzes.

INTRODUCTION

This motivation for a simpler and less expensive fuze mechanism and yet maintaining the capability to defeat a myriad of targets on a reliable basis has impelled fuze designers to seek novel means of accomplishing the operations of safing, arming, and functioning. One such means which has recently come to the fore is shown in Figure 2. This figure presents a cut-away view of a 20mm, high explosive projectile which does not utilize a conventional mechanical or electrical fuze mechanism. Most of the projectile's attributes/components, however, are of a traditional design. The projectile body, rotating band, external shape, nose cap, high explosive charge, etc., are typical of those employed in other cannon caliber ammunition. Moreover, the assembly of this projectile is effected via standard techniques. The uniqueness of the concept shown in Figure 2 lies in the fact that two different incendiary mechanisms are in the forward (projectile nose) and mid-regions of the projectile. The proposers and advocates of this concept contend that the safing, arming and functioning mechanisms of this concept are accomplished by a physical rearrangement of the forward incendiary mix as a result of ballistic loading. During launch, a 20mm, high-explosive projectile senses a set-back force of approximately 1.2×10^5 g's and a rotational velocity of 1.7×10^4 radians/second[2]. Typical in-barrel ballistic times are of the order of $2\text{-}3 \times 10^{-3}$ seconds and the flight time to a target 1000 meters distant is 3-4 seconds. It is within these loading and temporal constraints that the concept shown in Figure 2 must operate.

HYPOTHESIZED SAFING/ARMING/FUNCTIONING MECHANISM

The pre-launch state of the projectile shown in Figure 2 is safe. Since there is no detonator present (by virtue of the fact that there is no conventional fuze present), accidental or premature initiation is impossible. The safety of the projectile is limited only by the safety of the high explosive charge which, unless stimulated by a shock or pressure pulse, is a relatively insensitive material. Without the use of a detonator-type material to generate a pressure wave in the high explosive medium, it is extremely difficult to initiate accidentally the projectile.

PROBLEM STATEMENT

The concept shown in Figure 2 and hypothesized to operate as described in the previous narrative has been demonstrated and evaluated to the point where it may be added to the US's ammunition inventories. For the most part, the concept was matured through a trial-and-error, empirical approach. Given the concept's demonstrated success, it seems reasonable to explore fully all possible design options for fuzing which may attend the rearrangement of an incendiary composition under ballistic loading. For this reason, an analytical model was constructed to predict the movement of an incendiary subject to set-back and centripetal loading. The succinct purpose for formulating the anlaytical model and verifying the model's predictive capability with real-range data is to allow a convenient, rapid economical means to maximize the safety and performance capabilities of "fuzeless" projectile concept. Once the relationship between the local density of the incendiary and the cavity's formation is known, performance alternatives such as arming delays, delays after impact, super-quick functioning can all be incorporated into the basic design. The analysis which follows will then predict the motion of the locus of points at the interior surface of the projectile's nose under the influence of ballistic loading.

ANALYTICAL APPROACH

The approach pursued in developing the mathematical model is to separate the total event into two phases -- one, the result of set-back or inertial loading and the other attributable to the centripetal loading. The set-back loading will be strongly influenced by the pressure-time history of the propellant gases which cause the projectile's acceleration. The centripetal loading will be a function of the rotational velocity imparted to the projectile as a result of the barrel's rifling. The displacement realized by the forward incendiary due to the set-back loading will serve as the initial condition for the rearrangement due to centripetal loading.

ANALYSIS

The pressure-type history of the propellant gases recorded during the firing of a 20mm cartridge is presented in Figure 4 and is the curve labelled $P^{(2)}$. The curves identified V and T are respectively the projectile velocity and projectile travel. No attempt has been made to convert these data to SI units since they were abstracted directly from (2). The pressure-time curve has been divided into twenty-four time increments, thereby allowing an incremental loading of the projectile. In the first phase of the analysis, the force balance equation is $ma = PA$. The instantaneous set-back force, F_{se_i} , is the product of the projectile mass and the instantaneous acceleration. Figure 5 shows a sketch of the incendiary charge as it is defined by the interior surface of the projectile's nose and the simplification of this geometry to a right circular cylinder. The local stress concentration imparted to the forward face of the incendiary is classically given as

$$\sigma = \frac{F_s}{A_I}$$

Selected values for a, F_{se_i} and σ as a function of various increments of the pressure-time curve are given below:

$m(\ )$	$P\left(\frac{DYNE}{CM^2}\times10^{-8}\right)$	$a\left(\frac{CM}{SEC^2}\times10^{-7}\right)$	$F_{se}\left(DYNE\times10^{-7}\right)$	$\sigma\left(\frac{DYNE}{CM^2}\times10^{-7}\right)$
0	0	0	0	0
4	6.9	2.3	4.0	8.8
8	34.5	11.4	20.1	44.2
10	41.4	13.7	24.1	53.0
12	36.6	12.1	21.3	46.9

* All symbols are defined under the NOMENCLATURE heading.

14	24.2	8.0	14.1	31.0
20	9.7	3.2	5.6	12.3
24	6.2	2.0	3.5	4.4

The density profile of the incendiary composition in the projectile's nose is discussed in (3) and is portrayed in Figure 6. A linear approximation to the measured density profile has been effected to facilitate the mathematics. Reference (4) provides background data as to the values of typical densities of incendiary compositions encountered in cannon caliber ammunition. A maximum local density at $z=0$ (i.e. base of the projectile's nose) of 2.95 grams/cc is deduced from reference (4). Hence, the following range of values will be used to describe the local densities in the projectile's nose.

$\rho\left(\frac{\text{GRAM}}{\text{CC}}\right)$	z (CM)*
2.95	0-7.17
1.62	7.18-16.73
0.29	16.74-23.9

* z is measured from the base of the projectile's nose toward the ogive.

The displacement of the forward surface of incendiary charge will be the result of the compression of the incendiary in each of the three increments ($0 \le z \le 7.17$, $7.18 \le z \le 16.73$, $16.74 \le z \le 23.9$). In general, a material's compressibility is related to the local stress concentration through the Modulus of Elasticity. Classically,

$$\epsilon = \frac{\sigma}{E}$$

In order to calculate the overall displacement of the forward surface, the local stress concentration will be incrementally advanced in time in each of the three regions. Each increment of compression, in turn increases the local density which then requires an updated value for the Modulus of Elasticity. Therefore, for each of the three regions in the incendiary charge, the total compression will be given by:

$$\epsilon_{TOTAL} = \int_0^{t_{FINAL}} \epsilon(t)\,dt = \int_0^{t_{FINAL}} \frac{\sigma(t)}{E}\,dt$$

$$\epsilon_{TOTAL} = \frac{\Delta t}{15}\left[14\left[\frac{1}{2}\left(\frac{\sigma_0}{E_0} + \frac{\sigma_m}{E_m}\right) + \sum_{\substack{j=2\\ \text{EVEN}}}^{m-2} \frac{\sigma_j}{E_j}\right] + 16 \sum_{\substack{j=1\\ \text{ODD}}}^{m-1} \frac{\sigma_j}{E_j}\right] \quad (1)$$

Where each incremental σ_i requires an updated value of the Modulus of Elasticity. For each Δt equation (1) is applied to each of the three regions. The assumption is made that each region realizes the same local stress' concentration for a particular Δt .

Reference (5) provides data on the physical and mechanical properties of solid materials in the density range of 0.29 - 2.95 grams/cc. Porous graphite with a density of 1.02 grams/cc has a Modulus of Elasticity of 1.38 x 10^{10} dyne/cm^2. Local values for E which bracket this value are used as the local density is increased as a result of the compression. The displacement of the forward surface in the rearward direction is the product of the compression and instantaneous length.
The solution of equation (1) and multiplication by the instantaneous length is accomplished via computer and will not be discussed at any greater length. Bookkeeping of the updated values of E is also done within the computer. The range of Modulus of Elasticities assigned to the region adjacent to the ogive varies from 0.46 x 10^{10} to dyne/cm to 0.69 x 10^{10} dyne/cm^2. Multiplication of the resulting compressions and the instantaneous lengths yields movement of the forward surface by 2.43mm. Also, when equation (1) is applied to elemental discs in the mid and base regions of the incendiary charge where the nominal values of E are 1.86 x 10^{11} dyne/cm^2 and 8.38 x 10^{11} dyne/cm, respectively. The movement of these discs are of the order 10^{-3} and 10^{-4}mm, respectively. The conclusion is reached that the set-back loading perturbs the forward surface of the incendiary charge by displacing it 2.43mm in the rearward direction and that the densities in the mid and base regions of the incendiary are of such magnitude that there is no discernible motion which may be attributable to compression.
Once the initial displacement of the incendiary has been realized and the projectile exists the muzzle of the weapon beginning its free flight, the cavitation prediction is the next step in the analysis. Reference (6) provides a detailed analytical treatment of Couette Flow which involves the steady helical flow of a viscous medium between bounding cylinders rotating with different angular velocities Ω_1, and Ω_2. The analysis undertaken in reference (6) assumes that there is no axial loading. Under the assumption that each material point moves in a circle with speed $r\omega(r)$, the shear stress in the radial direction then becomes

$$S(r) = \frac{M}{2\pi r^2}.$$

Equation (16.11) of reference (6) gives the velocity profile as

$$\omega(r) - \Omega_1 = \int_{R_1}^{r} \frac{1}{\xi} \lambda\left(\frac{M}{2\pi\xi^2}\right) d\xi = \frac{1}{2} \int_{\frac{M}{2\pi r^2}}^{\frac{M}{2\pi R_1^2}} \frac{1}{S} \lambda(S)\, dS \qquad (2)$$

where S = shear stress concentration
λ = rate of shear function (an inverse function of S).

As a result of the high shear rates encountered in the spinning of the projectile during its trajectory, non-Newtonian fluids show a characteristic known as ultimate viscosity (second Newtonian viscosity). That is, the non-Newtonian effects are diminished or suppressed at high flow rates (those commensurate with angular velocity of 1.7×10^4 radians/second). This ultimate viscosity simplifies the relationship between the rate of shear function and the shear stress

$$\lambda(s) = \frac{s}{\eta_\infty}.$$

Substitution of the above expression into equation (2) and evaluation yields

$$\omega(r) = \frac{1}{R_2 - R_1}\left[r\left(\Omega_2 R_2^2 - \Omega_1 R_1^2\right) - \frac{R_1^2 R_2^2}{r}\left(\Omega_2 - \Omega_1\right)\right] \tag{3}$$

which is consistent with the classical Couette Flow problem solution. In order to predict the cavitation in the viscous medium, reference (6) is again used as the basis. Coleman, *et al* (6) provide the governing equation for the climbing effect in Couette Flow as equation (20.1)

$$\gamma = \int_{R_1}^{r} \left\{ \frac{1}{\xi}\left[\sigma_2\left(\frac{M}{2\pi\xi^2}\right) - \sigma_1\left(\frac{M}{2\pi\xi^2}\right)\right] - \rho\,\xi\,\omega(\xi)^2 \right\} d\xi - \sigma_1\left(\frac{M}{2\pi r^2}\right) + q(t) \tag{4}$$

where γ = total normal stress in the axial direction
ξ = variable of integration

$q(t)$ is determined from the balance of the total force in the axial direction

$$2\pi \int_{R_1}^{R_2} \gamma\, r\, dr = -\,p_0 \pi \left(R_2^2 - R_1^2\right). \tag{5}$$

Substitution of equations (4) and (5) into (3) and rearranging gives

$$q = -p_0 + \frac{1}{R_2^2 - R_1^2}\int_{R_1}^{R_2}\left\{\rho\left(R_2^2 - R_1^2\right) r\,\omega(r)^2 - \frac{R_2^2 - r^2}{r}\sigma\left(\frac{M}{2\pi r^2}\right) + \frac{R_2^2 + r^2}{r}\sigma\left(\frac{M}{2\pi r^2}\right)\right\} dr. \tag{6}$$

Denoting X as the excess of the atmospheric pressure p_0 over the thrust $-\Upsilon$ exerted by the fluid in the axial direction

$$X = -p_0 + \Upsilon.$$

In general, X is not zero and hence the face surface at the upper end of the fluid mass cannot be a plane z = constant. The derivative of X in the radial direction is obtained from equation (6)

$$\frac{\partial X}{\partial r} = -\rho r\,\omega(r)^2 + \frac{1}{r}\left[\sigma_2\left(\frac{M}{2\pi r^2}\right) - \sigma_1\left(\frac{M}{2\pi r^2}\right)\right] + \frac{M}{\pi r^3}\sigma_1\left(\frac{M}{2\pi r^2}\right)$$

In the above equation Ω_1 and R_1 were driven to zero to allow the Couette Flow to approximate the centripetal loading of the projectile.

If the normal stress functions are zero, then

$$\frac{\partial X}{\partial r} = -\rho r\,\omega(r)^2 < 0. \tag{7}$$

This inequality is regarded as an indication that the free surface will slope upwards from the inner to the outer cylinder. Solution of equation (7) and subsequent plotting is the cavitation profile. Figure 7 shows the calculated dependence of $\omega(r)$ on r which is used to calculate the cavitation profile shown in Figure 8.

EXPERIMENT

Recently, an experimental endeavor was undertaken to verify the existence of the cavitation in the forward incendiary composition. An array of X-ray tubes was positioned approximately 200 meters from the muzzle of the weapon in a position which was directly aligned with the projectile's flight path. The tubes were pulsed when the projectile interacted with a break circuit positioned immediately before the "vision" cone of the X-ray tubes. Due to differences in the material thicknesses of various portions of the projectile's body -- the nose is relatively thin, whereas the projectile body is rather thick -- it is impossible to view the entire contents of the projectile. For this reason, the exposure and power levels of the X-ray tubes were adjusted to view only the nose region. Figure 9 is a reproduction of a typical X-ray. Note the cavity shown in Figure 9 is very similar to that predicted from equation (7) and graphed in Figure 8.

CONCLUSIONS

1. Set-back forces are of sufficient magnitude to cause a rearward displacement of the forward surface of the incendiary by 2.43mm.
2. Centripetal forces are responsible for a cavity's formation. The shape of which may be predicted by equation (7) and graphed in Fig. 8.
3. The hypothesized safing and arming mechanism of the "fuzeless" concept has been verified.
4. The analysis described herein offers a design tool -- to maximize the effectiveness of the fuzeless concept particularly relative to definition of the local density.

REFERENCES

(1) MIL-STD-1316B, Military Standard, Fuze Design, Safety Criteria for, 15 February 1977.

(2) Corner, J., Theory of Interior Ballistics of Guns, N.Y., N.Y., John Wiley & Sons, Inc., 1950.

(3) Design Parameters and Functioning Mechanisms, The Multipurpose Concept for Multiple Effects Projectiles, Volume 2, A/S Raufoss Ammunisjonsfabrikker, Raufoss, Norway, December 1964.

(4) AMC Pamphlet 706-177, Engineer Design Handbook, Explosive Series, Properties of Explosives of Military Interest, 1964.

(5) Perry, Robert H. and Chilton, Cecil H., Chemical Engineer's Handbook, Fifth Edition, 1974.

(6) Coleman, B. D., Markovitz, H., Noll, W., Viscometric Flows of Non-Newtonian Fluids, Springer-Verlag New York, Inc., N.Y., N.Y., 1966.

NOMENCLATURE

Symbols are listed in the order in which they are used in the paper.

P = Instantaneous Chamber Pressure
T = Projectile Travel
V = Projectile Velocity
m = Projectile Mass
a = Instantaneous Acceleration
A = Bore Area
F_{SB} = Instantaneous Set-Back Force
σ = Local Stress
A_I = Effective Cross-Sectional Area of Incendiary Charge
n = Increment Number
ρ = Density
z = Axial Distance
ϵ = Compression
E = Modulus of Elasticity
t = Time
j = Summation Index
t_{exit} = Time to Projectile Exit from Muzzle
Ω_1 = Applied Angular Velocity
Ω_2 = Applied Angular Velocity
z = Displacement in Radial Direction
S = Shear Stress
M = Torque
ω = Angular Velocity (as a function of radial distance)
η_∞ = Ultimate Viscosity
λ = Rate of Shear Function
ξ = Variable of Integration
τ = Total Normal Stress in Axial Direction
q = Excess Atmospheric Pressure over Thrust
p_0 = Atmospheric Pressure

FIGURES

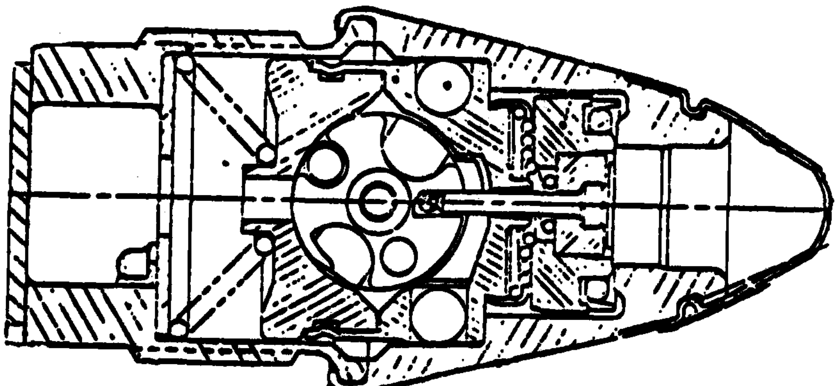

FIGURE 1. Sketch of a Conventional Mechanical Fuze

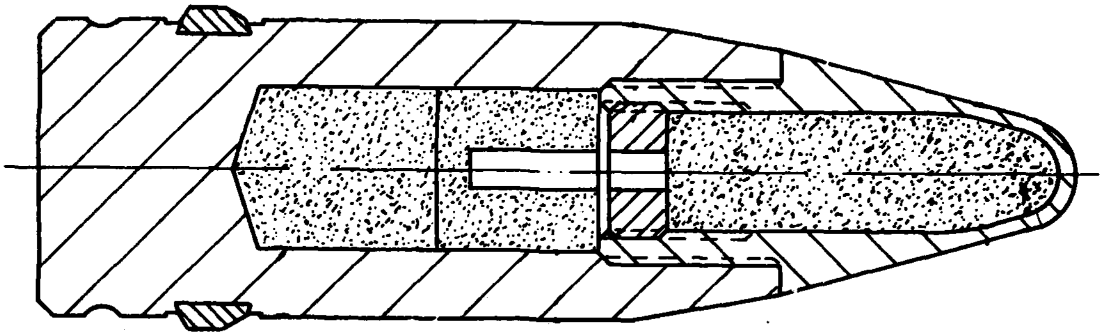

FIGURE 2. Novel High Explosive Projectile

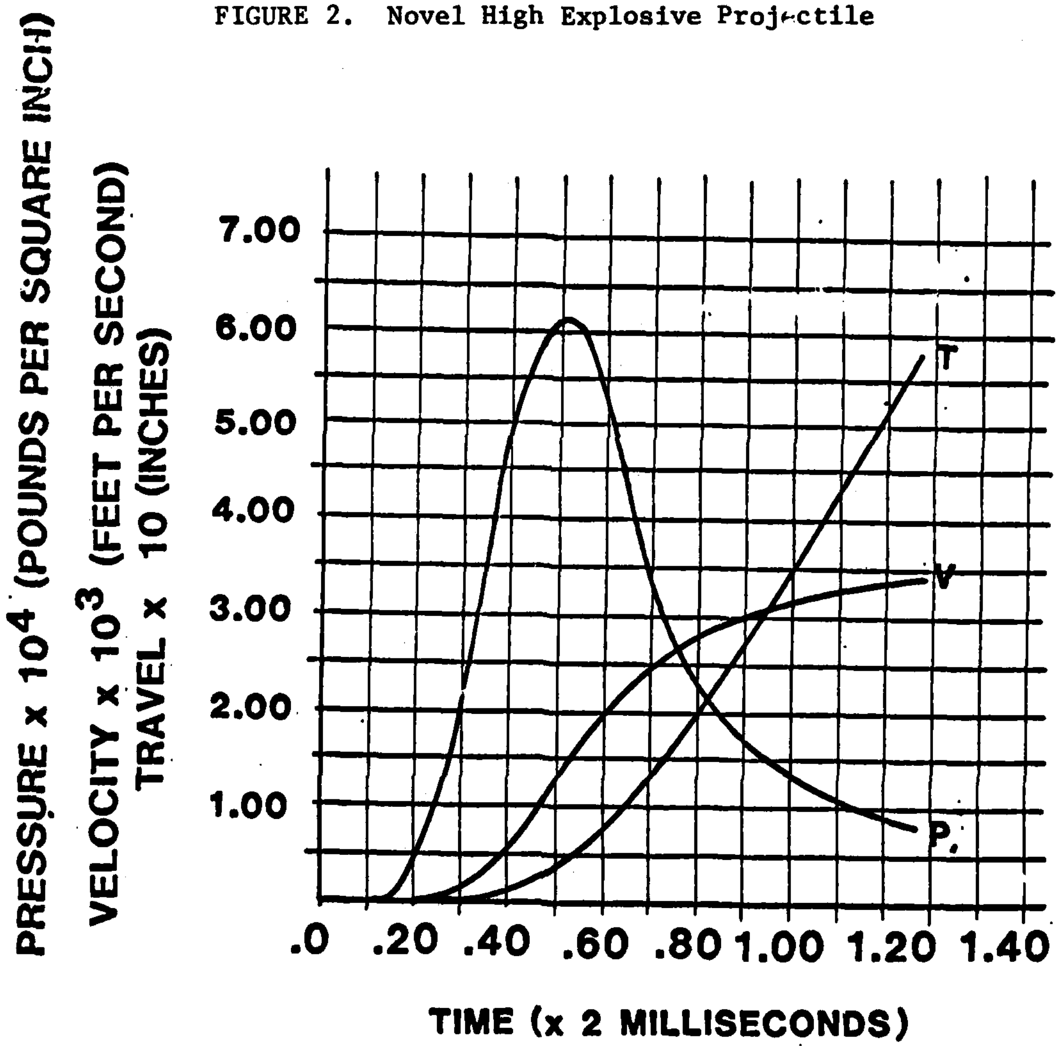

FIGURE 4. Pertinent 20mm Interior Ballistic Data

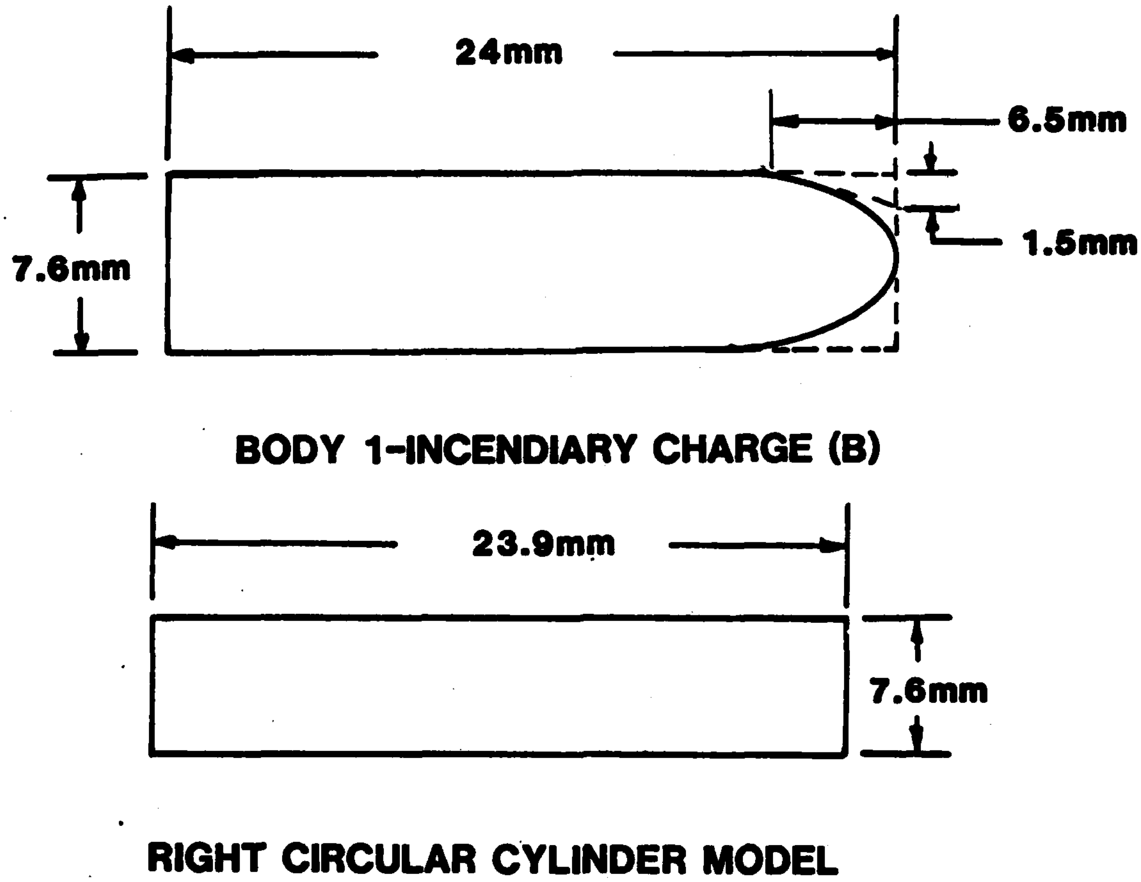

FIGURE 5. Dimensions and Simplifications of Forward Incendiary

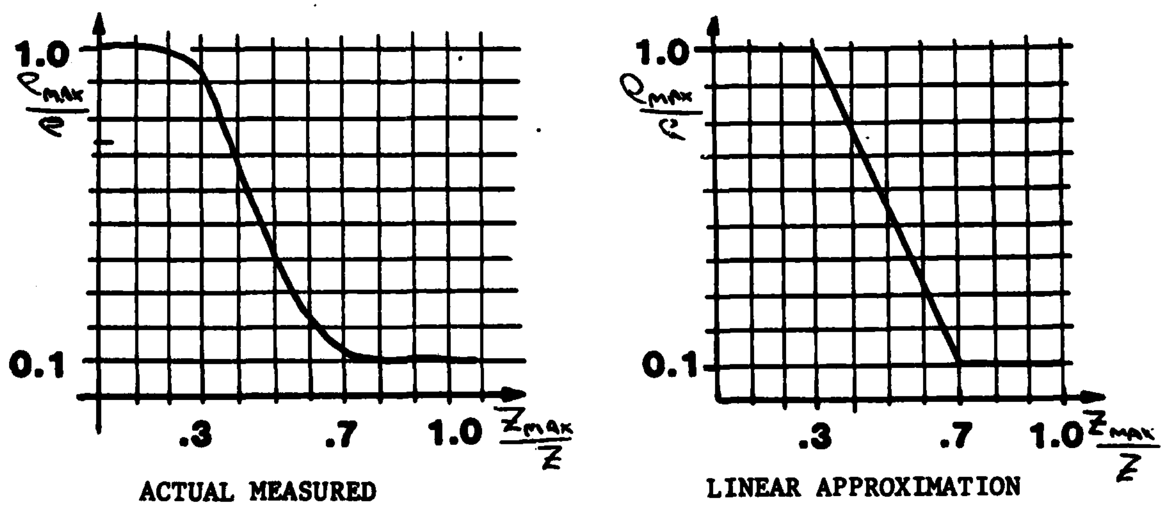

FIGURE 6. Density Profile and Approximation in Forward Incendiary Charge

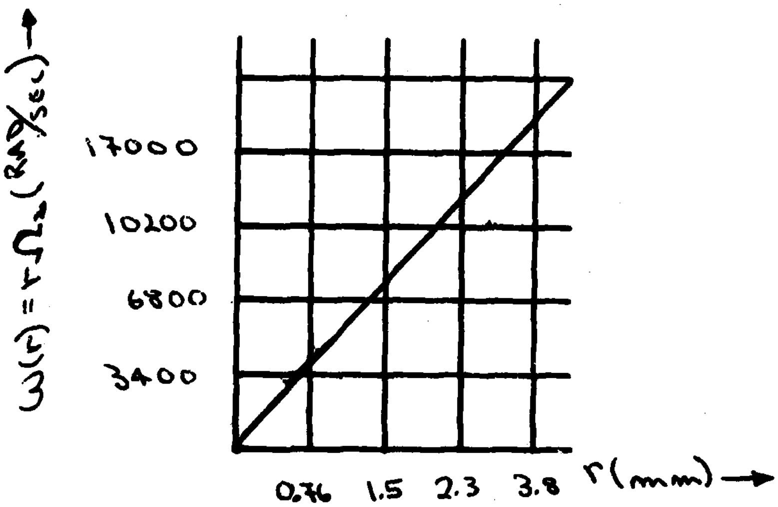

FIGURE 7. Plot of ω(r) Versus r Used to Evaluate Equation (7).

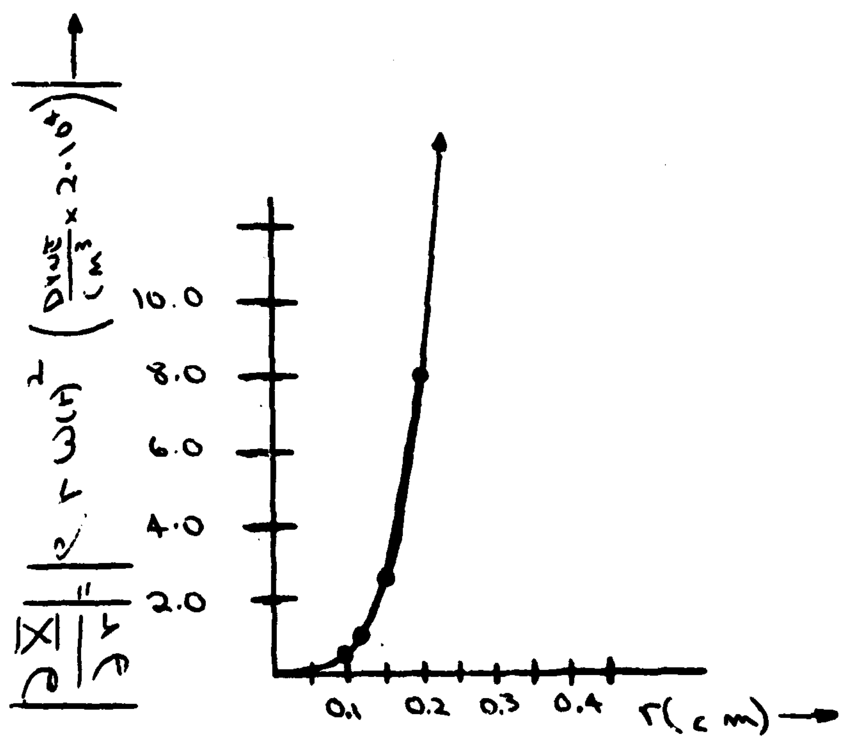

FIGURE 8. Plot of Equation (7) Showing Parabolic Shape of Cavity.

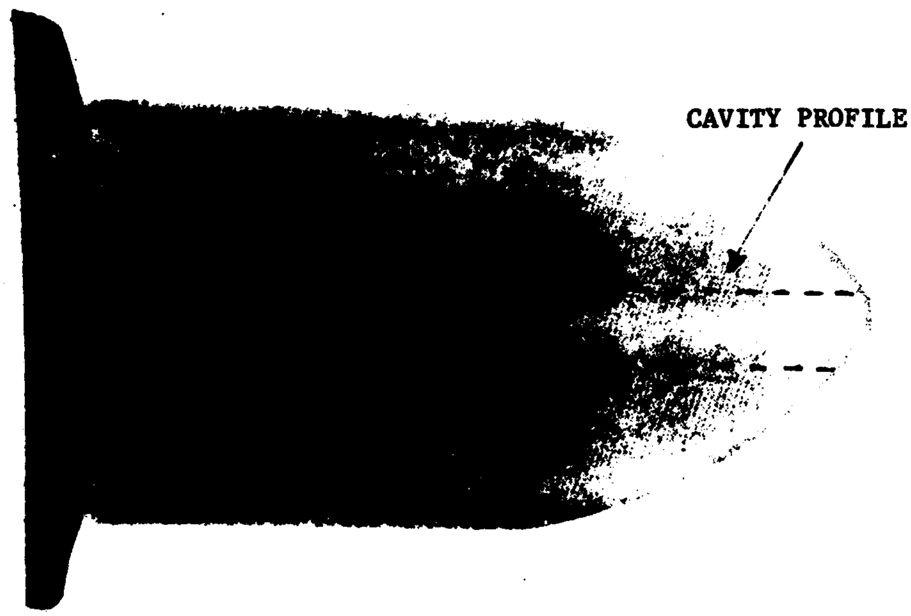

FIGURE 9. Dynamic X-ray of Forward Incendiary Showing Cavitation

THE RELATIONSHIP BETWEEN COMPANY LEADERSHIP CLIMATE AND OBJECTIVE MEASURES OF PERSONNEL READINESS (U)

BRUCE S. STERLING, Ph.D.
ARI FIELD UNIT, FORT HARRISON
FORT BENJAMIN HARRISON, INDIANA 46216

Many military leadership studies have related subordinates' perceptions of leader behavior to subjective (i.e., paper and pencil) measures of subordinate satisfaction and/or group effectiveness e.g., Halpin, 1954 (1); Reaser, Vaughan, and Kriner, 1974 (2); Bleda, Gitter, and D'Agostino, 1977 (3); O'Reilley and Roberts, 1978 (4). However, few studies have assessed the relationship between subordinates' perceptions of military leader behavior and objective measures of group effectiveness such as unit disciplinary rates, e.g., Affourtit, 1977 (5); Omara, In Press (6).

Also, only one level of leadership is often the focus of military leadership studies, such as Lange, 1960 (7); Olmstead, Christie, and Jacobs, 1975 (8), while research suggests that different leadership behavior may be required at different levels; e.g., Nealy and Blood, 1968 (9).

The purpose of the present research is to examine the relationship between perceptions of company leadership climate (by both leaders and lower enlisted) and objective measures of personnel readiness. However, before such a relationship can be explored, an instrument for examining overall company leadership climate must be constructed. Therefore, a secondary purpose of the research was to construct a valid measure of company leadership climate for both leaders and lower enlisted.

Method

Subjects

Subjects were 237 leaders (team leaders, squad leaders, platoon sergeants and platoon leaders) and 513 lower ranking enlisted (E1 to E4 in nonleadership positions) in a USAREUR infantry brigade. Most soldiers had spent about 12 months in the brigade. Sixty percent were in line units and 20% each were from combat support and headquarters units.

Instruments

Construction of the company leadership climate instruments began with interviews using lower enlisted and leaders concerning what constitutes effective leadership at company level and below. A draft instrument based on these interviews was pilot tested via administration to a sample of 75 leaders and 150 lower ranking enlisted. Items which were answered substantially the same by soldiers from all five companies (and thus were low in between unit variance) were eliminated. Remaining items were revised, reorganized and administered to a small sample of soldiers to ensure appropriate reading level. Final instruments contained 108 items and 67 items for leader and lower enlisted surveys, respectively. Each item was answered on a one to five scale. A typical item was "How fairly are small punishments, such as extra duty, given out in your company?"

Objective measures of personnel readiness (described in Appendix A) were collected from battalion records kept in the Personnel and Administration Center (PAC) for a six month period immediately preceding the survey. The number of occurrences of each measure was divided by unit strength figures to give ratios of occurrences in the past six months per number of soldiers for each of the 15 companies surveyed. These indicators are objective as they are a matter of record not subject to observer bias. However, they may not be definitive measures of personnel readiness.

Procedure

Surveys were administered to the 15 companies over a period of about four months. However, each unit took the survey during an identical part of their activity cycle to minimize differences in responses due to differences in recent missions. Surveys were administered to personnel during regular duty hours. An hour block was allotted but average administration time was about thirty minutes plus ten minutes for instruction. Eleven of the 15 companies were surveyed separately. Leaders and lower enlisted were always surveyed separately. Subjects were assured that responses would be reported in group form only and that the results would not serve as an official evaluation of the unit in general or any person in particular.

Results

Internal Validity

Factor analyses of the leader and lower enlisted instruments yielded four scales for leaders and seven for lower enlisted members (details are given in Appendix B). Resulting scales for leaders and lower enlisted are reported below.

Leader data: The leader structure scale had a Cronbach alpha[1] of .92 and contained 15 items measuring leaders' ability as trainers, effectiveness in maintaining standards among soldiers, agreement over use of punishment and supervision of subordinates.

The company level concern scale contained seven items (Cronbach alpha of .85) measuring the company commander's understanding of leaders' duties in training, troop handling and garrison tasks, as well as the fairness of punishment administered in the company and company leaders' (e.g., company commander or first sergeant) effectiveness in maintaining good morale, rewarding good performance, and showing concern.

The planning of training scale (Cronbach alpha of .80) contained eight items relating to the degree of involvement of various levels of leadership in planning training, the frequency with which training meetings are held, the reliability of the training schedule and the degree of realism in training.

The feedback scale (Cronbach alpha of .83) contained six items measuring leaders' agreement with use of both positive feedback mechanisms need as rewards and neutral to negative feedback mechanisms, such as inspections and counseling.

Intercorrelations between scale scores ranged from .52 to .65 with a median of .60, suggesting that, on average, scales shared about 36% of their variance.

Lower enlisted data: The squad level concern scale (Cronbach alpha of .89) contained eight items measuring the extent to which team and squad leaders helped soldiers in job-related areas and personal matters, maintained morale and showed concern.

The rewards scale (Cronbach alpha of .86) contained six items which tapped the extent to which soldiers agreed with the frequency of rewards such as awards, time off and promotion.

The training satisfaction scale (Cronbach alpha of .86) contained three items related to soldiers' satisfaction with time training as a squad, platoon and company.

---

[1]Cronbach alpha is a measure of the extent to which scale items tend to measure the same vs different concepts. It ranges from 0 to + 1, with scores over .60 generally accepted as showing reasonable scale internal validity.

The platoon level concern scale (Cronbach alpha of .90) consisted of nine items measuring the extent to which platoon sergeants and platoon leaders helped soldiers in job related and personal matters, maintained morale, rewarded good performance and showed concern.

The fairness and concern scale (Cronbach alpha of .88) contained ten items of a wider variety than other scales. Items on this scale measured fairness of rewards and punishments, the extent to which various leaders maintained morale, treated soldiers with respect, showed concern, were available to give job related help and evaluated job progress. This scale seemed to overlap squad level and platoon level concern to some extents.

The training instruction scale (Cronbach alpha of .80) contained five items measuring the extent to which leaders are enthusiastic about training, can answer questions on training, critique training and set the example.

The company level concern scale (Cronbach alpha of .80) contained three items relating to how helpful the company commander and first sergeant were in personal matters.

Intercorrelations between the scales ranged from .19 to .72 with a median of about .40, suggesting that an average scales had about 16% variance in common.

External Validity

For each objective measure, mean scale scores of soldiers from units above vs below the median on the objective measure were compared by t-tests. Results of these tests are discussed below, first for leader data then for lower enlisted data.

Leader data: The relationship personnel readiness measures and scale scores for leader data are summarized in Figure 1. This figure reveals that for all four scales, higher leadership ratings are related to relatively higher rates of IG complaints and field grade Article 15s. For all but the planning of training scale, higher leadership ratings are also related to lower sick call rates. Serious incident reports and requests for transfer show a mixed pattern. Higher scores on leader structure relate to higher rates of serious incident reports/requests for transfer, while higher scores on planning of training relate to lower rates of serious incident reports/requests for transfer. Concerning awards, leaders' ratings of company level concern are higher in units above the median in rates of certificates of achievement.

Lower enlisted data: The relationship between personnel readiness measures and scale scores for lower enlisted are summarized in Figure 2. Squad level concern, fairness and concern and training instruction all

	Action Line Complaints	IG Complaints	Company Grade Article 15s	Field Grade Article 15s	Total Article 15s	MSMs	ARCOMs	COAs	Total Awards	Sick Calls	SIRs	Requests for Transfer
Leader Structure		+		+	+					—	+	+
Company Level Concern		+		+				+		—		
Planning of Training		+	+	+	+						—	—
Feedback		+		+						—		

<u>NOTE</u>: + = scale mean of units above median on criterion measure is greater than ($p < .05$) scale mean of units below median on criterion measure.

\- = scale mean of units above median on criterion measure is less than ($p < .05$) scale mean of units below median on criterion measure.

Figure 1

RELATIONSHIP BETWEEN CRITERION MEASURES AND

SCALE SCORES: LEADER DATA

	Action Line Complaints	IG Complaints	Company Grade Article 15s	Field Grade Article 15s	Total Article 15s	MSMs	ARCOMs	COAs	Total Awards	Sick Calls	SIRs	Requests for Transfer
Squad Level Concern	+	+	+	+	+					—		
Rewards		+								—		
Training Satisfaction									+			
Platoon Level Concern		+								—		
Fairness and Concern		+		+	+					—		
Training Instruction		+		+	+					—		
Company Level Concern	—					+	+		+	—		

<u>NOTE</u>: + = mean of units above median on measure greater ($p < .05$) than mean of units below median on measure.

- = mean of units below median on measure greater ($p < .05$) than mean of units above median on measure.

Figure 2

RELATIONSHIP BETWEEN CRITERION MEASURES AND

SCALE SCORES: TROOP DATA

show a similar pattern. Higher ratings on these scales relate to higher rates of IG complaints, field grade Article 15s and total Article 15s as well as lower rates of sick calls. Concerning awards, soldiers' ratings of training satisfaction are higher in units earning relatively more total awards, and soldiers' rating of company level concern are higher in units earning relatively more meritorious service medals, army commendation medals and total awards. Higher ratings of company level concern also relate to lower rates of action line complaints and lower sick call rates.

Discussion

Concerning the first purpose of this research, the relationship between leadership climate and measures of personnel readiness, there appear to be consistent relationships between climate and readiness for both leaders and lower enlisted members. For both groups, more positive perceptions on a wide variety of leadership skills are associated with a relatively higher level of complaints, punishments and awards, as well as lower levels of sick calls. While these results may seem surprising at first, when one considered the maximum ratio of complaints (less than 2% per person per month) and punishments (less than 5% per person per month) it appears that good leadership is associated with moderate levels of complaints and punishments. This presents a picture of the effective leader as active leader, responding to subordinates' behavior appropriately, whether good or bad. Punishing those few who disrupt unit effectiveness rather than ignoring such behavior may earn the wrath of those few soldiers who do not want firm leadership (as evidenced by the relatively high complaint rate), but it satisfies the majority of soldiers as reflected by higher leadership ratings and lower levels of sick calls (absenteeism) a traditional measure of job satisfaction in the civilian literature.

Concerning the second purpose of this research, the documentation of perceptions of overall unit leadership climate, results appear promising. Leaders seem to define leadership climate in terms of leader structure, company level concern, planning of training and feedback. Also, lower enlisted members define leadership climate in terms of how well various levels fulfill their role responsibilities, as seen by soldiers (e.g., squad level concern, platoon level concern, company level concern), how well training is done (e.g., training satisfaction, training instruction) and use of rewards plus general fairness and concern of the overall leadership structure. Also, these scales all appear to be internally valid and each measure discrete aspects of company leadership climate.

In summary, two main conclusions can be drawn from this research. First, the effective leader may be more than a "nice guy" (person). The effective leader appears to be active, both punishing and rewarding behavior appropriately, and irritating a few people by doing so. A second conclusion logically following from this is that the tradiitional interpretation of official complaints and Article 15s as indicators of poor morale or discipline may not be correct. There may well be a curvilinear relationship between such measures and unit climate, with very low levels rereflecting a "milquetoast" and very high levels reflecting a "martinet."

References

(1) Halpin, A. W. The leadership behavior and combat performance of airplane commanders. Journal of Abnormal and Social Psychology, 1954, 49, 19-22.

(2) Reaser, J. M.; Vaugham, M. R.; & Kriner, R. E. Military leadership in the seventies: A closer look at dimensions of military leader behavior, Human Resources Research Organization (HUMRRO) Final Report: D7-74-133, 1974.

(3) Bleda, P. R.; Gitter, G. A., & D'Agostino, R. B. Enlisted men's perceptions of leader attributes and satisfaction with military life, Journal of Applied Psychology, 1977, 62, 43-49.

(4) O'Reilly, C. A.; & Roberts, K. H. Supervision iufluence and subordinate mobility aspirations as moderators of consideration and initiating structure. Journal of Applied Psychology, 1978, 63, 96-102.

(5) Affourtit, T. D. Measuring the impact of the Marine Corps' leadership (human relations) program: an empirical evaluation study. (Technical Report 77-2). Rockville, MD. Interaction Research Institute, January 1977.

(6) O'Mara, F. E. The organizational climate-organizational performance relationship in Army units. (Draft Technical Report), Alexandria, Army Research Institute for the Behavioral and Social Sciences, In Review.

(7) Lange, C. J. Leadership in small military units: Some research findings, Human Resources Research Office (HUMRRO), Professional Paper 24-67, 1960.

(8) Olmstead, J. A.; Christie, C. I.; & Jacobs, T. O. Leadership problems and behavior of U.S. Army company commanders in Europe. Human Resources Research Organization (HUMRRO) Final Report CD(C)-75-10, 1975.

(9) Nealy, S. M. & Blood, M. R. Leadership performance of nursing supervisors at two different organizational levels. Journal of Applied Psychology, 1968, 52, 414-422.

(10) Nie, N. H.; Hull, C. H.; Jenkins, J. G.; Steinbrenner, K.; & Bent, O. H. Statistical package for the social sciences; Second edition, McGraw Hill, New York, N.Y.; 1975.

Appendix A: Objective Performance Measures

Action Line Complaints

A type of local complaint whereby soldiers could directly call a number at brigade headquarters. The complaint was then given to their company commander, who had 24 hours to reply in writing to the brigade commander.

IG Complaints

Complaints filed with the inspector general (IG).

Company Grade Article 15s

A form of nonjudicial punishment (could be fines, confinement to quarters, etc.) given by the company commander.

Field Grade Article 15s

Similar to the company grade Article 15, but given by battalion commander. Maximum punishments are substantially larger.

Total Article 15s

Sum of company and field grade Article 15s.

MSMs

Meritorious Service Medals: A formal peacetime award given to service members to reward outstanding service over a period of time or an outstanding single achievement.

ARCOMs

Army Commendation Medal: A formal war or peacetime award given to reward service over a period of time or short term achievement. It is a lesser award than the MSM.

COAs

Certificates of Achievement: Informal recognition given generally to reward a single outstanding achievement (e.g., SQT score of 90 or over). Is a lesser reward (i.e., not an award) than the two above, but can be worth promotion points to lower enlisted.

STERLING

Total Awards

Sum of above three.

Sick Calls

Total incidents of people going on sick call (e.g., if one person sent on sick call on three different days, that represented three incidents of sick call).

SIRs

Serious Incident Reports: Military Police arrests for serious offenses (e.g., rape, robbery, etc.).

Requests for Transfer

Formal written requests for transfer submitted through the chain of command.

Appendix B: Creation of Scales for Leader and Lower Enlisted Data

Since these surveys were rather long, a method of reducing the number of items for further analysis was devised. Twelve t-tests (one for each objective measure) were performed. The difference in means between soldiers from units above vs below the median on each objective measure was tested for each item. Items which showed statistically significant $p < .05$ differences in means on at least two objective measures were selected for factor analysis. With an alpha of .05, an item has a probability of .46 of relating to at least one of the twelve measures by chance but a probability of roughly .12 of relating to at least two measures just by chance. This method reduced the number of items in the leader survey to about 45% of the original total and reduced the troop survey to about 74% of the prior total items.

Only about 69% of the leaders and 61% of the troops responded to all the remaining items in their surveys. However, 92% of the leaders and 94% of the troops answered at least 90% of the remaining survey items. Thus to gain more of the sample for factor analysis, the sample mean for a given item was used to replace the missing data for subjects missing between 1 to 5 items. This method does not substantially change the results of the factor analysis. All factor analyses used SPSS version seven by Nie, Hull, Jenkins, Steinbrenner, & Bent, 1975 (10).

Factor Solutions

Leader data. Data for both leaders and lower enlisted were analyzed using a principal components analysis. The unrotated factor matrix (principal factoring with iteration) for leader data showed that the eigenvalue dropped below one after six factors. Thus, a six factor solution was generated using varimax rotation. However, examination of the items loading .40 or greater on each of the six rotated factors suggested that several factors seemed to overlap in content, while other items which seemed similar loaded on separate factors. Thus, a five factor solution was generated. This factor eliminated most, but not all, overlap between factors. A four factor solution appeared to completely correct for factor overlap and gave the solution making the most intuitive sense. Percentage of total variance among items accounted for by each rotated factor was: leader structure (14%), company level concern (9%), planning of training (9%) and feedback (7%).

Scales scores for each factor were generated by adding together a leader's scores on all items loading .40 or greater on the factor.

Lower enlisted data. The initial unrotated factor matrix (principle factoring with iteration) showed that the eigenvalue dropped below one after the seventh factor. Thus, the seven factor solution was retained for varimax rotation. This rotation seemed to make good intuitive sense, and thus no further analyses were explored. The percentage of total item variance accounted for by each rotated factor is as follows: squad level concern (8%), rewards (7%), training satisfaction (5%), platoon level concern (8%), fairness and concern (9%), training instruction (6%), and company level concern (6%).

Scale scores for each factor were again created by adding together a subject's scores on all items loading .40 or more on the factor.

OCULAR EFFECTS OF RELATIVELY "EYE SAFE" LASERS (U)

*BRUCE E. STUCK, MS, DAVID J. LUND, BS,
EDWIN S. BEATRICE, COL MC
LETTERMAN ARMY INSTITUTE OF RESEARCH
PRESIDIO OF SAN FRANCISCO, CA 94129

Laser devices are an important part of current and future Army systems. Laser rangefinders, designators, communicators, and training devices are currently deployed or are in some stage of development. Most current laser rangefinders and designators, which enhance the effectiveness of the modern Army weapon systems, operate in the visible and near infrared region of the electromagnetic spectrum. The eye is particularly vulnerable in this wavelength region. The collimated laser radiation collected by the eye is transmitted by the ocular media with little attenuation and focused to a small spot on the sensory retina. The retinal irradiance is several orders of magnitude greater than that incident on the cornea; therefore, the total intraocular energy required to produce a retinal lesion is small. Lasers with output characteristic similar to those being fielded are capable of producing serious retinal injury at ranges that are tactically significant (1). The use of binoculars or magnifying optics increases the range at which these injuries can occur. Such devices cannot be used in training exercises without appropriate control restrictions or the use of protective devices. In some cases, training with the actual system in a realistic scenario is inhibited by these restrictions and troop proficiency may never be attained.

Ocular safety is particularly important for personnel using laser training devices where low power laser transmitters and sensitive receivers are used to evaluate the effectiveness of troops and tactics in two-way field exercises which simulate actual engagement scenarios. The MILES (Multiple Integrated Laser Engagement Simulator) program has resulted in the fabrication of laser transmitters configured to simulate several weapon systems. The gallium arsenide laser diodes used in these devices emit near 900 nm. The concern for eye safety when using this system stimulated careful bioeffects research (2) and a continual evaluation of maximum permissible exposures (MPE) given in AR 40-46 and TB MED 279 (3,4). If the emission from a laser system does not exceed the MPE as defined by TB MED 279 (3), then that system is a Class I system and can be referred to as "eye safe." To simulate weapon systems which are effective at longer ranges, lasers which emit more energy per pulse are required to offset losses due to atmospheric absorption and beam divergence. "Eye safe" lasers are desirable for these applications and for rangefinders and designators which can be used without restriction in training exercises. Laser systems operating beyond 1.4 μm have commonly been called "eye safe" and indeed, relative to lasers operating in the visible or near-infrared, the MPE for direct interbeam viewing is 2000 to 100,000 greater. However, only limited experimental biological effects data exist for wavelengths in this region of the spectrum.

In the spectral region from 1 to 3 μm, the outer ocular structures (cornea, aqueous, lens, vitreous) undergo the transition from highly transparent to essentially opaque. The absorption coefficient varies over 3 orders of magnitude (5). At 10.6 μm, where approximately 90% of the incident energy is absorbed in the first 70 μm of tissue, the corneal response at near threshold doses is confined to the corneal epithelium. Recovery from the insult occurs within 24 to 48 hours as observed by slit lamp microscopy (6,7). As the absorption decreases (in the 1-3 μm region), the incident energy is absorbed and is dissipated over a larger volume of tissue. The absorption of the incident radiation throughout a larger volume of tissue results in a higher threshold dose and therefore a reduced ocular hazard unless deeper structures such as the corneal endothelium or the crystalline lens are more sensative to the radiation insult. Consequently, the wavelength dependence of the dose-response relationships can be compared to the wavelength dependence of the absorption of the ocular media.

The ocular effects of infrared lasers for specific exposure conditions have been described (2, 6-14). In this paper, experimental ocular dose-response data obtained at 1.732 μm are presented and compared to bioeffects data obtained at other wavelengths in this spectral region.

METHODS

An erbium laser operating at 1.732 μm was fabricated in our laboratory and operated in the long pulse mode. The 1/4 by 3 inch erbium rod (obtained from Sanders Associates, Inc., Nashua, NH) was inserted into an eliptical cavity and pumped by a linear flash lamp (EG&G Inc., FX-42C3, Salem, MA). Energy input to the lamp was approximately 425 Joules. The maximum energy in a single pulse at 1.732 μm was 200 mJ. The emission duration was 225 μs (FWHM) and reached complete extinction at 380 μs. The measured beam divergence was 3.0 milliradian. The laser exposure system is schematized in Figure 1. Because of the limited total output energy, a lens was used to focus the laser energy at the corneal plane. The small amount of energy (100 μJ) transmitted through the highly reflective mirror at the rear of the cavity was proprotional to the energy measured at the cornea. Before exposure of the rhesus monkey's eyes, the ratio of the energy at the corneal plane to that at the reference detector was determined. Energy measurements were made with pyroelectric energy monitors (Laser Precision Corporation, Model RkP 335, Utica, NY). These detectors were calibrated with a disc calorimeter (Scientech Model 30-2002, Boulder, CO). Calibrated neutral density filters were placed in the beam to vary the energy per exposure. The point of intersection of the split beams from a helium neon laser was used to locate the corneal exposure plane and to facilitate selection of the corneal exposure site.

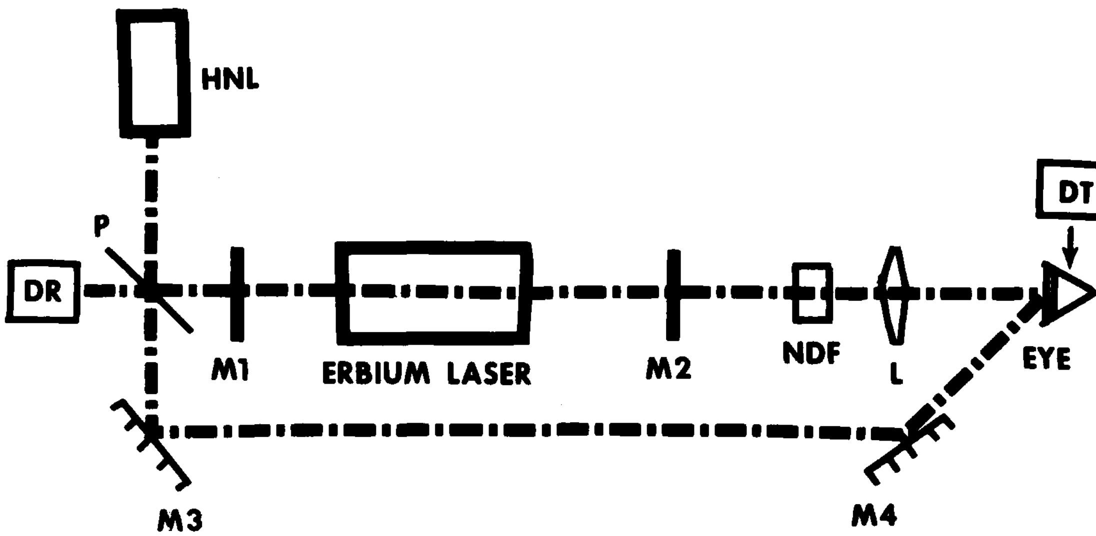

Figure 1. Erbium laser exposure system (emission wavelength = 1.732 µm). DR - Reference detector, DT - Target detector, HNL - Helium neon alignment laser, NDF - Neutral density filter holder, M1 to M4 - mirrors, P - pellicle, L - lens.

Four lenses were used to obtain a range of corneal irradiance diameters. The corneal exposure plane was located in the experimentally determined focal plane a distance of f_p from the lens. The intensity profile of the beam and the effective beam diameter at the corneal plane were measured by two techniques. 1) By systematically reducing the energy per pulse and irradiating developed photographic paper, the relative intensity distribution was displayed. 2) Apertures with progressively decreasing diameters were placed at the exposure plane, and the total energy through each aperture was measured. The intensity profile at the focal plane was "approximately" gaussian and the reported beam diameters ($d_{1/e}$) are the diameters at the 1/e intensity points. The radiant exposure is the peak radiant exposure obtained by dividing the total incident energy by the area defined by the beam diameter ($d_{1/e}$).

Rhesus monkeys (Maccaca mulatta) were tranquilized with ketamine intramuscularly and anesthetized with pentobarbital sodium intravenously. The ocular pupils were dilated with one drop each of 2% cyclopentolate hydrochloride and 10% phenylephrine hydrochloride to facilitate biomicroscopic evaluation. The outer ocular structures (cornea, aqueous, lens, and vitreous) were carefully evaluated before and after exposure by use of the slit lamp biomicroscope. Body temperature during anesthesia was maintained with a thermal blanket. The eyelid was held open with a pediatric eye speculum and the cornea was gently irrigated with physiological saline to prevent drying. Six to nine exposures were placed in each cornea in an array of independent sites (Table 1). The dose was incrementally varied over a preselected range.

TABLE 1. CORNEAL ED_{50}s FOR SINGLE 225 μs EXPOSURES AT 1.732 μm.

f_p cm	$d_{1/e}$ μm	ED_{50} (95% CI) J/cm^2	SLOPE	DOSE RANGE TESTED J/cm^2	No. ANIMALS/ EYES/ EXPOSURES
17.8	515	29 (27-31)	1.30	1.0-80	3/6/54
24.1	740	26 (23-29)	1.34	0.5-45	4/7/49
30.5	920	22 (20-23)	1.28	0.3-30	4/8/48
40.6	1200	>16*		14-16	1/2/8

* No ED_{50} was determined for this condition because of the limited energy per pulse available from the laser.

The corneas were evaluated immediately and at 1 hour after the exposure. The response criterion was the appearance of a lesion at the exposure site as observed with the slit lamp biomicroscope. Other evaluations were made at 24 hr, 48 hr, 1 week and up to 6 months after exposure. The crystalline lens was also carefully evaluated. The effective dose for a 0.5 probability of producing an observable response (ED_{50}), the 95% confidence intervals about the ED_{50}, and the slopes of the regression lines through the experimental data (slope = ED_{84}/ED_{50} = ED_{50}/ED_{16}) were determined by probit techniques (15).

RESULTS

The ED_{50}s for the production of a corneal lesion at 1.732 μm observed with the slit lamp biomicroscope and the exposure conditions are presented in Table 1. The ocular response for these exposure conditions was confined to the cornea. Corneal lesions generally involved the entire corneal thickness (Figure 2). Lesions near the ED_{50} were smaller and less dense than those produced at 1.5 to 2.0 times the ED_{50}. No lesion was observed at 24 or 48 hours that was not observed at one hour. No lenticular effects were observed at one hour or in the four animals that were evaluated up to 6 months after exposure. Some corneal lesions observed at one hour were not observed at 48 hours. Over the limited range of exposure conditions, the ED_{50} exhibits a dependence on the irradiance diameter (Figure 3). The radiant exposure required to produce a corneal lesion decreases as the irradiance diameter increases.

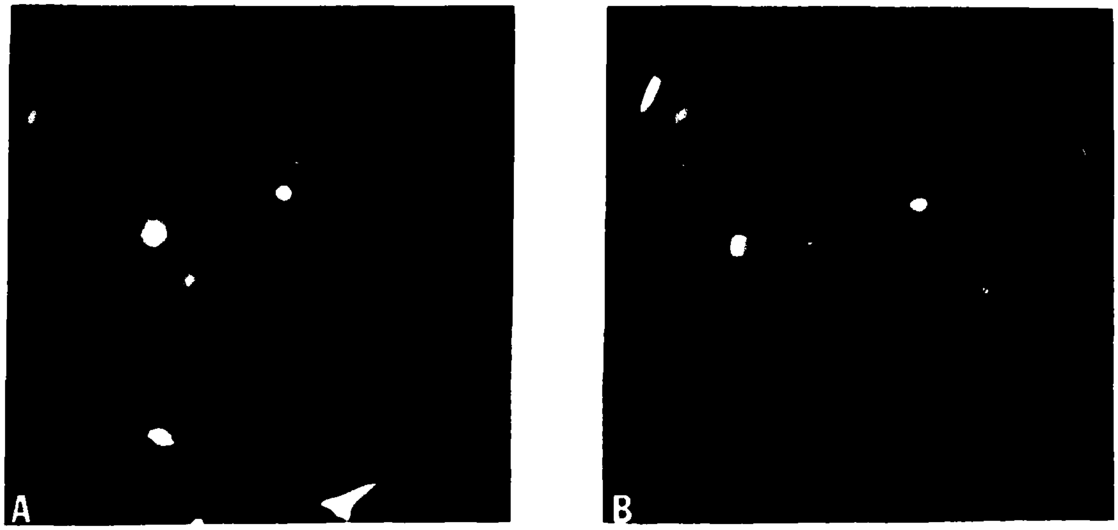

Figure 2. A. Slit lamp photograph of a corneal lesion one hour after exposure produced by an erbium laser operating at 1.732 μm (Corneal radiant exposure = 56 J/cm^2, Exposure duration = 225 μs (FWHM), Incident beam diameter at the 1/e intensity points = 515 μm). B. Slit lamp photograph of the same lesion shown in A illuminated with a narrow slit of light showing that the lesion extends through the entire thickness of the cornea.

DISCUSSION

The corneal response resulting from exposure to infrared laser radiation is considered to be the result of a temperature elevation of the tissue. Sufficient energy is absorbed in a finite volume resulting in a localized temperature rise that produces a coagulation or opacification of the medium. Predictive thermal model calculations based on a localized elevation of temperature to a "threshold peak temperature" have been used to estimate the threshold dose required to produce a corneal lesion (16). These thermal model results are considered to be in good agreement with most experimental data published in this wavelength region. Experimental data of this and other experiments are given in Table 2. The ED_{50}s for corneal injury at 1.732 µm are lower than the ED_{50} obtained at the 1.33 µm and higher than those obtained for erbium laser radiation at 1.54 µm. This trend was anticipated based on the relative absorption of cornea at these three wavelengths. Corneal effects at 1.732 µm were similar to those produced at 1.33 µm and 1.54 µm in that the observed response extended throughout the full corneal thickness.

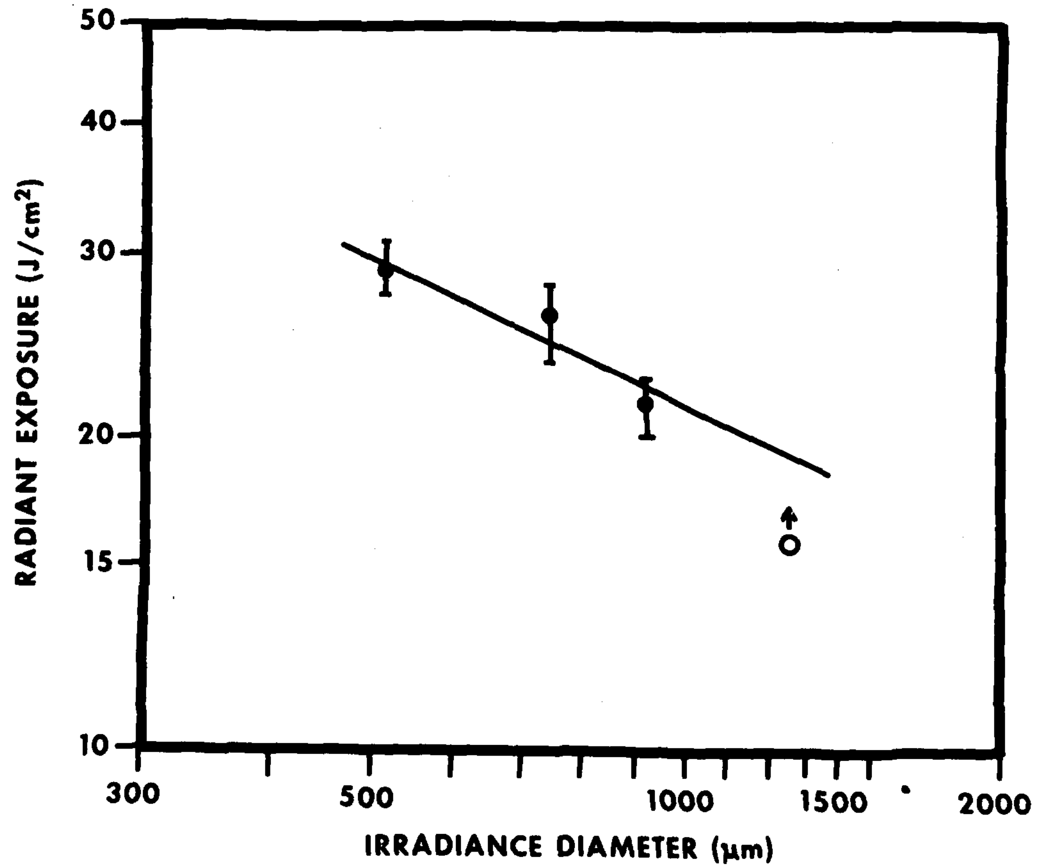

Figure 3. The ED_{50} and 95% confidence interval about the ED_{50} for the production of a corneal lesion as a function of the irradiance diameter of the incident beam ($d_{1/e}$). No corneal effect was observed for exposures made with the 1200 µm irradiance diameter (open circle with arrow).

TABLE 2. CORNEAL DAMAGE THRESHOLDS FOR INFRARED LASER RADIATION

WAVELENGTH	EXPOSURE DURATION	IRRADIANCE DIAMETER	CORNEAL ABSORPTION COEFFICIENT[a]	ED_{50}	REFERENCE
μm	s	mm	cm^{-1}	J/cm^2	
1.318-1.338[b]	.25 ms	.40	2.28	45	9
1.41	25 ns	1.1	15.9	2.1-4.2	12
1.54	40 ns	1-2	9.03	4.7	13
1.54	50 ns	1	9.03	21.0	8
1.54	.93 ms	1	9.03	9.6	10
1.54	1.0 ms	1-2	9.03	7.2	13
1.732	.225 ms	.515	5.88	29.0	c
1.732	.225 ms	.740	5.88	26.0	c
1.732	.225 ms	.920	5.88	22.0	c
1.732	.225 ms	1.20	5.88	>16.	c
2.06	42 ns	.32	28.2	5.2	10
2.06	50 ns	.351	28.2	3.25	15
2.06	.10 ms	1.8	28.2	2.9	10
2.6-2.9[d]	45 ns	0.82	>5000	.156	14
2.9	100 ns	10.0	12900	.006-.010[e]	11
3.6-3.9[f]	100 ns	.96	112-180	.377	14
10.6	1.4 ns	10.0	817	.013-.015[e]	11
10.6	100 ns	2.1	817	0.35	2

a Corneal absorption coefficients from Reference 5 for wavelengths less than 2.1 um. For wavelengths greater than 2.06 um the absorption coefficient of water which approximates that of the cornea is tabulated.

b Multiline neodymium laser with 40% of the energy at 1.318 um and 60% at 1.338 um.

c This report.

d Multiline hydrogen fluoride laser.

e No ED_{50}s was determined. The dose listed is the approximate threshold dose that an immediate response was observed.

f Multiline deuterium fluoride laser.

The ED_{50}s given in Table 2 are plotted in Figure 4 as a function of wavelength to exhibit the wavelength dependence of the damage threshold. Inherent to the wavelength dependence of the ED_{50} is the wavelength dependence of the ocular media absorption. The solid curve on Figure 4 is the depth at which 95% of the incident energy has been absorbed. The absorption coefficients of physiological saline which approximate that of the cornea and outer ocular media were used to calculate the 95% absorption depth. Let x_1 be the depth at which 95% of the incident radiation is absorbed. From Lamberts Law, $I/I_o = e^{-ax_1}$ where I_o is the incident intensity, I is the intensity transmitted through a thickness x_1 of medium with an absoption coefficient of a. By letting $I/I_o = .05$ (i.e. 95% of incident energy absorbed), the depth or thickness x_1 can be calculated for a given absorption coefficient a. The volume in which the radiation is absorbed is equal to Ax_1 where A is the cross sectional area of the incident beam. If Q is the incident energy, then the absorbed energy/ unit volume is Q/Ax_1. Assuming the absorbed energy per unit volume required to produce corneal damage is independent of wavelength, therefore $Q/Ax_1 = k$ at the threshold dose where k is a constant. Consequently, the radiant exposure Q/A is directly proportional to the absorption depth or $Q/A = kx_1$. There is a direct correlation between the dose at threshold and the penetration depth (Figure 4).

Even though the exposure conditions (exposure duration, beam diameter), calibration, and observation criteria of different investigators were not identical for the experimental data subjected to this analysis, the wavelength dependence of the corneal ED_{50}s is approximated by the shape of the absorption depth curve. Given identical experimental conditions across investigations and adjustment of absoption depth curve, a better fit to the experimental data may result. Doses required to produce an observable corneal response in the wavelength region between 1 and 2 µm were higher than those required at 2.8, 3.8, and 10.6 µm where absorption takes place within a much smaller volume. The corneal response of a near threshold exposure at the shorter infrared wavelengths involved the corneal stroma and did not exhibit the rapid repair as reported for the longer wavelengths where the threshold response only involved the corneal epithelium. The solid curve in Figure 4 supports that observation. Near threshold lesions at the shorter infrared wavelengths can be considered more severe since a long lasting stromal scar results.

For the exposure conditions evaluated to date at 1.732 µm, no retinal or lenticular effect has been observed; however, further evaluation for a collimated beam continues. The ED_{50} for an ophthalmoscopically visible retinal lesion was establish for the 1.3 µm neodymium laser (2). The beam divergence was 2.3 mr, pulse duration was 650 µs and the corneal beam diameter was 5.5 mm. The total intraocular energy was 356 mJ resulting in a corneal radiant exposure of 1.5 J/cm^2 a the ED_{50}. If this energy were averaged over a 7 mm pupil, the corneal radiant exposure required to

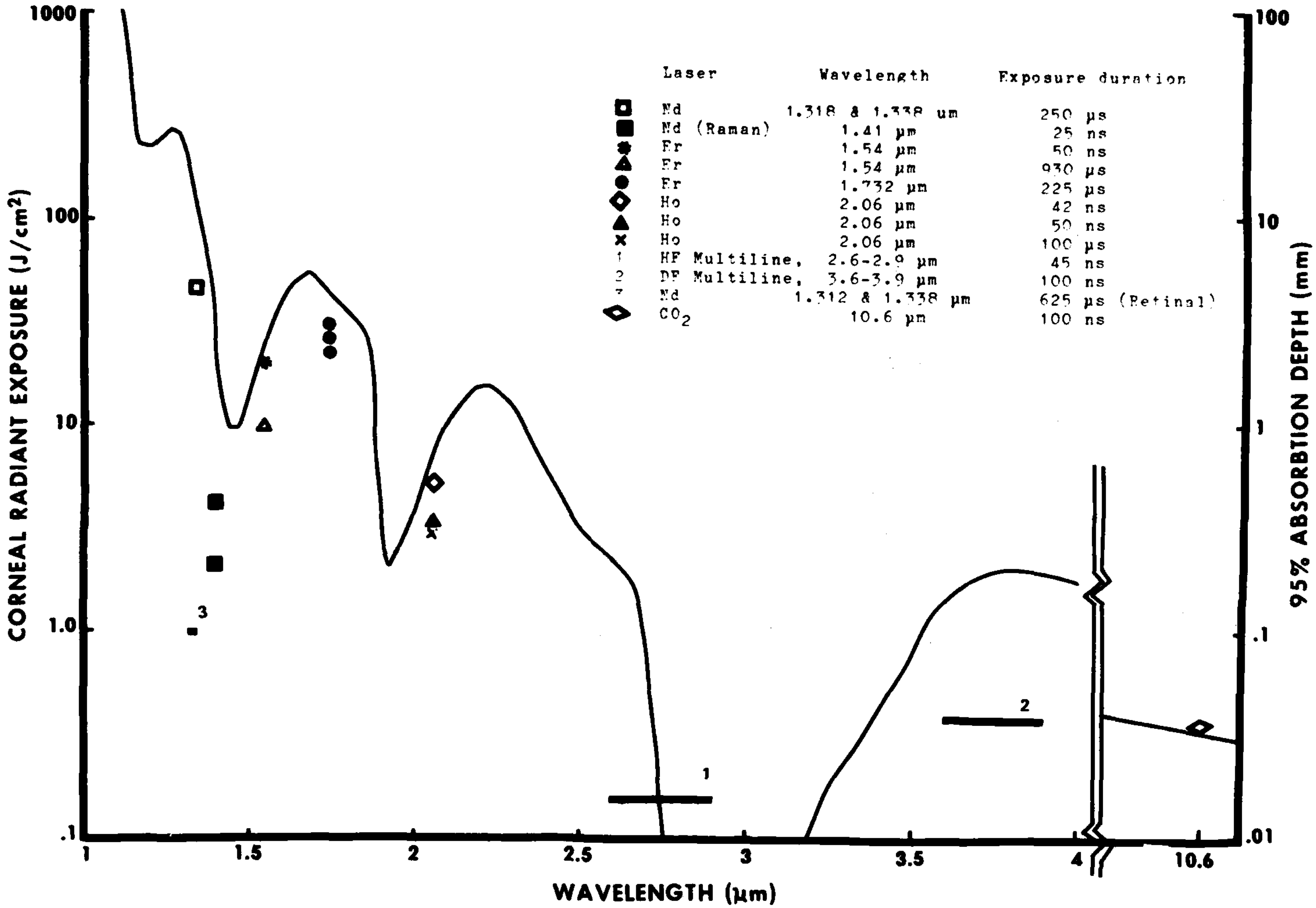

Figure 4. The ED_{50}s for the production of a corneal lesion for exposure conditions given in Table 2 as a function of wavelength. The solid curve is the depth (right hand axis) at which 95% of the incident energy is absorbed in physiological saline (the absorption properties of physiological saline approximate those of the outer ocular media). The data point at 3 is the ED_{50} for production of a retinal lesion obtained at the 1.33 μm.

produce retinal injury at 1.3 µm is 0.93 J/cm^2. This value is also plotted in Figure 4. At 1.3 µm, the corneal radiant exposure required to produce a retinal effect is much lower (Table 2) than that required to produce a corneal effect; nonetheless, the corneal radiant exposure required to produce a retinal response is 3 orders of magnitude greater than that required at 1.064 µm (2) and the MPEs for both lasers are identical (4).

The dependence of the corneal damage threshold on the irradiance diameter of the incident beam has not been described in previous investigations at any wavelength. Common to many of the investigations of the corneal effects in the infrared has been the necessity to focus the output energy on the cornea (8,9,10,12,13,15) because of the limited energy per pulse from typical laboratory laser devices operating in this wavelength region. Consequently corneal damage thresholds were obtained only for small irradiance diameters. For irradiance diameters from 500 to 1000 µm, the radiant exposure required to produce a threshold lesion decreased as the beam diameter increased (Figure 2) for 1.732 µm laser radiation. Accidental exposures to infrared lasers will probably involve exposure of the entire cornea (irradiance diameters greater than 10 mm). Further evaluation of this dependence at other wavelengths in this region is required in order that the potential implication to the establishment of permissible exposure limits can be ascertained.

The MPEs for ocular exposure to wavelengths greater than 1.4 µm currently depend only on the exposure duration. These values have been based primarily on the dose-response relationships reported for carbon dioxide laser radiation (10.6 µm). No wavelength dependence of the MPE has been included in laser safety standards. The only exception is the elevated permissible exposures for the Q-switched erbium laser (1.54 µm) where experimental data (5) existed when these permissible exposure limits were established (3). The MPE for a single exposure less than 100 µs in duration is 10 mJ/cm^2 for laser radiation with wavelengths greater than 1.4 um (1 J/cm^2 for 1.54 µm radiation). The MPE for ocular exposure to laser radiation at 1.732 µm or 2.06 µm is the same as the MPE at 10.6 µm, even though the ED_{50}s differ by a factor of 10 to 100. Although additional experimental dose-response data are needed in the 1 to 3 µm region for longer exposure durations, larger corneal irradiance diameters, and repetitive pulse conditions, a generalized wavelength correction to the MPE in the infrared spectral region is indicated by these experimental data. When compared to the MPEs for visible and near infrared radiation (the MPE ranges from 0.5 to 5 µJ/cm^2 for exposure durations less than 100 µs), lasers operating beyond 1.4 µm are relatively "eye safe." Lasers operating in the IR-B region which emit 100 mJ per pulse could be used without stringent range control restrictions or protective devices. With current permissible exposure limits, a 1.54 µm laser would be desirable since the MPE is 100 times that for other systems such as holmium (2.06 µm) or erbium (1.732 µm).

CONCLUSIONS

Ocular dose-response data obtained at 1.732 µm for exposure conditions examined thus far coupled with the other experimental data obtained in the wavelength region from 1.3 to 3.0 µm support consideration of including a wavelenght dependence in the maximum permissible exposure. This wavelength dependence should be based on the relative absorption properties of the ocular media. Lasers which operate in this wavelength region offer a distinct advantage to the system developer from an "eye safety" standpoint.

REFERENCES

1. STUCK, B.E., D.J. LUND, and E.S. BEATRICE. Another Look at the Ocular Hazard from Military Lasers. In: Proceedings of the Aerospace Medical Association, 224-225, 1981.

2. LUND, D.J., B.E. STUCK, and E.S. BEATRICE. Biological Research in Support of Project MILES. Institute Report No. 96. Presidio of San Francisco, CA, Letterman Army Institute of Research, 1981.

3. DEPARTMENT OF THE ARMY. Army Regulation 40-46, Control of Health Hazards from Lasers and Other High Intensity Optical Sources. Washington DC: Headquarters, Department of the Army, 1978.

4. DEPARTMENT OF THE ARMY. Technical Bulletin, TBMED 279. Control of Hazards to Health from Laser Radiation. Washington DC: Headquarters, Department of the Army, 1975.

5. MAHER, E.F. Transmission and Absorption Coefficients for the Ocular Media of the Rhesus Monkey. Report SAM-TR-78-32. Brooks Air Force Base, TX: USAF School of Aerospace Medicine, 1978.

6. BROWNELL, A.S., and B.E. STUCK. Ocular and Skin Hazards from CO_2 Laser Radiation. In: Proceedings of the 9th Army Science Conference. U.S. Military Academy, West Point, NY. 1: 23-37. 1974.

7. PEABODY, R.R., H. ROSE, H.C. ZWENG, N.A. PEPPERS, and A. VASSILIADIS. Threshold damage from CO_2 Lasers. Arch Ophthalmol 82: 105-107, 1969.

8. LUND, D.J., G.H. BRESNICK, M.B. LANDERS, J.O. POWELL, J.E. CHESTER, and C. CARVER. Ocular Hazards of the Q-switched Erbium Laser. Invest Ophthalmol 9: 463-470, 1970.

9. STUCK, B.E., D.J. LUND, and E.S. BEATRICE. Ocular Effects of Laser Radiation from 1.06 to 2.06 µm. In: Proceedings of the Society of Photo-Optical Instrumentation Engineers, 96: 115-120, 1980.

10. STUCK, B.E., D.J. LUND and E.S. BEATRICE. Ocular Effects of Holmium (2.06 µm) and Erbium (1.54 µm) Laser Radiation. Health Physics 40: 835-846, 1981.

11. MUELLER, H.A., and W.T. HAM . The Ocular Effects of Single Pulses of 10.6 µm and 2.5-3.0 µm Q-Switched Laser Radiation. Report to the Los Alamos Scientific Laboratory, L Division, Los Alamos, NM, 1976.

AD-A120 813 PROCEEDINGS OF THE 1982 ARMY SCIENCE CONFERENCE HELD AT 5/6
THE UNITED STATES..(U) DEPUTY CHIEF OF STAFF FOR
RESEARCH DEVELOPMENT AND ACQUISITIO.. 18 JUN 82

UNCLASSIFIED F/G 5/2 NL

END

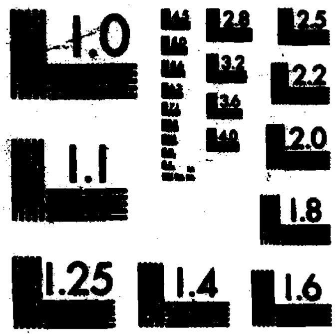

MICROCOPY RESOLUTION TEST CHART
NATIONAL BUREAU OF STANDARDS-1963-A

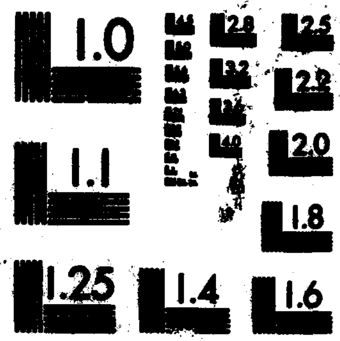

MICROCOPY RESOLUTION TEST CHART
NATIONAL BUREAU OF STANDARDS-1963-A

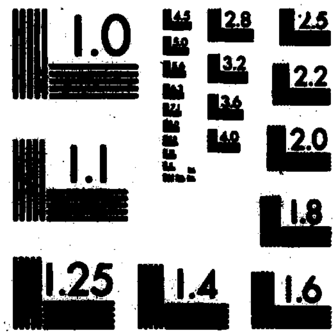

MICROCOPY RESOLUTION TEST CHART
NATIONAL BUREAU OF STANDARDS-1963-A

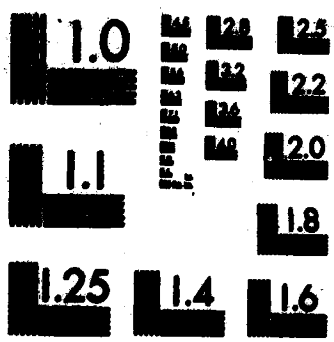

MICROCOPY RESOLUTION TEST CHART
NATIONAL BUREAU OF STANDARDS-1963-A

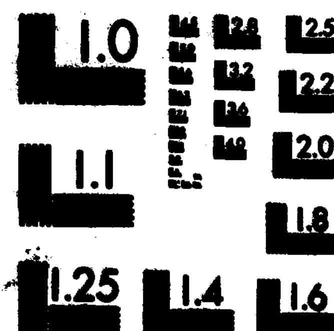

MICROCOPY RESOLUTION TEST CHART
NATIONAL BUREAU OF STANDARDS-1963-A

12. ARCHIBALD, C.J., and J. TABOADA. Damage to the Cornea Induced by 1.4 Micrometer Laser Light Pulses. In: Proceedings of the Aerospace Medical Association, 94-95, 1981.

13. AVDEEV, P.S., YU.D. BEREZIN, YU.P. GUDAKOVSKII, YU.R. MURATOV, A.G. MURZIN, AND V.A., FROMZEL. Experimental Determination of Maximum Permissible Exposure to Laser Radiation of 1.54 µm Wavelength. Soviet J Quant Elec 8: 137-139, 1978.

14. DUNSKY, I.L. and D.E. EGBERT. Corneal Damage Thresholds for Hydrogen Fluoride and Deuterium Fluoride Chemical Lasers. Report SAM-TR-73-51. Brooks Air Force Base, TX: USAF School of Aerospace Medicine, 1973.

15. VIVEASK, J.P. Median Effective Dose for Visible Damage to the Cornea by a Q-Switched Holmium Laser (2060 nanometers). IAM Report No. 588. Farnborough, UK: Royal Air Force Institute of Aviation Medicine, 1980.

16. FRISCH, G.D. Quantal Response Analysis. Frankford Arsenal Memorandum Report M70-27-1. Philadelphia, PA: Frankford Arsenal, 1970.

17. EGBERT, D.E., and E.J. MAHER. Corneal Damage Thresholds for Infrared Laser Exposures: Empirical Data, Model Predictions and Safety Standards. USAF Technical Report SAM-TR-77-29. Brooks Air Force Base, TX: School of Aerospace Medicine, 1977.

In conducting the research described in this report, the investigators adhered to the "Guide for the Care and Use of Laboratory Animals," as promulgated by the Committee on Revision of the Guide for Laboratory Animal Facilities and Care, Institute of Laboratory Animal Resources, National Academy of Sciences, National Research.

Citation of trade names in this report does not constitute an official endorsement or approval of the use of such items.

IN-BORE PROPELLANT MEDIA DENSITY MEASUREMENTS BY CHARACTERISTIC X-RAY RADIOGRAPHY

GEORGE M. THOMSON, Ph.D.
KEITH A. JAMISON, Ph.D.
BALLISTIC RESEARCH LABORATORY, ARRADCOM
ABERDEEN PROVING GROUND, MD 21005

Introduction

X-rays have long been used in ballistics for numerous tasks such as studying projectiles in flight, examining propellant beds, and diagnosing launcher conditions. Typically such experiments consist of a qualitative shadowgraphic examination of the attenuation that x-rays experience while passing through or near the system under study. Few, however, take advantage of the details of the relationship between x-ray absorption and media density that has prompted investigators in other disciplines to use x-rays for quantitatively characterizing gas properties under a variety of conditions. Density measurements of high accuracy can be performed with energetically well-defined x-rays from radioisotopes such as Fe^{55} (1). Unfortunately, the limited intensity and the small number of x-ray energies available from radioactive sources restricts their use to certain slow phenomena. In fast events conventional electron excited x-ray sources can be applied (2,3), but problems connected with stabilizing, measuring, and convoluting their x-ray energy distributions complicate quantitative measurement. In this work we report development of a new technique for fast, accurate density measurements in a wide range of multiphase media. It is based upon a determination of the in-bore absorption of a copious flux of transiting characteristic x-rays that is produced by the impact of fast protons upon metal films. The method, called characteristic x-ray radiography (CXR), has been successfully tested in a particularly difficult regime - the interior of a discharging firearm.

General Principles

If a flux of monoenergetic x-rays of initial intensity I_0 enters a medium, absorption occurs and only an intensity I passes through. The fraction $(I(t)/I_0)$ surviving passage through a distance (x) is related to the instaneous density of a media (ρ) by the mass absorption coefficient (μ) as described by the expression:

$$(1) \quad \frac{I(t)}{I_0} = e^{-\mu\rho(t)x}$$

The quantity μ is a function of the media's atomic composition and of the x-ray energy ε only. In cases of elemental substances values of μ have been extensively tabulated (4). For more complex compounds and mixtures μ can be readily calculated by weighing the μ values of each of its elemental constituents by its appropriate mass fraction. It is important to note that since μ is a function of the media's atomic composition, x-ray absorption is virtually independent of the detailed chemistry and phase of the absorber. An analysis of equation (1) shows that the sensitivity, i.e., the change in I for a given fractional change in ρ, is a maximum when $\mu\rho x = 1$. The minimum fractional error $\frac{\Delta\rho}{\rho}$ occurs when $\mu\rho x = 2$ for experiments in which there are normal statistical counting errors in I and in which I_0 is precisely known. Optimum performance may be achieved by selecting ε so that the value of $\mu\rho x$ provides a best compromise between the desired sensitivity and the errors inherent in the experiment.

It is essential when using x-rays to measure media densities that one know the energy distribution of the analyzing x-rays because μ is a strong function of ε. In designing the present experiment two alternate x-ray sources were considered, a conventional electron excited source and a proton excited source. Both are similar in that they use the passage of a charged particle through an atomic inner shell to create vacancies in that shell. When these vacancies decay radiatively they produce x-rays at a few well-defined characteristic energies. The two production schemes differ, however, in that the close passage of relatively light electrons near atomic nuclei strongly accelerates them and causes them to produce a broad-banded x-ray emission known as bremsstrahlung. During similar passage the more massive protons suffer no strong accelerations and as a result produce virtually no bremsstrahlung. The x-ray emission spectra for an electron excited (left) and a proton excited (right) x-ray source are shown in fig. 1. A molybdenum target was used in both cases. In order of increasing energy the two x-ray lines are the produc[illegible]lectrons filling vacancies in the 1s shells of the atoms from their 2[illegible] or their 3p shells. These are denoted as the K_α and K_β lines, resp[illegible]y. It is evident that the proton induced spectrum is far more amenable to application of eq. 1. The presence of bremsstrahlung in the electron excited spectrum requires that any density analysis be based upon integrals of μ over the entire x-ray energy distribution, which in turn must be empirically determined. The price for proton excited systems spectral simplicity however is not trivial. In

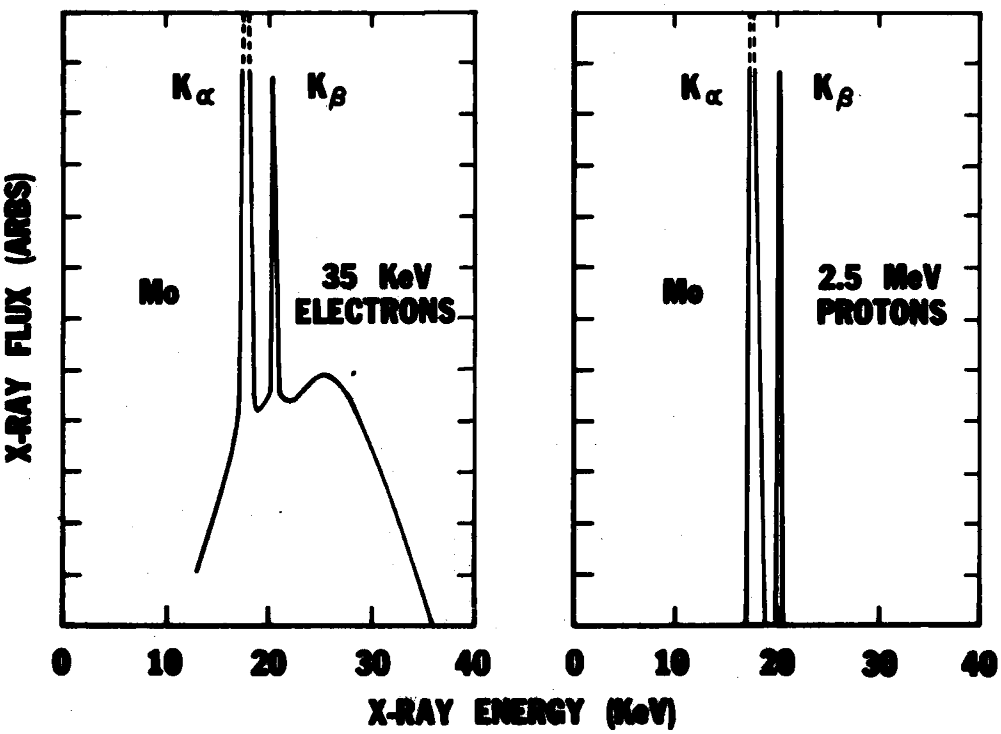

Figure 1. The x-ray spectra produced by the impact of electrons (left) and protons (right) on a molybdenum target.

order to project massive protons close to the repulsive nucleus proton energies of millions of electron volts are needed. For electrons, on the other hand, energies of only a few tens of thousands of electron volts are required. To get such protons one needs complex ion sources and accelerators instead of relatively simple x-ray tubes. Nonetheless, small (2-3 MeV) Van de Graaff accelerators capable of creating energetic protons are widely available. With most models enough x-rays can be produced to permit rapid density measurements to be made.

The efficacy of the x-ray technique in the interior ballistic environment is illustrated in fig. 2. Calculated transmission vs. x-ray energy profiles are shown for two sets of idealized (N_2 gas) conditions - those of typical muzzle and breech peak compressions. If one assumes the

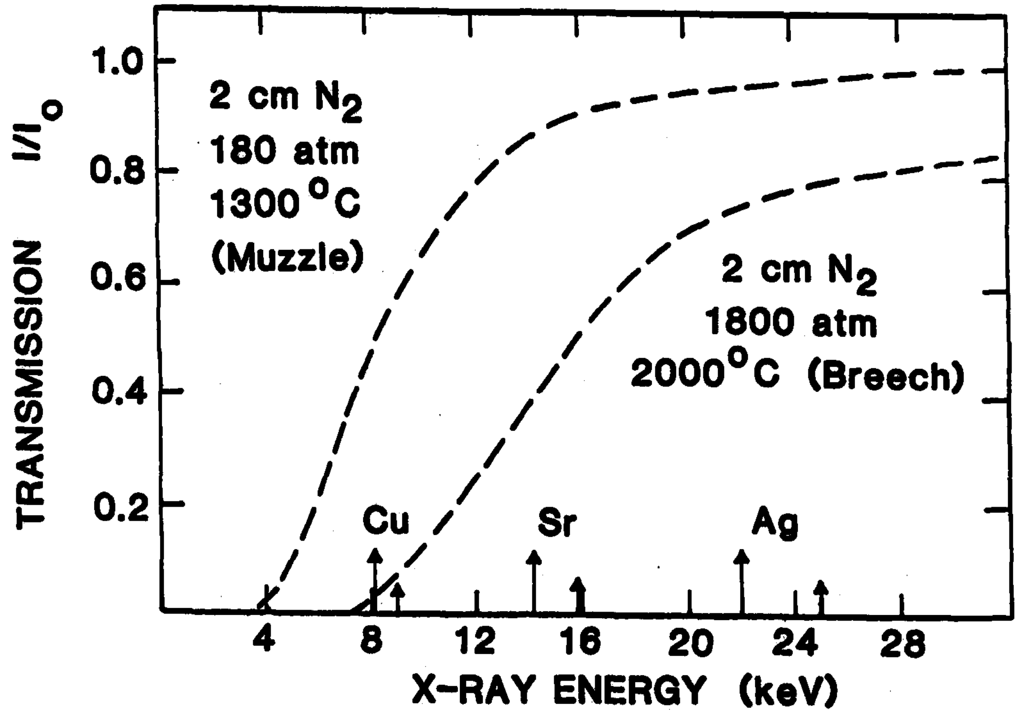

Figure 2. The transmission of x-rays under idealized breech and muzzle conditions.

sensitivity and error criteria previously stated, the optimum energy for analysis of these idealized muzzle conditions occurs when $1 < \mu\rho x < 2$ or correspondingly when $0.37 > I/I_0 > 0.13$. This lies near 8 keV. For breech conditions energies near 12 keV are more appropriate. In practice such energy selection can be achieved by merely changing the target material that the protons impact upon. The characteristic line pairs (K_α and K_β) for a few candidate target materials are shown on the abscissa of fig. 2.

There is another important design consideration, the window which allows the x-rays to enter and exit the weapon's bore and which maintains the bore seal integrity. The only material found sufficiently x-ray transparent is beryllium. Modern pressed powder alloys in virtually pure form of this substance are now available in x-ray transparent thicknesses which are strong and ductile enough to survive ballistic pressure/thermal pulses.

The new characteristic x-ray (CXR) method just described was first tested in a series of measurements in which a flux of copper characteristic K x-rays was passed through a 3 cm long chamber containing N_2 gas

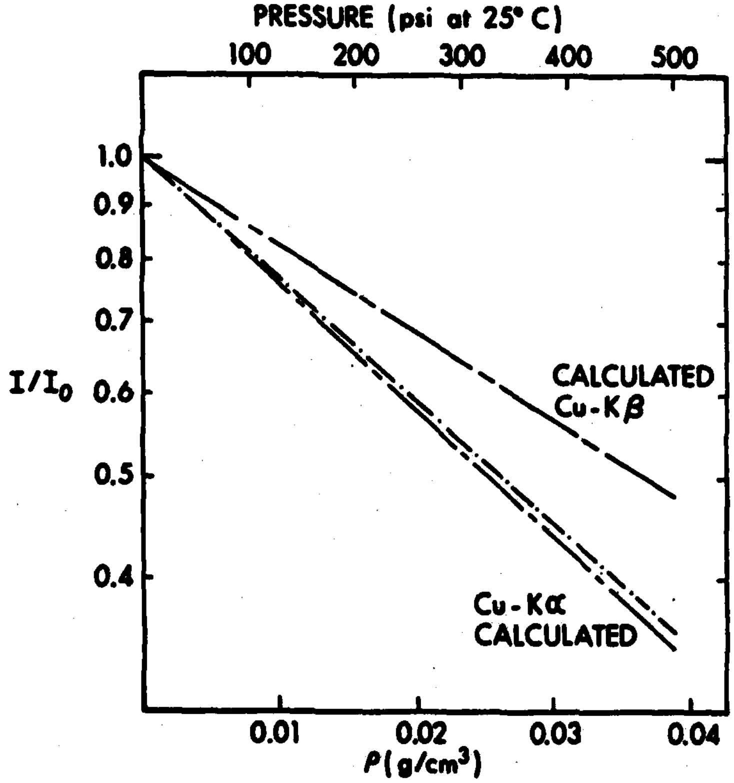

Fig. 3. The fraction of Cu x-rays surviving passage through 3 cm of N_2 gas under the conditions indicated (dots). Calculated transmissions for pure Cu-K_β x-rays (upper curve), for Cu-K_α x-rays (lower curve), and for the mixture of x-rays used in the experiments (dashed curve interrupted to reveal data points) are shown.

under conditions in which its temperature and pressure (and thus its density) could be precisely determined. The results of these measurements expressed as the fraction of the x-rays surviving passage while the gas density was incrementally raised are shown by the dots in fig. 3. The same figure also shows calculated values of I/I_0 for pure K_α and K_β x-rays (broken curves) and for the mixture of K_α and K_β x-rays actually present in the analyzing flux (dashed curve). The mixture was determined by a spectroscopic study of the x-rays conducted with a Si-Li detector. The agreement between the later calculated transmission and the experimental points is well within the errors of this measurement.

Apparatus

As a result of the success of the initial tests, an apparatus has been constructed for evaluating the CXR technique in a ballistic regime. It is illustrated schematically in fig. 4. To make a density measurement a current of 10-20 μamps of 2.35 MeV protons was taken from the BRL Van de Graaff accelerator, steered through an evacuated pipe, and directed upon a cooled thin target film of the appropriate material. X-rays created in the film enter and pass through the beryllium window mounted in the gun tube wall. Once inside the weapons bore some of the x-rays are absorbed photoelectrically by the propellant media. Those not absorbed may exit through a second beryllium window mounted in the opposite wall and strike a thin CaF_2 (Eu) scintillator. The light output from the scintillator then excites a photomultiplier which in turn produces an electrical current that is proportional to the instantaneous x-ray flux. That signal is next amplified and recorded on a digitizing oscilloscope. The resolving time of this system is limited to that time interval required to transmit the number of individual x-ray photons needed to establish counting statistics of the desired accuracy. In this apparatus transiting x-ray fluxes of $10^7 - 10^8$/sec are realized and resolving times of 10-20 μsec at a few percent uncertainty are achieved.

In its present configuration the apparatus uses a 5.56 mm weapon mounted to fire vertically downward. The weapon is equipped with piezoelectric pressure transducers (Kistler type 217C) placed adjacent to the cartridge throat and at the density measurement site. The amplified outputs of both transducers are recorded simultaneously with the x-ray

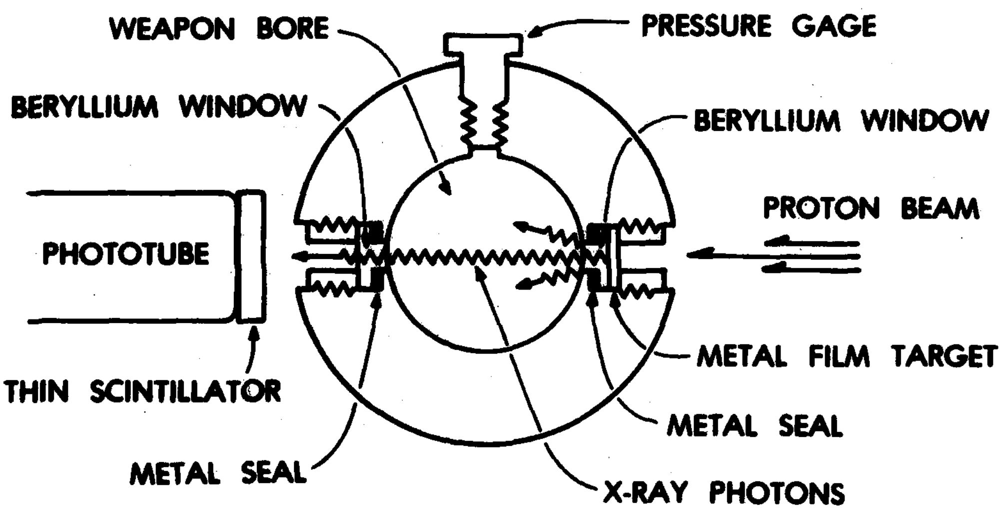

Figure 4. A schematic diagram of the apparatus used for the measurement of in-bore propellant densities.

attenuation signals. Measurements are now underway on three different weapons - these have measurement sites located 7.5 cm (near breech), 33 cm (the M-16 gas port location) and 45 cm (near muzzle) from the cartridge face.

Procedures and Results

The firing tests conducted to date have used M-193 ball ammunition containing WC-844 Olin propellant (10% nitroglycerine, 85% nitrocellulose, and 5% dibutyl phthalate). A typical raw x-ray flux profile at the 33 cm site is shown in fig. 5. Note that there are two types of fluctuations

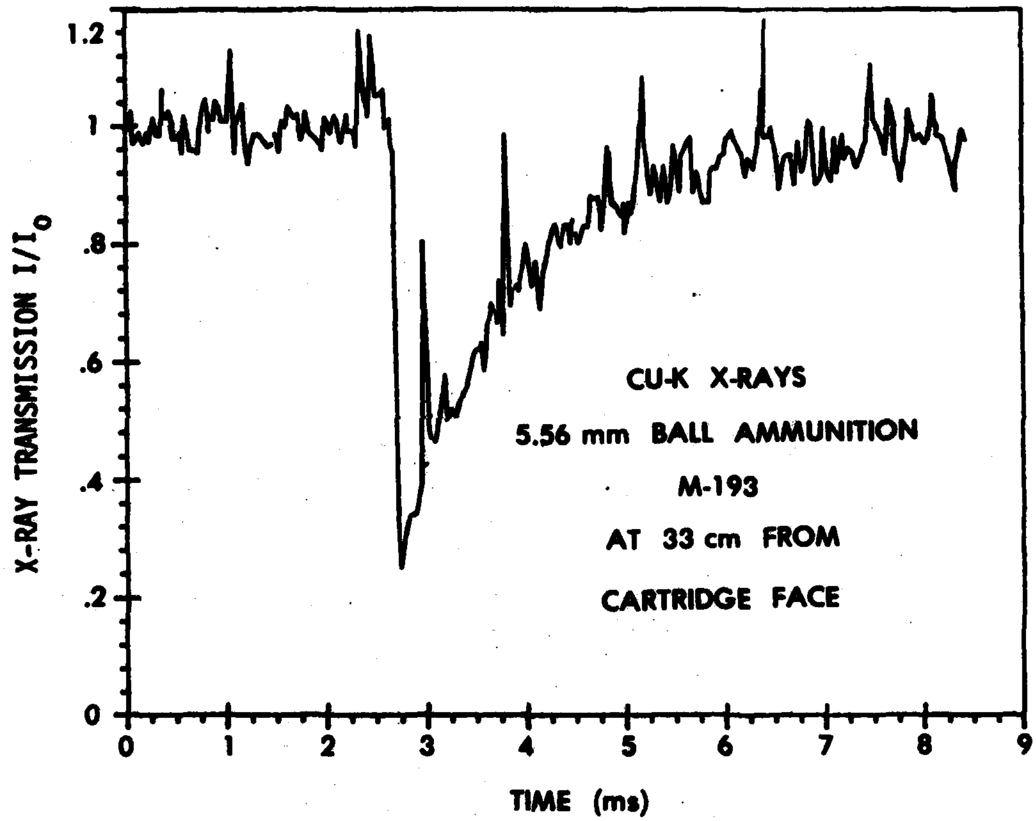

Figure 5. The attenuation of the Cu-K x-rays passing through the weapons bore during firing. The positive spikes are from extraneous nuclear reaction products.

associated with the x-ray flux profile, a random variation of a few percent amplitude and large positive-going spikes. The former are primarily the result of random statistical variations in the x-ray counts arriving during the resolving time of the apparatus. These may be significantly reduced by averaging over multiple shots. The larger fluctuations are produced by high energy products from nuclear reactions induced by proton impact. Inasmuch as the detailed shape of the individual spikes is characteristic of the electronic circuitry, they may be easily removed by signal processing.

The copper analyzing x-rays used in this experiment, like those in fig. 3, occur as a combination of K_α and K_β x-rays in a ratio which was determined with a Si-Li detector prior to weapon discharge. The propellant media has different attenuation coefficients for the K_α and K_β components, μ_α and μ_β, respectively. The scintillator cannot discriminate between components. It responds according to the relation:

$$(2) \quad \frac{I(t)}{I_0} = f\, e^{-\mu_\alpha \rho x} + (1-f) e^{-\mu_\beta \rho x}$$

where f is the ratio of K_α flux to the total x-ray flux. Given the experimentally determined parameters I/I_0 and f and values of μ_α and μ_β derived from the known composition of the propellant, it is possible to solve equation 2 for ρ numerically.

Density results are shown in fig. 6 which were derived from x-ray attenuation profiles taken at 33 cm from the cartridge face in a 5.56 mm weapon. Since the resolving time of the experiment is greater than the time of passage of the bullet over the 0.250 cm diameter x-ray aperture, the eclipse of the x-rays is not fully reproduced. At its peak the density is about 125 mg/cm^3 - 30% less than the density calculated for a uniform distribution of the 28 grain propellant charge over the bore volume between the window location and the cartridge face. The bulk of the trace in fig. 6 shows the venting of the weapon bore following the discharge of the projectile. The pressure profile determined at the density measurement site appears in fig. 7. Note that the pressure falls away faster than the density. Such behavior is to be expected of a cooling gas and/or a media in which less mobile condensed components are lagging behind its gaseous portions. It should be reemphasized at this point that the density reported here reflects the number of atoms per unit volume regardless of phase and chemical combination. The analysis also includes the assumption that the atomic composition is uniform throughout the media under study. This assertion is now being checked by repeating the measurements at multiple x-ray energies.

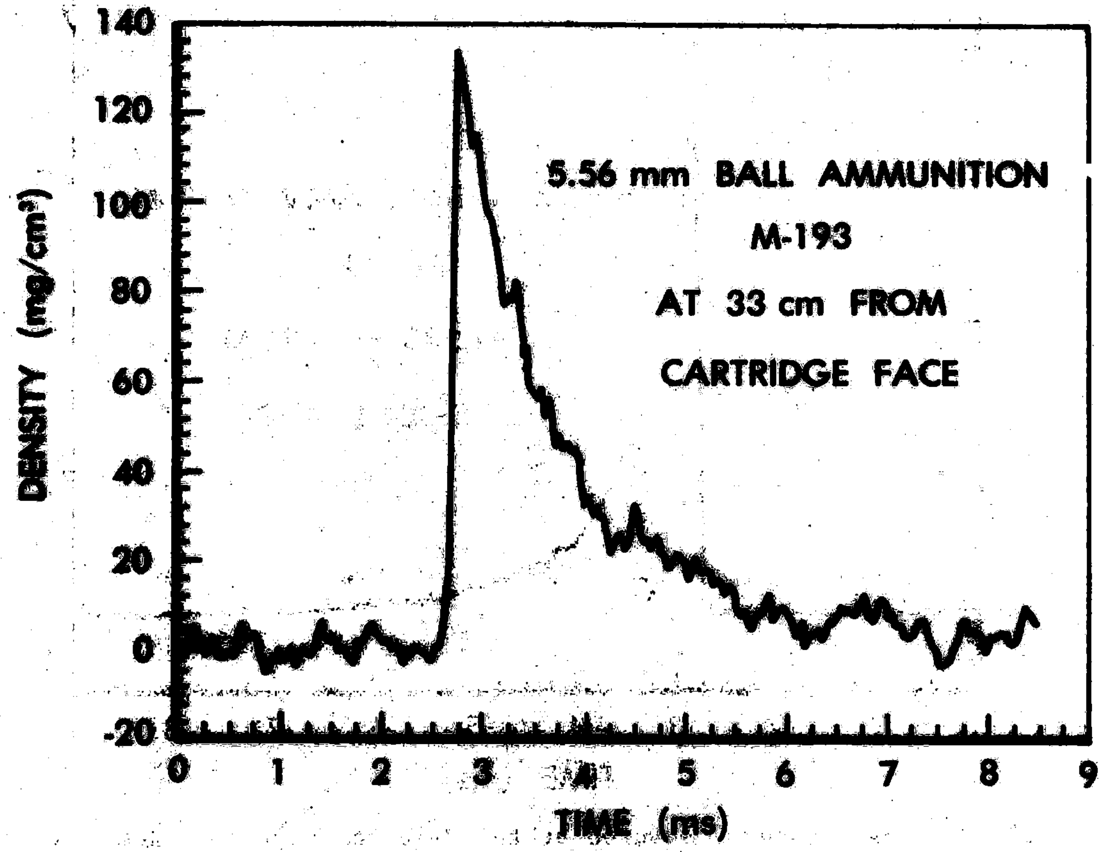

Figure 6. The propellant density measured in the bore of the weapon at the M-16 gas port location.

<u>Future Plans and Other Applications</u>

Our immediate goal is to improve the time resolution of the basic propellant density measurements, primarily by increasing the flux of proton induced x-rays. This is being done by raising the proton energy, by increasing the current delivered to the metal target, and by incorporating targets of increased efficiency. A parallel effort is also underway to replace the proton induced x-ray source with a conventional electron excited metal target operating in combination with a monochromator tuned to the K_α line. Most x-ray monochromators are diffraction-based and feature notoriously low transmission efficiencies (typically a few tenths to a few

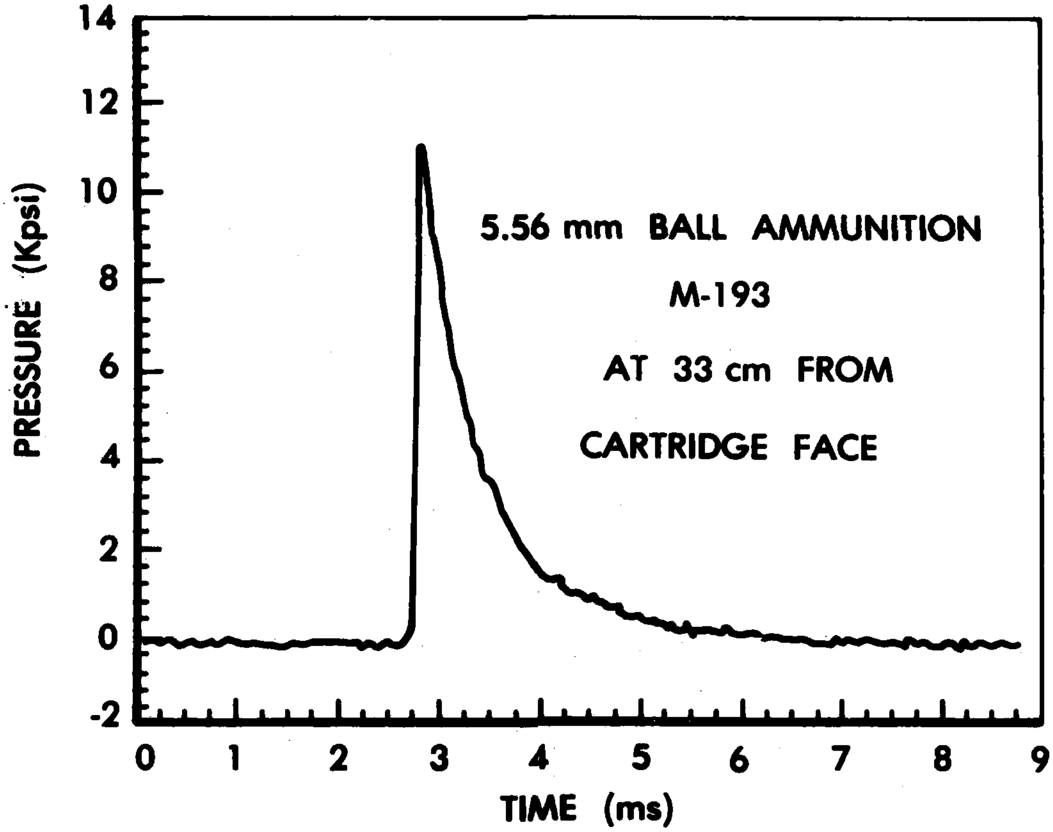

Figure 7. The pressure measured at the M-16 gas port location. A piezoelectric transducer was used in this determination.

hundredths of a percent). However, one type diffraction device, the mosaic crystal (5), does not suffer this handicap as severely as others. In preliminary tests mosaics have realized transmission efficiencies of a few percent. They are now undergoing further study in this laboratory.

The success of the 5.56 mm tests has also prompted planning of a series of density measurements with larger caliber weapons. Our objectives are two-fold. First, the radial density distribution will be obtained by passing the x-rays not only along the center of the bore cross section, but also across parallel chords. These data may be numerically unfolded into radial distributions, a quantity important in the study of flow dynamics and energy transfer processes within gun tubes. Second, the propellant bed will be seeded at a selected location with small quantities of materials of high atomic number Z. Since the x-ray attenuation will be dominated by these high Z materials, the increase in density observed with the additional material will indicate the evolution of propellant media from only the salted region of the bed. This type of information will be applied to studies of propellant combustion and additive action.

The characteristic x-ray radiographic (CXR) method lends itself to a broad range of non-invasive density measurements. Certainly it is capable of use in many gas dynamic devices such as shock tubes and internal combustion engines. It has been applied in this laboratory to study the pressurization, rupture and venting of gas cylinders with plastic rupture disks. The effects of disk deformation were clearly distinguishable (6). The utility of CXR is by no means limited to gaseous regimes. We have used silver K x-rays to search for variations in the density of 1.2 cm x 0.6 cm x 2.5 cm pressed solid gunpowder pellets. The anisotropic compression of the powder near the face that lay adjacent to the moveable side of the pellet press was observed and measured. Variations on the order of 1% were easily determined in profiling times of a few seconds. This was done while maintaining radiation exposure levels low enough to be inconsequential to the safety of the personnel nearby.

Conclusions

The experiments described demonstrate that characteristic x-ray radiography can provide quantitative density measurements on time scales of ballistic interest. The CXR method provides results that are relatively easy to analyze and are independent of the details of the chemistry or phase of the propellant. It appears that characteristic x-ray radiography will be usable both in continued ballistics applications for flow and combustion characterization and in a variety of other applications requiring rapid, non-invasive measurement.

References

(1) G.J. Mullaney, Rev. Sci. Instr. 28, 433 (1957).

(2) H.T. Knight and D. Venable, Rev. Sci. Instr. 29, 92 (1958).

(3) G.B. Kistiakowsky and P.H. Kydd, J. Chem. Phys. 25, 824 (1956).

(4) J.W. Robinson, editor, Handbook of Spectroscopy, Vol. I, CRC Press; Cleveland, Ohio (1974).

(5) R.W. Gould, S.R. Bates, and C.J. Sparkes, Appl. Spectros. 22, 549 (1968).

(6) G.M. Thomson and K.A. Jamison, IEEE Trans. Nuc. Sci. NS26, 1411 (1979).

A FRACTURE AND BALLISTIC PENETRATION RESISTANT LAMINATE

*MR. JOSEPH F. THROOP
US ARMY ARMAMENT RESEARCH AND DEVELOPMENT COMMAND
LARGE CALIBER WEAPON SYSTEMS LABORATORY
BENET WEAPONS LABORATORY
WATERVLIET, NY 12189

INTRODUCTION

The purpose of this paper is to suggest the way to attain exceptional ballistic penetration resistance and after-penetration fatigue-damage tolerance in metal/metal laminates. Although the optimum light-weight metallic laminate has not been perfected, the results of the exploratory tests of laminates reported here indicate the major factors of concern for optimizing performance.

Possible applications of the research are in
(a) light-weight armor for vehicles, vessels, and helicopters;
(b) structural components for helicopters and aircraft;
(c) crack arrester systems for aircraft and ships;
(d) concentrically laminated thick-wall pressure vessels.

This paper is a sequel to one presented in the 1974 Army Science Conference (1), in which the behavior and fatigue test results of steel laminates and aluminum laminates were presented. It was concluded then that damage tolerant metal laminates can be made by furnace brazing steel lamina or by explosive bonding Alclad 6061-T6 aluminum lamina. Also, fatigue crack retardation appeared to result from a "crack blunting" effect of plastic deformation at the interfaces, while fatigue crack arrest appeared to result from the crack turning into the direction of the interface and subsequent delamination.

That was followed by a paper published in 1978 on fracture resistant titanium/aluminum laminates (2) in which it was concluded that explosive bonding of alternate sheets of mill-annealed Ti-6AL-4V and Alclad 2024-T3 produces a laminate in which the fatigue crack rates, fracture toughness and impact resistance are superior to those of the component alloys.

The present paper attempts to indicate how such laminates may be developed with superior damage tolerance properties. It reports exploratory test results on the ballistic penetration resistance and after-penetration fatigue damage tolerance of three compositions of the titanium/aluminum laminates. Tests were made to compare their performance with that of rolled 6061-T6 aluminum alloy plate and that of rolled homogeneous steel (RHS) armor plate, using 0.30 caliber (44 grain) fragment simulator projectiles. The attributes of laminates which contribute to optimum performance are examined. An attempt was made to exploit as many attributes as possible in preparing the laminated materials for these tests.

BACKGROUND

Our early studies (1) were made with compact tension specimens, illustrated in Figure 1. We tested specimens of three configurations: (A) the crack arrest type in which a crack grown from a notch may be arrested by the interfaces between the composite layers, (B) the crack divider type, in which the crack growing from a notch is divided among the several layers, and (C) the coplanar type, in which the crack starting from a notch can be made to grow in the mid-thickness of a lamina for some distance before it veers into the bond layer and causes delamination of the bond.

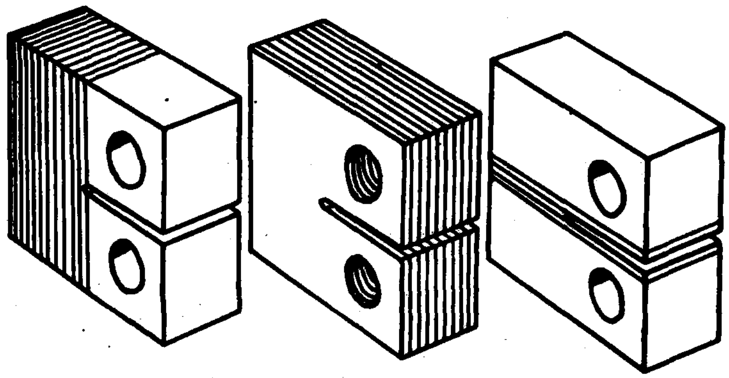

Fig. 1

The later work (2), on the titanium/aluminum laminates, was done with bending specimens. Crack divider and crack arrest specimens were tested. In the crack arrest specimens the notch was made so that its tip was either in an aluminum layer or a titanium layer, and then grown through that layer by cyclic loading to determine if it would go through the next bond layer or be arrested at the interface and start cyclic delamination. After measuring the crack growth rate by loading with a cyclic bending moment, we stopped the cyclic loading and loaded with a monotonically increasing load to measure the specimen's fracture toughness. Similar small standard Charpy impact specimens were made and used to measure the impact energy absorption C_v in both orientations of the notch.

These prior test results showed that ducile interfaces tend to decrease fatigue crack propagation rates in both orientations, and greatly enhance impact resistance in the crack arrest orientation. For resistance to ballistic penetration the laminate must resist fracture in the crack arrest configuration due to impact of a projectile. For complete penetration of the projectile it is necessary for the projectile and the associated cracks to pass through the several layers and interfaces of the laminate. Energy absorption by delamination and plastic deformation can be very effective in resisting penetration.

For subsequent fatigue service, however, the laminate must resist crack propagation in the crack divider orientation. The ballistically penetrated area may have so much damage that fatigue crack initiation is immediate and crack propagation life is very short. This is quite different from the usual fatigue crack propagation rate test in which a precracked specimen is cyclically loaded, or from a fracture toughness test in which a specimen is precracked and then monotonically loaded to failure. The ballistic penetration damage may be much more severe and the damaged area much more extensive than in the usual precracked specimen. It is appropriate then, to perform fatigue testing of specimens which have been subjected to actual ballistic damage.

Fracture Theory

Our experiments have been guided by the Cook and Gordon 1964 adaptation (3) of the Griffith (1921) fracture theory showing what may happen as a crack approaches normal to the interface between two solid materials. They showed that in an all brittle system a fracture may develop perpendicular to the advancing crack and well ahead of it because the maximum tensile stress in the direction of the crack advance occurs ahead of the crack tip and may exceed the strength of the material there. This applies especially at a weak interface in the crack arrest configuration of a laminate, and results in delamination of the interface.

McCartney et al (4) showed that this accounts for the arrest of super-critical cracks at interfaces in impact of laminates and of sub-critical cracks in fatigue of laminates. They postulated that the phenomenon is governed by the interfacial fracture strength gradient and the plastic zone size at the tip of the advancing crack. Thus a crack may either go through an interface or be arrested by delamination of the interface, depending upon the gradient of strength at the interface and the radius of the crack tip plastic zone when the crack arrives at the interface.

Our work has led us to postulate that the criterion for crack arrest at an interface in a given metal/metal laminate may be expressed as a constant product of the interfacial strength gradient γ times the radius of the crack tip plastic zone, r_p. The gradient is predetermined by the strengths of the chosen metals and thickness of bond layer at the interface. The plastic zone radius varies with the change of stress and with the increase in crack depth and can be calculated in terms of the fracture mechanics stress intensity factor. If their product is too great, either because of too steep a strength gradient or too large a plastic zone, the crack cannot advance into the stronger metal and a fracture occurs in the weaker metal and perpendicular to the advancing crack. Cyclic fatigue crack growth in the weaker metal along the interface then results in progressive delamination of the bond layer. In impact, the fracture of successive interfaces increases the energy absorption over that of the monolithic material.

Crack Arrest Criterion

Postulating that the crack arrest criterion can be expressed as a constant product of γ times r_p gives

$$\gamma\, r_p = C \tag{1}$$

as the limiting condition for delamination.

One can approximate the measured interfacial strength gradient γ by

$$\gamma = \frac{S_1 - S_2}{0.25\, t} \tag{2}$$

where S_1 is the ultimate tensile strength of the metal layer
S_2 is the ultimate tensile strength of the bond layer
t is the thickness of the bond layer
r_p is the crack tip plastic zone radius
C is a constant for a given composite

One can also approximate the crack tip plastic zone size for a static loading by the expression according to Irwin (5)

$$r_p^{s} = \frac{1}{2\pi}\frac{K^2}{S_y^{\,2}} \tag{3}$$

or for a cyclic loading by the expression according to Paris (6)

$$r_p^{c} = \frac{1}{8\pi}\frac{\Delta K^2}{S_y^{\,2}} \tag{4}$$

where S_y is the yield strength of material at the crack tip
$K = Y\sigma\sqrt{a}$, the stress intensity factor
ΔK is the cyclic range of stress intensity factor
Y is a term dependent upon the loading and geometry
a is the crack length
σ is the nominal stress

For a given combination of metal lamina, bond layer and bond thickness, the values of γ, S_y, and C are fixed and the likelihood of crack arrest by delamination depends upon the plastic zone radius at the crack tip. Thus

$$r_p = \frac{C}{\gamma} \tag{5}$$

indicates that a constant size plastic zone corresponds to the limiting condition for crack arrest by delamination.

Expressing this in terms of the fracture mechanics stress intensity factor, the condition for delamination becomes

$$K_{max} = \sqrt{2\pi}\, S_y \left(\frac{C}{\gamma}\right)^{1/2} \tag{6}$$

for crack arrest under static loading, and

$$\Delta K = \sqrt{8\pi}\, S_y \left(\frac{C}{\gamma}\right)^{1/2} \tag{7}$$

for crack arrest under cyclic loading. These indicate that the maximum stress intensity factor for delamination under cyclic loading is at least twice that required for delamination under static loading, hence the tendency for delamination is greater under static loading. Since the crack tip plastic zone will be even larger under an impact loading the tendency for delamination will be even greater under impact. Also, the delamination of successive bond layers under impact can absorb a large amount of energy in the deformation involved. These aspects of the hypothesis are in agreement with previously observed laminate behavior.

They also indicate that the criterion for crack arrest corresponds to a condition of constant K_{max} under static loading or of constant ΔK under cyclic loading. This has suggested an experiment for testing the validity of the hypothesis.

Experimental confirmation of the postulated crack arrest criterion has been demonstrated in a load shedding fatigue experiment in which it was possible to make a fatigue crack go through an interface by staying below the limiting value of ΔK, or make it be arrested by bond layer delamination by exceeding the limiting value of ΔK.

From Equation (7) and the stress intensity K-calibration for a given specimen type one can solve for the load to keep ΔK constant and corresponding to the criterion for crack arrest by delamination. For the compact tension specimen (7)

$$\Delta K = \frac{\Delta P}{BW^{1/2}} f(a/W) \tag{8}$$

From this and Equation (7) one gets

$$\Delta P = \frac{1}{f(a/W)} \left[\sqrt{8\pi}\, BW^{1/2}\, S_y \left(\frac{C}{\gamma}\right)^{1/2}\right] \qquad (9)$$

Similar expressions can be written for 3-point bending specimens (7) and for pure bending specimens (8). Since the terms within the brackets are all constants, Equation (9) indicates that in order to maintain a constant value of ΔK the cyclic load must be reduced as the inverse of $f(a/W)$. When the cyclic load is kept less than ΔP from Equation (9) the fatigue crack will grow through the interface and into the next metal layer. Reducing the load before reaching each successive bond layer permits the fatigue crack to grow through several layers. If, however, the load is not reduced below the limiting value the crack will be arrested and cyclic delamination will occur at the next interface it arrives at. To apply these expressions to any given laminate composition one must evaluate S_y, γ, and C experimentally for that laminate.

Figure 2 is an illustration of this load-shedding experiment. This is a plot of data from specimen A3A, a laminated beam of 6061-T6 explosively bonded with 0.012 inch thick 7072 aluminum alloy Alclad bond layers. It was fatigue cycled in pure bending under the prescribed load shedding procedure so that the load ΔP was kept less than the crack arrest limit as the crack approached each successive bond layer. The open circles represent the fatigue crack going through the interface at the load and crack depth plotted. Solid circles for other specimens represent the delamination and arrest of the crack at an interface corresponding to the plotted load and crack depth.

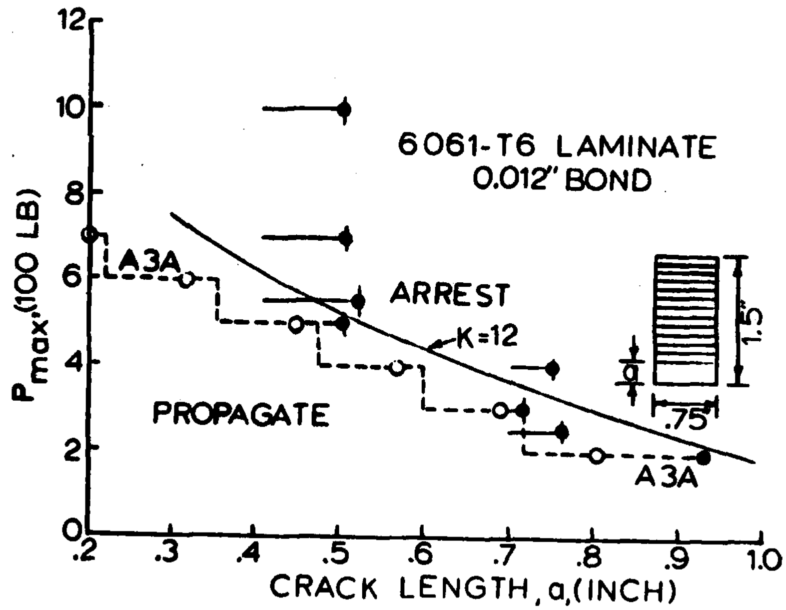

Fig. 2

One can see that in specimen A3A the load shedding kept the stress intensity factor range ΔK less than the value of 12 Ksi$\sqrt{\text{in}}$ and the crack proceeded through five successive bond layers before delamination occurred at the sixth. In the other specimens crack arrest and delamination occurred at interfaces at similar loads and crack depths because the loads were not reduced below the limiting value. This experiment has been performed successfully in several other metal lamina and bond layer combinations.

Crack Retardation

Even when the crack grows through the bond layer its growth is retarded, as shown in Figure 3. The curve labelled A shows fatigue crack growth in a crack arrester specimen of the Ti/AL laminate. The curve labelled B shows the fatigue crack growth on a crack divider specimen of the same laminate under the same loading conditions. As the crack approaches the bond layer in the crack arrester specimen (A) it slows down in the 2024 aluminum layer and takes a large number of cycles to traverse the soft Alclad bond layer. When it grows into the next Ti-6AL-4V layer it acquires approximately the same crack rate as that in the crack divider specimen, but as it approaches the next bond layer it again slows down. This repetitive retardation of crack growth at each interface has the cumulative effect of greatly lengthening the fatigue crack propagation life in comparison to monolithic specimens of the same materials or to crack divider specimens of the same laminate. We have previously shown that the crack rates of the Ti/AL laminates in both crack divider configuration and crack arrest configuration are less than those of the component material (2). Thus, even in the crack divider configuration the bond layers have some effect on the fatigue crack rate. This may be attributed to energy absorption and crack blunting in the soft bond layers, and to a tendency for plane stress behavior in the individual lamina.

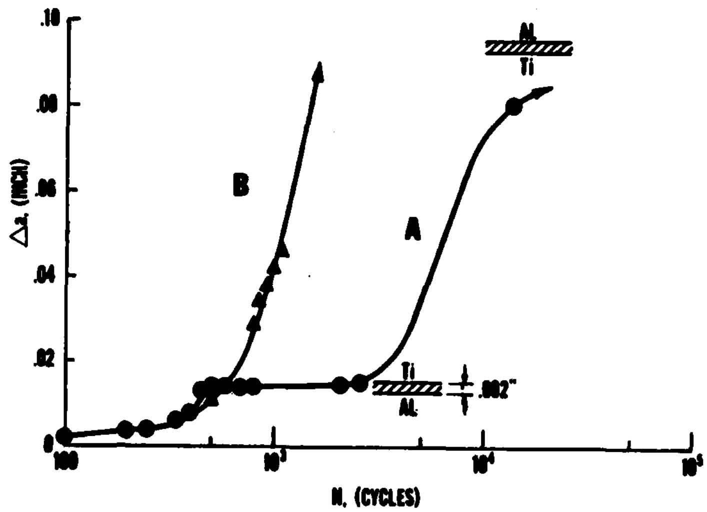

Fig. 3

Ballistic Damage Specimens

In the present study small plate specimen were prepared as shown in Figure 4, and tested first for their ballistic penetration resistance. Then loading holes were drilled and a saw cut was made into the ballistically damaged area and the specimens were tested as compact tension specimens for their after-damage fatigue life.

In Figure 4 the edge view labelled (A) shows the arrangement with 30% volume fraction of aluminum, the view labelled (B) shows the arrangement with 60% volume fraction and view labelled (C) shows the arrangement with 90% volume fraction. The shaded layers represent the titanium layers. The layer and laminate thicknesses are given in Table 1. Similar specimens were made of 6061-T6 plate and RHS armor plate, also listed in Table 1.

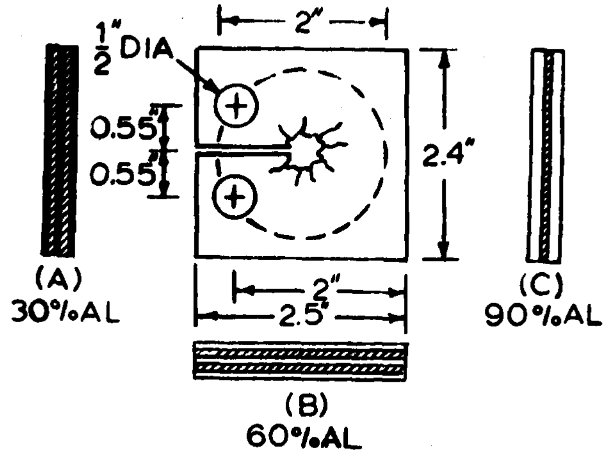

Fig. 4

Materials

The laminates for these specimens were composed of mill-annealed Ti-6AL-4V sheets and Alclad 2024-T3 aluminum alloy sheets, clad on both sides. In the finished laminates the thickness of the cladding was approximately 0.002 inch. In each composite the titanium sheets were interior layers and the exterior layers were Alclad aluminum alloy sheets.

These consisted of a five-layer laminate (AA) with three thin aluminum layers and two thick titanium layers, having approximately 30% volume fraction of aluminum; a five-layer laminate (AB) with three aluminum layers and two titanium layers all of equal thickness, having 60% volume fraction of aluminum; also a three layer laminate (AC) with two thick layers of aluminum and one thin layer of titanium, having approximately 90% volume fraction of aluminum. They were laminated by explosive bonding in the Fabrication and Quality Assurance Section of the Battelle Columbus Laboratories (9). They were compared with plates of 6061-T6 aluminum alloy and rolled homogeneous steel armor RHS. The five materials tested are listed with their layer dimensions in Table 1.

The 3/8 inch thick plate of 6061-T6 aluminum alloy and the 0.150 inch thick plate of homogeneous rolled steel armor (RHS) were supplied by the Fort Dix Test Facility of ARRADCOM, where the ballistic penetration testing was performed (10).

An attempt was made to have the laminated materials about 3/8 inch thick to compare with the 6061-T6 aluminum plate, and to approximate as nearly as possible the areal density of 6.12 pounds per square foot of the RHS plate, so as to facilitate the comparison of ballistic penetration and fatigue performance. In the final analysis the ballistic penetration velocities of the laminates and the aluminum were compared with published (10,11) values for RHS having the same areal density as that of each of these materials.

Ballistic Protection Velocity

The ballistic penetration tests were made by supporting the plate specimen against a steel plate with a two inch diameter hole in it at the point where the bore-sited projectile was aimed. Fragment similator projectiles of 0.30 caliber (44 grain) were fired at various velocities to obtain the ballistic protection velocity limit V_{50} at which 50% of the projectiles would just penetrate through the specimen. The resulting values of V_{50} for the materials tested are compared with V_{50} values for RHS of the same areal density in Table 2.

Areal Density

Figure 5 shows a plot of the volume fraction F_a of aluminum of the laminates versus the areal density d in pounds per square foot. The line shows the variation of F_a versus d for 3/8 inch laminate. The symbols on the graph show the volume fraction versus density of the laminates tested and their thickness, as well as that of the 6061 plate. The right side of Figure 5 shows the V_{50} of the laminates and the 6061-T6 plotted as a function of their areal density. The equation of the curve shown indicates that the V_{50} increases as the square of the areal density. The values of V_{50} of the three laminates exceed that of the RHS which had the areal density of 6.12 pounds per square foot, while that of 2024-T4 is slightly less and that of 6061-T6 is considerably less. These results will be compared with RHS on the basis of equal areal densities in a later section. The curve on Figure 5 indicates that the ballistic protection velocity V_{50} decreases in relation to the square power of the volume fraction of aluminum in the laminate. The interpretation is that the more titanium there is in the laminate the greater the V_{50} protection limit will be.

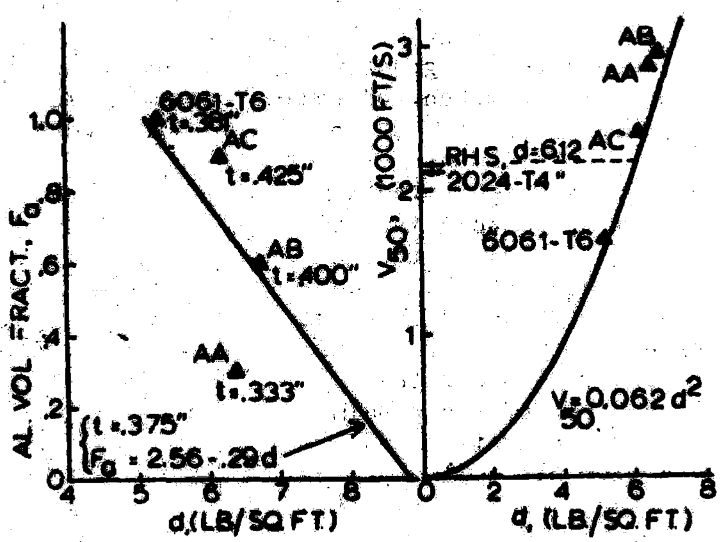

Fig. 5

Fatigue Lives

The number of fatigue cycles endured to failure for each of the ballistically damaged materials is listed in Table 3. In all three laminates, and the 6061-T6 as well, the lives of the drilled-hole specimens are much longer than those of the ballistically damaged specimens. It may be assumed that the ballistic damage practically eliminates the fatigue crack initiation cycles that are included in the lives for the drilled-hole specimens, and also that the damage extends to a larger radius from the center of the damage site.

Only the fatigue lives of those specimens which were impacted at the V_{50} velocity of the particular laminate or near it are amenable to consistent analysis. The ones that were only partially penetrated would have endured longer lives than measured if we had not made our saw cut to the middle of the damaged zone, because the fatigue cracks would have had to grow in the crack arrest orientation until they became through-cracks before growing in the crack divider orientation. The lives of the specimens which were penetrated at greater than the V_{50} velocity are quite variable because of the greater extent of damage from the higher velocity. Their lives are much shorter in general than those which were impacted at the V_{50}.

Focusing our attention on those which were impacted at velocities close to the V_{50} for each material, one may see in Figure 6 that the greater V_{50} velocity of the material the longer the fatigue life of the specimen at the given cycle load. These were all cycled at the same load, specifically from 175 lb. to 1,750 lb. and at 30 hertz. The triangle symbols represent ballistically damaged specimens, and the circles represent drilled-hole specimens of the laminates and the 6061-T6 plate.

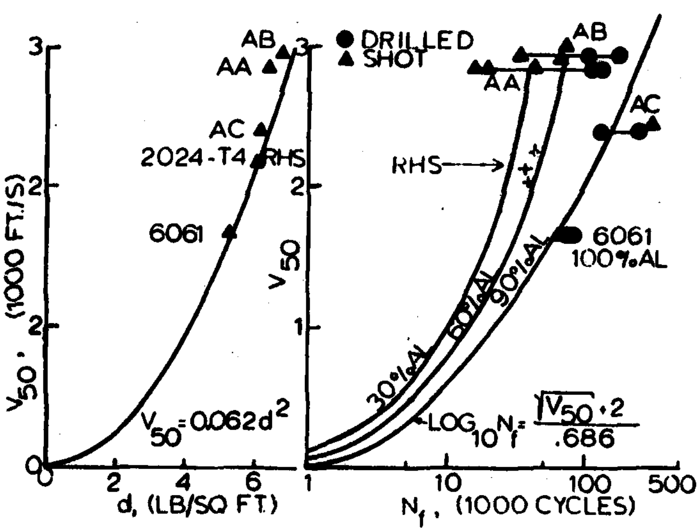

Fig. 6

Figure 6 also indicates that the greater the volume fraction of aluminum in the laminate the longer the fatigue life will be. Both AB and AC, as well as the 6061 aluminum plate have lives greater than the RHS specimens. The equation on Figure 6 indicates that the fatigue life of the

90 to 100% volume fraction specimens increases with the square root of V_{50}. The V_{50} was shown earlier to increase as the square of the areal density. Hence the fatigue life for 90 to 100% AL is seen to increase approximately as the areal density. However, the three curves representing 30%, 60%, and 90% volume fraction of aluminum indicate that the larger the aluminum content the longer is the after-damage fatigue life of the laminate.

It becomes apparent then that to optimize the laminate's performance in both ballistic penetration protection and after-damage fatigue tolerance, one must make a compromise in regard to the aluminum volume fraction, since decreasing F_a increases V_{50} but decreases N_f. On Figure 7 is plotted V_{50} for each material divided by the V_{50} of equal areal density RHS. Also plotted is N_f divided by the N_f of the 0.150 inch thick RHS tested. This shows that the best after-damage fatigue life is given by the 90% aluminum laminate. However, the best combination of ballistic protection velocity with fatigue life is given by the 60% aluminum laminate, with a V_{50} which is 22% greater than the RHS, and a fatigue life which is over 50% longer than the RHS.

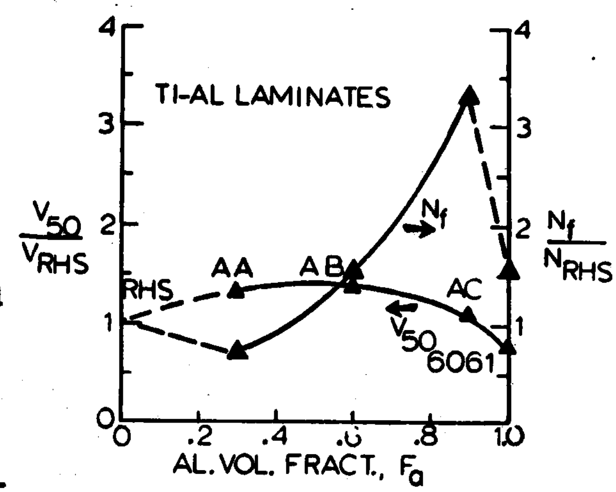

Fig. 7

Laminate Attributes

From the results reported earlier (1,2) and those reported here it is evident that there are several aspects of metal/metal laminates which can be exploited to develop maximum damage tolerance. Each of the following attributes of laminate construction can be enhanced toward optimizing the laminate performance for a given application. In the titanium/aluminum laminates they are:

1. Alternate soft and hard layers: Soft layers absorb energy and resist spalling of the hard layers, while the hard layers provide high strength. Soft Alclad layers on the exterior surfaces also resist corrosion from the surrounding environment.

2. Thin-sheet metal properties can be retained in thick sections: Superior mechanical properties are attainable in rolled sheet as compared to thick forged sections; heat treatment is more effective and plane stress K_c fracture toughness, rather than plane strain K_{Ic}, may be sustained.

3. Ductile bond layers resist fatigue and fracture: The Alclad surfaces on the aluminum sheets became the ductile bond layers and gave the effect of "crack blunting" at the interfaces. In steel laminates a ductile CuNi interleaf gave the same effect.

4. Laminate interfaces may be tailored to the application: The strength and thickness of the bond layer can be selected in relation to those of the metal layers so as to absorb energy, retard crack propagation and arrest cracks by delamination.

5. Favorable residual stresses can be developed by explosive bonding: Compressive residual stress in the aluminum layers retards initiation and propagation of fatigue cracks and increases the critical crack depth. The corresponding tensile residual stress in the alternate layers of higher-strength titanium tends to accelerate initiation and decrease the critical crack depth, but has little effect on the crack propagation rate and small effect on the after-penetration life.

6. Areal density of the composite can be adjusted from that of aluminum plate to that of titanium plate: The lighter weight permits thicker sections than steel of the same areal density, hence panels may be stiffer.

7. Volume fractions may be optimized by adjusting the number and thicknesses of layers: Increasing the volume fraction of aluminum in the Ti/Al laminate increases the after-penetration fatigue life but decreases the ballistic penetration protection velocity.

Since most of these attributes are interdependent it is important to seek the optimum combination of all of them if maximum performance is to be attained. However, as long as alternate soft and hard layers of thin sheet metal are bonded with suitable ductile bond layers it is possible to adjust the thicknesses, strengths, and numbers of interfaces and lamina to give a range of areal density and volume fraction as desired. Explosive bonding, in addition, permits lamination of dissimilar metals without brittle interfaces.

CONCLUSIONS

1. Delamination at ductile interfaces in metal/metal laminates can absorb much energy in impact and ballistic penetration, and can retard or arrest fatigue cracks in cyclic loading.

2. The results of exploratory tests show that a compromise between the ballistic penetration protection velocity limit and after-damage fatigue life may be necessary to achieve the optimum combination of these two qualities in a laminate.

3. The several attributes of metal/metal laminates which contribute to the above qualities are interdependent, therefore it is necessary to seek the optimum combination of these attributes to attain maximum performance of any given laminate composition.

4. An empirical criterion for crack arrest by delamination of laminate interfaces can be expressed in terms of the strengths and dimensions of the composite layers and as a function of a limiting value of the crack tip stress intensity factor.

ACKNOWLEDGEMENTS

My sincere gratitude goes to E. A. Webster, Jr. for ballistic testing, to Ronald T. Abbott and Gregory S. Leger for fatigue and fracture testing and to Ellen Fogarty for manuscript preparation. This work was performed under funding from DA Project 1L161102AH60 in the Army Armament Research and Development Command.

REFERENCES

1. Throop, J. F. and Miller, J. J., "Fatigue Behavior of Laminates," Proc. U.S. Army Science Conference, June 1974, Vol. III, pp. 229-243, AD785690.
2. Throop, J. F. and Fujczak, R. R., "Fracture Resistant Titanium-Aluminum Laminate," Toughness and Fracture Behavior of Titanium, ASTM STP 651, American Society for Testing and Materials, 1978, pp. 246-266.
3. Cook, J. and Gordon, J. E., Proceedings Royal Society of London, Vol. 282A, 1964, pp. 508-520.
4. McCartney, R. F., Richard, R. C., and Trozzo, P. S., "Fracture Behavior of Ultrahigh Strength Steel Laminar Composites," Trans. ASM, Vol. 60, 1967, pp. 384-389.
5. Irwin, G. R., "Fracture Mode Transition for a Crack Traversing a Plate," J. Basic Eng., Am. Soc. Mech. Eng., Series D, V. 82, No. 2, June 1960.
6. Paris, P. C., "The Fracture Mechanics Approach to Fatigue," in Fatigue, An Interdisciplinary Approach, Burke, J. J., Reed, N. L., Weiss, V., Editors, Syracuse University Press (1964), pp. 107-132.
7. ASTM Specification E-399-78, 1978 Annual Book of ASTM Standards, Part 10, Am. Soc. Test & Matls., Philadelphia, pp. 512-533.
8. Tada, H., Paris, P., and Irwin, G., "The Stress Analysis of Cracks Handbook," Del Research Corp., Hellertown, PA, 1973, p. 214.
9. Pattee, H. E., "Explosive Welding of Laminated Plates," Final Report to Watervliet Arsenal From the Fabrication and Quality Assurance Section of Battelle Columbus Laboratories, Columbus, OH, August 1979.
10. Webster, E. A., Private Communication and letter from James A. Donahue, Director, ARRADCOM Test Site, Fort Dix, NJ, February and March 1980.
11. AMMRC, "Ballistic Technology of Lightweight Armor," TR79-10, U.S. Army Materials and Mechanics Research Center, 1979 (U), Figure 410.

TABLE 1. DESCRIPTION OF MATERIALS AS PREPARED FOR TEST

Material Designation	No. of Layers (#)	Thickness (inch)	No. of Layers (#)	Thickness (inch)	Thickness (inch)	AL Vol. Fract. (%)	Areal Density (lb./sq. ft.)
Ti/AL-AA	3	0.031	2	0.120	0.333	28%	6.38
Ti/AL-AB	3	0.080	2	0.080	0.400	60%	6.71
Ti/AL-AC	2	0.045	1	0.045	0.425	89%	6.13
6061-T6 AL	1	-	0	-	0.381	100%	5.28
RHS Armor	0	-	0	-	0.150	0%	6.12

TABLE 2. COMPARISON OF BALLISTIC PROTECTION VELOCITIES

Material Tested	Thickness (inch)	Areal Density lb/sq. ft.	Test V_{50} ft/sec	RHS, V_{50} ft/sec	Ratio: $\frac{\text{Test}}{\text{RHS}}$
6061-T6	0.381	5.28	1660	2041	0.81
RHS	0.150	6.12	2170	2267	0.96
Ti/AL-AC 90% AL	0.425	6.13	2400	2270	1.06
Ti/AL-AA 30% AL	0.333	6.38	2850	2338	1.22
Ti/AL-AB 60% AL	0.400	6.71	2950	2427	1.22

TABLE 3. AFTER-DAMAGE FATIGUE TEST RESULTS

Material Tested	Aluminum Vol. %	$\left(\frac{V_{50}}{V_{RHS}}\right)$ *	N_f (Cycles)	$\left(\frac{N_f}{N_{RHS}}\right)$
6061-T6	100%	0.81	61,000	1.7
Ti/AL-AC	90%	1.06	128,000	3.6
Ti/AL-AB	60%	1.22	58,000	1.6
Ti/AL-AA	30%	1.22	27,000	0.7
RHS	0%	0.96	36,000	1.0

DOXYCYCLINE PROPHYLAXIS OF SCRUB TYPHUS

JOHN C. TWARTZ, MBBS, AKIRA SHIRAI, Ph.D., G. SELVARAJU, MBBS, J. PETER SAUNDERS, MBBS, *DAVID L. HUXSOLL, COL, VC, AND MICHAEL G. GROVES, LTC,VC
US ARMY MEDICAL RESEARCH UNIT
INSTITUTE FOR MEDICAL RESEARCH, KUALA LUMPUR, MALAYSIA

Scrub typhus is a febrile illness caused by infection with *Rickettsia tsutsugamushi*, the vectors of which are larval stages of trombiculid mites, frequently referred to as chiggers.

Although the disease was originally reported only from restricted areas in Japan, it is now known to have a widespread distribution within a large triangular area bounded by Siberia in the north, Australia in the south, and Pakistan in the west. The distribution of the disease parallels that of known vector mites.

Scrub typhus gained military importance among both Allied and Japanese forces during World War II. Records are incomplete on casualties suffered from the disease by Japanese forces, but estimates approaching 30,000 have been made (1). Among Allied forces, available statistics indicate that approximately 18,000 casualties occurred (2). Of 11,000 cases for which adequate data are available, there were nearly 650 deaths. In American troops, case fatality rates varied in different epidemics between less than one percent and thirty-five percent. Scrub typhus seriously jeopardized the operational efficiency of military units in which the sudden outbreaks occurred. In Vietnam, scrub typhus was a leading cause of fever of unknown origin in US soldiers (3,4).

The lack of an effective vaccine for scrub typhus has caused other methods of prevention to be considered. One method, dating from the 1940's, is chemoprophylaxis with antibiotics. Once weekly 4g doses of chloramphenicol were shown to provide successful scrub typhus prophylaxis if taken for a minimum of four weeks after exposure (5). Recognition of the risk of dose-related and idiosyncratic bone marrow toxicity, however, now precludes the prophylactic use of this antibiotic (6,7).

Tetracyclines are currently the drugs of choice for therapy of scrub typhus (8). In this group, doxycycline and minocycline have the most potential for prophylactic use because they have the longest half-lives and are the most active against gram negative bacilli (9). Whereas doxycycline is relatively free of serious side effects, minocycline has been associated with vestibular toxicity (10). Prophylactic doxycycline has been safely used in the prevention of traveller's diarrhea (11), acute exacerbations of chronic bronchitis (12), and infections after abdominal surgery (13). Doxycycline in single doses has already been reported to be effective treatment for two rickettsial diseases, scrub typhus (14) and louse-borne (epidemic) typhus (15).

Recently, doxycycline was used in a large scrub typhus prophylaxis study in Taiwan (16). The drug was well tolerated and apparently effective, but interpretation of the results of this study is hampered by the low incidence of scrub typhus in the control subjects and the failure of some treated subjects to comply with the prophylactic regimen.

We also have studied the efficacy of doxycycline as a prophylactic drug for scrub typhus. In our prospective, randomized, double-blind, placebo-controlled study, volunteers were given weekly 200 mg doses of doxycycline and deliberately infected. Additionally, we tested the efficacy of a single dose of doxycycline in the therapy of early scrub typhus. The results of these studies form the basis of this report.

Materials and Methods

Volunteers. The study population comprised 16 Malaysian and four American male members of our laboratory staff, ages 27-48 years. The volunteers were examined by an independent physician to determine their fitness to participate in the study. They were then divided by him into two similar groups according to several criteria: racial origin, age, body weight, and pre-existing antibody to *Rickettsia tsutsugamushi* as measured by the indirect fluorescent antibody (FA) test (17). Three placebo and two doxycycline subjects had pre-existing antibody (titers $\leq$1:50) to *R. tsutsugamushi*. All subjects were given single test doses of 200 mg doxycycline and 500 mg tetracycline hydrochloride before the start of the study to check for immediate hypersensitivity to either drug.

Infection. Our laboratory maintains a colony of *Leptotrombidium fletcheri* mites (18) infected with *R. tsutsugamushi* (19). The volunteers were infected by allowing chiggers from this colony to feed on them (20).

Prophylactic regimen. Doxycycline 100 mg capsules and identical looking placebo capsules containing calcium lactate were generously supplied by Pfizer (Japan). Subjects in the doxycycline group each received a single, weekly 200 mg oral dose of doxycycline for seven doses. The antibiotic was given under supervision after breakfast. The control group received their placebo capsules under the same circumstances. No other medications were allowed to be taken during the study except that dextropropoxyphene napsylate 100 mg (Eli Lilly) was available as an analgesic. Because this drug does not have an antipyretic effect (21), there was no masking of febrile responses in the volunteers.

Surveillance and criteria for diagnosis. All subjects were examined daily, and oral temperatures were recorded twice daily. Upon completion of the seven-week course of prophylaxis, the remaining healthy volunteers were kept under clinical surveillance for a further four weeks. During the prophylaxis period, venous blood was drawn every three days for standard hematological and biochemical tests, indirect FA, and rickettsial isolation. Subsequently, blood was drawn every week for two months. Indirect FA was measured against each of eight prototype strains of *R. tsutsugamushi*: Karp, Kato, Gilliam, TA678, TA686, TA716, TA763 and TH1817. Titers were expressed as the reciprocal of the highest positive serum dilution. A change in the indirect FA titer from zero (<25) to 50 or a four-fold rise between initial and subsequent sera was considered significant.

For rickettsial isolation, 0.2 ml of each blood sample was inoculated ip into three adult white mice. Twenty-eight days later, surviving mice were challenged ip with 10^3 mouse LD_{50} of the Karp strain of *R. tsutsugamushi*. Death after the first inoculation or survival after the challenge indicated the presence of *R. tsutsugamushi* in the original blood specimen (22). Further aliquots of each venous blood sample were stored at -70C. Subsequently, 0.2 ml of each blood sample was inoculated ip into five glycogen-treated mice. When these animals became sick or on day 14, peritoneal cells were harvested and examined for *R. tsutsugamushi* by the direct FA (23) test.

A clinical diagnosis of scrub typhus was based on either (1) coexistence of two or more of the cardinal signs - eschar, generalized lymphadenopathy, hepatomegaly and/or splenomegaly, and rash - or (2) fever greater than 37.6C for more than 48 hours.

Subjects considered to have scrub typhus on clinical grounds were treated on the third day of their illness with a single 200 mg oral dose of doxycycline. Recovery from scrub typhus was defined as absence of symptoms and a 24-hour period with temperature less than 37.2C. Relapse was defined as the presence of fever greater than 37.6C for 24 hours or the recurrence of fever in any two consecutive 24 hour periods after apparent recovery from scrub typhus. Therapy for relapse was tetracycline hydrochloride 500 mg sixth hourly for seven days.

Statistics. Prior to the study, an estimate of the required group sizes was made, using various infection rates for the placebo and drug group and a significance level of $p = 0.01$. For example, if the disease rates in placebo and drug groups were 0.8 and 0.2 respectively, eight subjects would be needed in each group for a significance level of $p = 0.01$. We chose 20 volunteers as a minimum number to allow for the possibility that some volunteers might withdraw from the study. Our results were analyzed in a two-tailed test of significance by Fisher's exact probability test.

Results

Chigger attachment. The day after the first dose of prophylaxis, a small plastic capsule (24) was glued to the medial aspect of the thigh of each volunteer. The next morning, adherence of the capsule was checked and ten chiggers were placed in each capsule. The chiggers were observed under a dissecting microscope for 15 minutes, by which time some had begun to attach in about half the volunteers. A dampened cotton swab was placed in the capsule to prevent dessication of the chiggers, and the cover of the capsule was taped closed. For those volunteers with slow attachment, the chiggers were replaced with a fresh batch and observed. In this way, 16 volunteers had chiggers attached on the third day after prophylaxis was started. Attachment and condition of the chiggers were rechecked later in the day. The four volunteers (two from each treatment group) with no chigger attachment had fresh chiggers inserted in the late afternoon and left overnight. The following day all of these volunteers had some chiggers attached.

Between two and 13 (mean 8.5) chiggers attached to each volunteer and between two and 13 (mean 7.1) engorged chiggers were recovered 48 hours after attachment. Direct FA staining of these engorged chiggers (25) showed all to be infected with R. tsutsugamushi.

Prophylaxis period. No significant adverse effects from doxycycline were reported. Mild epigastric discomfort was noted after one dose by two subjects; one other dose was vomited by one of these subjects and was repeated.

Starting between the third and ninth days post chigger attachment (PCA), all subjects, except three receiving doxycycline, developed tender inguinal lymphadenopathy adjacent to the site of chigger attachment. The three remaining subjects had similar findings during the succeeding eight days. By day 7 PCA, all the placebo group and two of the drug group had a small, indurated, erythematous nodule at this site. In none of the drug group did this progress, whereas in all but one of the placebo group a classical eschar developed. The one exception was an American volunteer, who had no past history of scrub typhus and no pre-existing scrub typhus antibody, but had had several years of occupational (laboratory) exposure to scrub typhus rickettsiae.

Between days 7-11 PCA, nine of the placebo group and one of the drug group were hospitalized with presumed scrub typhus (Table 1). The clinical diagnosis was subsequently confirmed by isolation of rickettsiae from blood with or without a four-fold rise in indirect FA titer.

TABLE 1. Scrub typhus in subjects receiving placebo or doxycycline prophylaxis*

Group	Number of subjects with	
	Scrub typhus	No disease
Placebo	9	1
Doxycycline	1	9

* p = 0.001 (two-tailed test of significance by Fisher's exact probability test).

The one placebo subject not diagnosed as having scrub typhus had pre-existing antibody. He never had fever but formed an eschar and in the third week PCA, as the eschar healed, developed generalized lymphadenopathy. He was not treated and recovered spontaneously.

The nine subjects in the doxycycline group who did not become ill reported some symptoms in the period from days 9-24 PCA. Malaise was the most common complaint, with abdominal pain and arthralgia occurring less frequently. In several volunteers there was a waxing and waning both of the minimal induration at the chigger attachment site and of the adjacent lymphadenopathy. Three subjects had intermittent fever $\leq$37.3C. Symptoms were maximal at the time of the next dose and resolved within 24 hours of medication. After day 24 PCA all symptoms were absent. However, in the fourth week PCA, five of the nine had a mild generalized non-tender lymphadenopathy.

<u>Post-prophylaxis period</u>. Ten to 14 days after the last dose of doxycycline, eight of the nine remaining subjects reported or exhibited further abnormalities that lasted up to seven days. These included malaise (four cases), abdominal pain (two cases), arthralgia (one case),

and lymphadenopathy (seven cases). Three subjects had low-grade fever ($\leq$37.6C) for one, two and four days. All these abnormalities were self-limiting. The volunteers were able to continue their normal duties except for one who was given sedentary work for one day.

Therapy. Subjects with scrub typhus were treated on the third day of disease, 48-64 hours after fulfilling the diagnostic criteria. Within 36 hours of receiving their single dose of doxycycline, all 10 patients with scrub typhus were afebrile and virtually symptom-free. However, five to ten days after therapy, all experienced a recurrence of one or more symptoms - headache, malaise, myalgia, arthralgia, photophobia. Six of the 10 were treated for relapse. A seventh patient had such severe constitutional symptoms, combined with tender hepatosplenomegaly and generalized lymphadenopathy, that he also was treated for a relapse. A week long course of tetracycline brought about rapid recovery in all seven subjects, and there were no further relapses. The three subjects with milder symptomatology, but no fever, recovered spontaneously.

Hematology. There was no characteristic alteration in total or differential leukocyte counts in the 10 subjects treated for scrub typhus. Platelet counts were $<200 \times 10^9/1$ in eight subjects during their acute illness, and in two of these the counts were $<150 \times 10^9/1$. There were no sequelae of the thrombocytopenias.

Biochemistry. One placebo subject had a mild elevation of aspartate aminotransferase (AST) during his acute scrub typhus infection. All other values of AST, lactic dehydrogenase, alkaline phosphatase, urea, and electrolytes were normal for all subjects in the study.

Evidence of infection. All subjects had rickettsiae isolated from peripheral blood at some stage during the study. In those developing scrub typhus, rickettsemia was demonstrated up to three days prior to the onset of fever and was frequently present three days after apparently successful therapy, when the subjects had neither fever nor symptoms. No rickettsiae were isolated from blood drawn at the time of relapse after single-dose therapy.

All placebo subjects and all but one doxycycline subject had at least four-fold rises in indirect FA titer to one or more strains of R. tsutsugamushi. The one exception was the sole failure of doxycycline prophylaxis; he had a low pre-existing indirect FA titer that remained unaltered despite clinical scrub typhus (with rickettsial isolation on four successive blood samples) and relapse.

Volunteers receiving doxycycline and remaining well developed significant antibody titers during the fourth week PCA. This corresponded to the time that most had a mild generalized lymphadenopathy. Antibody titers were declining in most subjects by the end of the seven week prophylaxis period. In the subsequent two months, however, three subjects had a significant rise in antibody titer and four other subjects had consistent two-fold rises in antibody.

Discussion

We conclude from our data that doxycycline in weekly 200 mg doses provides effective chemoprophylaxis of naturally transmitted scrub typhus if prophylaxis is started before exposure to infection and continued for six weeks after exposure ($p = 0.001$).

Laboratory-reared chiggers from our colony have previously been used to transmit scrub typhus to three volunteers (19). The isolation of _R. tsutsugamushi_ from all 20 volunteers in this study further attests to the reliability of this method, which simulates a naturally acquired infection.

The question arises why weekly prophylaxis is effective. Chloramphenicol and the tetracyclines are bacteriostatic agents and their roles in the therapy of scrub typhus are attributed to suppression of rickettsial growth while the body develops an immune response (25). Rickettsiae have slower _in vitro_ growth characteristics than most other bacteria, having a doubling time of approximately 10 hours (27). Appropriately timed prophylaxis can therefore allow sufficient increase in the antigenic load to induce immunity while preventing overt disease.

We have compared very closely the results of our study with those from previous scrub typhus chemoprophylaxis trials using chloramphenicol (5,28-30). Using an artificial method for inoculating rickettsiae, Smadel _et al_ derived a prophylactic regimen (30) that provided protection without any symptoms either during or following the prophylaxis period. However, in all their studies employing natural means of infection and lasting longer than three weeks, they noted fever $>$37.8C during the second and third weeks of prophylaxis around the time of the next dose of prophylaxis. The number of rickettsiae transmitted by each chigger in a naturally acquired infection is unknown but may well be greater than the dosage used in inoculation studies (29,30). The symptoms reported by our volunteers in the second and third weeks were mild by comparison, and fevers, all $\leq$37.3C, were observed in only three subjects. Some immunity is presumably developing by the time these symptoms completely disappear because significant antibody levels were found in eight of our nine subjects at this time.

If we assume that after four half-lives neither drug is suppressive, then a once weekly dose of doxycycline ($t_{1/2}$ 15 hours) would be effective for 60 hours, with a therapeutic hiatus of 4.5 days. Equivalent therapy would be achieved with chloramphenicol ($t_{1/2}$ 2.5 hours) given every five days. Approximately this interval was used in a Gilliam strain inoculation study (29), and mid-prophylaxis fevers, but no late symptoms, were observed in subjects who received prophylaxis for at least 21 days. With a slightly shorter interval (29), complete protection with no symptoms was achieved following the inoculation of Karp strain.

Minor modifications to our regimen might achieve a similar result. For example, a six day interval and a slightly lower dose may permit optimal rickettsial multiplication to stimulate immunity while preventing clinical disease. Although doxycycline is moderately expensive, our prophylaxis regimen may have a role in preventing scrub typhus in personnel temporarily exposed to infection in high-risk areas. Furthermore, doxycycline may be appropriate for use in a combined chemoprophylaxis-living vaccine using several strains of R. tsutsugamushi. Long-lasting homologous immunity develops after infection suppressed with chloramphenicol (31), and we expect similar immunity after doxycycline prophylaxis. Also we have found recently that some strains which are avirulent for laboratory animals protected monkeys against a subsequent challenge with a virulent strain (unpublished results). This may simplify the choice of vaccine strains.

The demonstration of rickettsemia as early as three days before clinical disease and for as long as three days (five days in one case) after apparently successful therapy extends previous data (30,32). Only those who relapsed had rickettsemia demonstrated two or more days after initial therapy but we were surprised at our inability to isolate rickettsiae from blood collected at the time of relapse. The symptoms experienced by the majority of the doxycycline group during the post-prophylaxis period were probably due to the multiplication of rickettsiae that was insufficient to cause serious clinical disease. Although no rickettsemias were demonstrated at this time, three subjects had significant rises in antibody titer and four subjects had one dilution rises in titer after prophylaxis was stopped.

Our findings on eschar formation were different from previous reports of scrub typhus chemoprophylaxis. Although Alson et al (16) in a doxycycline field study did observe eschar in some prophylaxis subjects, these subjects were necessarily failures of prophylaxis by virtue of their study design. Smadel et al (29) found eschar in eight of 28 prophylaxis subjects who were inoculated with rickettsiae intradermally. However, in field studies, Smadel et al (5) did not observe classical eschar in any prophylaxis subject. Similarly, none of our prophylaxis subjects, not even the one failure, developed eschar.

All eight Asian subjects in our control, regardless of their pre-existing antibody titer, developed classical eschar. The incidence of eschar in both non-immune and immune Asian subjects has been reported to be very low (28,33). Our data do not support the hypothesis that partial immunity prevents eschar formation even though generalized disease might occur (28). The large number of chiggers attaching to some volunteers does not explain the high frequency of eschar in our control group. Even two chiggers were sufficient to cause eschar and disease in one Malaysian volunteer. Furthermore, our method of transmitting infection may not have been very different from the natural situation because chiggers in nature tend to cluster in one area on the body before attaching.

The poor results of early, single-dose doxycycline therapy for scrub typhus were not unexpected. Previous experience with chloramphenicol and terramycin showed a high incidence of relapse after short courses of treatment early in the disease (26). The originators of single-dose doxycycline therapy for scrub typhus (14) were unable to draw any conclusions on the merits of early treatment because their patients were treated on mean day 10 of disease. We believe that antibiotic treatment for scrub typhus should span at least seven days unless therapy is started late in the disease.

The findings of this study have provided the basis for a recommendation that military personnel deployed to a scrub typhus endemic area be given weekly doses of 200 mg doxycycline to protect them against the disease.

Acknowledgments

The study was approved by three human use committees at the Institute for Medical Research, Kuala Lumpur, Malaysia, at the Walter Reed Army Institute of Research, and the US Army Human Subjects Research Review Board, Washington, DC. Human subjects participated in these studies after giving their free and informed voluntary consent. Investigators adhered to AR 70-25 and USAMRDC Reg 70-25 on Use of Volunteers in Research.

In conducting the research described in this report, the investigators adhered to the "Guide for the Care and Use of Laboratory Animals," prepared by the Committee on Care and Use of Laboratory Animals of the Institute of Laboratory Animal Resources, National Research Council (DHEW Publication No. (NIH) 78-23, Revised 1978).

The authors are grateful to the Malaysian Armed Forces, who provided hospital facilities and an independent physician for the study. We are especially grateful to Colonel I. Natarajan and staff of Kinrara Hospital who assisted us. We would like to thank Dr. George F. de Witt, Director, Institute for Medical Research, for his enthusiastic support and his permission to publish this paper.

References

1. Savoor, S.A. and Audy, J.R. - Typhus. In The Institute for Medical Research 1900-1950. Studies from the Institute for Medical Research, Federation of Malaya, Jubilee Volume, No. 25, Government Press, Kuala Lumpur, 1951, pp. 184-209.

2. Department of the Army Technical Bulletin, TB Med. 31 - Scrub typhus (mite-borne typhus fever, tsutsugamushi disease). US Government Printing Office, 1962.

3. Deller, J.J. and Russell, P.K. - An analysis of fevers of unknown origin in American soldiers in Vietnam. Ann Intern. Med., 66: 1129-1143, 1967.

4. Berman, S.J. and Kundin, W.D. - Scrub typhus in South Vietnam. A study of 87 cases. Ann Intern. Med., 79:26-30, 1973.

5. Smadel, J.E., Traub, R., Frick, L.P., Diercks, F.H., Bailey, C.A. Chloramphenicol (chloromycetin) in the chemoprophylaxis of scrub typhus (tsutsugamushi disease). III. Suppression of overt disease by prophylactic regimens of four week duration. Am. J. Hyg. 51:216-228, 1950.

6. Erslev, A. Hematopoietic depression induced by chloromycetin. Blood 8:170-174, 1953.

7. Wallerstein, R.O., Condit, P.K., Kasper, C.K., Brown, J.W., Morrison, F.R. Statewide study of chloramphenicol therapy and fatal aplastic anemia. JAMA 208:2045-2050, 1969.

8. Sheehy, T.W., Hazlett, D., Turk, R.E. Scrub typhus. A comparison of chloramphenicol and tetracycline in its treatment. Arch. Intern. Med. 132:77-80, 1973.

9. Barza, M., Schiefe, R. T. Antimicrobial spectrum, pharmacology and therapeutic use of antibiotics. Part I; Tetracycline. Am. J. Hosp. Pharmacol. 34:48-57, 1977.

10. Allen, J.C. Minocycline. Ann. Intern. Med. 85:482-287, 1976.

11. Sack, R.B., Frochlich, J.L., Zulich, A.W., Hidi, D.S., Kapikian, A.Z., Orskov, F., Orskov, I., Greenberg, H.B.. Prophylactic doxycycline for travelers' diarrhoea. Results of a prospective double blind study of Peace Corps volunteers in Morocco. Gastroenterology 76:1368-1374, 1979.

12. Ferguson, G.C. A comparison of oxytetracycline with doxycycline in the winter chemoprophylaxis of chronic bronchitis. Br. J. Clin. Pract. 28:131-133, 1974.

13. Hojer, H., Wetterfors, J. Systemic prophylaxis with doxycycline in surgery of the colon and rectum. Ann. Surg. 187:362-368, 1978.

14. Brown, G.W., Saunder, J.P., Singh, S., Huxsoll, D.L., Shirai, A. Single dose doxycycline therapy for scrub typhus. Trans. R. Soc. Trop. Med. Hyg., 72:412-416, 1978.

15. Krause, D.W., Perine, P.L., McDade, J.E., Awoke, S. Treatment of louse-borne typhus fever with chloramphenicol, tetracycline or doxycycline. East Afr. Med. J. 52:421-427, 1975.

16. Olson, J.G., Bourgeois, A.L., Fang, R.C.Y., Collbaugh, J.C., Dennis, D.T. Prevention of scrub typhus. Prophylactic administration of doxycycline in a randomized double blind trial. Am. J. Trop. Med. Hyg. 28:989-997, 1980.

17. Robinson, D.M., Brown, G., Gan, E., Huxsoll, D.L. Adaptation of a microimmunofluorescence test to the study of human Rickettsia tsutsugamushi antibody. Am. J. Trop. Med. Hyg. 25:900-905, 1976.

18. Rapmund, G., Upham, R.W., Kundin, W.D., Manikumaran, C., Chan, T.C. Transovarial development of scrub typhus rickettsiae in a colony of vector mites. Trans. R. Soc. Trop. Med. Hyg. 63:251-258, 1969.

19. Shirai, A., Huxsoll, D.L., Dohany, A.L.,Montrey, R.D., Werner, R.M., Gan, E. Characterization of Rickettsia tsutsugamushi strains in two species of naturally infected, laboratory-reared chiggers. Am. J. Trop. Med. Hyg. (in press)

20. Shirai, A., Saunders, J.P.,Dohany, A.L., Huxsoll, D.L., Groves, M.G. Transmission of scrub typhus to human volunteers by laboratory-reared chiggers. Jpn. J. Med. Sci. Biol. (in press)

21. Prescott, L.F. Analgesics. Practitioner 200:84-92, 1968.

22. Blake, F.G., Maxcy, K.F., Sadusk, J.F., Jr., Kohls, G.M., Bell, E.J. Studies on tsutsugamushi disease (scrub typhus, mite-borne typhus) in New Guinea and adjacent islands: epidemiology, clinical observations, and etiology in the Dobadura area. Am. J. Hyg. 41:243-373, 1945.

23. Robinson, D.M., Roberts, L.W., Dohany, A.L., Gan, E., Chan, T.C. Huxsoll, D.L. Virulence and antigenic properties of *Rickettsia tsutsugamushi* in a naturally infected laboratory colony of *Leptotrombidium* (*Leptotrombidium*) *arenicola*. Southeast Asian J. Trop. Med. Publ. Health 8:227-231, 1977.

24. Dohany, A.L., Cromroy, H.L., Manikumaran, C. A new capsule for feeding chiggers on hosts (Acarina: Trombiculidae). J. Med. Entomol. 14:491-492, 1977.

25. Dohany, A.L., Shirai, A., Robinson, D.M., Ram, S., Huxsoll, D.L. Identification and antigenic typing of *Rickettsia tsutsugamushi* in naturally infected chiggers (Acarina: Trombiculidae) by direct immunofluorescence. Am. J. Trop. Med. Hyg. 27:1261-1264, 1978.

26. Smadel, J.E., Bailey, C.A., Diercks, F.H. Chloramphenicol (chloromycetin) in the chemoprophylaxis of scrub typhus (tsutsugamushi disease). IV. Relapse of scrub typhus in treated volunteers and their prevention. Am. J. Hyg. 51:229-241, 1950.

27. Bozeman, F.M., Hopps, H.E., Danauskas, J.X., Jackson, E.B., Smadel, J.E. Study on the growth of rickettsiae. I. A tissue culture system for quantitative estimations of *Rickettsia tsutsugamushi*. J. Immunol. 76:475-488, 1956.

28. Smadel, J.E., Traub, R., Ley, H.L., Jr., Philip, C.B., Woodward, T.E., Lewthwaite, R. Chloramphenicol (chloromycetin) in the chemoprophylaxis of scrub typhus (tsutsugamushi disease). II. Results with volunteers exposed in hyperendemic areas of scrub typhus. Am. J. Hug. 50:75-91, 1949.

29. Smadel, J.E., Ley, H.L., Jr., Diercks, F.H., Traub, R., Tipton, V.J., Frick, L.P. Immunization against scrub typhus. I. Combined living vaccine and chemoprophylaxis in volunteers. Am. J. Hyg. 53:317-325, 1951.

30. Ley, H.L., Jr., Diercks, F.H., Paterson, P.Y., Smadel, J.E., Wisseman, C.L., Jr., Traub, R. Immunization against scrub typhus. IV. Living Karp vaccine and chemoprophylaxis in volunteers. Am. J. Hyg. 56:303-312, 1952.

31. Smadel, J.E., Ley, H.L., Jr., Diercks, F.H., Paterson, P.Y., Wisseman, C.L., Jr., Traub, R. Immunization against scrub typhus: duration of immunity in volunteers following combined living vaccine and chemoprophylaxis. Am. J. Trop. Med. Hyg. 1:87-97, 1952.

32. Smadel, J.E., Woodward, T.E., Ley, H.L., Jr., Lewthwaite, R. Chloramphenicol (chloromycetin) in the treatment of tsutsugamushi disease (scrub typhus). J. Clin. Invest. 28:1196-1215, 1949.

33. Brown, G.W., Robinson, D.M., Huxsoll, D.L. Scrub typhus: a common cause of illness in indigenous populations. Trans. R. Soc. Trop. Med. Hyg. 70:444-448, 1976.

34. Audy, J.R. The ecology of scrub typhus. In J.M. May (ed.). Studies in Disease Ecology. Vol. 2, Hafner, New York, pp. 389-432, 1961.

SPEECH COMMAND AUDITORY DISPLAY SYSTEM (SCADS) (U)

*JAMES W. VOORHEES, CPT, PhD, MS
KRISTINE M. MARCHIONDA, Ms., & VALERIE L. ATCHISON, Ms.
U.S. ARMY AEROMECHANICS LABORATORY
MOFFETT FIELD, CA 94035

INTRODUCTION

The missions of the helicopter, within both the military and the civil sector, have changed rather dramatically over the last 20 years. The military's experience in Southeast Asia during the 1960's demonstrated the wide range of missions that could be accomplished by rotary wing aircraft: fire fighting, heavy lift, and large scale medical evacuations, as well as tactical missions of troop transport and close air support. The post-Vietnam civilian uses for helicopters have duplicated several of the military missions, resulting in an added interest in helicopters in both the military and the civilian sectors. This increased interest has also led to rapid advances in rotorcraft technology. As helicopters have become much more capable, there has been an increasing sophistication in flight controls, power plant systems, and in cockpit displays. This combination of the increase of types of missions and the increase in cockpit sophistication has created a new set of problems. The limiting factor for many types of helicopter missions is now the pilot; and the limitation appears to be specifically related to information transfer. This information transfer is in the form of aircraft status information to the pilot, and information transfer from the pilot back to the aircraft in the form of control manipulations.

One of the most pressing problems within the military helicopter flight procedures is Nap-of-the-Earth flight (NOE). NOE flight occurs at altitudes below the surrounding terrain features and vegetation - so that pilots fly between trees or down a canyon below the level of the walls. NOE flight is performed by a team of two aviators who share the effort. The pilot controls the aircraft and visually interacts with the outside world in order to avoid obstacles. Although he monitors flight information on his instrument panel, this activity is restricted because it diverts his visual attention from the outside scene where the most pressing dangers exist. The co-pilot monitors the position of the vehicle on a map, and provides "look ahead" guidance information to the pilot so that they arrive at their destination. Although pilot and co-pilot may feel apprehensive

METHOD

Subjects

Fourteen subjects served as paid volunteers in the study. They were college students recruited from a local university. The age range was from 18 - 31, with a mean age of 22.5 years. There were nine males and five females. All subjects were right handed with normal hearing and vision. None had previous flight experience.

Apparatus

The maze was a computer (PDP 11/70) generated graphic display using an Evans & Sutherland picture system. The task to be performed by the subjects consisted of moving a circular cursor (0.8 cm in diameter) representing a helicopter rotor disk, through mazes of obstacles representing trees. The maze was presented in a stationary "plan" view; that is the subject viewed the obstacles and his helicopter symbol from above. (see Figure 1.) The 49 obstacles were shaped like "plus" signs and were of five sizes (ranging from 1.0 to 0.1 cm). The size of these obstacles varied with the altitude of the helicopter in a ratio of 0.2 cm/20 feet of altitude. The centers of the obstacles were 2.0 cm apart, so that two of the largest trees, located adjoining each other, completely closed the space between them at zero feet of altitude. To move the helicopter through this space the subject had to be at a minimum of 40 feet indicated altitude.

The subject had two controls with which to maneuver the helicopter. The right hand control (representing the cyclic) was a centering joystick which controlled direction and acceleration. The left hand control (representing the collective) was a slide potentiometer which controlled the torque. The PDP 11/70 was programmed with a helicopter model (based on the UH-60 Blackhawk) which controlled the movements of the circular cursor via input from the subject controls. Subjects were located in an IAC sound attenuating chamber.

Experimental Condition

There were three display formats that presented airspeed, altitude, and torque information to the subject.

1. Conventional Dials (CC): Subjects received information from three single needle dials located on a console in front of them and below the level of the viewing screen for the maze. The location of the console was consistent with military cockpit specifications as to distance and viewing angle. Dials were illuminated with indirect lighting, and the numbers were white on a black background. The airspeed and torque gauges had red lines at 75 knots and 42 pounds of torque; the altimeter was not red lined.
2. Head-up-Display (HUD): Ribbon type gauges were drawn by the graphics system on the CRT around the periphery of the maze: (see Figure 1.) the altimeter on the left side, the torque gauge on the

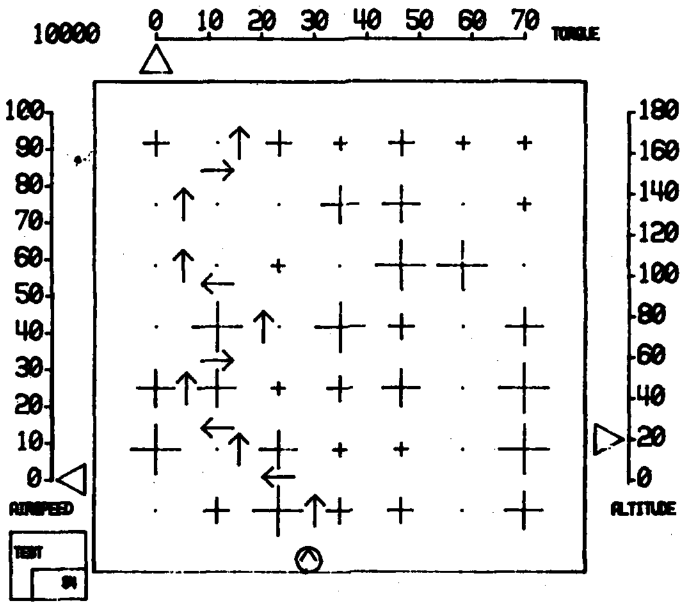

Figure 1 - The maze as displayed on the experimenter's screen showing the path along which the subject maneuvered the helicopter symbol. This maze is shown with the Head-up Display (HUD), the point count (upper left), and all of the direction arrows. The subject's maze displayed only two arrows at a time, for two seconds.

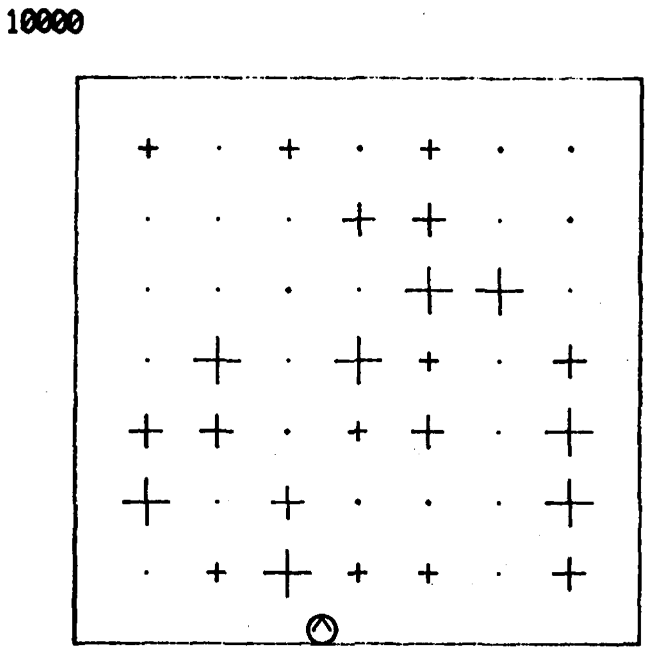

Figure 2 - The maze as displayed on the subject's screen for the conventional dial gauges and the auditory display conditions. The point count is shown in the upper left. In the Head-up Display condition the HUD would appear around the maze as in Figure 1.

top, and the airspeed gauge on the right side. Readings were presented via pointers moving up and down the gauge, which flashed when any of the limits were exceeded.

3. Auditory Display (AF): Subjects received synthesized speech feedback responses to spoken requests for airspeed, altitude, and torque. Spoken requests by the subject were received by an Interstate Electronics Voice Recognizer and interfaced with the PDP 11/70. Instrument readings were computed by the 11/70, and transfered to a SOL microprocessor, the output was given to the subject by a Votrax ML-2 speech synthesizer. There were also unrequested voice warning messages if the subject exceeded parameter limits.

During all display conditions there was a background cockpit noise tape playing at 90 db(A). The subjects wore a headset which had a 40 - 45 db attenuation. All speech responses, as well as communications with the experimenter were via the headset.

The subject's performance was monitored on a second screen located outside of the IAC chamber at the experimenter's station. The experimenter also had a video monitor which allowed for the monitoring of eye movements.

Procedures

Fifteen subjects were selected on the basis of preliminary screening with a critical tracking task. One dropped out after two weeks so the remaining fourteen were used. Subjects were instructed to maneuver their helicopter through the maze as fast as possible while staying as low as possible. The subjects were required to follow a path through the maze. This path was made up of arrows which flashed on between the trees showing the next two turns to take. (see Figure 2.) The arrows were only illuminated for two seconds, and if the subject missed seeing the arrows he/she had to say the word "direction" into the voice recognizer which illuminated the arrows. If the subject did not pass over each correct space the maze would not reset and the subject had to return to the place where he/she deviated from the path and retrace that portion of the maze. Subject's current score (out of a possible total of 10,000 per maze) was displayed in the upper left corner of the subject screen as continous feedback. After a subject completed a maze, the helicopter was automatically reset back to the bottom of the screen and a new maze displayed. Each subject performed one session per week; a session consisted of 20 mazes for the first two weeks and 30 mazes for the third and fourth weeks. All runs during this training phase were with conventional dial gauges. At the end of the fourth week, the fourteen subjects were formed into three matched groups based on their scores. One group (n=4) remained on dial gauges (CC), one group (n=5) shifted to a Head-up-Display (HUD), and the remainder (n=5) now received auditory feedback (AF) with no visual instrument information. The experimental display phase lasted three weeks, with 30, 35, and 35 mazes on weeks 5, 6, and 7 respectively. All subjects received the same mazes (each of which was different) in the same order during a session. At the end of week 7 the HUD and AF groups transitioned back to the conventional dial gauges. All three groups then completed an additional three sessions consisting of 30, 35, and 35 mazes on weeks 8, 9, and 10 respectively. Average session length decreased from two hours to one hour per session from the first to the sixth week as the subject's performance improved.

In the conditions where subjects were using the conventional dial gauges, an experimenter watched each subject's face on a closed circuit monitor, and recorded eye movements to the gauges by actuating a button connected to the PDP 11/70. This allowed the experimenter during subsequent data analysis to determine at what point in a maze the subject looked down at the gauges, and for how long.

RESULTS

A scoring system was developed whereby the subject was penalized by having points deducted for various events from an initial total of 10,000 points at the start of each maze. Penalties were assessed for the following: (1) length of time in the maze; (2) passing between two trees at higher than the minimum altitude necessary; (3) hitting a tree; (4) flying off course; (5) asking for "direction"; (6) hitting the ground while moving forward; and (7) exceeding limitations in airspeed, altitude, or torque. Subjects were debriefed at the end of each session as to how they had lost points.

The total number of points lost per maze per subject per group were log transformed and subjected to analysis of variance for week 4 (end of training phase), week 7 (end of test phase), and week 10 (end of return to dial gauges). The results for week 7 are presented in Table 1. At week 7 the ANOVA showed a significant difference (p .01) between groups. A Scheffe test for multiple comparisons was run on the week 7 data (Table 2).

Analysis of Variance Summary Table

Source	SS	df	MS	F
Between Groups	.000946	2	.000473	4.637*
Within Groups	.049709	487	.000102	

$*p < .01$

Table 1. - ANOVA for scores from the 7th week of testing. (scores were log transformed)

Scheffe Multiple Comparison

	CC	HUD	AF
	139.276	139.321	139.389
CC 139.276	-	.0450*	.1130*
HUD 139.321		-	.0680*
AF 139.389			-

$p < .01$
$CR_s = .0247$

Table 2. - Comparison of the three experimental groups on 7th week performance. CC-conventional dial gauges, HUD-head-up display, AF-auditory feedback.

Results of this test showed a significant improvement in performance ($p < .001$) in the HUD group compared to the control group (CC) and in the auditory feedback (AF) over both the control group (CC) and the HUD group. The week 10 data showed the AF and HUD groups performance returning to the control level (although the AF group's performance was still significantly better).

DISCUSSION

This research was undertaken to answer two basic questions. First, could a relatively simple graphics task simulation be developed to investigate NOE flight problems? Second, would the use of a synthetic speech display of aircraft flight parameters be as effective as conventional dial gauges of a head-up-display in conveying information to a subject flying an NOE simulation?

In the first area, the task development, we believe that the "plan" view maze task has shown itself to be sensitive to various manipulations such as type of information display. This type of task similarity to NOE flight, as opposed to visual similarity is encouraging, particularly for small scale laboratory investigations. It remains to be determined, of course, if trained helicopter pilots would respond in a similar manner to non-pilot subjects. This type of task may prove very useful in examining an issue such as side arm controller vs. conventional controls.

In the second area, that of the use of speech feedback for instrument information, the results are clearer. Performance (as measured by the previously described metric) significantly improved when the visual workload of gathering instrument information was off-loaded to the auditory channel. The significant improvement in performance for the AF group over the HUD is particularly interesting. Several investigators have advocated the use of HUDs to replace conventional dial gauges to eliminate the pilot's need to look at the instrument panel. Our results bear out their contention that this system is an improvement over dials, but we also find that the use of an auditory display of instrument information is significantly better than the HUD or the dials. With the advent of various night vision systems, and the possibility of a single pilot scout helicopter on the horizon, speech technology should be considered as a major candidate for information transfer systems.

The development of this type of laboratory task for task simulation of a procedure like NOE flight could be very useful in the area of standardization. One of the major problems that has consistently recurred in human performance testing in aviation simulation has been the problem of different task demands imposed by the testing procedures. The area of workload measurement is an example of how this procedure difference has frustrated attempts to understand the phenomena of concern. The use of an easily transferred task such as the maze task used in this research, offers an inexpensive simulation that can be used for a wide variety of testing, within a standardized framework.

STUDIES ON BUTYRYLCHOLINESTERASE INHIBITORS

ALAN D. WOLFE, PH.D., CLARENCE E. EMERY, B.S., JEFF S. VERDIER, B.S.
AND DOROTHY A. PRICHARD
WALTER REED ARMY INSTITUTE OF RESEARCH
WASHINGTON, D.C. 20012

The ultimate object of the present studies is the elucidation of the structure, function, and physiological significance of the enzyme, butyrylcholinesterase (BuChE, E.C.3.1.1.8). It occurs in the blood, tissues, ganglia and cytosol of organisms and cells (1,2,3), and its structure (4), substrate, and inhibitor patterns resemble those of acetylcholinesterase (AChE). Both enzymes possess many inhibitors in common, including organophosphate (OP) threat agents, but preferential inhibition of either enzyme frequently occurs. Among the compounds which preferentially suppress BuChE in comparison with AChE are those which exert significant neuropharmacological effects, for example, the phenothiazines, tropates, phencyclidines, butyrophenones, imipramines, and curariforms (1,5,6,7,8,9). Phenothiazines, butyrophenones and imipramines are tranquillizers, tropates are spasmodics, and phencyclidines are hallucinogens. BuChE inhibition relative to the pharmacologic or toxic influence of such drugs and threat agents is is unknown, despite the overt medical importance these compounds possess. In addition, they possess unusual military significance, since phenothiazines and atropine, in particular, are frequently included in OP antidotal formulations (10,11). Therefore ample justification may be found systematically to investigate BuChE, its function, and its known or potential inhibitors. Present research has focused on inhibitors of BuChE, and has resulted in four principal conclusions: 1) heterocycles containing sulfur, regardless of the presence or absence of a ring nitrogen, may be potent and and preferential BuChE inhibitors, 2) inhibitor potency may be related to planar area, 3) benzilates are highly effective preferential BuChE inhibitors, and 4) BuChE inhibitor potency may be useful as a simple, primary screen for detection or identification of OP antidote agents.

MATERIALS AND METHODS

BuChE was purchased from the Sigma Chemical Co., St. Louis, Mo., and AChE from the Worthington Biochemical Corp., Freehold, N.J. The colorimetric assay of Ellman (12) was adapted for use with 1.0 ml reaction volumes. Both enzyme concentrations were adjusted to catalyze the hydrolysis of approximately 7uM of either butyryl- or acetylthiocholine in 5 minutes. Drug-free reaction systems exhibited linear kinetics during this period. Thiocholine substrates were normally used at concentrations of 9.8×10^{-5}M. A Gilford Instrument Laboratory, (Oberlin, Ohio) model 2600 programmable spectrophotometer, adjusted to 412 nm, and at ambient temperature, was used in conjunction with a Hewlett-Packard (San Diego, Calif.) model 7225A plotter, and a Gilford thermal printer II, to record reaction rates. Substrates were purchased from Sigma, and drugs were obtained from the Division of Experimental Therapeutics, the Walter Reed Army Institute of Research.

RESULTS: I. EVALUATION OF POTENCY

Compounds evaluated for their BuChE inhibitory potency were selected upon the basis of four criteria: 1) inclusion in formulations designed to protect against OP threat agents, 2) relation to protective formulation components, 3) central nervous system (CNS) influence, and 4) DNA intercalation. The latter criterion was included because many DNA intercalants, including phenothiazines, inhibit cholinesterases (13,14,15,16). Figure 1 depicts the structures of major compounds investigated. Such compounds fall into two broad groups: 1) heterocycles, and 2) esters. Table 1 lists many of the screened compounds, their chemical groups, the concentrations estimated to cause 50% inhibition (I-50), and the number of aromatic rings contained by the drug. Table 1 also lists additional experimental data with respect to specific compounds. Figure 2 is an illustration of the dose response probit transforms from which I-50s were estimated. In most instances, compounds were tested against AChE as well as BuChE, but results are reported primarily with respect to their potency against BuChE.

Atropine was the least inhibitory compound for which I-50s were obtained. Benzilates, acridines, and phenothiazines exerted appreciably greater inhibition. Proflavine, perphenazine, and aprophen were the most inhibitory drugs of their respective groups. Pyridinium oximes were also tested. Pyridinium-2-aldoxime methylchloride (2-PAM) was appreciably less effective against BuChE than the bis-pyridinium oximes TMB-4 and HI-6. Tested oximes did not appear to inhibit preferentially either enzyme.

The thiaxanthone, miracil D, was the most inhibitory compound tested in this series. Figure 3 illustrates miracil D inhibition kinetics with BuChE. Miracil D BuChE inhibition appears competitive; were it mixed, or non-competitive, the curves would intersect on the abscissa. Similar analysis has also indicated chlorpromazine (1,5), a phenothiazine, to inhibit BuChE competitively, but Hofstee plots suggest chlorpromazine inhibition also occurs, to a limited extent, by a non-competitive mechanism. This

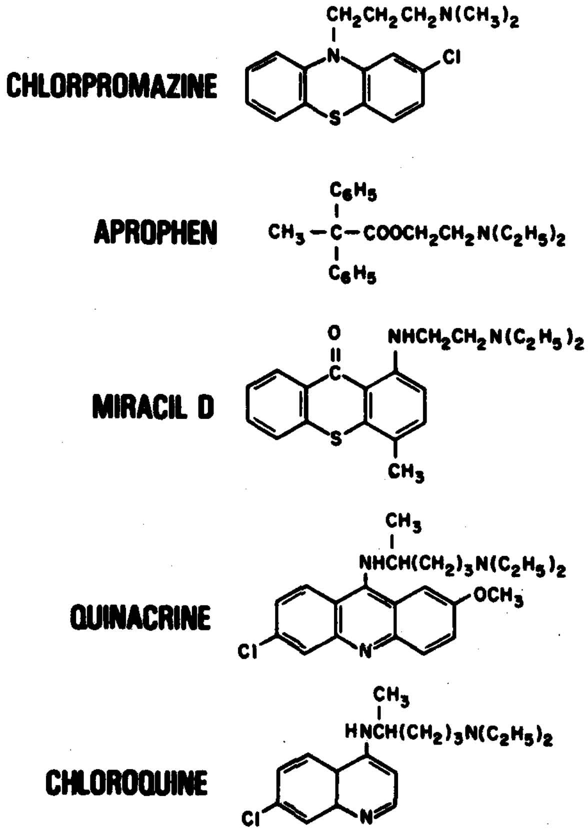

Figure 1. The structures of the major compounds investigated. Table 1 indicates the chemical group to which each compound belongs. Compounds were normally dissolved in dimethylsulfoxide (DMSO), and drug-free reaction systems contained DMSO in volumes equal to the drug aliquot used. Routine DMSO concentrations did not exceed 5%, and these concentrations of DMSO did not alter reaction rates in drug-free systems.

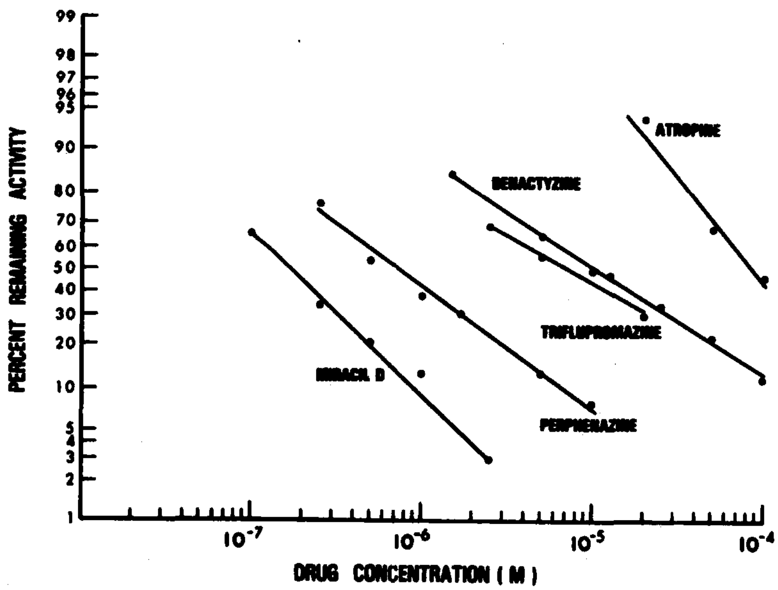

Figure 2. The percent remaining BuChE activity as a function of graded drug concentrations. The dose responses are depicted on a probit transform from which the drug concentration which produced 50% inhibition (I-50) is easily estimated.

TABLE 1

STRUCTURAL CLASS	COMPOUND	I-50 (M)	AROMATIC RINGS
TROPATE	ATROPINE	8.6×10^{-5}	1
BENZILATE	BENACTYZINE	1.1×10^{-5}	2
"	ADIPHENINE	3.3×10^{-6}	2
"	APROPHEN	1.5×10^{-6}	2
QUINOLINE	CHLOROQUINE	9.0×10^{-6}	2
DIBENZAZEPINE	IMIPRAMINE	3.1×10^{-6}	3
ACRIDINE	NITROAKRIDIN 3582	2.5×10^{-6}	3
"	NITROAKRIDIN NK-2	1.3×10^{-6}	3
"	QUINACRINE	1.2×10^{-6}	3
"	PROFLAVINE	3.7×10^{-7}	3
PHENOTHIAZINE	TRIFLUPROMAZINE	7.0×10^{-6}	3
"	PROMAZINE	1.7×10^{-6}	3
"	PHENERGAN	1.7×10^{-6}	3
"	CHLORPROMAZINE	1.7×10^{-6}	3
"	MEPAZINE	1.0×10^{-6}	3
"	PERPHENAZINE	6.0×10^{-7}	3
THIAXANTHONE	MIRACIL D	1.5×10^{-7}	3
		% I at 10^{-5} M	
QUINOLINEMETHANOL	MEFLOQUINE	< 15	2
"	QUININE	62	2
PHENANTHRENEMETHANOL	WR 122,455	86	3
		% I at 2×10^{-4} M	
OXIME	2-PAM	47	1
"	HI-6	65	2
"	TMB-4	85	2

I-50 = 50% INHIBITOR CONCENTRATION
SUBSTRATE CONCENTRATION = 9.8×10^{-5} M BUSCH

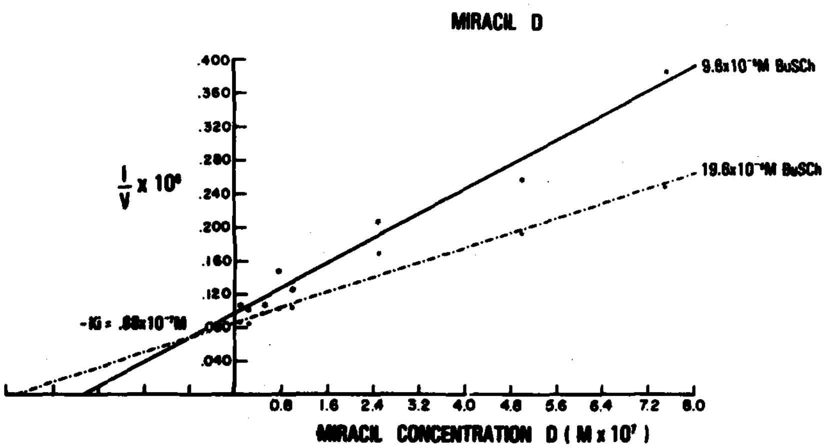

Figure 3. Dixon-Webb analysis of the kinetics of miracil D inhibition of BuChE. Inhibition appears competitive, and the K_i, and substrate concentrations are indicated on the diagram. Curves were obtained by linear regression analysis using a Hewlett-Packard electronic calculator model 9810A, and a Hewlett-Packard calculator plotter model 9862A.

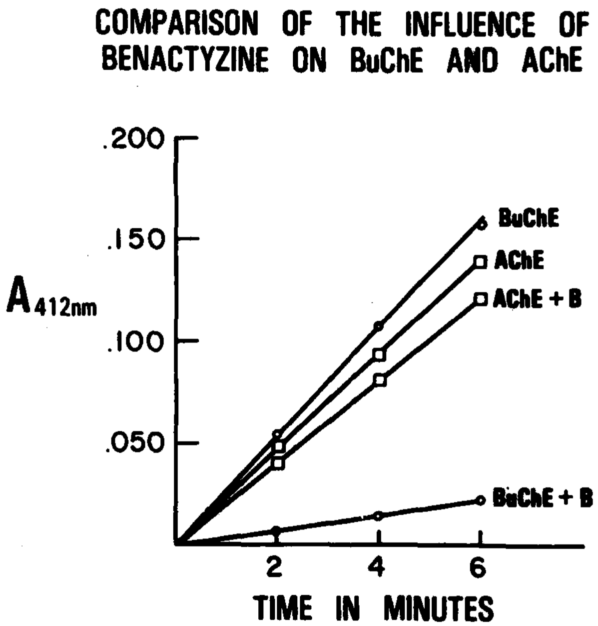

Figure 4. A comparison of the influence of a concentration of 1 x 10^{-4}M benactyzine (B) on BuChE and AChE. Benactyzine is B-diethylaminoethyl benzilate.

potential aspect of miracil D action is under investigation. A concentration of 1 x 10^{-5} M miracil D was also tested against eel AChE, and produced 55% inhibition, whereas this drug concentration did not alter the AChE activity in lysates of the bacterium, Pseudomonas aeruginosa. These data contrast strongly with the estimated I-50 for miracil D with BuChE.

The benzilates benactyzine and aprophen were also tested against AChE as well as BuChE. Figure 4 reveals that benactyzine inhibited BuChE much more effectively than it did AChE. Figure 6 depicts similar results with aprophen, obtained as ancillary information incidental to the object of the experiment.

RESULTS: II. BUCHE AS AN ANALYTICAL SCREENING AGENT

BuChE sensitivity to neuropharmacological agents suggests its use as a probe for the detection of new or unknown compounds which may modulate central nervous system function. Therefore an experimental formulation, of composition unknown to the authors, was prepared, and analyzed. Aliquots of the dissolved mixture, at an original concentration of 1 mg/ml methanol, were tested against both BuChE and AChE, and whereas a 1/200 dilution appreciably inhibited BuChE, a 1/10 dilution failed to inhibit AChE. High pressure liquid chromatography (HPLC), accompanied by UV analysis, suggested the mixture contained 50 ng aprophen/mg solid, and additional components. A 50 ng/ml methanol standard aprophen solution was prepared, and both the standard, and the experimental mixture, at a concentration of 1 mg/ml methanol, were tested to determine relative potencies. Figure 5 depicts the dose response curves generated by the standard aprophen solution, and the experimental formulation. The probit transform permitted an I-50 estimation of 1.7 x 10^{-6} M aprophen, in good agreement with the previous estimate. The mixture was approximately 15% more inhibitory than the standard aprophen solution at every employed dilution, suggesting that the mixture contained slightly more aprophen than concluded, or that additional inhibitory components were present in low concentration. An additional sample of the mixture was then subjected to HPLC fractionation, and fractions analyzed enzymatically. Figure 6 depicts the enzyme inhibition patterns obtained by such analysis. Aprophen elutes, in this HPLC system, at approximately 6.5 minutes, and this fraction exhibited intense and preferential inhibition of BuChE. The material which eluted at 2.5 minutes was moderately more effective against BuChE than AChE, whereas the material contained in the 4.0 minute fraction preferentially inhibited BuChE.

Thus use of BuChE, in conjunction with HPLC, revealed the presence of three compounds, whereas use of AChE revealed the presence of a single compound, and did not detect aprophen. Further enzymatic characterization of compounds which putatively modulate neurophysiological function may be achieved by kinetic analysis to obtain rate constants and inhibition modes, although absolute identification of compounds, as, for example, those which

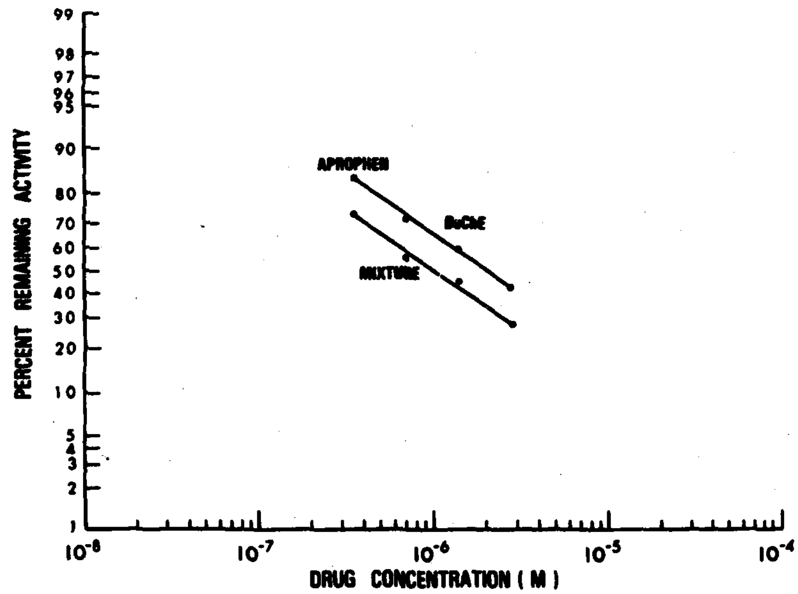

Figure 5. A composite probit transform of BuChE activity in the presence of aliquots of an experimental preparation of unknown composition, and a standard aprophen solution at a concentration equal to that determined to be present in the preparation. Equal volumes of each solution were tested for their ability to inhibit BuChE activity. Although the mixture and the standard contained equal concentrations of aprophen, the mixture consistently caused greater inhibition of the enzyme than aprophen caused.

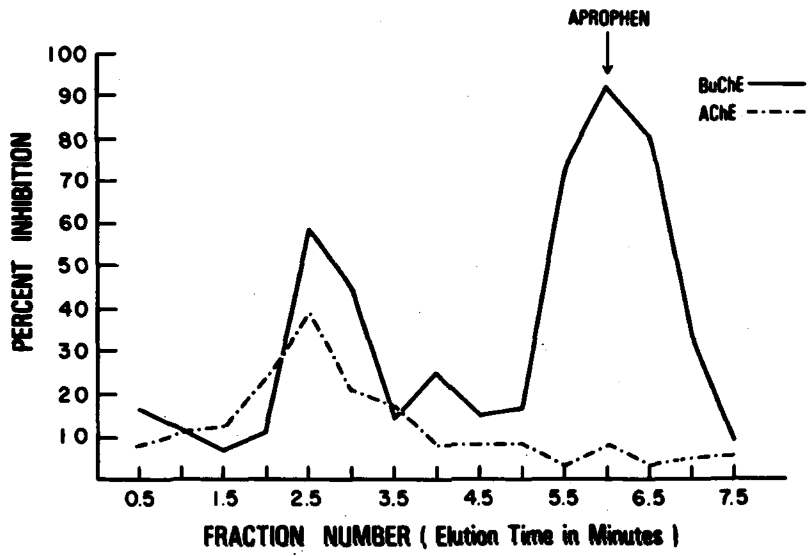

Figure 6. Analysis of BuChE and AChE inhibition in the presence of aliquots of the HPLC fractioned experimental mixture. A 1.0 ml aliquot of a methanol solution containing 2.5 mg mixture/ml was fractionated, using a solvent system consisting of 60% methanol, 40% acetonitrile, and 0.01% triethylamine. Fractions were collected every 30 seconds, the solvent evaporated, and fractions were redissolved in 200 ul methanol. Enzyme activity was assayed in the presence of 20 ul aliquots of each fraction, and compared with a standard assay system containing 20 ul methanol. Fractionations were conducted on a Waters Associates (Milford, Mass.) model ALC/GPC 204 liquid chromatograph.

eluted at 2.5 and 4.0 minutes, require modern analytical techniques.

DISCUSSION

The ultimate objective of these investigations is the determination of the structure, function, and physiological significance of the enzyme, BuChE. The present experiments were undertaken for specific, limited objectives. The first was to determine if the enzyme BuChE could be a useful tool for the detection and identification of OP antidotal agents. The second objective, in part dependent upon achievement of the first objective, was to discover such potential agents through the use of BuChE. A third objective was to obtain information with respect to the many neuropharmacological agents which are potent but apparently incidental BuChE inhibitors. Many of these agents are of particular interest, since they have been used in clinical or experimental OP antidote formulations. For example, the TAB formulation contains the bis-pyridinium oxime, TMB-4, to reactivate non-aged, OP complexed cholinesterases, atropine, a muscarinic cholinolytic, to reduce the influence of accumulated acetylcholine, and benactyzine, to prevent convulsions. An experimental formulation, comprised of pyridinium-2-methanesulfonate, the phenothiazine, triflupromazine, and the parpanit congener, G-3063, increased the sarin LD-50 in mice 23 fold (11). Thus the possibility of screening many actual or potential OP antidote mixture components, or mixtures, rapidly, simply, and inexpensively, while conducting basic biochemical and pharmacological studies, appeared promising.

Atropine and the benzilates were the first compounds screened. High concentrations of atropine moderately inhibited BuChE, in confirmation of Japanese investigators who observed atropine to inhibit a bacterial BuChE preferentially in comparison with a bacterial AChE (3). Benactyzine, adiphenine, and aprophen were found to be potent BuChE inhibitors, and the order of their potency parallelled the hydrophobic sequence OH-H-CH_3 of their methyl substituents. These compounds apparently have not been tested against BuChE. It is of interest that these four tested compounds are esters, and therefore potential substrates as well as inhibitors. Tested oximes inhibited both BuChE and AChE with equal intensity, although the bis-pyridinium oximes were considerably more effective than 2-PAM.

Acridines and propidium iodide intercalate into DNA, thereby providing information with respect to the base pairing and helical properties of this polymer. N-methyl acridinium chloride, and propidium iodide also inhibit both AChE and BuChE, and both active and peripheral sites on AChE have been thereby studied (13,14). Similar structural studies on BuChE have yet to be performed. It is noteworthy that the tested heterocycles do not possess reactive groups such as comprise oximes and esters; intercalant inhibition of BuChE must rely upon reciprocal steric features, provided, potentially, by the terminal dialkylamino group, the aromatic ring, and the enzyme. Parenthetically, it should be noted that the benzilates possess such terminal dialkylamino residues. Since the pKs of quinacrine and chloroquine are similar (7.7 and 10.8 vs 8.3 and 10.4), the only important difference between these molecules lies in their respective planar areas: $38Å^2$ vs $28Å^2$ (15,17, 18). Quinacrine was more than 7 times as potent as chloroquine. It also intercalates into DNA with much greater affinity than chloroquine. Similarly, planar area appears influential with respect to the BuChE inhibitory potency of the phenanthrenemethanol, WR 122,455, in comparison with the quinolinemethanol, mefloquine. This hypothesis might also be considered with respect to the efficacy of the bis-pyridinium oximes in contrast to the mono-pyridinium oximes.

DNA intercalant inhibition of BuChE has led to the unexpected finding that the antischistosomal drug, miracil D, is a potent inhibitor of BuChE. Miracil D appears to be the first thiaxanthone evaluated with respect to potency against BuChE. Hycanthone, the oxygenated congener of miracil D, and an even stronger antischistosomal agent, has been demonstrated to inhibit schistosomal and hookworm AChEs more effectively than the carbamate, physostigmine, whereas this agent more effectively inhibited eel and bovine AChE (19). Hycanthone caused non-competitive AChE inhibition (19). However, it is of unusual interest that hycanthone also appears to block the acetylcholine receptor in schistosomes (20). Fluorescence associated with dansylated acetylcholine becomes localized in the head of the schistosome in the absence of hycanthone; in the presence of the drug, the fluorescence fails to localize. Thus hycanthone, and by inference, miracil D, possess two influences in schistosomes: 1) inhibition of an AChE, and 2) blockade of a neurotransmitter receptor. It should be noted that schistosomes also contain a BuChE (21). Additionally, the intercalating acridine, quinacrine, remains the drug of choice with respect to tapeworm infections (15). It may prove fruitful to evaluate the action of quinacrine in the light of data on miracil D. It is noteworthy that gastrointestinal disturbances are among the principal side effects of both hycanthone and quinacrine in humans (19,15). The basis for such side effects is not apparent, but it is reasonable to speculate that both molecules may interact with a common site, be it receptor or enzyme.

Data accumulated through these experiments, and through the literature, suggest that BuChE may well be considered an enzyme which is sensitive to agents which block neurotransmitter receptors. Benzilates are reported to be cholinolytic (10), while atropine is a well recognized muscarinic cholinolytic. Propidium iodide exhibits competitive blockade at the neuromuscular junction (14). The tricyclic antidepressants amitriptyline, nortriptyline, imipramine, and desimipramine have been observed to alter the characteristics of activated but non-conducting species of a nicotinic ACh receptor ion channel (22). Thus data suggest that BuChE possesses a dual sensitivity which permits detection of both specific receptor blockers or ligands, and cholinesterase inhibitors. However, the differences between primary neuropharmacological action, and enzyme inhibition, require independent standardization, if atropine is used as an example. Atropine strongly blocks muscarinic ACh receptors, but only weakly inhibits BuChE. Compounds structurally related to atropine, but which possess three or four times its cholinolytic potency (10,11), may be comparably better inhibitors of BuChE, thereby permitting a simple, preliminary evaluation of candidate cholinolytic agents. Each class of compounds may best be evaluated through use of an internal standard.

The present results merge research on a number of subjects of military and medical interest. BuChE has been used to detect compounds in OP antidotal formulations; it may well be a useful indicator for cholinolytic activity and potential. In addition, its sensitivity to miracil D invites further research with respect to schistosomes and related parasites, and its sensitivity to antimalarial agents, many of which have been synthesized under the auspices of the U.S. Army Malaria program, may provide further information with respect to the physiological influence of these drugs, and the function of this enzyme. It is noteworthy that a nicotinic pressor response in atropinized cats is inducible in the order butyrylcholine > proprionylcholine > acetylcholine (23), and that BuChE is present in the cat superior cervical ganglion (2). Thus the present studies, and their continuation, permit concurrent research on chemical defence, on parasites, on the function and structure of an enzyme, and the relation between receptors, ligands, and cholinesterases.

SUMMARY

This paper is the first in a series devoted to military, medical, and biochemical aspects of the enzyme, butyrylcholinesterase. This enzyme is inhibited by many neuropharmacological agents which are used in therapeutic formulations, and BuChE has proven a useful agent for the the screening and identification of formulation components. In addition, benzilic acid esters, which are used in such formulations, have been also shown to be preferential inhibitors of BuChE, while miracil D, a congener of the antischistosomal drug, hycanthone, was found to be a highly potent BuChE inhibitor.

LITERATURE CITED

1. Rush, R.S., Main, A.R., and Faulkner, G.D. J. Pharm. Exp. Ther. 216, 586, (1980)
2. Davis, R., and Koelle, G.B. J. Cell Biol. 78, 785, (1978)
3. Tani, Y., Nagasawa, T., Oda, H., and Ogata, K. Agr. Biol. Chem. 39, 105 (1975)
4. Vigny, M., Gisiger, V., and Massoulie, J. Proc. Nat. Acad. Sci. U.S.A. 75, 2588 (1978)
5. Usdin, V.R., Su, S.C., and Usdin, E. Proc. Soc. Exp. Biol. Med. 108, 457 (1961)
6. Maayani, S., Weinstein, H., Ben-Zvi, N., Cohen, S., and Sokolovsky, M. Biochem. Pharm. 23, 1263 (1974)
7. Michalek, H. Biochem. Pharm. 23, 1067 (1973)
8. Ho, A.K.S., Freeman, S.E., Freeman, W.P., and Lloyd, H.J. Biochem. Pharm. 15, 817 (1966)
9. Kamaric, L. Biochem. Pharm. 24, 1663 (1975)
10. Coleman, I.W., Little, P.E., and Bannard, R.A.B. Can J. Biochem. Phys. 40, 815 (1962)
11. Coleman, I.W., Little, P.E., and Bannard, R.A.B. Can.J. Biochem. Phys. 40, 827 (1962)
12. Ellman, G.L., Courtney, K.D., Andres, V., Jr., and Featherstone, R.M. Biochem. Pharm. 7, 88 (1961)
13. Mooser, G., Schulman, H., and Sigman, D.S. Biochem. 11, 1595 (1972)
14. Taylor, P. and Lappi, S. Biochem. 14, 1989 (1975)
15. Wolfe, A.D., in Antibiotics III, 202 (1975). Ed.: Corcoran, J.W., and Hahn, F.E. Springer-Verlag, Berlin-Heidelberg-New York
16. Allison, R.G., and Hahn, F.E. Antimicr. Agents Chemother. 11, 251 (1977)
17. Bednarczyk, D.J., and Medzihradsky, F. Mol. Pharm. 13, 99 (1977)
18. Wolfe, A.D., in Prog. in Mol. Subcell. Biol. 2 247 (1971): Ed. Hahn, F.E. Springer-Verlag, Berlin-Heidelberg-New York
19. Hillman, G.R., and Senft, A.W. Amer. J. Trop. Med. Hyg. 24, 827 (1975)
20. Hillman, G.R., and Gibler, W.B. Biochem. Pharm. 24, 1911 (1975)
21. Bueding, E. Brit. J. Pharm. 7, 563 (1952)
22. Schofield, G.G., Witkop, B., Warnick, J.E., and Albuquerque, E.X. Proc. Nat. Acad. Sci. U.S.A. 78, 5240 (1981)
23. Sekul, A.A., and Holland, W.C. J. Pharm. 133, 313 (1961)

LASER OCULAR FLASH EFFECTS (U)

H.ZWICK, Ph.D.
KENNETH R. BLOOM, B.A
DAVID J. LUND, B.S.
E.S.BEATRICE, M.D., COL. MC
LETTERMAN ARMY INSTITUTE OF RESEARCH
PRESIDIO OF SAN FRANCISCO, CALIFORNIA 94129

INTRODUCTION

During this decade, lasers on the modern battlefield will become a directed energy threat to the eyes of ground force military personnel(1,2,3). One needs only to reflect on the enormous increase in electro-optical battlefield devices presently being developed to both train and equip troops for combat to suspect that a dramatic increase in accidental and intentional exposure incidence may well occur. Laser rangefinders (single pulse) and designators (multiple pulse) are anticipated to be commonplace in the modern electronic battlefield. While the future may hold to the concept of a laser injury as radiation that "vaporizes" its target, now we need only to be concerned with those devices that disrupt the complex man-machine interface by ocular injury. Such interfaces are critical to a modern equipped Army, and ocular injury will severely affect this complexity. Laser devices that inflict such ocular damage are easily available and will be prolific in ground battlefield scenarios. The present investigation was designed to incorporate several key features of the military scenario in order to address the question of a low level laser threat to the eye and acute vision.

To understand the nature of the low level laser threat, we need to understand some critical aspects of ocular anatomy, vision, and the nature of a laser exposure made under field conditions. The retina is the sensory tissue that is responsible for transducing light into simple visual sensation. Such sensations, processed as electrical impulses both within the retina and in the visual brain centers, produce our most complex visual experience. If a portion of this tissue is destroyed, vision can be permanently or temporarily altered. The photoreceptors, the actual biological transducers of light impulses into electrical impulses, are not uniformly distributed. The cone photoreceptors, concentrated in the fovea, are responsible for acute vision, maximal visual acuity, and fine spatial vision. If the fovea is damaged, visual acuity is dramatically altered and the visual scene is blurred. The fovea, a relatively small piece of the human sensory retina, is at the center of the optical axis of the eye. Thus, use of military optics places the fovea in a most vulnerable position.

In several previous experiments we demonstrated that foveal laser exposure could dramatically alter the ability to resolve fine spatial detail, i.e. visual acuity (4,5). These experiments demonstrated both permanent, as well as transient changes in acuity associated with moderate to low levels of laser flash exposure. But all of these previous experiments were done with relatively large retinal spot sizes (150-350 microns). In the field, however, the laser flash will produce a small retinal spot (30-50 microns) because of the laser's low divergence. Our questions in the present experiment were: will such exposure produce a significant effect on the retina and visual acuity? Will small punctate foveal exposures have an effect on visual acuity similar to that of larger retinal spot exposures, where the entire fovea was involved? Will small spot foveal exposure affect retinal areas outside the fovea?

By measuring contrast sensitivity across a range of acuity target sizes, we were able to assess the possible lateral influence of small spot laser flash exposure. While visual acuity expresses the very finest target that can be resolved spatially, it does not reflect spatial visual function for larger targets. In order to measure the effects on liminal spatial vision for large as well as small targets we measured contrast thresholds as well as visual acuity. The reciprocal of the minimum contrast ratio threshold is contrast sensitivity, and one may plot a function relating contrast sensitivity to acuity target size or spatial frequency. In the contrast sensitivity function the smallest resolveable target has the lowest contrast sensitivity, requiring the highest contrast threshold.

In this experiment we have not only simulated battlefield exposures with small retinal spot exposure but, because many field laser systems are repetitively pulsed, we have also employed a repetitively pulsed laser system. The wavelength of the laser source (532nm) is close to the peak of the daytime maximum color sensitivity of the human and monkey eye (550nm).

METHODS

Rhesus monkeys were trained on a visual acuity task in which exposure to a laser flash could be administered during task performance (4,5,6). Animals were trained for many months to discriminate bright achromatic Landolt ring acuity targets, rings with gaps ("C's"), from other bright ring targets that lack this gap ("O's"). The minimum resolveable spatial detail (visual angle) for the rhesus monkey is similar to that of the human.

The rhesus is also quite comparable to the human in its minimum contrast threshold for various target sizes. To measure contrast sensitivity, the gap of the Landolt ring was expressed as an aperiodic spatial frequency.

In order to expose an animal and track the immediate visual consequence of a laser exposure in a reliable manner for at least a half hour post-exposure, very stable visual function baselines were required. Spatial vision thresholds (visual acuity and contrast sensitivity) were determined by a method that allows instantaneous determination of threshold (7). The rhesus were trained to titrate either the size or the contrast of the acuity targets about their threshold. Following initial discrimination learning and determination of acuity or contrast sensitivity for a given acuity target, animals were trained to yield highly stable baselines with minimum variation over a period of at least an hour. Stability criteria of approximately 0.2 to 0.4 log units in either acuity or contrast sensitivity maintained over a 30 to 60 minute period were generally required before any animal was considered ready for exposure.

For two animals trained to track only their high contrast acuity, three to four exposure sessions were given to establish reliability of a given exposure level. Exposure levels were increased until a criterion deficit of about 90 % of baseline acuity could be obtained for about 2 minutes post-exposure. For three contrast sensitivity animals, the effect of laser flash exposure was determined on one spatial frequency at a time for three to four exposure sessions.

Laser flash effects were obtained for small spot pulsed visible laser (532 nm) flash exposure on visual acuity, and contrast thresholds for spatial frequencies from 38.5 cycles/degree to 2.2 cycles/degree, (i.e. Snellen acuity notation from 20/15 to 20/267). All exposures were made with the flash presented through the gap in a .78 minute of arc (20/15) Landolt ring. This assured foveal exposures, as the fovea was required for accurate discrimination of this size target. An exposure was made if the daily pre-exposure baseline was within 0.4 log units of the previous session's baseline for acuity or constrast sensitivity. A frequency doubled Neodymium laser (532 nm) operating at 20 Hz was used. Exposure consisted of six 20 nsec pulses delivered within a 300 msec time window. In the early portions of this experiment a 10 Hz pulse repetition frequency (PRF) was employed and six pulses were cumulated over three successive trials spanning a period of 36 seconds. The average calculated nominal Total Intraocular Energy (TIE) per pulse was 3.0 uJoules for a 5 mm pupil in high contrast acuity recovery tests. All contrast threshold functions were measured against a 70 ft L. background and, therefore, a 3 mm pupil was assumed for calculation of the total intraocular energy (1.1 uJoules). All TIE levels are nominal values with variation of TIE about $\pm$ 20% within a given animal.

Five animals were used in these experiments. All had pretraining refractive errors of less than a 1/2 diopter; all had normal appearing fundi prior to exposure. Fundi of selected animals were reexamined only after an entire exposure series for the given animal was complete.

RESULTS

An acuity threshold session, lasting about 60 minutes, from one animal is presented in Figure 1. Landolt rings presented to this animal immediately after exposure had to be increased in size to a Snellen acuity level of 20/108 before tracking of post-exposure recovery could be

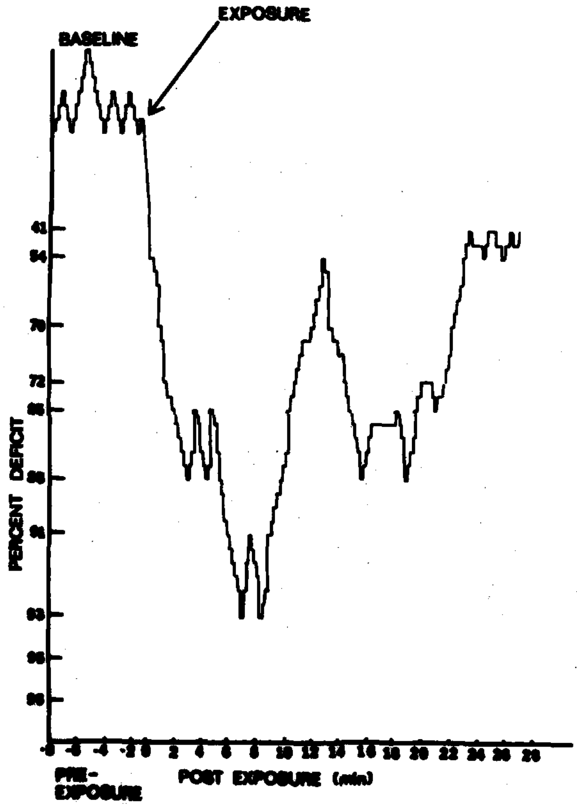

Figure 1. Raw data taken from an acuity exposure session is shown. The Y-axis is an ordinal scale where the location of Landolt rings in a size graded series of acuity targets is expressed as a percent deficit relative to the pre-exposure baseline. The last 8 minutes of the pre-exposure acuity baseline is followed by a laser exposure. A maximum acuity deficit of approximately 93% was seen as long as 8 minutes post-exposure. At 28 minutes, recovery was to about 50%, with full recovery occurring within 1 hour post-exposure.

achieved. This post-exposure threshold acuity level corresponded to at least a 90% deficit with respect to pre-exposure acuity baseline, and was persistent for several minutes post-exposure. Even after recovery began, it was slow and incomplete at the end of 30 minutes. At the end of the actual 50 minute post- exposure session, however, the animal's acuity baseline had returned to pre-exposure levels. No subsequent deficit was noted on successive test sessions.

In Figure 2, recovery curves for visual acuity (2a) and contrast sensitivity (2b) are presented. Two acuity recovery functions are shown in 2a. Both of these functions were obtained in a manner similar to that shown in Figure 1, except here we have averaged the acuity for each two minute block of post-exposure data over several exposure sessions for one animal. The lower curve was obtained from exposure to 6 pulses at a 10 Hz pulse repetition frequency, while the upper curve was obtained from exposure to 6 pulses at a 20 Hz pulse repetition frequency. In the former,

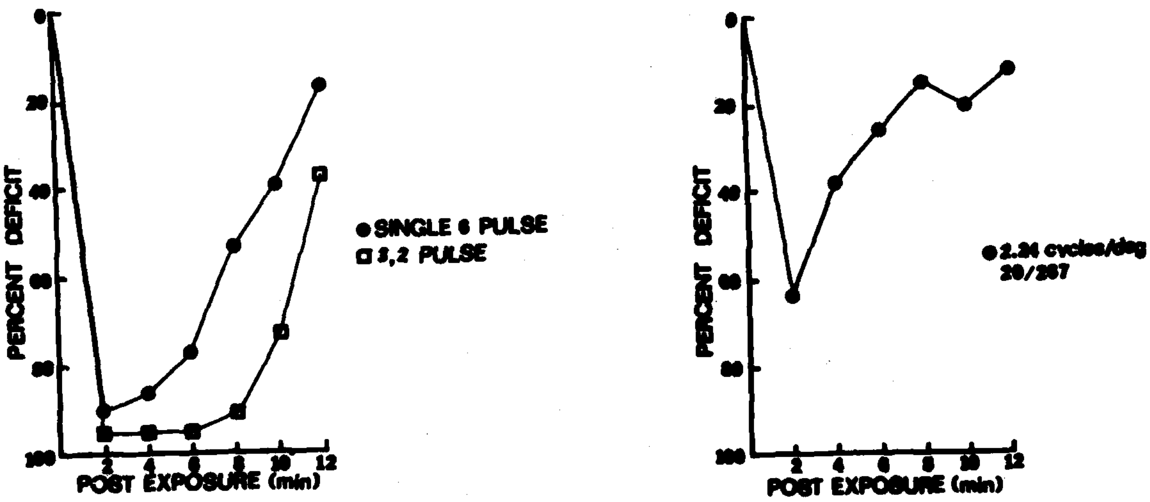

Figure 2. Post-exposure recovery curves for acuity (2a) and contrast sensitivity (2b) are presented as percent deficit relative to pre-exposure baselines. Significant initial deficits and recovery from such deficits are represented. The recovery curve for contrast sensitivity (2b) was measured with a large target having a spatial frequency of 2.24 cycles/degree. The acuity recovery curves represent the average of 4 exposure sessions for each condition, while the contrast sensitivity recovery curve is an average of 20 exposure sessions across 3 animals. By inspection, these average curves are highly representative of all individual recovery functions.

six pulses were delivered in 2 pulse bursts on three consecutive Landolt ring trials over a 36 second period, whereas in the latter curve the 6 pulses were delivered in a 300 msec interval on a single Landolt ring trial. While a more prolonged recovery time is evident for the 10 Hz repeated trial exposure, both require close to 20 minutes for full recovery to occur.

Figure 2b is a recovery function of the contrast sensitivity for an acuity target equivalent to 20/267 Snellen, or a spatial frequency of 2.2 cycles/degree. It is a large target that involves foveal as well as parafoveal stimulation. Initial deficits in contrast sensitivity, and recovery times for such size targets were essentially the same as those for targets requiring much smaller foveal areas. Similar curves for 20/15 Snellen acuity targets, or spatial frequencies of 38.5 cycles/degree, were essentially equivalent in the time course of recovery. Both small and large targets showed little recovery during the first two to four minutes post-exposure. After the initial four minutes post-exposure, full recovery required about 15 minutes. Post-exposure contrast threshold 95% confidence limits did not overlap those of baseline in any specific animal until about 6 minutes post-exposure. Statistical significance of post-exposure relative to pre-exposure thresholds for $p<.05$ was obtained during the first 4 to 6 minutes in all animals. Recovery became more variable both within and across animals beyond 6 minutes post-exposure.

Although an immediate and substantial deficit in spatial vision was usually produced, not every exposure produced the same initial loss. The histograms of Figure 3 show the percentages of exposure trials required to produce criterion deficits of 40, 60, or 70 % within the first 2 min post-exposure. Data were taken from three contrast sensitivity animals from all exposures where 38.5, 10.0, and 2.24 cycles/degree were used as test spatial frequencies. A total of 92 exposure sessions are represented.

Most exposure sessions produced a 40% deficit over the first 2 min of exposure regardless of spatial frequency. About 90% of all exposures tabulated produced a deficit >40% for these initial 2 min post-exposure; about 60% of all exposures produced deficits >60%; and, between 35 and 60% produced deficits >70%. In all three categories, the largest spatial frequency was affected at least to the same degree as was the finest spatial frequency. The intermediate spatial frequency seemed somewhat less affected than those at the spatial frequency extremes. When the complete spatial frequency spectrum is plotted, it is evident that intermediate spatial frequencies were somewhat less affected initially and recovered more rapidly than either the largest or the finest spatial frequencies.

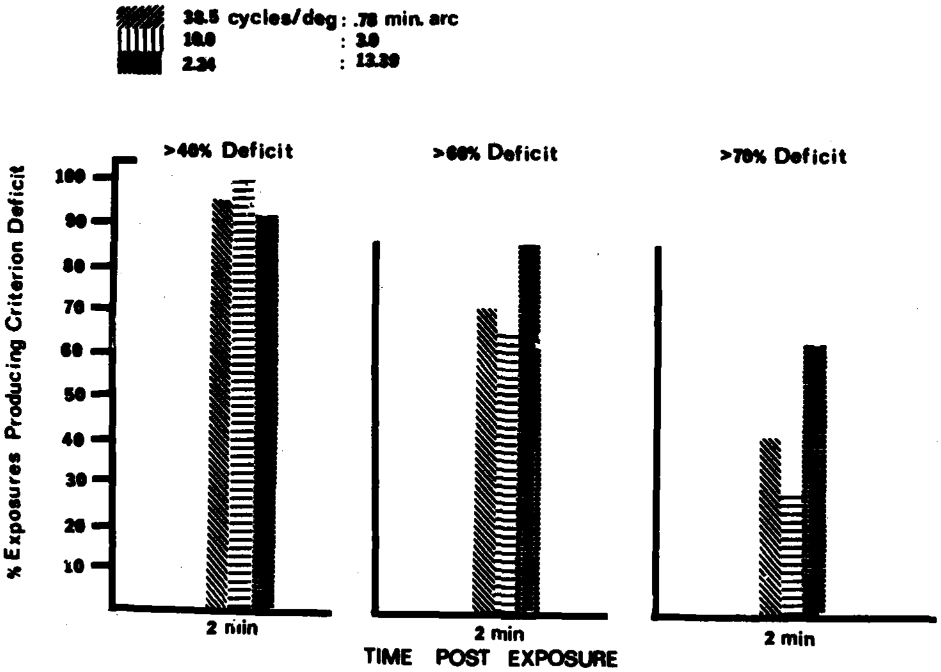

Figure 3. The degree of maximum deficit in contrast sensitivity was not uniform for all exposures. Variability can be seen in the amount of post-exposure change, with less than 50% of the exposures resulting in deficits greater than 70% of baseline levels, while deficits greater than 40% were produced on more than 90% of all exposures. Deficits greater than 60% were produced on 60-80% of the exposures. These data represent a total of 92 exposure sessions across 3 animals.

Several exposure sessions produced deficits in either acuity or contrast sensitivity that lasted more than the duration of the test session, and appeared more selective to the highest spatial frequencies. Such effects, however, were difficult to quantify fully because of their infrequence in the present study. However, recovery from these exposures always occurred with several post-exposure sessions.

Fundus observations of animals examined after the completion of all laser exposure sessions revealed small punctate lesions in the foveal areas including the foveola, the central portion of the fovea. A fundus photograph taken from one of the subjects is shown in Figure 4.

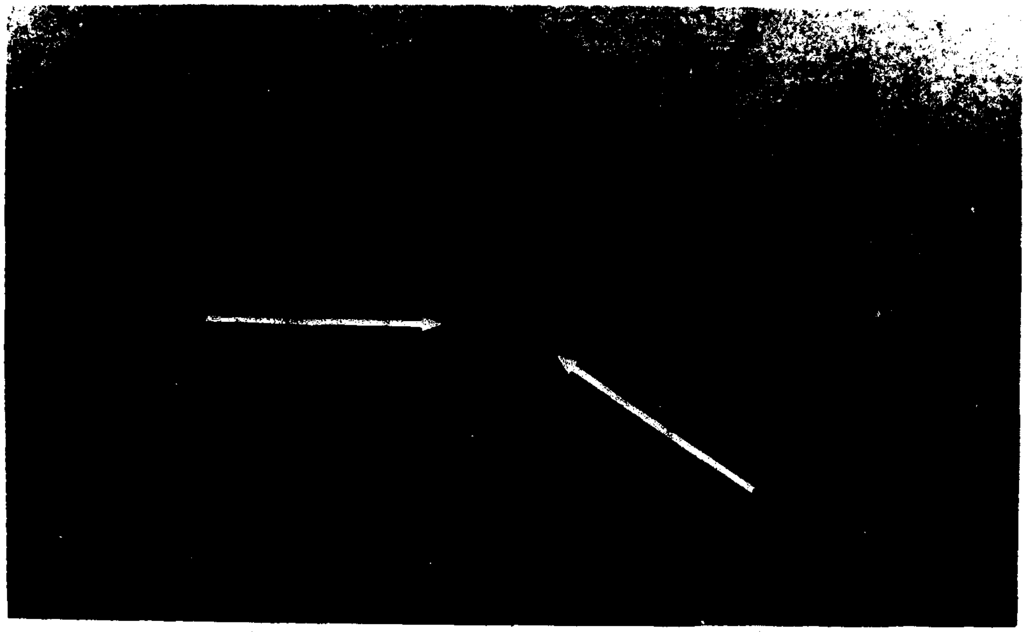

Figure 4. Rhesus fundus showing "punctate" foveal lesions. Arrows indicate the location of the lesions.

DISCUSSION

We have demonstrated that small spot laser flash exposures produce transient changes in high contrast visual acuity and contrast sensitivity These data indicate that effects may involve areas greater than the predicted retinal image diameter of 30 to 50 microns.

Several possible explanations are applicable to these findings. Most exposures in this experiment involved trains of Q-switched pulses. Such exposure conditions in combination with small eye movements may have "painted " a larger effective retinal spot across the fovea than would have been possible with a single pulse alone. In our early experiments, we used a 10 Hz PRF, and distributed six pulses over a 36 second period, 2 pulses per trial. This exposure condition (Figure 2a-lower curve) produced a longer lasting initial deficit than a single burst of six pulses delivered over 300 milliseconds.

As most exposures made were at the ED_{50} for retinal burn criterion, a second factor, local retinal edema, is possible as well. Local edema and its spread to neighboring retinal areas might well have affected parafoveal areas for a short period of time. Such a phenomenon was suggested to explain analogous effects for total foveal damage (4).

Neural retinal interactions are a third element in the explanation of these effects. The visual fields of foveal photoreceptor neural systems (foveal receptive fields) typically are considered to be small, subserving a small number of photoreceptors located within the fovea. While these results do not comment on the size of foveal receptive fields directly, they suggest that foveal receptive fields may overlap parafoveal areas, so that a foveal alteration could affect parafoveal processing of photoreceptor input.

In addition to producing large changes in fine spatial vision, these flashes frequently produced initial delays in the recovery function. Such delays were generally evident during the first 2 to 4 minutes following flash exposure. A similar finding has been reported for longer pulse widths (100 msec) and larger retinal spot sizes (150 to 350 microns) (5). Such delays in recovery after flash increased with exposure power up to permanent acuity losses. Temporary delays in recovery may be reflective of foveal neural "inelasticity" or foveal "blanking" as well as local retinal edematous changes.

Permanent changes lasting more than a single session were not as evident as those obtained in previous work, where large spot-induced foveal damage produced long-term loss in visual acuity that required at least six months for recovery, and longer term residual loss in color vision (4,8). In the present experiment, while portions of the fovea may be damaged, the long term effects are either non-existent or difficult to measure, perhaps requiring more sensitive spectral measurement(4,8). Nevertheless, obvious lesions were produced in and around the fovea. The possibilities that foveal receptive fields are larger or more dynamic than originally conceived (9,10) or normal foveal function can be maintained by the "spared" foveal areas are suggested as explanatory factors.

These results have significant implications for lasers on the modern battlefield. We have shown that minimal spot laser exposure can affect liminal spatial visual function, as well as foveal retinal tissue. Tactically, a compromise in the ability to resolve fine spatial detail in low contrast ground environments may produce an immediate field casualty. Subtle changes in lighting conditions as occur at dawn or dusk, in target reflections and glare, contribute to altering subtle contrast and fine spatial detail required in any complex target acquisition task. Under such conditions, a small induced change in minimal spatial resolution threshold or contrast threshold could result in failure to acquire a critical target. On the other hand , many military scenarios require acquisition of high contrast targets where the requirement for the resolution of fine spatial detail is less stringent. Such situations could be affected to a lesser degree by point source flashes(11), although alteration of retinal foveal tissue is still as likely as in the above military scenario.

We have shown that laser flash exposure can produce significant changes in fine spatial vision and that such effects can be produced with small spot retinal flashes that are likely from highly collimated fielded laser systems. These effects may produce injury to the retina as well as transient loss in fine spatial detail and alteration of normal contrast requirements for optimal target acquisition functions. Such transient effects may, therefore, interfere with mission completion as well as having unknown long term consequences for normal foveal vision. These effects represent a potentially serious Army field hazard regarding both present and near term development of Army laser systems.

In conducting this research, the investigators adhered to the "Guide for Laboratory Animal Facilities and Care", as promulgated by the Committee on the Guide for Laboratory Animal Facilities and Care of the Institute of Laboratory Animal Resources, National Academy of Sciences- National Research Council.

REFERENCES

1. Proceedings of Conference on Combat ocular Problems, Letterman Army Institute of Research, (Beatrice,E.S.) , 1980.

2. Stuck, B.E., Lund, D.J., and Beatrice, E.S.: Another look at the ocular hazards from military lasers. In: Proceedings of the 1981 Annual Scientific Meeting of the Aerospace Medical Association, 1981, 224-225.

3. Gibbons, W.D. and Allen, R.G.: Retinal damage from suprathreshold Q-switch laser exposure. Health Physics. 1978, 35 461-469.

4. Zwick, H. Bedell, R.B. and Bloom K.: Spectral and visual deficits associated with laser irradiation. Mod. Prob. Ophthalmol. 1974, 13, 299-306.

5. Robbins, D.O.,Zwick,H. and Holst, G.C.: A method for producing foveal retinal exposures in an awake, task-oriented rhesus monkey. Behav. Res. Meth. Instr. 1973, 5, 457-461.

6. Bloom K.R. and Zwick, H.: Rhesus spectral acuity for static and moving targets. Presidio of San Francisco, CA.:Letterman Army Institute of Research, 1979, Technical Note No. 79-9TN.

7. Dixon, W.J. and Massey, F.J. : Introduction to statistical analysis. New York: McGraw-Hill, 1957.

8. Robbins,D.O., Zwick,H. and Haenlein,M.: Changes in spectral acuity following laser radiation. In: Proceedings of the Human factors Society. 1980,24,162-166.

9. Kelly, D.H.: Photopic contrast sensitivity without foveal vision. Optics Letters. 1978, 2, 79-81.

10. Zwick,H., Robbins, D.O., and Knepp, A.: Changes in tectal spectral sensitivity and receptive field organization following coherent light exposure. Color Vision Deficiencies 1980, 5,151-156.

11. Callin, G.D., Devine, J.V. and Garcia, P.: Visual compensatory tracking performance after exposure to flashblinding pulses: II Sub-damage threshold laser irradiation of rhesus monkey subjects. SAM-TR-81-7, 1981. Brooks Air Force Base, USAF School of Aerospace Medicine.

*U.S. GOVERNMENT PRINTING OFFICE: 1982--542-006/711

AD-A120 813 PROCEEDINGS OF THE 1982 ARMY SCIENCE CONFERENCE HELD AT 6/6
THE UNITED STATES..(U) DEPUTY CHIEF OF STAFF FOR
RESEARCH DEVELOPMENT AND ACQUISITIO.. 18 JUN 82

UNCLASSIFIED F/G 5/2 NL

END

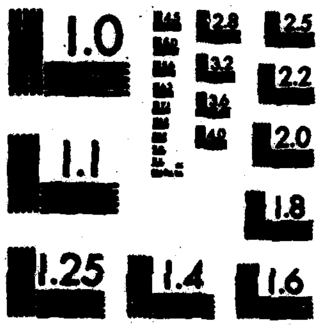

MICROCOPY RESOLUTION TEST CHART
NATIONAL BUREAU OF STANDARDS-1963-A

SUPPLEMENTAR[illegible]

INFORMATION

AD-A120 813

ERRATA

The paper starting on page 107 by Lockwood Reed has the referenced 19 figures missing and they are not available per the author.

DTIC-DDAC
6 May 83